CROCOPY RESOLUTION TEST CHART
NATIONAL BUREAU OF STANDARDS 1963 A

AFGL-TR-85-0322

COCHISE Atmospheric Nitrogen/Oxygen Excitation Studies

W.T. Rawlins
L.G. Piper
A. Gelb
G.E. Caledonia
P.E. Nebolsine
G. Weyl
H.C. Murphy
L.M. Cowles
B.D. Green

Physical Sciences Inc.
Research Park, P.O. Box 3100
Andover, MA   01810

DTIC
SELECTED
SEP 2 3 1986
D

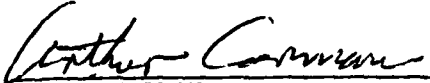December 1985

Final Report
23 March 1982 – 22 March 1985

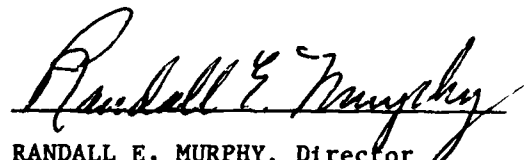APPROVED FOR PUBLIC RELEASE;
DISTRIBUTION UNLIMITED

86   9 23 011

"This technical report has been reviewed and is approved for publication"

ARTHUR CORMAN
Contract Manager

ROBERT R. O'NEIL, Chief
Infrared Dynamics Branch

FOR THE COMMANDER

RANDALL E. MURPHY, Director
Infrared Technology Division

This report has been reviewed by the ESD Public Affairs Office (PA) and is releasable to the National Technical Information Service (NITS).

Qualified requestors may obtain additional copies from the Defense Technical Information Center. All others should apply at the National Technical Information Service.

If your address has changed, or if you wish to be removed from the mailing list, or if the addressee is no longer employed by your organization, please notify AFGL/DAA, Hanscom AFB, MA 01731. This will assist us in maintaining a current mailing list.

REPORT DOCUMENTATION PAGE

1a. REPORT SECURITY CLASSIFICATION	1b. RESTRICTIVE MARKINGS
Unclassified	AD-A172 234

2a. SECURITY CLASSIFICATION AUTHORITY	3. DISTRIBUTION/AVAILABILITY OF REPORT
	Approved for public release; distribution unlimited
2b. DECLASSIFICATION/DOWNGRADING SCHEDULE	

4. PERFORMING ORGANIZATION REPORT NUMBER(S)	5. MONITORING ORGANIZATION REPORT NUMBER(S)
PSI-050/TR-509	AFGL-TR-85-0322

6a. NAME OF PERFORMING ORGANIZATION	6b. OFFICE SYMBOL (If applicable)	7a. NAME OF MONITORING ORGANIZATION
Physical Sciences Inc.		Air Force Geophysics Laboratory

6c. ADDRESS (City, State and ZIP Code)	7b. ADDRESS (City, State and ZIP Code)
Research Park, P.O. Box 3100 Andover, MA 01810	Hanscom Air Force Base Massachusetts 01731

8a. NAME OF FUNDING/SPONSORING ORGANIZATION	8b. OFFICE SYMBOL (If applicable)	9. PROCUREMENT INSTRUMENT IDENTIFICATION NUMBER
		F19628-82-C-0050

8c. ADDRESS (City, State and ZIP Code)	10. SOURCE OF FUNDING NOS.			
	PROGRAM ELEMENT NO.	PROJECT NO.	TASK NO	WORK UNIT NO.
	61102F	2310	G4	AY

11. TITLE (Include Security Classification) COCHISE Atmospheric Nitrogen/Oxygen Excitation Studies

12. PERSONAL AUTHOR(S) W.T. Rawlins, L.G. Piper, A. Gelb, G.E. Caledonia, P.E. Nebolsine, G. Weyl, H.C. Murphy, L.M. Cowles, and B.D. Green

13a. TYPE OF REPORT	13b. TIME COVERED	14. DATE OF REPORT (Yr., Mo., Day)	15. PAGE COUNT
FINAL	FROM 3/23/82 TO 3/22/85	1985 December	564

16. SUPPLEMENTARY NOTATION

17. COSATI CODES			18. SUBJECT TERMS (Continue on reverse if necessary and identify by block number)
FIELD	GROUP	SUB. GR	Infrared emission, Ozone Atmospheric backgrounds
			Oxygen Molecular dynamics
			Nitrogen Vibrational excitation

19. ABSTRACT (Continue on reverse if necessary and identify by block number)

This Final Report describes related COCHISE and FAKIR studies of (1) excited nitrogen reactions which can influence atmospheric molecular emission in the short-to middle-wavelength infrared; and (2) the phenomenology of ozone vibrational fluorescence in the long-wavelength infrared. COCHISE observations of the excitation of NO, CO, N_2O, and electronic states of N_2 by energy transfer in discharge-excited nitrogen are presented, and related FAKIR measurements of the kinetic behavior of metastable N and N_2 are given. Other related FAKIR studies of the products of discharged N_2O are discussed.

20. DISTRIBUTION/AVAILABILITY OF ABSTRACT	21. ABSTRACT SECURITY CLASSIFICATION
UNCLASSIFIED/UNLIMITED ☐ SAME AS RPT. ☐ DTIC USERS ☐	Unclassified

22a. NAME OF RESPONSIBLE INDIVIDUAL	22b. TELEPHONE NUMBER (Include Area Code)	22c. OFFICE SYMBOL
Arthur Corman	(617) 861-3694	AFGL/LSI

DD FORM 1473, 83 APR EDITION OF 1 JAN 73 IS OBSOLETE.

TABLE OF CONTENTS

QUALITY INSPECTED 1

Availability Codes

Dist | Avail and/or Special

A-1

iii

TABLE OF CONTENTS (CONTINUED)

TABLE OF CONTENTS (CONTINUED)

v

LIST OF ILLUSTRATIONS

LIST OF ILLUSTRATIONS (CONTINUED)

x

LIST OF ILLUSTRATIONS (CONTINUED)

xi

LIST OF ILLUSTRATIONS (CONTINUED)

LIST OF TABLES

1. EXECUTIVE SUMMARY

The COCHISE facility, located at the Air Force Geophysics Laboratory, is a cryogenic reactor/spectrometer apparatus designed for the study of upper atmospheric infrared fluorescence phenomena. This complex facility provides a unique capability for the study of the fundamental kinetic paths and product distributions produced by chemical reactions between various excited species, free radicals, and neutral molecules. Such studies, although of basic interest in their own right, prove to be invaluable in the understanding of radiative/energy transfer phenomenology occurring at rarified gas densities such as auroral or nuclear phenomena in the non-equilibrium upper atmosphere.

The COCHISE infrared kinetic and spectroscopic measurements are supported by detailed, state-to-state rate coefficient measurements on the FAKIR flow reactor facility, located at Physical Sciences Inc. This device possesses a wide range of diagnostic capabilities in the vacuum and near ultraviolet, visible, and near infrared, including the highly sensitive techniques of atomic and molecular resonance fluorescence, and has been used to make fundamental measurements in support of the direct infrared observations performed on COCHISE.

This Final Report describes related COCHISE and FAKIR studies of (1) excited nitrogen reactions which can influence atmospheric molecular emission in the short- to middle-wavelength infrared; and (2) the phenomenology of ozone vibrational fluorescence in the long-wavelength infrared. COCHISE observations of the excitation of NO, CO, N_2O, and electronic states of N_2 by energy transfer in discharge-excited nitrogen are presented in Section 2, and related FAKIR measurements of the kinetic behavior of metastable N and N_2 are given in Chapter 3 and Appendix G. Other related FAKIR studies of the products of discharged N_2O are discussed in Appendix C.

COCHISE investigations of the spectroscopy and kinetics of vibrationally excited ozone formed in discharged oxygen are described in Sections 4 and 5. In support of these experimental measurements, we have pursued theoretical

studies of the detailed collision dynamics of ozone formation by three-body recombination, discussed in Section 6 and Appendices E and F, and modeling calculations to describe the physics and chemistry of discharged oxygen-argon mixtures, Section 7. Also as a by-product of the O_3 investigations, we have obtained and analyzed infrared spectra of argon Rydberg transitions, Appendix D. Finally, support of laser-induced breakdown/plasma studies on the LINUS project at AFGL, we engaged in theoretical assessments of the data and the characteristics of the recombining plasma, as given in Appendices A and B.

The investigations reported here are fundamental in nature, and specific results and conclusions are best found in the individual sections. In terms of general and important results, we have gained a vastly improved, highly detailed understanding of ozone excitation phenomena as they occur in the upper atmosphere. This arises from a multi-pronged attack on the problem, including the development of a large data base on COCHISE and the interpretation of that data base as assisted by kinetic modeling and theoretical collision dynamic computations. In related work, we have applied this knowledge to the interpretation of high altitude ozone fluorescence data with success. Furthermore, we have pursued and identified several relevant infrared fluorescence excitation processes involving excited forms of atomic and molecular nitrogen which are likely to be important in the electron disturbed upper atmosphere. Much of what we report here constitutes preliminary scoping work, and more detailed studies are continuing. These studies have resulted in numerous Air Force technical reports, journal articles, and conference presentations, as referenced herein, and have led to a new level of sophistication in our view of high-altitude energy deposition.

2. SWIR/MWIR EFFECTS OF METASTABLE NITROGEN

2.1 Introduction

Recent experimental investigations on the COCHISE facility have been focussed upon the kinetics and spectroscopy of potential auroral radiators in the short-wavelength (SWIR, 2-4 μm) and middle-wavelength (MWIR, 4-8 μm) infrared spectral regions. The band systems being investigated include the NO fundamental and overtone bands near 5.4 and 2.7 μm, respectively, the CO fundamental band near 4.7 μm, and numerous electronic bands of N_2 between 2 and 6 μm. The NO and CO features are excited by interactions of O_2 and CO with the effluents of Ar/N_2 discharges, and the N_2 features may reflect the nature of energy-carrying metastables which are formed in such discharges. Consequently, conclusive studies of the excitation kinetics for these features requires parametric investigations as functions of N_2/Ar flow conditions through the discharges. We report here the results of preliminary scoping experiments, and their implications for future measurements.

In addition, we have carried out a series of measurements to assess the potential for the formation of vibraluminescent N_2O in a chemical reaction between N_2 and vibrationally excited $O_3(v)$, and from discharged $N_2/O_2/Ar$ mixtures. We will discuss the experimental data and a preliminary analysis of the results, and will examine the potential of further experimentation along these lines.

2.2 Experimental Methods

All the experiments are performed in the standard COCHISE configuration using balanced mass flow rates of discharged and counterflow gas at $\sim$ 0.1 g s^{-1}. Ar is used as the diluent for the discharge gas mixture with 1-10% levels of N_2 or O_2. Typical discharge conditions are 1.3 torr, 80-100 K, 50 W. The effluents of the microwave discharges interact in the low pressure ($\sim$ 4 mtorr) reaction zone with counterflows of O_2, Ar, N_2, or mixtures of Ar and CO. The

choices of discharge and counterflow constituents are dictated by the specific excitation process being investigated.

Infrared emission from the interaction zone is observed by the scanning monochromator with a typical spectral resolution of ~ 0.013 μm in first order (1 mm slits, 3 μm grating, 150 lines/mm, 0.5 m focal length). Order-sorting filters with cut-ons near 2 and 4 μm are used to isolate the 2-4 and 4-8 μm spectral regions. Spectral responsivities are determined by calibration with a 350-400 K blackbody and are in the range 2-5 $\times$ 10^5 V/(W cm^{-2} sr^{-1} μm^{-1}) between 2 and 8 μm.

2.3 Results and Discussion

The experiments to be discussed here address three different research topics which are somewhat interrelated: (1) fluorescence from NO(v) in the reaction of discharged N_2/Ar mixtures with O_2, and the accompanying emission from electronic states of N_2 excited in the discharges; (2) fluorescence from CO(v) excited by energy transfer from discharged Ar/N_2 mixtures, and the concomitant emission from hitherto unidentified species; and (3) emissions observed near 4-5 μm in the interaction of N_2 with discharged O_2/Ar mixtures. We discuss below the results of preliminary scoping experiments and data analysis performed to date, as well as the definition of more detailed test matrices for further investigations of each topic.

2.3.1 Fluorescence from NO and N_2

Previous COCHISE studies, done prior to refurbishment of the apparatus, have addressed the kinetics and spectroscopy of vibraluminescence from the fundamental and overtone[2,3] bands of NO(v) produced in the interaction between discharged N_2/Ar mixtures and O_2. By a series of kinetic arguments, it was concluded that the reaction responsible for the observed emission is[1]

$$N(^2D, \, ^2P) + O_2 \rightarrow NO(v) + O \, . \tag{1}$$

In an attempt to measure the vibrational-state-dependent relative transition probabilities of the overtone and fundamental bands,[2] we observed, in a very limited data base, values similar to those predicted by the theory of Billingsley[4] over the range $4 < v' < 12$. This result is similar to that obtained in LABCEDE[5] for $3 < v' < 7$. However, the COCHISE results reported in Ref. 2 were seriously affected by interference from neighboring emission bands; we have previously identified[3] some of these bands as features of the $W^3\Delta \to B^3\pi$ system of N_2 (also known as the Wu-Benesch system). A conclusive delineation of the relative transition probabilities for levels $2 < v' < 13$ is needed for prediction of NO radiation levels at 2.7 μm in auroral events.

The improved flexibility and sensitivity of COCHISE allows us to revisit this problem to obtain conclusive results. Our approach employs: (1) improved spectral resolution (1 mm slits as opposed to 1.5-2.0 mm as used earlier) in order to distinguish and identify the interfering radiators; (2) the use of reactive (O_2) and non-reactive (Ar, N_2) counterflows to aid in correcting the NO spectra for contributions from underlying radiators and from NO(v) formed from impurities in the discharges; and (3) a parametric study over at least an order of magnitude variation in N_2 mole fraction in the discharge gas, to aid in identifying the background radiators and to provide supporting kinetic data on the NO precursors, i.e., to distinguish between $N(^2D)$, $N(^2P)$, and excited states of N_2.

2.3.1.1 NO Fundamental Band

Spectra obtained for the highest and lowest N_2 flows, with O_2 and Ar counterflows, are shown in Figs. 1 to 4. The band between 5.25 and 7.0 μm is predominantly fluorescence from NO ($1 < v' < 14$) produced from Reaction (1). Preliminary least squares analysis of the spectral distribution of Fig. 1 gives relative vibrational populations which are consistent with those reported by Ref. 1; however, Figs. 3 and 4 show that there is a small but significant contribution from NO(v) formed in the discharge by impurities. We have since taken steps to reduce leakage of air into the discharge mixture,

INTENSITY, 10^{-8} W CM-2 SR-1 μM-1

WAVELENGTH, μM
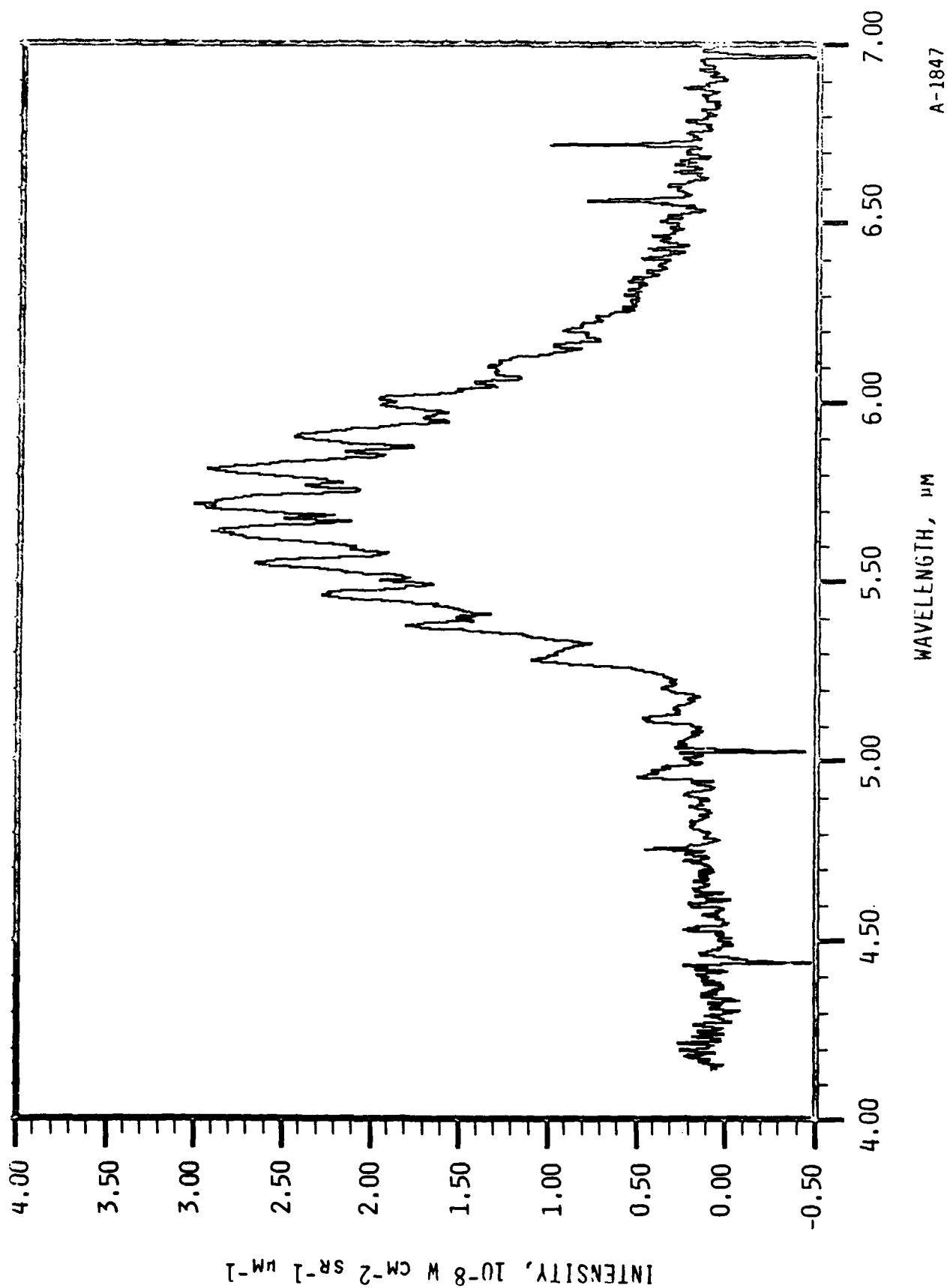
Figure 1. NO fundamental band, 12.1% N_2 in N_2/Ar discharge 100% O_2 counterflow.

A-1847

2-4
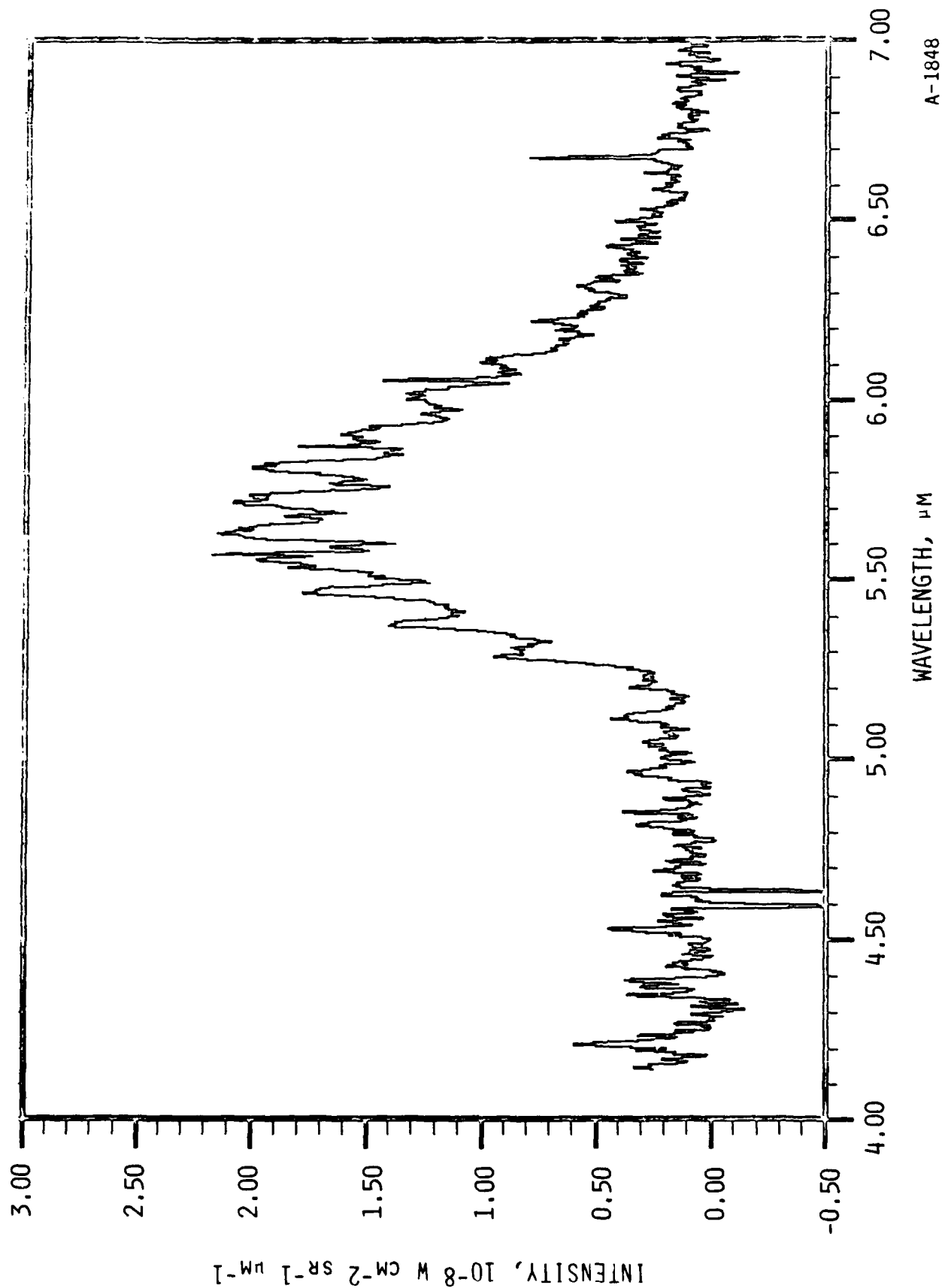
Figure 2. NO fundamental band, 1.04% N_2 in N_2/Ar discharge, 100% O_2 counterflow.

A-1848

WAVELENGTH, μM

INTENSITY, 10^{-8} W CM^{-2} SR^{-1} μM^{-1}
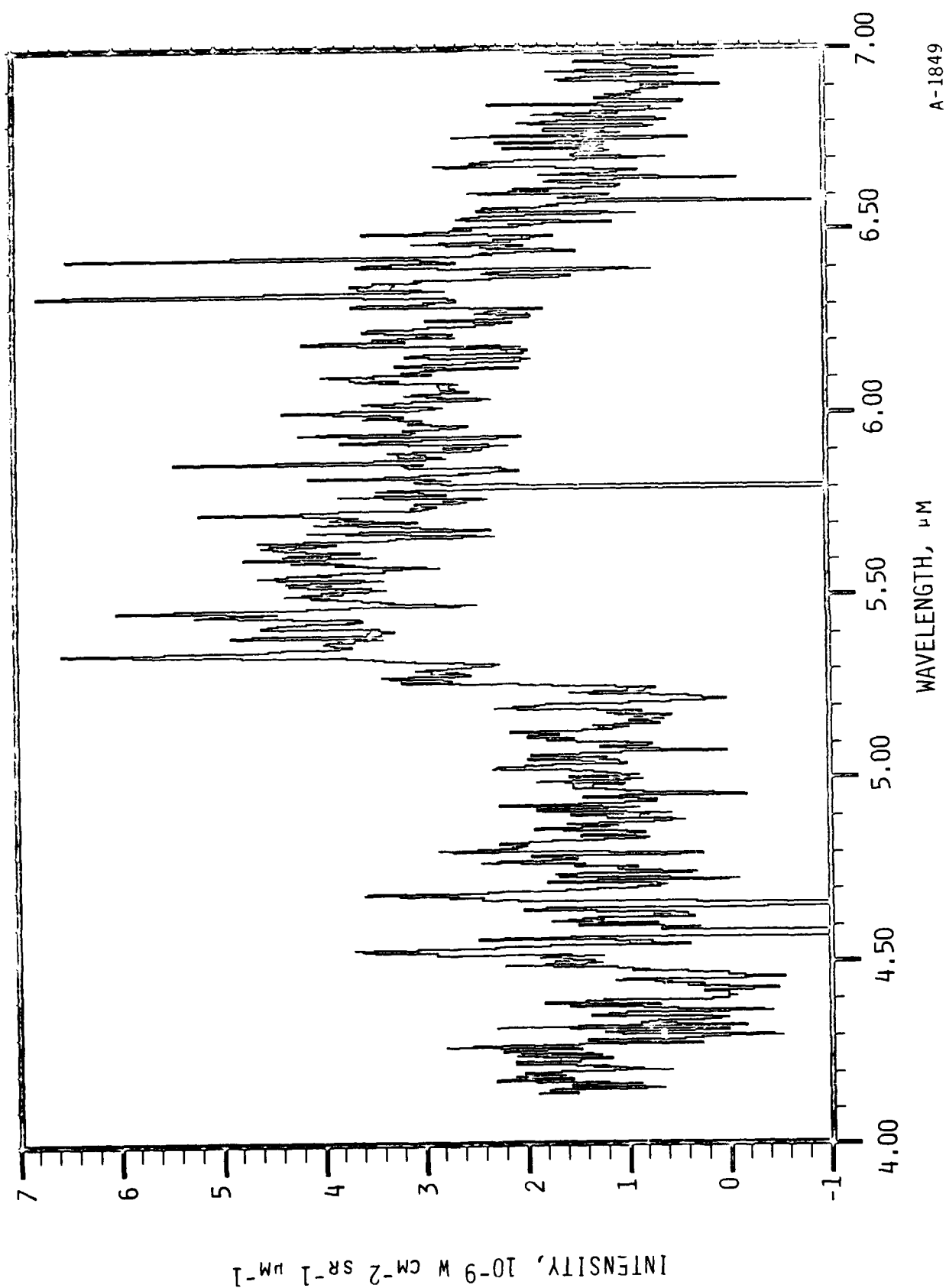
Figure 3. NO fundamental band, 12.1% N_2 in N_2/Ar discharge, 100% Ar counterflow.

A-1849

WAVELENGTH, μM

INTENSITY, 10^{-9} W CM-2 SR-1 μM-1
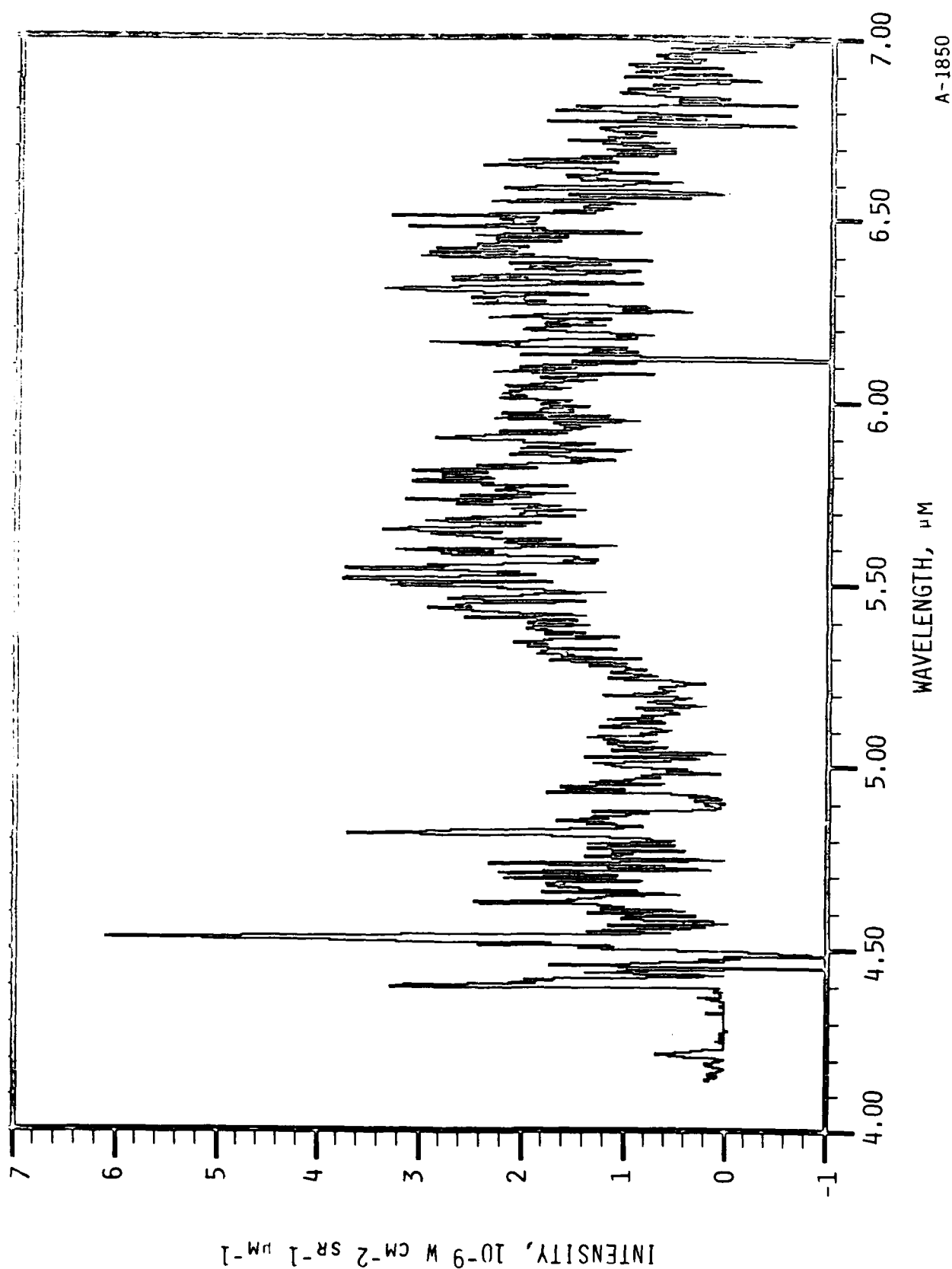
Figure 4. NO fundamental band, 1.04% N_2 in N_2/Ar discharge, 100% Ar counterflow.

A-1850

2-7

and future analysis will employ subtraction of each observed background spectrum prior to spectral fitting.

Comparison of the intensities in Figs. 1 and 2 shows that the NO(v) fluorescence intensity decreases by only about 20-30% when the N_2 flow rate admitted to the discharge is decreased by a factor of 13.7. This indicates that the discharge-produced precursor of NO(v) is a species whose yield from the discharge is insensitive to N_2 number density. This is characteristic of the atomic metastables, $N(^2D, \ ^2P)$, but not of excited molecular species, which show pronounced "quenching" at higher N_2 levels.[6] It remains to be seen whether contributions from $N(^2D)$ and $N(^2P)$ can be separated by this approach; detailed characterization of metastable yields from similar discharges is in progress on the FAKIR apparatus. The spectral distributions in Figs. 1 and 2 exhibit only minor variations; more data are required to establish a statistical basis for these differences. At present, there is no indication for more than one excitation mechanism, in accord with the conclusions of Ref. 1.

The results of Ref. 1 for v' = 1 were compromised by weak, overlapping contributions from an unidentified radiator near 5.2 μm. In our present work, we are attempting to isolate and identify these bands and to correct the NO data for their presence. The interfering radiation appears in Figs. 1 through 4 as a group of features between 4.9 and 5.3 μm. Othe rfeatures near 4.2, 4.5, and 4.8 μm are also observed and exhibit kinetic behavior similar to that of the 5 μm group. These features do not appear to be related to Ar Rydberg emission observed in the absence of added N_2.[7] It is especially interesting to note that (1) the band intensities depend upon N_2 flow in much the same way as the NO emission intensity, and (2) the 5 μm band intensity is considerably greater in an O_2 counterflow than in the Ar "blank" case. This indicates that the appearance of this feature may be related somehow to the interaction with O_2 rather than to a discharge-produced radiator. We suggest three possibilities. First, the emission could arise from electronic transitions of electronically excited O_2 formed by energy transfer *from* discharge-excited N_2 metastables. However, this does not seem likely, since the electronic states of O_2 have long radiative lifetimes (there are no dipole-allowed transitions

in O_2) which probably preclude their observation under the conditions of these experiments. Second, the emission could be due to electronic transitions of NO, which is first formed by Reaction (1) and then excited by energy transfer from discharge-produced N_2 metastables. We have not yet explored this possibility, and it will probably prove rather laborious to examine all the possible infrared transitions of NO. However, this type of sequential excitation process is discriminated against by the near-single-collision conditions attained in the COCHISE reaction cell.

Third, the emission may arise from electronically excited states of N_2 which are populated in deactivation of higher-lying states of N_2 by O_2. Following this approach, we have examined a few of the more likely band systems of N_2, namely $B^3\pi \rightarrow A^3\Sigma$, $W^3\Delta \rightarrow B^3\pi$, and $B^3\pi \rightarrow W^3\Delta$ (clearly, several other systems should also be considered). Our approach has utilized a spectral simulation code recently developed at PSI. This code computes detailed electronic spectra in any desired wavelength region, given spectroscopic data for the upper and lower electronic manifolds. Of the N_2 bands tested to date, the $\Delta v = 1$ transitions of the B $\rightarrow$ W system lie at roughly the same wavelengths as the observed radiation. A computed spectrum is shown in Fig. 5; the computations use the experimental resolution of 0.013 μm, unit relative vibrational populations in the upper electronic state, and a rotational temperature of 80 K. The correspondence between computed and observed transitions in encouraging. In particular, the $(v', v'') = (3,2)$ band corresponds well to the observed 4.8-5 μm group, and the (2,1) band overlaps with the short-wavelength edge of the NO fundamental band. Unfortunately, the corresponding $\Delta v = 2$ transitions of B $\rightarrow$ W between 2.4 and 3 μm cannot be identified as they are largely obscured by the NO overtone and W $\rightarrow$ B emission (see Section 2.3.1.2).

Clearly, the present data are too noisy and too limited in scope to allow conclusive identification of the interfering bands near 5 μm. However, such identification is essential, as their contributions to the apparent NO(low v') populations cannot be obtained directly from the background spectra. We hope to improve the COCHISE data base for those bands by making more systematic spectral scans, possibly at lower resolution to improve the S/N, and by more carefully examining the dependence of their intensities upon N_2 and O_2 levels.
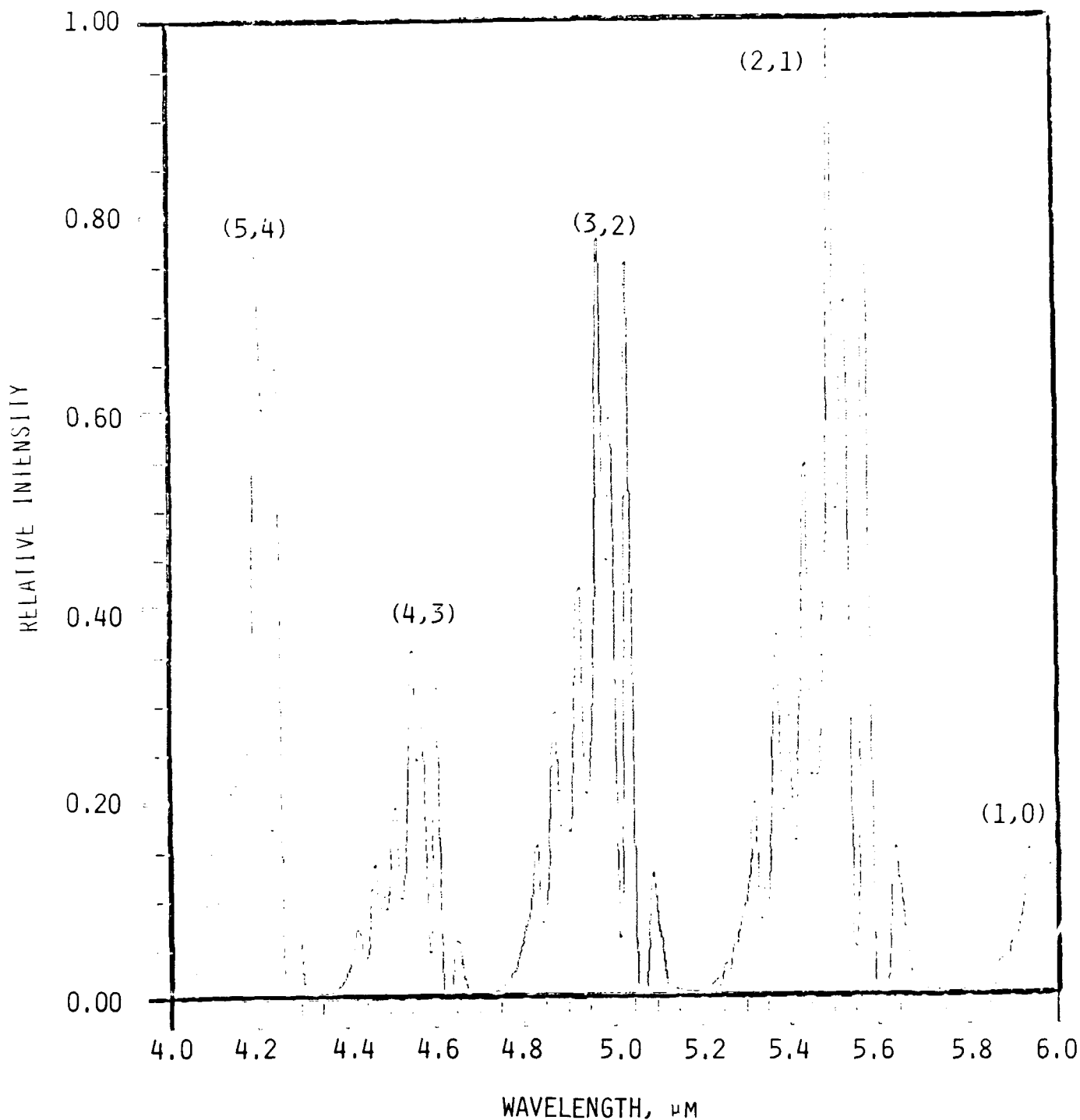
Figure 5. Computed bandshapes for $N_2(B^3\pi \rightarrow W^3\Delta)$ transitions near 5 μm. The computations used a temperature of 80 K, resolution of 0.013 μm, and unit upper state populations. Values of (v', v") are indicated for each band.

A-1851

2.3.1.2 NO Overtone Band (N_2^* Spectroscopy)

Spectra obtained for the highest and lowest N_2 flow rates, with O_2 and Ar counterflows, are shown in Figs. 6 to 9. The fluorescence from NO extends from 2.65 μm to about 3.4 μm, but the portion beyond 3.2 μm is obscured by the (2,0) band of the $W^3\Delta - B^3\pi$ (Wu-Benesch) transition of N_2 (see below). Indeed, the most striking observation in Figs. 6 to 9 is the overwhelming presence of numerous spectral features both in and out of the bandpass of the NO radiation. At low N_2 flow rates, the "background" features are stronger and the NO emission is weaker to the point that analysis of the NO spectral distribution is seriously compromised. In our future observations of NO($\Delta v = 2$) fluorescence, we will use high N_2 levels in the discharge to minimize the interfering emissions, and we will correct for these features by subtracting out the background spectra.

The emission features observed between 2 and 4 μm appear to be primarily due to electronic transitions from high-lying states of N_2 which are excited in the discharge and survive the traversal into the field of view. The band intensities increase substantially when the N_2 mole fraction is decreased, suggesting discharge-related kinetic effects. Furthermore, the intensities decrease by a factor of ~ 2 when the counterflow gas is turned off, meaning that the radiation arises from discharge-excited species which survive to reach the field of view rather than from scattered light or species excited within the field of view. Finally, the intensities of most of the features are only weakly affected by switching from Ar to O_2 counterflow, so the counterflow interaction has only a small effect on the excited state distributions.

The transitions observed here do <u>not</u> correspond to any known Rydberg transitions of Ar[7] or N[8], and therefore appear to be electronic bands of N_2. While it is important to understand and remove the interference of these bands with the NO overtone band for the present experiments, these N_2 bands are worthy of study in their own right owing to the potential for their excitation in the electron-disturbed upper atmosphere. These emissions could not only
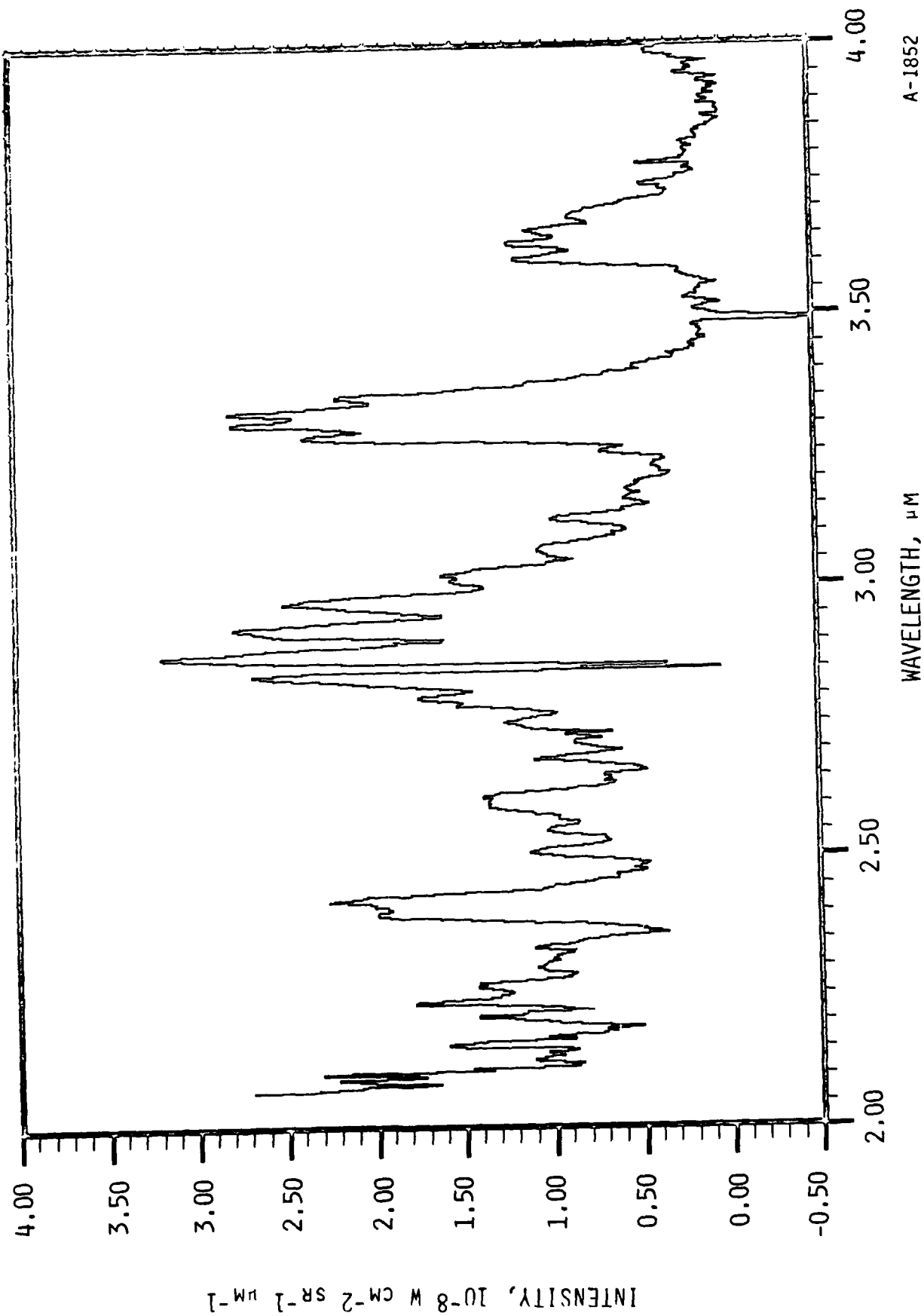
Figure 6. NO overtone region, 12% N_2 in N_2/Ar discharge, 100% O_2 counterflow.

A-1852

INTENSITY, 10^{-8} W CM^{-2} SR^{-1} μM^{-1}

WAVELENGTH, μM
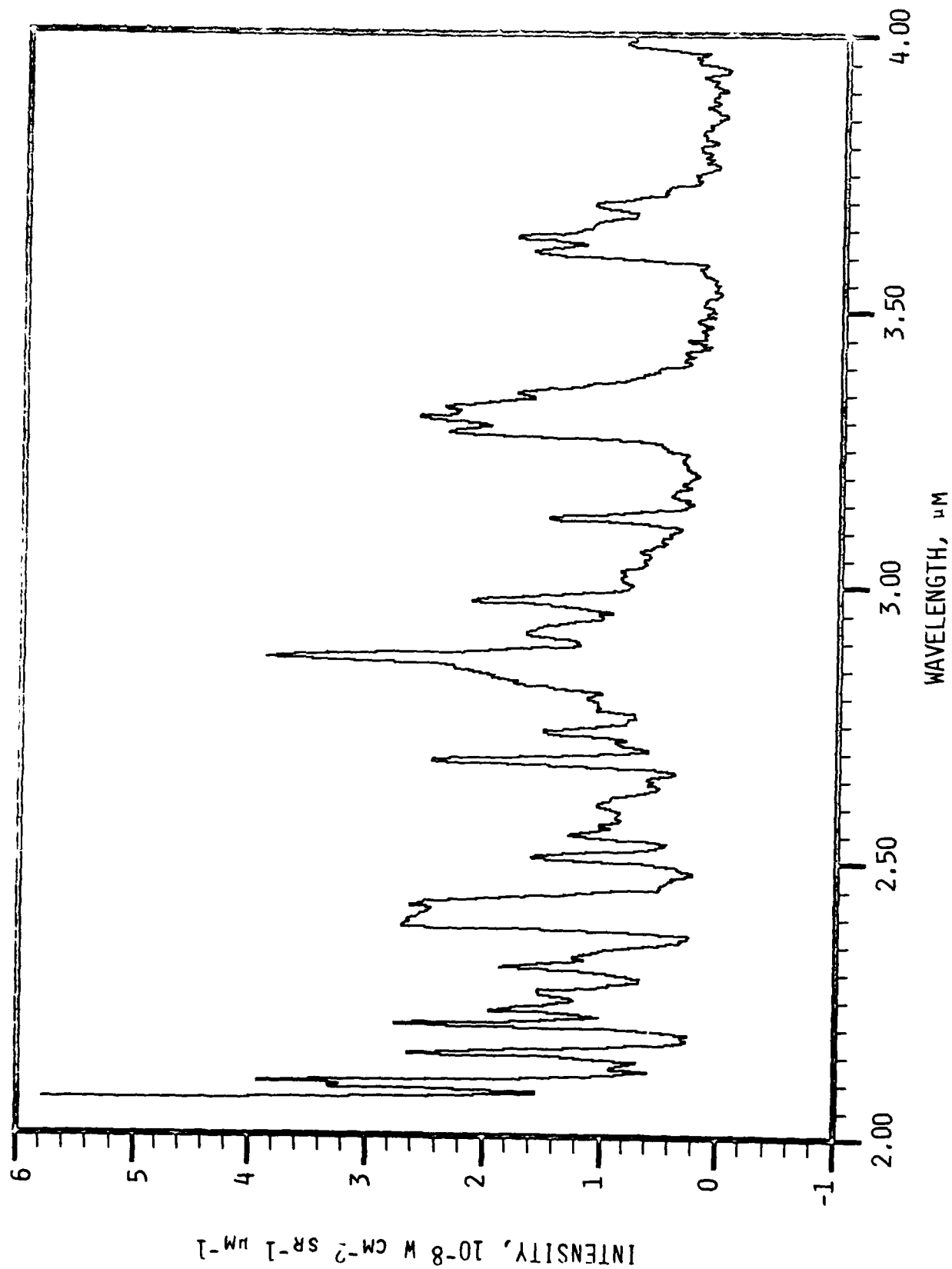
Figure 7. NO overtone region, 1% N_2 In N_2/Ar discharge, 100% O_2 counterflow.

A-1853
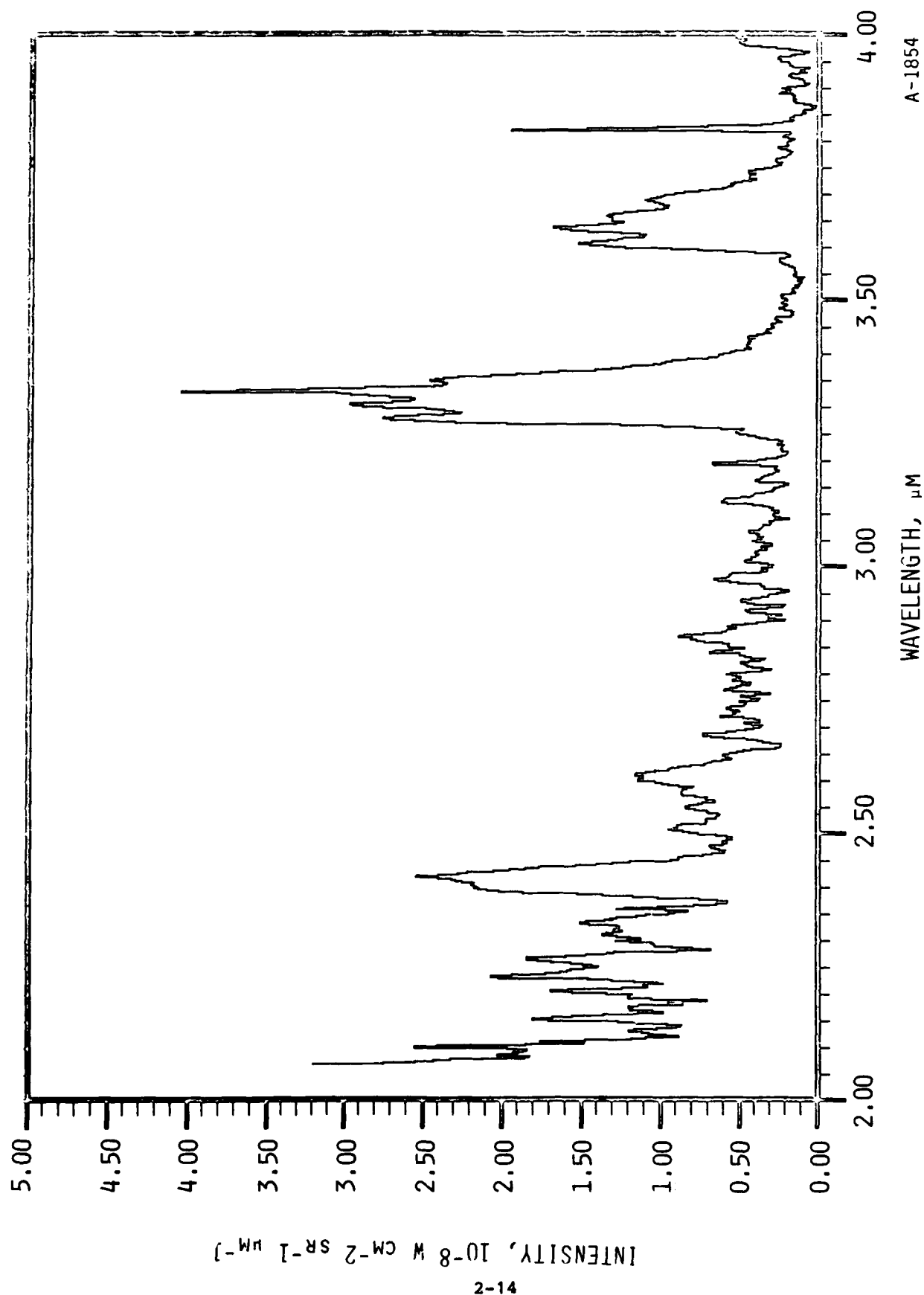
Figure 8. NO overtone region, 12% N_2 in N_2/Ar discharge, 100% Ar counterflow.

A-1854
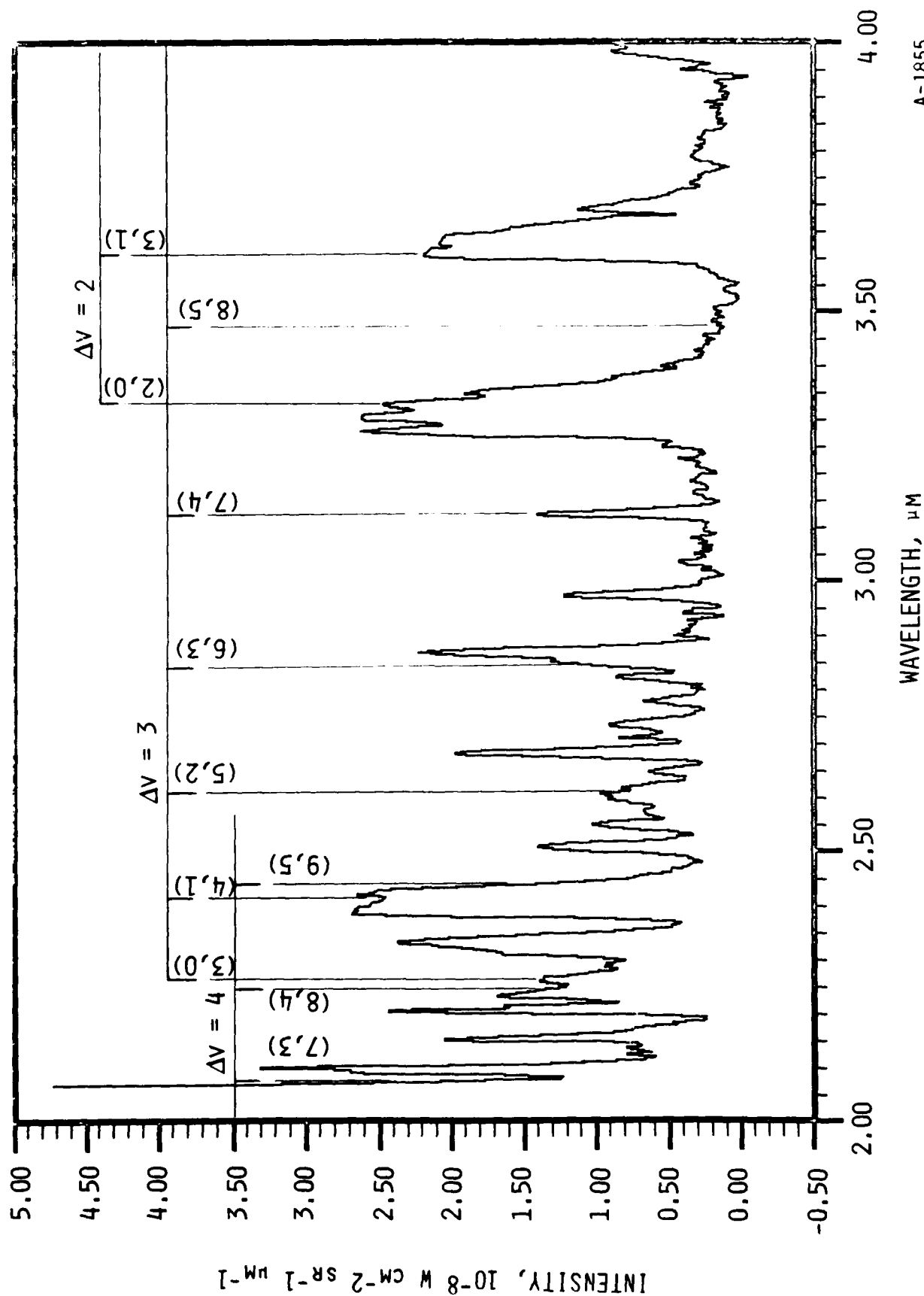
Figure 9. NO overtone region, 1% N_2 in N_2/Ar discharge, 100% Ar counterflow. Band centers for N_2 $W(^3\Delta) + B(^3\pi)$ (Wu–Benesch) transitions are indicated.

A-1855

affect high-altitude sensors, but may also serve as diagnostics for highly energetic forms of N_2 formed in auroras. Part of the energy carried by these metastable species will ultimately degrade to IR radiation through chemical reaction and energy transfer processes. For this reason, we have examined the spectra of Figs. 6 to 9 to determine the feasibility of utilizing COCHISE to investigate the spectroscopy and kinetics of discharge-produced excited nitrogen, N_2^*. While the spectral analysis is far from complete, we are able to assign many of the features and to infer the identities of several others. Further investigations will be aided by an improved data base under conditions similar to those in Fig. 9, with higher spectral resolution where possible, and with a spectral simulation/fitting analytical procedure. We summarize here the results of our first-pass inspection of the data.

The most prominent features of the spectrum are the $\Delta v = 2$ and $\Delta v = 3$ sequences of the $W^3\Delta - B^3\pi$ (Wu-Benesch) system; we have identified these bands in previous COCHISE SWIR spectra.[3] A computed spectrum of the $W \rightarrow B$ transitions, assuming unit relative vibrational state populations in the upper electronic state, is shown in Fig. 10. The (2,0), (3,1), and (4,2) bands are readily identifiable between 3.3 and 4 μm. Furthermore, the observed relative intensities suggest similar populations in the $v' = 2$, 3, 4 levels of the W state for the low N_2 case. In the $\Delta v = 3$ sequence between 2 and 3 μm, the transitions are somewhat less prominent, but the (3,0), (4,1), and (5,2) transitions can be identified. However, the intensity distributions in this sequence compared to those with the same v' in the $\Delta v = 2$ sequence are not in accord with the computed spectra, perhaps due to uncertainties in the computed transition probabilities or, more likely, to an artifact of the blackbody calibration at short wavelengths. We will attempt to verify the blackbody calibration in future experiments, and will consider implementing a hotter blackbody to facilitate calibration below 2.5 μm (see next section). The (6,3) transition is more difficult to identify, as the 2.8 μm feature peaks at slightly longer wavlength. The feature near 3.1 μm corresponds well to the expected wavelength of the (7,4) transition, but its intensity in the low N_2 case is surprisingly large relative to those for lower v'. The (8,5) transition near 3.5 μm is not evident. Many of the other features in the 2-3 μm
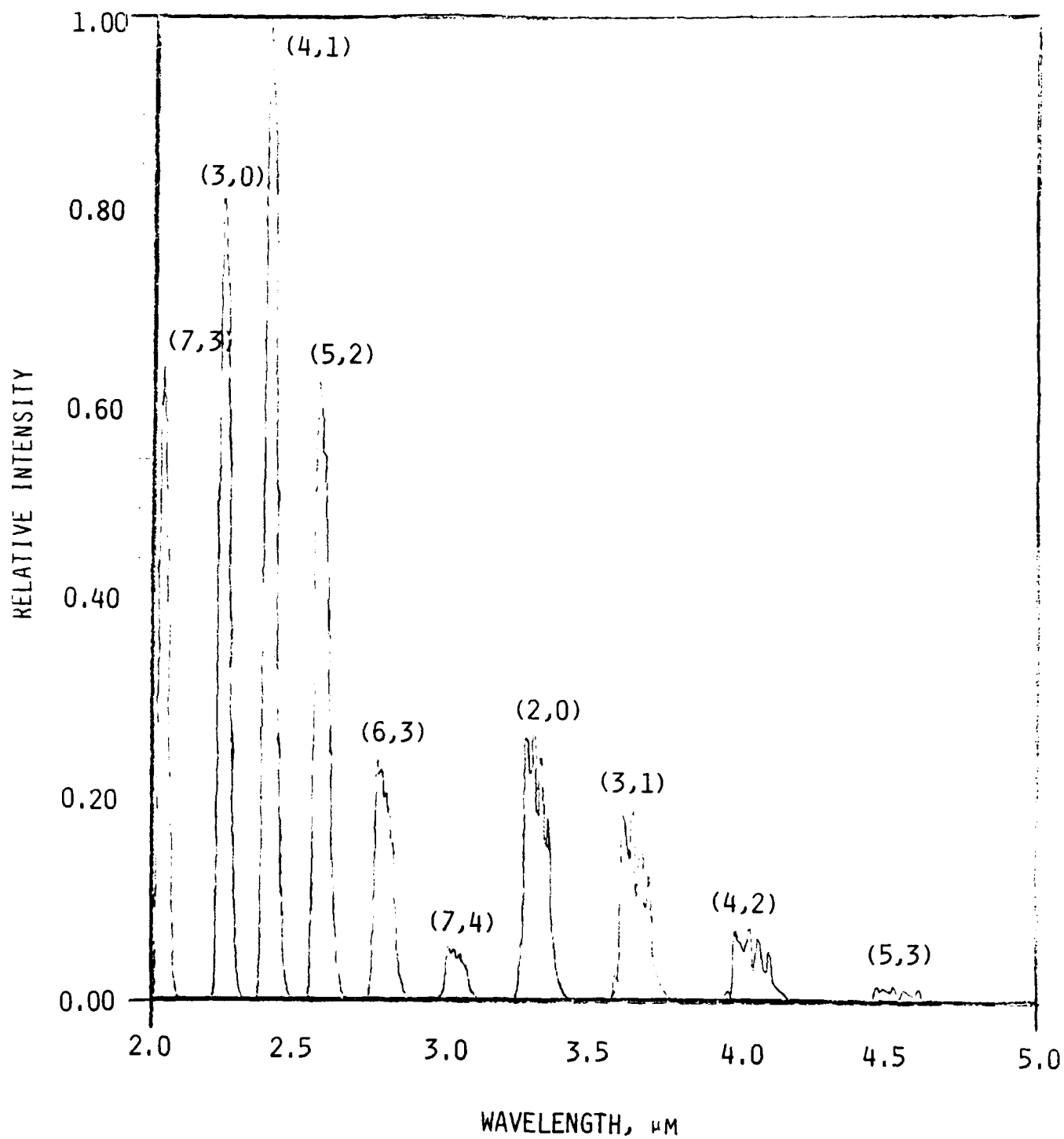
Figure 10. Computed band shapes for N_2 $W^3\Delta \rightarrow B^3\pi$ transitions, assuming $T = 80$ K, $\delta\lambda = 0.013$ μm, and unit populations of the upper state.

A-1856

region correspond well to expected wavelengths for transitions of the $B^3\pi$ - $A^3\Sigma$ systems: (7,13), (1,5), and (4,9) near 2.2 μm; (6,12), (0,4), and (3,8) near 2.4 μm and (5,11) near 2.7 μm. The highest excited levels observed correspond to energies of $\sim$ 8.5 eV in the discharge-excited products. The states observed have radiative lifetimes of typically several hundred μs, i.e., similar to the sum of the $\sim$ 500 μs cell transit time and the $\sim$ 300 μs residence time in the field of view. We emphasize that many of these assignments are extremely tentative and cannot be made conclusively without a detailed band-shape analysis (i.e., spectral fitting) and a more consistent data base.

Many prominent transitions cannot yet be identified even tentatively, but may arise from the long-postulated $A^3\Sigma$ - $B^3\pi$ system or from electronic transitions in the singlet manifold of N_2. For example, the strong feature near 3 μm corresponds well to the (10,0) transition of the A-B system. Complete analysis of these types of spectra under various discharge and counterflow conditions would provide valuable spectroscopic data on relative transition probabilities, N_2* excitation and energy transfer mechanisms, and vibrational and electronic redistribution processes within the B, W, and vibrationally excited A states. This information is closely related to recent observations in FAKIR of energy transfer in discharge-excited N_2/Ar mixtures.[6] Further analysis of the present data base will continue, but more definitive experiments will be conducted in the near future.

2.3.1.3 NO Overtone/Fundamental Ratio.

We have performed a first-pass least squares fitting analysis of a matched pair of NO overtone and fundamental spectra obtained at high N_2 flow. The spectra were not corrected for background radiation, nor were the computed fits optimized for rotational temperature. The results are consistent with those obtained previously,[2] namely that the Einstein coefficient ratios for each v' agree with the Billingsley[4] theory for v' > 4 but deviate significantly at lower v'. This deviation is in the direction of too much apparent radiation in the overtone band at low v', and is at least partially an artifact due to the background radiation near 2.7 μm. We are developing

background correction techniques before pursuing the spectral fitting any further. Also, we have obtained a more substantial data base of matched pairs of NO spectra at high N_2 flows to establish a good statistical base.

A crucially important consideration in these measurements is the accuracy of the blackbody calibration at short wavelengths. This is especially important in comparing radiation measurements at 5.4 and 2.7 μm, since the maximum blackbody temperature we can use is only 400 K. At this temperature, the short-wavelength range of the apparatus is well into the steep portion of the blackbody radiation curve; the spectral radiance of the blackbody drops by a factor of $\sim$ 250 in going from 4 μm down to 2 μm, presenting difficulties in accurately defining the system responsivity below 2.5 μm. Furthermore, the calibration in this wavelength range will be much more sensitive to uncertainties in the blackbody temperature. The blackbody spectral radiance in W cm^{-2} sr^{-1} μm^{-1} is given by:

$$N_\lambda = \frac{11909}{\lambda^5} \left(e^{14388/\lambda T} - 1 \right)^{-1} \tag{2}$$

where λ is in μm. For cold blackbodies at short wavelengths, i.e., for $\lambda T < 3 \times 10^3$, Eq. (2) reduces to

$$N_\lambda = \frac{11909}{\lambda^5} e^{-14388/\lambda T} . \tag{3}$$

Then

$$\frac{dN_\lambda}{dT} = N_\lambda \frac{14388}{\lambda T^2} \tag{4}$$

and

$$\frac{\delta N_\lambda}{N_\lambda} = \frac{14388}{\lambda T} \frac{\delta T}{T} .$$

(5)

We see from Eq. (5) that, for a 400 K blackbody source, the uncertainty in the absolute calibration is 18 $\delta T/T$ at 2 μm and 7.2 $\delta T/T$ and 5 μm. The relative uncertainty in <u>ratio</u> measurements for these two wavelengths would then be the square root of the sum of the squares or 19.4 $\delta T/T$. Thus, it is necessary to determine $\delta T/T$ in order to confirm the accuracy of the ratio measurements.

Values of $\delta T/T$ can be inferred from ratios of blackbody measurements at two different temperatures. The observed signal in volts is

$$S = F(\lambda)N_\lambda$$

(6)

where $F(\lambda)$ is the spectral responsivity of the optical system. At a given wavelength and two temperatures $T_1 < T_2$,

$$\frac{S_2}{S_1} = \frac{e^{-14388/\lambda T_2}}{e^{-14388/\lambda T_1}} = e^{\frac{14388}{\lambda}\left(\frac{1}{T_1} - \frac{1}{T_2}\right)}$$

(7)

Then

$$\ell n \, S_2/S_1 = \frac{14388}{\lambda} \frac{T_2 - T_1}{T_1 T_2} .$$

(8)

So plots of $\ell n \, S_2/S_1$ vs. $14388/\lambda$ for blackbody scans at different nominal temperatures, say 400 and 350 K, will have slopes $(T_2-T_1)/T_1 T_2$. The deviation of the observed slope from the expected one should allow an assessment of the uncertainty in T. A more detailed approach could also be employed, plotting $1/S\lambda^5$ vs. $1/T$ for several different wavelengths to obtain slopes $14388/\lambda$ as

2-20

described in Ref. 2. However, this would require about ten blackbody scans at various temperatures, and may not be necessary if implementation of Eq. (8) provides sufficient confirmation of the calibrations.

One possible option in dealing with the 2-2.5 μm calibration problem is to implement a higher-temperature blackbody source. A commercial source capable of 800 K has been used in the past in COCHISE, but was very expensive and presented severe problems in the determination of its actual radiometric temperature.[2] This probably occurred because the epoxy attaching the thermocouple to the cavity failed at cryogenic temperatures. Conversely, the low-temperature epoxy on the present source is susceptible to failure near or above 200 F(366 K). Thus, it is not clear whether there is an easy solution to the problem. The major advantage in raising the blackbody temperature from 400 to 800 K lies in the 4-order-of-magnitude increase in intensity at 2 μm rather than in the factor-of-two decrease in sensitivity to temperature uncertainties (cf. Eq. (5)). Increasing the intensity near 2 μm is important for defining the system responsivity near the short-wavelength cutoffs of both the 2 μm long-pass filter and the Ge optical components. However, it may be possible to achieve a satisfactory solution at 400 K merely by making some measurements at the largest possible slit width, i.e., 3 mm as opposed to the usual 1 mm setting employed in calibration measurements. This will enhance the signal by a factor of 9. We will address these calibration questions in a series of COCHISE measurements in the near future.

2.3.2 Interaction of N_2* with CO

The excitation of CO(v) by energy transfer from discharged N_2 has been observed for several years in COCHISE,[9] but a definitive study has not been performed. The interaction has been used routinely to provide a wavelength calibration via the band center of the CO(1→0) transition at 2143 cm^{-1}. However, as we shall see below, the interaction is extremely complicated, and a meaningful study must explore a large parameter space.

In the wavelength calibration measurements, fluorescence between 4.5 and 5.2 μm from vibrationally excited CO is observed in the reaction zone upon the interaction of discharged Ar/N_2 mixtures with counterflow mixtures of CO diluted in O_2, N_2 or Ar. Presumably, the $v' = 1$ level of CO is readily excited by rapid V-V transfer from $N_2(v)$ produced in the discharge, but the presence of higher-v' fluorescence at longer wavelengths has not been explained. In an earlier discussion,[9] multi-quantum V-V transfer from $N_2(v)$ to CO was suggested as a source of the higher levels of CO. Multi-step sequences of V-V "pumping" of $CO(v' = 1)$ by itself or $N_2(v)$ have not yet been ruled out, but are unlikely in the near-single-collision conditions of COCHISE. Also, in the early work of Ref. 9, a single spurious spectral scan showed the presence of an unusual spectral signature which was then suggested to be due to vibrationally excited CN. We are now able to reproduce this observation under controlled conditions, at higher resolution, and with better wavelength accuracy, and have found that the original assignment was incorrect (see below). However, CN electronic fluorescence has been observed in mixtures of active N_2 and CO,[10] and we cannot yet rule out the possibility of its formation in the COCHISE experiments.

In addition to $N_2(v)$, electronically excited N_2^* and $N(^4S, {}^2D, {}^2P)$ can interact with CO. The N_2^* process is likely to lead to direct E-V or E-E,V energy transfer from N_2^* to CO rather than chemical reaction, owing to the "stiffness" of the two bonds relative to those of NCO and to the four-center nature of the reaction to form CN and NO. (However, vibrational energy in the CO molecule could lead to a different result.) The reaction

$$N(^4S) + CO \rightarrow CN + O \tag{9}$$

is endoergic by 76.9 kcal/mol, and would thus require $CO(v' > 13)$ in order to proceed at low temperatures. Similarly, the reaction

$$N(^2D) + CO \rightarrow CN + O \tag{10}$$

is endoergic by 21.9 kcal/mol and would require $CO(v' \geq 4)$. It seems unlikely that such secondary processes involving $CO(v)$ as a reaction partner would be significant under our conditions. However, $N(^2D)$ can transfer energy in an E-V process:

$$N(^2D) + CO \rightarrow N(^4S) + CO(v \leq 9) . \tag{11}$$

This reaction proceeds with a total rate coefficient of about 2×10^{-12} cm^{-3} at room temperature. (The kinetics of quenching of $N(^2D, ^2P)$ by CO have been studied by several previous investigators (see Ref. 6), but the reported rate coefficients are in considerable disaccord. We are currently pursuing definitive measurements on the FAKIR flow reactor, cf. Section 3.) The reaction with $N(^2P)$,

$$N(^2P) + CO \rightarrow CN + O \tag{12}$$

is exoergic by 5.1 kcal, but there is no adiabatic route for this process.[11] Furthermore, vibrationally excited CN cannot be formed directly unless the reactant CO is vibrationally excited. Thus, we find no direct routes for formation of $CN(v)$ in the primary processes occurring in the reaction zone, and only a relatively slow route for possible formation of $CN(v = 0)$, i.e., Reaction (12). $CN(v)$ fluorescence would then have to arise from secondary and tertiary processes and is therefore expected to be very weak at best. The quenching of $N(^2P)$ can proceed by two branches:

$$N(^2P) + CO \rightarrow N(^2D) + CO(v \leq 4) \tag{13}$$

$$N(^2P) + CO \rightarrow N(^4S) + CO(v \leq 15) . \tag{14}$$

We conclude from this discussion that the primary interaction between discharged N_2 and CO will consist of excitation of $CO(v)$ by energy transfer from $N_2(v)$, $N(^2D)$, and $N(^2P)$, and possibly excitation of electronically excited CO

by energy transfer from N_2 metastables. Formation of CN and excitation of CN(v) or CN* can only occur through secondary and tertiary processes initiated by reactions of CO(v), and should not be observable in the COCHISE experiments.

The experiments discussed here were performed using discharge gas mixtures of 3-12% N_2 diluted in Ar, at reaction zone pressures of 4.5-5.0 mtorr and nominal gas temperatures of 80-100 K. The range of CO number density in the reaction zone was 2-12 × 10^{13} cm^{-3}, in considerable excess over the 10^{9-10} cm^{-3} ranges we expect for $N(^2D, ^2P)$. Fluorescence measurements were made in two modes of discharge operation, modulated at 23 Hz (i.e., the normal mode employed in other COCHISE studies), and CW, where the detected fluorescence is modulated by the tuning fork chopper. Spectra for the two different modes and several combinations of N_2 and CO flow rates are shown in Figs. 11 to 17.

The spectra obtained with the modulated (AC) discharges are shown in Figs. 11 to 14 for combinations of high and low flow rates of N_2 and CO. Several different spectral signatures appear in these data. The CO(v = 1) → CO(v = 0) band is prominent for high N_2 flow rates (Figs. 13 to 14) and can be recognized by its sharp band center near 4.7 μm and its relatively broad R and P branches peaking near 4.6 and 4.8 μm, respectively. The resolution of the AC measurements is 0.013 μm, which is insufficient to resolve the rotational structure of CO. Fluorescence from the higher vibrational levels of CO will extend to longer wavelengths (cf. Figs. 15 to 17), and may be responsible for the general envelope of the spectra extending to ~ 5 μm. Weak fluorescence between 5.2 and 6 μm may be due to NO formed in the discharges from trace impurities in the Ar/N_2 mixture. The most striking feature of these spectra is the sharply structural set of features which appear throughout. These features fall into two categories: (1) a grouping of 5-6 "lines" which lie between 4.3 and 4.6 μm, and which appear consistently in all spectra; and (2) a system of transitions extending to longer wavelengths, which are most prominent at high N_2 and low CO (Fig. 13). We measured the phase differences of the various features relative to ArI radiation scattered from the discharges. These measurements show that the CO-related

2-24
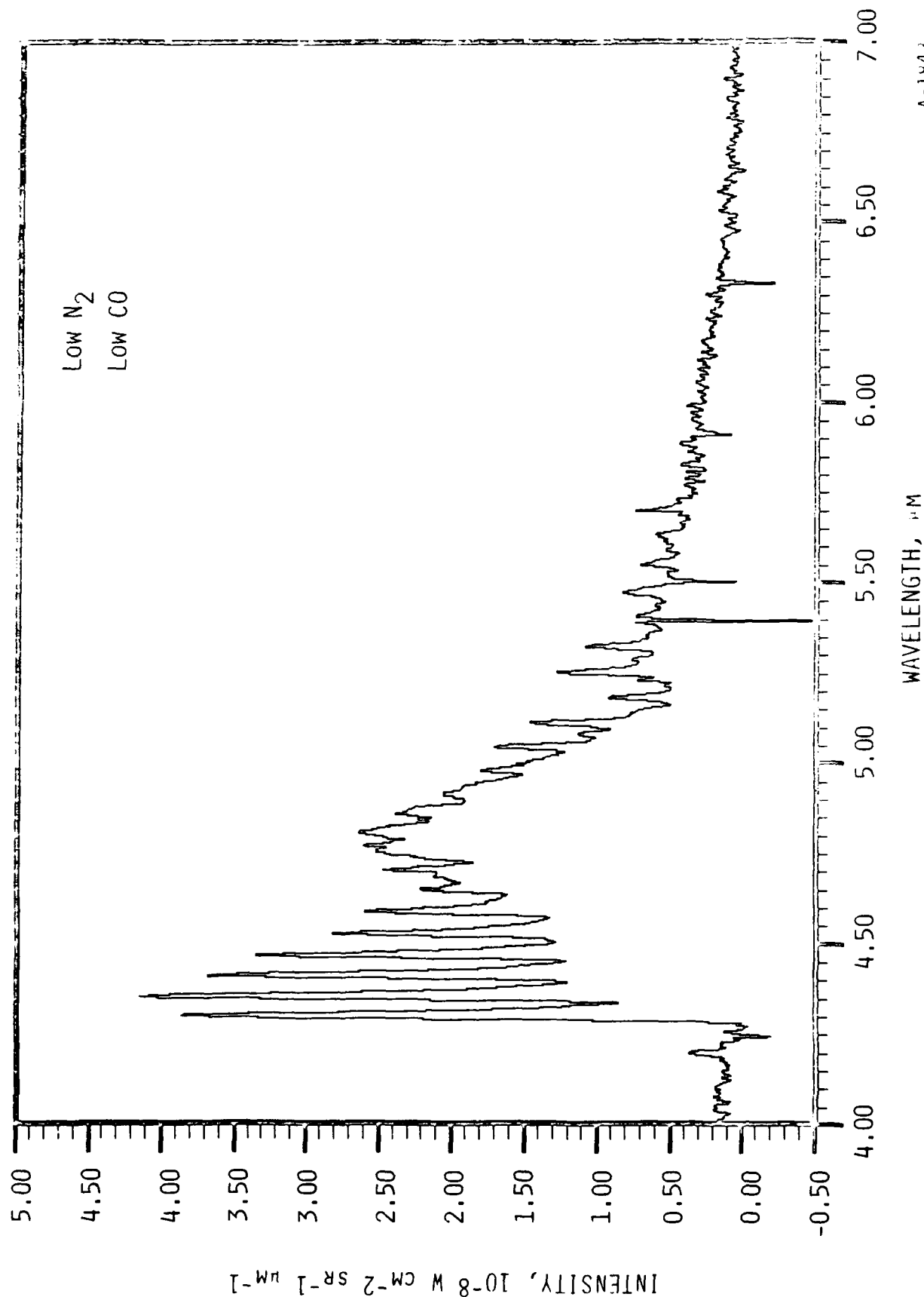
Figure 11. CO fundamental band region, AC discharges. Discharge mixture: mixture: 4.9% N_2 in Ar. Counterflow mixture: 8.6% CO in Ar. [CO] $\approx 2 \cdot 10^{13}$ cm^{-3} in the mixing zone. T = 80 K, P = 4.5 mt, $\ell \approx 0.013$ m.

A-1843
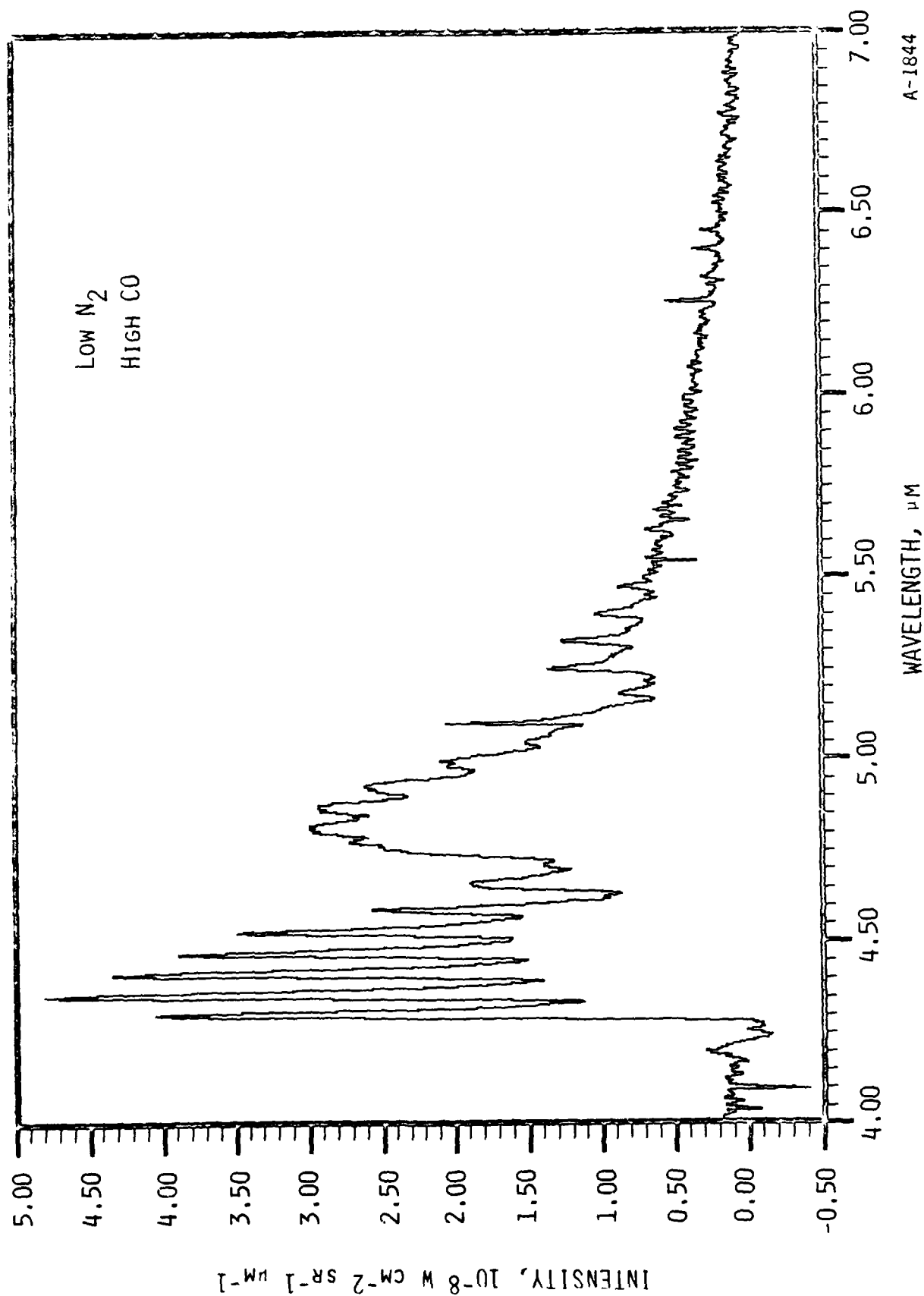
Figure 12. CO fundamental band region, AC discharges. Discharge mixture: 2.9% N₂ in Ar. Counterflow mixture: 45.5% CO in Ar. [CO] ≈ 1.2 x 10¹⁴ cm⁻³ in the mixing zone. Other conditions are the same as in Fig. 11.

A-1844
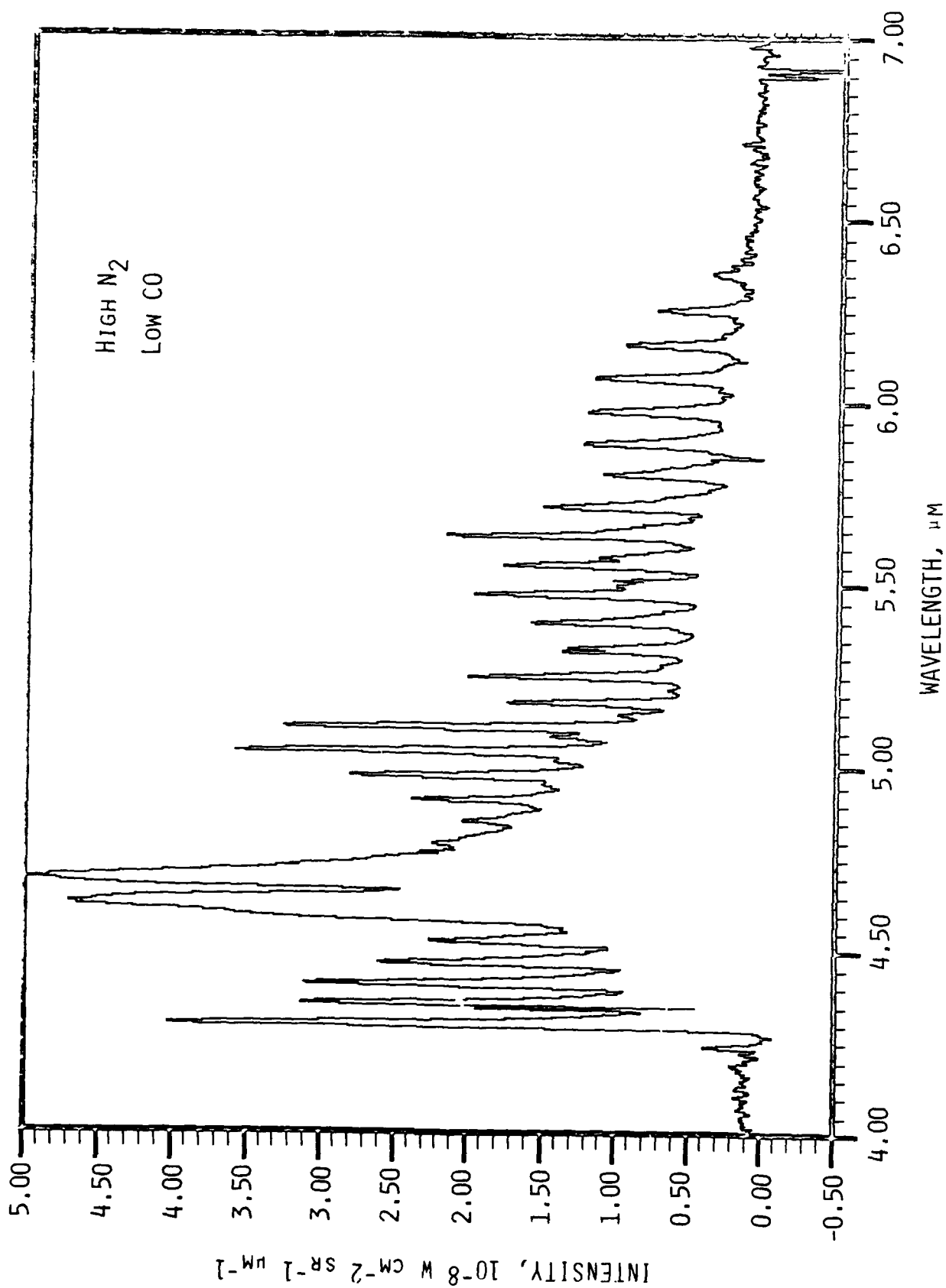
Figure 13. CO fundamental band region, AC discharges. Discharge mixture: 12% N_2 in Ar. Counterflow mixture: 8.6% CO in Ar. [CO] = 2×10^{13} cm^{-3} in mixing zone. Other conditions as given in Fig. 11.

A-1845
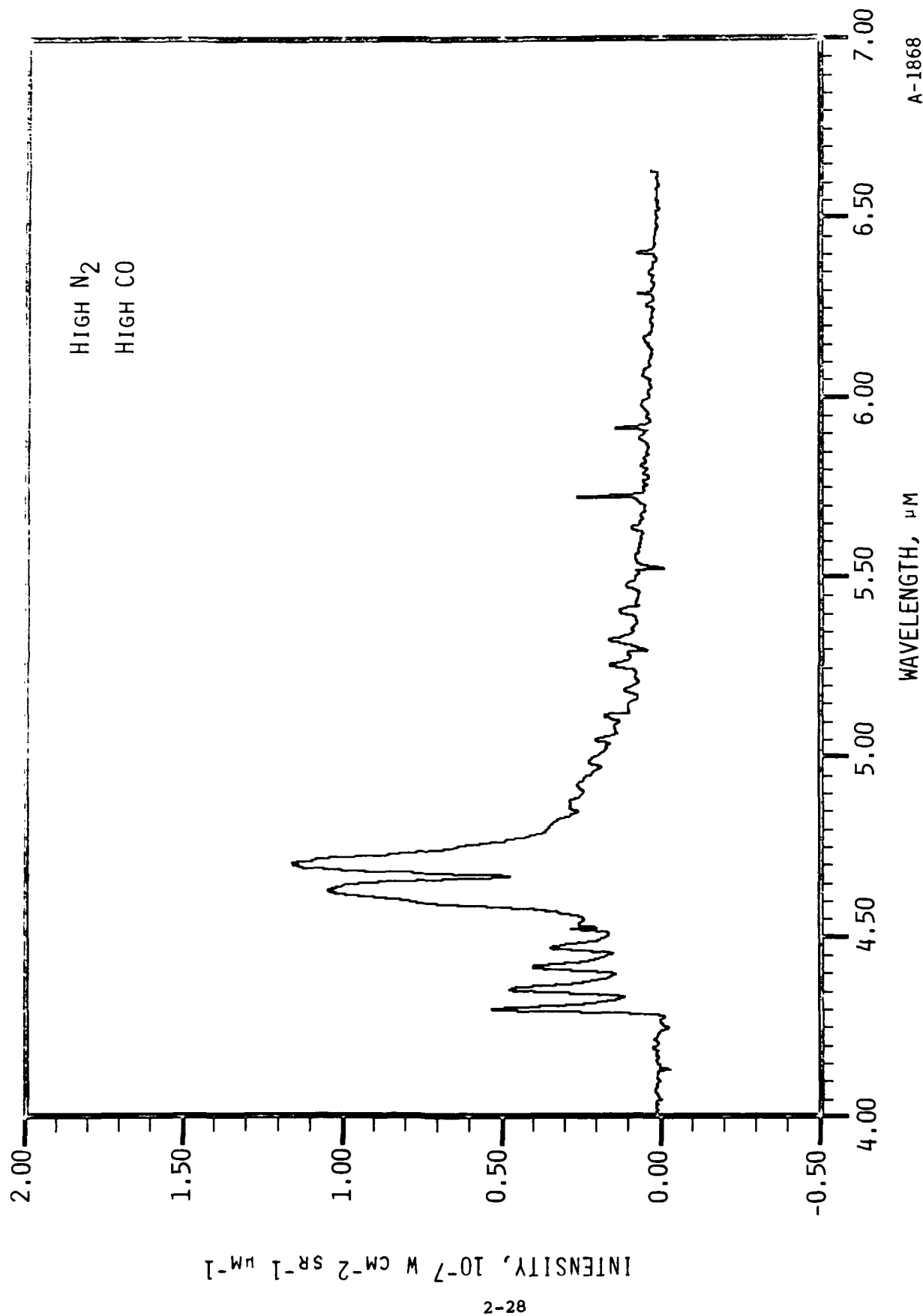
Figure 14. CO fundamental band region, AC discharges. Discharge mixture: 12% N₂ in Ar. Counterflow mixture: 45.5% CO in Ar. Other conditions as given in Fig. 11.

A-1868
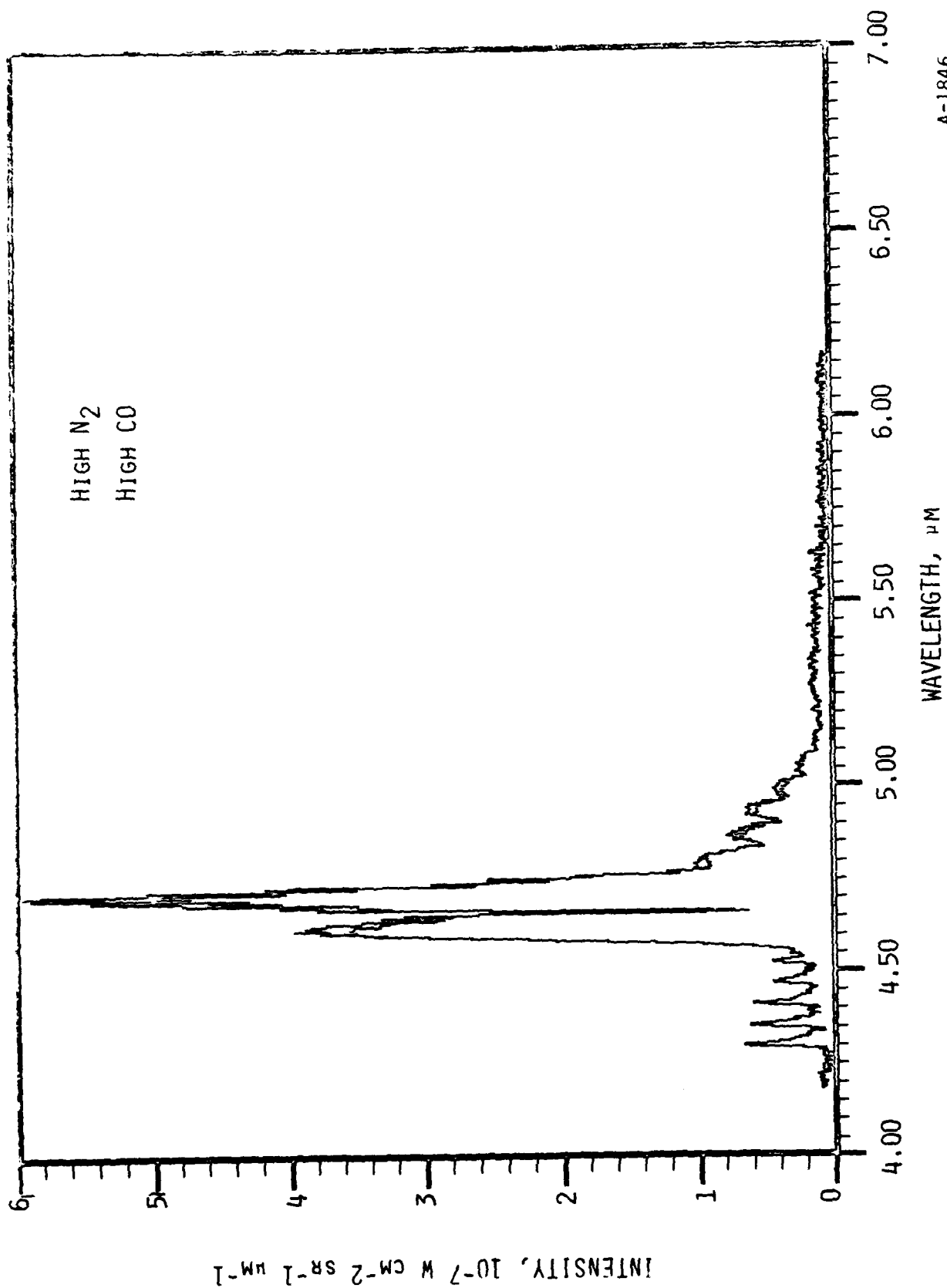
Figure 15. CO fundamental band region, CW discharges. Nominal flow conditions: discharge, 10% N_2 in Ar; counterflow: 30% CO in Ar. T = 80 K, P = 3.5 mt, $\delta\lambda$ = 0.007 μm.

A-1846
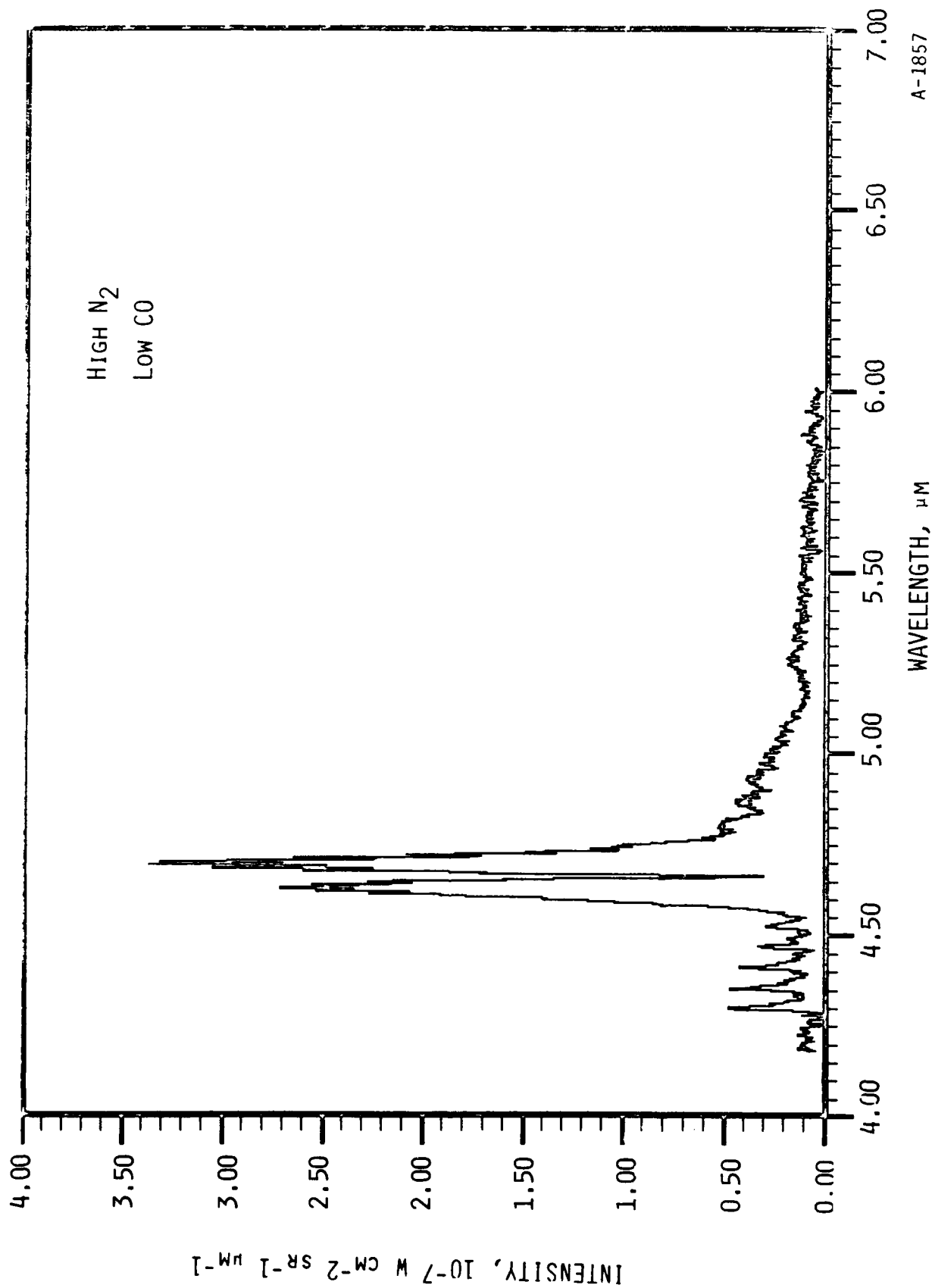
Figure 16. CO fundamental band region, CW discharges. Nominal flow conditions: discharge, 10% N_2 in Ar; counterflow, 4% CO in Ar. Other conditions same as in Fig. 15.

A-1857

INTENSITY, 10^{-7} W CM^{-2} SR^{-1} μM^{-1}

WAVELENGTH, μM

HIGH N_2
LOW CO
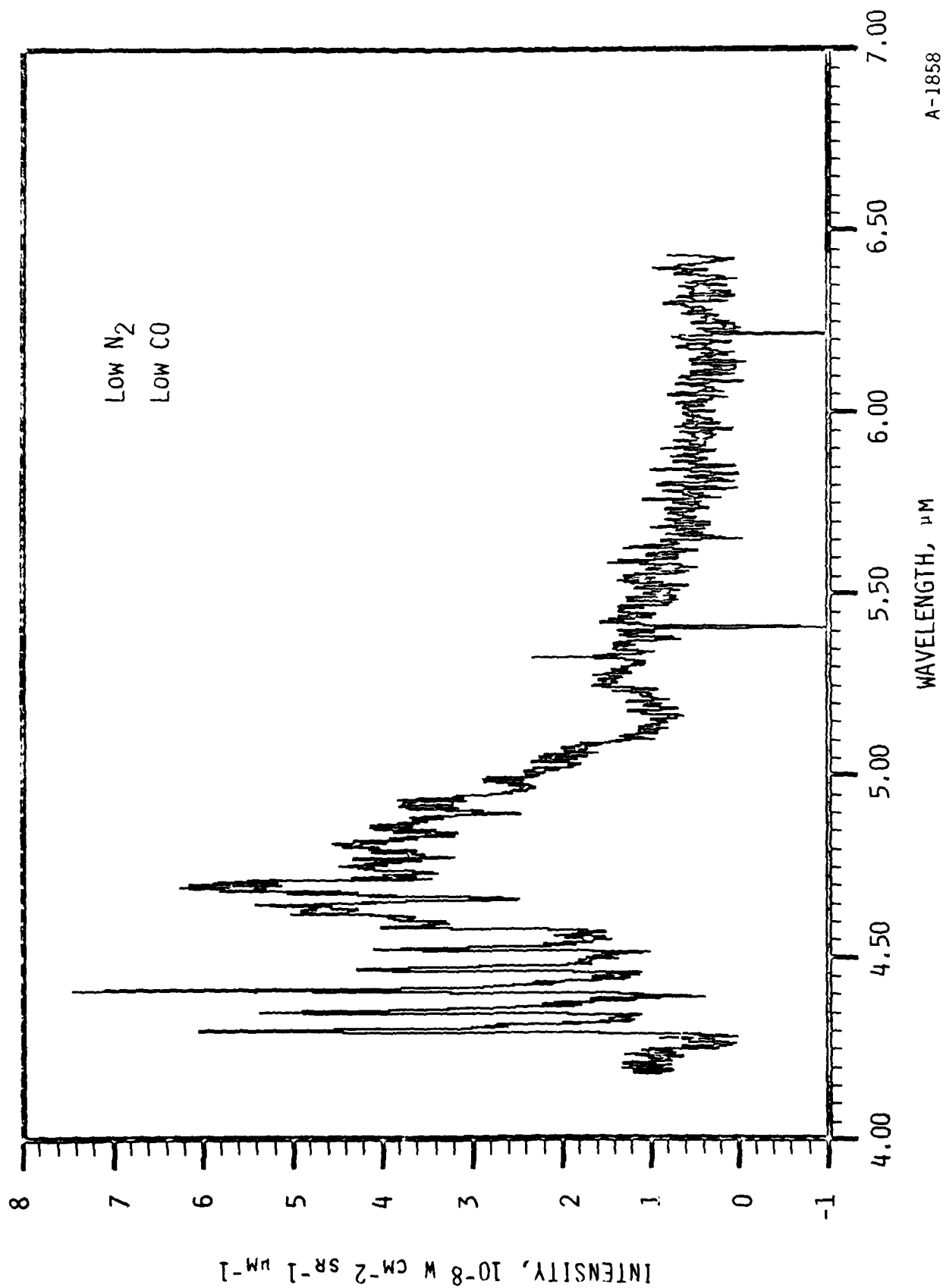
Figure 17. CO fundamental band region, CW discharge. Nominal flow
conditions: discharge, 2% N_2 in Ar; counterflow, 4% CO
in Ar. Other conditions same as in Fig. 15.

A-1858

2-31

fluorescence is out of phase with the discharges by 550 µs for the 4.3 µm system, 680 µs for the CO(1 → 0) band, and ~ 1000 µs for the sharp, longer wavelength features. These values are to be compared to our estimated values of ~ 500 µs for transit from the discharge tube outlet to the center of the reaction cell and ~ 300 µs for the residence time in the field of view. Thus, the appearance of the 4.3 µm system and the CO(1 → 0) fluorescence are consistent with direct excitation within the field of view, but the longer wavelength features are not. These features must then arise from secondary processes, perhaps involving species which have returned to the field of view following collisions with the cell walls.

The sharp, line-like features between 4.7 and 6.5 µm are strongest at lower flows of CO. We have occasionally observed these features even in the absence of added CO, provided CO had previously been used as a reagent. These are essentially the same features as those that were previously thought[9] to be CN(v). Examination of these new spectra shows that the band centers of the CN ($\Delta v = 1$) transitions are ~ 10 cm^{-1} to the blue of each observed peak above 4.9 µm, but the band centers of CO($\Delta v = 1$) transitions correspond exactly with each peak. The narrowness of the features must result from an extremely low rotational temperature, which tends to collapse all the intensity into low J' transitions in the P-branch. The spectrum of Fig. 13 is replotted in Fig. 18; this is to be compared to the computed vibrational basis functions (no population weighting) for CO at 5 K shown in Fig. 19. The correspondence between computed and observed features is exact. We conclude that the sharp spectral features between 4.7 and 6.5 µm are due to ($\Delta v = 1$) transitions from rotationally cold CO. It seems likely that the excited CO has re-entered the field of view following multiple collisions with the wall and with other molecules, or may be adsorbed on a surface. The observed rotational temperature appears to be < 10 K, which is somewhat colder than we might expect for the reaction cell walls (10-15 K), but may not be inconsistent in view of the difficulty of determining absolute hardware temperatures in this range. The spectrum of Fig. 13 shows contributions from as high as v' = 23. This corresponds to an excitation level of ~ 5.4 eV. The excitation could arise from transfer from $N_2(v)$ or N_2^* metastables, or from deactivation of electronically excited CO formed by N_2^*. In any case, it appears that the fluorescence results at least
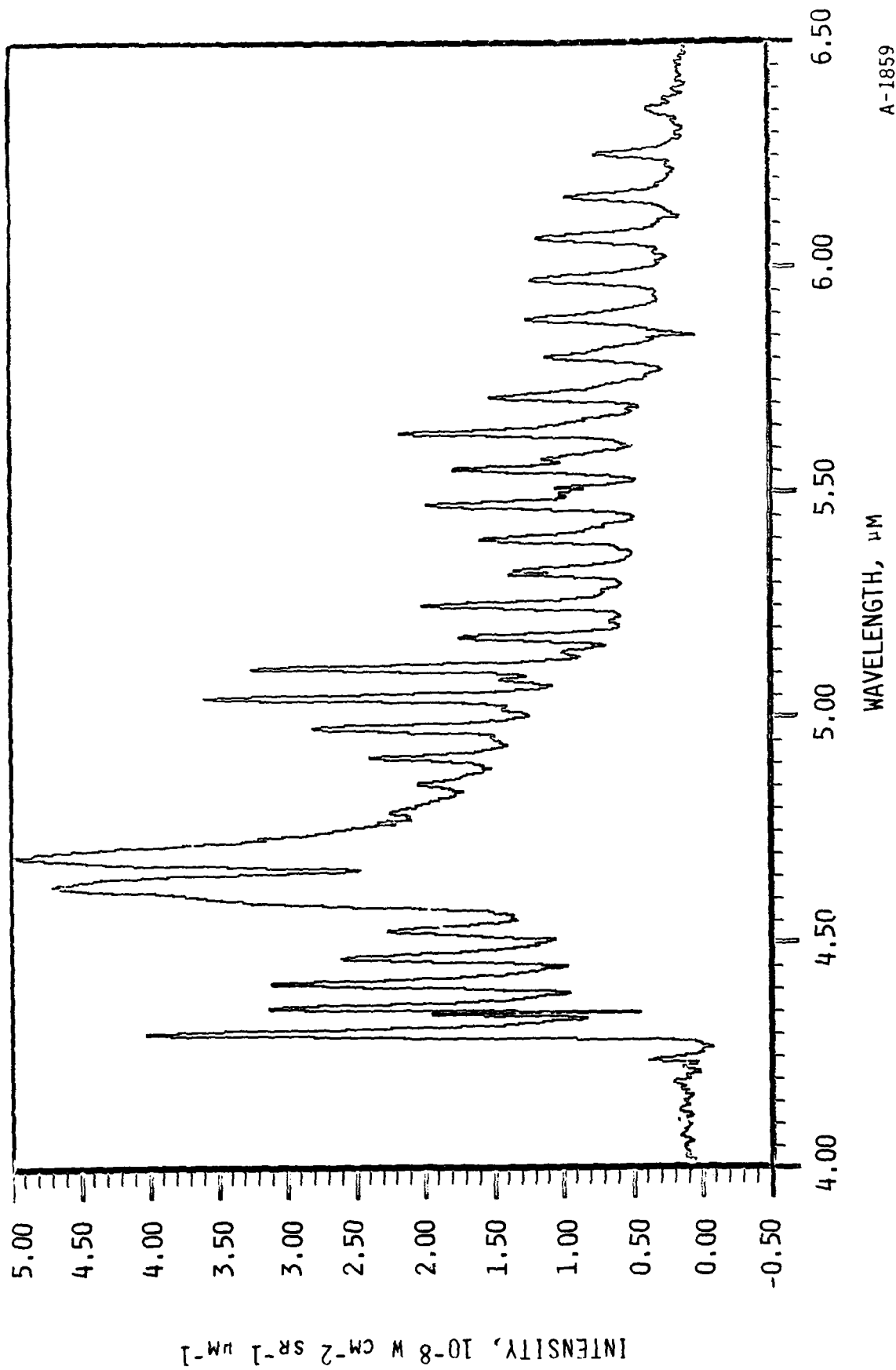
Figure 18. Spectrum of Fig. 13 on expanded scale for comparison with computed spectrum in Fig 19.

A-1859

2-33
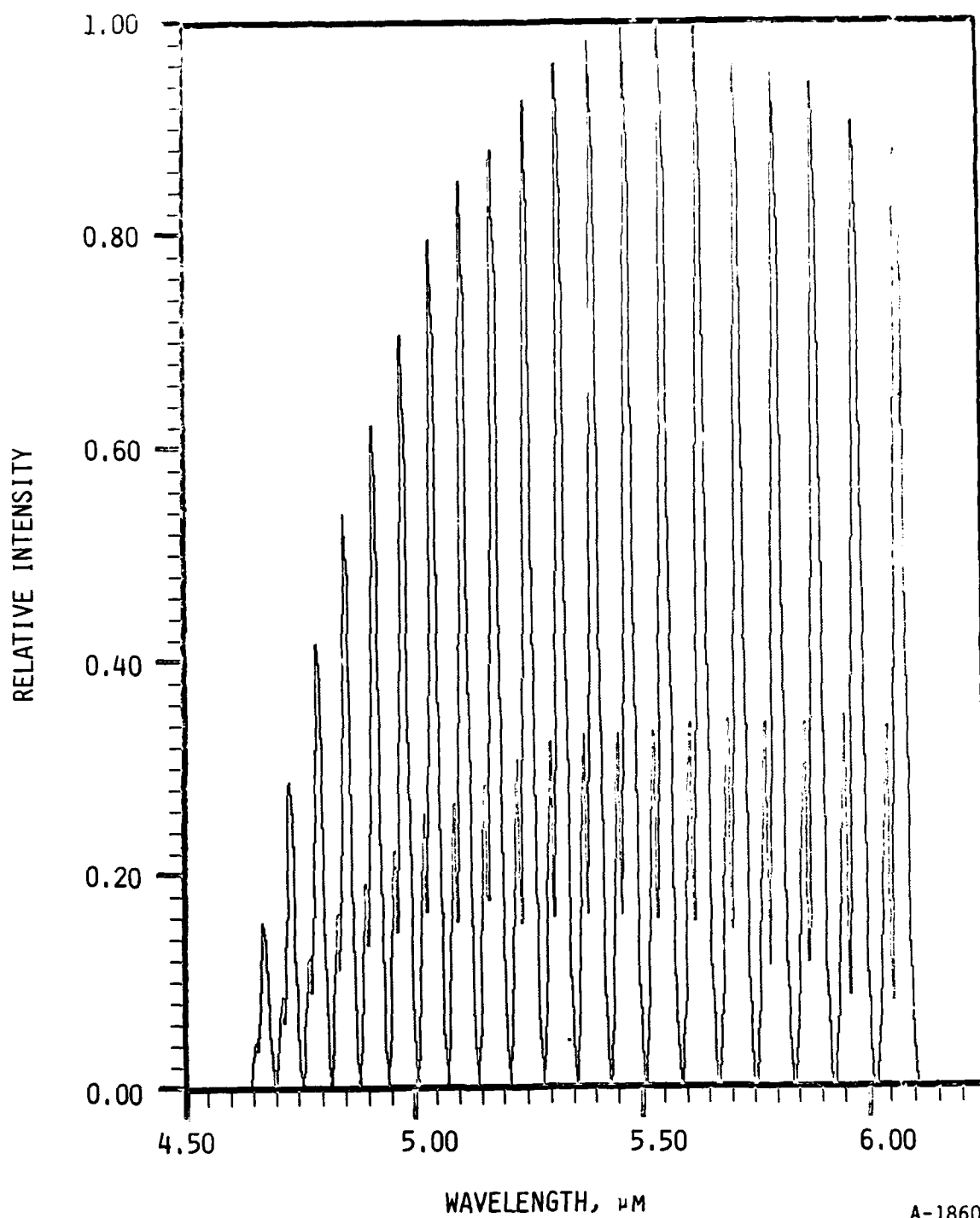
Figure 19. Computed basis functions of CO($\Delta v=1$) fluorescence for T_{ROT} = 5 K and equal vibrational state populations.

A-1860

2-34
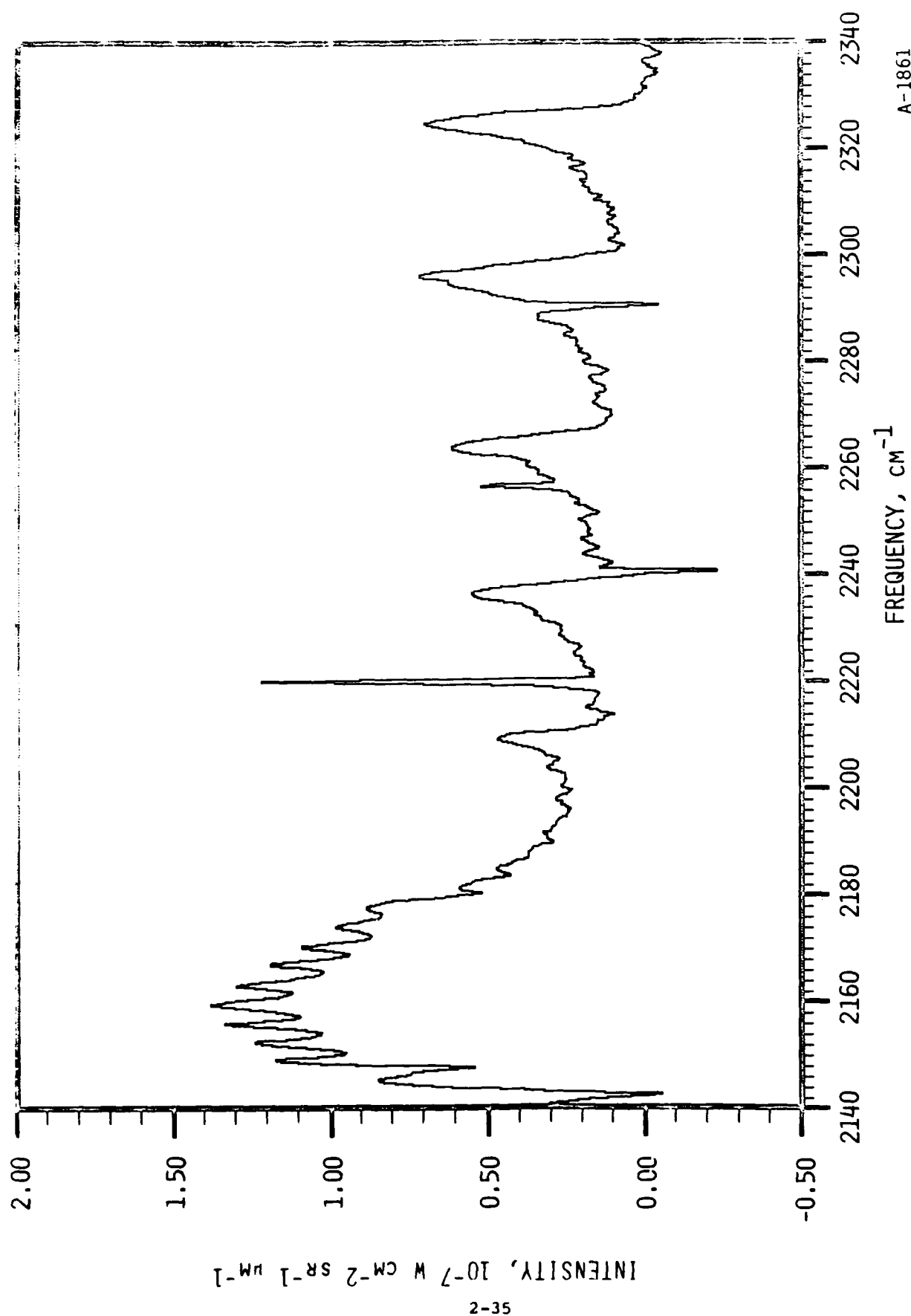
Figure 20. Frequency spectrum of unidentified fluorescence near 4.5 μm. Conditions are the same as in Fig. 14, except $\delta\lambda = 0.007$ μm (~ 3.6 cm^{-1} at 4.3 μm). The CO(1,0) band center and R branch are at 2143 cm^{-1} and 2143-2180 cm^{-1}, respectively.

A-1861

partially from multi-collisional processes occurring outside the field of view and, as such, will be difficult to characterize more fully. The addition of more CO seems to diminish their relative contribution, probably because of the enhanced rate of direct excitation of CO(v). It should be noted that, due to the phase lag between the direct and indirect CO excitation spectra, it is often difficult to optimize the phase setting for the direct fluorescence. This problem can be alleviated by using the CW-discharge mode (see below).

The other CO-related grouping which remains to be identified is the set of features near 4.3 μm. A high resolution scan (0.007 μm, 3.7 cm^{-1}) is plotted in frequency space in Fig. 20. The features appear as five sharp-headed, red-degraded bands beginning at 2325 cm^{-1} and progressing to the red with a spacing of (29 ± 2) cm^{-1}. A sixth peak near 2180 cm^{-1} underlies the R-branch of the CO(1 → 0) band. The intensities of these peaks vary in much the same way as that of the CO(Δv = 1) band with variations in CO flow. These features could be due to either vibration-rotation transitions or electronic bands of some molecule present in the reaction chamber. If they are vibration-rotation bands, the rotational temperature would have to be extremely low to account for the narrowness of the bands. If the system is treated as (Δv = 1) transitions of a diatomic molecule, the spectroscopic parameters are ω_e = 2354 cm^{-1} and $\omega_e x_e$ = 14.5 cm^{-1}. These values are startlingly close to those for $N_2(X^1\Sigma)$, 2358.57 and 14.324 cm^{-1}. Of course, we do not expect $N_2(v)$ to radiate, except perhaps via a collision-induced dipole in the frozen matrix on the walls, and we do not understand why such radiation would occur only in the presence of CO. We will continue to pursue that possibility, since such an observation is likely to be quite unique. We have thus far been unable to identify any other species with these spectroscopic properties. We have also pursued the possibility of electronic transitions of CO, using the data in Krupenie's monograph.[12] However, there are no clear assignments, with the possible exception of the (0,6) band of the $d^3\Delta_i \rightarrow a^3\pi$ system, which falls at 2331 cm^{-1}. We will pursue this tack in more detail with the spectral simulation code discussed in Section 2.3.1. If this system is an electronic transition, other bands corresponding to different values of Δv should be evident at other wavelengths. We plan to survey the 2-4 μm region in future experiments.

If electronic states of CO are indeed excited by energy transfer from N_2^*, there is potential for electronic transitions in the LWIR to occur.

Measurements with the discharges operating CW produce substantially different results (Figs. 15 to 17). In these measurements, the 0.007 µm resolution allows partial resolution of the rotational structure of CO, and the rotational distributions for all vibrational levels are similar to what one would expect for the nominal gas temperatures of 80-100 K. In this case, the entire CO spectrum appears to be the result of direct excitation. A least squares spectral analysis of one of the spectra is depicted in Figs. 21 to 23. The (1-0) transition is prominent, but as many as 8 or 9 vibrational levels of CO can be identified. This would be consistent with excitation of CO by energy transfer from $N_2(v)$, which excites predominately $CO(v = 1)$, and from $N(^2D, ^2P)$, which could excite the higher levels. The $N_2(v)$ component is strong at higher N_2 flow, but disappears at low $N_2(v)$ in the discharge. The N^* component, however, is much less sensitive to N_2 flow, as we observe in the $NO(v)$ experiments described above.

The dependence of the intensity on CO flow rate is rather weak, but this is a consequence of the reduced metastable number density in the presence of CO. The kinetics are in steady state, according to the following:

$$\frac{d[CO(v)]}{dt} = k[N^*][CO] - k'[CO^*] = 0 \tag{15}$$

$$\frac{d[N^*]}{dt} = \phi_{N^*} - (k' + k[CO])[N^*] = 0 \tag{16}$$

where N^* denotes $N(^2D, ^2P)$ and/or $N_2(v)$, ϕ_{N^*} is the production rate of N^* from the discharges into the field of view, k is the rate coefficient for excitation of CO by N^*, and k' is the reciprocal of the residence time in the field of view. Combining Eqs. (15) and (16) gives

$$[CO(v)] = \frac{k\phi_{N^*}[CO]}{k'(k' + k[CO])} . \tag{17}$$
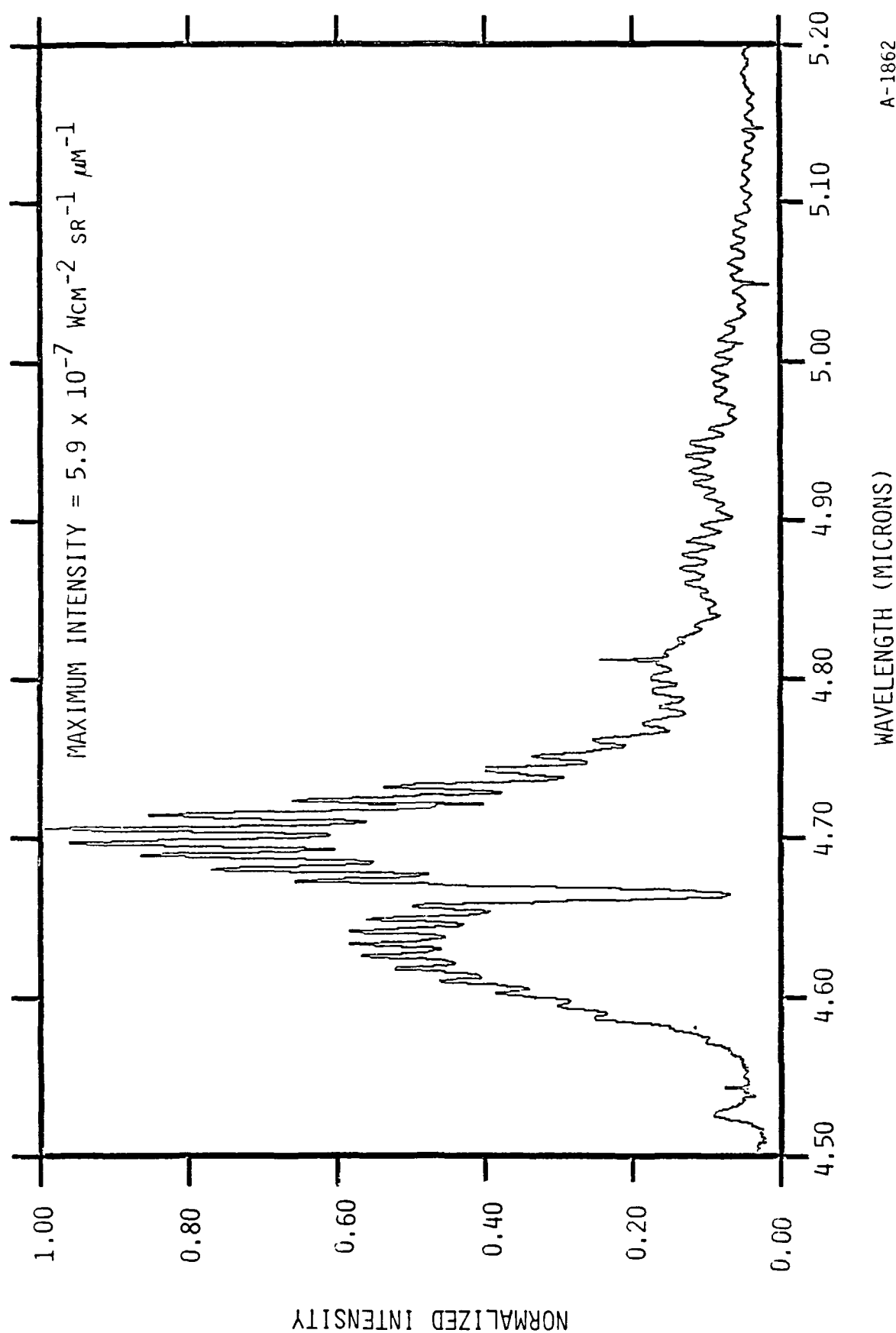
Figure 21. Experimental CO spectrum for comparison to least squares analysis shown in Fig. 22. Experimental conditions are the same as those in Fig. 15.

A-1862

2-38
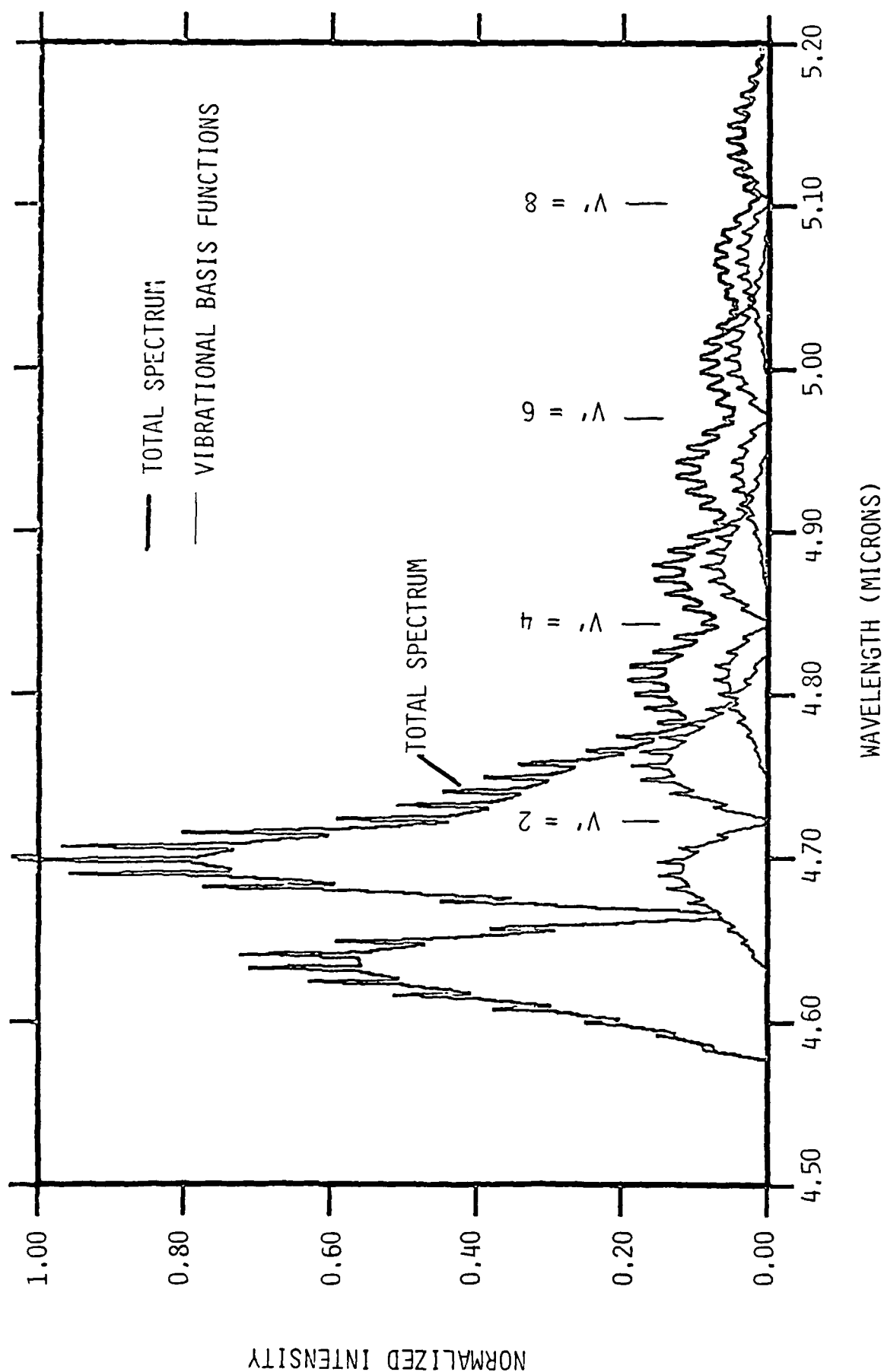
Figure 22. Computed least squares spectral fit to the experimental CO spectrum of Fig. 21. $T_{ROT} = 80$ K, $\delta\lambda = 0.007$ µm.

A-1863

2-39

DISCHARGES CW
DISCHARGE: 10% N_2/AR
COUNTERFLOW: 30% CO/AR
T = 80 K
P = 3.5 MT

[CO(v)], cm^{-3}

VIBRATIONAL ENERGY, cm^{-1}
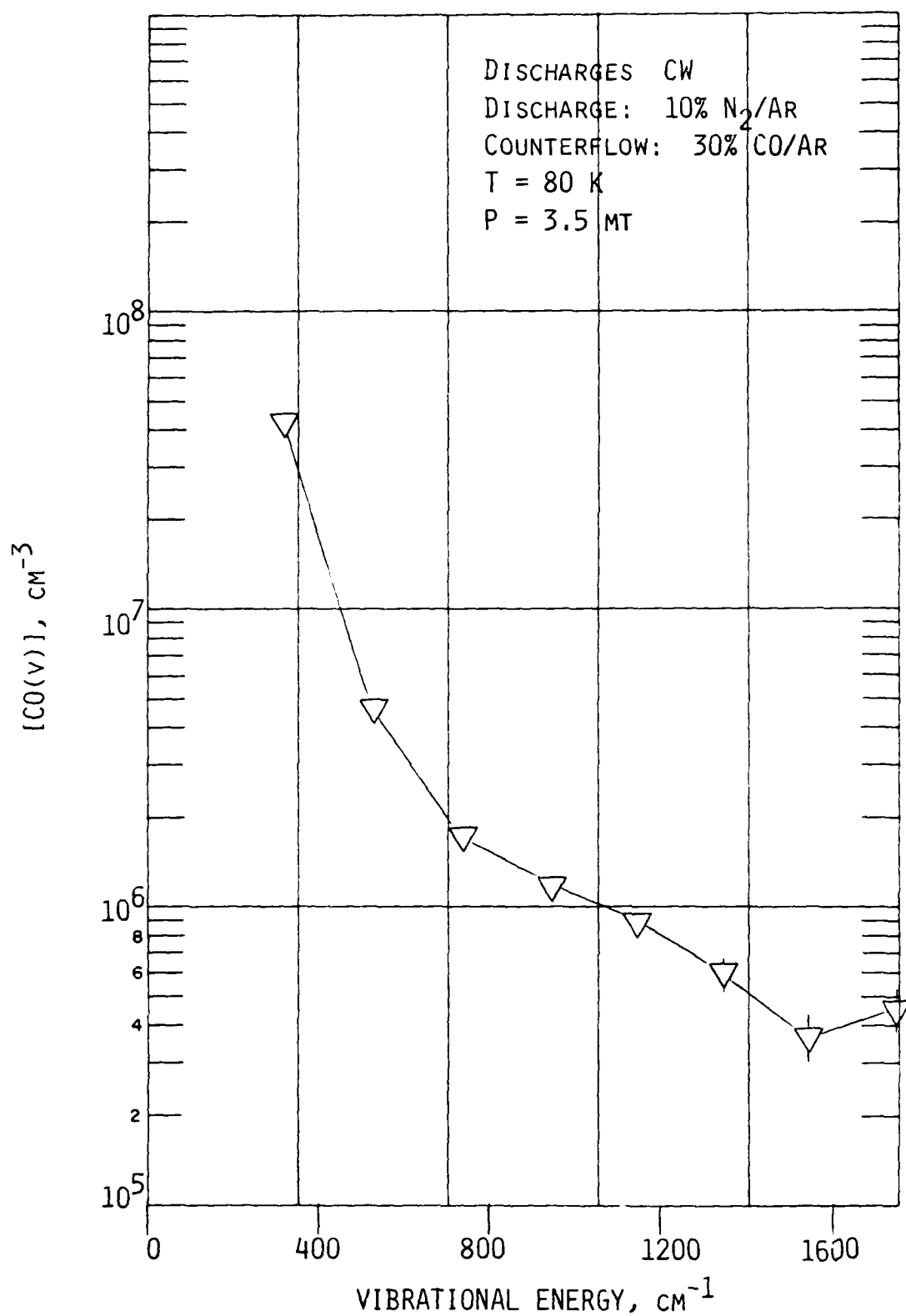
A-1864

Figure 23. CO vibrational state number densities determined from least squares analysis of Figs. 21, 22.

2-40

Thus, by studying the yield of CO(v) as a function of added CO, it should be possible to determine ϕ_{N*} for a given discharge condition. Such measurements would be extremely useful as a calibration technique for other experiments such as the NO(v) measurements.

Clearly, the CO excitation studies are in their infancy but have already raised several fascinating and important questions. Why do the AC and CW discharge methods give such disparate results? How does the rotationally cold CO(v) spectrum arise? What is the radiating species at 4.3 μm, and does it exhibit signatures in the SWIR and LWIR? Can we isolate the $N(^2D, \ ^2P)$ and $N_2(v)$ mechanisms for pumping CO? Can we effectively use this reaction as a titration technique for determining $N(^2D)$ number densities? We hope to address these questions in future experimental studies on COCHISE, with supporting kinetic measurements on FAKIR. We must also perform a complete literature search on all aspects of the problem.

2.3.3 Interaction of $O_3(v)$ with N_2

The chemical formation of N_2O at high altitudes is an important issue in studies of the quiescent and auroral upper atmosphere. Numerous workers have observed the formation of N_2O in electron-irradiated air. N_2O can be formed at high pressures by the reaction

$$N + NO_2 \rightarrow N_2O + O$$

where NO_2 is formed by three-body recombination processes. However, this route will not operate at high altitudes characteristic of auroral and airglow processes. N_2O formation has also been observed in low-pressure air discharges, most notably in COCHISE and LABCEDE. Several mechanisms for its formation at low pressure have been postulated,[13] such as the following reactions:

$$N_2(A^3\Sigma) + O_2 \rightarrow N_2O + O$$

$$OH(A^2\Sigma) + N_2 \rightarrow N_2O + H \ .$$
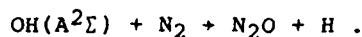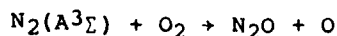
Other reactions could certainly be suggested, involving various combinations of metastable O_2, N_2, and O_3. These reactions should be sufficiently exoergic to form vibrationally excited N_2O, which will radiate strongly in the infrared. This fluorescence occurs at 4.5, 7.8, and 17 μm for the ν_3, ν_1, and ν_2 bands, respectively; excitation of higher levels would, of course, cause some redshifting of each band. The strongest of these bands by far is the ν_3 band near 4.5 μm (A_{001} = 258 s^{-1}).

An interesting possible atmospheric source of $N_2O(v)$ is the reaction of N_2 with vibrationally excited O_3:

$$O_3(v) + N_2 \rightarrow N_2O(v) + O_2 . \tag{18}$$

In the absence of reactant vibrational energy, Reaction (18) is exoergic by 14.4 kcal/mol; each vibrational quantum of $O_3(\nu_3)$ adds another $\sim$ 3 kcal/mol. Thus, $O_3(v)$ carries enough energy to excite several vibrational quanta of N_2O (6.4 kcal/mol per quantum of ν_3 excitation). Observations of $O_3(v)$ fluorescence in COCHISE[14] and in the upper atmosphere[15] show that as many as 6 ν_3 quanta of excitation in $O_3(v)$ are present at high altitudes. This would result in a maximum excitation in N_2O of v_3 = 4, extending the ν_3-band signature to about 4.7 μm.

We have attempted to observe Reaction (18) in COCHISE by searching for $N_2O(\nu_3)$ fluorescence in the direct interaction of discharge-produced $O_3(v)$ with counterflowing N_2. Unfortunately, in the rarefied conditions of the COCHISE reaction cell, a chemiluminescence reaction must be relatively efficient to produce easily measurable fluorescence. As will be shown below, we do not observe any $N_2O(v)$ fluorescence from Reaction (18), but the resulting upper bound on the rate coefficient is still rather large in the context of the potential atmospheric production of N_2O.

The experiments were performed by interacting a pure N_2 counterflow with discharge gas mixtures of $\sim$ 86 μmol s^{-1} of O_2 and 625 μmol s^{-1} of Ar in each of the four discharge tubes at 1.3 torr and 80 K. The discharges were

operated in the usual AC mode. The N_2 flow rate in each injection tube was 1006 μmol s^{-1}. The resulting total pressure in the reaction zone was $\sim$ 4.4 mtorr. The concentration of N_2 in the reaction zone was then $\sim 3 \times 10^{14}$ cm^{-3}.

Recent COCHISE experiments on the discharge-excited $O_3(v)$ fluorescence at 10 μm have established that the maximum $[O_3(v)]$ we can obtain from these discharges is $\sim 10^9$ cm^{-3}, and occurs at the 12% O_2 condition we have employed here. The vibrational distribution under these conditions is bimodal with primary and secondary maxima at $v_3' = 1$ and $v_3' = 4$, respectively, indicating that much of the vibrational excitation may be occurring via metastable energy transfer processes. Some of the $O_3(v)$ is also clearly being formed by three-body recombination of O and O_2. The $(v_1 + v_3)$ combination states are also found to be populated under these conditions. A detailed discussion of our $O_3(v)$ results is presented in Sections 4 and 5.

The results depicted in Figs. 24 to 26 are typical of those obtained in several measurements for each of three separate COCHISE experiment cycles. The spectrum observed for an N_2 counterflow is shown in Fig. 24; this is to be compared to spectra obtained with an unreactive Ar counterflow (Fig. 25) and with an Ar counterflow and only Ar in the discharge (Fig. 26). It can be seen that the sharp features between 4 and 5 μm are due to ArI Rydberg transitions, as we have described in detail elsewhere.[7] The band shapes of the N_2O (001) and $O_3(101)$ bands are also sketched in Fig. 24. The N_2O band is sketched as it appears in COCHISE in AC-discharge measurements for air/Ar mixtures at the same spectral resolution (observed in recent measurements as well as reported in Ref. 2). The $O_3(101 \rightarrow 000)$ transition is sketched as computed for our experimental conditions using data from the AFGL line-parameters compilation.[16] The broad feature appearing between 4.6 and 5.1 μm is undoubtedly the $(v_1 + v_3)$ band of O_3, with most of the radiation arising from vibrationally excited "hot" bands. The phase settings were locked into this feature for the measurements. The fluorescence peaks at $\sim$ 4.9 μm or 2041 cm^{-1}. This corresponds within 1 cm^{-1} to the band center of the 102$\rightarrow$001 transition. In the 10 μm $O_3(v)$ fluorescence measurements, the (102) state is observed to be
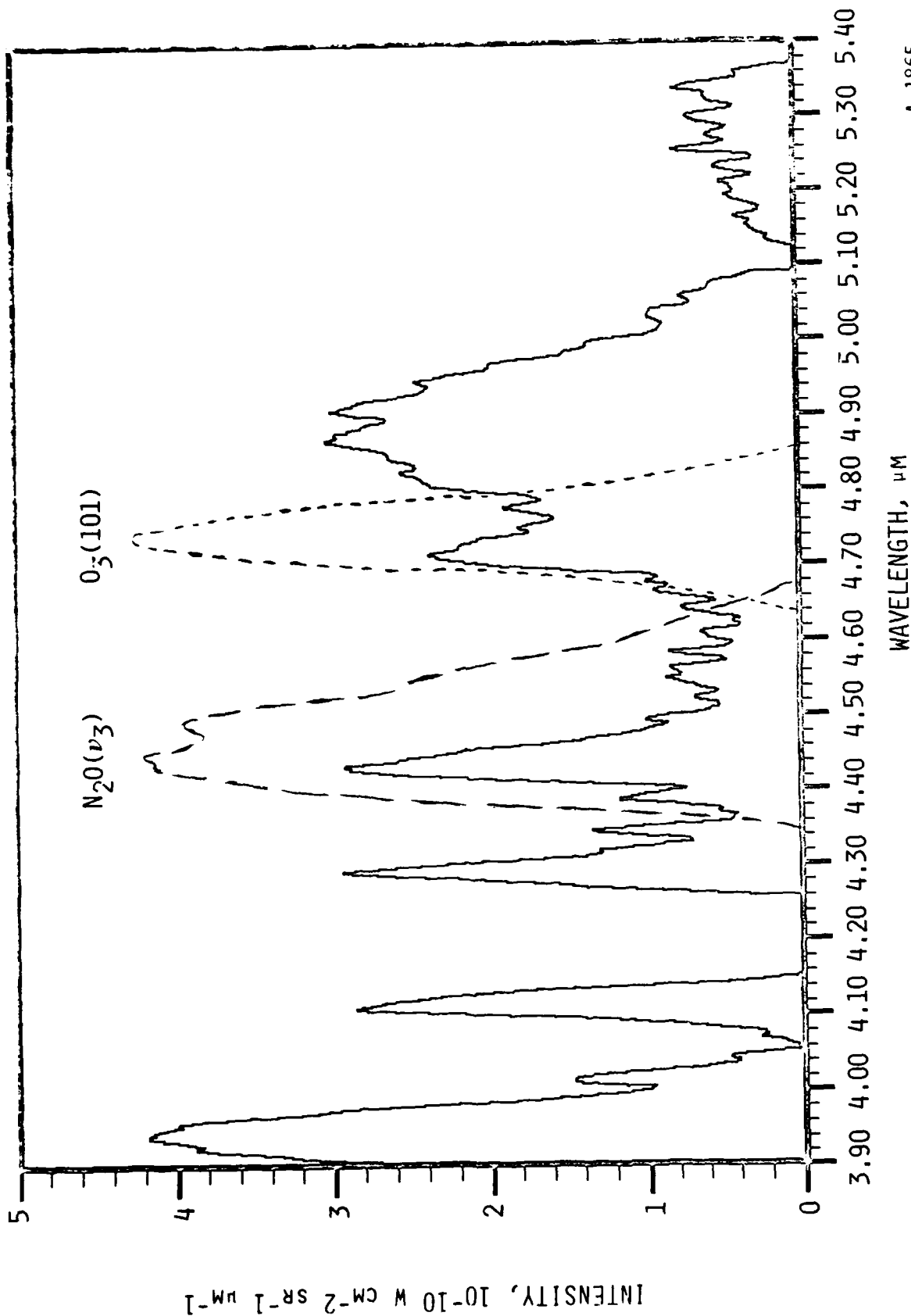
Figure 24. Spectrum of the interaction between $O_3(\nu)$ and N_2. Discharges: 86 and 625 μmol s^{-1} of O_2 and Ar, respectively. Counterflow: 1006 μmol s^{-1} of N_2. $T = 80$ K, $P = 4.4$ mt, $\delta\lambda = 0.04$ μm. The expected band shapes of the $N_2O(\nu_3)$ and the $O_3(101)$ bands are given by the dotted curves.

A-1865
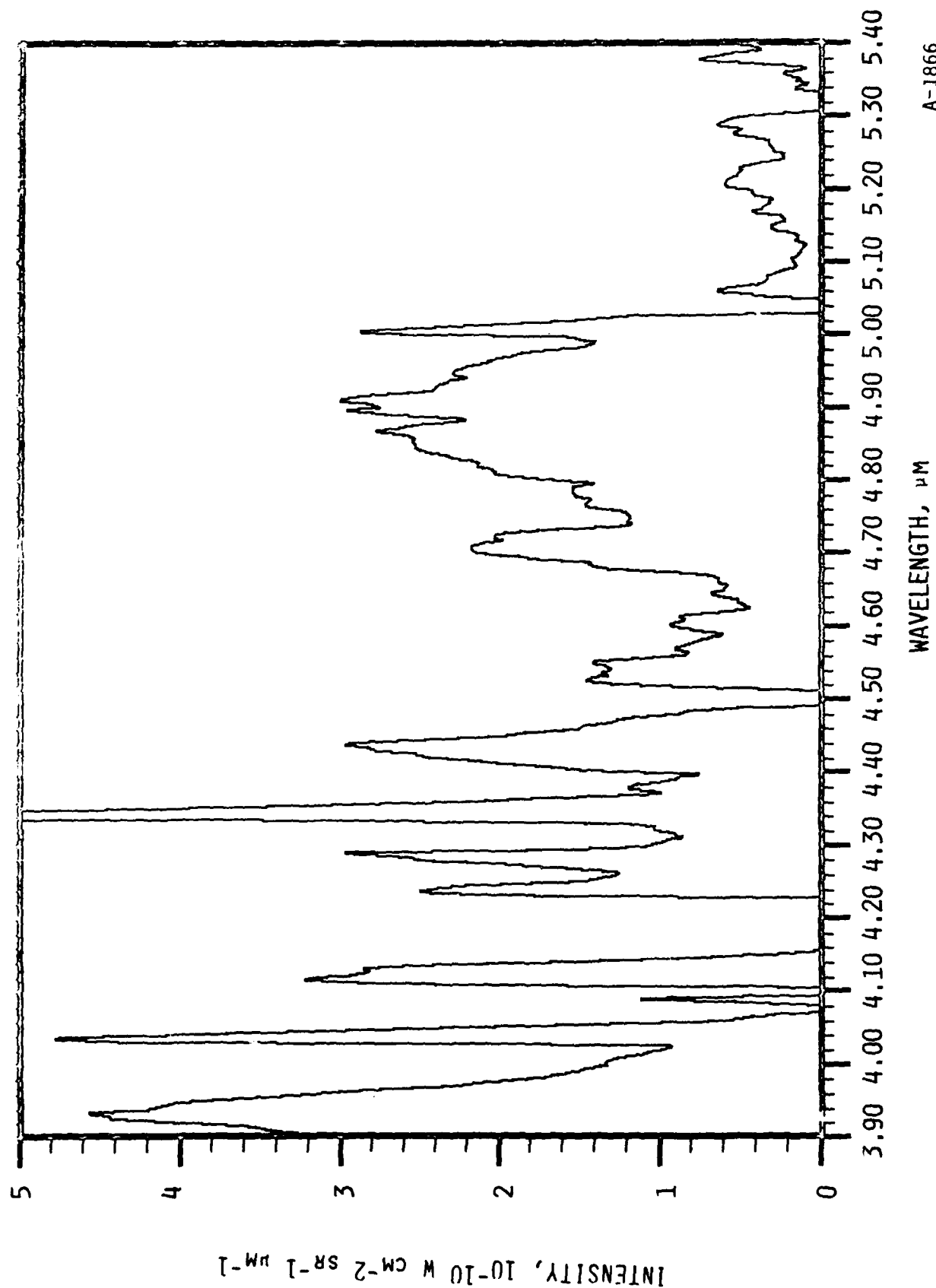
Figure 25. Spectrum of the interaction between $O_3(v)$ and Ar. Conditions same as in Fig. 24 except counterflow is 100% Ar.

A-1866
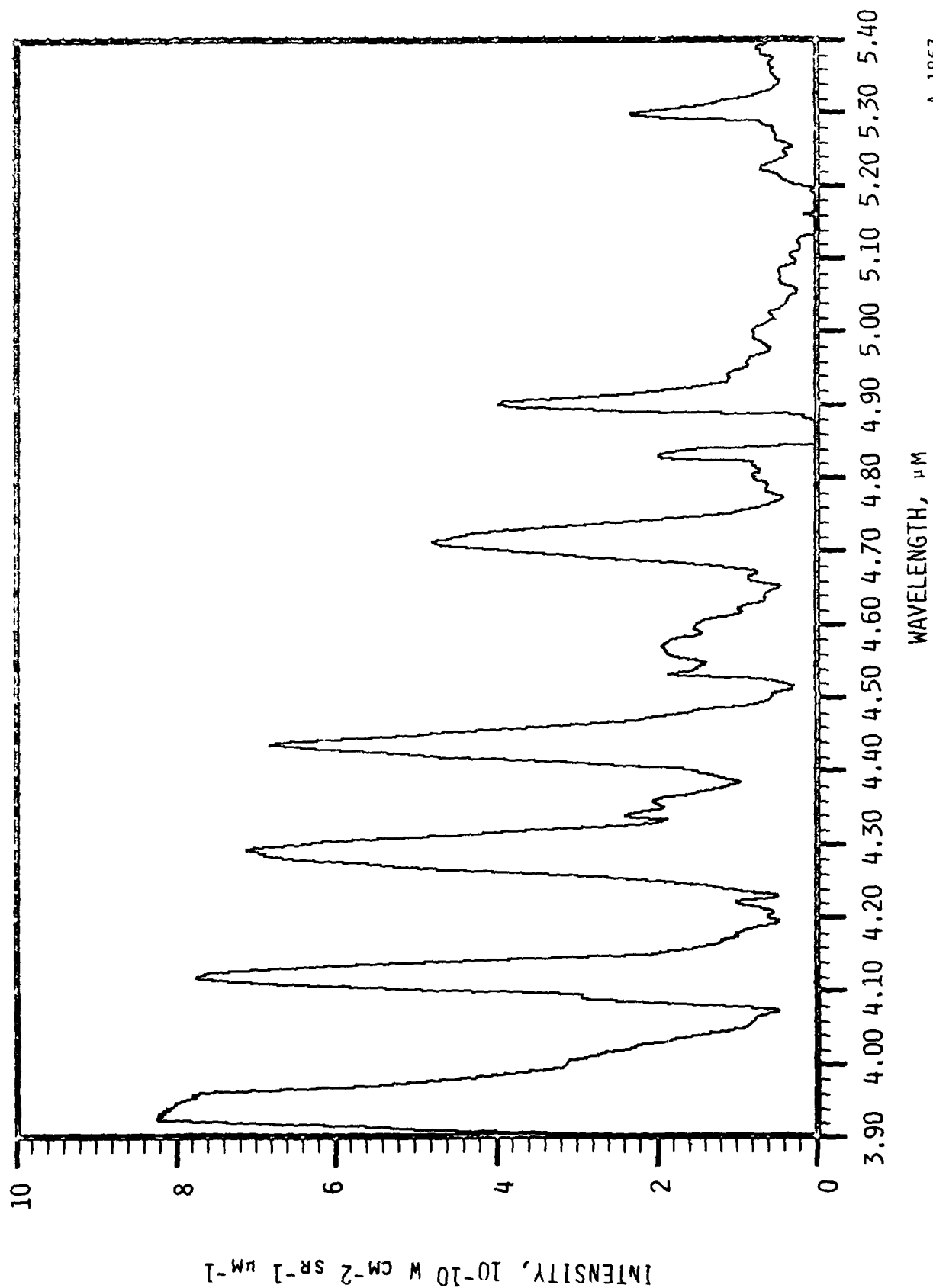
Figure 26. Spectrum observed when only Ar is admitted to both the discharge and counterflow sides. Other conditions same as in Fig. 24.

WAVELENGTH, μM

INTENSITY, 10-10 W CM-2 SR-1 μM-1

A-1867

2-46

the most strongly populated combination state under these discharge conditions, so the present observations are consistent with the ν_3-band data.

Fluorescence from N_2O should occur near 4.5 μm, with possible hot bands extending to the energetic limit near 4.8 μm. There is evidence of a broad emission feature between 4.4 and 4.7 μm underlying the Ar lines. However, this also appears in the Ar counterflow case, so it is not likely to be due to N_2O. The emission could be due to weak, unresolved Ar lines, or possibly to strong OI Rydberg transitions which are predicted to occur at these wavelengths.[8] In any case, there is no evidence of $N_2O(v)$ formation from Reaction (18).

This negative observation places an upper bound on the rate coefficient for $N_2O(v)$ formation from Reaction (18). From comparison of the spectra with N_2 and Ar counterflows (Figs. 24 and 25), the $N_2O(v)$ fluorescence at 4.5 μm is less than 3×10^{-11} W cm^{-2} sr^{-1} μm^{-1}. For a bandwidth of 0.2 μm, this transforms to 3.4×10^7 photons cm^{-3} s^{-1}, or

$$[N_2O(v)] < 1.3 \times 10^5 \text{ cm}^{-3} \ .$$

In the steady-state conditions of the reaction zone, we have

$$[N_2O(v)] = \frac{k_{18}[O_3(v)][N_2]}{k'} \tag{19}$$

where k_{18} is the rate coefficient for Reaction (18) and k' is the inverse of the residence time in the field of view. For the typical conditions $[O_3(v)]$ $\sim 10^9$ cm^{-3}, $[N_2] = 2.6 \times 10^{14}$ cm^{-3}, and $(k')^{-1} \sim 300$ μs, we obtain

$$k_{18} < 2 \times 10^{-15} \text{ cm}^3 \text{ s}^{-1} \ .$$

It must be stressed that this upper bound pertains only to the formation of vibrationally excited N_2O, not to formation of ground state N_2O which, of

course, cannot be observed in COCHISE. However, for lack of better information, it is consistent with our experience with vibraluminescent processes to assume that the reaction to form $N_2O(v = 0)$ will be kinetically similar to that forming vibrationally excited N_2O.

The upper bound obtained in COCHISE is still too large to rule out significant atmospheric and auroral production of $N_2O(v)$ by Reaction (18). In the quiescent atmosphere, values of $[O_3(v)]$ are typically in the 10^5 cm^{-3} range near 80-100 km and range up to as high as 10^6 cm^{-3} at 70 km in the daytime.[15] We would then predict upper bounds to the $N_2O(v)$ production rate of $\sim 10^6$ cm^{-3} s^{-1} at 70 km (daytime) and $\sim 10^{4-5}$ cm^{-3} s^{-1} at 90 km (day or night). These are very large production rates for these altitudes, being comparable to the excitation rates of $O_3(v)$ by recombination and earthshine absorption.[15] By comparison, Zipf and Prasad,[13] using an incorrect description of the kinetics of $N_2(A^3\Sigma^+)$, predicted auroral production rates for total N_2O from the postulated reaction of $N_2(A)$ with O_2 to be of order 10^3 cm^{-3} s^{-1} near 100 km. Since the chemical lifetime of N_2O at high altitudes is quite long,[13] only a very small production rate is required to produce significant quantities of _total_ N_2O. Thus, the present COCHISE measurements do not give a sufficiently definitive answer to the question of atmospheric production of N_2O.

We can see from this analysis that, because of the rarefied conditions of the reaction volume, COCHISE experiments on direct excitation of $N_2O(v)$ may be extraordinarily ϵ sitive but cannot provide definitive results for the upper atmosphere unl. the reaction in question proceeds with a significant reaction probability, i.e., at least 10^{-5}. However, as alluded to above, we _have_ been able to observe $N_2O(v)$ fluorescence excited in low-pressure, discharged mixtures of N_2, O_2 and Ar. This intriguing observation offers another, albeit less direct, avenue for studying $N_2O(v)$ formation in electron-disturbed air. In the higher pressures and longer contact times available in the discharge tubes, slower processes can occur which would not otherwise be observed in the reaction chamber. The principle difficulty with such experiments lies in the conclusive identification of the species and reactions responsible for the observed product formation. However, at this stage of the N_2O problem, we do

not even know whether the key reactants are metastables of N_2 or of O_2, and a discharge experiment can address this most fundamental point. We know from discharged N_2/Ar experiments that $N(^2D, ^2P)$ yields decrease only slightly at low N_2 levels, while $N_2(v)$ yields are large at high N_2 and yields of the high-lying metastables of N_2 are largest at low N_2. Similarly, from discharged O_2/Ar experiments, we have documented the variation of $O_3(v)$, $O_2(v)$, and meta-stable O_2 with O_2 flow into the discharges. In addition, we are developing kinetic models for the excitation of O_2, N_2, and Ar in the COCHISE discharges. Thus, a systematic kinetic study of $O_2/N_2/Ar$ discharges in which N_2 and O_2 are independently varied should allow us to deduce the relative importance of several discharge-excited species in the formation of $N_2O(v)$. The results of some preliminary experiments are discussed in Section 2.3.4.

2.3.4 COCHISE IR Emission from $N_2/O_2/Ar$ Discharges

Some preliminary scoping experiments were performed on COCHISE to examine IR emission (2 to 8 μm) observed in the reaction chamber following discharge excitation of $N_2/O_2/Ar$ mixtures. The measurements were made for a constant Ar flow of ~3.7 std ℓ/min, both in excess N_2 and in fixed O_2. In excess N_2, the N_2 flow rate was set to ~0.2 std ℓ/min and the O_2 flow rate was varied from 10 to 200 std cm^3/min. In fixed O_2, the O_2 flow rate was set to ~0.1 std ℓ/min and the N_2 flow rate was varied from 10 to 400 std cm^3/min. Discharge tube pressures ranged from 1.0 to 1.7 torr. The temperature of the side arms was maintained at ~80 K for almost all the measurements. No coun-terflow was employed. The purpose of these measurements was to: 1) identify the various bands comprising the spectral signature of discharged N_2/O_2 mix-tures; 2) examine the variation of intensities and spectral distributions as functions of separately varied N_2 and O_2 flow rates to check for quenching or metastable effects; and 3) define an optimum range of experimental conditions for carrying out more detailed investigations. Particular emphasis was placed on characterizing the $N_2O(v_3)$ band near 4.5 μm. We present here a summary of the data in its raw, uncalibrated form as obtained in COCHISE.

SWIR spectral signatures were observed between 2 and 4 μm. Typical spectra showed sharp bands and/or lines atop a weaker, broad continuum peaked near 3 μm. Some of this continuum may result from $NO(\Delta v = 2)$ radiation, but the continuum persists outside the NO bandpass. The NO-O air afterglow is a possible source of continuum emission in this spectral region. The molecular bands arise predominately at the shorter wavelengths, i.e., nearer 2 μm, with the Wu-Benesch $(\Delta v = 2)$ features, normally so prominent between 3 and 4 μm for N_2/Ar discharges, strongly suppressed by the presence of O_2. The features between 2 and 3 μm await identification and comparison to our earlier data for N_2/Ar, but may arise in part from the First Positive system of N_2. As the O_2 level is increased to excess O_2 conditions, more of the intensity shifts into the 2 to 3 μm bands until the relative contributions of the 3 to 4 μm bands and the continuum are barely discernible. Thus, in general, the SWIR spectral distribution is markedly different than in N_2/Ar, favoring shorter-wavelength features near 2 to 2.5 μm. These features show a pronounced increase in intensity with increasing O_2. By comparison, previous experiments with Ar/O_2 showed only Ar lines in this spectral region, with intensities decreasing with increasing O_2. Since the Ar lines are even more strongly "quenched" in N_2, it is not likely that there are any prominent Ar lines in the $N_2/O_2/Ar$ spectra. We plan to analyze these data together with the N_2/Ar data to identify these transitions.

MWIR spectra were taken between 4 and 8 μm for excess N_2 and excess O_2 conditions. A representative excess-N_2 spectrum (low resolution, 0.04 μm) is shown in Figure 27 for the lowest O_2 flow rate (10 std cm^3/min). The prominent negative-going feature near 4.5 μm appears to be N_2O emission which is 180° out of phase with the rest of the radiating species; we will examine this point further below. The NO fundamental band arises near 5.3 μm and extends to longer wavelengths. Indeed, the "tail" of this band appears to persist all the way to nearly 8 μm in this particular spectrum. $NO(v)$ is undoubtedly formed in the discharge by reaction of $N(^2D)$ with O_2 and is relaxed to a steady-state distribution by a variety of collisional processes. The spectral distribution shown here is strongly peaked to low v, but exhibits bimodal behavior at middle v (~ 6 μm), and the extended "tail" is indicative of population of higher vibrational levels than are commonly observed in more
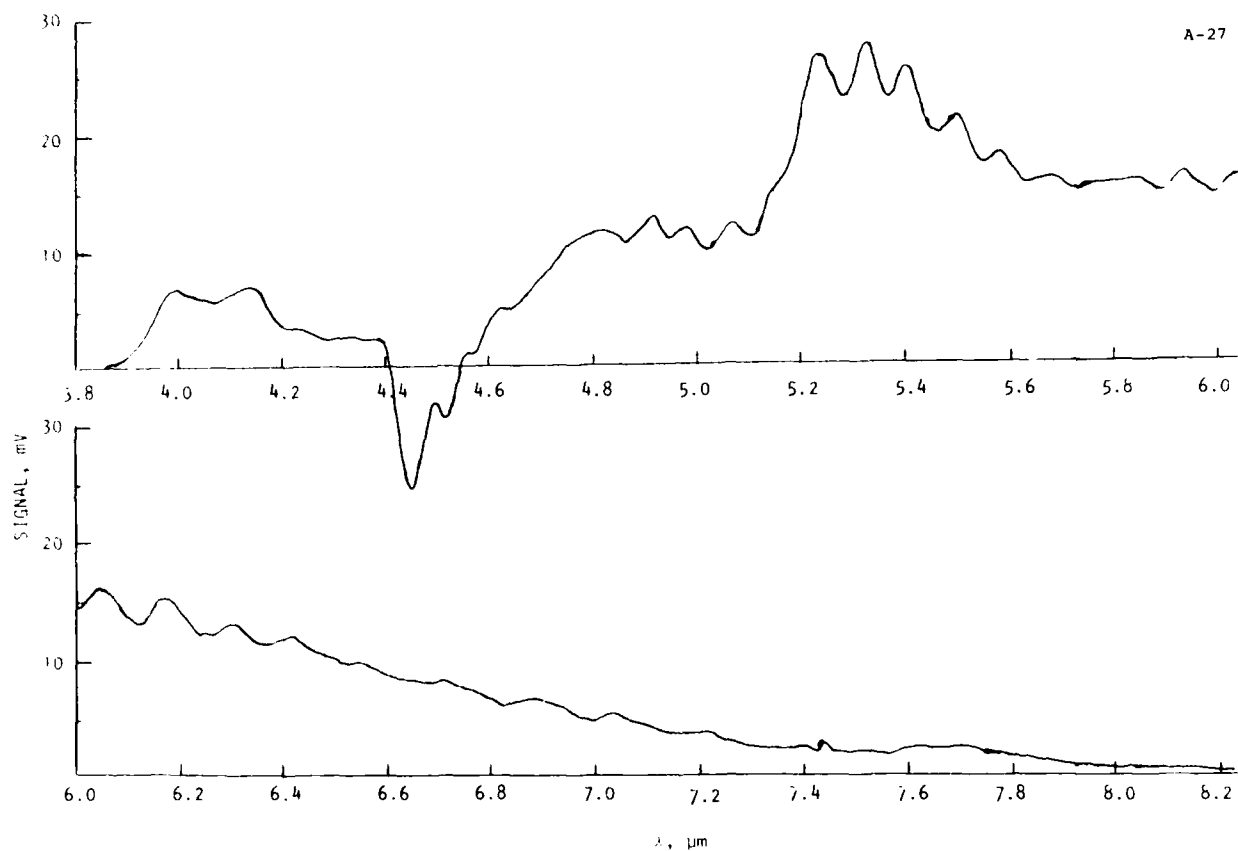
Figure 27. MWIR Signature for Discharged N_2/O_2 Ar Mixture, Excess N_2. Experimental conditions are as follows: $N_2/O_2/Ar$ = 0.2/0.010/3.7 std ℓ/min, T = 80 K, P = 1.3 torr, resolution = 0.04 μm (Expt. 312405)

2-51

conventional COCHISE experiments. Of course, contributions from underlying radiators cannot yet be ruled out, but other excitation sources for NO(v) are suggested by these data.

The band near 4 μm appears to be due in part to the (4-2) band of the Wu-Benesch (W-B) system of N_2; however, the origin of the emission between 4 and 4.5 μm is not yet known. Some of the emission near 4.7 to 5 μm could be due to the O_3 ($\nu_1 + \nu_3$) combination band and its hot bands. The sharp bands near 5 μm are the same as those previously observed in the interaction of dis-charged N_2/Ar with O_2, but we do not yet know their identity conclusively.

In excess fixed N_2 (0.2 std ℓ/min), as the O_2 flow rate increases from 10 to 200 std cm^3/min, the intensities of all the bands decrease except for that of the out-of-phase N_2O feature, which passes through a maximum near the 1 percent O_2 level. This latter behavior is similar to that of O_3(v ≥ 2) as observed in the O_2/Ar discharge experiments. If this trend is supported in future experiments, it could implicate O_3(v ≥ 2) as a percursor of the observed N_2O(v). The decrease in intensity of the other features with increasing O_2 could be due to collisional deactivation by O_2, O, and/or O_3, as well as to colder electron energy distributions in the discharge.

For a fixed O_2 flow rate of ~0.1 std ℓ/min, N_2 flow rates were varied from 10 to 400 std cm^3/min at nominal temperatures of 60 K. In the fixed-O_2 case, the intensities of all spectral features decrease uniformly with decreasing N_2 flow rate. The general spectral distribution is similar to that of the fixed-N_2 spectra, except for some slight variations observed at the lowest N_2 flow rate as shown in Figure 28. Here the N_2O feature is no longer observable, and the NO band exhibits a secondary maximum near 6.5 μm. It remains to be determined whether this feature arises from another NO(v) excitation reaction (perhaps N(^{2}P) + O_2?) or from vibrationally excited NO_2 formed in the discharge.

At the highest N_2 flow rates, the S/N was high enough to permit high resolution scans of the N_2O band. Such a scan is shown in Figure 29 for
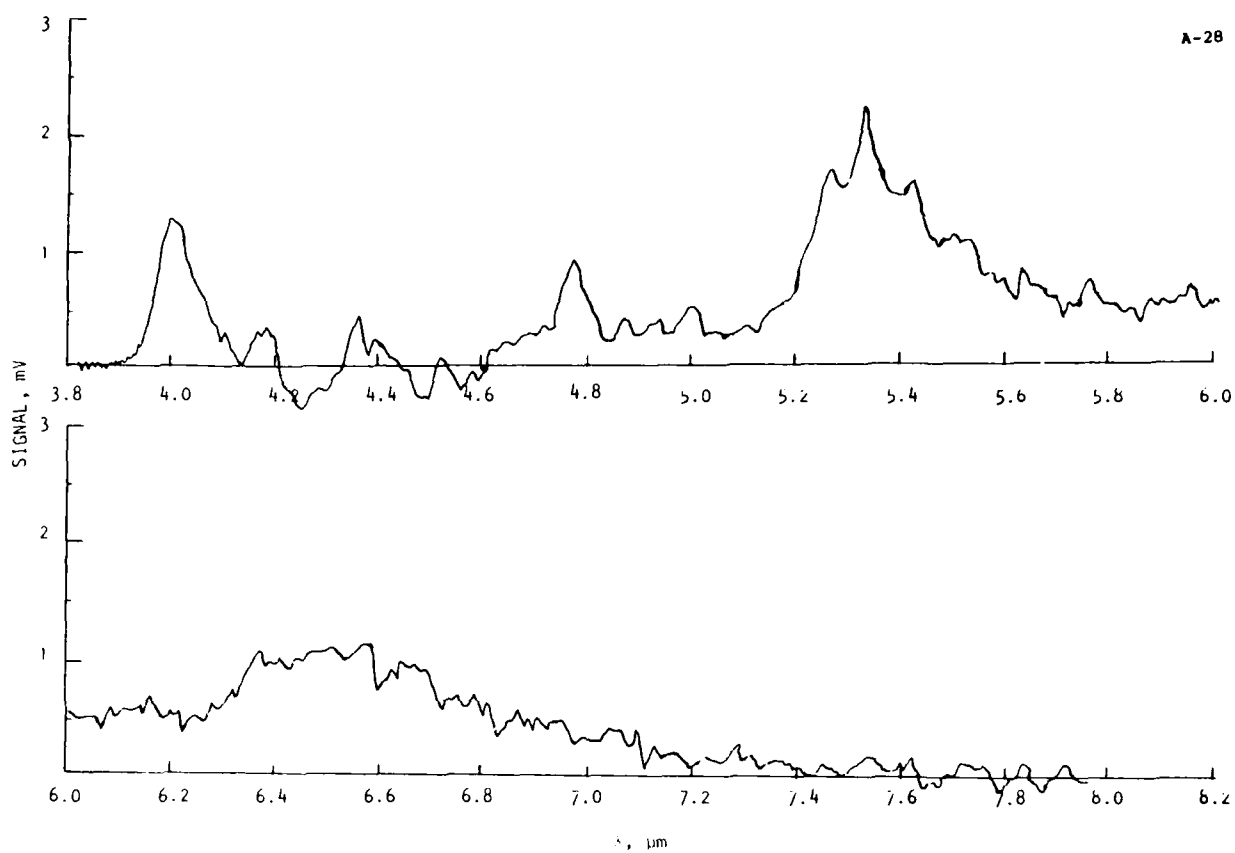
Figure 28.   MWIR Signature of Discharged $N_2/O_2/Ar$ Mixture, Excess O_2.
Experimental conditions are as follows: $N_2/O_2/Ar$ =
0.010/0.1/3.7 std ℓ/min, T = 80 K, P = 1.5 torr,
resolution = 0.04 μm (Expt. 312422)

2-53
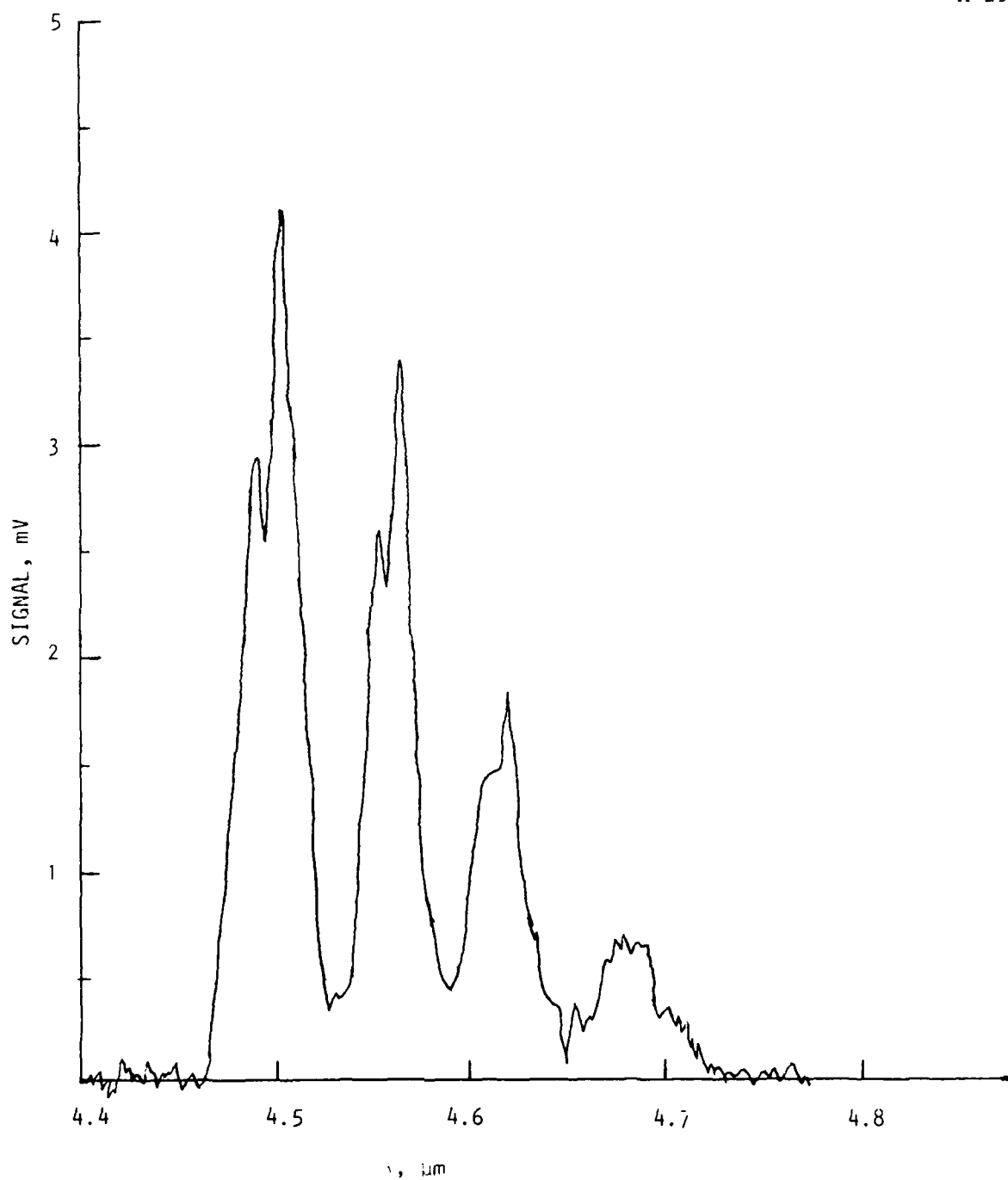
Figure 29. High Resolution Scan of Out-of-Phase Emission from $N_2O(\nu_3)$. $N_2/O_2/Ar = 0.4/0.1/3.7$ std ℓ/min, T = 80 K, P = 1.5 torr, resolution = 0.0067 μm or 3.3 cm^{-1} (Expt. 312424)

0.5 mm slits (0.007 μm resolution). The system consists of four distinct bands, each of which appears to be a vibration-rotation band of the $N_2O(\nu_3)$ mode. Preliminary inspection of the raw data gives $\omega_3^0 = 2226 \pm 3$ cm^{-1}, $x_{33} = 15 \pm 1$ cm^{-1}, in excellent agreement with the values for N_2O used in the AFGL line parameters compilation (2223.76 cm^{-1}, 15.06 cm^{-1}). *The narrowness of the bands suggests a very low rotational temperature; however, since the rotational constant for N_2O is only ~0.42 cm^{-1}, this conclusion cannot be stated with certainty until we perform a spectral fitting analysis.*

When the sidearm temperature was elevated to 120 K, part of the N_2O emission became in phase with the NO emission. This is demonstrated in Figure 30 by comparison of spectra obtained for the same flow conditions at 80 K and 120 K. Emission from the lowest vibrational level is in phase with NO at 120 K, but emission from the higher levels is not, resulting in a peculiar composite positive-and negative-going spectrum for N_2O. If the excited N_2O were being formed by reactions occurring in the active discharge, we would expect to see the N_2O fluorescence roughly in phase with the NO and N_2 emissions. When the N_2O emission is out of phase, this means that most of the fluorescence seen by the detector occurs after the discharges are off, i.e., in the absence of discharge-excited species. In other words, the out-of-phase N_2O emission arises from a slug of undissociated gas. It is difficult to account for this phenomenon. However, the 120 K results suggest that, in the lower temperature experiments, transport of N_2O out of the discharge tubes may be impeded by condensation of discharge-produced N_2O on the walls. (The vapor pressure of N_2O is 10^{-6} torr at 80 K and 0.1 torr at 118 K). Thus, in the 80 K experiments, discharge-produced N_2O would condense and accumulate in the sidearms, exerting its equilibrium vapor pressure. The small amount of N_2O vapor may be destroyed in the active discharge, such that gas phase N_2O only escapes into the viewing region during the period when the discharges are off. It is fascinating to consider that the N_2O appears to retain considerable vibrational excitation in this process. Clearly, these experiments should be repeated at elevated temperatures, 120 to 150 K, and a systematic study of temperature dependence is required. In any case, it is clear that N_2O is indeed formed in discharge-excited mixtures of N_2, O_2, and Ar.
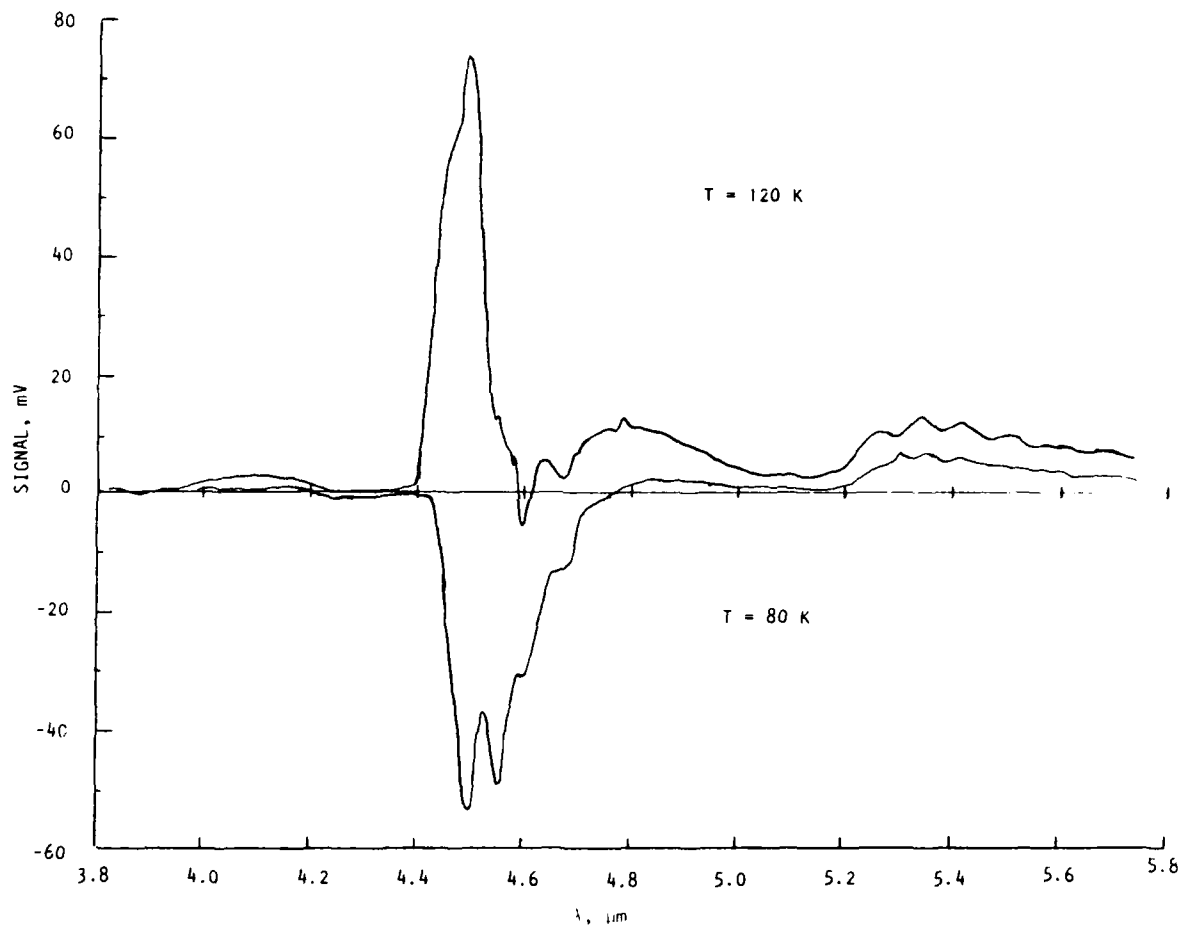
Figure 30.   Reversal of $N_2O(\nu_3)$ Phasing with Temperature.
$N_2/O_2/Ar$ = 0.4/0.1/3.7 std ℓ/min,
P = 1.7 torr, resolution = 0.04 μm
(Expts. 312426, 312423)

Identification of the processes responsible for this will be pursued in further investigations.

In summary, we have performed a series of scoping experiments to examine the IR signatures of discharged $N_2/O_2/Ar$ mixtures under a variety of conditions. Band systems of N_2 and NO are observed, but with significantly different spectral distributions than observed in previous experiments employing N_2/Ar discharges and O_2 counterflows. In addition, emission from the ν_3 and, in some cases, ν_1 bands of N_2O are also observed; however, these data are clouded because the sidearm temperature was too low. It appears that systematic variation of N_2 and O_2 flow rates can be employed to probe the kinetics of the N_2O formation processes. Further experiments should be performed at temperatures above 120 K and with the highest possible resolution, over the same ranges of flow rates employed here. In the meantime, the present data base should be subjected to spectral fitting analysis for quantitative comparisons to previous N_2/Ar discharge work.

2.4 Conclusions: Further Studies

We have reviewed a recently acquired, preliminary data base on chemi-excitation of $NO(v)$, $CO(v)$, and $N_2O(v)$. Examination of these data has suggested a great deal of further experimentation which is needed to address the various problem areas as well as to provide the final data base. We list these as follows:

(1) NO fundamental/overtone measurements

(a) Fundamental band: more exhaustive data on N_2 variations; more detailed characterization of unknown 5 μm bands for spectral subtraction (use lower resolution, compare to spectral simulations); correct for impurity $NO(v)$.

(b) Overtone band: use highest possible N_2 flows, subtract N_2^* background; obtain at least five matched overtone and fundamental spectra, all at the same conditions, for good statistics.

(c) Blackbody calibration: test with two-temperature ratio method; extend to shorter wavelengths by using wider slits, no filter.

2-57

(2) N_2^* SWIR fluorescence

   (a) Obtain more data at low N_2, use highest possible resolution

   (b) Analyze by spectral simulation/fitting

   (c) Examine state redistribution as function of discharge conditions, relate to FAKIR observations

   (d) Potential for measurements of transition branching ratios

(3) Excitation of CO

   (a) Unidentified bands: survey shorter wavelengths for related transitions; use spectral simulations; search literature for possible radiators and related kinetics.

   (b) CO(v) excitation mechanisms: direct comparison of AC and CW discharge experiments; more extensive study of N_2, CO dependencies; temperature dependence; recalibrate flowmeter for CO (potential titration for $[N(^2D)]$).

(4) Formation of $N_2O(v)$: examine 4.5 μm signature as function of N_2 and O_2 flows in $N_2/O_2/Ar$ discharges; shorten discharge tubes to cut down interference from ArI lines.

2.5 References

1. Kennealy, J.P., DelGreco, F.P., Caledonia, G.E., and Green, B.D., "Nitric Oxide Chemi-excitation Occurring in the Reaction Between Metastable Nitrogen Atoms and Oxygen Molecules," J. Chem. Phys. __69__, 1574 (1978).

2. Rawlins, W.T., Piper, L.G., Green, B.D., Wilemski, G., Goela, J.S., and Caledonia, G.E., "LABCEDE and COCHISE Analysis II. Volume I. Final Report." Physical Sciences Inc. TR-207A, February 1980.

3. Rawlins, W.T., Piper, L.G., Caledonia, G.E., and Green, B.D., "Final Technical Report: COCHISE Research," Physical Sciences Inc. TR-298, September 1981.

4. Billingsley, F.P., "Calculated Vibration Rotation Intensities for $NO(X^2\pi)$," J. Molec. Spectrosc. __61__, 53 (1976).

5. Green, B.D., Caledonia, G.E., and Murphy, R.E., "A Determination of the Nitric Oxide Einstein Coefficient Ratios," J. Quant. Spectrosc. Radiat. Transfer __26__, 215 (1981). AFGL-TR-81-0263 ADA104749.

6. Piper, L.G. and Rawlins, W.T., "COCHISE Atmospheric Nitrogen/Oxygen Excitation Studies: Studies on Metastable Nitrogen Atoms." Physical Sciences Inc. TR-411, September 1983.

7. Rawlins, W.T. and Gelb, A., "COCHISE Atmospheric Nitrogen/Oxygen Excitation Studies: COCHISE Observations of Ar Rydberg Emission from 2 to 16 µm," Physical Sciences Inc. TR-383, March 1983.

8. Biemont, E. and Grevesse, N., "Infrared Wavelengths and Transition Probabilities for Atoms, $3 \leqslant z \leqslant 20$," Atomic Data and Nuclear Data Tables 12, 217 (1973).

9. Caledonia, G.E., Green, B.D., and Simons, G.A., "LABCEDE and COCHISE Analysis. Volume I. Final Report," Physical Sciences Inc. TR-83, February 1977.

10. Stair, A.T., Jr., Kennealy, J.P., and Murphy, R.E., "A Study of Some Inelastic Collision Processes using Active Nitrogen and Carbon Monoxide," J. Chim. Physique 1, 52 (1967).

11. Donovan, R.J. and Husain, D., "Recent Advances in the Chemistry of Electronically Excited Atoms," Chem. Rev. 70, 489 (1970).

12. Krupenie, P.H., "The Band Spectrum of Carbon Monoxide," NSRDS-NBS 5, 1966.

13. Zipf, E.C. and Prasad, S.S., "Production of Nitrous Oxide in the Auroral D and E Regions," Nature 287, 525 (1980); Zipf, E. C., "On the Formation of Nitrous Oxide by the Reaction Between N_2 and Excited OH Radicals," Nature, to be published.

14. Rawlins, W.T., Caledonia, G.E., and Kennealy, J.P., "Observation of Spectrally Resolved Infrared Chemiluminescence from Vibrationally Excited $O_3(\nu_3)$," J. Geophys. Res. 86, 5247 (1981).

15. Green, B.D., Rawlins, W.T., and Caledonia, G.E., "Atmospheric Radiation Infrared Signature Analysis," Physical Sciences Inc. TR-366, June 1983.

16. McClatchey, R.A., Benedict, W.S., Clough, S.A., Burch, D.E., Calfee, R.E., Fox, K., Rothman, L.S., and Garing, J.S., "AFCRL Atmospheric Absorption Line Parameters Compilation," AFCRL-TR-73-0096, Jan. 1973. AD762904.

3. KINETICS OF EXCITED NITROGEN ATOMS AND MOLECULES

3.1 Introduction

Metastable nitrogen atoms, $N(^2D, ^2P)$, play an important role in the chemistry of disturbed atmospheres. $N(^2D)$ through its reaction with molecular oxygen,

$$N(^2D) + O_2 \rightarrow NO(v) + O \qquad (1)$$

is an important precursor for producing vibrationally excited nitric oxide in the upper atmosphere. Both the rate coefficient for removal of $N(^2D)$ by O_2[1] and the relative distribution of $NO(v>1)$ produced from reaction (1) are fairly well established.[2] What is not known is the absolute rate coefficient for producing $NO(v)$ from the reaction, i.e. the branching fraction into $v=0$.

In addition to understanding fully the product side of reaction (1) one must also understand whether or not $N(^2D)$ is quenched significantly by atomic oxygen before the total importance of reaction (1) in producing vibrationally excited nitric oxide in the upper atmosphere can be assessed.[3] Two laboratory measurements[1,4] seem to indicate that the rate coefficient for reaction (2),

$$N(^2D) + O \rightarrow N(^4S) + O \qquad (2)$$
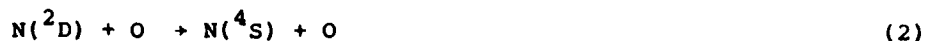
is about 2×10^{-12} cm^3 molecule^{-1} s^{-1}. Aeronomic predictions, however, favor a value which is much lower, and because both the laboratory measurements were plagued with various uncertainties, this issue is far from settled.

We have begun to do some experiments on the FAKIR apparatus to try to address the above two issues. One approach to the issue of the absolute rate coefficients for $NO(v)$ formation from reaction (1) would be to repeat the classic COCHISE measurement on the $NO(v)$ distribution from reaction (1) with a

simultaneous measurement of the absolute $N(^2D)$ number density in the reaction volume. Several years ago[5] we designed a VUV absorption lamp to fit into COCHISE which would measure $N(^2D)$ number densities. We have recently begun to try to measure the yield of atomic oxygen from reactions (3) plus (4)

$$N(^2D) + CO_2 \rightarrow CO + NO \qquad (3)$$

$$N(^4S) + NO \rightarrow O + N_2 \qquad (4)$$

By comparing these yields with absorption measurements of $N(^2D)$ number densities, we hope to obtain an absolute calibration of the VUV resonance lamp. Some of our previous publications have detailed the necessity for establishing absolute calibrations of VUV resonance lamps which use microwave discharge excitation.[5]

We have also begun a series of experiments aimed at determining the rate coefficient for reaction (2). Our preliminary results are in rough accord with the previous laboratory measurements, but need significant further refinement. Our basic approach is to try as many different sources of atomic oxygen as possible, hoping to obtain congruent results from all, and thereby demonstrate that difficult-to-detect species which may accompany some of the sources, such as $O_2(a^1\Delta)$, are not a factor in the measurements.

To support these measurements, we found it necessary to determine accurate values of the rate coefficients for the reaction of $N(^2D)$ with a number of atmospheric species including, CO, CO_2, N_2O, O_2 and H_2. Thus during the course of this program we developed a sensitive VUV resonance fluorescence diagnostic and added a moveable injector to our flow reactor. These improvements give us state-of-the-art facilities for studying $N(^2D)$ kinetics.

The following sections: describe the apparatus; discuss the lamp absorption measurements; and give results of some preliminary measurements using a

resonance fluorescence technique of $N(^2D)$ quenching-rate coefficients by several quenchers including atomic oxygen.

3.2 Experimental

The apparatus is a modification of one we have used previously in a number of other studies.[6-10] It consists of a two-inch flow tube pumped by a Leybold-Heraeus Roots blower/forepump combination capable of producing linear velocities up to 5×10^3 cm s^{-1} at pressures of one torr. The flow-tube design is modular (see Fig. 31), with separate source, reaction, and detection sections which clamp together with O-ring joints. The detection region is a rectangular stainless-steel block bored out internally to a two-inch circular cross section and coated with Teflon® (Dupont Poly TFE #852-201) to retard surface recombination of atoms.[11] The surface was primed with black primer prior to the Teflon® coating to reduce scattered light inside the block. Two sets of viewing positions consisting of circular ports on each of the four faces of the block are separated by a distance of 7.5 cm. The circular ports, all of which contain MgF$_2$ windows, accommodate vacuum ultraviolet resonance lamps, VUV and visible monochromator interfaces, laser delivery side-arms and a spatially filtered photomultiplier/interference filter combination.

The upstream observation position is fitted with two microwave-discharge resonance lamps placed normal to each other, and a 0.2 m vacuum ultraviolet monochromator (Minuteman 302 VM) diametrically opposite one of the resonance lamps. The lamp which is viewed by the monochromator is used in absorption studies, while the lamp normal to the monochromator's optical axis is used to excite resonance fluorescence of atomic species formed in the flow reactor. The lamps and the monochromator are separated from the flow tube by 25 mm diameter MgF$_2$ windows which have a short wavelength cutoff of 115 nm. In addition, a MgF$_2$ lens in the optical train of the monochromator collects light from the flow tube.

A schematic showing the resonance lamps and detection cell is given in Fig. 32. The lamps are constructed from 13 mm (o.d.), medium-wall Pyrex® tubing. He or Ar flow through each lamp at rates of ~ 150 μmol s^{-1} and total
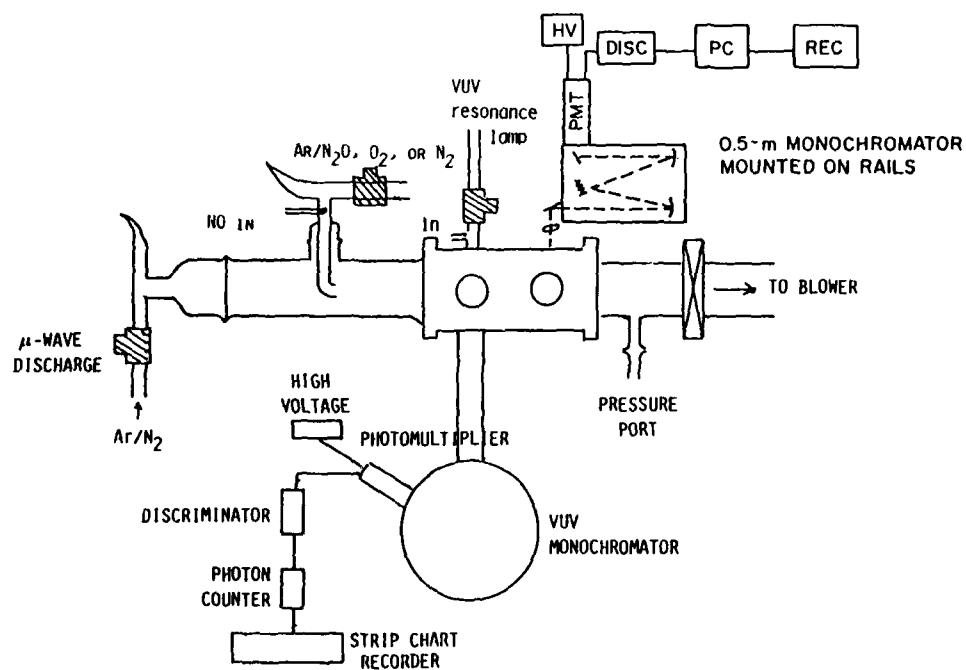
Figure 31. Apparatus for N* (^{2}D, ^{2}P) studies.
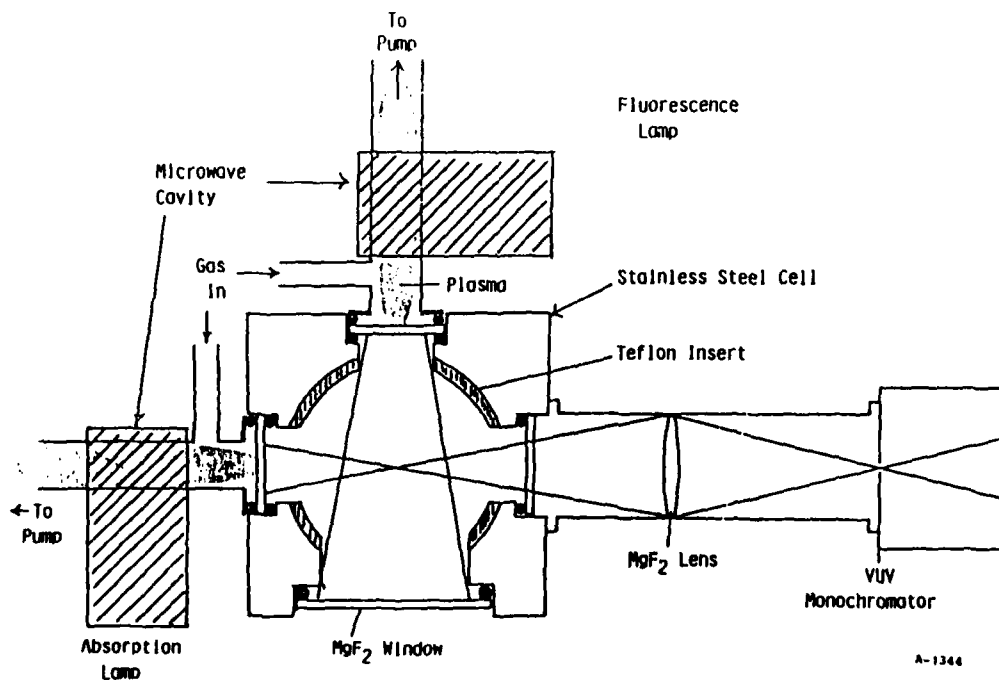
Figure 32. Cross sectional view of the absorption/fluorescence cell showing
the placement of the lamps. The direction of the flow in the
reactor is perpendicular to the figure.

pressures of ~ 1.5 torr. The discharge plasmas are excited by Evenson[12] cavities powered by 2.45 GHz supplies (Raytheon PGM-10) operating at a power of about 20 W for the absorption lamp and 50 W for the resonance-fluorescence lamp. The gas flow enters the lamp near the window and passes from front to back. This procedure inhibits the buildup of pockets of absorbing atoms between the emitting region and the exit window. Occasionally, controlled amounts of air are added to the lamp to enhance nitrogen emissions, but usually the impurity level of N_2 (i.e., a few ppm) in the He and Ar bath gases is sufficient to give intense but optically thin multiplets at 149 and 174 nm. The absence of self-absorption is determined spectrally by confirming that the observed intra-multiplet line ratios are consistent with those predicted from spin-orbit sum rules.[13] Instability in the emission intensity, due to long-term variations in the lamp cooling rate and thereby in the steady-state operating temperature of the lamp (typically 500-600 K), is minimized by regulating the flow of cooling air to the cavity.

Atomic nitrogen metastables are made in the flow tube by discharging mixtures of nitrogen and either argon or helium in a McCarroll[14] cavity powered by another Raytheon 2.45 GHz supply. Molecular nitrogen is moderately efficient at quenching the atomic metastables $(k_{N(^2D) + N_2} = 1.6 \times 10^{-14}$ cm^3 molecule^{-1} s^{-1}),[13,15] so that the best metastable yields come from fairly dilute mixitures of N_2 in Ar or He, typically < 1% N_2.

Quenchers or titration reagents are injected into the flow tube through fixed or a moveable injectors. The fixed injectors are a one-inch diameter loop constructed from 2 mm o.d. polyethylene tubing, with numerous small holes around both the inside and outside surfaces of the loop, and several hook-shaped injectors whose outlet orifices are coaxial with the main flow tube. Atomic oxygen for quenching measurements is made up-stream in one of the hook injectors by discharging Ar/N_2O or Ar/O_2 mixtures or by titrating N-atoms with NO in the injector with N-atoms being made further upstream in an Ar/N_2 discharge. NO formation from the Ar/N_2O discharge is eliminated by using large flows of argon (≈600 μ moles^{-1}) and relatively high discharge powers

($\simeq$ 70 W). We have characterized this source of atomic oxygen in a previous report.[16]

The moveable injector consists of a 0.25 inch diameter length of stain- less steel with a teflon loop epoxied into its downstream end. The loop is slightly more than an inch in diameter and is set on the stainless steel tube so that it is concentric with the flow reactor. A number of small holes have been drilled around both the inside and outside of the loop to allow reagent gas to escape into the gas stream, and the quality of mixing was checked by observing the air afterglow when NO was added through the loop injector to a flow containing O-atoms. The 0.25 inch stainless tube slides along the bottom of the flow reactor, and exits it through a Swagelok® fitting in the end flange of the flow reactor. The Swagelok® fitting has been slightly modified for this purpose by boring it out completely to accept the tube, using a double o-ring seal in place of the front ferrule, and by reversing the rear ferrule. The zero of the scale relating the distance between the injector and the detection region was calibrated by measuring the point at which the scat- tered light from the resonance fluorescence lamp suddenly increased as the injector was moved into the detection region.

Mass-flow meters monitor the flow rates of argon or helium and nitrogen, rotameters measure those of quenching reagents and of argon through the O-atom discharge, and measurement of the rate of increase in pressure with time in a calibrated volume determines the flow rate of nitric oxide which was needed to calibrate an O-atom resonance lamp and to measure O-atom yields from the Ar/O_2 or Ar/N_2O reagent discharges. All flow meters were calibrated by measuring rates of increase of pressure with time into 6.5 or 12 ℓ flasks, using appro- priate differential pressures transducers (Validyne DP-15) which had them- selves been calibrated with silicon oil or mercury manometers. Typically the flow rates for argon or helium, nitrogen, and quencher were 2000-5000, 50, and 0-120 $\mu mole\ s^{-1}$, respectively. The total pressure was generally 1-3 torr, and the flow velocity was 1000-3500 $cm\ s^{-1}$.

3-6

The argon or helium and the nitrogen flow through molecular-sieve traps to remove water and carbon dioxide prior to entry into the flow reactor, while the argon through the injector flowed straight from the cylinder. Most experiments used quenchers, N_2O, CO_2, or O_2, straight from their cylinders without further purification.

Nitric oxide was purified by flowing it slowly at atmospheric pressure and room temperature through an Ascarite® trap, then through a trap immersed in a liquid nitrogen/methanol slush bath (175K). It was stored in a 5 ℓ bulb. Final nitric oxide purification involved several freeze, pump, thaw cycles of the gas in the storage bulb. The Ascarite® trap previously had been baked overnight under vacuum.

Some spectral observations were made in the visible/near UV using a 0.5 m monochromator equipped with a thermoelectrically cooled photomultiplier having an S-20 response. A photon-counting rate meter monitored the output of the photomultiplier. VUV observations also employed the photon-counting rate meter, or in some cases, a scaler counted individual photons. Since the dark count of the VUV solar blind PMT was about 0.4 Hz, count rates well below 10 Hz could be determined with reasonable precision. When pulse counting, the procedure generally was to average 4-10 sets of 10 second counts.

Atomic-oxygen number densities produced from reactions (3) plus (4) in the lamp calibration experiments were measured using resonance absorption at 130 nm. The absorption diagnostic was calibrated by adding NO to excess N and then equating the O produced with the NO consumed. This diagnostic lacks sufficient sensitivity to be used accurately at O-atom number densities above 10^{13} atoms cm^{-3} which are required for measurements of reaction (2). For those experiments atomic oxygen number densities were determined by measuring the intensity of the O/NO air afterglow when known amounts of NO were added to the reactor with the main Ar (or He)/N_2 discharge turned off.[7,16-18] The filtered photomultiplier at the second observation position detected this light. We have described elsewhere in great detail how we calibrate and use this diagnostic to monitor O-atom number densities.[7,16,18]

3-7

3.3 $N(^2D, ^2P)$ Kinetics

3.3.1 Production of Atomic Oxygen in the Reaction Between $N(^2D)$ and CO_2

The basic concept behind these measurements is straightforward: one wants to relate the atomic oxygen produced in reactions (3) plus (4) to measurements of the $N(^2D)$ fractional absorption in order to determine an effective temperature for the emission line in the $N(^2D)$ lamp. The data are complicated to interpret, however, because even in the absence of added O_2, $N(^2D)$ is removed from the system by diffusion to the reactor walls. The $N(^2D)$ absorption measurements, therefore, determine the $N(^2D)$ number density at the observation point, whereas the atomic oxygen measurements relate to $N(^2D)$ number densities between the injector and the observation position. Atomic oxygen is essentially unperturbed by collisions with reactor walls. We have modeled the reaction system to analyze our data and thereby correct for the diffusive losses of $N(^2D)$.

The differential equation for the loss of $N(^2D)$ in the reactor is

$$\frac{\bar{v}d[N(^2D)]}{dz} = -0.62 \left\{ \frac{D_o}{\Lambda^2_P} + k_3 [CO_2] \right\} [N(^2D)] \tag{5}$$

where

- D_o is the diffusion coefficient of $N(^2D)$ in Ar or He buffer,
- Λ is the characteristic diffusion length $(r/2.405)^2$,
- z is the distance from the injector to the detector,
- $\bar{v}$ is the bulk flow velocity, and the factor 0.62 corrects for the coupling of a radial density gradient in $N(^2D)$ with a radial velocity profile.

Because the added CO_2 is in great excess compared to the $N(^2D)$ in the reactor, pseudo first-order conditions prevail and Eq. (24) has the solution

$$[N(^2D)] = [N(^2D)]^\circ e^{-0.62\left(\frac{D_o}{\Lambda^2 P} + k_3[CO_2]\right)z/\bar{v}}$$
(6)

The differential equation for the production of atomic oxygen in reactions (3)
plus (4) is

$$\frac{d[O]}{dt} = k_3[CO_2][N(^2D)] \quad .$$
(7)

The formation of O from $N(^4S)$ and CO_2 is negligibly small under our condi-
tions,[19] as is the loss of O in wall recombination.[20] Using Eq. (6) for
$[N(^2D)]$ we can solve Eq. (7) to get

$$[O] = \frac{[N(^2D)]^\circ}{1+k_D/k_3[CO_2]} \left\{ 1 - e^{-0.62\,(k_D + k_3[CO_2])z/\bar{v}} \right\}$$

where

$$k_D = \frac{D_o}{\Lambda^2 P}$$

We can use Eq. (25) in the absence of added CO_2 to determine $[N(^2D)]^\circ$ at the
injector in terms of the number density at the detector, $[N(^2D)]^\circ_{obs}$. The
ratio of $[O]/[N(^2D)]^\circ_{obs}$ is then

$$\frac{[O]}{[N(^2D)]^\circ_{obs}} = \frac{e^{0.62\,k_D z/\bar{v}}}{1 + k_D/k_3[CO_2]} \left\{ 1 - e^{-0.62(k_D + k_3[CO_2])z/\bar{v}} \right\}$$
(9)

We wrote a computer program to generate values of the ratio $[O]/[N(^2D)]^\circ_{obs}$
a function of $[CO_2]$ for the various sets of experimental conditions in our
reactor and using $D_o(Ar) = 240$ cm^2 s^{-1} torr^{-1},[13] $D_o(He) = 750$ cm^2 s^{-1}
torr^{-1},[13] and $k_3 = 3.6 \times 10^{-13}$ cm^3 molecule^{-1} s^{-1} (see below). Figure 3
compares model predictions with observations for two cases.

3-9
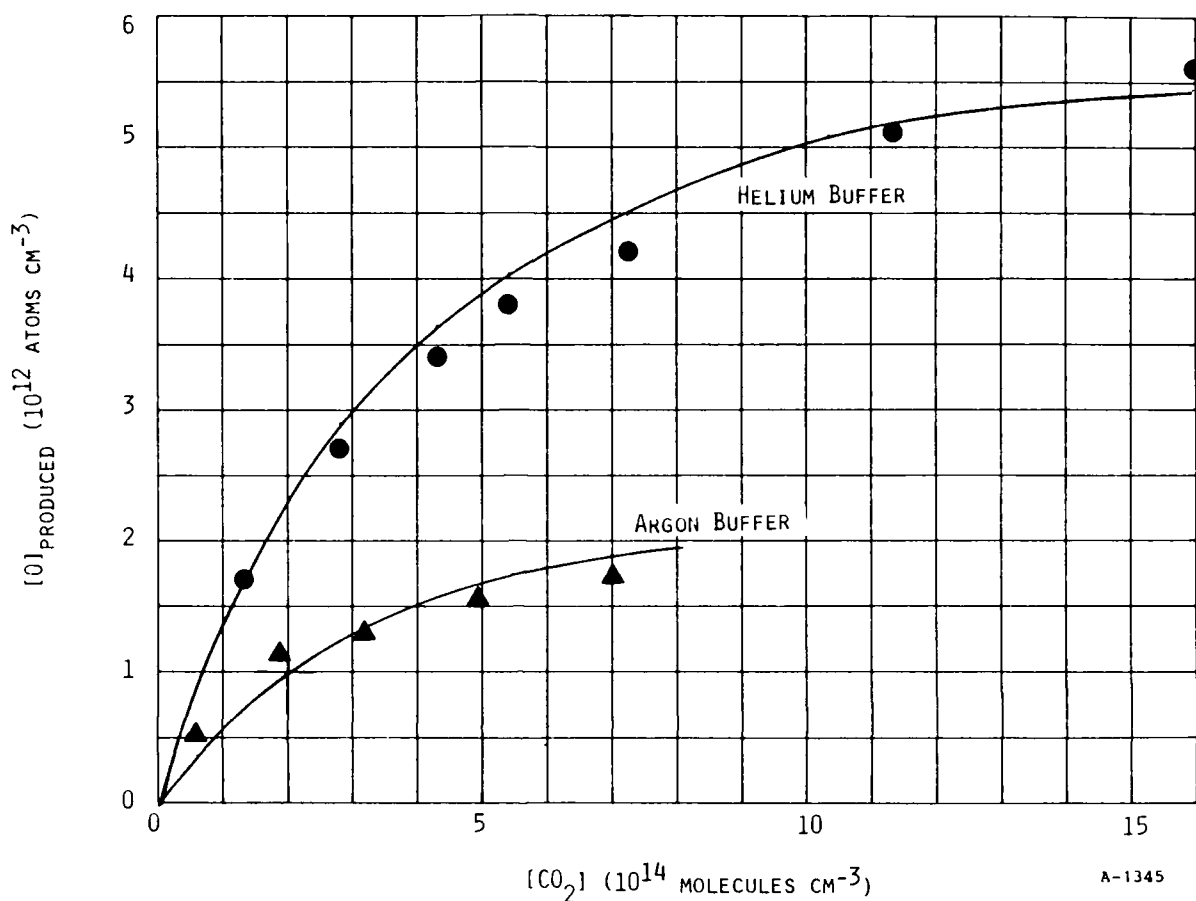
Figure 33. The production of atomic oxygen from excited nitrogen plus CO_2. The lines through the data points are from the kinetic model described by Eq. (28).

The absolute $N(^2D)$ number density at the detector is given by the ratio of the measured atomic-oxygen number densities to the ratio $[O]/[N(^2D)]°_{obs}$ calculated from Eq. (28). This absolute $[N(^2D)]°_{obs}$ can then be compared to various lamp models to extract an effective temperature for the $N(^2D)$ absorption multiplet.

Relative metastable nitrogen number densities are given by the relation $[N(^2D)]_{rel} = \ell n(1/(1-A))$ where A is the fractional absorption of the 149 nm resonance multiplet. This expression is a Beer's law analogue which we

have shown previously to apply to our conditions.[18] The results of the fitting indicate that $[N(^2D)]_{rel} = 1.0$ corresponds to absolute number densities of 6.5 and 9 x 10^{12} atoms cm^{-3} for runs in helium and argon buffer respectively. These data translate to effective lamp temperatures of 6,000 and 13,000 K determined from runs in helium and argon buffer respectively.

We have several good reasons to believe that the temperature in the resonance lamp using a helium buffer is actually more like the 500-600 K ambient temperature in the discharge.[5] If the lamp temperature is as suspected, then the experimental data imply that roughly 2.7 and 3.7 atoms of oxygen are produced per atom of $N(^2D)$ consumed in the helium and argon buffer experiments respectively. The only way that excess oxygen atoms can be produced is for there to be other energy carriers in the discharged Ar/N_2 or He/N_2 mixtures. Figures 34 and 35 show that this is undoubtedly the case. These figures show spectra of the nitrogen first-positive bands downstream from an Ar/N_2 discharge. The spectral distribution in Fig. 34 is what one expects to see when the first-positive emission is produced by nitrogen-atom recombination. Figure 35 which was taken at a much shorter delay time between the discharge and the observation region, shows a much different spectral distribution.

This spectrum was taken 9 ms downstream of the discharge, so the emission cannot result from $N_2(B^3\Pi_g)$ excited in the discharge and then carried downstream because the $N_2(B)$ state has a lifetime of only about 8 μs. Thus the spectrum must be excited by some metastable energy carrier in the gas flow which can be collisionally converted to $N_2(B)$. The metastable species in question is <u>not</u> $N_2(A^3\Sigma_u^+)$ because the ground-state atomic-nitrogen number density is so great as to quench $N_2(A)$ to an insignificant level in the 9 ms transit time from the discharge to the observation region.[21] <u>The identity of this $N_2(B)$ precursor could have important atmospheric implications and should be pursued further</u>.

Three other experiments also show there must be additional energy carriers in the discharge effluent. Two runs in argon buffer with only one third of the transit time from the discharge to the injector as compared to the other argon runs gave a value of 14 x 10^{12} atoms cm^{-3} for unit $[N(^2D)]_{rel}$
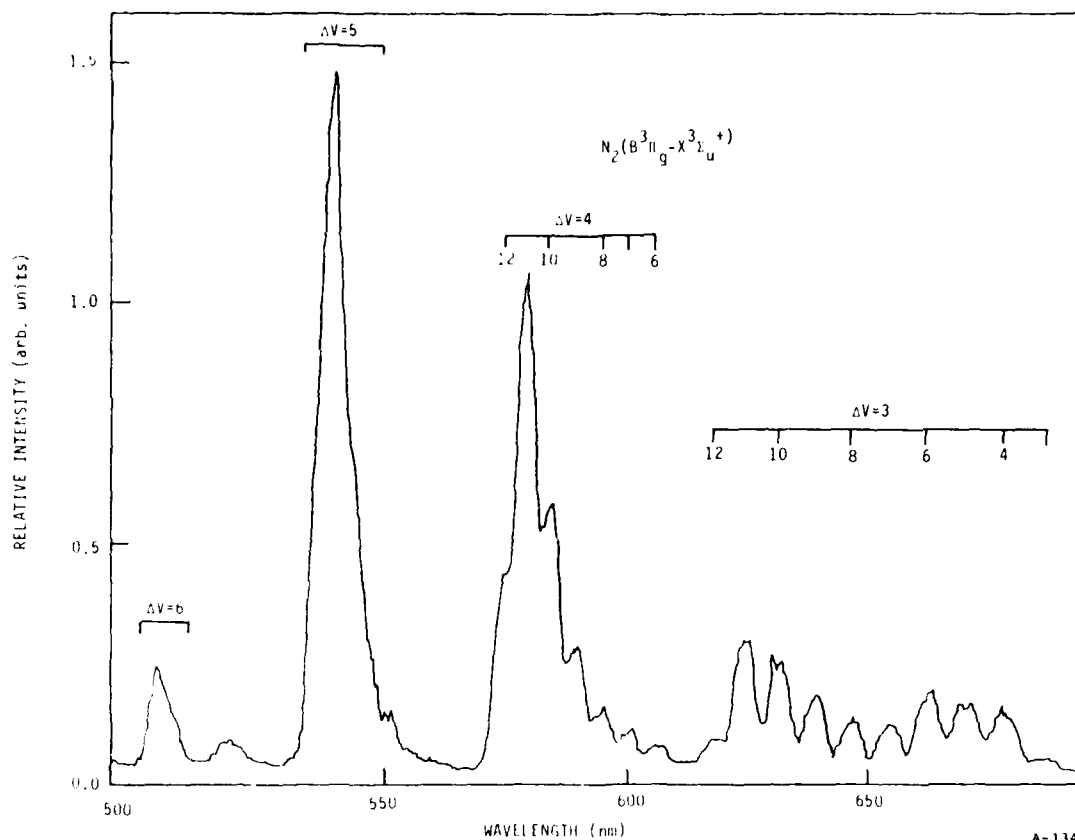
Figure 34. Nitrogen first-positive emission, $N_2(B\ ^3\Pi_g - A\ ^3\Sigma_u^+)$, excited by N-atom recombination.
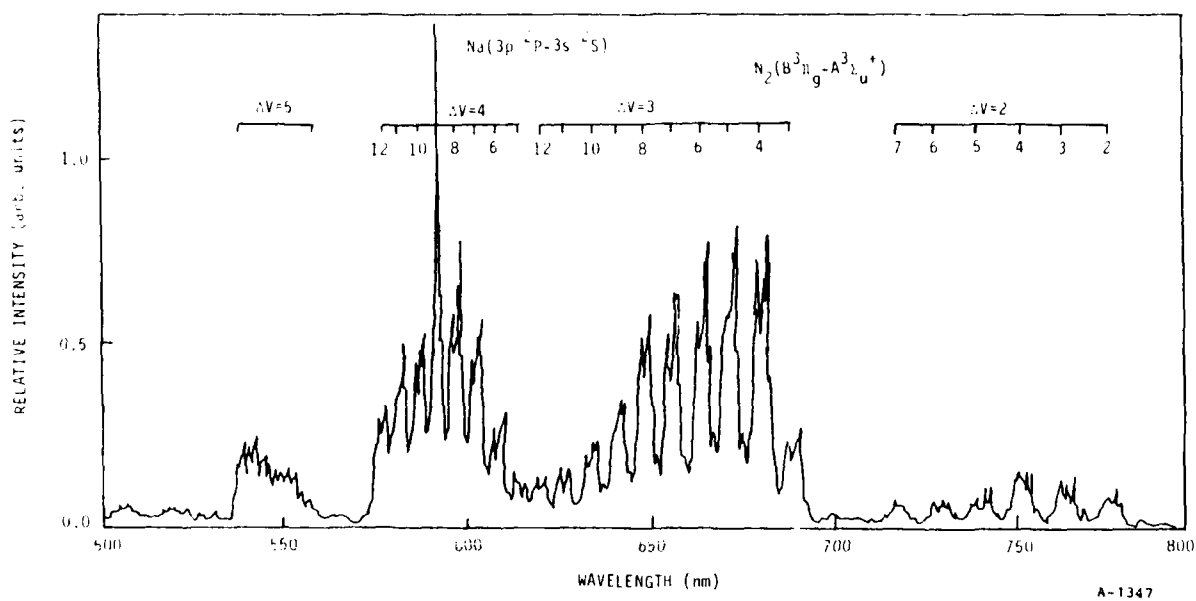
Figure 35. Visible spectrum 9 ms downstream from an Ar/N_2 discharge $X_{N_2} = 0.02$.

3-12

while one run in which some CO was added to the discharge effluent upstream from the injector gave a value of 1.75×10^{12} atoms cm^{-3} for unit relative $N(^2D)$ number density. These experiments indicate that the precursor state is relaxed either by longer contact time with argon or else by wall collisions as evidenced by the great differences in the argon runs with a long flow time to the injector compared to the runs with a short flow time. In addition, the precursor state is quenched efficiently by carbon monoxide, but lacks sufficient energy to dissociate it. Some further experiments with the pre-quenched discharge effluent are needed to get good quantitative results on the production of O from reaction (1), but our CO run indicates that the yield of O per $N(^2D)$ consumed is unity, and that the temperature of the helium lamp is indeed 500-600 K.

3.3.2 $N(^2D, ^2P)$ Quenching Measurements

Rate coefficients are determined from measurements of the change in the natural log of the metastable nitrogen number density as a function of number density of added quenching reagent with fixed reaction distance z:

$$- \frac{d\ell n[N(^2D)]}{d[Q]} = 0.62 \ k_Q z/\bar{v} = \Gamma(z) \tag{10}$$

This analysis requires corrections to the reaction distance, z, to account for imperfect mixing at the injector. Thus one must measure decays at several different distances with all other conditions fixed, and then determine the reaction coefficient from a plot of Γ versus z.

A resonance fluorescence technique monitors the atomic-nitrogen-metastable number density in the reactor. At sufficiently low number densities, the metastable-nitrogen number density is directly proportional to the intensity of the observed resonance fluorescence (see Fig. 36). The two metastable nitrogen atoms, $N(^2D)$ and $N(^2P)$ have a common upper state for their resonance lines so that one of the lines must be filtered from the lamp to discriminate between the two levels. A laser reflector centered at about 175 nm on a MgF_2 substrate discriminates moderately well against the 174 nm line which is absorbed by
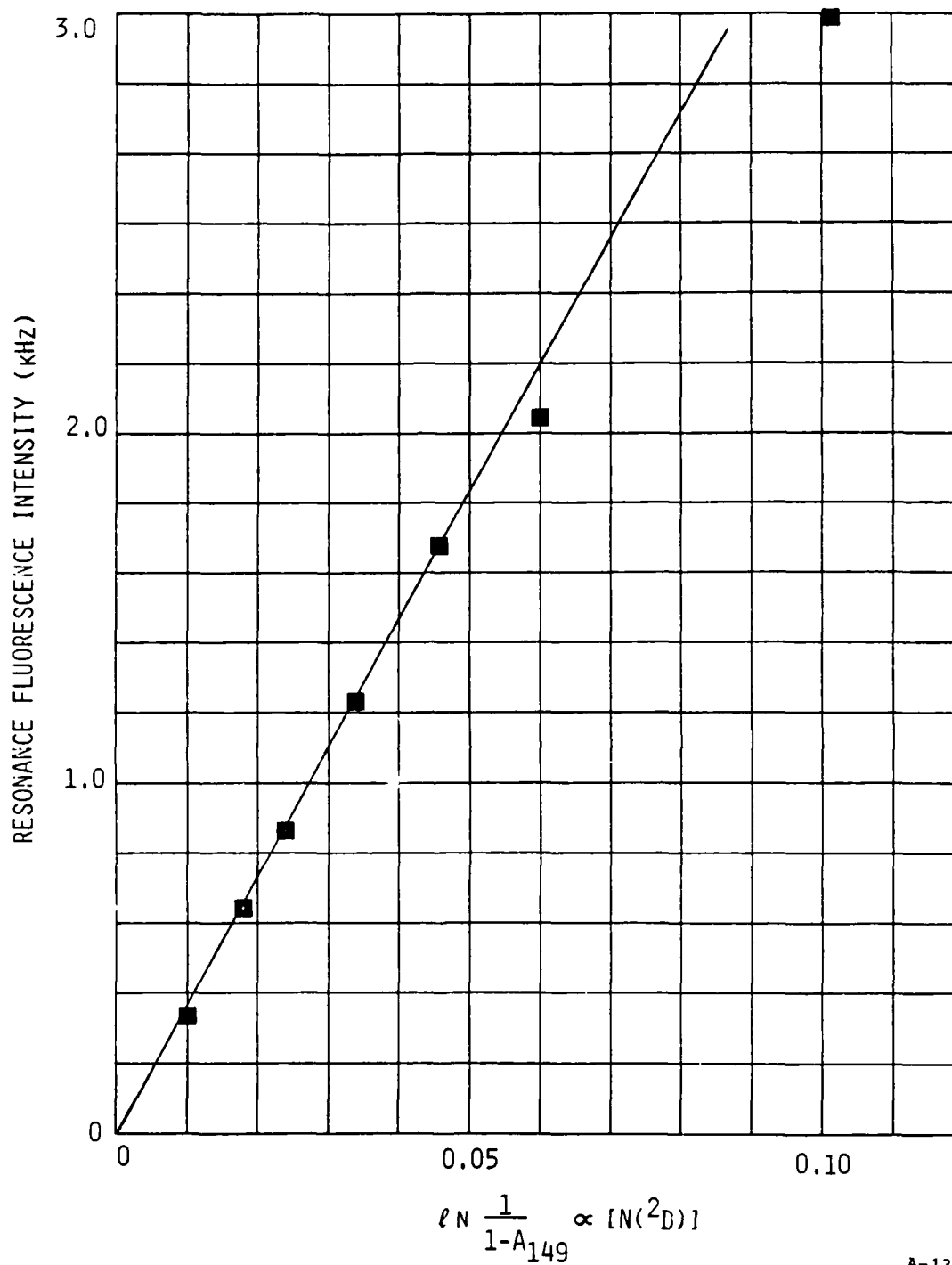
Figure 36. Variation in $N(^2D)$ resonance fluorescence intensity at 174 nm as a function of relative $N(^2D)$ number density. Ar buffer: 250 μm Slits.

A-1348

3-14

$N(^2P)$ while passing the 149 nm multiplet which is absorbed by $N(^2D)$. We found that commercially available reflectors were imperfect, however, giving a transmission ratio, T_{149}/T_{174} of about 8:1. Some further discrimination which enhances resonance fluorescence from $N(^2D)$ pumping over that from $N(^2P)$ pumping results from a greater intensity in the 149 nm multiplet, a slightly larger oscillator strength for 149 nm absorption, and by the fact that $N(^2D)$ outnumbers $N(^2P)$. Absorption measurements on the ratio of $[N(^2D)]$ to $[N(^2P)]$ showed a variation of greater than 7:1 in argon to as little as 2.5:1 in helium. The fraction of the initial resonance fluorescence observed in argon which could be attributed to $N(^2P)$ pumped by leakage through the lamp filter was only about 1%, but was as much as 3-5% in helium buffer. This leakage causes severe problems in getting reliable kinetic data because the $N(^2P)$ is much less readily quenched than is $N(^2D)$--by one to two orders of magnitude-- so that after only one e-fold in measured resonance-fluorescence decay, as much as 15% of the residual resonance-fluorescence signal comes from unquenched $N(^2P)$. Thus decay plots in helium can become severely non-linear over less than an order of magnitude decay. Such non-linearity is unaccept- able for obtaining reliable quenching measurements. One would like two orders of magnitude of linear decay if possible, and given the low background counts in the system, several orders of magnitude in resonance fluorescence decay as a function of added quencher is certainly attainable.

We tried a non-linear least-squares fit to the decay plots using the sum of two exponential decays, one relating to $N(^2D)$ and the other to $N(^2P)$. Ade- quate fits were possible only in cases in which the decays were carried out to very high quencher additions where all of the resonance fluorescence signal could be attributed solely to $N(^2P)$ pumping. In those cases, however, hand fits were equally good. Such a case is shown in Fig. 37 which shows the decay in the resonance fluorescence signal as a function of added N_2O for two runs in helium buffer, one in which only N_2O was added through the injector, and another in which a flow of argon, comprising about 12-14% of the total flow, was added through the injector along with the N_2O. The two interesting points to notice about the data with the large argon flow are that the initial signal in the absence of N_2O addition is much larger than the initial signal without the added argon, and the data with the added argon decay to a much lower
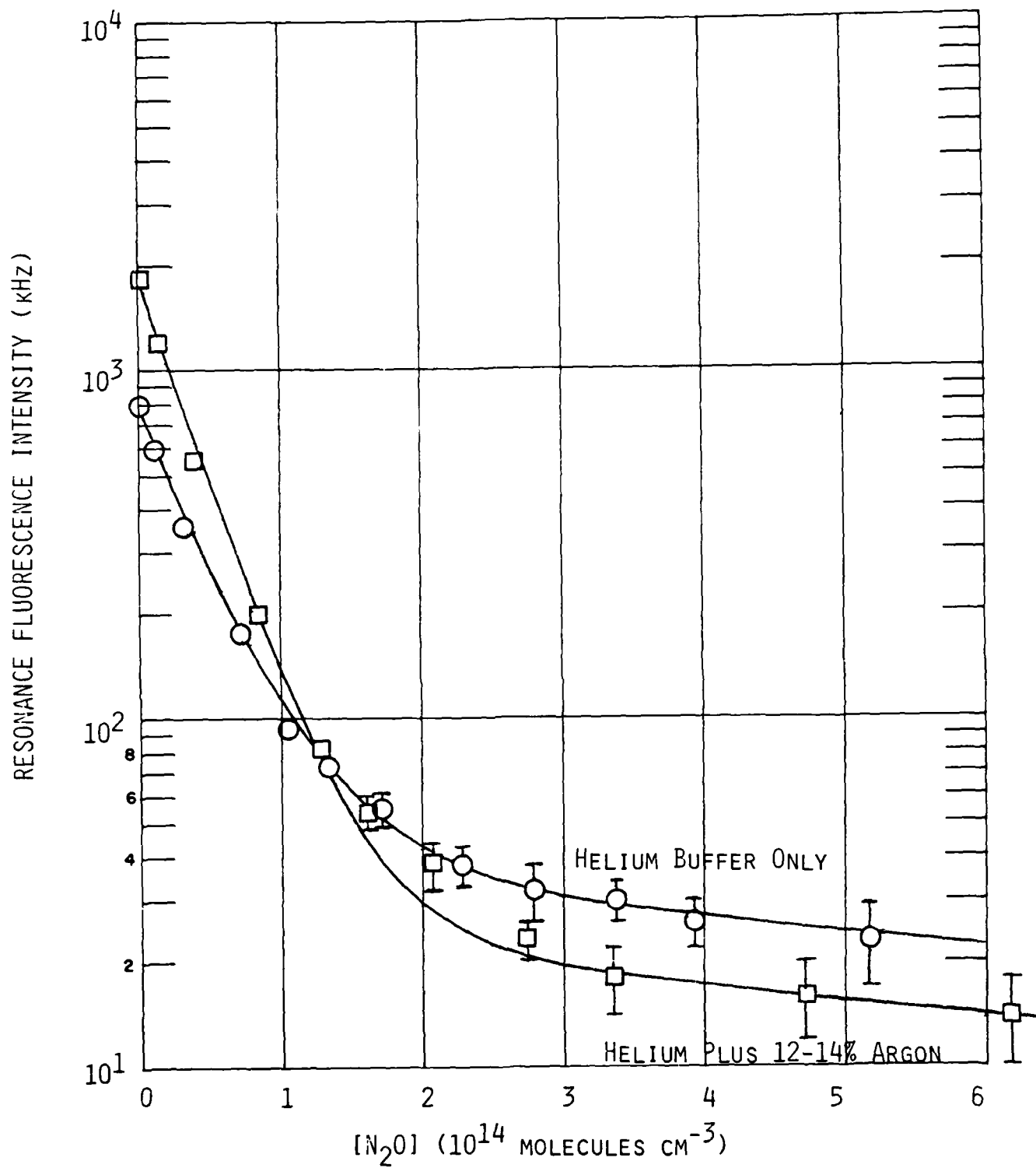
Figure 37.   The quenching of N(^{2}D, ^{2}P) by N$_2$O in helium buffer with and
without the addition of 12-14% argon.

residual N(2P) resonance-fluorescence intensity. The initial signal is larger because the addition of the argon slows down the loss of metastable nitrogen by diffusion to the walls. The lower $N(^2P)$ plateau results because argon is a more efficient quencher of $N(^2P)$ than it is of $N(^2D)$. We estimate from these and some other data that $N(^2P)$ is quenched by argon with a rate coefficient of about 2×10^{-15} cm^3 molecule^{-1} s^{-1}.

We overcame the problems of residual $N(^2P)$ resonance fluorescence interference by using two filters back-to-back to discriminate against 174 nm line from the lamp, and by making measurements at moderately high pressures of argon buffer. With this procedure we could obtain decays of two orders of magnitude (see Fig. 38). The slopes of the lines in Fig. 38 are the decay coefficients, $\Gamma(z)$, as defined by Eq. (29). The slope of a plot of Γ versus effective reaction time, $\bar{z}/v$, determines the reaction rate coefficient. Figure 39 illustrates this for the data of Fig. 38. Note the non-zero intercept indicating a finite mixing time for the experimental conditions employed. Figures 40 and 41 show data for another quencher, CO. Table 1 lists our results along with other measurements in the literature. In general our measurements are more accurate because they cover a much greater dynamic range in experimental parameters than most other studies.

The effects of adding small amounts of a heavier gas to slow diffusive losses in helium were, as demonstrated in Fig. 37, also evident in comparing changes in $N(^2D)$ number density (measured in absorption) as a function of the amount of N_2 added to the reactor. With helium buffer, increasing the molecular nitrogen from 0.5 to 5% of the total flow attenuated the metastable-nitrogen-atom number density only slightly (<7%), whereas similar increases in N_2 in an argon buffer dropped the metastable nitrogen atom number density by more than 70%. The molecular nitrogen quenches the $N(^2D)$ reasonably efficiently (our data suggest a quenching rate coefficient of $(4 \pm 1) \times 10^{-14}$ cm^3 molecule^{-1} s^{-1}), but in helium this more rapid quenching by higher number densities of N_2 is offset by the slowing of diffusive losses with higher N_2 mole fractions in the reactor. The CO_2 and CO measurements are critical to the analysis of the O-atom production studies, the N_2O and O_2 values are critical to the analysis of the O-atom quenching measurements to be reported below, and the H_2 measurement is needed for analy is of results on the LABCEDE facility at AFGL.

3-17
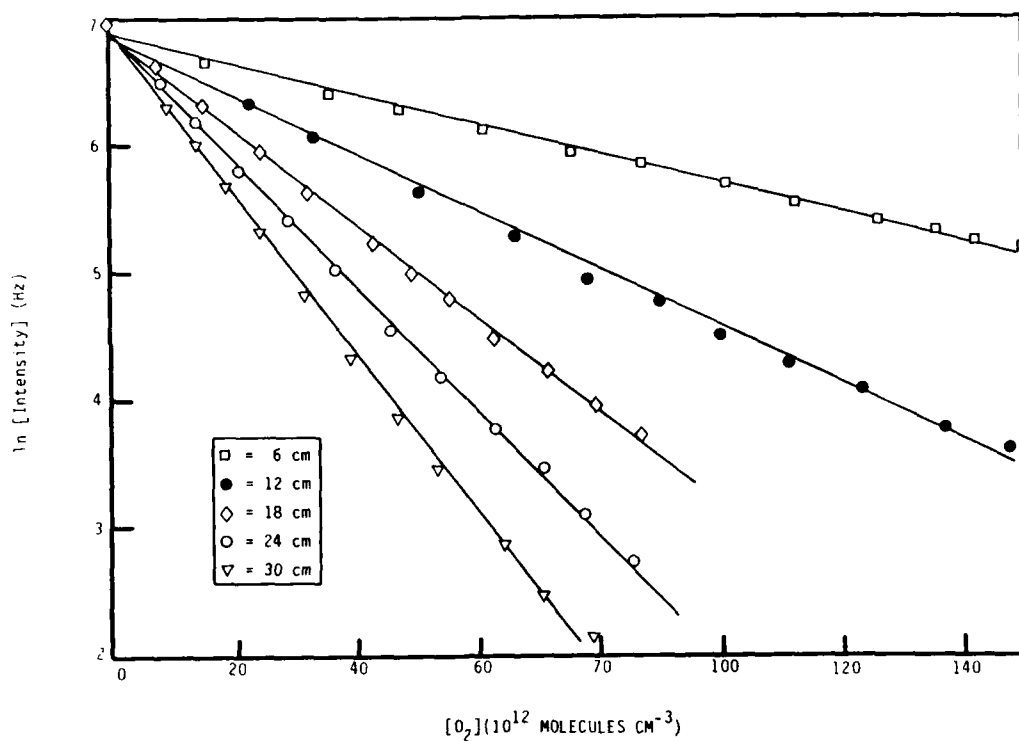
A-1264

Figure 38. Decay of the log of [N(^{2}D)] as a function of [O$_2$] at five
different reactio·: distances.
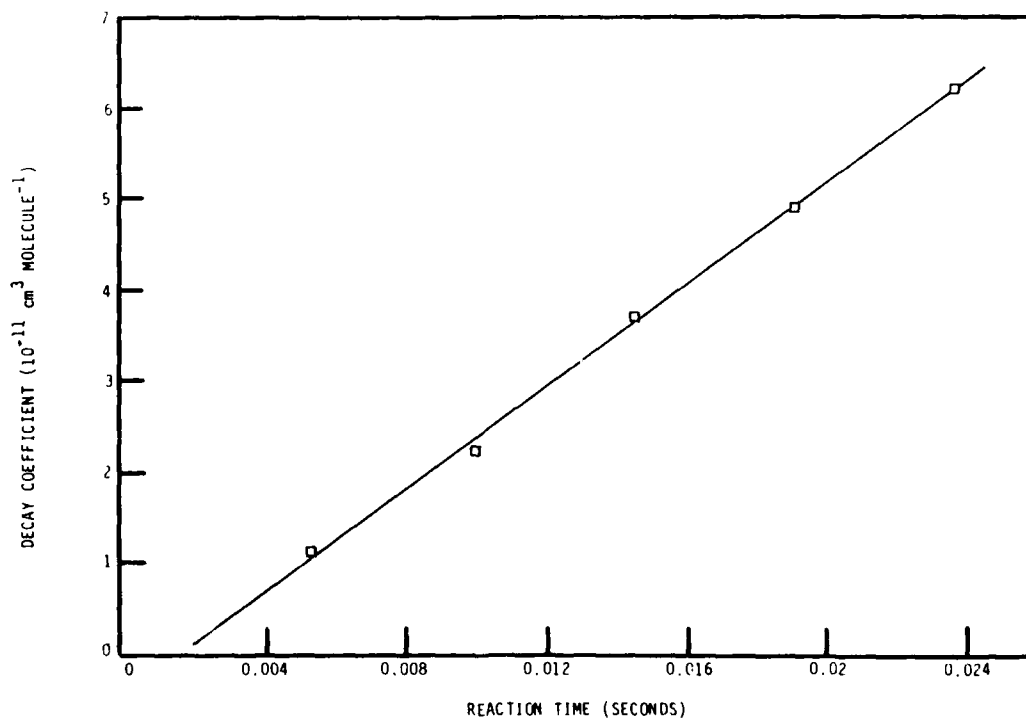
A-1265

Figure 39. Variation in decay constant with reaction time for N(^{2}D) + O$_2$
reaction. The ordinates of the data points are determined
from the slopes of the lines in Fig. 39.

3-18
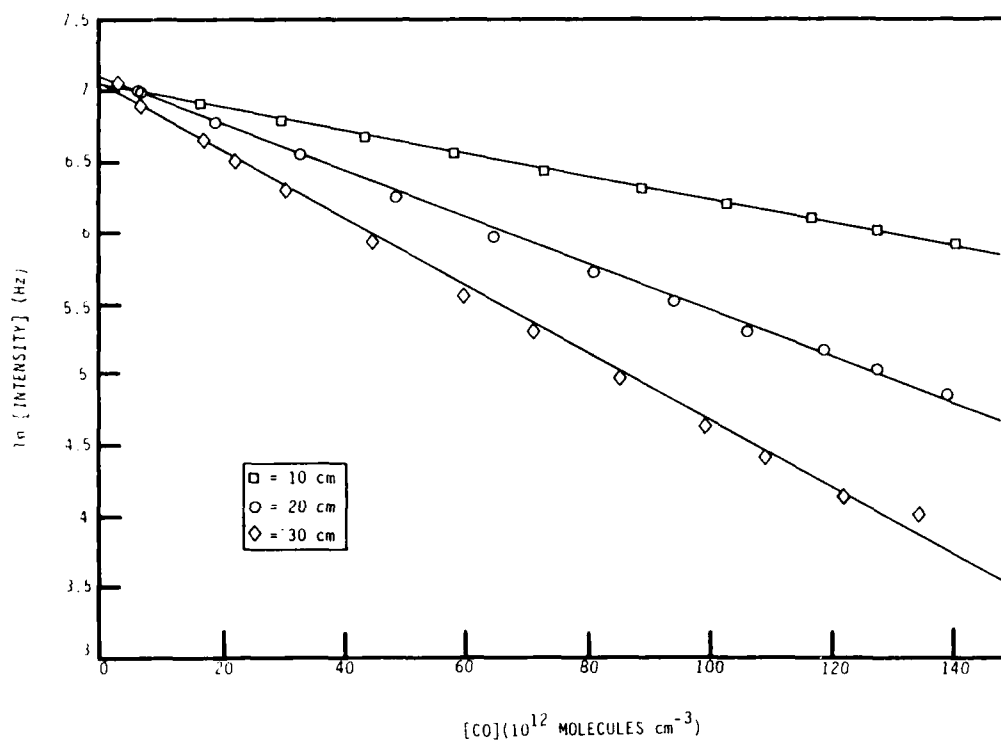
Figure 40. Decay of the log of [N(^{2}D)] with [CO] for different
reaction times.
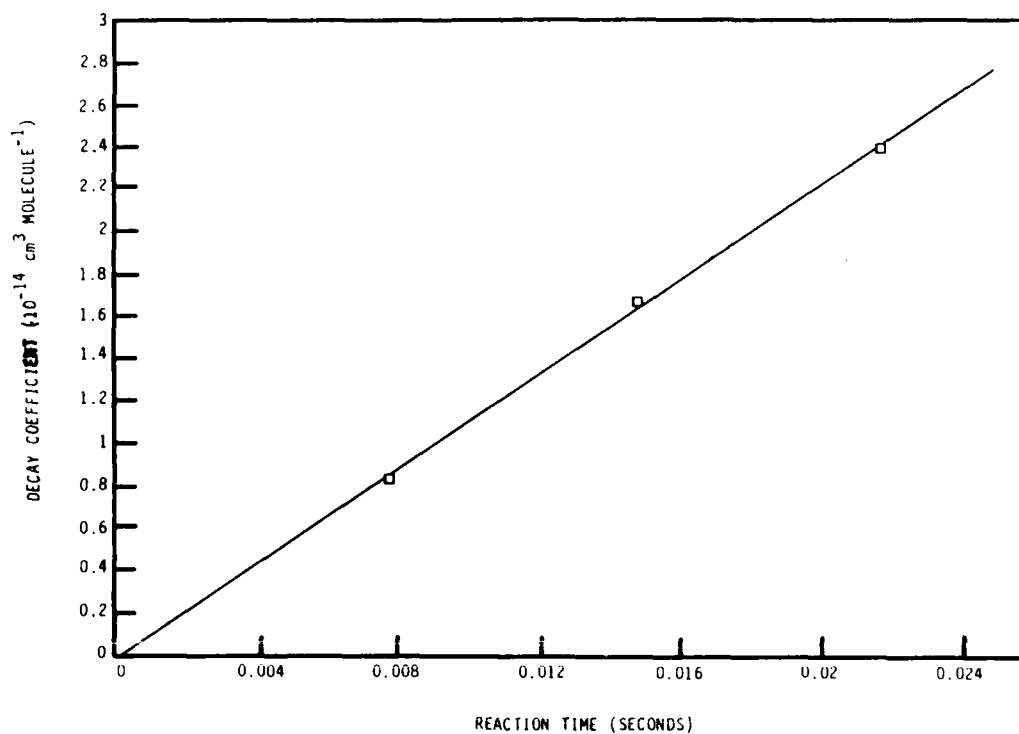
Figure 41. Variation in decay coefficient, Γ, with reaction time for the
N(^{2}D) + CO reaction. The data points are derived from
Fig. 40.
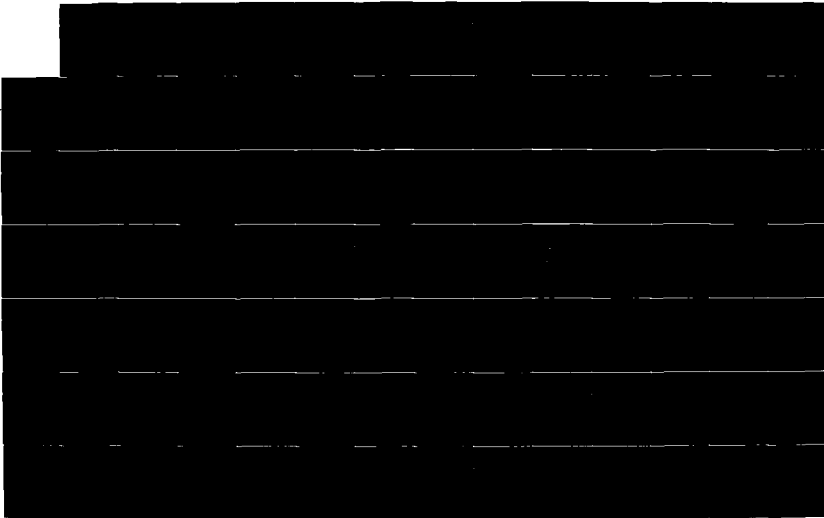
TABLE 1. PRELIMINARY RATE COEFFICIENTS.

$N(^2D)$ Quenching Molecule	Value	Reference
CO_2	$(3.6\pm0.4) \times 10^{-13}$	FAKIR
	$(1.8\pm0.2) \times 10^{-13}$	Husain, Mitra, Young[15]
	$(5\pm2) \times 10^{-13}$	Lin and Kaufman[13]
	6×10^{-13}	Black, Slanger, Young[24]
	$(6.8\pm2.0) \times 10^{-13}$	Fell, Rivas, McFadden[23]
N_2O	$(2.3\pm0.2) \times 10^{-12}$	FAKIR
	1.6×10^{-12}	Husain, Mitra, Young[15]
	$(3.5\pm1.2) \times 10^{-12}$	Lin and Kaufman[13]
	3×10^{-12}	Black, Slanger, Young[24]
	$3\pm1 \times 10^{-12}$	Fell, Rivas, McFadden[23]
O_2	$(4.7\pm0.4) \times 10^{-12}$	FAKIR
	$(5.2\pm0.4) \times 10^{-12}$	Husain, Mitra, Young[15]
	$(6\pm2) \times 10^{-12}$	Lin and Kaufman[13]
	7.4×10^{-12}	Black, Slanger, and Wood[25]
	$(6.1\pm1.8) \times 10^{-12}$	Fell, Rivas, McFadden[23]
	$(5.3\pm0.5) \times 10^{-12}$	Ianuzzi and Kaufman
CO	$(1.7\pm0.4) \times 10^{-12}$	FAKIR
	$(2.1\pm0.2) \times 10^{-12}$	Husain, Mitra, Young[15]
H_2	$(3\pm1) \times 10^{-12}$	FAKIR
	$(2.1\pm0.3) \times 10^{-12}$	Husin, Mitra, Young[15]
	5×10^{-12}	Black, Slanger, Young[24]
	$(3.5\pm1) \times 10^{-12}$	Fell, Rivas, McFadden[23]
N_2	4×10^{-14}	FAKIR
	1.5×10^{-14}	Husain, Mitra, Young[15]
	1.6×10^{-14}	Lin and Kaufman[13]

$N(^2P)$ Quenching

	Value	Reference
CO_2	7×10^{-15}	FAKIR
	1.1×10^{-15}	Husain, Mitra, Young[15]
N_2O	7×10^{-14}	FAKIR
	$(5\pm2) \times 10^{-14}$	Husain, Mitra, Young[15]
Ar	2×10^{-15}	FAKIR
	7×10^{-16}	Lin and Kaufman[13]
	4×10^{-16}	Ianuzzi and Kaufman[1]
H_2	1×10^{-14}	FAKIR
	2×10^{-15}	Husain, Mitra, Young[15]

The data with the single 174 nm rejection filter for which decays extended to sufficiently high quencher number density so as to eliminate all resonance fluorescence from $N(^2D)$ should give rate coefficients for quenching $N(^2P)$. Our measurements give values of 7×10^{-15} and 1.2×10^{-13} cm^3 molecule^{-1} s^{-1} for quenching by CO_2 and N_2O respectively. We tried taking some better data by monitoring only $N(^2P)$ resonance fluorescence. These studies used a suprasil window as a lamp filter. This filter passes the 174 nm emission for $N(^2P)$, but rejects the 149 nm emission which $N(^2D)$ absorbs. Under conditions we employed, we obtained highly non-linear decays which we tried fitting to sums of two or three exponentials (Fig. 42). Initial decays from CO_2, N_2O, and H_2 addition all were quite fast, consistent with quenching rate coefficients $>10^{-12}$ cm^3 molecule^{-1} s^{-1}. The decays plateaued to slowly decaying components at large additions of reactant. The slowly decaying plateau in the presence of H_2 is consistent with an $N(^2P)$ + H_2 rate coefficient $\sim 1 \times 10^{-14}$ cm^3 molecule^{-1} s^{-1}. We didn't follow the CO_2 and N_2O decays far enough out to extract meaningful estimates for $N(^2P)$ quenching rate coefficients.

The initial decays, which represented the bulk of the signal, were clearly the result of quenching of some precursor state which was coupled collision- ally to $N(^2P)$. The $N(^2P)$ then was essentially just a tracer of this other species. We found that we could raise the level of the slowly decaying plateau relative to the initial signal by working with fairly large mole fractions of nitrogen. Thus molecular nitrogen appears to quench this precursor state also. However, our $N(^2P)$ measurements were still severely contaminated by some species which was coupled to $N(^2P)$ (spectral scans of the resonance fluorescence signal eliminated the possibility of our detection system being contaminated by extraneous emission). We do not feel that a microwave discharge in N_2/Ar or He mixtures provides an adequately clean source of $N(^2P)$ for kinetic measurements. We plan to develop a clean source of $N(^2P)$ based upon the energy transfer reac- tion between $N_2(A\ ^3\Sigma_u^+)$ and $N(^4S)$. After developing this source, we shall be able to study $N(^2P)$ kinetics free from extraneous interferences.
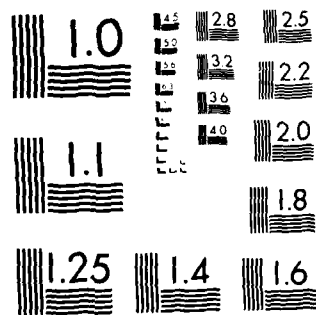
CROCOPY RESOLUTION TEST CHART
NATIONAL BUREAU OF STANDARDS 1963 A
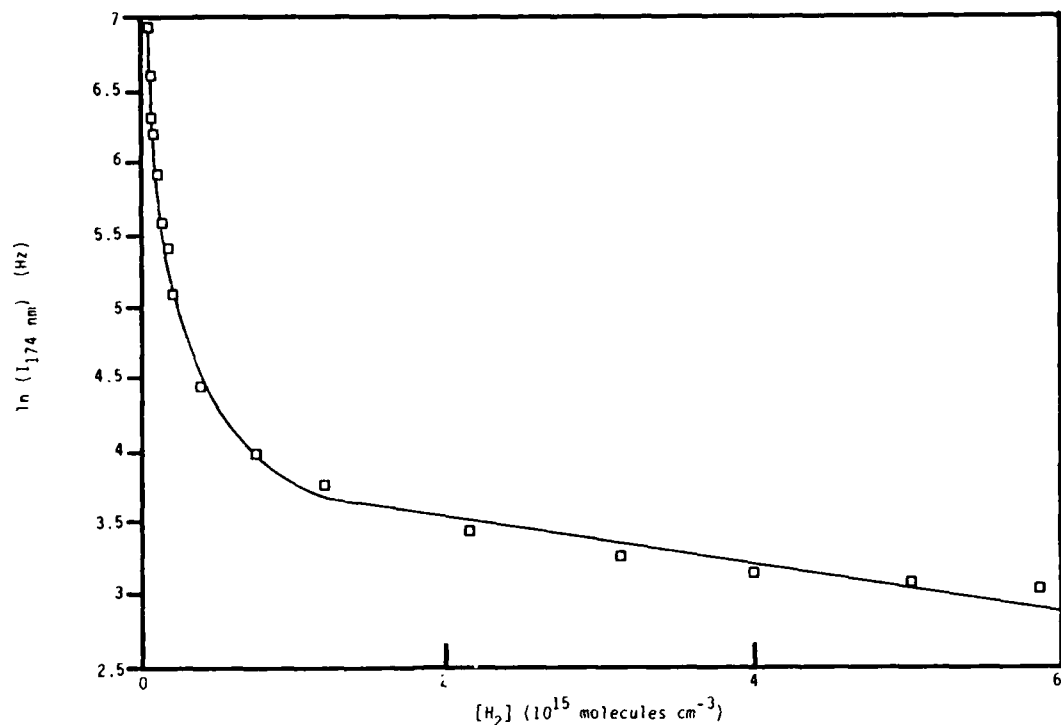
Figure 42. Decay of N(^{2}P) resonance fluorescence with added molecular hydrogen for a reaction time of 18 ms.

3.3.3 The Quenching of N(^{2}D) By Atomic Oxygen

Two preliminary measurements on the quenching of N(^{2}D) by atomic oxygen were made by comparing the differences in the N(^{2}D) attenuation as a function of added quencher in the presence and absence of a microwave discharge to dissociate the reagent gases. Figure 43 displays results taken using N_2O as the reagent gas. Clearly, discharging the gas reduces the N(^{2}D) attenuation, showing that atomic oxygen is less efficient than N_2O in quenching N(^{2}D).

With the discharge off the equation governing the resonance fluorescence intensity is given by

$$\ln I_{off} = \ln I_o - \left(k_D + k_{N_2O}(N_2O)\right)z/\bar{v} \qquad (11)$$

and with the discharge on, the equation is

3-22
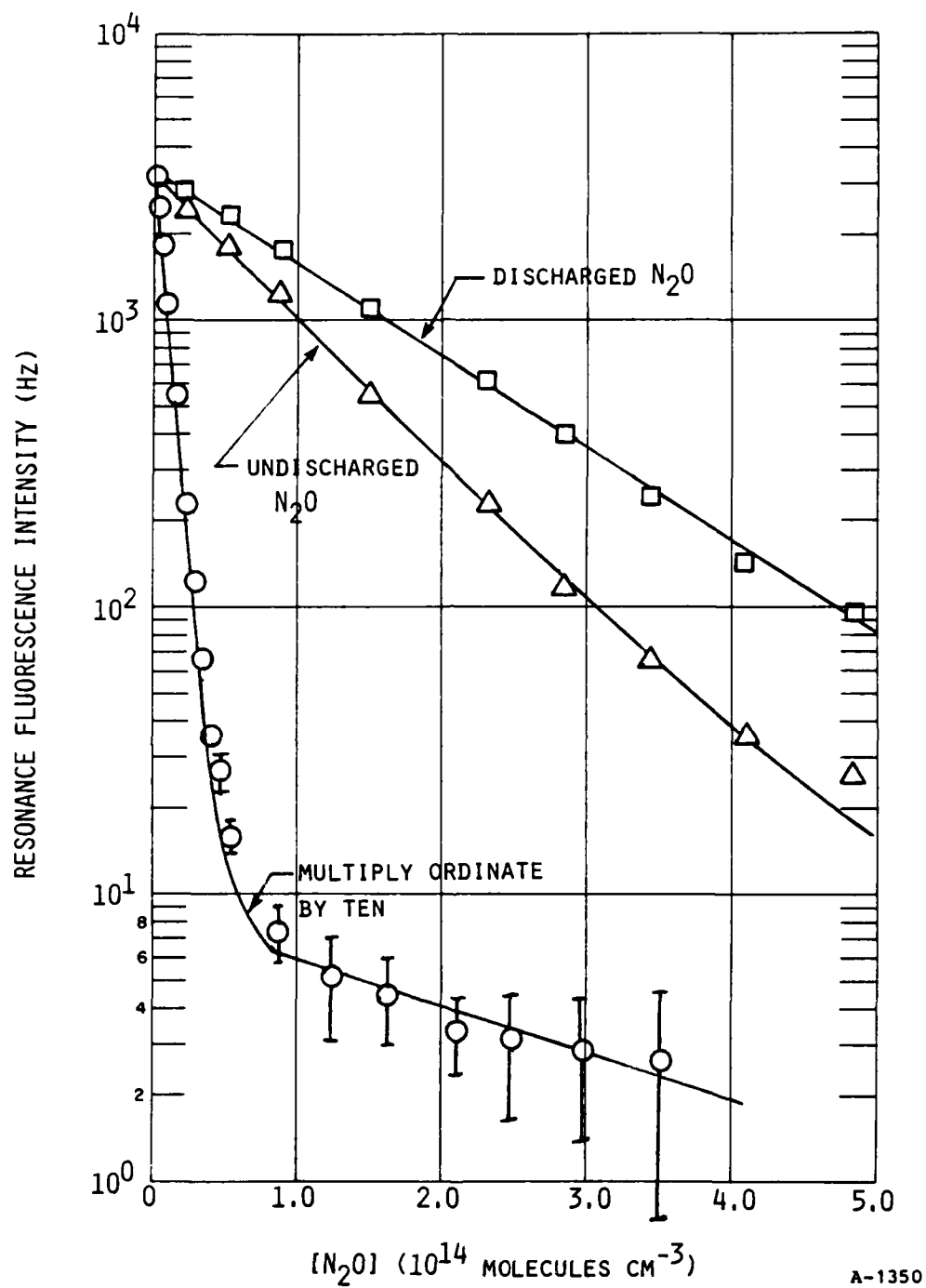
Figure 43. Variation in resonance fluorescence intensity of $N(^2D, ^2P)$ as a function of added N_2O for both discharged and undischarged N_2O.

$$\ln I_{on} = \ln I_o - \left(k_D + k_O[O] + k_{O_2}[O_2]\right)z/\bar{v} \qquad (12)$$

We tried to measure the efflux of undissociated N_2O from the discharge by
monitoring the attenuation of the 129.6 nm Xe resonance line as N_2O was added
to the discharge. Our measurements indicated no N_2O exited the discharge,
thus implying that the N_2O was completely dissociated and that any discrepancy
between O produced and N_2O consumed must be the result of O-atom recombination
or reaction of $O(^1D)$ with N_2O to produce O_2, some of which may well be in the
$a^1\Delta$ state. With the discharge on, the number density of atomic oxygen is

$$[O] \approx \alpha[N_2O]_o \qquad (13)$$

and that for molecular oxygen is

$$[O_2] = \frac{1-\alpha}{2} [N_2O]_o \qquad (14)$$

where α is calculated from the ratio of the measured atomic-oxygen number
density to the N_2O number density with the discharge off. Using these above
two relations in Eq. (12) and combining with Eq. (11) gives the working equa-
tion for our data analysis

$$\ln \frac{I_{on}}{I_{off}} = \left(k_{N_2O} - \alpha k_O - \frac{1-\alpha}{2} k_{O_2}\right)[N_2O]_o z/\bar{v} \qquad (15)$$

For experiments with discharged O_2 the analysis equation is

$$\ln \frac{I_{on}}{I_{off}} = \left(k_{O_2} - 2k_O\right)\alpha[O_2]_o z/\bar{v} \qquad (16)$$

where in this case α is defined as the fractional O_2 dissociation or

$$\alpha = \frac{[O_2]-[O_2]_o}{[O_2]_o} = \frac{[O]}{2[O_2]_o} \qquad (17)$$

3-24

Figure 44 shows a plot of the data according to Eq. (15) for the experiments with discharged N_2O while Fig. 45 shows the results of the experiment with discharged O_2. The two sets of data give O-atom quenching rate coefficients of 0.5 and 1×10^{-12} cm^3 molecule^{-1} s^{-1} for the N_2O and O_2 experiments respectively. The fractional dissociations in both experiments were not particularly impressive ($\approx$30%). We hope to boost the fractional dissociations and thereby enhance the O-atom number densities relative to the molecular discharge products. We also plan some experiments in which atomic oxygen is made by titrating excess N in the upstream part of the injector with NO. This latter approach produces O free from other reactive species if recombination in the injector is avoided. It cannot produce such large number densities of atomic oxygen as the other two techniques, however, thus making decay measurements more tenuous.

Our preliminary measurements indicate a rate coefficient for reaction (2) which is marginally smaller than previous laboratory measurements, but further, more precise data are required before a definitive conclusion can be reached.
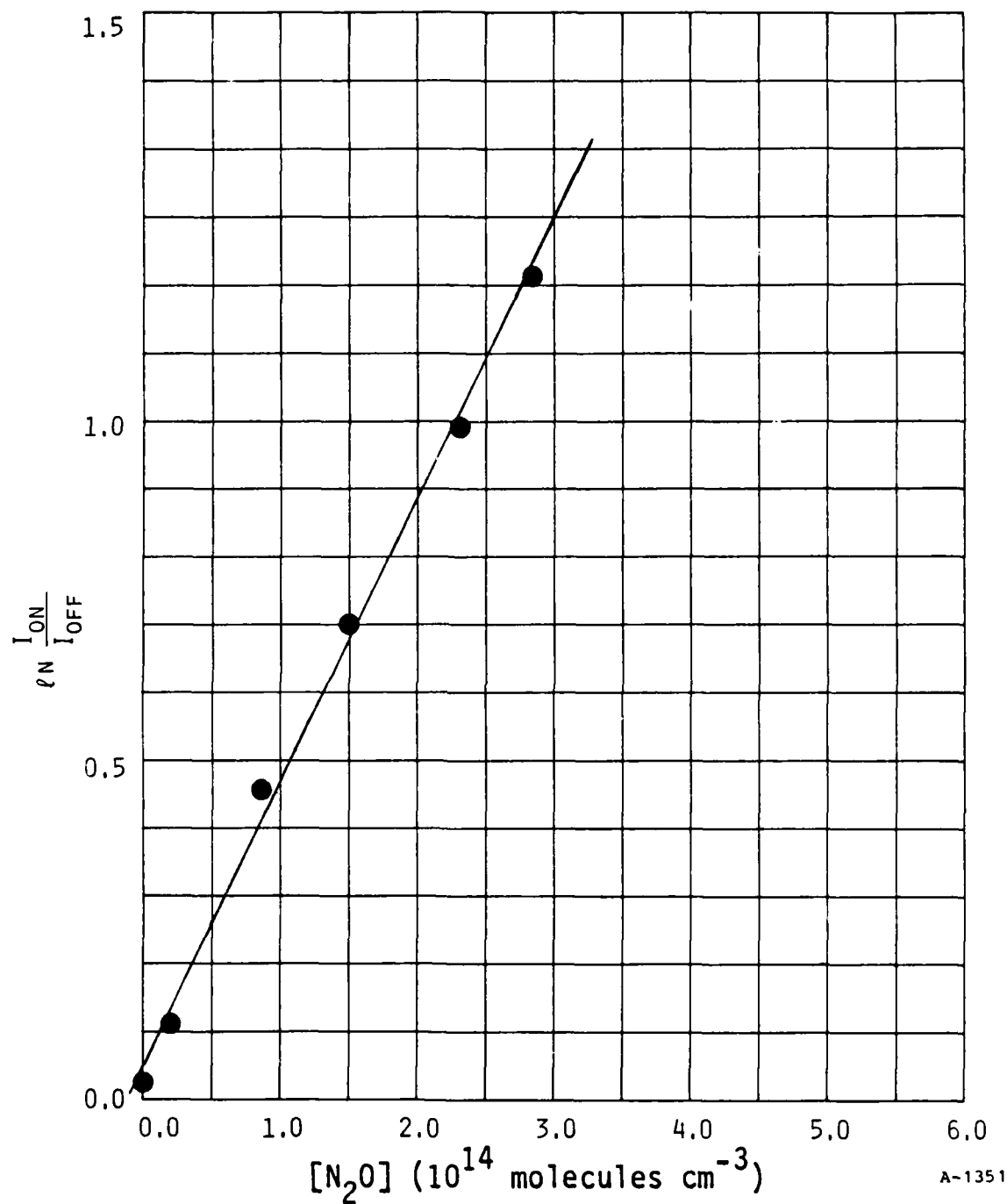
Figure 44. Variation in log of the ratio of $N(^2D)$ resonance fluorescence intensity in the presence of microwave discharged N_2O to that in the presence of undischarged N_2O.

3-26
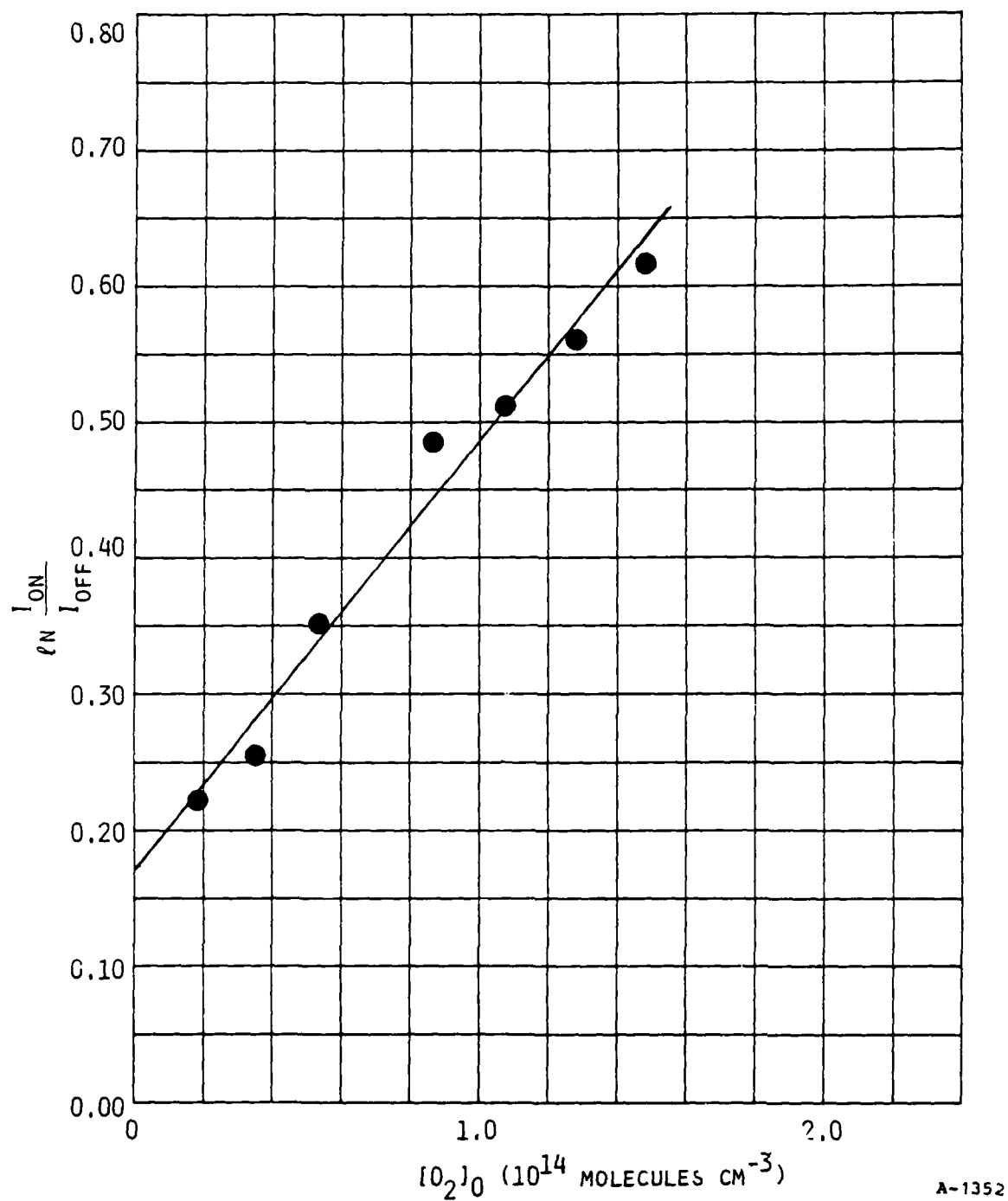
Figure 45. Variation in the log of the ratio of the N(^{2}D) resonance
fluorescence intensity in the presence of microwave
discharged O_2 to that in the presence of undischarged O_2
as a function of initial molecular oxygen number density.

3-27

3.4 Summary

We have reported preliminary measurements on the yield of atomic oxygen from the reaction of $N(^2D)$ with CO_2 and quenching rate coefficients of $N(^2D)$ by a number of species including atomic oxygen. Our results indicate a large number density of energetic species in addition to $N(^2D)$ which also produce atomic oxygen when they interact with CO_2. These species appear to be quenched more efficiently by carbon monoxide than is $N(^2D)$.

Our quenching measurements are comparable to other measurements in the literature, although our rate coefficient for quenching $N(^2D)$ by atomic oxygen is about half that previously reported. Definitive measurements of these processes are now in progress.

3.5 References

1. Iannuzzi, M.P. and Kaufman, F., "Rates of Some Reactions of $N(^2D$ and $^2P)$ Near 300 K," J. Chem. Phys. 73, 4701 (1980).

2. Kennealy, J.P., DelGreco, F.P., Caledonia, G.E., and Green, B.D., "Nitric Oxide Chemi-excitation Occurring in the Reaction Between Metastable Nitrogen Atoms and Oxygen Molecules," J. Chem. Phys. 69, 1574 (1978).

3. Caledonia, G.E. and Kennealy, J.P., "NO Infrared Radiation in the Upper Atmosphere," Planet. Space Sci. 30, 1043 (1982).

4. Davenport, J.E., Slanger, T.G., and Black, G., "The Quenching of $N(^2D)$ by $O(^3P)$, J. Geophys. Res. 81, 12 (1976).

5a. Rawlins, W.T. and Kaufman, F. "Characteristics of O(I) and N(I) Resonance Line Broadening in Low Pressure Helium Discharge Lamps," J. Quant. Spectrosc. Radiat. Transfer 18, 561 (1977).

5b. Clyne, M.A.A. and Piper, L.G., "Kinetic Spectroscopy in the Far Vacuum Ultra-Violet, Part 3: Oscillator Strengths for the 3s, 4s and 5s $^3S - {}^2P^4\, {}^3P_2$ Transition in Atomic Oxygen," JSC Faraday II 72, 2178 (1976).

6. Piper, L.G., Caledonia, G.E., and Kennealy, J.P., "Rate Constants for Deactiviation of $N_2(A)v'=0,1$ by O_2," J. Chem. Phys. 74, 2888 (1981).

7. Piper, L.G., Caledonia, G.E., and Kennealy, J.P., "Rate Constants for Deactivation of $N_2(A\, ^3\Sigma_u^+, v'=0,1)$ by O," J. Chem. Phys. 75, 2847 (1981).

8. Piper, L.G., "The Excitation of $O(^1S)$ in the Reaction between $N_2(A\ ^3\Sigma_u^+)$ and $O(^3P)$," J. Chem. Phys. $\underline{77}$, 2373 (1982).

9. Rawlins, W.T. and Piper, L.G., "Effects of Excitation Mechanism on Line-width Parameters of Conventional Vacuum Ultraviolet (VUV) Discharge Line Sources," Proc. Soc. Photo.-Opt. Instrum. Eng. $\underline{279}$, 58 (1981).

10. Piper, L.G., Clyne, Michael A.A. and Monkhouse, Penelope B., "Electronic Energy Transfer between Metastable Argon Atoms and Ground-state Oxygen Atoms," J. Chem. Soc., Faraday Trans. 2 $\underline{78}$, 1373 (1982).

11. Berg, H.C. and Kleppner, D., "Storage Technique for Atomic Hydrogen," Rev. Sci. Instrum. $\underline{33}$, 248 (1962).

12. Fehsenfeld, F.C., Evenson, K.M., and Broida, H.A., "Microwave Discharge Cavities Operating at 2450 MHz," Rev. Sci. Instr. $\underline{36}$, 294 (1965).

13. Lin C., and Kaufman, F., "Reactions of Metastable Nitrogen Atoms," J. Chem. Phys. $\underline{55}$, (1971).

14. McCarroll, B., "An Improved Microwave Discharge Cavity for 2450 MHz," Rev. Sci. Instr. $\underline{41}$, 279 (1970).

15. Husain, D., Mitra S.K. and Young, A.N., "Kinetic Study of Electronically Excited Nitrogen Atoms, $N(2^2D_J, 2^2P_J)$, by Attenuation of Atomic Resonance Radiation in the Vacuum Ultra-Violet," JCS Faraday II $\underline{70}$, 1721, (1974).

16. Piper, L.G. and Rawlins, W.T., and Armstrong, R.A., "O-Atom Yields from Microwave discharges in N_2O/Ar Mixtures," AFGL-TR-83-0031, Air Force Geophysics Laboratory, Hanscom AFB, MA 1983. Available from the authors on request. ADA130429.

17. Kaufman, F., "The Air Afterglow and Its Use in the Study of Some Reactions of Atomic Oxygen," Proc. Roy. Soc. (London) A $\underline{247}$, 123 (1958).

18. Kaufman, F., "The Air Afterglow Revisited," Chemiluminescence and Bioluminescence, M. J. Cormier, D. M. Hercules, and J. Lee, eds. pp. 83-100 (1973).

19. Rawlins, W.T. and Kaufman, F., "The Reaction of CO_2 with Active Nitrogen," J. Chem. Phys. $\underline{64}$, 1128 (1976).

20. Kaufman, F., "Reactions of Oxygen Atoms," Prog. React. Kinet. I.. 1(1961).

21. Meyer, J.A., Setser, D.W., and Stedman, D.H., "Energy Transfer Reactions of $N_2(A^3\Sigma_u^+)$. II. Quenching and Emission by Oxygen and Nitrogen Atoms," J. Phys. Chem. $\underline{74}$, 2238 (1970).

22. Rawlins, W.T., Piper, L.G., Caledonia, G.E, and Green, B.D., "COCHISE Research," PSI TR-298 (1981). Available from the authors upon request.

23. Fell, B., Rivas, I.V., and McFadden, D.L., "Kinetic Study of Electronically Metastable Nitrogen Atoms, $N(2\ ^2D_J)$, by Electron Spin Resonance Absorption," J. Phys. Chem. $\underline{85}$, 224 (1981).

24. Black, G., Slanger, T.G., St. John, G.A., and Young, R.A., "Vacuum-UV Photolysis of N_2O, 4, deactivation of $N(^2D)$," J. Chem. Phys. $\underline{51}$, 116(1969).

25. Slanger, T.G., Wood, B.J., and Black, G., "Temperature Coefficients for $N(^2D)$ Quenching by O_2 and N_2O," J. Geophys. Res. $\underline{76}$, 8430 (1971).

4. SPECTROSCOPY OF VIBRATIONALLY EXCITED OZONE

4.1 Introduction

The three-body recombination of atomic and molecular oxygen to form ozone

$$O + O_2 + M \rightarrow O_3 + M \qquad (1)$$

has long been a problem of special interest in the study of recombination reactions in polyatomic systems. The large negative temperature coefficient and relatively small room-temperature rate coefficient for this reaction offer intriguing questions which have not yet been answered in terms of reaction rate theory. In addition to its relevance to fundamental reaction rate theory, Reaction (1) is a crucial component of the oxygen/ozone photochemical cycle which governs the chemistry of the Earth's atmosphere.

Direct observation of vibrationally excited ozone, $O_3(v)$, formed in Reaction (1) offers new insight into the dynamics of three-body recombination. Spectrally resolved studies of $O_3(v)$ formation under conditions of minimal collisional deactivation can probe detailed vibrational state population distributions at early to intermediate stages in the complex recombination sequence, i.e., following the initial stabilization of the O_2-O collision complexes but prior to complete thermalization of the newly formed molecules. This type of measurement provides a unique data base which can be used to assess the detailed recombination dynamics, including questions regarding the participation of the chaperon or radical-molecule-complex mechanism, the possible influence of electronically excited states of O_3, the initial distribution among the internal vibrational modes, the deactivation of excited $O_3(v)$, and the possible chaotic behavior of the higher vibrational states.

The presence of recombined $O_3(v)$ in the upper atmosphere is also a matter of considerable interest. A significant fraction of vibrationally excited

molecules can lead to a redshift in the Hartley continuum ultraviolet absorption spectrum, resulting in increased solar photodissociation of atmospheric ozone. In addition, $O_3(v)$ may be an important energy carrier in the upper atmosphere, and could exhibit enhanced reactivity over vibrationally cold O_3. At high altitudes (90 ± 20 km), airglow from $O_3(v)$ is one of the dominant sources of infrared radiation in the upper atmosphere, its variations in intensity and spectral distribution reflecting the complex interplay of the O_2/O_3 photochemical cycle.

Direct observation of $O_3(v)$ infrared chemiluminescence from Reaction (1) is difficult owing to the need to make high-sensitivity emission measurements at relatively long wavelengths (approximately 10 μm for the v_3 band, the strongest of the O_3 bands - See Table 2). The first such measurements were reported by von Rosenberg and Trainor[1-3] in an excellent series of flash photolysis studies at room temperature and relatively high pressures ($[M] = 2 - 13 \times 10^{18}$ cm^{-3}). However, this work involved only bandpass observations of the infrared emissions, and the extent of collisional intermode and intramode coupling was clearly rather large. The extension of the data base to lower pressures and higher spectral resolution has required rather extreme measures, namely the construction of a totally cryogenic discharge-flow apparatus to eliminate thermal infrared backgrounds.

We have previously reported on spectrally resolved $O_3(v)$ chemiluminescence observed from Reaction (1) at ~1 torr and 80-120 K.[4] These experiments utilized the cryogenic COCHISE reactor/spectrometer facility[5] at the Air Force Geophysics Laboratory, and constitute the first laboratory measurements of spectrally resolved infrared emission from vibrationally excited O_3. We have subsequently applied the spectroscopic and kinetic information developed in that work to the analysis and kinetic interpretation of high altitude $O_3(v)$ infrared emission spectra.[6-8] However, a number of key issues remained unresolved in the laboratory measurements. First, the spectroscopic description of the $O_3(v)$ emission was only approximate, and the detailed excited state distributions and number densities could not be determined unambiguously. Second, the excited state distributions were clearly affected by collisional

TABLE 2.   OZONE FUNDAMENTAL AND OVERTONE VIBRATIONAL BANDS[a].

Band	Band Origin, μm	Einstein Coefficient, s^{-1}
ν_1	9.07	0.63
ν_2	14.27	0.23
ν_3	9.60	11.4
$2\nu_3$	4.86	0.35
$3\nu_3$	3.29	0.77
$\nu_1 + \nu_3$	4.74	3.8
$\nu_2 + \nu_3$	5.79	0.12
$\nu_1 + \nu_2$	5.57	0.55
$\nu_1 + \nu_2 + \nu_3$	3.59	0.14

[a]Data from Ref. 11.

deactivation processes, with relative contributions from higher-lying states increasing with decreasing O_2 and O mole fractions. Third, because of the limited spectral resolution, it was not possible to assess the degree of intermode coupling via spectral contributions from combination states. Fourth, bimodal vibrational distributions were observed at higher O_2 mole fractions, suggesting the occurrence of additional excitation mechanisms for $O_3(v)$. Finally, under all conditions the $O_3(v)$ emission spectra extended no further than ~ 11 μm, despite the potential for high-lying O_3 vibrational states to radiate near 12 μm. This behavior signifies population of O_3 states only in the lower half of the O_2-O potential well, a characteristic not expected in a recombination sequence unless collisional deactivation of the high-energy states is extensive.

Following extensive modifications to the optical, thermal, and electrical subsystems of the COCHISE facility, the overall sensitivity of the apparatus has been improved by over an order of magnitude,[5] such that it became possible to address the above issues in detail. We have thus acquired an extensive data base for $O_3(v)$ chemiluminescence over a wide range of kinetic effects (i.e., initial O_2/Ar mixing ratio, gas temperature, etc.) and at sufficiently high spectral resolution to permit conclusive spectroscopic analysis. These results support and extend the preliminary conclusions of our earlier work. Studies of the kinetics and mechanisms for $O_3(v)$ formation and destruction are presented in a Section 5. In the present paper, we present a spectroscopic analysis of the observed $O_3(v)$ fluorescence near 10 μm. The results show that: (1) observed vibrational transition frequencies are close to those predicted from a Darling-Dennison perturbation treatment; (2) little intermode ($\nu_3 \to \nu_1$, ν_2) coupling occurs in the early stages of the recombination sequence, with evidence only for weak contributions from the lowest ν_1 level; and (3) the possibility of near-resonant V-V energy transfer from molecular O_2 is indicated. The assumptions for scaling the band-integrated Einstein transition probabilities with vibrational quantum number are examined in detail to assess the uncertainties in transforming the observed band intensities into vibrational state number densities.

4.2 Experimental Measurements

The design and operation of the COCHISE facility have been described in detail elsewhere.[5] In brief, the entire radiative environment of the experiment is maintained at a base temperature of approximately 20 K, which effectively eliminates background radiation within the 2-20 μm operating range of the apparatus. The detection system consists of a scanning grating monochromator and a liquid-helium-cooled Si:As detector. Reagent gases are introduced through temperature-controlled feed lines to the reaction cell as shown in Figure 46. A flowing O_2/Ar mixture at approximately 1 torr passes through four parallel microwave discharges (2450 MHz, 50 W) prior to expanding into a low-pressure (approximately 3 mt), cryogenically pumped interaction volume. A counterflow gas (usually O_2 or Ar) enters the volume from the opposite side to combine with the discharged gas in a stagnation region near the axis of the cell, which coincides with the axis of the cylindrical field-of-view of the detector. In some cases (e.g., Ref. 10), this interaction consists of a chemical reaction under nearly single-collision conditions. However, in the present experiments, Reaction (37) is too slow to occur significantly in the interaction zone at 3 mt, and all the O_3 emission observed arises from processes occurring in the discharge sidearms. This is readily confirmed by substituting non-reactive counterflow gases and obtaining no change in the observed emission intensity.

In the experiments reported here and in Section 5, the reagent gases were introduced at temperatures of 80-150 K; most of the experiments were conducted at 80-90 K. In the discharged gas, the Ar flow rate was held at 640 μmole/s, and the O_2 flow rate was varied from 2.3 to 86 μmole/s (0.3 to 12% O_2). Under these conditions, the residence time in the chemically active portion of the sidearm is approximately 2 ms, and vibrational deactivation of $O_3(v)$ occurs mainly via collisions with O and to a lesser extent with O_2 and the surface of the discharge tube.[4,9]

Vibraluminescence from $O_3(v)$ was observed with spectral resolutions of 0.027 to 0.080 μm (2.7 to 8.0 cm^{-1}). A typical spectrum is shown in
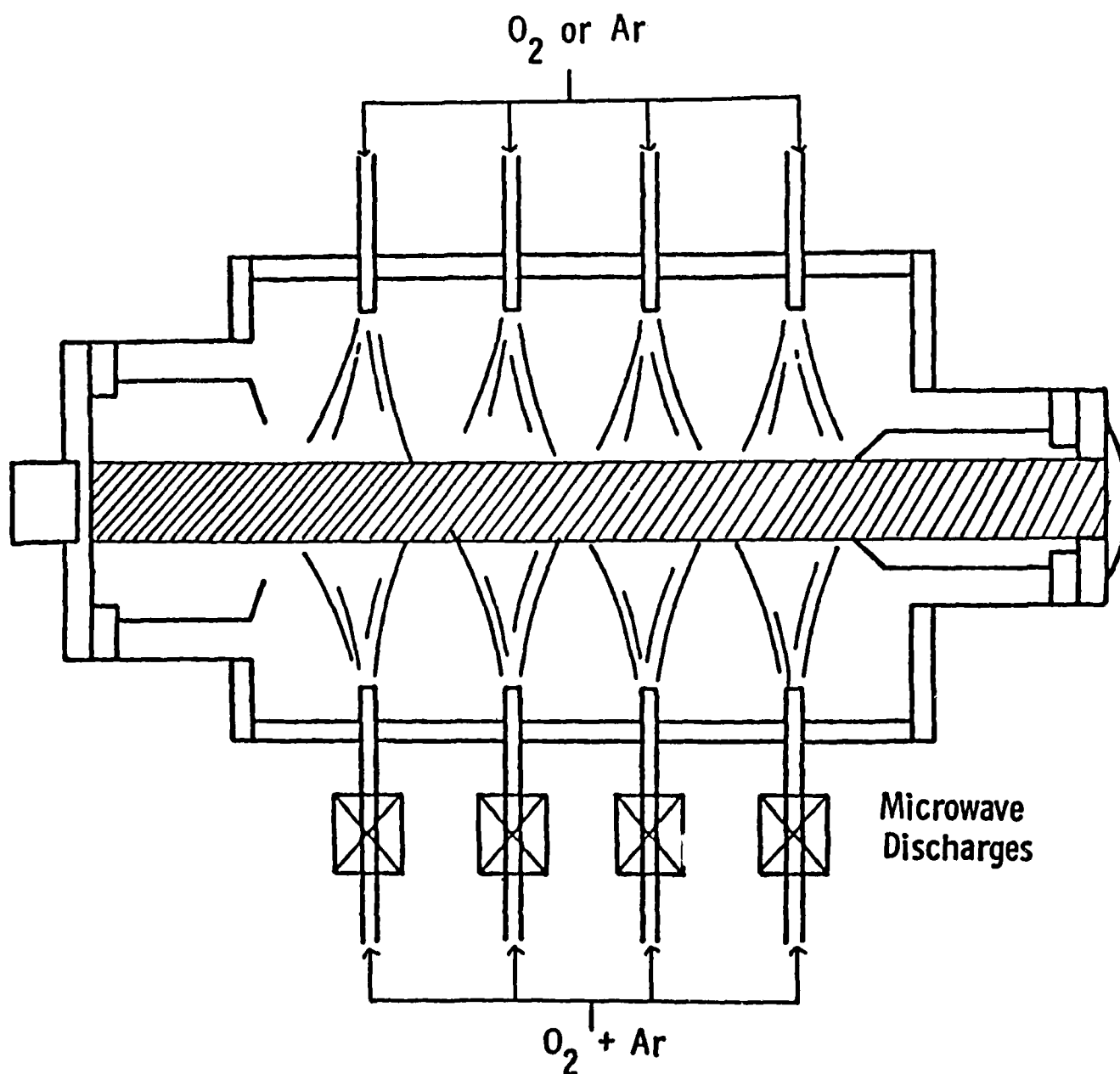
Figure 46. COCHISE reaction chamber. The cross-hatched region
delineates the field-of-view of the detector (not shown).

4-6

Figure 47, illustrating the readily identifiable (001)-(000) transition centered at 9.6 μm and the characteristic extension to longer wavelengths due to $\Delta v_3 = 1$ fluorescence from higher vibrational states. All spectral data were acquired by an on-line computer and were corrected to radiometric units using blackbody calibrations of the spectral responsivity of the detection system. Detailed spectroscopic analyses were restricted to the data with high spectral resolution, intermediate O_2 mole fraction, and low reagent temperature. However, the results of the analysis were applied to all the data and were found to provide consistent representations of the observed spectra over the entire range of experimental conditions.

4.3   Method of Spectral Analysis

The $O_3(v_3)$ spectral data are analyzed by a least-squares spectral fitting procedure[5] originally applied to O_3 spectra in Ref. 4. In this formulation, the transition frequencies and band strengths for the appropriate vibration-rotation transitions are computed or estimated from spectroscopic data in the literature, are convolved with the instrumental scan function, and are fit to the observed spectra to determine number densities of $O_3(v)$ in various emitting vibrational states. A complete spectral analysis would treat all $\Delta v_3 = 1$ transitions for all possible (v_1, v_2) combinations; however, such a treatment is extremely difficult owing to the overlap between adjacent emission bands and to the lack of spectroscopic data on highly vibrationally excited ozone (above two quanta). As will be shown in the next section, the spectral resolution of the present data is sufficient to allow clear identification of contributions and band center frequencies for emission from $(00v_3)$ and $(10v_3)$ states with up to five quanta of excitation. This result permits a more definitive representation of the emission spectrum than was possible in the previous work.

Detailed information on the rotational line positions and strengths of the (001)-(000), (002)-(001), (101)-(100), and (011)-(010) transitions is available from the absorption line parameter compilation of the Air Force Geophysics Laboratory;[11] these data are collected from the results of many

4-7
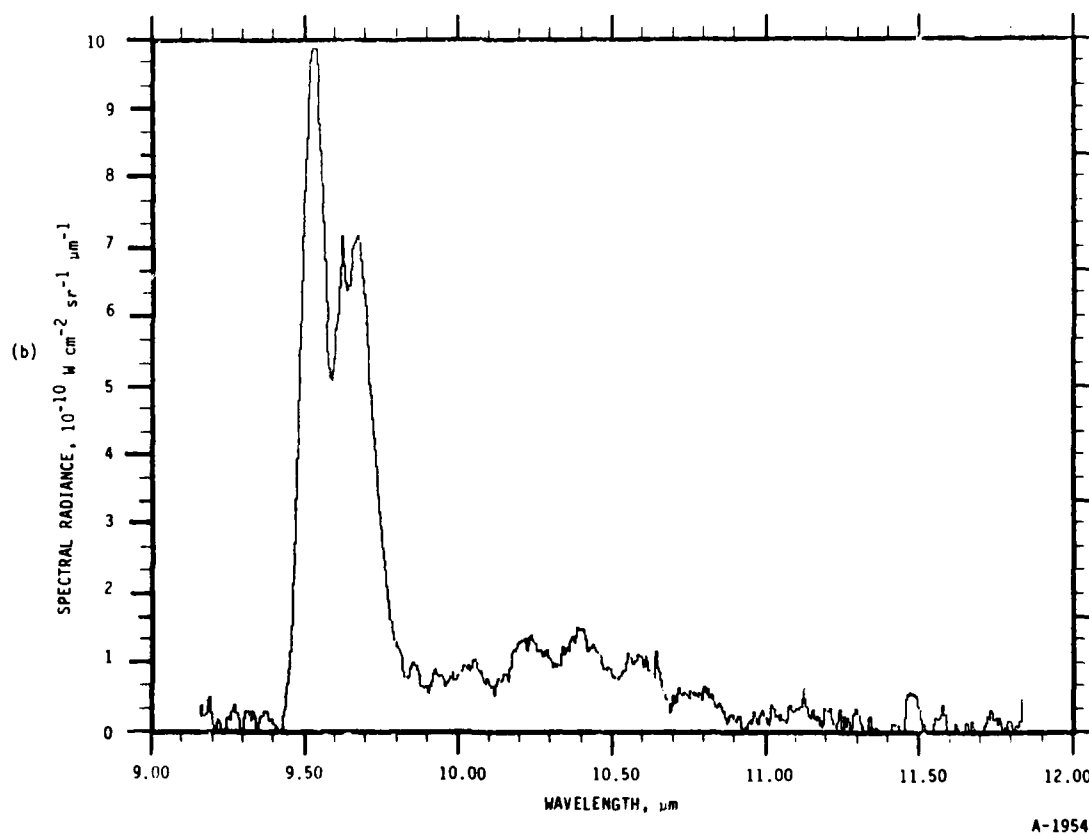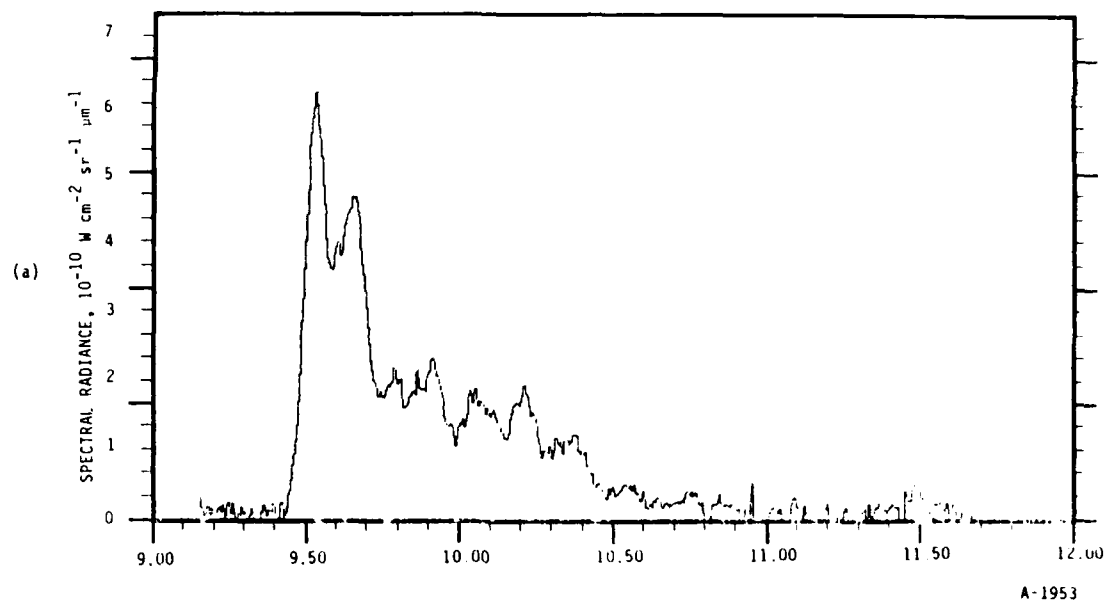
Figure 47. Observed $O_3(v)$ chemiluminescence spectra, medium resolution. $T = 80$ K, spectral resolution = 0.04 μm. (a) 1.0% O_2 in Ar; (b) 10.0% O_2 in Ar.

4-8

recent high resolution absorption measurements.[12-15] To describe the bandshapes for $\Delta v_3 = 1$ emission from higher-lying vibrational states, it is necessary to estimate the upper state emission band centers $\tilde{\nu}_0(v_1 v_2 v_3)$ from some description of the anharmonicity of the molecule. In our previous work,[4] the band centers were estimated from the simple first-order anharmonicity formula:

$$\tilde{\nu}_0(00v_3) = \tilde{\nu}_0(001) - 2 \, x_{33}(v_3-1) \tag{2}$$

with $x_{33} = 12.3 \text{ cm}^{-1}$ after the results of Barbe et al.[16] However, since O_3 exhibits Darling-Dennison resonance, a second-order coupling between upper levels of the symmetric and asymmetric stretching modes,[17] a more precise description of the vibrational energy levels can be obtained from the perturbation treatment presented by Barbe et al.[12] Adler-Golden and Armstrong[18] extended this treatment to incorporate additional high-lying states relevant to the present study. The transition frequencies at band center as determined from the vibrational state energies predicted by Adler-Golden and Armstrong[18] are used in the present analysis, with only slight adjustments as required to improve the comparison between observed and computed spectral features (see next section).

With the band center frequencies chosen as described above, the rotational line spacings and relative strengths within each band are taken to be the same as those given by Ref. 11 for the (001)-(000) band. This treatment thus neglects the effects of vibration-rotation interactions, an approximation which has no obvious impact on the analysis of the data reported here. The rotational population distributions are described by the usual Boltzmann factor using a single assumed rotational temperature. The assumed values of rotational temperature are adjusted to optimize the fit to the envelope of the R-branch of the (001)-(000) band, where there are no underlying contributions from other states. The contribution to the total integrated intensity due to each $\Delta v_3 = 1$ band is then given by

4-9

$$I_{v'} = hc \, \tilde{v}_{0v'} \, N_{v'} \, A_{v' \to v''} \qquad\qquad (3)$$

where v' and v" denote the upper and lower $(v_1 v_2 v_3)$ states, $N_{v'}$ is the number density of species in each upper state, and $A_{v' \to v''}$ is the band-integrated Einstein coefficient for each transition. The sum of the $dI_{v'}/d\lambda$ contributions, convolved with the instrumental slit function, is matched to each experimental spectrum by a linear least squares fit in which the quantities $\{N_{v'} \, A_{v' \to v''}\}$ are the solutions which minimize the sum of the squares of the intensity differences between experimental and computed spectra. The values of $N_{v'}$ can then be determined if values for $A_{v' \to v''}$ can be specified. The estimation of $A_{v' \to v''}$ is discussed in the next section.

4.4 Results and Discussion

4.4.1 Spectral Analysis

A representative comparison between observed and computed high-resolution spectra is illustrated in Figure 48. Also shown in Figure 48 are the individual contributions of the identifiable vibrational bands to the total spectral intensity. At the present spectral resolution of 0.027 μm, the P, Q, and R branch structures of many of the individual vibrational bands can be clearly identified, especially with the aid of the spectral fitting analysis. Spectral fits incorporating only $(00v_3)$ transitions are clearly inadequate at this resolution, failing to account for the spectral intensity observed near 10.0, 10.3, and 10.7 μm. Incorporation of $(10v_3)$ bands into the calculations provides a good match to the observed spectral structure. Further incorporation of other $(v_1 v_2)$ combinations is unnecessary to explain the data, and leads to an overspecification of the least squares fitting due to extensive band overlap. Indeed, spectral calculations show that if the v_1 and v_2 modes are excited to the extent observed for v_3, the resulting band overlap would cause a smoothing effect on the total spectrum, i.e., the vibrational structure would be more "washed out" than we observe. Thus we conclude that the v_1 and v_2 modes are not significantly excited in these experiments.
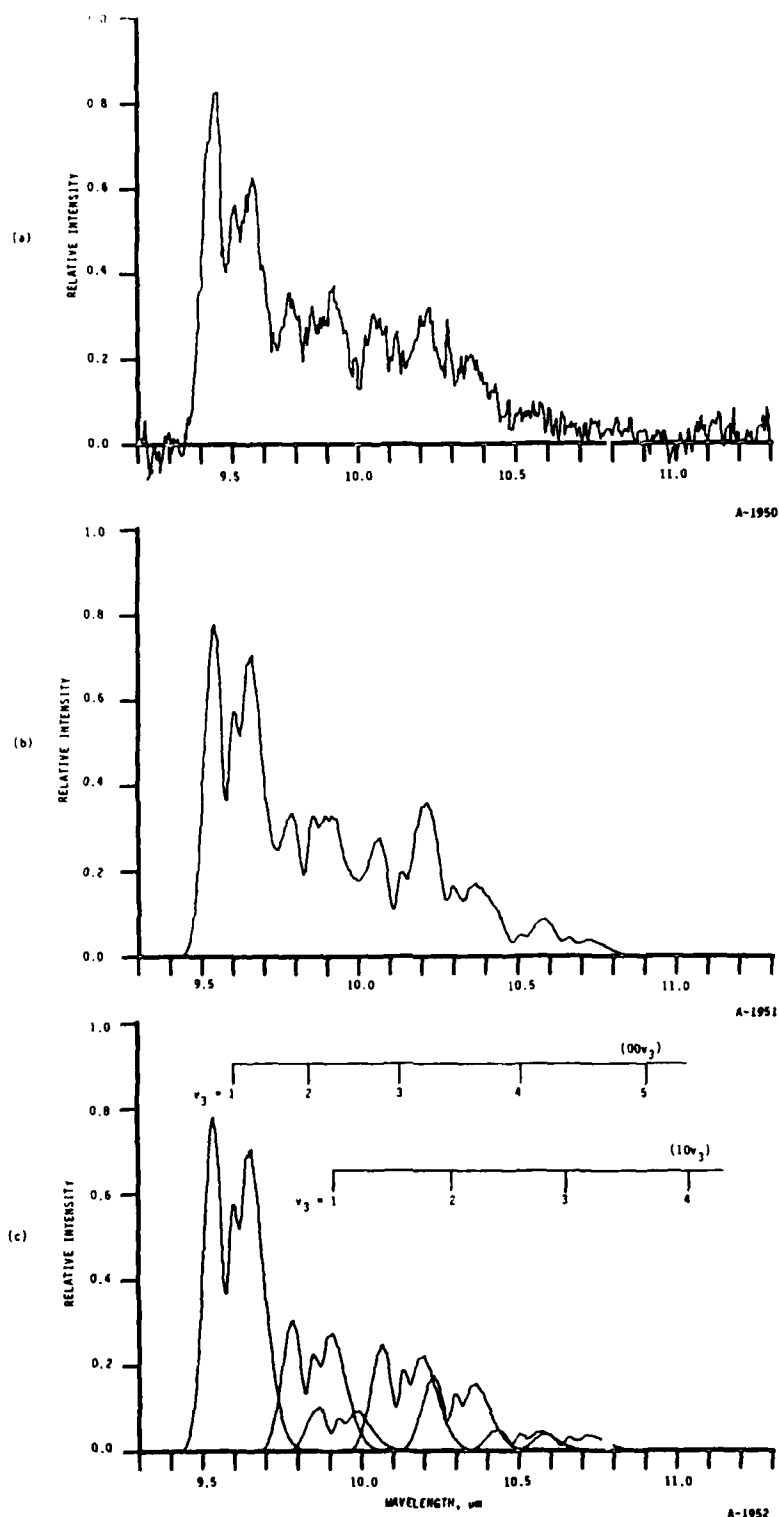
Figure 48. Observed and computed $O_3(v)$ chemiluminescence spectra, high resolution. (a) Experimental spectrum, 1.0% O_2 in Ar, T = 80 K, spectral resolution = 0.027 μm, corrected for spectral responsivity. (b) Computed spectrum, least squares fit, T_{ROT} = 50 K. (c) Contributions from individual vibrational bands. Data for the five-quantum states are available in spectral scans of lower resolution and better S/N near 11.0 μm.

4-11

From the comparison of best fit and experimental spectra, it is possible
to determine the band center frequencies which provide the best alignment.
The values of $\nu_{0v'}$ determined from calculations of Ref. 18 (i.e., Darling-
Dennison perturbation of a harmonic oscillator, fit to the spectroscopic data
of Barbe et al.[12]) provide a reasonable fit to the data; however, we find it
necessary to adjust these values slightly to give the best results. The band
centers determined in this fashion are listed in Table 3, along with the har-
monic Darling-Dennison values. The observed values agree with the results of
Barbe et al.[12] and the predictions of Adler-Golden and Armstrong[18] within
approximately 3 cm^{-1}. i.e., well within the uncertainties of both the present
experiment and the predictions. Also listed in Table 3, and in significant
disagreement with the present results, are values of $\nu_{0v'}$ as determined from:
(1) the simple anharmonic oscillator approximation of Eq. (38) (used in our
previous work);[4] (2) spectroscopic data of Imre et al.;[19] and (3) a fit to the
data of Imre et al.[19] using an algebraic formulation for coupled anharmonic
modes.[20]

An additional factor which aids in spectral separation of the vibrational
bands is the low rotational temperature observed in the experiments
($T_{ROT} \sim 50$ K in Fig. 48). The temperature of the discharge sidearm is typi-
cally 80 K or higher. As the discharged gas expands into the reaction chamber
(Fig. 46), it undergoes a rather crude free expansion where rotational energy
is partially converted to translation. When an equal mass flow of opposing
counterflow gas is admitted to the reaction cell, a stagnation region develops
along the axis, and most of the initial rotational energy is recovered.[21]
This is confirmed by observation of rotational temperatures consistent with
the sidearm temperature, as reported previously.[4] However, when no opposing
counterflow is introduced, there is no well-defined quasi-static region within
the field of view, and the recovery of rotational energy is incomplete. This
results in lower rotational temperatures and correspondingly reduced spectral
overlap between adjacent vibrational bands. Indeed, close examination of the
P and R branch structure of the (001)→(000) band (Fig. 48) reveals that the
observed rotational distribution is multi-modal and is not adequately
represented by our Boltzmann approximation. The higher-energy wings of the

TABLE 3. BAND ORIGINS (cm^{-1}) FOR OBSERVED $\Delta v_3 = 1$ TRANSITIONS.

State	This Work ($\pm$ 3 cm^{-1})	Darling-Dennison Perturbation[a]	Algebraic Hamiltonian[b]	Anharmonic Oscillator[c]
001	1042	1042.1	1040.94	1042
002	1016	1015.8	1013.32	1018
101	1008	1007.6	1003.96	-
003	987	987.3	983.57	993
102	971	974.5	969.81	-
004	952	955.4	949.59	968
103	939	941.6	935.37	-
005	916	918.8	910.61	944
104	904	907.1	899.64	-
006	-	87C.6	868.86	919
105	-	871.0	862.54	-
007	-	847.7	827.35	-
106	-	833.6	824.45	-

[a]Ref. 18, fit to spectroscopic data of Ref. 12.

[b]Ref. 20, fit to spectroscopic data of Ref. 19.

[c]Approximation used in Ref. 4, spectroscopic data of Ref. 16.

band are well fit by the value 50 ± 5 K, but the ratio of the R and P branch maxima is characteristic of a much higher rotational temperature near that of the discharge gas prior to expansion. Thus the lower rotational levels appear to be collisionally thermalized on the time scale of the measurement, while the higher levels are not. For comparison, the transit time from the discharge tube outlet to the field of view is approximately 0.5 ms and the residence time in the field of view is approximately 0.2-0.3 ms. The 50 K distribution found for the higher rotational levels suggests that R→T transfer in the expansion is collision-limited for our apparatus. Thus the observed rotational structure is not fully accounted for in the spectral analysis. However, as we have observed for other molecular systems,[5-10] minor discrepancies in the rotational fine structure of the spectrum do not significantly affect the analysis of the much coarser vibrational envelope, so the results of the spectral fitting are not sensitive to the above uncertainties in the rotational distribution.

4.4.2 Estimation of Band Einstein Coefficients

As described above (Eq. (3)), values of the band-integrated Einstein coefficients $A_{v'\to v''}$ are required to transform the spectral fitting solutions into $O_3(v)$ number densities. Values for low-lying vibrational states accessible in thermal absorption measurements are well documented and are available in the literature.[11] However, no such data exist for the higher vibrational states of O_3 (i.e., three quanta or more). It is therefore necessary to estimate values for the higher states based on possible scalings of $\Delta v_3=1$ transition probabilities with vibrational energy.

The Einstein coefficients for the $\Delta v_3=1$ emissions observed here may be scaled from the well-known[11] values for $(001)\to(000)$ and $(101)\to(100)$ transition via the relationship

$$\frac{A_{v'v''}}{A_{10}} = \left(\frac{\nu_{v'v''}}{\nu_{10}}\right)^3 \left(\frac{R_{v'v''}}{R_{10}}\right)^2 \tag{4}$$

where $R_{v'v''}$ is the transition moment matrix element connecting states v' and v'', and the subscript 10 denotes the (001)-(000) or (101)-(100) transitions as appropriate. If the system is electrically harmonic, Eq. (5) reduces to

$$A_{v'v''} = v' A_{10} \left(\frac{\nu_{v'v''}}{\nu_{10}} \right)^3 \qquad (5)$$

In this case the transition probabilities scale with vibrational quantum number, but are moderated by the mechanical anharmonicity of the oscillator. We have used this scaling formula in our previous work.[4] However, it is highly likely that this approximation will break down at some point for higher vibrational levels. This could occur by one or more of several mechanisms, including electrical anharmonicity, near-resonant intermode coupling (e.g., Darling-Dennison coupling or accidental resonances), vibronic coupling with a possible bound electronically excited triplet state,[22] or the approach to ergodic behavior[23] near the dissociation limit. With the possible exception of electrical anharmonicity, these effects will tend to reduce the transition probabilities from the values predicted by Eq. (41). We expect vibronic coupling and ergodic behavior, if they occur, to be more significant for vibrational levels higher than those observed here; indeed, such effects may be partially responsible for our failure to observe emission from O_3 states near the dissociation limit.

The effects of Darling-Dennison coupling and transition moment variations have been investigated theoretically by Adler-Golden and coworkers.[18,24,25] Adler-Golden and Armstrong[18] report $(R_{v'v''}/R_{10})^2$ values determined from the first-order matrix elements obtained from overlap integrals of the perburbed harmonic oscillator wavefunctions of Barbe et al.[12] These calculations predict lower values of $A_{v'v''}$ then Eq. (41), the deviation being less than ten percent for $v_3' \leq 3$ but more substantial at higher v_3'. The two sets of values are compared in Fig. 49. Also shown in Fig. 49 are values of $A_{v'v''}$ determined from the perturbed harmonic oscillator wavefunctions together with an ab initio dipole moment function.[24,25] These latter calculations indicate
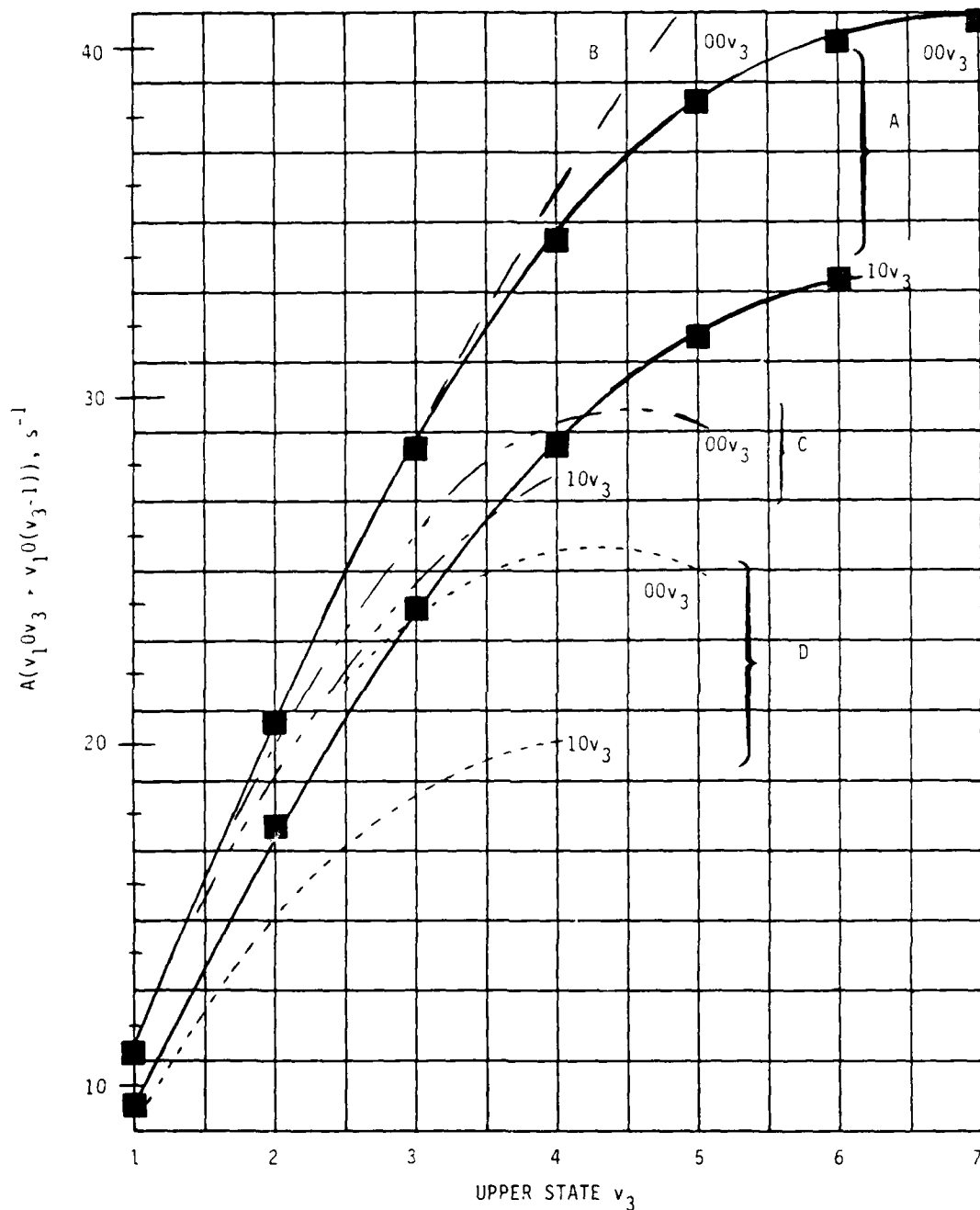
A-1956

Figure 49. Estimated Einstein coefficients for $O_3(\nu_3)$ emission.
A: Eq. (41) with observed band origins, used in this
work; B: Eq. (41) with anharmonic oscillator estimation
of band origins, used in Ref. 4; C: Darling-Dennison
+ electrical harmonicity, derived in Ref. 18 from
data of Ref. 12; D: Darling-Dennison + ab initio
dipole moment of Ref. 24, reported in Ref. 25.

that the effects of electrical anharmonicity may be substantial for $v_3 \geq 5$. However, it should be noted that the quartic potential surface[12] used in these calculations is accurate only near the bottom of the potential well, and may not be adequate for treatment of the higher vibrational levels.

For the range of vibrational levels observed in our experiments, we have elected to use the $A_{v'v''}$ values given by Eq. (5). It appears upon comparison to complex theoretical calculations[25] that the uncertainty in these values is minimal for $v_3' \leq 3$, and that Eq. (5) provides, at worst, upper bounds to $A_{v'v''}$ for higher v_3'. Thus the vibrational state number densities inferred from our analysis may actually be lower bounds for $v_3' = 4\text{-}5$, the values being perhaps 50 percent low for $v_3' = 5$. We await definitive measurements of either $A_{v'v''}$ or $(R_{v'v''}/R_{10})^2$ to resolve this remaining uncertainty.

4.4.3 Vibrational Population Distributions

The values of $N_{v'}A_{v'v''}$ obtained from the spectral fitting analysis were transformed into vibrational state number densities using $A_{v'v''}$ values estimated from Eq. (5). Representative vibrational distributions obtained for different initial O_2 mole fractions are shown in Fig. 50. The error bars, indicated where larger than the data point symbols, are the statistical standard deviations in the least-squares solutions (67 percent confidence) as determined from the variance-covariance matrix for each spectral fit. (It should be noted that this error analysis assumes Gaussian statistics, which may not be strictly correct for non-orthogonal solutions as pertain here.) The variations in both absolute number density and relative distribution as functions of initial O_2 mole fraction in the discharges are clearly seen. For low O_2 levels, the vibrational distributions are roughly Boltzmann in character, with the relative contribution from higher levels increasing as the O_2 is reduced. In contrast, at high O_2 mole fraction, the distribution is sharply bimodal. In our previous work,[4] we interpreted similar observations to represent steady-state distributions resulting from excitation and deactivation processes occurring in the discharge tubes: (1) three-body recombination
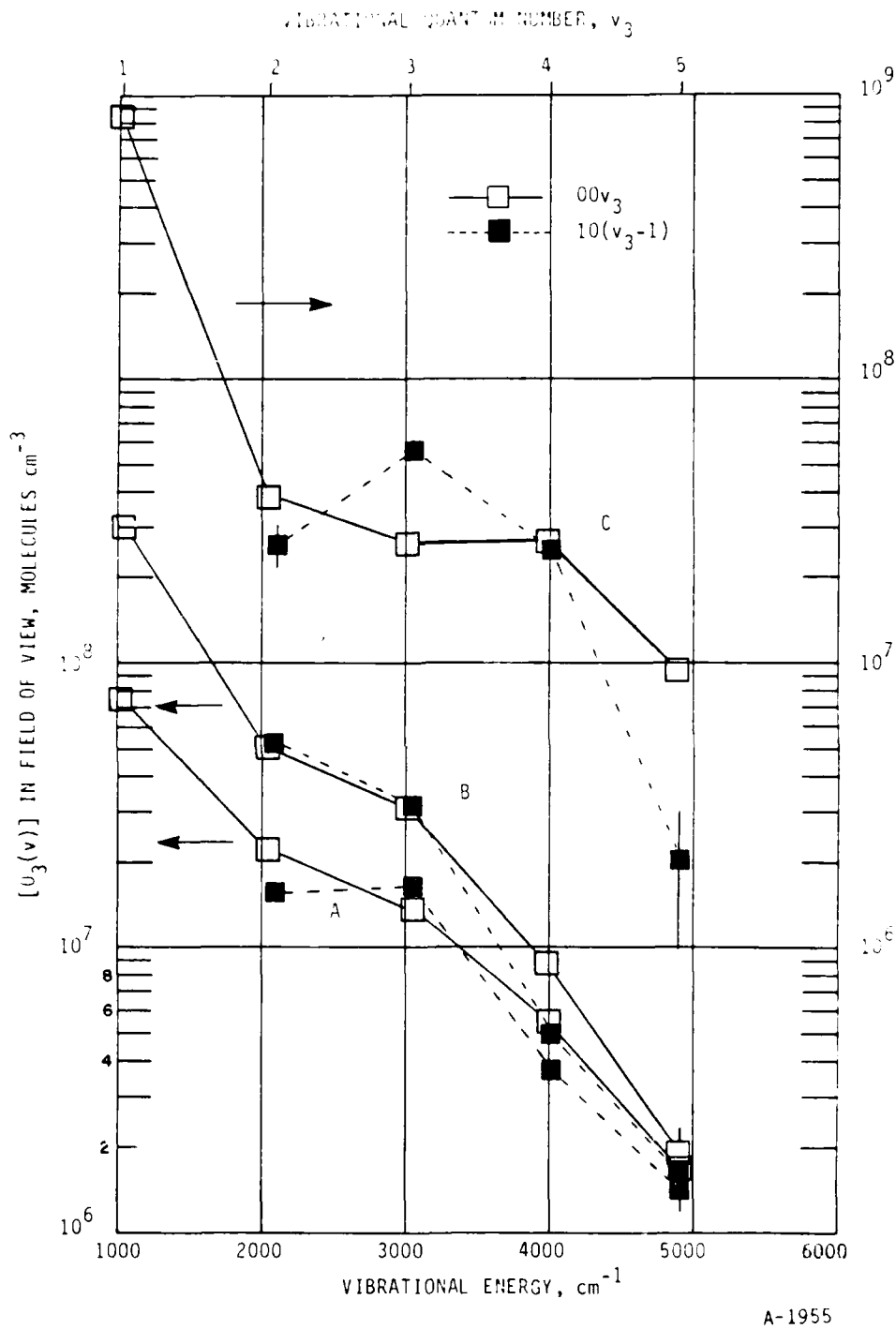
Figure 50. Example $O_3(v)$ vibrational population distributions, T = 80 K. A: 0.24% O_2 in Ar; b: 1.46% O_2 in Ar; C: 10.1% O_2 in Ar.

4-18

of O and O_2 at low O_2 levels, with deactivation by O and Ar; and (2) one or more additional $O_3(v)$ excitation processes at high O_2. These interpretations are supported and amplified by more detailed kinetic measurements of this type, as described in Section 5.

Another effect can be seen upon examination of the combination state number densities. The $\nu_1 + (n-1)\nu_3$ states lie closer in energy to the corresponding $n\nu_3$ levels than any of the other vibrational levels of O_3. Indeed, they are the only levels within $\sim kT$ at the bath temperature of 80 K, having Boltzmann factors at that temperature, $N_{10(v_3-1)}/N_{v_3}$, of 0.39, 0.52, 0.62 and 0.77 for $v_3 = 2$, 3, 4, and 5, respectively. Within the statistical fitting uncertainties, the observed population ratios for the $v_3 = 4$, 5 states match the 80 K Boltzmann factors for the low O_2 mole fraction cases (i.e., the recombination-dominated regime). This observation is consistent with population of the 103 and 104 states by rapid, near-resonant collisional V$\rightarrow$T energy transfer from the 004 and 005 states initially populated in the recombination/deactivation sequence. However, the 102 and 101 populations are significantly larger than dictated by Boltzmann factors; in particular, the population of the 102 state is enhanced by as much as a factor of 3, giving rise to its prominence in the spectrum as discussed above. This type of observation indicates a direct source of $O_3(102)$ other than deactivation of higher states. We note that $O_3(102)$, which lies at an energy of 3085 cm^{-1}, is nearly resonant with $O_2(v=2)$ at 3089 cm^{-1}. Since $O_2(v)$ is surely an important species in discharged oxygen effluents, it is possible that $O_3(102)$ is efficiently produced by the rapid V-V exchange:

$$O_2(v=2) + O_3(000) \rightarrow O_3(102) + O_2(v=0) \tag{6}$$
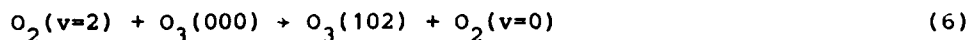
We then expect $O_3(101,002,003)$ to be formed by collisional deactivation of $O_3(102)$.

The ν_2 mode does not appear to be significantly populated by collisional energy transfer in our experiments; this is consistent with the slow rates for

transfer from the stretching to the bend modes observed by other workers.[26-30] Perhaps more surprisingly, higher levels of the ν_1 mode ($v_1 > 1$) are also not observed in the spectra. These results imply that the recombination/ deactivation sequence is mode-selective, with only near-resonant transfer to $v_1 = 1$ states branching into the symmetric stretch mode. This point will be examined in more detail in Section 5.

4.5 Summary and Conclusions

In summary, we have obtained moderate-resolution spectra of infrared emission from vibrationally excited ozone, formed principally by three-body recombination of O and O_2 (Reaction (37)) in flowing, microwave-discharged O_2/Ar mixtures near 1 torr and 80 K. The observed emission occurs entirely in the ν_3-mode fundamental band near 10 μm. The ν_1 and ν_2 bands at 9 and 14 μm, respectively, are too weak to be observed in our experiments, implying excited state number densities in those modes that are factors of $50(\nu_1)$ and $14(\nu_2)$ less than those for the ν_3-band radiating species.

From the emission spectra, we are able to identify the band centers for $\Delta v_3 = 1$ transitions from $(00v_3)$ and $(10v_3)$ vibrational levels with up to 5 quanta of stretching excitation. The band center frequencies for these transitions are consistent with those predicted from a Darling-Dennison coupling analysis.[18]

We have determined individual vibrational state number densities from a least squares spectral fitting analysis. Central to this determination is the description of the variation of the Einstein transition probabilities with vibrational quantum number, which is fairly reliable near the bottom of the potential well but becomes highly uncertain for levels above those identified here.

The results presented here are consistent with those of our previous work,[4] which was performed over a less extensive range of experimental conditions. In that work, a simple kinetic analysis was used to establish

4-20

that Reaction (1) is responsible for the observed emission for most conditions; furthermore, evidence for a secondary excitation of the $v_3' = 4$, 5 levels is observed at larger O_2 mole fractions. In addition to these effects, the improved spectral resolution of the present work reveals that $O_3(102)$ appears to be selectively excited relative to the other vibrational levels; we take this to be evidence for a rapid, near-resonant V-V exchange between $O_3(000)$ and $O_2(v=2)$ (Reaction (6)). The detailed excitation and deactivation kinetics of $O_3(v)$ are the subject of Section 5.

The observed spectra also indicate an absence of states with significant excitation in the v_1 and v_2 modes. This implies a rather surprising degree of selectivity for asymmetric stretching motion in the recombination sequence. The observed $O_3(v)$ molecules have undergone approximately 10^4 collisions with Ar and O, which should result in substantial collisional deactivation following their initial formation, and thus they represent the recombination products at some intermediate stage in the thermalization sequence. Despite this rather advanced stage of the reaction, most of the excitation is still in the v_3 mode, i.e., there has been little or no collisional or intramolecular randomization of the recombination energy. This has interesting implications for the detailed dynamics of association and stabilization of the nascent O_2-O complex: perhaps the ensemble of complexes which form stable vibrationally excited molecules retain a "memory" of the original approach configuration (i.e., the internuclear motion is not substantially altered upon stabilization), and the subsequent deactivation to well-defined energy states in the lower half of the potential well is so rapid that equilibration of the internal vibrational modes is kinetically limited for our experimental conditions. Indeed, trajectory calculations for Ar-O_3 collisions indicate rapid deactivation of highly excited ozone through V→R→T energy transfer.[31,32] A possible alternative hypothesis is that the mode selectivity could arise from formation of $O_3(v)$ by the chaperone mechanism, via the complex ArO. The chaperone mechanism for Reaction (37) has been suggested by Troe and coworkers[33] on the basis of the anomalously low reaction rate coefficient at high pressure.

As a final point, the absence of higher vibrational levels deserves comment. The O_3 potential well can accommodate up to 8 or 9 bound vibrational levels in the ν_3 mode; however, under no conditions do we observe more than five quanta of excitation. Thus the chemiluminescence spectrum never extends substantially beyond approximately 11 μm (at our spectral resolution and low rotational temperatures). The five-quantum level occurs at an energy of 4919 cm^{-1}, or about 58 percent of the dissociation energy of O_3. Possible explanations for this apparent spectral "cutoff" include kinetic interference of the long-postulated triplet excited state of O_3,[22,34] or a catastrophic loss of transition strength at high energies due to anharmonic or resonance effects or quantum "chaos"[23] as discussed above. If any of these hypotheses are correct, then the 11-12 μm fluorescence from higher vibrational levels of O_3 may never be observable, even in the rarefied conditions of the upper atmosphere. However, it is clear that collisional deactivation by both Ar and O is important in our experiments, and the "hottest" vibrational distributions are obtained at low initial O_2 mole fractions where the total fluorescence signal is very small, so the fluorescence from the higher states may simply lie below our detection limit because of rapid collisional deactivation. In that case, 11-12 μm fluorescence may be detectable at low pressures if sufficient detector sensitivity can be attained. The kinetic data and analysis presented in Section 5 address this issue.

4.6 References

1. von Rosenberg, C.W. and Trainor, D.W., "Observations of Vibrationally Excited Ozone Formed by Recombination," J. Chem. Phys. 59, 2142 (1973).

2. von Rosenberg, C.W. and Trainor, D.W., "Vibrational Excitation of Ozone Formed by Recombination," J. Chem. Phys. 61, 2442 (1974).

3. von Rosenberg, C.W. and Trainer, D.W., "Excitation of Ozone Formed by Recombination, II," J. Chem. Phys. 63, 5348 (1975).

4. Rawlins, W.T., Caledonia, G.E., and Kennealy, J.P., "Observation of Spectrally Resolved Infrared Chemiluminescence from Vibrationally Excited $O_3(\nu_3)$," J. Geophys. Res. 86, 5247 (1981).

5. Rawlins, W.T., Murphy, H.C., Caledonia, G.E., Kennealy, J.P., Robert, F.X., Corman, A., and Armstrong, R.A., "COCHISE: Laboratory Studies of Atmospheric Infrared Chemiluminescence in a Cryogenic Environment," Appl. Opt. 23, 3316 (1984).

6. Rawlins, W.T., Caledonia, G.E., Gibson, J.J., and Stair, A.T., Jr., "HIRIS Rocketborne Spectra of Infrared Fluorescence in the $O_3(\nu_3)$ Band Near 100 km," J. Geophys. Res. 40, 2896 (1985).

7. Green, B.D., Rawlins, W.T., Nadile, R.M., "Diurnal Variability of Vibrationally Excited Mesospheric Ozone as Detected by SPIRE," J. Geophys. Res., in press, 1985.

8. Rawlins, W.T., "Chemistry of Vibrationally Excited Ozone in the Upper Atmosphere," J. Geophys. Res., in press, 1985.

9. Rawlins, W.T., and Caledonia, G.E., "Dynamics of Vibrationally Excited Ozone Formed by Three-Body Recombination. II: Kinetics and Mechanism," J. Chem. Phys., to be submitted, 1985.

10. Kennealy, J.P., DelGreco, F.P., Caledonia, G.E., and Green, B.D., "Nitric Oxide Chemiexcitation Occurring in the Reaction Between Metastable Nitrogen Atoms and Oxygen Molecules," J. Chem. Phys., 69 (4), 1574 (1978).

11. Rothman, L.S., Gamache, R.R., Barbe, A., Goldman, A., Gillis, J.R., Brown, L.A., Toth, R.A., Flaud, J.M., and Camy-Peyret, C., "AFGL Atmospheric Absorption Line Parameters Compilation: 1982 Edition," Appl. Opt. 22, 2247 (1983).

12. Barbe, A., Secroun, C., and Jouve, P., "Infrared Spectra of $^{16}O_3$ and $^{18}O_3$: Darling and Dennison Resonance and Anharmonic Potential Function of Ozone," J. Mol. Spectrosc. 49, 171 (1974).

13. Barbe, A., Secroun, C. Jouve, P., Monnanteuil, N., Depannemaecker, J.C., Duterage, B., Bellet, J., and Pinson, P., "Infrared and Microwave High-Resolution Spectrum of the ν_3 Band of Ozone," J. Mol. Spectrosc. <u>64</u>, 343 (1977).

14. Flaud, J.M., Camy-Peyret, C., Barbe, A., Secroun, C., and Jouve, P., "Line Positions and Intensities for the $2\nu_3$, $\nu_1+\nu_3$, and $2\nu_1$ Bands of Ozone," J. Mol. Spectrosc. <u>80</u>, 185 (1980).

15. Barbe, A., Secroun, C., Jouve, P., Goldman, A., and Murcray, D.G., "High-Resolution Infrared Atmospheric Spectra of Ozone in the 10 μm Region: Analysis of the ν_1 and ν_3 Bands - Assignment of the $(\nu_1+\nu_2)-\nu_2$ Band," J. Mol. Spectrosc. <u>86</u>, 286 (1981).

16. Barbe, A., Secroun, C., and Jouve, P., "Spectre d-Absorption Infrarouge de l'Ozone Gazeux," Compte Rendeu Acad. Sci, Paris, <u>274</u>, 615 (1972).

17. Herzberg, G., <u>Infrared and Raman Spectra of Polyatomic Molecules</u>, D. van Nostrand Company, 1945.

18. Adler-Golden, S.M., and Armstrong, R.A., "Spectroscopic Parameters for Ozone from Infrared and Ultraviolet Techniques," AFGL-TR-82-0231, Air Force Geophysics Laboratory, Hanscom AFB, MA (1982). ADA124315.

19. Imre, D.G., Kinsey, J.L., Field, R.W., and Kateyama, D.H., "Spectroscopic Characterization of Repulsive Potential Energy Surfaces: Fluorescence Spectrum of Ozone," J. Phys. Chem. <u>86</u>, 2564 (1982).

20. Benjamin, I., Levine, R.D., and Kinsey, J.L., "High-Lying Levels of Ozone Via an Algebraic Approach," J. Phys. Chem <u>87</u>, 727 (1983). See also comments by Lehmann, K.K., J. Phys. Chem. <u>88</u>, 1047 (1984) and authors' reply.

21. Caledonia, G.E., Green, B.D., Simons, G.A., Kennealy, J.P., Robert, F.X., Corman, A., and DelGreco, F.P., "COCHISE Studies I: Fluid Dynamical and Infrared Spectral Analysis," AFGL-TR-77-0281, Air Force Geophysics Laboratory, Hanscom AFB, MA (1977). ADA053218.

22. Wilson, C.W., Jr., and Hopper, D.G., "Theoretical Studies of the Ozone Molecule. I. Ab Initio MCSCF/CI Potential Energy Surfaces for the X^1A_1 and a^3B_2 States," J. Chem. Phys. <u>74</u>, 595 (1981).

23. Hansel, K.D., "On the Dynamics of Multiphoton Dissociation of Polyatomic Molecules II. Application to O_3," <u>Laser-Induced Processes in Molecules</u> (K.L. Kompa and S.D. Smith, Editors), Springer Series in Chemical Physics, Vol. 6, Springer, Berlin (1979).

24. Adler-Golden, S.M., Langhoff, S.R., Bauschlicher, C.W., Jr., and Carney, G.D., "Theoretical Calculation of Ozone Vibrational Intensities," J. Chem. Phys. <u>83</u>, 255 (1985).

25. Adler-Golden, S.M., "Recommended Einstein Coefficients for Ozone Chemiluminescence in COCHISE," SSI-TR-54, Spectral Sciences Inc., Burlington, MA, 1984.

26. Rosen, D.I., and Cool, T.A., "Vibrational Deactivation of $O_3(101)$ Molecules in Gas Mixtures," J. Chem. Phys. 59, 6097 (1973).

27. Rosen, D.I., and Cool, T.A., "Vibrational Deactivation of O_3 Molecules in Gas Mixtures, 2," J. Chem. Phys. 62, 466 (1975).

28. Hui, K.K, Rosen, D.I., and Cool, T.A., "Intermode Energy Transfer in Vibrationally Excited O_3," Chem. Phys. Lett. 32, 141 (1975).

29. Adler-Golden, S.M., and Steinfeld, J.I., "Vibrational Energy Transfer in Ozone by Infrared-Ultraviolet Double Resonance," Chem. Phys. Lett. 76, 479 (1980).

30. Jones, J.A., Burkholder, J.B., and Bair, E.J., "Vibrational Relaxation in Ozone Recombination," J. Chem. Phys. 76, 5902 (1982).

31. Stace, A.J., and Murrell, J.N., "A Classical Trajectory Study of Collisional Energy Transfer in Thermal Unimolecular Reactions," J. Chem. Phys. 68, 3028 (1978).

32. Gelb, A., "Classical Trajectory Study of Energy Transfer Between Argon Atoms and Vibrationally-Rotationally Excited Ozone Molecules," J. Phys. Chem, in press, 1985.

33. Croce de Cobos, A.E., and Troe, J., "High Pressure Range of the Recombination $O+O_2+O_3$," Int. J. Chem. Kinet. 16, 1519 (1984).

34. Swanson, N., and Celotta, R.J., "Observation of Excited States in Ozone Near the Dissociation Limit," Phys. Rev. Lett. 35, 783 (1975).

5. KINETICS OF VIBRATIONALLY EXCITED OZONE

5.1 Introduction

The chemical kinetics of vibrationally excited ozone, $O_3(v)$, is a complex problem of fundamental importance in studies of atmospheric photochemistry as well as in basic molecular dynamics. Experimental observations of $O_3(v)$ formed during three-body recombination sequence

$$O + O_2 \rightleftharpoons O_3^{\ddagger} \tag{1a}$$

$$O_3^{\ddagger} + M \rightarrow O_3(v) + M \tag{1b}$$

$$O_3(v) + M \rightarrow O_3(v-n) + M \tag{1c}$$
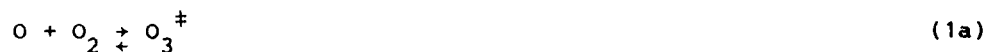
can provide insight to the detailed dynamics of the initial formation of $O_3(v)$ and to the subsequent vibrational deactivation and intermode exchange. In particular, low-pressure observations of discrete $O_3(v)$ states formed in early stages of the recombination sequence can provide a unique data base on a marginally understood problem in chemical kinetics: the molecular dynamics and mechanisms of recombination and energy transfer in polyatomic systems.[1]

The kinetics of $O_3(v)$ formation and deactivation have been addressed by a number of investigators. In general, $O_3(v)$ is usually formed by laser excitation of the v_3-mode or by three-body recombination following flash photolysis, and is detected by ultraviolet absorption or broadband infrared fluorescence. Rosen and Cool[2-4] studied the quenching of infrared fluorescence from low-lying, laser-excited vibrational states of O_3 by several reagents, and showed that vibration-to-translation (V→T) energy transfer near the bottom of the potential well is rate-limited by deactivation from the well-coupled symmetric (v_1) and asymmetric (v_3) stretching modes through the poorly coupled bending (v_2) mode. Using similar techniques, West et al.[5,6] studied the deactivation of low levels of $O_3(v)$ by O, concluding that the deactivation pathway was primarily V-T energy transfer rather than chemical conversion to O_2.

Von Rosenberg and Trainor[7-9] were the first to observe $O_3(v)$ formed in three-body recombination, reporting on the production and deactivation of broadband infrared fluorescence in the ν_3, $\nu_1 + \nu_3$, and ν_2 bands. Working at total pressures of 100 to 400 torr, they found greater excitation in the bending than in the stretching modes, presumably because of the extensive collisional deactivation and intermode transfer by both V→T and V→V ($O_3(v) + O_3$ intermode equilibration) processes that occurred under these conditions. More recently, the kinetics of laser-initiated and recombination-generated $O_3(v)$ have been re-investigated using ultraviolet absorption in the Hartley bands as the diagnostic for $O_3(v)$.[10-15] These studies are somewhat less definitive than the infrared fluorescence measurements owing to the greater difficulty of resolving contributions from different modes to the observed absorption spectra; however, the results are generally consistent with the analogous infrared fluorescence data. It is noteworthy that Joens et al.,[15] investigating recombination under conditions of V→T-dominated collisional deactivation, inferred initial formation of $O_3(v)$ in the stretching modes followed by kinetically limited collisional transfer to the bending mode, in contrast to the results of von Rosenberg and Trainor.[7-9]

Except for the $O + O_3(v)$ studies,[5,6] all of the above experiments were performed in a flash-photolysis mode, with relatively high pressures of order 10^2 torr, observation times of 10 to 100 µs, and room temperature. Thus the newly formed $O_3(v)$ molecules experienced on the order of $10^4 - 10^6$ collisions on the time scale of the observations. In many cases, O_3 was a significant collision partner, providing the avenue of rapid V→V equilibration. In contrast, in the upper atmosphere (e.g., altitudes of 80 to 100 km, where $O_3(v)$ effects are most pronounced), an excited $O_3(v)$ molecule suffers only about $10^2 - 10^3$ collisions in the time scale of its radiative lifetime; the principal collision partners are N_2 and O_2, which we expect to induce simple V→T cascade down the vibrational ladder, and O, which may give more complex deactivation pathways. Thus it is important to probe the earliest possible stages of the recombination sequence, where the effects of V→T cascade (Reaction (1c)) are minimized, in order to determine the range of vibrational levels which are likely to be populated in high-altitude atmospheric conditions.

We report here on studies of the $O + O_2$ recombination sequence in flow-ing, microwave-discharged O_2/Ar mixtures near 1 torr and at low temperatures, 80 to 100 K. Prior to their observation, the $O_3(v)$ molecules experience $\sim 10^4$ collisions, primarily with Ar, a relatively inefficient V$\rightarrow$T transfer partner. Thus collisional effects are significant but are not severe enough to destroy information about the early stages of the recombination sequence. The mea-surements were made by directly observing the spectrally resolved infrared chemiluminescence from $O_3(v)$ in the v_3 band near 10 μm, using the cryogenic COCHISE infrared reactor/spectrometer facility[16] at the Air Force Geophysics Laboratory. Our initial investigation,[17] with a limited set of experimental conditions, produced the first laboratory spectra of $O_3(v)$ fluorescence, attributed this fluorescence to three-body recombination in steady state with collisional deactivation, demonstrated the effects of deactivation by atomic oxygen, and hinted at the possibility of other discharge-related excitation mechanisms. We have now reinvestigated this problem with greater dynamic range so that more definitive conclusions can t made regarding both spectro-sopic and kinetic/mechanistic issues which arose in the earlier work. The detailed spectroscopic observations have been reported in Chapter 4.[18] We report here on the results and interpretations of kinetic/ spectroscopic experiments whose objectives are to: 1) determine a quasi-initial state dis-tribution from the recombination reaction, for use in atmospheric modeling; 2) assess the kinetic effects of deactivation by atomic oxygen; and 3) charac-terize and identify other $O_3(v)$ excitation mechanisms arising in the dis-charged gas. The results of this work are generally consistent with those from the initial studies,[17] and serve to validate and extend our interpreta-tions[19-21] of the high-altitude chemistry of vibrationally excited ozone.

5.2 Experiments and Spectral Data

The COCHISE facility is described in detail elsewhere,[16] and the con-figuration of the $O_3(v)$ experiments is described thoroughly in Section 4. $O_3(v)$ is produced in four parallel microwave discharges (2450 MHz, 50W) of

rapidly flowing O_2/Ar mixtures at ~1 torr total pressure and selected temperatures between 80 and 150 K. The discharge effluents expand into a low-pressure (~3 mt), cryogenically pumped chamber, where they enter the collimated field of view of a scanning monochromator/infrared detector assembly. Optional opposing flows of O_2 or Ar may be used to create a quasi-static interaction region along the centerline of the field of view. The use of this counterflow thus gives some increase in the observed effluent fluorescence intensities, but also causes incomplete rethermalization of the expansioncooled rotational distributions. Thus in most of the experiments, counterflows were not employed in order to keep the rotational temperatures lower and minimize spectral overlap. The use of O_2, Ar, and N_2 counterflows give essentially identical results; the absence of a counterflow gives the same vibrational spectral distributions but colder rotational distributions and about half the total intensity. These results confirm the expectation that measurable $O_3(v)$ is formed only in the discharge tubes and not in the low-pressure viewing region.

Vibraluminescence from $O_3(v)$ was observed with spectral resolutions of 0.027 to 0.080 μm (2.7 to 8.0 cm^{-1}). For convenience and optimized signalto-noise (S/N) ratio, the lower resolution was employed for most of the measurements. Higher resolution scans for selected conditions were used to develop and verify the spectroscopic model used in the analysis as described in Section 4.

The primary thrust of these experiments is to examine the variation in $O_3(v)$ number densities and relative population distributions with varying O_2 mole fraction in the discharge gas. Our previous work[17] showed: 1) at low O_2 mole fractions, $\chi_{O_2} < 10^{-2}$, the relative contributions of the higher-lying states increased as χ_{O_2} decreased, presumably due to reduced collisional deactivation by atomic oxygen formed in the discharge; and 2) for $\chi_{O_2} \sim 10^{-1}$, bimodal vibrational distributions were obtained, implying the onset of another excitation reaction pumping the higher vibrational states. Accordingly, in

the present experiments, the Ar flow rate was maintained at 640 μmoles s^{-1} and the O_2 flow rate was varied from 2.3 to 86 μmoles s^{-1} (0.3 to 12 percent O_2), all at a constant discharge tube temperature of 80 K. Under these conditions, the residence time in the chemically active portion of the discharge tubes is ~2 ms. The dynamic range of χ_{O_2} was limited by poor S/N at the low end and difficulty of remote discharge ignition at the upper end of the range. The variations in spectral distribution over this range are illustrated in Figure 51.

For selected constant O_2 and Ar flow rates, the discharge sidearm and gas supply temperatures were varied systematically from 80 to 150 K. The effect of the observed spectra is illustrated in Figure 52. The spectral distribution is seen to be invariant with temperature, however the total intensity exhibits a strong negative temperature coefficient. These data lend credence to the interpretation that the observed $O_3(v)$ derives either directly or indirectly from ozone formed in three-body recombination, which follows a similar temperature dependence.[22] We will pursue this point further in the next section.

Prior to analysis of the spectral data, it was necessary to correct the observed spectra for atomic argon Rydberg lines appearing as scattered light from the discharge tubes. This was a straightforward procedure involving subtraction of background spectra obtained with no O_2 added to the discharges. This contamination was at worst only a minor effect near 10.0 and 10.3 μm, with stronger features near 11.1, 11.4, and 12.3 μm lying generally beyond the maximum spectral extent of the $O_3(v)$ emission. The spectroscopy of these argon emission features is interesting in its own right, and a detailed investigation has been reported elsewhere.[23]

During the course of the measurements, spectral surveys were conducted over the entire 2 to 16 μm range of the apparatus in search of other ozone emission bands besides the prominent v_3 band reported here. The only other O_3-related feature we could detect was the $v_1 + v_3$ combination band, which
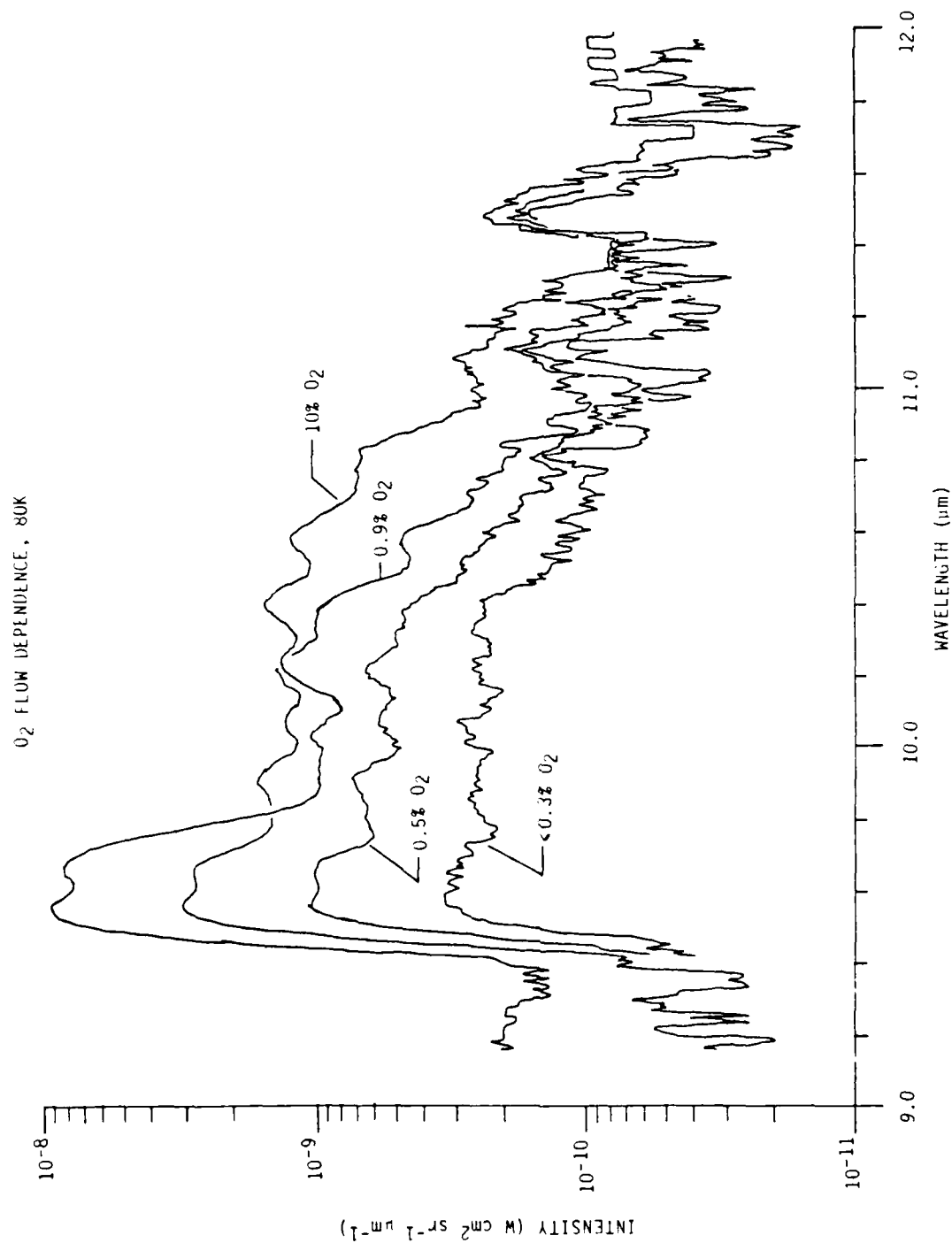
Figure 51. Effect of O_2 level in discharged O_2/Ar mixtures on observed spectral distributions (no counterflow, 80K, 640 μmole/s Ar, 0.08 μm resolution).

A-1932

TEMPERATURE DEPENDENCE, 1% O_2/Ar

80K

115K

135K

WAVELENGTH (μm)

INTENSITY (W cm^2 sr^{-1} μm^{-1})
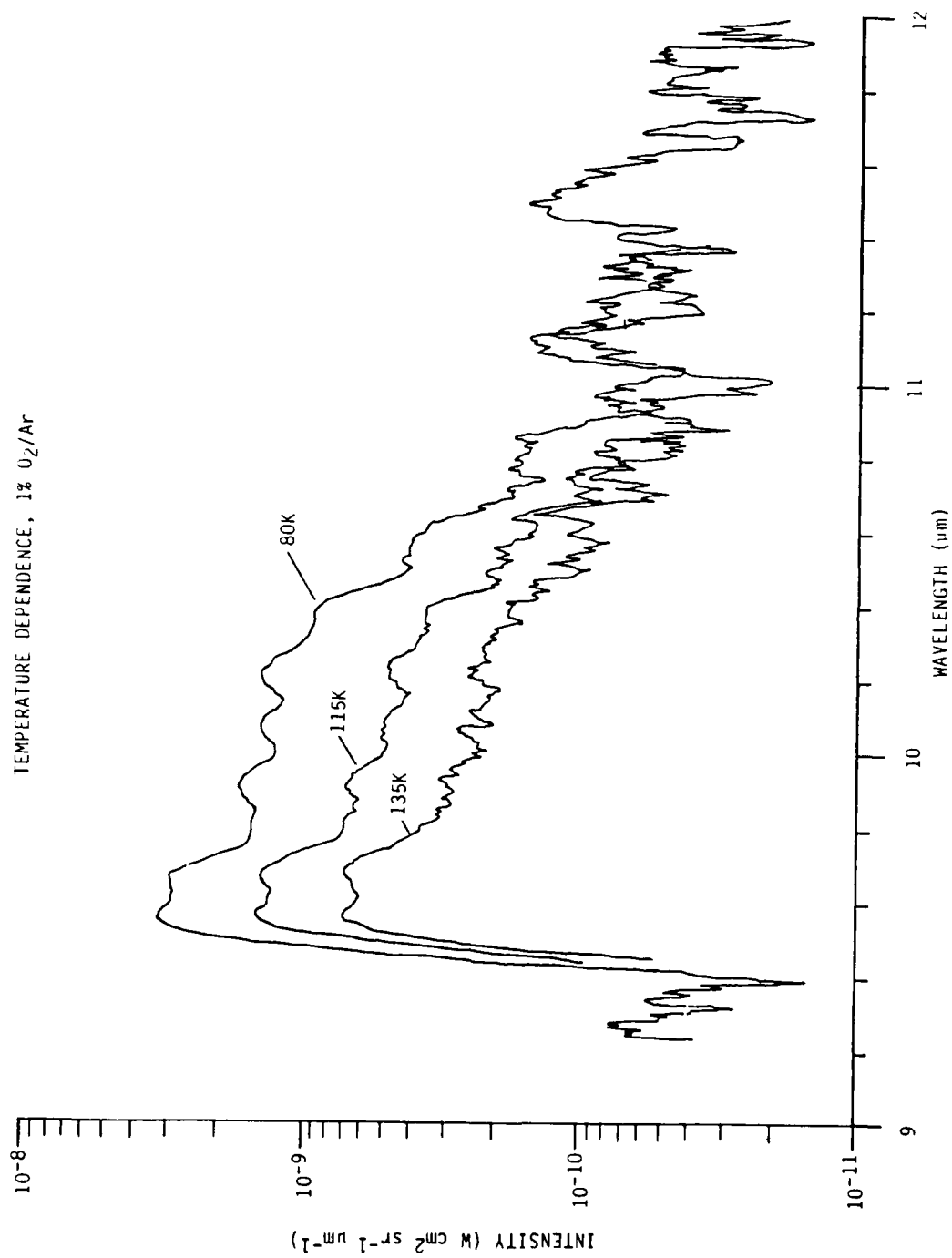
A-1933

Figure 52. Effect of temperature, low-O_2 case (no counterflow, 640 μmole/s Ar, 1% O_2, 0.08 μm resolution).

originates near 4.7 μm. The ν_1 and ν_2 bands, which are factors of 22 and 45 weaker than ν_3,[24] were not observable under any conditions of flow, temperature, or spectral resolution. Based on blackbody calibrations of the spectral responsivity, examination of the S/N of the ν_3 data, and the results of the spectral fitting analysis described below, we estimate a minimum detection limit for $O_3(001)$ of 1×10^6 molecules cm^{-3}, which in turn corresponds to detection limits of 2×10^7 cm^{-3} and 6×10^7 cm^{-3} for $O_3(100)$ and $O_3(010)$, respectively. Also unobservable was any O_3-related fluorescence near 6.6 and 8 μm, observed at high pressure by von Rosenberg and Trainor[9] and attributed by them to electronic and vibrational transitions of electronically-excited triplet ozone.

5.3 Analysis and Results

Individual excited state number densities were determined from the spectral data using the linear least-squares spectral fitting method described in Section 4. As discussed there, high resolution spectra showed evidence for emission from $(00v_3)$ and $(10(v_3-1))$ states up to $v_3 = 5$, with no observable features from states with $v_1 > 1$ or $v_2 > 0$. Accordingly, the $(00v_3)$ and $(10(v_3-1))$ states were included in all the spectral fits. An important aspect of this fitting procedure is that the solutions are values of $N_{v'}A_{v'v''}$, where $N_{v'}$ is the number density for the emitting state and $A_{v'v''}$ is the Einstein coefficient for the radiative transition to the lower state v''. As discussed in Section 4, the scaling of $A_{v'v''}$ with v' is highly uncertain, and we have chosen a course which could result in underestimates of the values of $N_{v'}$. We believe these estimates are reasonably accurate for up to 3 quanta of stretching excitation, but become progressively more uncertain for the higher levels, with perhaps as much as 50 percent uncertainty for 5 quanta. The error bars shown in the following figures reflect only statistical uncertainties from the fitting unless otherwise stated.

An example least squares fit to spectral data is illustrated in Figure 53. The slight mismatch between observed and computed rotational distributions, most noticeable in the P/R branch structure of the prominent
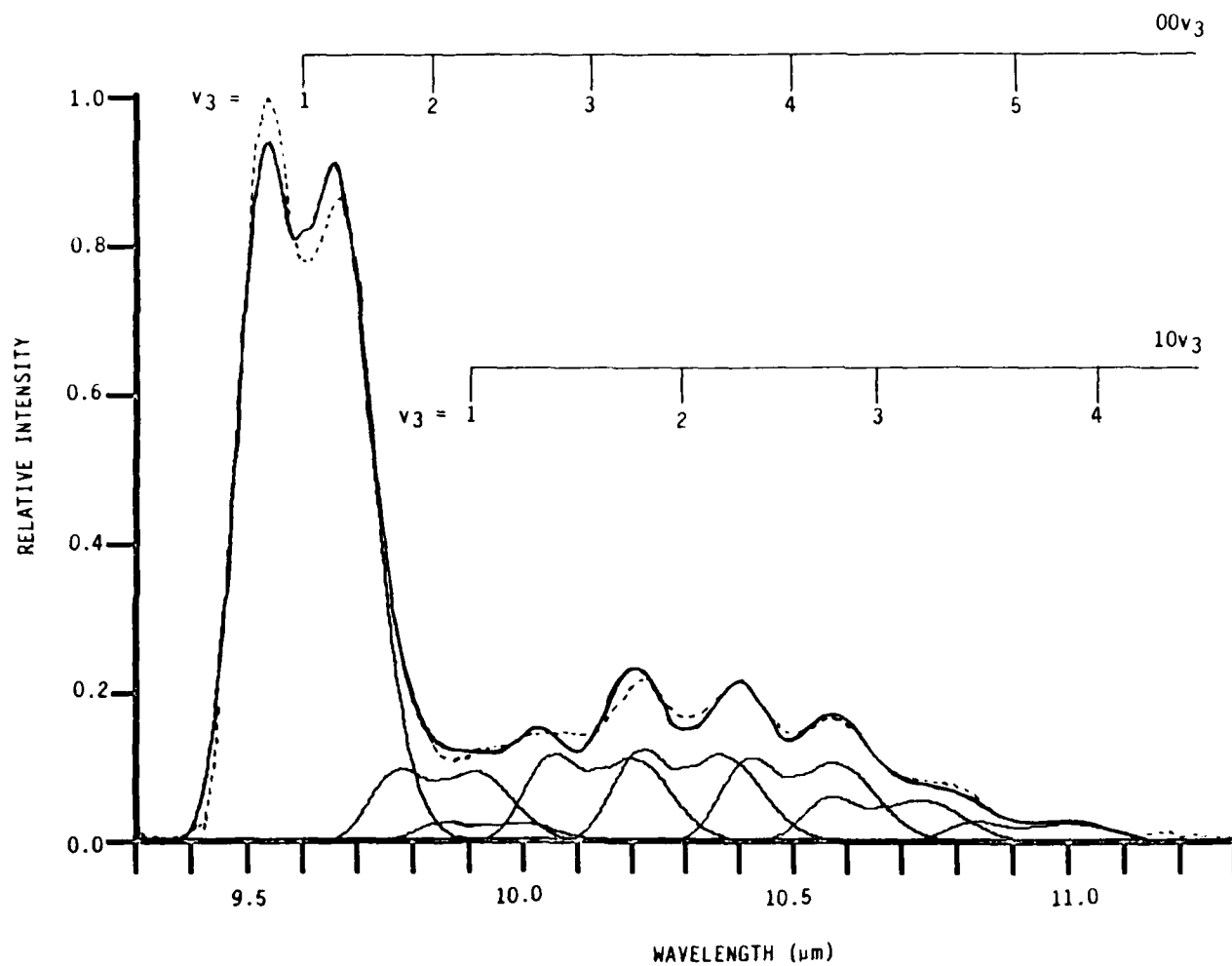
Figure 53.   Comparison of observed and computed (least squares fit)
             Spectra. (11.8% O_2 in Ar, $T = 80$ K, spectral resolution =
             0.08 μm; -----, experimental spectrum; _____, computed
             spectrum and individual vibrational bands, $T_{rot} = 60$ K)

5-9

(001)→(000) band near 9.6 μm, appears to be due to a non-Boltzmann rotational distribution resulting from collision-limited R → T transfer in the low-pressure expansion region of the reaction chamber. However, since the vibrational state number densities are determined from the much coarser band integrals, the results are insensitive to such small discrepancies in the fine structure of the spectrum. Examples of the detailed vibrational state number densities determined from such fits are shown in Fig. 50 of Section 4.

5.3.1 Temperature Dependence

The $O_3(v)$ temperature dependence was studied from 80 to 150 K for initial O_2 mole fractions of 0.0067, 0.030, 0.109, and 0.118. In all cases, the individual relative vibrational state populations did not change with temperature, but the total absolute number densities varied by almost an order of magnitude. Accordingly, the total vibrationally excited number densities, $\sum_{v>1}[O_3(v)]$, were normalized to a common value at 100 K in order to collapse the data onto a single temperature dependence curve. The results are shown in Figure 54.

The normalized $\sum[O_3(v)]$ values can be fit quite well by a T^{-n} dependence, where $n = (3.2 \pm 0.3)$ at the 95 percent confidence level. This is considerably larger than $n \cong 2$ as commonly observed for $O + O_2$ recombination with Ar near 300 K.[22] However, in Arrhenius form, as plotted in Figure 55, the COCHISE data extrapolate well to the higher temperature results for the recombination reaction,[25-28] with approximate asymptotes of $e^{500/T}$ at high T and $e^{250/T}$ at low T. The close correspondence of the temperature dependence of $O_3(v)$ and that of the three-body recombination reaction

$$O + O_2 + Ar \rightarrow O_3 + Ar \qquad (2)$$

is evidence that the $O_3(v)$ observed in COCHISE is formed either directly in Reaction (2) or by excitation of ground-state O_3 formed in that reaction.
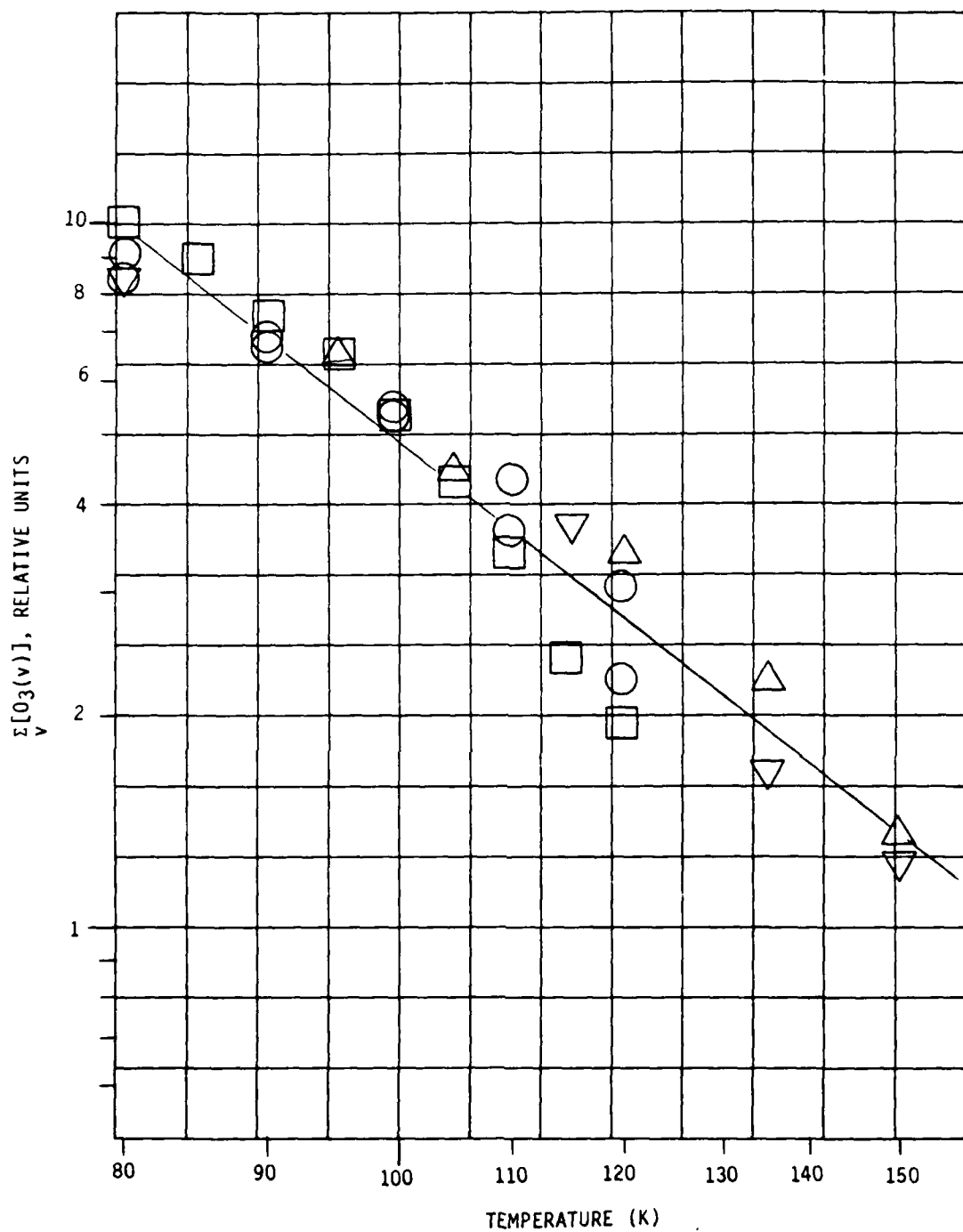
Figure 54. Temperature dependence of total $[O_3(v)]$. (∇, 0.67% O_2; O, 3.0% O_2; Δ, 10.9% O_2; $\square$, 11.8% O_2. The solid line is a least squares fit to the data, $\sum_v [O_3(v)] \propto T^{-3.2 \pm 0.3}$ (95% confidence level).
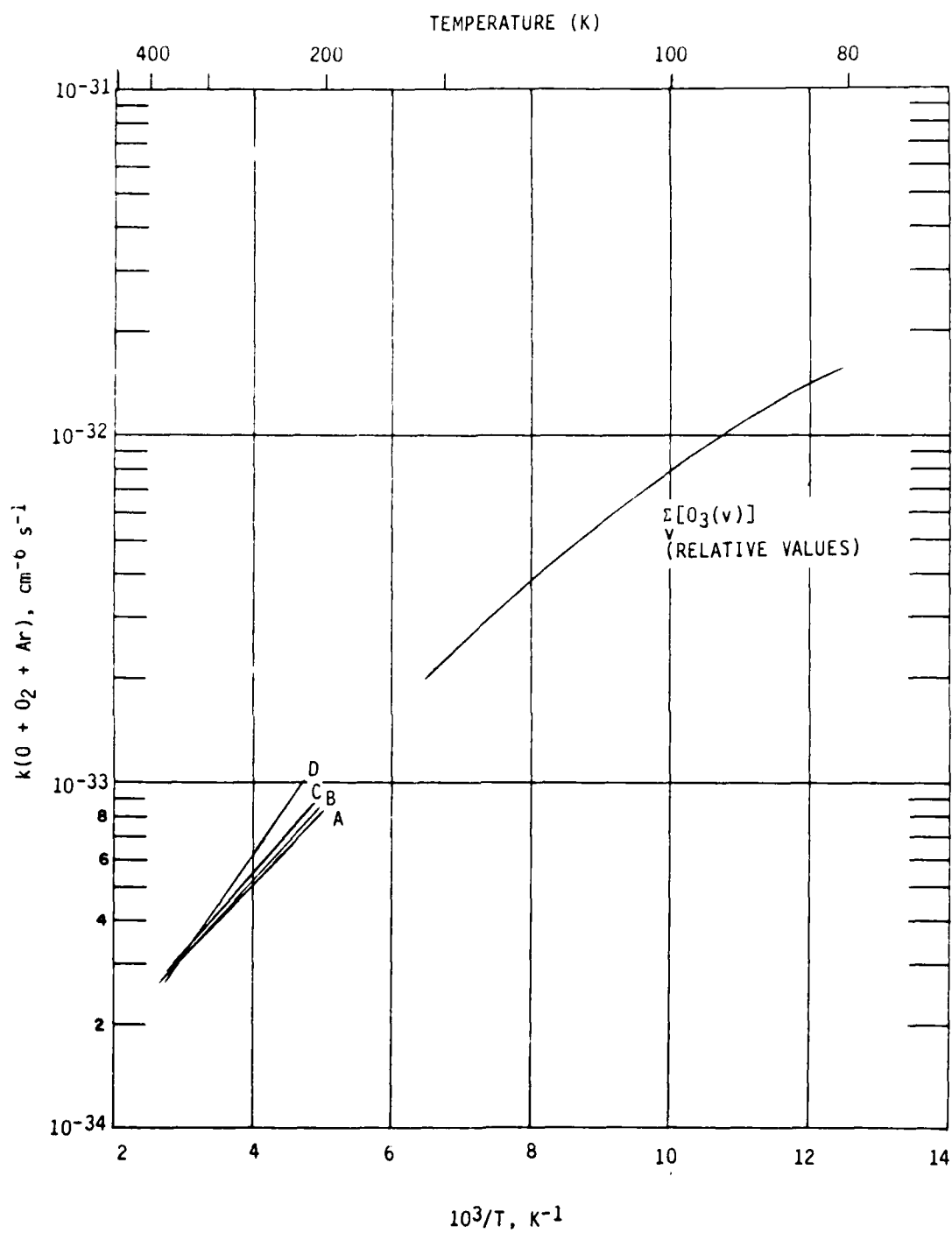
Figure 55. Arrhenius plot comparing the observed $\sum_v [O_3(v)]$ temperature dependence to that observed for the recombination rate coefficient. (A: Ref. 25; B: Ref. 26; C: Ref. 27; D: Ref. 28)

A-1936

Since the observed $O_3(v)$ is actually in steady-state with collisional deactivation processes, one might expect the temperature dependencies of those processes to influence either the behavior of the relative distributions or the net number densities. The apparent absence of such effects indicates that the overall temperature dependence is controlled by that of the O_3 production rate. For V-T deactivation processes, viz. $Ar + O_3(v)$, one might expect a weak positive temperature coefficient, perhaps $T^{1/2}$. However, the downward curvature in the data at low T indicates a decreasing $O_3(v)$ production efficiency rather than a decreasing deactivation rate. Thus it appears that the reactions controlling $O_3(v)$ deactivation are not strongly temperature dependent.

5.3.2 Variation of O_2 Mole Fraction

$O_3(v)$ number densities were determined for a variation of χ_{O_2} over slightly more than two orders of magnitude for constant discharge pressure (1.3 torr) and temperature (80 K). For clarity, we display the results in three figures, Figs. 56 through 58. The overall results, comparing $\Sigma[O_3(v)]$, $[O_3(001)]$, and $\Sigma[O_3(v > 1)]$, are plotted in Fig. 56. Breakdowns of the individual $(00v_3)$ and $(10(v_3-1))$ number densities for $v_3 > 1$ are plotted in Figs. 57 and 58 respectively. In general, the data show a roughly first-order dependence on O_2 at low χ_{O_2}, a strong quenching effect for the higher levels above $\chi_{O_2} \sim 0.01$, and a striking increase in $O_3(v)$ production near $\chi_{O_2} \sim 0.1$ which results in population inversions among the higher levels.

The first-order behavior below $\chi_{O_2} = 0.01$ is consistent with our earlier view[17] of $O_3(v)$ formation by Reaction (1) balanced by destruction principally by atomic oxygen. The regime above $\chi_{O_2} \sim 0.01$ exhibits a substantial increase in the $O_3(v)$ loss rate, especially for the higher levels; the implication is the onset of another reaction with some discharge-produced species which reaches large concentration at this O_2 level. As we will discuss in the next section, we do not expect O, O_3, or O_2 to be responsible for this behavior.

PERCENT O_2 IN DISCHARGE GAS (1.2 torr, 80K)
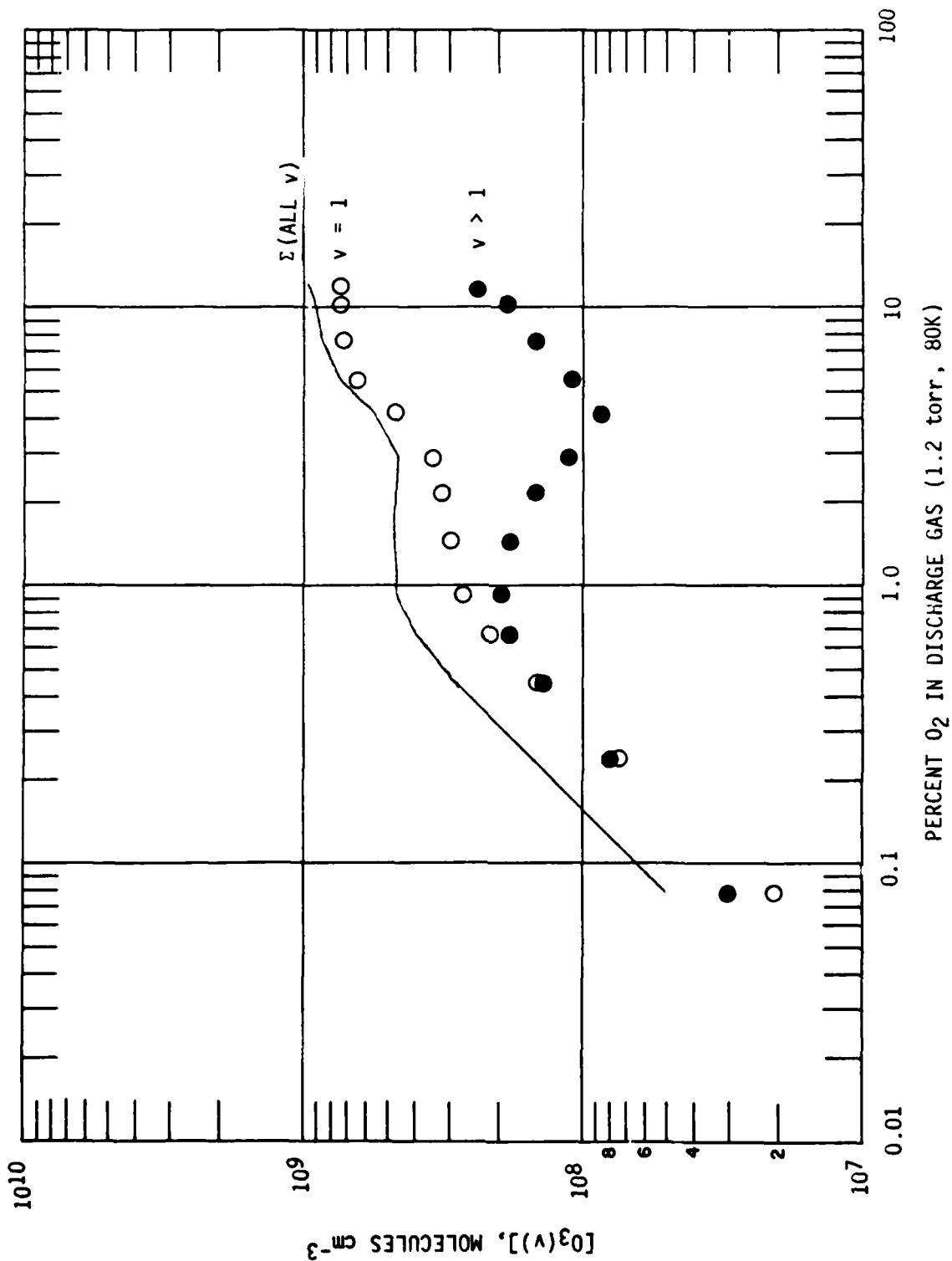
A-1937

Figure 56. Observed $O_3(v)$ number densities for all v, v=1, and v>1 (number densities are those observed in the field of view at 3 to 5 mt)

PERCENT O_2 IN DISCHARGE GAS (1.2 torr, 80K)
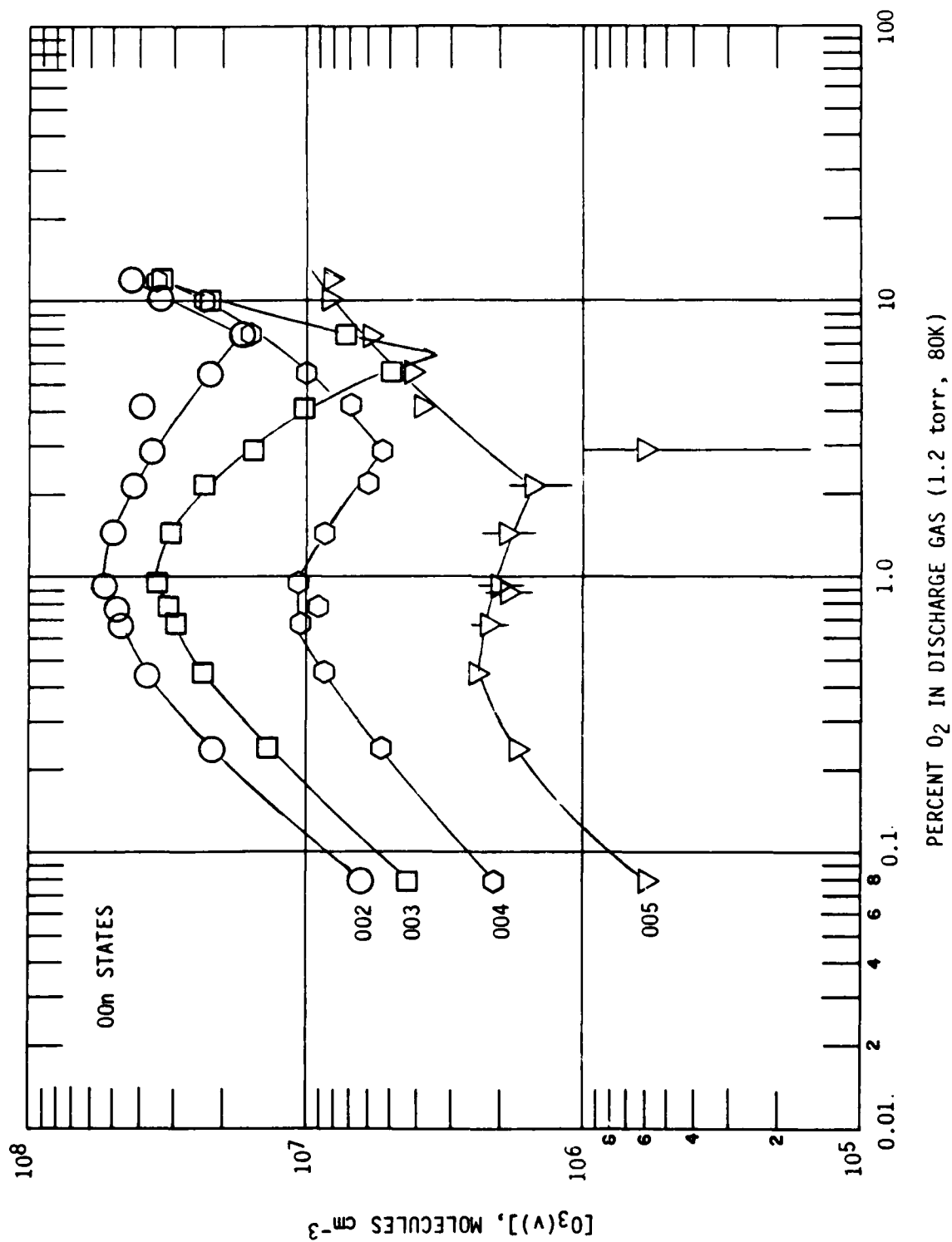
Figure 57. Observed $O_3(v)$ number densities in field of view $(00v_3, v_3 > 2)$ only.

A-1939

5-15
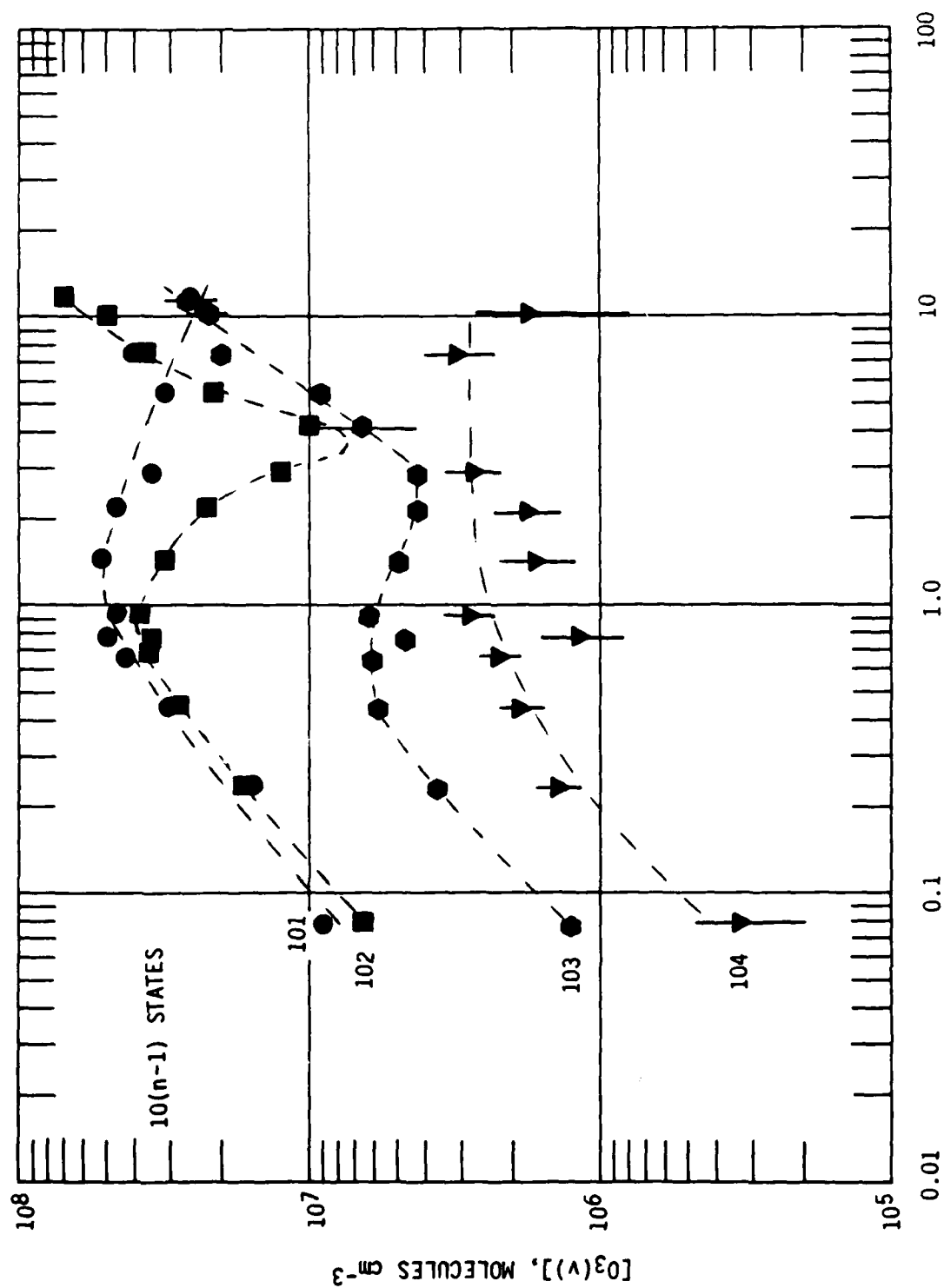
Figure 58. Observed $O_3(v)$ number densities in field of view ($(10v_2)$ states).

A-1938

The increase in $O_3(v)$ production at large χ_{O_2} seems to originate in the highest observed levels, $v_3 = 4\text{-}5$. The production of these levels begins to increase at substantially lower χ_{O_2} than for the lower levels, $v_3 = 2\text{-}3$, as if the high levels are directly excited and the lower levels are increasingly populated from above by collisional cascade as χ_{O_2} is increased. Since $O_3(006)$ is not observed even though there is sufficient sensitivity, $\left([O_3(005)]/[O_3(006)] > 10\right)$, the excitation reaction responsible for these observations must have an energetic limit in the 5000 to 6000 cm^{-1} range. Furthermore, since the temperature dependence of $O_3(v)$ tracks with that of recombination even in this regime of χ_{O_2}, the reaction must involve excitation of ground-state O_3, formed from deactivation of recombination-generated $O_3(v)$. The dramatic increase with χ_{O_2} points to an energetic excitation partner which is formed from electron-irradiated O_2. The possibilities then are V-V transfer to O_3 from $O_2(v)$, or E-V transfer from an electronic metastable species. The energy defect we require, ~4900 to 5800 cm^{-1}, is significantly off resonance with the states of $O_2(v)$; for example, the v=3 and 4 states of O_2 lie at energies of 4598 and 6085 cm^{-1}, respectively. However, the observed energetics correspond well to the energy difference between $O_2(b^1\Sigma_g^+)$ and $O_2(a^1\Delta_g)$ of 5230.5 cm^{-1}. We therefore invoke the reaction

$$O_2\left(b^1\Sigma_g^+\right) + O_3 \rightarrow O_2\left(a^1\Delta_g\right) + O_3(005) \ . \tag{3}$$
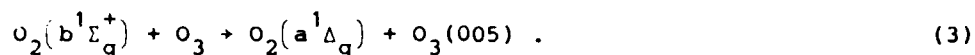
The quenching of $O_2(b)$ by O_3 has been observed to occur at room temperature with a rate coefficient of 2.2×10^{-11} cm^3 molecule^{-1} s^{-1} and a branching fraction of 2/3 for dissociation of O_3.[29] As will be discussed in the next section, if the remaining 1/3 of the quenching proceeds by Reaction (3), we anticipate that there is sufficient $O_2(b)$ produced in the discharge to account for the observations at large χ_{O_2}.

As discussed in Section 4, in the recombination-dominated regime of χ_{O_2}, we observe population of the combination states (103) and (104) in thermal equilibrium with the "pure-v_3" states (004) and (005), and have interpreted this observation in terms of initial recombination into the v_3 mode followed

by rapid, near resonant V-T transfer with Ar to populate the nearby $(10(v_3-1))$ states. In addition (also in Section 4), we observe a strong enhancement of $[O_3(102)]$ and a minor enhancement of $[O_3(101)]$ which is most likely the result of resonant V-V exchange with $O_2(v=2)$

$$O_2(v=2) + O_3(000) \rightarrow O_2(v=0) + O_3(102) \qquad (4)$$

$$O_3(102) + M \rightarrow O_3(101) + M . \qquad (5)$$
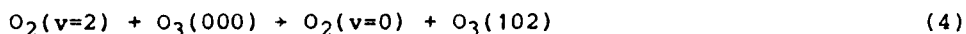
It is also likely that $O_3(002, 003)$ are enhanced to some extent by deactivation of $O_3(102)$. We have attempted to estimate a lower bound to the total $O_3(v)$ formed from V-V exchange by computing from the data the total amount of $O_3(101, 102)$ in excess of the thermal equilibrium with $O_3(002, 003)$ expected for recombination. These values are plotted in Fig. 59. For $[O_3(000)]$ estimated by extrapolation of the observed $O_3(v)$ distributions, a value of $\sim 10^{-11}$ cm^3 s^{-1} for rapid V-V exchange, and deactivation by O as described below, the levels of $O_3(v)$ observed in Fig. 59 require an $O_2(v)$ vibrational temperature of $\sim 10^3$ K, which is well within the range expected for microwave discharges such as those used here. In addition, the behavior with χ_{O_2} shown in Fig. 59, i.e., a first-order dependence below $\chi_{O_2} = 0.01$ and constant within experimental scatter above that point, has a bearing on formation kinetics of $O_3(000)$; this point will be addressed in the next section.

We now wish to isolate the effect of recombination kinetics on the vibrational distributions at low χ_{O_2}. In the recombination-dominated regime of χ_{O_2}, we view the observed $O_3(v)$ as being formed in recombination either directly or by collisional cascade from higher levels (the mathematical formalism is the same in either case), and destroyed primarily by atomic oxygen. In the steady-state approximation, we have

$$[O_3(v)] = \frac{k_F(v) \, [O] \, [O_2] \, [Ar]}{k_D(v) \, [Ar] + k_o(v) \, [O]} \cong \frac{k_F(v)}{k_o(v)} [O_2] \, [Ar] \qquad (6)$$

There is also some contribution from the V-V exchange Reaction (4), which can be subtracted from the data using the results of Fig. 59. (Note that there
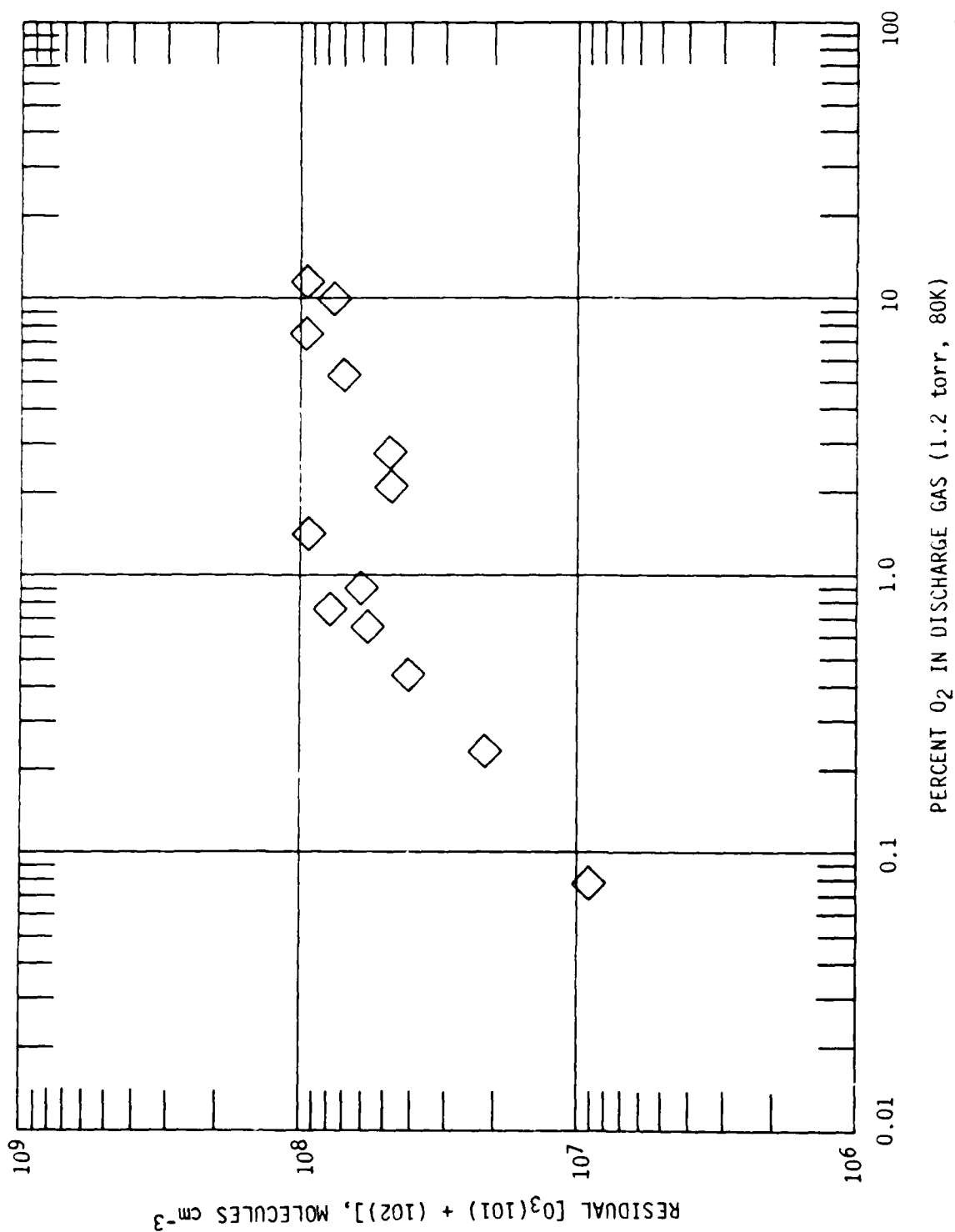
Figure 59. Estimated contribution from $O_2(v)$ + O_3 exchange. (Number densities (field of view values) represent sum of (102) and (101) values, corrected for their estimated levels due to recombination/deactivation (see text).)

A-1940

is probably some residual contribution from Reaction (4) in the (003) and
perhaps (002) populations which we cannot evaluate.) Finally, we correct for
resonant V-T transfer to the combination states by adding the population of
each $(10(v_3-1))$ state to that of the corresponding $(00v_3)$ state. A plot of the
resulting relative vibrational state populations, $[O_3(00v_3)]/\sum_{v_3>1}[O_3(00v_3)]$,
as functions of χ_{O_2} is shown in Fig. 60. For $\chi_{O_2} < 0.01$, the data fit well
to an exponential empirical expression, with well-defined intercepts at
$\chi_{O_2} = 0$. Since [Ar] is constant throughout, the slopes of the lines reflect
variations in the atomic oxygen deactivation rates with χ_{O_2}; variation in the
slopes suggests a vibrational level-dependent rate coefficient which increases
with v_3. The intercepts reflect an effective vibrational distribution which
is affected only by collisions with argon. A least-squares analysis of the
$\chi_{O_2} = 0$ vibrational distribution gives a vibrational "temperature" of
$2070 \pm 210(1\sigma)$ K. In the next section, we will attempt to extract from these
data further details about the atomic oxygen deactivation and about the
nascent or quasi-nascent $O_3(v)$ distribution from three-body recombination.

As a final point in the data analysis, we note the striking difference
between the kinetic behavior of $O_3(001)$ and that of the higher levels (cf.
Figs. 56 and 60). The relative (001) contribution increases steadily with
χ_{O_2}, showing none of the sensitivity to O_2-related loss processes that are
evident in the data for higher v. While a number of hypotheses might account
for this, the simplest explanation which satisfies both the reaction order and
temperature dependence is that significant $O_3(001)$ might be formed by secon-
dary electron impact excitation of $O_3(000)$, which undoubtedly accumulates in
the recombination process. If this is true, then $O_3(001)$ and $O_3(000)$ might
well be in a quasi-equilibrium, especially at higher χ_{O_2} where $O_3(000)$ buildup
is more substantial. Similar excitation of the higher levels may also occur;
however, from inspection of the data, this does not seem to be a dominant con-
tribution. If optical selection rules (e.g., Franck-Condon overlap) apply in
the electron excitation process, we would not expect significant multiquantum
excitation from O_3.
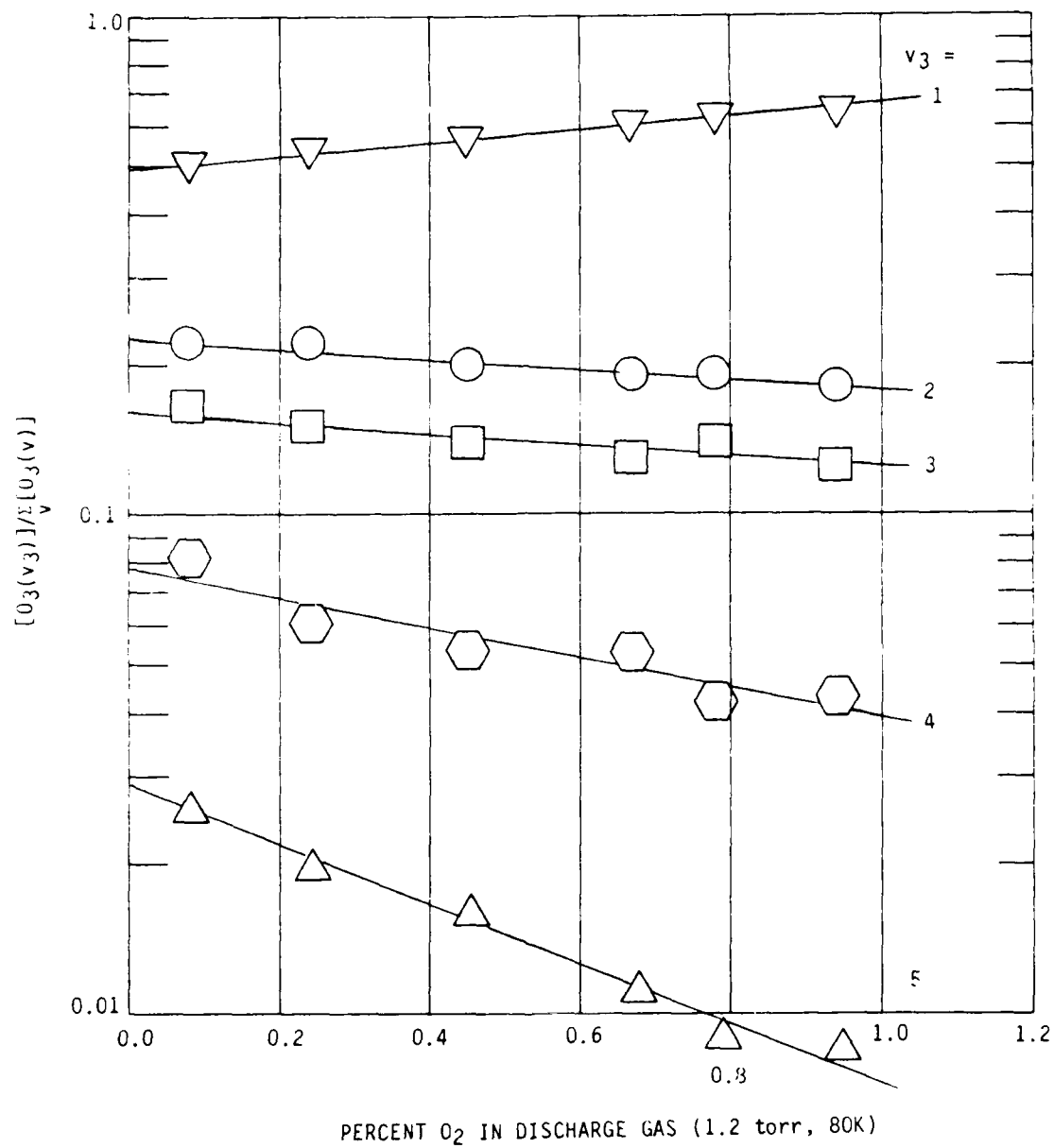
Figure 60. Dependence of relative vibrational distributions from recombination upon O_2 mole fraction in discharge gas (the solid lines are least squares fits to the data points).

5.4 Kinetic Interpretations

In order to fully interpret the data in terms of production and loss mechanisms for $O_3(v)$, we must assess species number densities, rate coefficients, and scalings with χ_{O_2} and T for the relevant reactions which we expect to occur in the microwave discharges. In this section, we first address the physics and chemistry of the discharge in order to estimate number densities of the key species. We then apply these values in a comparative assessment of the various possible $O_3(v)$ production and loss processes. This leads to the derivation of a rigorous steady-state kinetic analysis, which we can then use to interpret the experimental results.

5.4.1 Discharge Conditions

The COCHISE discharges are of the conventional microwave type, whose operating conditions are governed by ambipolar diffusion.[30,31] For the conditions of these experiments, we estimate an electric field/density ratio of $E/N \sim 3 \times 10^{-16}$ V cm^2; from energy balance considerations, this leads to an estimated electron number density of $\sim 10^{11}$ cm^{-3}. We have solved the Boltzmann transport equation, treating all the inelastic processes occurring in the discharge to the accuracy with which their cross sections are known, to obtain a characteristic electron energy of ~ 8 eV for dilute O_2/Ar mixtures. This characteristic energy is roughly constant from $\chi_{O_2} = 0$ to 0.01, and then decreases with increasing χ_{O_2} due to increasing collision frequency of electrons with O_2, approaching a value of ~ 2 eV for 100 percent O_2. Application of the electron energy distributions obtained in this fashion to energy-dependent excitation cross sections available in the literature gives the effective excitation rate coefficients as functions of E/N and χ_{O_2}.

We have used this treatment to estimate rate coefficients for the key electron impact processes, including O_2 dissociation (O formation), excitation

of $O_2(v)$ and of the O_2 metastables $a^1\Delta_g$, $b^1\Sigma_g^+$, $c^1\Sigma_u^-$, and dissociation of O_3 (a key O_3 loss process). An important aspect of these calculations is that, since the electron energy distribution is unaffected by O_2 at low χ_{O_2}, the excitation rate coefficients are constant below $\chi_{O_2} = 0.01$, i.e., in the recombination-dominated regime. This means that the production rates for O, $O_2(v)$, and $O_2(a,b,c)$ are linearly dependent upon $[O_2]$ in this regime. We will use these rate coefficients in the steady-state analysis presented below. Further details on the Boltzmann transport solutions are given in the Section 7.

5.4.2 Excitation of $O_3(v)$

We wish to evaluate and compare the $O_3(v)$ production rates for the most likely reactions: three-body recombination, electron-impact excitation, and resonant V-V transfer from $O_2(v=2)$, resonant E-V transfer from $O_2(b^1\Sigma_g^+)$, the possible chemical reaction between O_2 and one or more of the high-lying metastables $O_2(A^3\Sigma_u^+, A'^3\Delta_u, c^1\Sigma_u^-)$. The reactions considered are listed in Table 4, along with their estimated rates for $\chi_{O_2} = 10^{-3}$, 10^{-2}, and 10^{-1}.

To estimate the three-body recombination rate, we use values of $[O]$ given by the discharge analysis. O is formed by electron-impact dissociation of O_2, and its number density is limited by the residence time t in the discharge. Thus we have $[O]/[O_2] = 2\, k_E^{O_2}[e^-]/t$. For $k_E^{O_2}$ as determined for the COCHISE discharges, we get $[O]/[O_2] \sim 1$ for $\chi_{O_2} < 10^{-2}$ and $[O]/[O_2] \sim 0.2$ for $\chi_{O_2} = 10^{-1}$. From Figure 55, we estimate a recombination rate coefficient of $\sim 2 \times 10^{-32}$ cm^6 s^{-1} at 80 K; this then gives a product $k_R[O][O_2][Ar] = 2 \times 10^{13}$, 2×10^{15}, and 4×10^{16} cm^{-3} s^{-1} for $\chi_{O_2} = 10^{-3}$, 10^{-2}, and 10^{-1} respectively.

The next three reactions involve excitation by energy transfer to $O_3(000)$, whose number density must be estimated from the discharge calculations. The only efficient means of forming $O_3(000)$ in the discharge is by the recombination/vibrational relaxation pathway; the above total $O_3(v)$ production rates provide an upper bound for $O_3(000)$ formation. The principal loss process for $O_3(000)$ is most likely by electron-impact dissociation; we estimate a loss rate on the order of 10^3 s^{-1} based on the discharge predictions.

TABLE 4. ESTIMATED RATES* OF $O_3(v)$ FORMATION IN MICROWAVE DISCHARGES OF O_2/Ar, 1.3 TORR, 80 K.

Reaction	$\chi_{O_2} = 10^{-3}$	10^{-2}	10^{-1}
$O + O_2 + Ar \rightarrow$ $O_3(v) + Ar$	2 (13)	2 (15)	4 (16)
$e + O_3 \rightarrow$ $O_3(001) + e^-$	<2 (12)	<2 (14)	<4 (16)
$O_2(v=2) + O_3 \rightarrow$ $O_3(102) + O_2$	2 (12)	2 (14)	2 (16)
$O_2(b^1\Sigma) + O_3 \rightarrow$ $O_3(005) + O_2$	1 (11)	1 (14)	6 (15)
$O_2(c^1\Sigma) + O_2 \rightarrow$ $O_3(001,002) + O$	--	1 (13-14)	--

*Rates are in units of molecules $cm^{-3} s^{-1}$.

Dissociation of O_3 by metastables of O, O_2, or Ar proves to be more than an order of magnitude slower by comparison. Thus we estimate upper-bound values for $[O_3(000)]$ for 2 x 10^{10}, 2 x 10^{12}, and 4 x 10^{13} cm^{-3} for χ_{O_2} = 10^{-3}, 10^{-2}, and 10^{-1}. The value at χ_{O_2} = 10^{-2} is consistent with extrapolation of the observed vibrational distribution and correction for the expansion ratio, i.e., $[O_3(000)]/[O_3(001)] \sim 25$. The actual $[O_3(000)]$ value may be considerably less than this owing to incomplete vibrational relaxation.

Vibrational excitation of O_3 by low-energy electrons is difficult to assess since its cross section is unknown and the effective electron density is ill-defined. If we describe the process in terms of the total electron density and an effective rate coefficient of 10^{-9} cm^3 s^{-1}, the upper-bound excitation rates are about an order of magnitude smaller than those for recombination. Thus this reaction may compete with recombination for formation of $O_3(001)$, but does not appear to be effective for general excitation of $O_3(v)$.

$O_2(v)$ is formed in the active discharge by electron-impact excitation of O_2, and is removed by deactivation by O and electron-impact dissociation. For low vibrational levels, the O-atom reaction is the dominant loss process by 1 to 2 orders of magnitude. From the discharge predictions and a likely $O + O_2(v)$ rate coefficient of $\sim 10^{-11}$ cm^3 s^{-1}, we expect $[O_2(v=2)]$ = 8 x 10^{12}, 8 x 10^{12}, and 4 x 10^{13} cm^{-3} at χ_{O_2} = 10^{-3}, 10^{-2}, and 10^{-1}, corresponding to vibrational "temperatures" of about 1700, 900, and 800 K, respectively. For a V-V transfer rate coefficient of $\sim 10^{-11}$ cm^3 s^{-1}, we obtain $O_3(102)$ production rates which are competitive with those expected for recombination. The values listed in Table 4 are also consistent within a factor of 2 with the apparent $O_3(102)$ production rate determined from the data of Fig. 59 using the deactivation rates derived below. The $O_2(v)$ + O_3 hypothesis therefore appears to be quite credible in terms of both the data and the expected discharge kinetics.

$O_2(b^1\Sigma_g^+)$ is formed and dissociated by electron impact. The dissociation cross section is not known, but the effective rate coefficient can be scaled from the $O_3(v)$ data. From the onset of the $O_3(v)$ enhancements shown in

Fig. 57, together with an E → V rate coefficient of 7×10^{-12} cm^3 s^{-1} (in keeping with the results of Slanger and Black),[29] we estimate $[O_2(b)]$ values which, taken with the discharge-predicted $O_2(b)$ production rates, correspond to an $O_2(b)$ dissociation rate coefficient which is about five times larger than that for $O_2(X^3\Sigma_g^-)$. This gives $[O_2(b)] = 10^{12}$, 10^{13}, and 2×10^{13} cm^{-3} for $\chi_{O_2} = 10^{-3}$, 10^{-2}, and 10^{-1}. The resulting $O_3(005)$ production rates, shown in Table 4, are seen to be competitive with recombination only at large χ_{O_2}.

Lastly, we consider the reaction

$$O_2^* + O_2 \rightarrow O_3(v) + O \tag{7}$$

where O_2^* is one of the Herzberg states: $A^3\Sigma_u^+$, $A'^3\Delta_u$, and $c^1\Sigma_u^-$. This type of reaction was implicated in high altitude auroral measurements,[19,21] but has yet to be demonstrated in the laboratory. The reaction with $O_2(A,v=0)$ is exoergic enough to form O_3 with up to 2 quanta of stretching vibration. For $\chi_{O_2} = 10^{-2}$, we estimate from the discharge predictions for $O_2(c)$ and O_2^* production rate of $\sim 6 \times 10^{16}$ cm^{-3} s^{-1}. By analogy with the other metastables, the loss rate by dissociation is probably 10^4–10^5 s^{-1}, so we expect $[O_2^*] \sim 10^{11}$–10^{12} cm^{-3}. This means that Reaction (7) may compete successfully with recombination if the rate coefficient is in the 10^{-13} cm^3 s^{-1} range, which is consistent with quenching measurements at room temperature for $O_2(A)$.[32] However, the strong negative temperature coefficient observed for all $O_3(v)$ under all χ_{O_2} conditions argues against the contribution of Reaction (7) in the COCHISE measurements at cryogenic temperatures.

5.4.3 Deactivation of $O_3(v)$

The principal loss of $O_3(v)$ occurs through collisions with Ar, the wall of the discharge tube, and atomic oxygen. Deactivation by O_2 is not important at these dilutions. In addition, we will consider dissociation of $O_3(v)$ by electrons, $O_2(a^1\Delta_g)$, and $O_2(b^1\Sigma_g)$. The relevant reactions are listed in Table 5.

TABLE 5. ESTIMATED LOSS RATES* FOR $O_3(v)$ IN MICROWAVE DISCHARGES OF
O_2/Ar, 1.3 TORR, 80 K

Reaction	$X_{O_2} = 10^{-3}$	10^{-2}	10^{-1}
$O_3(v) + Ar \rightarrow$ $O_3(v-1) + Ar$		700v	
$O_3(v) \xrightarrow{wall} O_3(v-n)$		<300	
$O_3(v) + O \rightarrow$ $2O_2$ or $O_3(v-n) + O$	1 (3)	1 (4)	2 (4)
$O_3(v) + e^- \rightarrow$ $O_2 + O$	1 (3)	1 (3)	1 (3)
$O_3(v) + O_2(a^1\Delta_g^+) \rightarrow$ $2O_2 + O$	1 (2-3)	1 (3-4)	4 (4-5)
$O_3(v) + O_2(b^1\Sigma_g) \rightarrow$ $2O_2 + O$	--	1 (2)	--
*Rates are in units of molecules s^{-1}			

The deactivation of low levels of $O_3(v)$ by Ar has been studied at room temperature.[2-4,12] We have scaled those data by $vT^{1/2}$ to apply to our conditions. Based on the state distributions we observe, it appears that the deactivation occurs mainly by $\Delta v_3 = 1$ changes until the (001) state is reached, after which it may proceed through (010) into (000) as suggested by Rosen and Cool.[2,3] For this type of V→T transfer, we expect single quantum cascade down the vibrational ladder. The assumed Ar deactivation rates are therefore in the 10^3 s^{-1} range, with a significant dependence on vibrational level.

Deactivation of $O_3(v)$ on the wall of the discharge tube was estimated from lowest mode diffusion[30] by analogy to CO_2,[17,33] assuming unit deactivation efficiency. This gives an upper bound of ~300 s^{-1}, which is of minor importance for our conditions. This value is comparable to 500 s^{-1} corresponding to the inverse of the residence time in the active discharge prior to expansion, so little influence of wall collisions on the vibrational distributions is expected.

Deactivation of $O_3(v)$ by O is a critical reaction which is difficult to treat. West et al.[5] studied this reaction for $O_3(v=1)$ and found efficient removal of $O_3(v)$ by O, with a rate coefficient of either ~10^{-11} or ~10^{-12} cm^3 s^{-1}, depending upon whether chemical reaction or V→T transfer occurred. These same investigators[6] later reported no significant loss of O in the process, implicating V→T transfer as the dominant pathway, at least for $O_3(v=1)$. The behavior for higher v is not known, although statistical arguments[34] favor deactivation by multiquantum energy transfer. For reasons discussed later in this chapter, we suspect that the chemical reaction pathway is important in our experiments. For the present purposes, we invoke a rate coefficient of 10^{-11} cm^3 s^{-1} with no dependence upon vibrational level. For this value, we can see that deactivation by O is competitive with Ar at the lowest χ_{O_2} and faster for larger χ_{O_2}. In the analysis to follow, we will use the data to obtain better estimates for the rate of this process.

The rate of dissociation of $O_3(v)$ by electrons was estimated by analogy with $O_3(000) + e^-$ rates determined above, assuming no large increase in the cross section with O_3 vibrational energy. This loss process may be a minor factor at low χ_{O_2}, but does not appear to be generally important except to determine the overall loss rate of total ozone.

The dissociation of $O_3(v)$ by $O_2(a^1\Delta_g)$ is an interesting possibility and may provide an explanation for the anomalously large loss rates for $O_3(v>2)$ which are evident in the data (Figs. 56 through 58) for $\chi_{O_2} > 10^{-2}$. Quenching of vibrationally cold $O_2(a)$ by ground state O_3 is known to be slow;[22] however, excitation of at least one vibrational quantum of either partner would permit dissociation of the O_3, and might therefore lead to a substantial increase in the reaction cross section. Based on the discharge predictions, we estimate $[O_2(a)] \sim 10^{14}$ to 4×10^{15} cm^{-3} for $\chi_{O_2} = 10^{-2}$ to 10^{-1}. Thus we can account for the observations with a rate coefficient in the 10^{-11} to 10^{-10} cm^3 s^{-1} range. We know of no other possible hypotheses to explain the observed depletion in $O_3(v>2)$ above $\chi_{O_2} = 10^{-2}$.

Finally, we have evaluated the dissociation of $O_3(v)$ by $O_2(b^1\Sigma_g^+)$ using the discharge predictions given above for $[O_2(b)]$ and the total quenching constant of Slanger and Black[29] for ground-state O_3. As shown in Table 2, this turns out to be an insignificant loss process for $O_3(v)$.

5.4.4 Steady-State Kinetic Analysis

Comparison of the estimated $O_3(v)$ production and loss rates in Tables 4 and 5 allows us to confidently verify our initial belief that, for $\chi_{O_2} < 10^{-2}$, $O_3(v)$ is formed primarily through three-body recombination and is removed by collisions with O and Ar. The values of Tables 1 and 2 give predicted steady-state $O_3(v)$ number densities in the field of view of $\sim 3 \times 10^7$, 7×10^8, and 3×10^9 cm^{-3} for $\chi_{O_2} = 0.001$, 0.01, and 0.1, respectively. The first two values are within a factor of ~ 2 of the observations (cf. Fig. 56), which is well within the uncertainty of the calculations. The predicted value at $\chi_{O_2} = 0.1$ is high by a factor of ~ 3, suggesting that we may have under-estimated some of the loss rates for this discharge condition.

The excited ozone observed in these experiments is in low vibra-
tional states, v<5, which are unlikely to have been formed directly upon
stabilization of the O_2-O collision complex. We define here a true nascent
distribution, $O_3(v^*, J^*)$, as being the earliest rotational-vibrational distri-
bution for which collisional redissociation is insignificant compared to
radiative and/or collisional deactivation. This distribution is likely to
encompass vibrational states in the upper half of the potential well, and is
also probably extremely short-lived, perhaps surviving for only 100 collis-
ions. On this time scale there will evolve a secondary vibrational distribu-
tion, $O_3(v)$, which is the quasi-initial distribution that precedes the deacti-
vation observed here. In terms of the steady-state analysis for $[O_3(v)]$, it
is easy to show that a steady-state assumption of $O_3(v^*, J^*)$ formation by
three-body recombination and removal by Ar gives the same form for the produc-
tion rate for $O_3(v)$ as if we assume direct recombination into $O_3(v)$. We can
therefore write the level-dependent steady-state equations:

$$[O_3(v)] = \frac{k_v^R [O] [O_2] [Ar]}{k_v^O [O] + R_v} \tag{8}$$

$$\sum_v [O_3(v)] = \frac{\sum_v k_v^R [O] [O_2] [Ar]}{k_L^O [O] + R_1} \tag{9}$$

where k_v^R is the apparent rate coefficient for "direct" recombination into
state v, k_v^O is the rate coefficient for collisional removal of state v by O,
and R_v represents the removal of state v by all oxygen-independent processes,
mainly Ar and wall collisions. In Eq. (51), k_L^O represents the rate-limiting
step for removal of all $O_3(v)$ by O. For example, if the $O + O_3(v)$ step
proceeds by single quantum cascade, this is given by $k_L^O = k_1^O$; if the process

is a chemical reaction or involves total multiquantum deactivation to $O_3(v=0)$,
we have $k_L^O = \sum_v k_v^O [O_3(v)]/\sum_v [O_3(v)]$.

Several important conclusions can now be stated upon examination of the reaction orders observed in Figs. 56 through 58. First, the observed number densities of $\Sigma[O_3(v)]$ and $[O_3(v)]$ are first-order in O_2 even at the lowest χ_{O_2}, corresponding to $[O_2] = 1.3 \times 10^{14}$ cm^{-3}. From the discharge predictions, we expect $[O]/[O_2]$ to be constant throughout this regime, with an estimated ratio of unity. From the condition required for first-order behavior, $k_v^o[O] > R_v$ and R_v given by Table 5, we conclude $k_1^o > 8 \times 10^{-12}$ cm^3 s^{-1}, etc., up to $k_5^o > 3 \times 10^{-11}$ cm^3 s^{-1}. Further information on the deactivation step can be gleaned from the V-V transfer results plotted in Fig. 59. From the discharge predictions, we expect $[O_2(v=2)]$ to be constant from $\chi_{O_2} = 10^{-3}$ to 10^{-2}. The first-order behavior in $[O_3(102)]$ exhibited in Fig. 59 must therefore be due to a similar dependence in $[O_3(v=0)]$. First-order behavior of $[O_3(v=0)]$ cannot occur if there is significant formation of $O_3(v=0)$ by $O + O_3(v)$. This indicates that the major route of this step is by chemical reaction to form O_2.

To assess the level-dependent kinetic effects, we examine the relative vibrational distributions

$$\frac{[O_3(v)]}{\sum_v [O_3(v)]} = \frac{k_v^R}{\sum_v k_v^R} \frac{k_L^o [O] + R_1}{k_v^o [O] + R_v} \tag{10}$$

It can be shown after considerable algebra that, over the range of [O] and relative population observed here, Eq. (52) is approximated by the empirical exponential form plotted in Fig. 60. The empirical slopes are related to the kinetic parameters via

$$\frac{d \ln\left([O_3(v)]/\sum_v [O_3(v)]\right)}{d [O_2]} = \frac{f k_L^o}{R_1} - \frac{f k_v^o}{R_v} \tag{11}$$

to within ~30 percent, where $f = [O]/[O_2] \approx 1$. The first-order kinetics in $[O_2]$ provides us with the lower bound $k_L^o/R_1 > 8 \times 10^{-15}$ cm^3. Using the Ar and wall deactivation rate coefficients from Table 4, and the empirical slopes

from Fig. 60, we can evaluate lower bounds for k_v^o (0.8, 1.4, 2.0, 2.7, and 3.6) x 10^{-11} cm^3 s^{-1} for v = 1, 2, 3, 4, and 5, respectively.

The χ_{O_2} = 0 intercepts from Figure 60 can be used to determine the quasi-initial $O_3(v)$ distribution from recombination. From Eq. (52) at [O] = 0, we obtain

$$\left(\frac{[O_3(v)]}{\sum_v [O_3(v)]}\right) = \frac{k_v^R}{\sum_v k_v^R} \frac{R_1}{R_v} \tag{12}$$

where $k_v^R/\sum_v k_v^R$ are the quantities we seek. The observed intercepts and the values corrected for R_v/R_1 are plotted in Fig. 61. The error bars reflect the combined uncertainties in R_v/R_1 (i.e., with and without wall collisions) and in the Einstein coefficients used in the spectral analysis. Also plotted in Fig. 61 is the statistical nascent distribution which would obtain if the entropy change of the reaction were maximized, i.e., if all final states within the v_3 mode equally probable. In the language of surprisal theory,[35] this is called the "prior" or "zero surprisal" distribution of states, and is given by[36]

$$P^o(v) = \frac{(1 - E_v/E)^{3/2}}{\sum_v (1 - E_v/E)^{3/2}} \tag{13}$$

where E_v is the energy of vibrational state v and E is the total energy available (E = 8468 ± 140 cm^{-1}). The close correspondence between the COCHISE quasi-initial distribution and the zero-surprisal distribution is striking. It appears from this that the energy contained in the truly nascent $O_3(v^*,J^*)$ states is rapidly randomized throughout the asymmetric stretching mode of the molecule in collisions with the Ar bath gas.

5.5 Discussion

The detailed dynamics of the three-body recombination are summarized in Table 6. In the energy transfer or association/deactivation mechanism, we

Y-axis label: $[O_3(v)]/\sum_{v \neq 0}[O_3(v)]$

X-axis label: VIBRATIONAL ENERGY (cm^{-1})
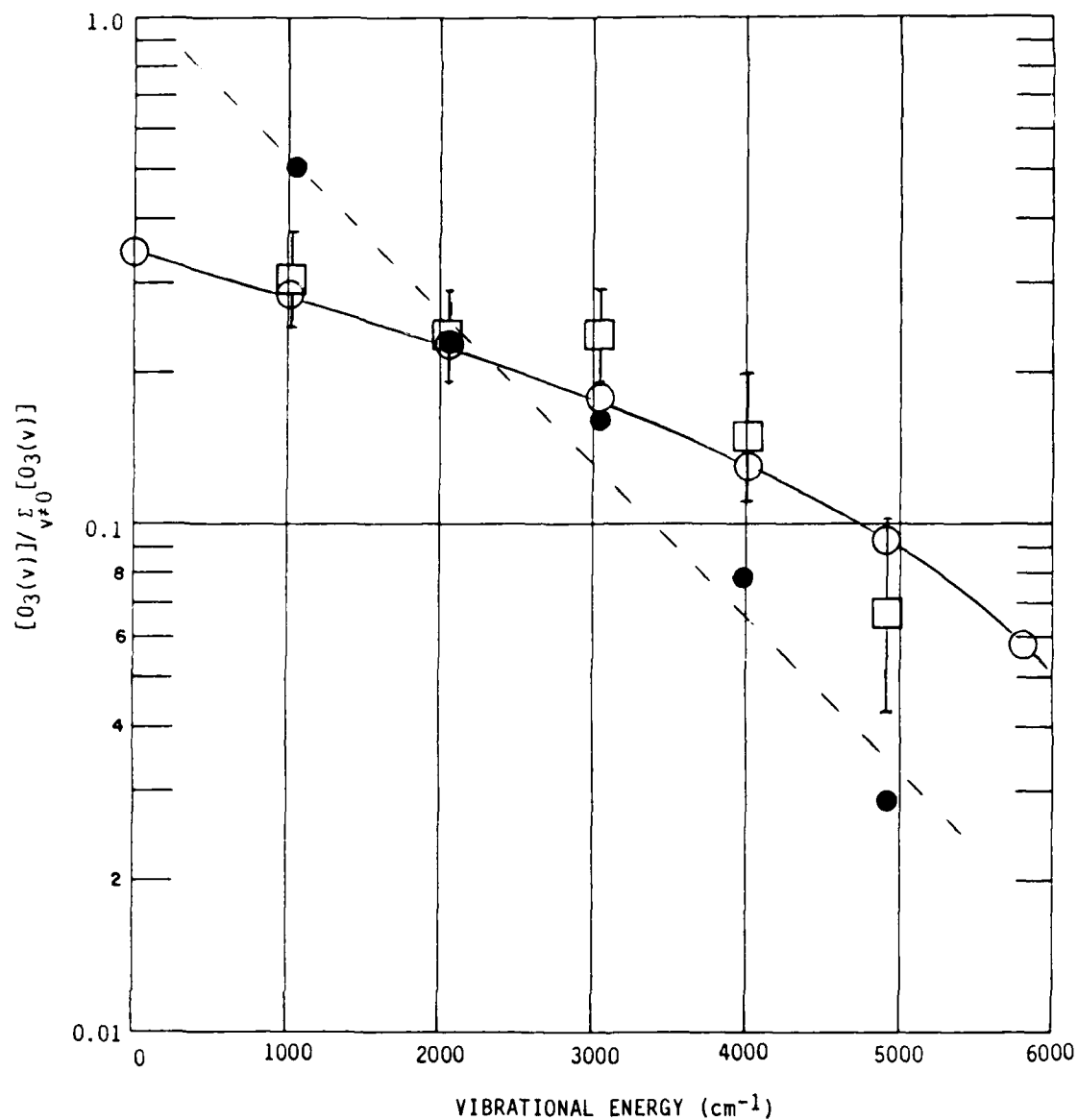
A-1942

Figure 61. Quasi-initial vibrational distribution of $O_3(v)$ formed in
recombination. (---●---, $XO_2 = 0$ intercepts, with least
squares fit ($T_{vib} = 2070 \pm 210(1\sigma)$ K); □, zero-O_2 values
adjusted for Ar deactivation; ───○───, computed statistical
distribution (including v=0))

envision the formation of an unbound but associated $O---O_2$ complex which can live long enough to collide with an Ar atom. This collision results in either dissociation of the complex or formation of slightly bound $O_3(*)$. Further collisions of $O_3(*)$ result in either redissociation or stepwise deactivation until finally the non-dissociative nascent distribution $O_3(v^*,J^*)$ is attained. The state distribution continues to evolve downwards by collisional cascade, at first rapidly through V,R → T transfer until the rotational distribution is thermalized, and then more slowly by conventional V→T transfer thereafter. Within the framework of this model, we require rapid scrambling of the recombination energy throughout the v_3 mode. This is not unreasonable, since trajectory calculations for Ar + $O_3(v,J)$ collisions indicate efficient energy transfer with large ΔE for excited ozone molecules with high rotational energy.[37,38] The observed preference for asymmetric stretching motion is also striking; it seems that the newly formed molecules (probably in a quasi-continuum of states) are deactivated into the non-chaotic portion of the potential well so rapidly that they retain "memory" of the original approach configuration. The decrease in the recombination rate with increasing temperature can be ascribed, qualitatively at least, to less efficient complex formation and increased collisional redissociation prior to formation of the nascent distribution.

In an alternative recombination scheme, the chaperon or radical-molecule complex mechanism, O and Ar may exist in equilibrium with the weakly bound van der Waals molecule ArO, which can react with O_2 to either dissociate or form excited O_3. Troe[39] has suggested that this mechanism may be responsible for the anomalously low values for the three-body and high-pressure rate coefficients observed for the reaction at room temperature. We can find no evidence in our data to preclude the occurrence of this mechanism. A detailed study of these mechanisms using classical trajectory calculations is currently under way in our laboratory.[40]

TABLE 6.   DYNAMICS OF THREE-BODY RECOMBINATION

(1)   Association/deactivation mechanism

Complex formation: $O + O_2 \rightarrow O\text{---}O_2 \rightarrow O + O_2$

$O\text{---}O_2 + M \rightarrow O + O_2 + M$

$O\text{---}O_2 + M \rightarrow O_3(*) + M$

Stabilization: $O_3(*) + M \rightarrow\rightarrow\rightarrow O + O_2 + M$

$O_3(*) + M \rightarrow\rightarrow\rightarrow O_3(v^*, J^*) + M$

Deactivation: $O_3(v^*, J^*) + M \rightarrow\rightarrow\rightarrow O_3(v) + M$

$O_3(v) + M \rightarrow\rightarrow\rightarrow$ Rotational thermalization
Vibrational cascade

(2)   Chaperon mechanism

$O + M \rightleftharpoons OM$

$O_2 + OM \rightarrow O_2 + O + M$

$O_2 + OM \rightarrow O_3(v^*, J^*) + M$

$O_3(v^*, J^*) + M \rightarrow\rightarrow\rightarrow$ Rotational thermalization
Vibrational cascade

5-35

The elusive triplet excited state of ozone[41,42] may also be involved in the recombination sequence, perhaps as a collisional precursor to the quasi-initial $O_3(v)$ distribution. Our data neither support nor contradict this; however, there is no spectral evidence for significant triplet ozone,[18] nor do we need to invoke its presence to account for the results.

The COCHISE data have profound significance in the interpretation and modeling of high-altitude $O_3(v)$ chemistry.[19-21] We expect the observed quasi-initial distribution to correspond fairly well to the three-body recombination reaction in the upper atmosphere. The effects of N_2 and O_2 as third bodies and V→T collisional deactivation partners should be similar to those observed here for Ar. Furthermore, the large rate coefficients we find for reaction of $O_3(v)$ with O indicate that the atomic oxygen reaction will be important between 80 and 100 km for some (but not all) atmospheric conditions. Finally, the characterization of other discharge-related $O_3(v)$ excitation processes has an important bearing on the interpretation and scaling of auroral observations.

5.6 Conclusions

By a detailed analysis of spectrally resolved $O_3(v)$ fluorescence data over a wide range of experimental conditions, we have been able to characterize completely the kinetics of $O_3(v)$ formed in microwave discharges of dilute, flowing O_2/Ar mixtures. The primary result of this effort is the determination of the quasi-initial distribution of $O_3(v)$ states formed in three-body recombination of O with O_2,

$$O + O_2 + Ar \rightarrow O_3(v) + Ar$$
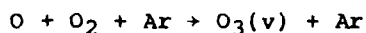
The results indicate statistical behavior in the asymmetric stretch mode, but little or no transfer into the other modes on the time scale of the measurements. An analysis of the change in vibrational distribution with changing O_2 mole fraction leads to the conclusion that deactivation of $O_3(v)$ by O proceeds via chemical reaction

$$O + O_3(v) \rightarrow O_2 + O_2$$
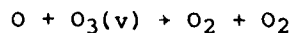
with rate coefficients in excess of 10^{-11} cm^3 s^{-1} and increasing with v. As an interesting aside, this reaction can lead to considerable vibrational and electronic excitation in O_2, including the formation of the metastables $A^3\Sigma_u^+$, $A'^3\Delta_u$, and $c^1\Sigma_u^-$.

Additional evidence was obtained for other $O_3(v)$ excitation processes. These include: resonant V$\rightarrow$V transfer from $O_2(v)$,

$$O_2(v=2) + O_3 \rightarrow O_2(v=0) + O_3(102) \quad ;$$

E$\rightarrow$V transfer from $O_2(b^1\Sigma_g)$,

$$O_2(b^1\Sigma_g^+) + O_3 \rightarrow O_2(a^1\Delta_g^+) + O_3(005) \quad ;$$
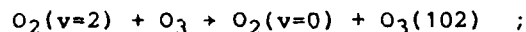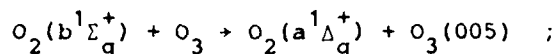
and possible electron-impact excitation of O_3,

$$e^- + O_3 \rightarrow O_3(001) + e^- \quad .$$
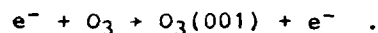
Finally, indirect evidence suggesting rapid dissociation of $O_3(v_3 > 1)$ by $O_2(a^1\Delta_g)$ was obtained:

$$O_3(v_3 > 1) + O_2(a^1\Delta_g) \rightarrow O + O_2 + O_2 \quad .$$
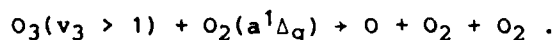
Much of the information presented here was inferred from indirect and often circuitous analysis of a complex data base. For this reason, these results are by no means definitive. Nevertheless, they represent the current state of the art for this difficult problem, and the development of a more definitive data base will undoubtedly prove to be extraordinarily difficult. We eagerly await the testing of the concepts and models presented here by advanced theoretical and experimental methods.

5-37

5.7 References

1. Troe, J., "Atom and Radical Recombination Reactions," Ann. Rev. Phys. Chem. 29, 223 (1978).

2. Rosen, D.I. and Cool. T.A., "Vibrational Deactivation of $O_3(101)$ Molecules in Gas Mixtures," J. Chem. Phys. 59, 6097 (1973).

3. Rosen, D.I. and Cool, T.A., "Vibrational Deactivation of O_3 Molecules in Gas Mixtures, 2," J. Chem. Phys. 62, 466 (1975).

4. Hui, K.K., Rosen, D.I., and Cool, T.A., "Intermode Energy Transfer in Vibrationally Excited O_3," Chem. Phys. Lett. 32, 141 (1975).

5. West, G.A., Weston, R.E., Jr., and Flynn, G.W., "Deactivation of Vibrationally Excited Ozone by $O(^3P)$ Atoms," Chem. Phys. Lett. 42, 488 (1976).

6. West, G.A., Weston, R.E., Jr., and Flynn, G.W., "The Influence of Reactant Vibrational Excitation on the $O(^3P)$ + O_3† Bimolecular Reaction Rate," Chem. Phys. Lett. 56, 429 (1978).

7. von Rosenberg, C.W. and Trainor, D.W., "Observations of Vibrationally Excited Ozone Formed by Recombination," J. Chem. Phys. 59, 2142 (1973).

8. von Rosenberg, C.W. and Trainor, D.W., "Vibrational Excitation of Ozone Formed by Recombination," J. Chem. Phys. 61, 2442 (1974).

9. von Rosenberg, C.W. and Trainor, D.W., "Excitation of Ozone Formed by Recombination, II," J. Chem. Phys. 63, 5348 (1975).

10. McDade, I.C. and McGrath, W.D., "IR-Laser-Induced Changes in the UV Absorption Spectrum of Ozone. A New Technique for Vibrational Energy-Transfer Studies," Chem. Phys. Lett. 72, 432 (1980).

11. McDade, I.C. and McGrath, W.D., "IR-Laser-Induced Changes in the UV Absorption Spectrum of Ozone. The Hartley Continuum of the Vibrationally Excited Components," Chem. Phys. Lett. 73, 413 (1980).

12. Adler-Golden, S.M. and Steinfeld, J.I., "Vibrational Energy Transfer in Ozone by Infrared-Ultraviolet Double Resonance," Chem. Phys. Lett. 76, 479 (1980).

13. Adler-Golden, S.M., Schweitzer, E.L., and Steinfeld, J.I., "Ultraviolet Continuum Spectroscopy of Vibrationally Excited Ozone," J. Chem. Phys. 76, 2201 (1982).

14. Kleindienst, T., Burkholder, J.B., and Bair, E.J., "The Spectrum of Ozone During Formation by Recombination," Chem. Phys. Lett. 70, 117 (1980).

15. Joens, J.A., Burkholder, J.B., and Bair, E.J., "Vibrational Relaxation in Ozone Recombination," J. Chem. Phys. 76, 5902 (1982).

16. Rawlins, W.T., Murphy, H.C., Caledonia, G.E., Kennealy, J.P., Robert, F.X., Corman, A., and Armstrong, R.A., "COCHISE: Laboratory Studies of Atmospheric Infrared Chemiuluminescence in a Cryogenic Environment," Appl. Opt. 23, 3316 (1984).

17. Rawlins, W.T., Caledonia, G.E., and Kennealy, J.P., "Observation of Spectrally Resolved Infrared Chemiluminescence from Vibrationally Excited $O_3(\nu_3)$," J. Geophys. Res. 86, 5247 (1981).

18. Rawlins, W.T. and Armstrong, R.A., "Dynamics of Vibrationally Excited Ozone Formed by Three-Body Recombination. I: Spectroscopy," J. Chem. Phys., to be submitted (1985).

19. Rawlins, W.T., Caledonia, G.E., Gibson, J.J., and Stair, A.T., Jr., "HIRIS Rocketborne Spectra of Infrared Fluorescence in the $O_3(\nu_3)$ Band Near 100 km," J. Geophys. REs. 40, 2896 (1985).

20. Green, B.D., Rawlins, W.T., and Nadile, R.M., "Diurnal Variability of Vibrationally Excited Mesospheric Ozone as Detected by SPIRE," J. Geophys. Res., in press (1985).

21. Rawlins, W.T., "Chemistry of Vibrationally Excited Ozone in the Upper Atmosphere," J. Geophys. Res., in press (1985).

22. Baulch, D.L., Cox, R.A., Hampson, R.F., Jr., Kerr, J.A., Troe, J., and Watson, R.T., "Evaluated Kinetic and Photochemical Data for Atmospheric Chemistry: Supplement II," J. Phys. Chem. Ref. Data 13, 1259 (1984).

23. Rawlins, W.T., Gelb, A., and Armstrong, R.A., "Infrared Spectra (2-16 μm) of ArI Rydberg Emission from a Microwave Discharge Plasma," J. Chem. Phys. 82, 681 (1985).

24. Rothman, L.S., Gamache, R.R., Barbe, A., Goldman, A., Gillis, J.R., Brown, L.A., Toth, R.A., Flaud, J.M., and Camy-Peyret, C., "AFGL Atmospheric Absorption Line Parameters Compilation: 1982 Edition," Appl. Opt. 22, 2247 (1983).

25. Huie, R.E., Herron, J.T., and Davis, D.D., "Absolute Rate Constants for the Reaction of $O + O_2 + M \rightarrow O_3 + M$ over the Temperature Range 200-346 K," J. Phys. Chem. 76, 2653 (1972).

26. Arnold, I. and Comes, F.J., "Temperature Dependence of the Reactions $O(^3P) + O_3 \rightarrow 2O_2$ and $O(^3P) + O_2 + M \rightarrow O_3 + M$," Chem. Phys. 42, 231 (1979).

27. Klais, O., Anderson, P.C., and Kurylo, M.J., "A Reinvestigation of the Temperature Dependence of the Rate Constant for the Reaction $O + O_2 + M \rightarrow O_3 + M$ (for $M = O_2$, N_2, and Ar) by the Flash Photolysis Resonance Fluorescence Technique," Int. J. Chem. Kinet. 12, 469 (1980).

28. Lin, C.L. and Leu, M.T., "Temperature and Third-Body Dependence of the Rate Constant for the Reaction $O + O_2 + M \rightarrow O_3 + M$," Int. J. Chem. Kinet. <u>14</u>, 417 (1982).

29. Slanger, T.G. and Black, G., "Interactions of $O_2(b^1\Sigma_g^+)$ with $O(^3P)$ and O_3," J. Chem. Phys. <u>70</u>, 3434 (1979).

30. Kaufman, F., "The Production of Atoms and Simple Radicals in Glow Discharges," in Advances in Chemistry Series #80, (Chemical Reactions in Electric Discharges)," American Chemical Society (1969), pp. 29-47.

31. Brown, S.C., "Breakdown in Cases: Alternating and High Frequency Fields," in Encyclopedia of Physics, Vol. XXII Gas Discharges II, ed. S. Flugge, Springer-Verlag, Berlin (1956), pp. 531-575.

32. Kenner, R.D. and Ogryzlo, E.A., "Deactivation of $O_2(A^3\Sigma_u^+)$ by O_2, O, and Ar," Int. J. Chem. Kinetics <u>12</u>, 501 (1980).

33. Hirschfelder, J.O., Curtiss, C.F., and Bird, R.B., <u>Molecular Theory of Gases and Liquids</u>, John Wiley, New York (1954).

34. Quack, M. and Troe, J., "Complex Formation in Reactive and Inelastic Scattering: Statistical Adiabatic Channel Model of Unimolecular Processes III," Ber. Bunsenges. Phys. Chem. <u>79</u>, 179 (1975).

35. Bernstein, R.B. and Levine, R.D., "Role of Energy in Reactive Molecular Scattering: An Information-Theoretic Approach," in <u>Advances in Atomic and Molecular Physics II</u>, ed. by D.R. Bates and B. Bederson (Academic Press, New York, 1975), pp., 216-297; Levine, R.D., and Bernstein, R.B., "Thermodynamic Approach to Collision Processes," in <u>Modern Theoretical Chemistry, Vol. II: Dynamics of Molecular Collisons, Part B</u>, ed. by W.H. Miller (Plenum Publishing Co., New York, 1975) Chapter 7.

36. Kennealy, J.P., Del Greco, F.P., Caledonia, G.E., and Green, B.D., "Nitric Oxide Chemiexcitation Occurring in the Reaction Between Metastable Nitrogen Atoms and Oxygen Molecules," J. Chem. Phys. <u>69</u>(4), 1574 (1978).

37. Stace, A.J. and Murrell, J.N., "A Classical Trajectory Study of Collisional Energy Transfer in Thermal Unimolecular Reactions," J. Chem. Phys. <u>68</u>, 3028 (1978).

38. Gelb, A., "Classical Trajectory Study of Energy Transfer Between Argon Atoms and Vibrationally-Rotationally Excited Ozone Molecules," J. Phys. Chem., in press (1985).

39. Croce de Cobos, A.E. and Troe, J., "High Pressure Range of the Recombination of $O + O_2 \rightarrow O_3$," Int. J. Chem. Kinet. <u>16</u>, 1519 (1984).

40. Gelb, A. and Rawlins, W.T., work in progress.

41. Swanson, N. and Celotta, R.J., "Observation of Excited States in Ozone Near the Dissociation Limit," Phys. Rev. Lett. 35, 783 (1975).

42. Wilson, C.W., Jr. and Hopper, D.G., "Theoretical Studies of the Ozone Molecule. I. Ab Initio MCSCF/CI Potential Energy Surfaces for the X^1A_1 and a^3B_2 States," J. Chem. Phys. 74, 595 (1981).

6. DYNAMICS OF VIBRATIONALLY EXCITED OZONE AND THREE-BODY RECOMBINATION

6.1 Introduction

Ozone has long been known to be an important infrared radiator in the lower thermosphere and upper mesosphere.[1,2] A significant level of understanding of the radiation-producing mechanisms for this species has developed from recent high-altitude in situ measurements[3-7] and kinetic modeling of the quiescent and disturbed upper atmosphere.[8,9] This work has been well supported by a variety of laboratory studies of the relevant production and loss processes. However, the modeling efforts have identified crucial problems in the kinetic schemes which are difficult to solve unambiguously by experiment. For example, in the case of infrared emission from $O_3(v_3)$, the nascent vibrational distribution formed in $O-O_2$ recombination

$$O + O_2 + M \rightarrow O_3(v') + M$$

and its subsequent collisonal relaxation

$$O_3(v') + M \rightarrow O_3(v'') + M$$

need to be characterized in detail.

Although experimental studies of this and other reactions are ongoing, particularly in research groups at the Air Force Geophysics Laboratory, Massachusetts Institute of Technology, and Physical Sciences Inc., these reactions are extremely difficult to study unambiguously in the laboratory. The difficulties arise from the requirements to produce large but uncontaminated fluxes of atomic oxygen, to form and/or detect very low levels of state-specific reactants and products using sophisticated infrared and ultraviolet fluorescence techniques, and to isolate collisional cascade effects. Furthermore, the eventual results of such experiments need to be interpreted and validated

in terms of fundamental concepts of reaction dynamics. Thus, it is important that the laboratory work, as well as continued atmospheric modeling, be supported by detailed theoretical efforts aimed at increasing our understanding of how these reactions occur. We now summarize the salient features of the O_3 problem from the viewpoint of modeling the high-altitude chemistry of O_3.[9,10]

In the quiescent upper atmosphere, $O_3(v)$ containing more than one quantum of vibrational energy is thought to be formed by three-body recombination of O and O_2. This occurs over a narrow altitude range with a maximum rate near 80 km. The production rate by recombination is negligible above 110 km, and below 70 km at night, but may persist to lower altitudes during the daytime. The principal collision partners in this altitude region are N_2, O_2, and O. Collisional deactivation of $O_3(v)$ by N_2 and O_2 is important below 90 km, and O may be an important collision partner between 90 and 110 km under certain conditions. The rate coefficients of these processes for the higher vibrational levels are totally unknown. In particular, the possibility of O-atom encounters that are reactive,

$$O + O_3\dagger \rightarrow O_2 + O_2$$

offers the potential for an odd-oxygen loss mechanism which has not been considered in atmospheric photochemical models.

The principal laboratory investigations of high-altitude $O_3(v)$ chemistry have been performed on the COCHISE facility at AFGL.[11,12] These experiments are performed at 80-150 K, with Ar as the principal third body and O as a dominant relaxation partner, and yield a lower bound to the "nascent" vibrational distribution formed in recombination. By contrast, the atmospheric temperature near the mesopause (100 km) is about 200 K, and the major collision partners are N_2, O_2 and O. A major objective of the theoretical effort discussed here is to verify the supposition that the experiments performed in COCHISE indeed provide a useful representation of the high altitude chemistry despite these differences. The growing data base now emerging from the

COCHISE experiments will provide valuable benchmarks with which the theoretical results can be compared.

The results to be presented here are the initial results from a project designed to investigate several aspects of the reaction dynamics of complex energy transfer processes which are important in high altitude infrared fluorescence mechanisms. Our present work is focussed on a theoretical description of the O_3 system. This system offers a unique opportunity to examine the closely coupled dynamics of recombination and collisional deactivation, a topic which has been addressed previously only for relatively simple atom-atom systems (see below). The basic technical approach is to perform classical trajectory calculations for the deactivation of quasi-bound O_2-O by selected collision partners; several methods will be used to define the initial O_2-O orbiting complexes and the required potential surfaces.

Work thus far has treated collisional relaxation of high vibrational-rotational states of ozone by Ar. In particular, we have examined energy transfer as a function of ozone vibrational-rotational excitation and relative translational energy. Ab initio calculations of the ozone potential energy surface at extended configurations have been performed (see Appendix F) and also preliminary calculations on multicollisional relaxation of excited ozone. Before presenting our results to date, some details and background of the computational approaches will be presented. Finally we outline the next steps in this project.

6.1.1 References

1. Stair, Jr., A.T.; Ulwick, J.C.; Baker, D.J.; Wyatt, C.L, and Baker, K.C., "Altitude Profiles of Infrared Radiance of $O_3(9.6 \ \mu m)$ and $CO_2(15 \ \mu m)$," Geophys. Res. Lett. 1(3), 117 (1974).

2. Stair, Jr., A.T.; Ulwick, J.C.; Baker, K.D., and Baker, D.J., "Rocketborne Observations of Infrared Emissions in the Auroral Region," in Atmospheres of the Earth and the Planets, edited by B. M. McCormack, pp. 335-346, D. Reidel, Dordrecht-Holland, (1975).

3. Stair, Jr., A.T.; Pritchard, J.; Coleman, I.; Bohne, C.; Williamson, W.; Rogers, J., and Rawlins, W.T., "The Rocketborne Cryogenic (10 K) High Resolution Interferometer Spectrometer Flight-HIRIS: Atmospheric and Auroral Infrared Emission Spectra," Applied Optics, in press, 1983.

4. Rawlins, W.T. Caledonia, G.E., Gibson, J.J. and Stair, Jr., A.T., "Infrared Emission from $NO(\Delta v = 1)$ in an Aurora: Spectral Analysis and Kinetic Interpretation of HIRIS Measurements," J. Geophys. Res. 86, 1313 (1981).

5. Rawlins, W.T.; Caledonia, G.E.; Gibson, J.J., and Stair, Jr., A.T., "HIRIS Rocketborne Spectra of Infrared Fluorescence in the $O_3(\nu_3)$ Band near 100 km," J. Geophys. Res., to be submitted.

6. Nadile, R.M., Stair, Jr., A.T.; Wheeler, N.B.; Frodsham, D.G.; Wyatt, C.L.; Baker, D.J., and Grieder, W.F., "SPIRE-Spectral Infrared Rocket Experiment (Preliminary Results)," AFGL-TR-78-0107, Air Force Geophy. Lab. Bedford, MA, 1978.

7. Green, B.D., Rawlins, W.T., and Nadile, R.M., "Diurnal Variability of Vibrationally Excited Ozone in the Mesosphere," J. Geophys. Res. (to be submitted).

8. Caledonia, G.E., and Kennealy, J.P., "NO Infrared Radiation in the Upper Atmosphere," Planet. Space Sci. 30, 1043 (1982).

9. Rawlins, W.T., "Chemistry of Vibrationally Excited Ozone in the Upper Atmosphere," manuscript in preparation.

10. Green, B.D., Rawlins, W.T., and Caledonia, G.E., "High Altitude Radiation Signatures," PSI-TR-296, Physical Sciences Inc., Andover, MA, 1982.

11. Rawlins, W.T., Caledonia, G.E. and Kennealy, J.P., "Observation of Spectrally Resolved Infrared Chemiluminescence from Vibrationally Excited $O_3(\nu_3)$," J. Geophys. Res., 86, 5247 (1981).

12. Rawlins, W.T. and Armstrong, R.A., "COCHISE Observations of O_3 Formed by Three-Body Recombination of O and O_2," AFGL-TR-82-0273, Air Force Geophysics Laboratory, Hanscom AFB, MA, 1982.

6.2 Theoretical Methods

6.2.1 Introduction

The present program is a theoretical study of the dynamics of ozone recombination. Our goal is to predict nascent vibrational and rotational distributions for recombined ozone and to compute relaxational rates of the newly formed molecules. These calculations will provide a basis for the theoretical prediction of radiation from recombined ozone in the upper atmosphere. Our approach is to use classical and semi-classical trajectory methods to compute the outcome of the collision of unbound O_2-O complexes with third body partners such as atomic oxygen and argon.

The recombination of ozone by collision with oxygen atoms is assumed to occur by the following sequence of reactions:

a) $O_2 + O \rightarrow O_3^*$

b) $O_3^* + O \rightarrow O_3(v) + O.$
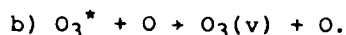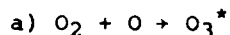
In reaction a) an oxygen atom and molecule collide to form an unbound or quasibound ozone molecule. This complex is unstable and reverts to O_2 and O unless stabilized by collision. In reaction b) the quasibound O_3^* collides to form rotationally-vibrationally excited ozone. The excess (above the dissociation limit) energy of O_3^* is removed by collision with the incident oxygen atom. Initially, we will adopt reactions a) and b) as the sole mechanism for ozone recombination. Other mechanisms involving collision with O_2 or N_2 as the stabilizing third body, or complexes formed from O_2-O_2 collisions colliding with oxygen atoms, can be addressed at a later time. We will also consider laboratory situations such as the COCHISE experiment in which Ar is the likely collision partner. A similar recombination mechanism is assumed. In the upper atmosphere, however, oxygen atoms are a major species, and it is possible that reactions a) and b) describe an important mechanism for the formation of ground-state ozone.

Some discussion has been made with regard to ozone recombination via ozone triplet states. We will not address that issue here directly. Estimates will be made for models of ozone excited states within a single potential surface treatment. Our initial effort will not include the possibility of curve crossings or radiation from recombined triplet states of ozone. The complexities of such an extension would be beyond the scope of our initial study.

6.2.2 Classical Trajectory Studies of Ozone Recombination

The use of classical trajectories to study chemical reactions dates back to the work of Eyring and Polanyi.[1] However until the advent of large computers in the late 1950's classical trajectory studies were quite restricted. The first large scale Monte Carlo trajectory calculations were done by Bunker[2a] (1962) and Karplus, Porter and Sharma[2b] (1964). Since then classical trajectory techniques have been widely applied to the study of many chemical processes including three-body exchange reactions, unimolecular decomposition reactions and energy transfer processes.[3,4]

Relatively little work using classical trajectory techniques has been done to address molecular recombination dynamics. Shui[5] used Keck's variational phase space technique[6] to calculate $H + H + H \rightarrow H_2 + H$ rates. Burns and coworkers[7] have calculated recombination rates for halogen atoms by rare gas atoms. They examined the relative contributions from the radical molecule complex mechanism:

$$X + M = XM$$

$$XM + X \rightarrow X_2 + M$$

and the energy transfer mechanism

$$X + X = X_2^*$$

$$X_2^* + M = X_2 + M.$$

6-6
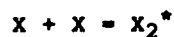
Correction factors for subsequent collisional dissociation of the nascent mol-
ecules have been computed by using classical trajectories to effect a solution
to the Boltzmann equation.[8] This correction factor is quite large (0.6-0.8)
for halogen atom recombination[7d] with inert gas third-body colliders.

The appeal of the classical trajectory technique is its relative com-
putational tractability. Accurate quantum mechanical calculations of poly-
atomic recombination are not possible on even the fastest computers. Exper-
ience has shown that classical trajectory calculations are accurate in cases
when tunneling and interference phenomena are not important. This indeed
should be the case in ozone recombination.

6 2.3 Classical Trajectory Methodology

The calculation of classical trajectories consists of three tasks:
(1) selection of initial conditions, (2) integration of Hamilton's equations
of motion and (3) final state analysis. Several reviews have described each
of these tasks in considerable detail. The reader is referred especially to
the reviews by Bunker[3] and Porter and Raff.[9] Only points specific to the
present calculations will be discussed here.

Coordinate System

We use a four-body coordinate system with fixed center of mass at the
origin. A convenient coordinate system for integration of Hamilton's equa-
tions of motion is defined by the following relations:

$$\bar{q}_i = \bar{r}_i - \bar{r}_4$$
$$i = 1,2,3$$
$$\bar{p}_i = m_i \dot{\bar{r}}_i$$

where $\bar{r}_i$ are the coordinates of the four particles relative to the center of
mass and are defined by the relations

6-7

$$\sum_{i=1}^{4} m_i \bar{r}_i = 0$$

$$\sum_{i=1}^{4} m_i \dot{\bar{r}}_i = 0.$$

In the $\bar{q}_i$ coordinate system the Hamiltonian, H, becomes

$$H = 1/m_4 \sum_{i=1}^{3} (m_i + m_4) \bar{p}_i^2 / 2m_i + 1/m_4 \sum_{i>j} \bar{p}_i \cdot \bar{p}_j + U$$

where U is the potential energy function. Hamilton's equations are written as:

$$\dot{\bar{q}}_i = \frac{\partial H}{\partial p_i} = \frac{m_i + m_4}{m_i m_4} \bar{p}_i + \frac{1}{m_4} \left(\bar{p}_{j \neq i} + \bar{p}_{k \neq j \neq i} \right)$$

and

$$\dot{\bar{p}}_i = -\frac{\partial H}{\partial \bar{q}_i} = -\frac{\partial U}{\partial \bar{q}_i}$$

Method of Integration

The numerical integrations were performed using a fourth order fixed stepsize Runge-Kutta integrator for the first five integration points. Subsequent points were computed using a fixed stepsize, fourth order Adams-Moulton integrator.

Computed trajectories were checked for numerical accuracy by back integration of selected trajectories and observation of conservation of energy and angular momentum. In most cases total energy was constant to a few parts in 10^6. Angular momentum components were conserved to better than 1-2 parts in 10^6. The integrations were performed using 60 bit CDC single precision arithmetic. Most calculations were performed on the Cyber 175 computer at the Air Force Geophysics Laboratory.

Potential Surface

For collisions of Ar with O_3 we use the Varandas-Murrell potential surface.[10] The ozone portion of this potential was derived using available spectroscopic data by Murrell et al.[10,11].

The potential function is written as

$$U = V_{Ar-O_3} + V_{O_3}$$

where V_{Ar-O_3} is the Ar-O_3 interaction and V_{O_3} is the potential function for ozone. V_{Ar-O_3} is given by a sum of pairwise Ar-O Lennard-Jones 6-12 potential between the Ar atom and each oxygen atom, i.e.

$$V_{ArO_3} = \sum_{i=1}^{3} 4\varepsilon_{ArO} \left[\left(\frac{\sigma}{|\bar{q}_i|} \right)^{12} - \left(\frac{\sigma}{|\bar{q}_i|} \right)^{6} \right]$$

The ozone interaction, V_{O_3}, is written as a function of the oxygen interatomic distances, r_1, r_2, and r_3, defined by

$$\bar{r}_1 = \bar{q}_1 - \bar{q}_2$$

$$\bar{r}_2 = \bar{q}_2 - \bar{q}_3$$

$$\bar{r}_3 = \bar{q}_1 - \bar{q}_3$$

and is given by:

$$V_{O_3} = \left[P(r_1 r_2 r_3) + G(r_1 r_2 r_3) \right]\left[1 - \tanh 2.2\varrho_1 \right]$$

$$+ V_{O_2}(r_1) + V_{O_2}(r_2) + V_{O_2}(r_3)$$

6-9

where

$$V_{O_2}(r) = C_1\left[1 + C_2(r-C_3)\right] e^{-C_4(r-C_3)},$$

$$Q_1 = C_{12}\left[(r_1-C_{13}) + (r_2-C_{13}) + (r_3-C_{13})\right],$$

$$Q_2 = C_{14}\left[(r_2-C_{13}) - (r_3-C_{13})\right],$$

$$Q_3 = C_{15}(r_1-C_{13}) + C_{16}(r_2-C_{13}) + C_{17}(r_3-C_{13}),$$

$$P = C_5 + C_6 Q_1 + C_7 Q_1^2 + C_8(Q_2^2+Q_3^2) + C_9 Q_1(Q_2^2+Q_3^2)$$

$$+ C_{10}(Q_3^3 - 3Q_2^2 Q_3) + C_{11}(Q_2^2 Q_3^2)^2,$$

$$G = g_1(1+g_3 Q_1)g_P^5 e^{-g_4(Q_2^2+Q_3^2)}$$

and

$$g_P = \left[g_3 + \sum_{\substack{i=1 \\ i \neq j \\ i=h}}^{3} (r_i^2 - r_j^2 - r_h^2)/2r_j r_h\right].$$

6-10

6.3 Classical Trajectory Calculations

6.3.1 Test Matrix

6.3.1.1 Single Collision Calculations of Energy Transfer in Ar-O_3 Collisions

The first effort in this project was devoted to a systematic study of
energy relaxation of highly vibrationally-rotationally excited ozone by colli-
sion with argon. Calculations were performed at fixed Ar-O_3 relative transla-
tional energy. Translational energies of 0.5, 1.0, 2.0 and 4.0 kcal/mol were
considered (corresponding to average kinetic energies for temperatures of 250,
500, 1000 and 2000 K). Ozone molecular energies of 25, 20, 15 and 10 kcal/mol
were used for each translational energy. (The ozone dissociation energy on
this potential surface is approximately 26 kcal/mol from the well minimum.)
For each ozone internal energy the molecular angular momentum was varied
between 0 and a value for which almost all the molecular energy was in rota-
tion. For calculations at fixed ozone angular momentum, impact parameters
were chosen randomly with maximum value 4Å. Calculations were done in batches
of 500-1000 (usually 750) for each set of translational energy, molecular
energy and molecular angular momentum. Approximately 80,000 trajectories were
computed for this effort.

Calculations were also performed at fixed total molecular energy with
different partitionings of molecular energy (set equal to 25 kcal/mol) between
rotation and vibration. Initial vibrational energy was equal to 0, 12.5 and
25 kcal/mol. Each calculation was done for a relative translational energy
of 2 kcal/mol and fixed impact parameter. Impact parameters were varied be-
tween 0 and 4Å in steps of 0.5Å. Batches of usually 1000 trajectories were
done for each set of initial conditions. About 27,000 trajectories were com-
puted for these initial conditions.

6.3.1.2 Multiple Collision Calculations

Initial multiple collision simulations of vibrationally-rotationally
excited ozone have also been begun. These calculations provide an approximate
description of the temporal behavior, i.e. relaxation, of ozone in a bath of

argon. The relaxation of ensembles of 60 ozone molecules by 250 sequential collisions with argon has been computed. Two cases were treated, both with initial total molecular energy equal to 15 kcal/mol. The two batches differed by the amount of angular momentum in the initial molecules. The relative translational energy for each collision in the sequence was fixed at a value of 2.388 kcal/mol corresponding to an approximate bath temperature of 597°K. Some calculations have also been performed for relaxation and dissociation of highly excited ozone with 25 kcal/mol initial vibrational energy.

Multiple collision simulations of the relaxation of an ensemble of vibrationally-rotationally excited ozone in a bath of argon atoms have been performed. The calculations provide an approximate description of the temporal behavior, i.e., relaxation of ozone in a bath of argon atoms.

Initial computations treated the relaxation of an ensemble of 60 ozone molecules by 250 sequential collisions with argon atoms. Two cases were treated, both with initial total molecular energy equal to 15 kcal/mol. The two batches differed by the amount of angular momentum in the initial molecules. The relative translational energy for each collision in the sequence was fixed at a value of 2.388 kcal/mol corresponding to an approximate bath temperature of 597 K.

Multiple collisional calculations were performed to simulate the behavior of ozone molecules initially excited to within 1-2 kcal/mol of the dissociation limit. Of particular interest in these simulations is the influence of partitioning of the initial molecular energy between rotation and vibration on the dissociation dynamics. Calculations were also performed to investigate the influence of the argon atom bath temperature on rates of energy relaxation and molecular dissociation probabilities.

Calculations of 50 sequential collisions with argon were performed for molecules initially excited 25 kcal/mol above the well minimum with zero angular momentum at argon atom bath temperatures of 200, 300, 400, 500, and 750 K. At the lower bath temperature, batch sizes of at least 150 initial

ozone molecules were used. At bath temperatures of 500 and 750 K, the batch size was 200. Relative translational energies were determined from the appropriate Boltzmann distribution to simulate the temperature of the bath.

Two batches of ozone molecules were excited 26 kcal/mol above the well minimum in a thermal bath at 300 K. For one batch, the initial molecular angular momentum was set equal to zero, whereas for the other, initial angular momentum equalled 16 h. Fifty sequential collisions were computed.

A total of approximately 85,000 single collisional events were computed for these multiple simulation studies.

6.3.1.3 O-O$_2$ Collisions: Complex Formation Calculations

Calculations were performed for the simulation of ozone complex formation by the collision of an oxygen atom with an oxygen molecule. Since the trajectories cannot be integrated without end, an arbitrary cutoff time was chosen beyond which an O$_3$ complex was said to have been formed. In the vast majority of collisions, the O$_3$ collision complex dissociated to O$_2$-O with 10,000 integration steps (1 integration step = 3 x 10^{-16} s) or 3 x 10^{-12} s. We designate a collision complex that does not dissociate within 400,000 integration steps (1.2 x 10^{-10} s) as a stable complex.

Complex formation calculations were performed as a function of relative translational energy and O$_2$ rotational energy. The oxygen molecule vibrational energy was fixed at a value of 0.2 kcal/mol, corresponding to a classical vibrator at T = 200 K. It is inappropriate to include, in this classical simulation of complex formation, the quantum mechanical zero point energy of the diatom vibrational mode. This is so because in a purely classical picture, there is no mechanism to restrict the zero point energy from participating in the complex dissociation by transferring energy from vibrational to relative translational energy. In real (quantum mechanical) molecules, the zero point energy is conserved and may not be transferred to translation. Therefore, a consistent classical picture omits the diatom zero point energy

for these calculations. Note, however, that in most classical calculations of atom-exchange collisions, it is found that it is best to include zero point energies, i.e., use quasiclassical initial conditions. This would indeed be the case for a treatment of the $O-O_2$ isotopic exchange reaction. It is, however, not appropriate for these calculations.

Calculations were performed at relative O_2-O translational energies of 0.01, 0.02, 0.03, 0.04, 0.05, 0.06, 0.07, 0.08, 0.09, 0.10, 0.11, 0.12, 0.13, 0.14, 0.15, 0.17, and 0.20 machine energy units (1 machine energy unit = 23.88 kcal/mol). At translational energies below 0.12 machine energy units calculations were done at rotational energies of 0, 0.01, 0.02, 0.03, and 0.04 machine energy units and above 0.13 units translational energies for rotational energies of 0 and 0.01 machine energy units. In most cases, more than 500 trajectories were computed for each translational and rotational energy. Calculations were also performed at fixed impact parameter with zero rotational energy at translational energies of 0.01 and 0.02 machine units with 0 and 0.01 rotational energies. Approximately 40,000 trajectories were computed.

6.3.2 Results and Discussion

6.3.2.1 Single Collision Calculations

In the first part of this effort we have examined energy transfer from highly excited ozone by collision with argon. The focus has been to examine energy transfer from highly excited ozone as a function of molecular angular momentum, i.e. the effect on energy transfer of partitioning of the total molecular internal energy between rotation and vibration. The primary quantity of interest is the mean energy transferred in a collisional event, $\langle \Delta E \rangle$. This quantity is computed by suitably averaging over an ensemble of trajectories with randomly chosen initial conditions. Computed values of $\langle \Delta E \rangle$ versus initial ozone angular momentum are shown in Figs. 62 to 65, for total ozone internal energies of 25, 20, 15 and 10 kcal/mol respectively. For each initial ozone internal energy, relative translational energies of 0.5, 1.0,
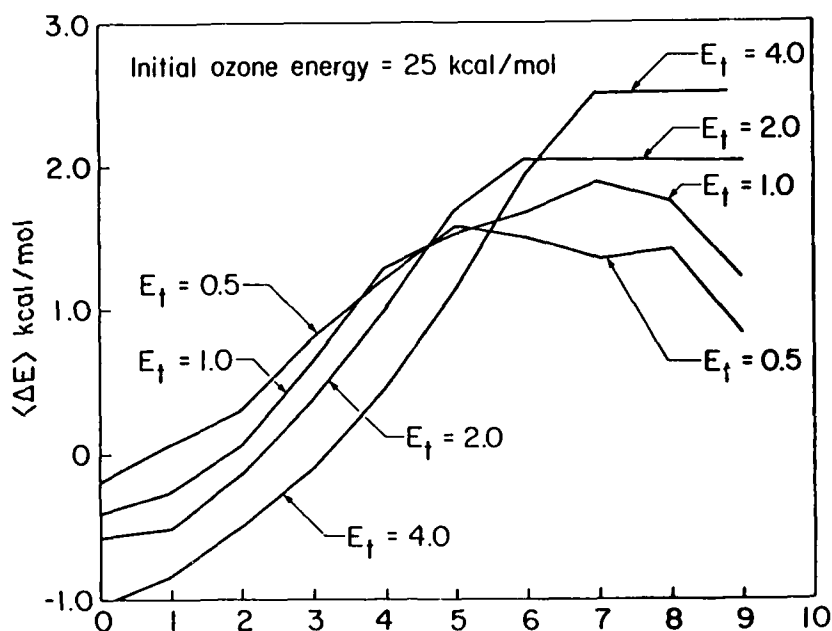
Figure 62. Average energy transferred per collision, <ΔE>, between ozone and argon as a function of initial ozone molecular angular momentum, J_{mol}, for relative translational energies of 0.5, 1.0, 2.0 and 4.0 kcal/mol. Initial ozone molecular energy equal to 25 kcal/mol.
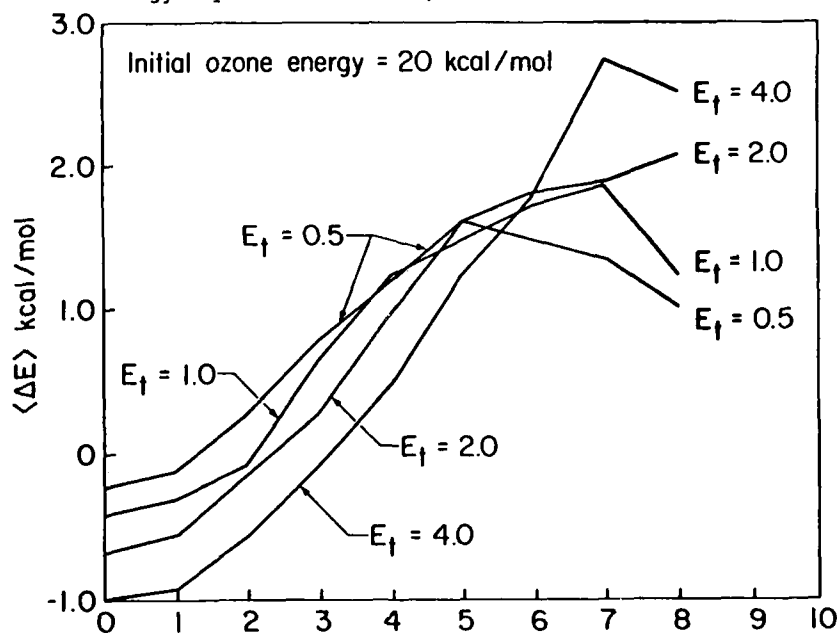
Figure 63. Average energy transferred per collision, <ΔE>, between ozone and argon as a function of initial ozone molcular angular momentum, J_{mol}, for relative translational energies of 0.5, 1.0, 2.0 and 4.0 kcal/mol. Initial ozone molecular energy equal to 20 kcal/mol.
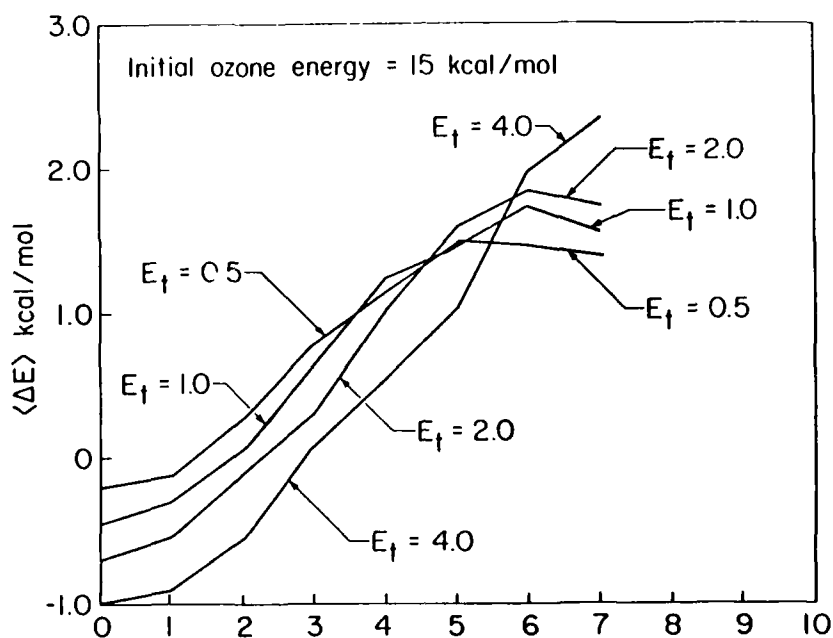
Figure 64. Average energy transferred per collision, <ΔE>, between ozone and argon as a function of initial ozone molecular angular momentum, J_{mol}, for relative tran .ational energies of 0.5, 1.0, 2.0 and 4.0 kcal/mol. Initial ozone molecular energy equal to 15 kcal/mol.
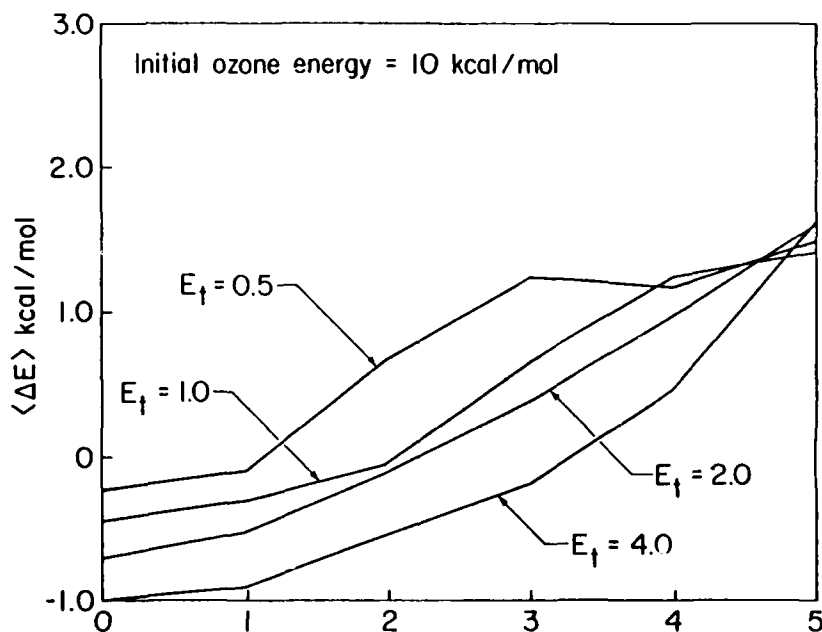
Figure 65. Average energy transferred per collision, <ΔE>, between ozone and argon as a function of initial ozone molecular angular momentum, J_{mol}, for relative translational energies of 0.5, 1.0, 2.0 and 4.0 kcal/mol. Initial ozone molecular energy equal to 10 kcal/mol.

2.0 and 4.0 kcal/mol were considered. Molecular angular momentum was varied from zero (non-rotating molecule) to a value such that almost all the internal energy was present as rotational energy. Molecular angular momentum is plotted in units of 16 $\hbar$ for convenience. The significance of these initial calculations to the relaxation of nascent recombined ozone molecules will be discussed briefly later.

We discuss first the results for collisions with ozone with 25 kcal/mol internal excitation. The adiabatic dissociation energy of ozone via the reaction

$$O_3 \rightarrow O_2 + O$$
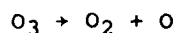
requires slightly more than 26 kcal/mol (from the well bottom, neglecting zero point energy). Thus in this case we are considering energy transfer from molecules excited to within 1 kcal/mol of their dissociation limit. The computed values of $\langle \Delta E \rangle$ are displayed in Fig. 62. Two points are immediately obvious and noteworthy. First, despite the high internal energy, molecules with low angular momentum gain energy per collision. This occurs for all relative translational energies. This gain in energy is correlated with a transfer of relative orbital angular momentum into molecular angular momentum. Second, as the molecular angular momentum is increased the energy transfer is reversed and the ozone molecules lose energy per collision. The results indicate that transfer of energy to ozone by collision occurs most readily by transfer into rotational energy. The implication of this for relaxation of newly recombined ozone is that despite high vibrational excitation, relaxation occurs when substantial angular momentum is available. Low angular momentum molecules will gain energy and have a high probability of redissociation.

We note also the dependence of energy transfer on relative translational energy. At zero initial ozone angular momentum the average energy transferred per collision, $\langle \Delta E \rangle$, decreases with increasing translational energy, i.e. the

amount of energy into the molecule increases with increasing translational energy. Thus for the range of translational energy considered here, which corresponds to a translational temperature range of 250-2000 K, the net effect of collisions with non-rotating ozone is to pump energy into the molecule and the magnitude of the energy transferred increases with the available translational energy. As the initial ozone angular momentum is increased the sign of the energy transfer begins to change and energy transfer from the molecule occurs. Energy transfer from the molecule as a function of molecular angular momentum occurs first for the lowest translational energy, 0.5 kcal/mol. Thus at intermediate values of molecular angular momentum the average energy transfer varies inversely with relative translational energy. As the molecular angular momentum is increased further the dependence of the energy transferred on translational energy changes again. At high values of initial molecular angular momentum $\langle \Delta E \rangle$ again increases with increasing translational energy. This transition occurs for the translational energies considered when a large fraction of the 25 kcal/mol is available as rotational energy. (Note however that at internal energies of 25 kcal/mol a strict separation of rotational and vibrational energy is not feasible.)

A qualitative understanding of the dependence of energy transfer on molecular angular momentum may be obtained by consideration of the relative time scales of the translational, rotational and vibrational motion. Characteristic time scales for rotational and translational motion are similar. Thus exchange between these modes is quite facile. However the characteristic time scales (or frequencies) for vibration are much faster than translation. Hence the argon atom impinging on the vibrating ozone sees a rapidly fluctuating forcefield that averages the energy transfer over the course of a trajectory to zero.

At low initial angular momentum the impinging Ar atom sees a cold rotational mode and transfers energy into it. As mentioned, the vibrational motion is highly energetic but does not couple readily to the atom translation. Thus the net effect is energy transfer into the molecule. At intermediate values of molecular angular momentum the rotational mode and

translational energy are balanced so that they do not exchange energy. Energy
exchange between vibration and translation does not occur readily and the net
effect is that the average energy passes through zero for each translational
energy. As expected, this occurs at higher values of molecular angular momen-
tum for higher translational energies. At high values of molecular angular
momentum the impinging atom sees a hot rotational mode which readily loses
energy to translation and thus the net effect of collisions is that the mole-
cule loses energy. If molecular angular momentum could be increased indefi-
nitely its characteristic time scale would become too short to effectively
couple with translation and a decrease in energy transfer is expected.

The computed values of $\langle \Delta E \rangle$ for ozone internal energies of 20,15 and
10 kcal/mol are shown in Figs. 63, 64 and 65 respectively. These results
are extraordinarily similar to those for internally excited ozone of
25 kcal/mol. This result is in accordance with the fact that energy transfer
occurs primarily between translational and rotational modes. At the lower
vibrational energies this should be even more true due to the shorter time-
scale of vibrational motion as one goes down into the potential well.

Selected calculations have been performed for $\langle \Delta E \rangle$ as a function of
impact parameter. Three cases for ozone with initially 25 kcal/mol internal
energy have been computed: (1) all internal energy in vibration, (2) the
internal energy (arbitrarily) divided equally between vibration and rotation
and (3) all internal energy as rotation. The calculations are for relative
translational energy of 2 kcal/mol. The results are displayed in Fig. 66.

For the non-rotating case ($E_{ROT} = 0$) the energy transfer is negative
at all impact prameters, i.e. energy is pumped into the molecule. This shows
that the net negative values discussed earlier which were averaged over impact
parameters had no positive energy transfer range. The magnitude of the energy
transfer increases initially due to the increasing orbital angular momentum of
the relative translational motion. At large impact parameters the energy
transfer decreases rapidly due to the fairly rapid drop-off of the potential
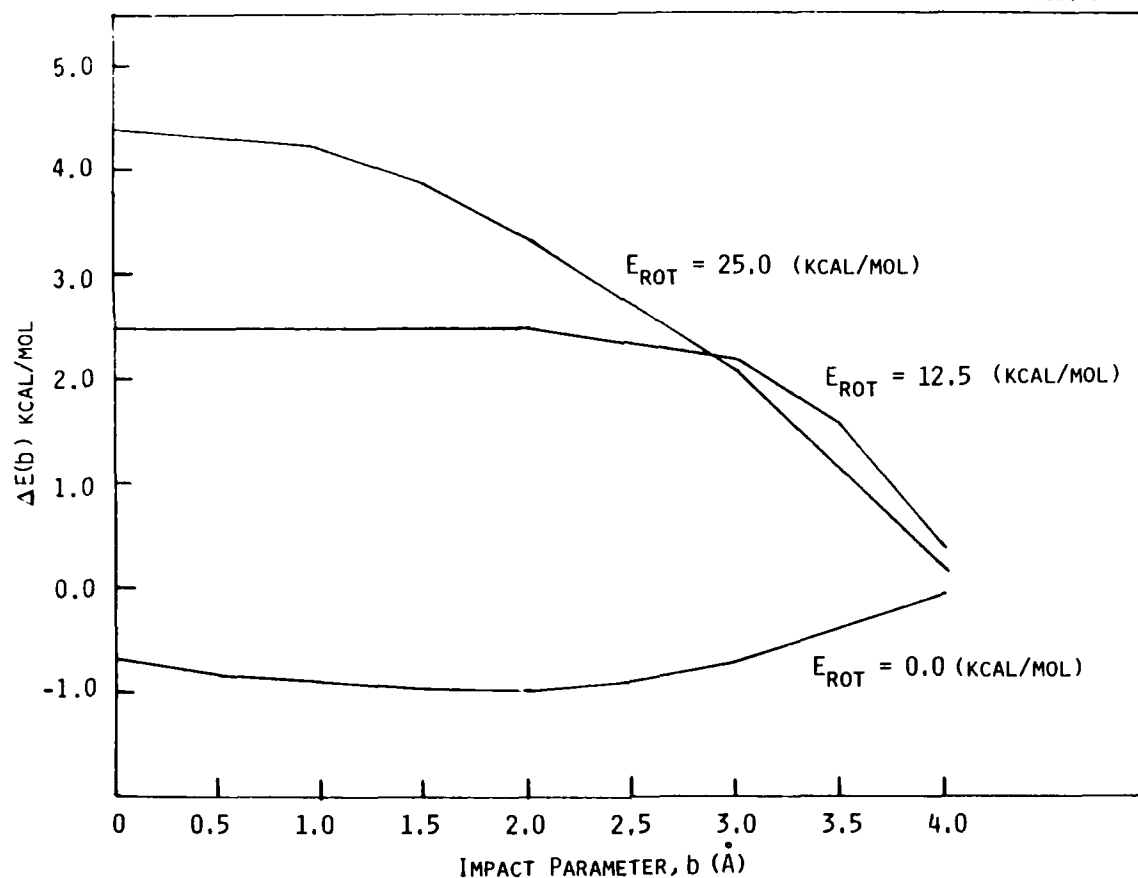
Figure 66. Average energy transferred per collision, $\Delta E(b)$, between ozone and argon as a function of impact parameter for initial ozone rotational energy equal to 0, 12.5 and 25 kcal/mol. Total initial ozone molecular energy is equal to 25 kcal/mol.

with intermolecular distance. For the case when all the initial triatom energy is in rotation, very large average energy transfers are computed. In this case the average energy transfer decreases monotonically with increasing impact parameters. The case of equally divided initial rotational and vibrational energy resembles the $E_{VIB} = 0$ case. Here the magnitude of energy transferred per collision is somewhat reduced due to the lesser amount of rotational energy.

It is also of interest to examine the distribution of energy transfers per collision. Distributions of magnitudes of energy transfers are shown in Fig. 67 for initial molecular excitation of 25 kcal/mol, and translational energy of 2 kcal/mol for two values of initial angular momentum: 31 $\hbar$ and
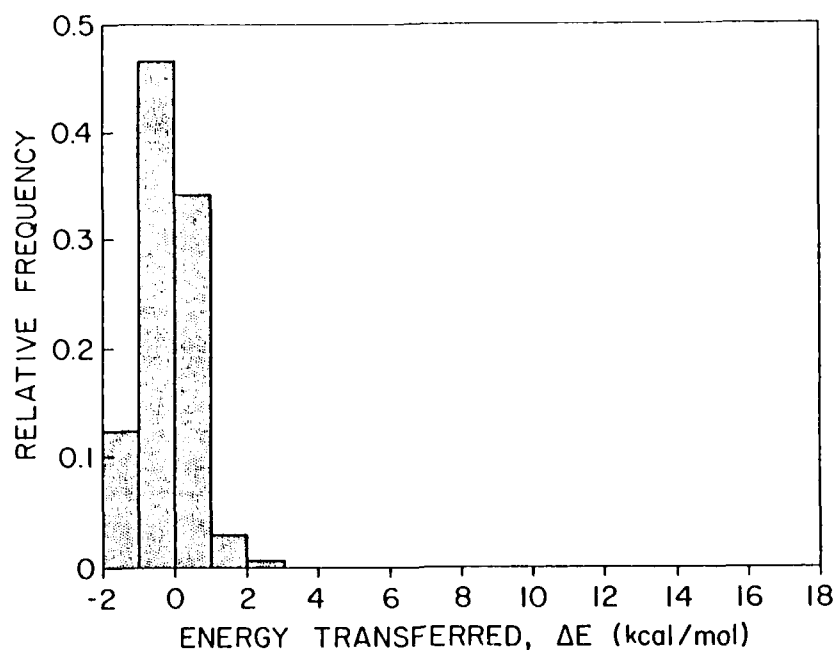
Figure 67. Relative frequency of energy transfers, ΔE, in argon-ozone
collisions at initial relative translational energy of
2 kcal/mol, ozone molecular energy of 25 kcal/mol and
initial molecular angular momentum equal to 31 $\hbar$

125 $\hbar$. As before, positive values of energy transfer signify energy is lost
from the molecule while for negative values the molecule gains energy in a
collision. As seen in both Figs. 67 and 68 most collisional encounters lead
to small energy transfers due to the fairly large maximum impact parameter of
4Å used in the calculations. For the lower value of molecular angular momen-
tum there are very few encounters in which more than 1-2 kcal/mole is trans-
ferred out of the molecule. Hence as previously mentioned the net collisional
transfer is into the ozone molecule despite its initial high vibrational-
rotational excitation. The higher molecular angular momentum case is quite
different. The average energy transfer is from the molecule to relative
translational motion. Additionally there are a substantial number of large
energy transfer collisions. The total cross section for energy transfers
greater than 10 kcal/mol is computed to be 2.4 Å^2. It is clear that the pres-
ence of large molecular angular momentum qualitatively changes the energy
transfer.

6-21
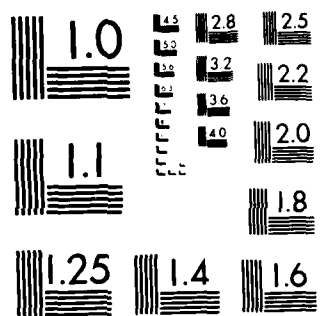
CROCOPY RESOLUTION TEST CHART
NATIONAL BUREAU OF STANDARDS 1963-A
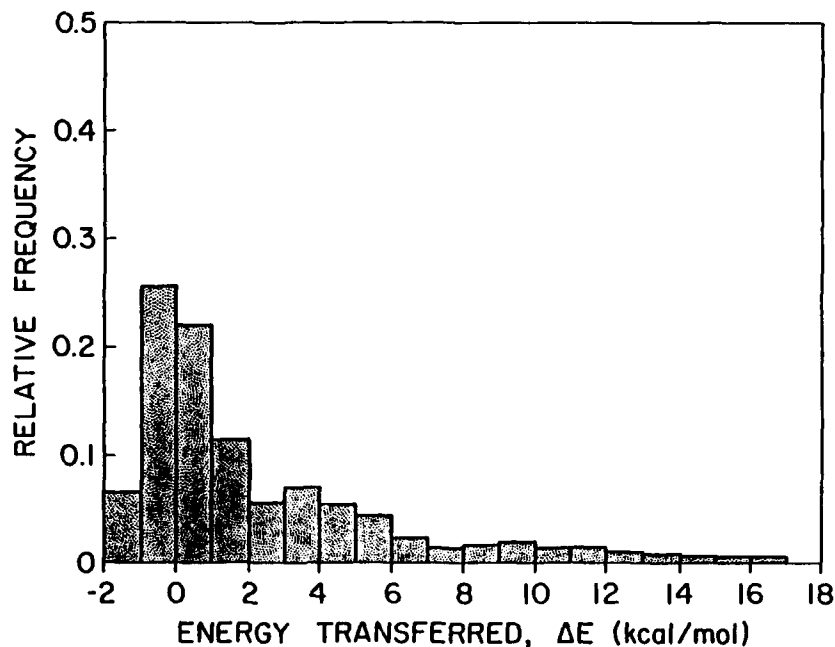
Figure 68. Relative frequency of energy transfers, ΔE, in argon-ozone
            collisions at initial relative translational energy of
            2 kcal/mol, ozone molecular energy of 25 kcal/mol, and
            initial molecular angular momentum equal to 125 $\hbar$

6.3.2.2 Multiple Collision Calculations

Multiple collision calculations were performed to simulate the relaxation
of excited ozone in a bath of argon. Two cases were treated in a preliminary
effort; (a) molecules initially excited with 15 kcal/mol with angular momentum
equal to 16 $\hbar$ and (b) molecules excited 15 kcal/mol with angular momentum
equal to 63 $\hbar$. The average molecular energy versus collision is plotted in
in Fig. 69 for both cases. A fixed value of the relative translational
energy equal to 2.3 kcal/mol was chosen.

The effect of initial molecular angular momentum is readily seen. Ini-
tially the low angular momentum molecules gain energy as angular momentum is

built up by collisions. On the other hand the higher angular momentum molecules undergo a rapid energy loss initially associated with a loss in average molecular angular momentum. The difference in behavior between the two ensembles is highly transitory. After approximately fifty collisions the characteristic relaxation behavior of each ensemble becomes identical. This behavior, however, has serious implications for the early relaxation of recombined molecules formed very close to the dissociation limit. For molecules with low angular momentum, energy will be pumped into the molecule as angular momentum is increased by collisions. This will lead to dissociation for some molecules. However, molecules formed with high angular momentum will lose energy and should have a substantially lower probability of dissociation.

Preliminary calculations of the relaxation of 25 kcal/mol vibrationally excited ozone (with zero angular momentum) show that on the order of one-third of the molecules are dissociated after 25 collisions. Dissociation, curiously, is a very low probability single collision event. Approximately 10,000 trajectories were computed in which the total energy exceeded the ozone dissociation energy. However only one trajectory was observed to lead to dissociation. The multicollisional calculations imply that dissociation is quite important for very highly excited molecules and makes a very significant contribution to the computed rates of recombination and relaxation. These early calculations would seem to establish the need for describing non-equilibrium effects in any realistic description of ozone recombination.

The average molecular angular momentum versus collision number is shown in Fig. 70 for both cases. The ensemble initially with low angular momentum rapidly (10-20 collisions) gains angular momentum while the relatively high initial angular momentum ensemble loses angular momentum. This behavior correlates well with the short time increase in the average molecular energy of the low initial angular momentum ensemble. The initial decrease of the average angular momentum of the high initial value ensemble also correlates well with the initial rapid decrease in the average molecular energy of this ensemble. Thus, we may readily associate the difference in the early time behavior of these ensembles with rotational relaxation of the initial ensemble.
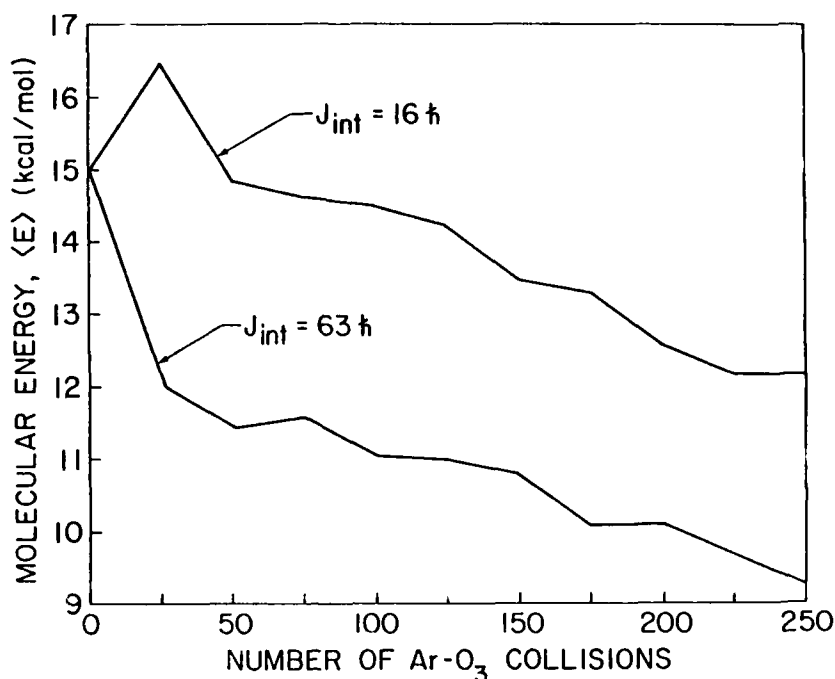
Figure 69. Average molecular internal energy of an ensemble of ozone
molecules as a function of number of collisions with argon
atoms. The results for two ozone ensemble initial conditions
are shown: (1) total ozone energy equal to 15 kcal/mol and
initial ozone angular momentum, J_{int}, equal to 16 ℏ and
(2) total ozone energay equal to 15 kcal/mol and J_{int} - 63 ℏ.
Relative translational energy is equal to 2.3 kcal/mol in
both cases.

A study of the multiple collision relaxation of an ensemble of ozone
molecules initially excited 25 kcal/mol above the well minimum was performed
as a function of the argon bath temperature. The initial ozone ensemble was
given zero initial angular momentum. For these initial conditions,
substantial dissociation occurs.

The probability of dissociation, i.e., fraction of ozone molecules that
dissociated after 50 collisions, is shown as a funccion of bath temperature in
Fig. 71. At a bath temperature of 200 K, relatively few molucu₋es are dis-
sociated, i.e., less than 10 percent of the initial ensemble. The dissocia-
tion probability rapidly rises with temperature and, for a bath temperature in
excess of 750 K, more than half the ensemble dissociates after several
collisions.
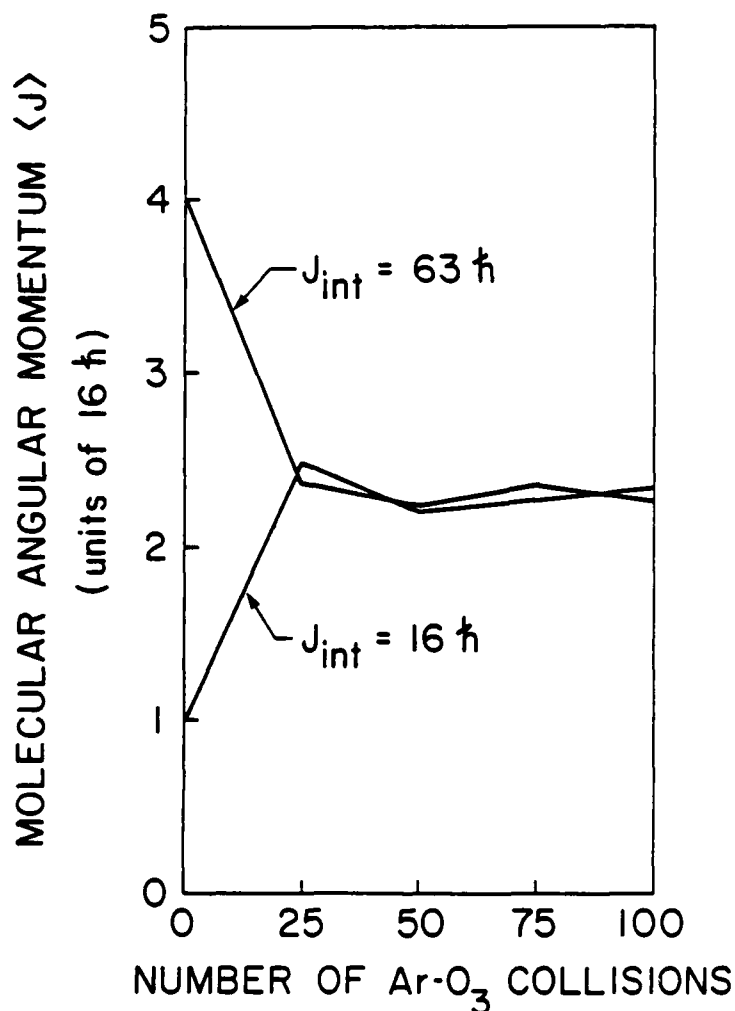
Figure 70. Average molecules angular momentum versus collision number.
Same initial conditions as in Fig. 69.

It is anticipated that ozone molecules formed by recombination will have
internal energies only a few kilocalories below the dissociation limit. Given
the rather large probabilities for dissociation shown in Fig. 71, it is
necessary to account for relaxation behavior after formation. The measureable
dissociation rate will be determined by the rate at which quasibound complexes
are stabilized by collision, and the rate at which these highly excited mole-
cules are relaxed. Molecules formed at energies near the dissociation limit
will either relax or be redissociated. Clearly, redissociated molecules do
not contribute to the measured recombination rate. Thus, again, the simula-
tion of measured rates and temperature dependencies requires proper accounting

6-25
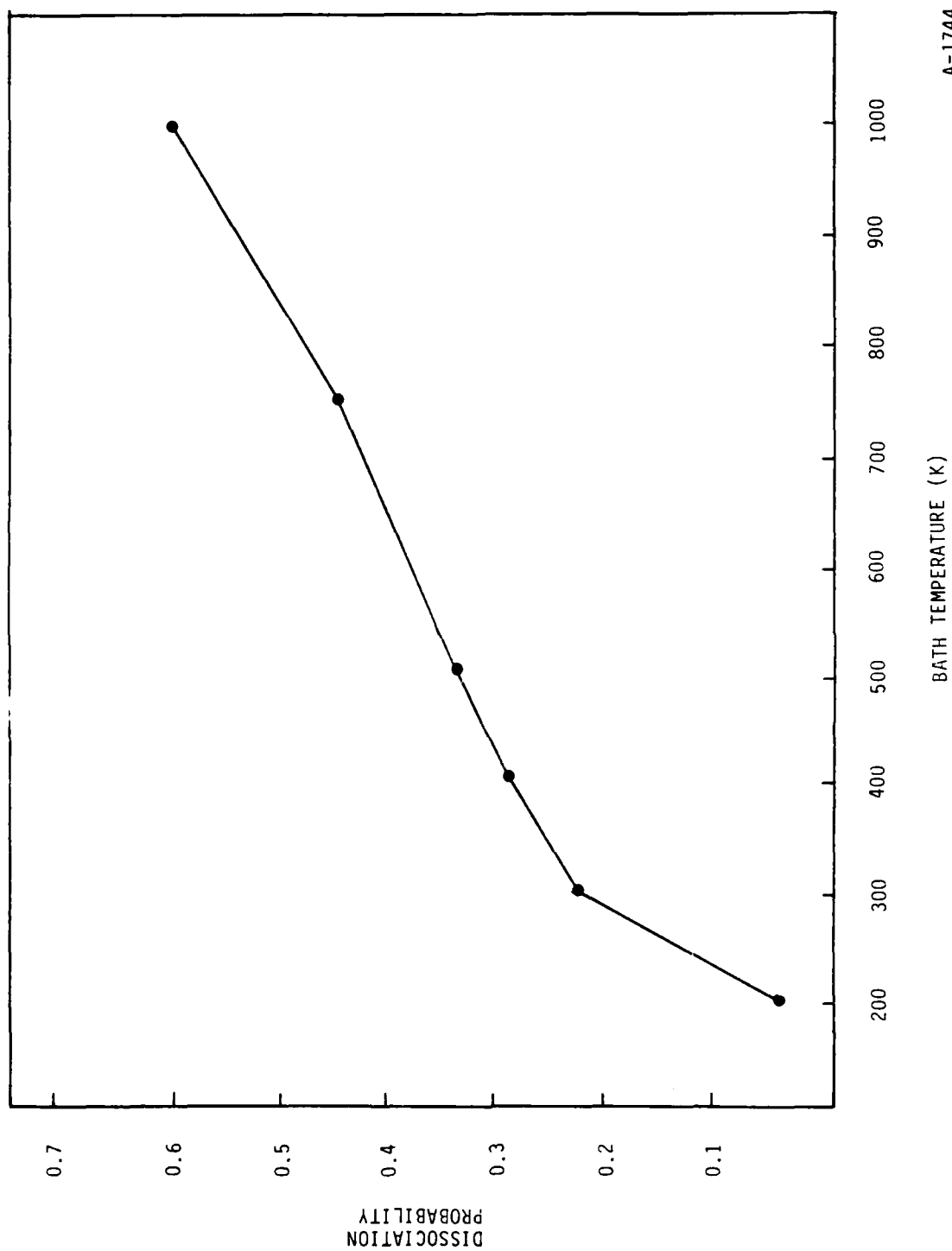
Figure 71. Probability of ozone dissociation versus bath temperature (Initial O_3:25 kcal/mol Internal Energy, J = 0)

A-1744

6-26

of such non-equilibrium effects as redissociation. From the results presented in Fig. 71, it is anticipated that redissociation will scale single collision rates by 30-60 percent. Most significantly, they will increase the temperature dependence at lower temperatures due to the rapid increase in the dissociation probability with bath temperature.

Multiple collision calculations were performed for two ensembles of ozone molecules excited 26 kcal/mol above the well minimum (i.e., within about 0.5 kcal/mol of the dissociation limit). The initial ensemble differed by the amount of molecular angular momentum. In one case, the initial molecules had zero angular momentum, and in the other, they had initial angular momentum corresponding to 7 kcal/mol rotational energy. The argon bath temperature was 300 K. The average relative translational energy of a collision was 1.2 kcal/mol.

The energy relaxation of both ensembles is shown in Fig. 72. As for the case discussed earlier (see Fig. 69), the low (zero) initial angular momentum gains energy over the first few collisions while the hotter rotational energy does not. The difference in energy relaxation behavior is again highly transitory and disappears after approximately 20 sequential collisions with the argon bath. The dissociation probability versus number of collisions is shown in Fig. 73. Several points are noteworthy.

The initial zero angular momentum ensemble undergoes approximately 35 percent dissociation, whereas the other undergoes only about 12 percent dissociation. Clearly, vibrational energy is more effective in inducing dissociation. However, the effect is somewhat subtle in that it is the lack of rotational energy that promotes energy accumulation in the molecules and hence, dissociation. It is also interesting to note the energy and time scales for dissociation.

Figure 72. Relaxation of ozone initially excited 26 kcal/mol in 300 K Argon atom bath.
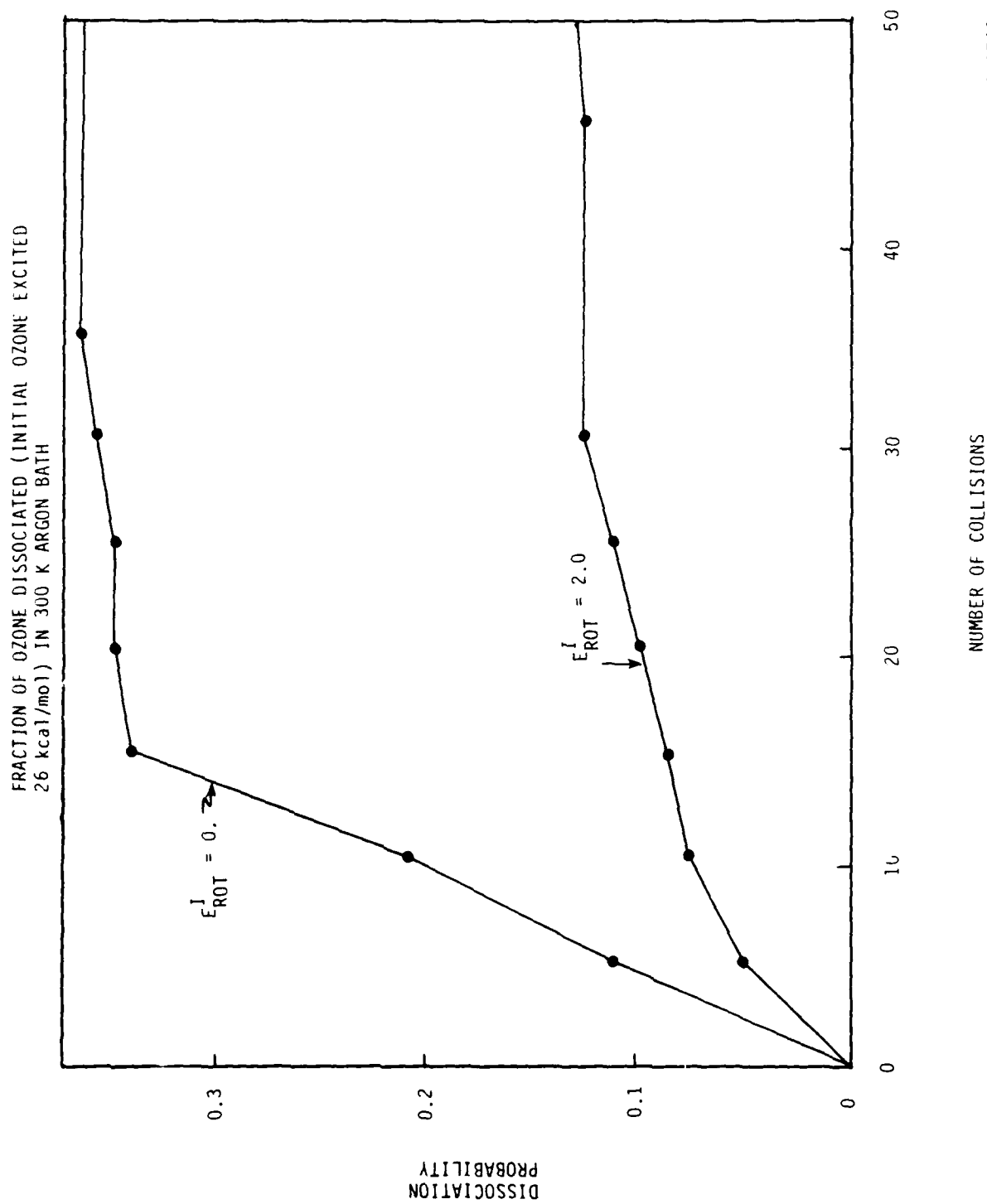
Figure 73. Fraction ozone dissociated (initial ozone excited 26 kcal/mol) in 300 K Argon bath.

A-1743
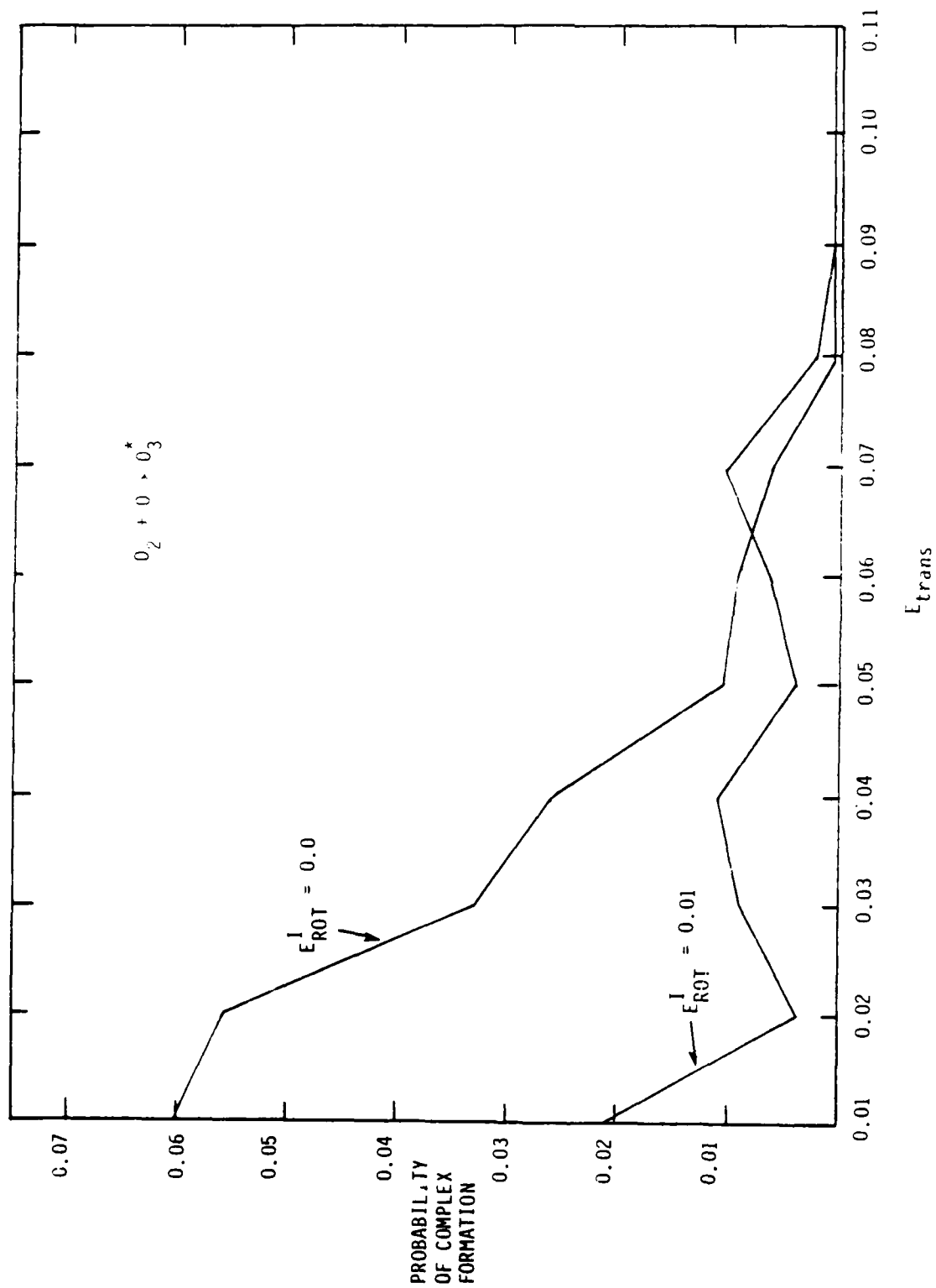
Figure 74. Complex formation as a function of translation energy.

For both ensembles, dissociation ceases to be a significant event after about 20 collisions, although there are some rare cases out to 50 collisions. This corresponds for both ensembles to average internal energies of about 22 kcal/mol. At 22 kcal/mol energy above the well minimum, molecules need about 4.5 kcal/mol to dissociate. This is approximately 8 kT for the argon bath. Calculations of the dissociation of diatomics in thermal baths indicate that dissociation ceases once the average molecular energy is 5-10 kT below the dissociation limit. A similar value seems to be indicated for the $Ar-O_3$ system at 300 K bath temperatures.

Dissociation, like rotational relaxation, is a short time phenomenon occurring on a time scale of 10-20 collisions. This is readily seen since molecules relaxed several kT below the dissociation limit have very low probabilities of dissociation.

6.3.2.3 $O-O_2$ Collision: Complex Formation Calculations

The simulation of ozone recombination dynamics consists of three steps: 1) formation of complexes of unbound ozone by collisions of O with O_2, 2) stabilization of the unbound complexes by collision with argon atoms to form highly excited ozone molecules, and 3) relaxation of highly excited molecules in a thermal bath of argon atoms. The first step in this simulation has been systematically investigated to uncover the dependence of complex formation on relative translational energy and diatom rotational energy.

Complex formation probabilities as a function of relative translational energy for two values of diatom rotational energy are shown in Fig. 74. It is readily seen that complex formation decreases rapidly with relative translational energy. Beyond approximately 0.08 machine units (about 2 kcal/mol), the probability of forming $O_3^\dagger$ is very unlikely. This is because complexes formed at higher energies have too much energy to remain bound for long periods of time.

The addition of rotational energy to the colliding diatom causes a marked decrease in complex formation probability at lower translational energy. This effect disappears when the translational energy is increased substantially above 0.05 machine units (1.2 kcal/mol).

This general behavior implies a strong temperature dependence on temperature for complex formation and, in turn, on the ozone recombination rate. Current work is using the computed complexes as initial conditions for the stabilization and relaxation calculations.

6.3.3 Implication for COCHISE and High Altitude Processes

In the COCHISE apparatus radiation is measured from recombined ozone. The measurements are made after the nascent molecules have undergone between 10^2 and 10^4 collisions. Analysis of the measured spectra indicates vibrational states above the fifth quantuum level are not detected. The conclusion of the present study is that the COCHISE measurements are from ensembles of recombined ozone that have undergone substantial molecular relaxation and thus do not directly reflect the nascent distribution of very highly excited ozone vibrational states.

It is important to make a comparison between the conditions of the COCHISE experiment and high altitude processes. At 100 km collision frequencies are about 3000 ms^{-1}. Radiative lifetimes from highly excited vibrational states of ozone are predicted to be 20 ms. Thus on the average, 50 collisions occur before radiation is emitted. The calculations presented here imply that substantial relaxation of very highly excited molecular states could occur on this time scale. Thus the radiation emitted from recombined ozone at these altitudes could reflect a partially relaxed distribution of molecular states.

To compare the degree of relaxation in the COCHISE experiments to that in the upper atmosphere we first note that it is expected that the rate of collisional relaxation of the uppermost ozone states should be faster than that of lower states. Two factors should make this true: (1) very highly excited states may be depleted both by energy loss and by energy gain via dissociation

and (2) for lower states the energy gap between states increases and coupling between rotational and vibrational modes decreases. Our tentative conclusion is that the very uppermost states are relaxed in both the COCHISE apparatus and at 100 km altitude. Substantially more relaxation occurs in the COCHISE experiments. However, this additional effect should be considerably less dramatic due to the slower relaxation of less excited states. The kinetic analyses of Chapter 5 have been used to extrapolate COCHISE observations to a quasi-initial distribution more representative of the upper atmosphere.

6.3.4 Future Work

The goal of this project is to develop a theoretical description of ozone recombination dynamics in order to aid in the interpretation of available data. Thus far we have developed the computational machinery for this effort and have completed a systematic study of energy relaxation of vibrationally-rotationally excited ozone by collision with argon atoms. Additionally, we have examined the time evolution of excited ozone in a thermal bath of argon atoms. When this is completed, our future efforts will become more specifically directed towards recombination simulation studies.

The first step will be characterization of unbound O_3 complexes. Two approaches will be used: (1) a classical trajectory search for long-lived O_3^* formed by O_2-O collisions and (2) a semiclassical calculation of resonance states[12-14] above the dissociation limit (by D. Noid and M. Koszykowski). Classical calculations have been completed. Collision rates (one-way fluxes) will then be calculated for stabilization of O_3^* by argon atoms and ensembles of nascent recombined ozone will be generated. The relaxation of the nascent ensembles will be studied using multi-collision calculations. The results of these calculations should provide a valuable insight into the experimental data. In addition to the Ar-O_3 system we shall begin work on the O-O_3 system.

In continued investigations, we will also investigate recombination dynamics via the chaperon mechanism, i.e., by collision of Ar-O with O_2. Additionally, it is anticipated that a study of the relaxation of vibrationally-rotationally excited oxygen by O atoms will be of interest.

6.4 References

1. Eyring, H. and Polanyi, M., Z. Phys. Chem. $\underline{B12}$, 279 (1931).

2a. Bunker, D.L., "Monte-Carlo Calculation of Triatomic Dissociation Rates I N_2O and O_3," J. Chem. Phys., $\underline{37}$, 393 (1962).

 b. Karplus, M., Porter, R.N. and Sharma, R.D., "Dynamics of Reactive Collisions: The H + H2 Exchange Reaction," J. Chem. Phys. $\underline{40}$, 2033 (1964).

3. Bunker, D.L., "Classical Trajectory Methods," Meth. Comp. Phys. $\underline{10}$, 287 (1971).

4. Porter, R.N. "Molecular Trajectory Calculations," Am. Rev. Phys. Chem. $\underline{25}$, 317 (1974).

5. Shui, V.H., "Thermal Dissocation and Recombination of Hydrogen According to the Reactions H_2 + H ~ H + H + H," J. Chem. Phys. $\underline{58}$, 4068 (1973) and earlier references

6. Keck, J.C., Advanc. At. Mol. Phys. $\underline{8}$, 39 (1972).

7a. Clarke, A.G. and Burns, G., "Trajectory Studies of Atomic Recombination Reactions," J. Chem. Phys. $\underline{55}$, 4717 (1971).

 b. Clarke, A.G. and Burns, G., "Trajectory Studies of Atomic Recombination Reactions. II. The Energy Transfer Mechanism and Nonequilibrium Effects," J. Chem. Phys. $\underline{56}$, 4636 (1972).

 c. Clarke, A.G. and Burns, G., "Trajectory Studies of Atomic Recombination Reactions. III. Energy Transfer in Bromine Inert Gas Systems," J. Chem. Phys. $\underline{58}$, 1908 (1973).

 d. Wong, W.H. and Burns, G., "Trajectory Studies of Atomic Recombination Reactions. IV. Recombination of Iodine Atoms," J. Chem. Phys. $\underline{58}$, 4459 (1973).

 e. Burns, G. and Young, A.W., "Trajectory Study of Atomic Recombination. VIII. The Energy Transfer Mechanism," J. Chem. Phys. $\underline{72}$, 3630 (1980).

8. Gelb, A., Kapral, R. and Burns, G., "Non-Equilibrium Effects in Atomic Recombination Reactions," J. Chem. Phys. $\underline{56}$, 4631 (1972).

9. Porter, R.N. and Raff, L.M., "Classical Trajectory Methods in Molecular Collisions," in Dynamics of Molecular Collisions Part B, edited by W.H. Miller, Plenum, New York (1976).

10. Varandas, A.J.C. and Murrell, J.N., "Dynamics of the $^{18}O + ^{16}O_2(v=0)$ Exchange Reaction on a New Potential Energy Surface for Ground State Ozone," Chem. Phys. Lett. 88, 1 (1982).

11. Carter, S.; Mills, I.M.; Murrell, J.N., and Varandas, A.J.C., "Analytical Potential for Diatomic Molecules IX," Molec. Phys., 45, 1053 (1982).

12. Marcus, R.A., "Semiclassical Theory for Collisions Involving Complexes (Compound State Resonances) and for Bound State Systems," Fara. Disc. Chem. Soc., 55, 34 (1973) and reference therein.

13. Noid, D.W. and Marcus, R.A., "Semiclassical Calculation of Bound States in a Multidimensional System. Use of Poncare's Surface of Section," J. Chem. Phys. 62, 2119 (1975).

14. Noid, D.W. and Marcus, R.A., "Semiclassical Calculation of Bound States in a Multidimensional System for Nearly 1:1 Degenerate Systems," J. Chem. Phys. 67, 559 (1977).

7. DISCHARGE EXCITATION OF O_3:
A MODEL OF THE PHYSICS AND CHEMISTRY
OF MICROWAVE DISCHARGES IN Ar/O_2 MIXTURES

The COCHISE gases are excited via microwave discharge techniques. Under typical operating conditions gases at a pressure of $\sim$ 1 Torr and temperatures of $\sim$ 80 K are passed through cylindrical inlet tubes of 0.55 cm radius. The discharge is struck across McCarroll-modified Evenson electrodeless cavities operating at a frequency of 2.45 GHz and with a power output of 50 W. The experiments directed towards the study of ozone formation have been performed in gas mixtures of O_2 dilute in Ar.

We must diagnose the processes occuring in the discharge in order to provide a kinetic interpretation of the ozone observations. Such an analysis requires three distinct steps: (1) a definition of the characteristic field strengths of the discharge; (2) specification of the electron-neutral excitation rates within the discharge; and (3) development of a complete electron-ion-neutral chemical kinetic scheme to predict the coupled interaction of all states of interest. The development of this model is described below.

7.1 Operating Conditions for Microwave Discharges

When a low pressure (0.1-10 Torr) DC glow discharge is struck between cathode and anode a rich axially structured light pattern is observed between the plates characterized by number of regions with distinct optical and electrical properties.[1] Much of this structure is specific to the cathode and anode regions, however a relatively uniform region, called the positive column, fills the major part of the discharge.

The use of high frequency electrodeless discharges eliminates the complications of anode and cathode regions and provides a relatively uniform glow which resembles the positive column of an equivalent DC discharge.[2] The excitation mechanism is, of course, distinct in the AC discharge, inasmuch as the electrons gain energy through collisions with neutral molecules as they

oscillate with the field. These collisions act to disturb the phase relations (90° in vacuum) between field and electrons, allowing energy transfer between the two, as well as promoting a modest energy transfer between electrons and neutrals. The electrons continue to gain energy in this manner until a balance is struck between energy gain from the field and energy loss through inelastic collisions with neutrals. It can readily be shown[2,3] that an AC discharge with electric field E_o is equivalent to a DC discharge of effective field E_e defined by

$$E_e = E_o \left(\frac{\nu^2}{\nu^2 + \omega^2} \right)^{1/2}$$

where ν is the collision frequency for momentum transfer and $\omega = 2\pi f$, where f is the field frequency, 2.5 GHz for COCHISE. For purposes of reference it has been shown[4] that collision frequencies in Ar Discharges will be of order 3×10^{10} s^{-1} at densities of $10^{17}/cm^3$.

Definition of the appropriate field strength is not so obvious however. Such discharges are diffusion dominated and thus operating conditions are determined by a balance between diffusive losses and volume ionization. Specifically the steady operating condition depends upon gas, pressure, and discharge diameter. The defining equation for electron density may be written as

$$d^2n/dr^2 + \frac{1}{r} \, dn/dr + \frac{Z}{D_a} \, n = 0 \tag{1}$$

where cylindrical geometry and a constant volume ionization rate has been assumed. Here n is electron density, Z is the number of ionizing collisions per second per electron and D_a is the ambipolar diffusion coefficient. (See Reference 5 for a discussion of deviations from the ambipolar limit.) Equation (1) has the solution

$$n_e = n_o J_o \ (r \ \sqrt{Z/D_a}) \tag{2}$$

where J_o is a Bessel function of zero and the solution is only valid to the first zero of the function which occurs when

$$r = R = 2.405 \ \sqrt{D_a/Z} \tag{3}$$

where R is the tube radius. Thus

$$Z = 5.8 \ D_a/R^2 \tag{4}$$

The ambipolar diffusion coefficient is defined by the relationship

$$D_a = \frac{De \ \mu_+ + D_+ \mu_e}{\mu_e + \mu_+} \tag{5}$$

where De, μ_e and D_+, μ_+ are the free diffusion and mobility coefficients of the electron and ion respectively. The quantity D/μ is called the character-istic energy of the distribution which we will donate by ε_k or ε_+ for electrons and ions respectively. Generally, $\varepsilon_k \gg \varepsilon_+$ in discharges whence

$$D_a \approx \varepsilon_k \ \mu_+ \tag{6}$$

(Note that characteristic energies are often related to "temperature," although not in the Maxwellian sense, and Eq. (6) is often rewritten[2] as $D_a \approx D_+ \ Te/T_+$. There is no difference between these two definitions. Because of the low mobility of the positive ions T_+ is typically of the order, but necessarily higher, than the gas translational temperature.)

It has been found that the ionic mobility does not vary significantly with field strength.[6] This is demonstrated in Fig. 75 where measured ionic mobility for several typical ions diffusing in an argon carrier are plotted over a range of two orders of magnitude in density-normalized field strength. Similar results pertain for other carriers such as N_2. Reference 6 does not report results for O_2^+ in an argon carrier, however O_2^+ should behave

similarly to N_2^+. Note that the ionic diffusion coefficients tend to be smaller than those for their neutral counterparts. This is a result of the increased collision cross section resulting from the charged particle/ polarizable neutral interaction.

The standard mobility in Fig. 75 is normalized to standard temperature and pressure. It may be related to the mobility at P, Torr and T, K by the relationship

$$\mu_o = \mu(P/760)\,(273/T)$$

The classical approach[1] to characterize the discharge is to assume a Maxwellian electron distribution and a kinetic ionization rate of the form

$$Z = A\,\sqrt{T_e}\,e^{-I/T_e} \tag{7}$$

where I is the ionization potential for the gas and it is assumed the $\varepsilon_k = kT_e$. In this case Equation (4) becomes a transcendental equation which can be solved for T_e. Typical solutions are given in Cobine[1] where it is found that for gases such as Ar and N_2 and COCHISE conditions of R = 0.5 cm, p ~ 1 Torr the electron temperature is ~ 1.5 eV. Unfortunately, although this approximation appears reasonable for N_2, it is quite poor for Ar. This is apparently so because the large Ramsauer minimum in the electron/argon collision cross section drives the electron energy to a very non-Maxwellian distribution.

Fortunately there are measured values available for the ionization rate and characteristic energy for gases such as N_2 and Ar as a function of E/N (field strength/number density). Typical measured results are provided in Table 7 (see review in Reference 7). Listed in order, are E/N, ionization coefficient, drift velocity, characteristic energy (D/μ) and ionization rate. As can be seen the properties of Ar and N_2 are quite different.

7-4
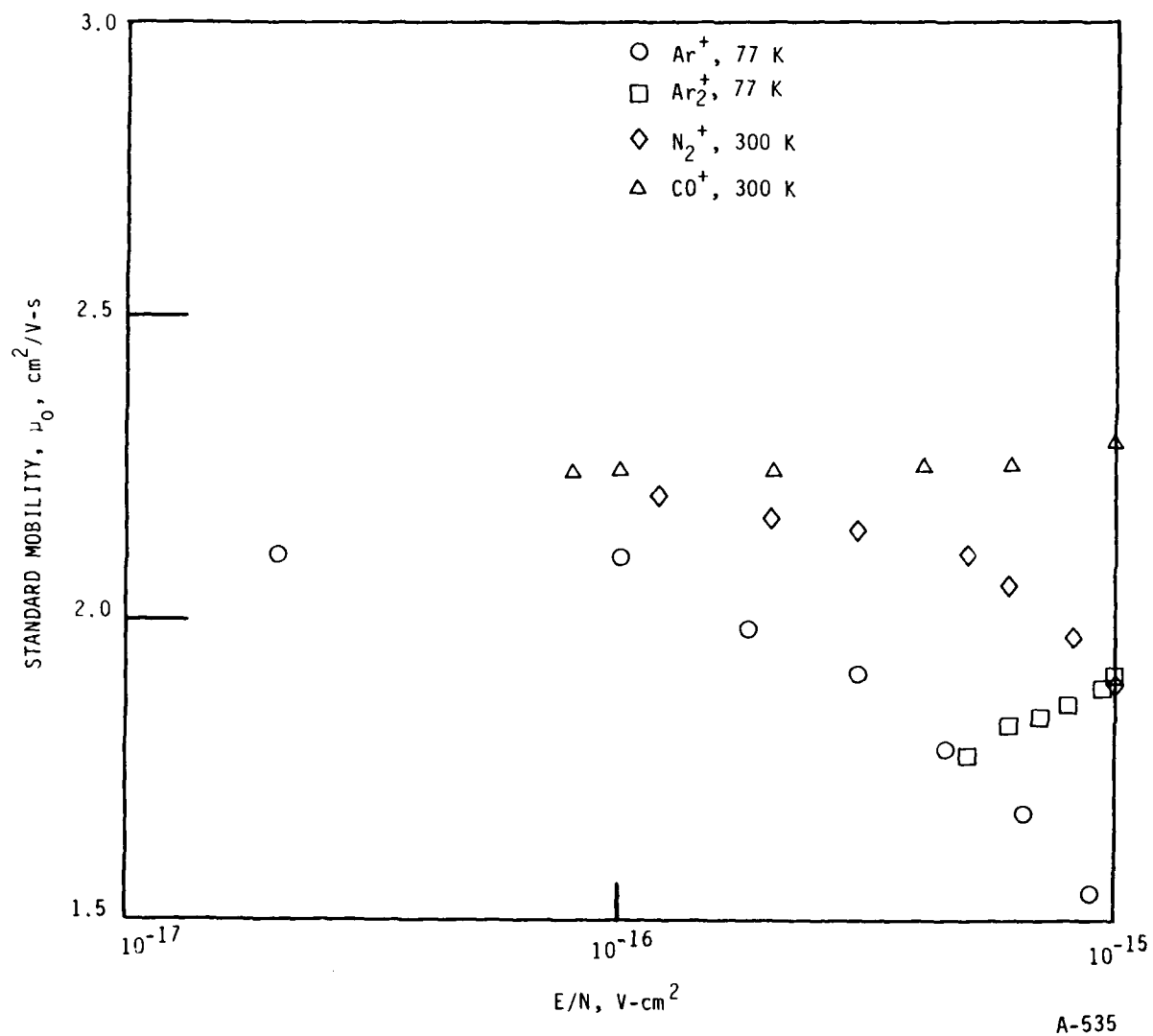
Figure 75.   Standard mobility versus density normalized field
strength for positive ions in argon. (Reference 6)

TABLE 7. SELECTED DISCHARGE PROPERTIES OF N_2/Ar (REFERENCE 7).

Gas	$E/N \times 10^{16}$ $V\text{-}cm^2$	α/N cm^2	$W \times 10^{-6}$ $cm\text{-}s^{-1}$	ε_k eV	Z/N cm^3/s
Ar	2	$3.\times10^{-20}$	1.7	~ 8	5.1×10^{-14}
	3	2.5×10^{-19}	2.5		6.3×10^{-13}
	4	6.8×10^{-19}	3.3		2.2×10^{-12}
	5	1.6×10^{-18}	4.0		6.4×10^{-12}
	7	4×10^{-18}	5.0	~ 8	2.0×10^{-11}
	10	9.5×10^{-18}	7.4		$7.\times10^{-11}$
	20	3.4×10^{-17}	14.		4.8×10^{-10}
N_2	8.5	1.8×10^{-20}	9.5	1.7	1.7×10^{-13}
	10	$7.\times10^{-20}$	10.5		7.4×10^{-13}
	15	$\sim 1.\times10^{-18}$	14.	~ 2.7	1.4×10^{-11}
	20	$5.\times10^{-18}$	19.5		9.8×10^{-11}

Equation (59) can be evaluated using the data in Table 7. Taking a generic value of μ_0 of 2 cm^2/V-s and a radius of 0.55 cm one can rewrite Eq. (4) as

$$Z/N \approx \frac{10^{21}}{N^2} \varepsilon_k \ (eV) \tag{63}$$

Evaluations of Eq. (63) for total number densities of 10^{16} and 10^{17} cm^{-3} are provided in Table 8. We note that nitrogen requires slightly higher E/N's than argon although the characteristic energies are considerably lower. These values of E/N are required to make detailed rate predictions as described in Section 7.2. Recall that E is the effective field rather than the real AC field.

As pointed out earlier, the high characteristic energies in Ar result from the Ramsauer minimum in the electron-collision cross-section which causes argon to be near transparent to low energy electrons. This cross section behavior provides for a very non-Maxwellian electron energy distributions in

argon microwave discharges. An example of a predicted electron energy distribution in argon at an E/N of 2×10^{-16} V-cm^2 is shown in Fig. 76. (The details of this prediction are discussed later.) The characteristic energy of this distribution is 7.6 eV. This prediction is contrasted in the figure with Maxwellian distributions at electron temperatures of 1.5 and 7.4 eV. We note that below $\sim$ 10 eV the Ar distribution is similar to that of the 7.5 eV Maxwellian and then falls off precipitously at higher energies. Interestingly enough the predicted Ar distribution crosses the 1.5 eV Maxwell distribution at $\sim$ 15.8 eV, the ionization potential for argon. The latter distribution would actually exhibit a _larger_ ionization rate.

We note that the power supplied by the field is just

$$P = N \, N_e \, e \, W \, E/W \, V \tag{64}$$

where V is the volume of the discharge. For argon the active discharge is estimated to have a length of 17.5 cm and radius of 0.55 cm for a volume of $\sim$ 17 cm^3, and provides a total power of 50 W. Thus, for perfect conversion efficiency

$$N_e = 1.8 \times 10 \leftarrow {}^{19}/(N \, E/N \, W) \tag{65}$$

For example for an N of 10^{17}, E/N = 3×10^{-16}, W = 2.9×10^6 cm/s we find,

$$N_e = 2.0 \times 10^{11} \ /cm^3 \tag{66}$$

TABLE 8. PREDICTED OPERATING CONDITIONS FOR COCHISE DISCHARGES.

Gas	N cm^{-3}	z/N cm^3/s	T_e eV	E/N$\times 10^{16}$ V-cm^2	E V/cm
Ar	10^{17}	$8. \times 10^{-13}$	8	3.2	32
	10^{16}	$8. \times 10^{-11}$	8	10	10
N$_2$	10^{17}	1.8×10^{-13}	1.8	9	90
	10^{16}	2.8×10^{-11}	2.8	16	16
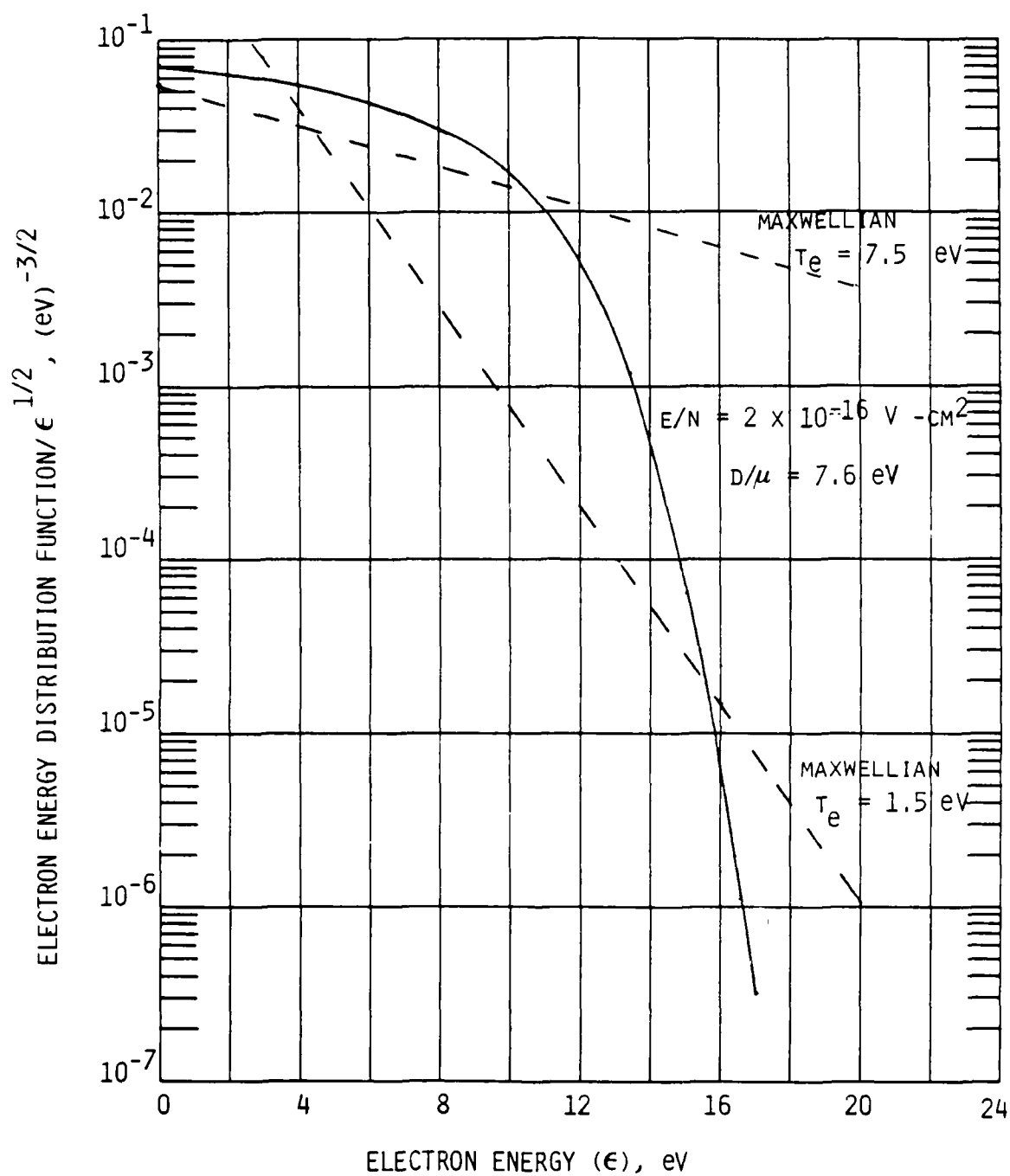
Figure 76. Predicted electron energy distribution in argon for
$E/N = 2 \times 10^{-16}$ V-cm^2 contrasted with Maxwellian
distribution.

This quantity is not well defined. In particular there are a number of losses in the system and it has been estimated that as little as one-third of the power may be delivered to the gas.

There are additional complications in deducing operating conditions for high power devices such as used in COCHISE. For instance, the diffusion analysis assumes that the field is homogeneous throughout the gas. This will only be true if the microwave frequency is much larger than the plasma frequency.

$$\omega_p^2 = \frac{4\pi N_e e^2}{m}$$

For $N_e = 2 \times 10^{11}$ cm^{-3}, $\omega_p = 2.5 \times 10^{10}$ s^{-1}, and is approximately the same as the microwave frequency. Thus the field cannot penetrate and both field and ionization rate will be peaked near the walls and decrease sharply towards the center. Ferreira and Loureiro[5] point out that there has been some analysis of such effects and it is found that the magnitude of the ionization rate in the center required to sustain the discharge is lower but still comparable to that for uniform ionization. Such an analysis is well beyond the scope of the present effort; however the expected trend suggests that Eqs. (64) to (66) may provide an upper bound on the electron density.

A more important point, which will be discussed in the next section, is the effect of stepwise ionizatin. Specifically the discharge properties reported in Reference 7 are for very low electron densities. As the electron density increases, secondary processes involving excited states created in the discharge, i.e.,

$$e + X^* \rightarrow X^+ + 2e \qquad (12)$$

can also lead to ionization and thus lower the required E/N to reach a required ionization rate.

7.2 The Prediction of Excitation Rate Constants in O_2/Ar Discharges

We present here predictions for excitation rates in O_2/Ar microwave discharges. These calculations not only incorporate the collective effects of ground state excitation of O_2 but also include excitation of discharge created species such as cross sections for O atom excitation, ozone dissociation, and ionization of argon metastable states.

We have used a computer model which solves the Boltzmann transport equation to evaluate the excitation rates characteristic of the O_2/Ar discharges used in the COCHISE ozone studies. Discharge predictions were performed for various O_2/Ar mixtures as a function of E/N (electric field per unit length normalized by total number density). The inputs to these calculations are the electron energy dependent cross sections for the inelastic processes occurring in the discharge while the outputs include discharge characteristics such as characteristic electron energy and drift velocity as well as excitation rate constants. The calculational techniques are straight-forward and well understood (see for example Reference 4).

The predictions are, of course, only as accurate as the cross sections employed. In the case of argon all the cross sections are well known with the exception of those for electronic excitation. We have characterized electronic excitation with two processes representing s state excitation with an energy loss of 11.6 eV and p state excitation with an energy loss of 13.1 eV. The respective recommended cross sections are tabulated in Table 9. Note that these are meant to be aggregate cross sections and include the effect of excitation to other states such as the [1]P levels. These latter states, although optically allowed, will be radiatively trapped, and will behave similarly to the metastables. These cross sections were used with the more standardly accepted cross sections for momentum transfer and ionization for Ar[4,8] to predict the transport properties of argon discharges.

The discharge properties of argon have been the subject of numerous measurements.[7] The transport properties are integral measurements of the

TABLE 9. ELECTRONIC EXCITATION CROSS SECTIONS FOR Ar.

Ar(3P-4S)		Ar(3P-4P)	
E,eV	$\sigma \times 10^{16}$, cm^2	E,eV	$\sigma \times 10^{16}$, cm^2
0	0	0	0
11.58	0		
12	0.017		
13	0.065	13.1	0
14	0.12	14	0.10
15	0.17	15	0.21
17.5	0.28	17.5	0.49
20	0.38	20	0.77
25	0.42	25	1.00
30	0.46	30	1.12
40	0.45	40	1.36
100	0.40	100	1.06

electron energy distribution. Therefore, a necessary, but not sufficient, criterion for the validation of any set of excitation cross sections is that they can be used to predict these properties successfully. A comparison between data and prediction is given in Table 10, where the data is representative of that presented in Reference 7. Comparisons are provided for drift velocity, characteristic energy and ionization coefficient. As can be seen, the comparison is reasonably good. The cross sections could have been fine-tuned to provide a better comparison but such an effort was not warranted for the needs of the present study.

For the case of O_2 the cross section data base discussed extensively by Phelps and coworkers[9-11] has been used. These cross sections provided reasonable agreement with O_2 discharge data and limited measurements of O_2 metastable state excitation rates.[9,10] The processes considered include momentum transfer, rotation and vibrational excitation, electronic excitation of several states, dissociation, dissociative attachment and ionization. Several of the key cross sections are tabulated in Table 11.

Several excitation processes involving O and O_3 have also been included in the analysis. These species have been treated as traces and thus do not affect the discharge electron energy distribution. Electron impact excitation

TABLE 10. TRANSPORT PROPERTIES IN Ar DISCHARGES.

$E/N \times 10^{16}$, V cm^2	$W \times 10^{-6}$, cm/s		ε_K, eV		$\alpha/N \times 10^{19}$, cm^2	
	Exp.	Theory	Exp.	Theory	Exp.	Theory
1.	~1.03	1.03	7.8	7.66	0.0	0
2.	1.83	2.0	7.8	7.75	0.35	0.17
3.	2.6	2.9	8.0	7.94	1.6	1.9
4.	~3.5	3.7	8.0	8.1	6.8	6.8
5.	~4.2	4.5	8.0	8.24	16	15

TABLE 11. SELECTED EXCITATION CROSS SECTIONS FOR O_2.

$O_2(^3\Sigma) \rightarrow O_2(^1\Delta)$		$O_2(^3\Sigma) - O_2(^1\Sigma)$		$O_2(^3\Sigma) \rightarrow 2O\ (^3P)$	
E, eV	$\sigma \times 10^{17}$, cm^2	E, eV	$\sigma \times 10^{17}$, cm^2	E, eV	$\sigma \times 10^{17}$, cm^2
0.0	0.0	0.0	0.0	0.0	0.0
0.977	0.0	1.627	0.0	6.0	0.0
1.5	0.058	2.0	0.026	7.0	1.5
2.0	0.153	3.0	0.097	7.8	2.3
3.0	0.380	3.5	0.133	9.0	2.3
3.5	0.490	4.0	0.149	10.0	2.1
4.0	0.570	5.0	0.182	12.0	1.65
5.0	0.740	5.69	0.194	15.0	1.05
5.62	0.825	6.54	0.194	17.0	0.65
5.91	0.862	7.34	0.191	20.0	0.475
6.19	0.888	8.41	0.183	45.0	0.19
6.53	0.908	9.26	0.174	100.0	0.0
6.99	0.914	10.0	0.160		
7.61	0.891	13.0	0.131		
7.89	0.863	14.9	0.117		
8.96	0.768	17.0	0.103		
10.04	0.679	19.4	0.092		
13.0	0.527	20.7	0.086		
15.1	0.455	22.5	0.080		
17.5	0.387	24.0	0.072		
20.5	0.324	28.0	0.061		
24.9	0.256	35.1	0.047		
30.9	0.196	41.9	0.034		
41.0	0.137	45.1	0.031		
45.0	0.120	100	0.0		
100.0	0.0				

of $O(^3P)$ to $O(^1D)$ and $O(^1S)$ has been specified by the cross sections recommended by Jackman et al.,[12] and dissociation of O_3 by the analysis of Keto.[13] The latter treatment is theoretical with no experimental validation. These cross sections are shown in Fig. 77.

Similarly, electron impact ionization of the Ar(4S, 4P) states have also been incorporated. These cross sections, shown in Fig. 78, have been taken from the theoretical treatment in Reference 14. The cross sections for Ar(4S) have been validated experimentally. Ar metastables were only treated as a trace in the calculations. Note however that this stepwise ionization process can change the discharge operating conditions if the Ar metastable state concentration becomes sufficiently large.

These cross-sections have been used to calculate discharge properties and excitation/de-excitation rate constants of various O_2/Ar mixtures as a function of E/N. Such predictions are shown in Figs. 79 to 86. The excitation rate constants for Ar metastables are displayed in Fig. 79. They can be seen to fall off at higher O_2 mole fractions where the lower energy O_2 excitation processes dominate the electron energy distribution functions. There appears to be only one measurement of metastable excitation rates in argon discharges[15] and these values fall approximately a factor of two below those shown in Fig. 79 at low O_2. We have decided not to adjust the cross sections given the uncertainty in the measured rate constants. Predicted argon metastable electron impact ionization and de-excitation (i.e., superelastic collisions) rates are shown in Fig. 80. Note that these rate constants are quite large, reflecting the high characteristic energies of the discharge, and these processes can ultimately limit the concentration of argon metastables in the discharge. Similar predictions for the O_2 metastables $a^1\Delta$, $b^1\Sigma$ and $c^1\Sigma$ are shown in Fig. 81. These states are found to have significant excitation rates over the full range of discharge parameters. Tne rate constants for electron impact dissociation of O_2 are shown in Fig. 82. Two processes are shown: (1) the excitation of continuum states leading to $2O(^3P)$ atoms; and (b) excitation of the $B^3\Sigma$ state which we have assumed leads to formation of $O(^1D) + O(^3P)$ with unit efficiency in the discharge. Similar predictions for the O_2 metastables $a^1\Delta$, $b^1\Sigma$ and $c^1\Sigma$ are shown in Fig. 81. These states are
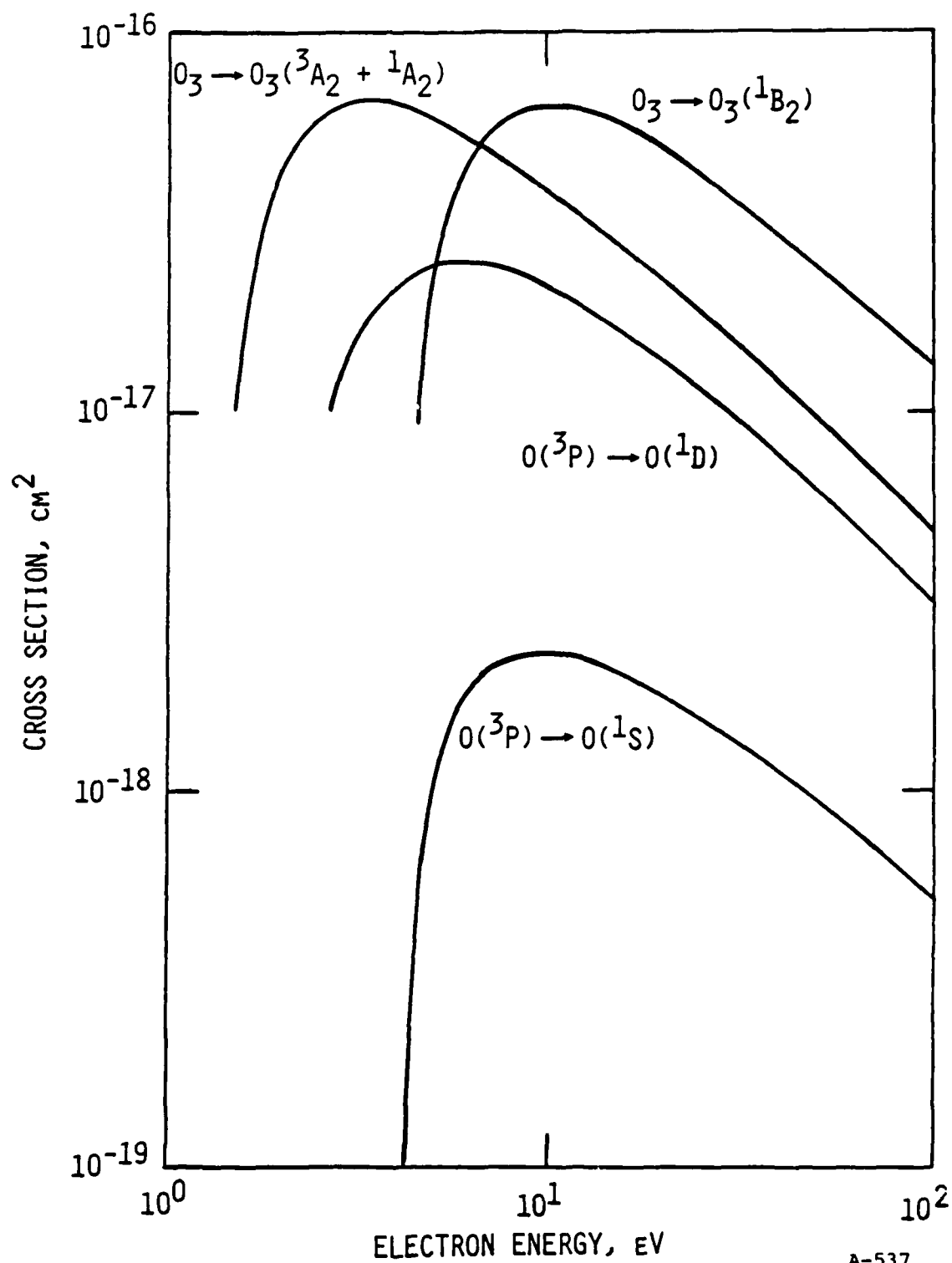
Figure 77. Electron impact excitation cross sections. The excited states of O_3 are dissociative.

7-14
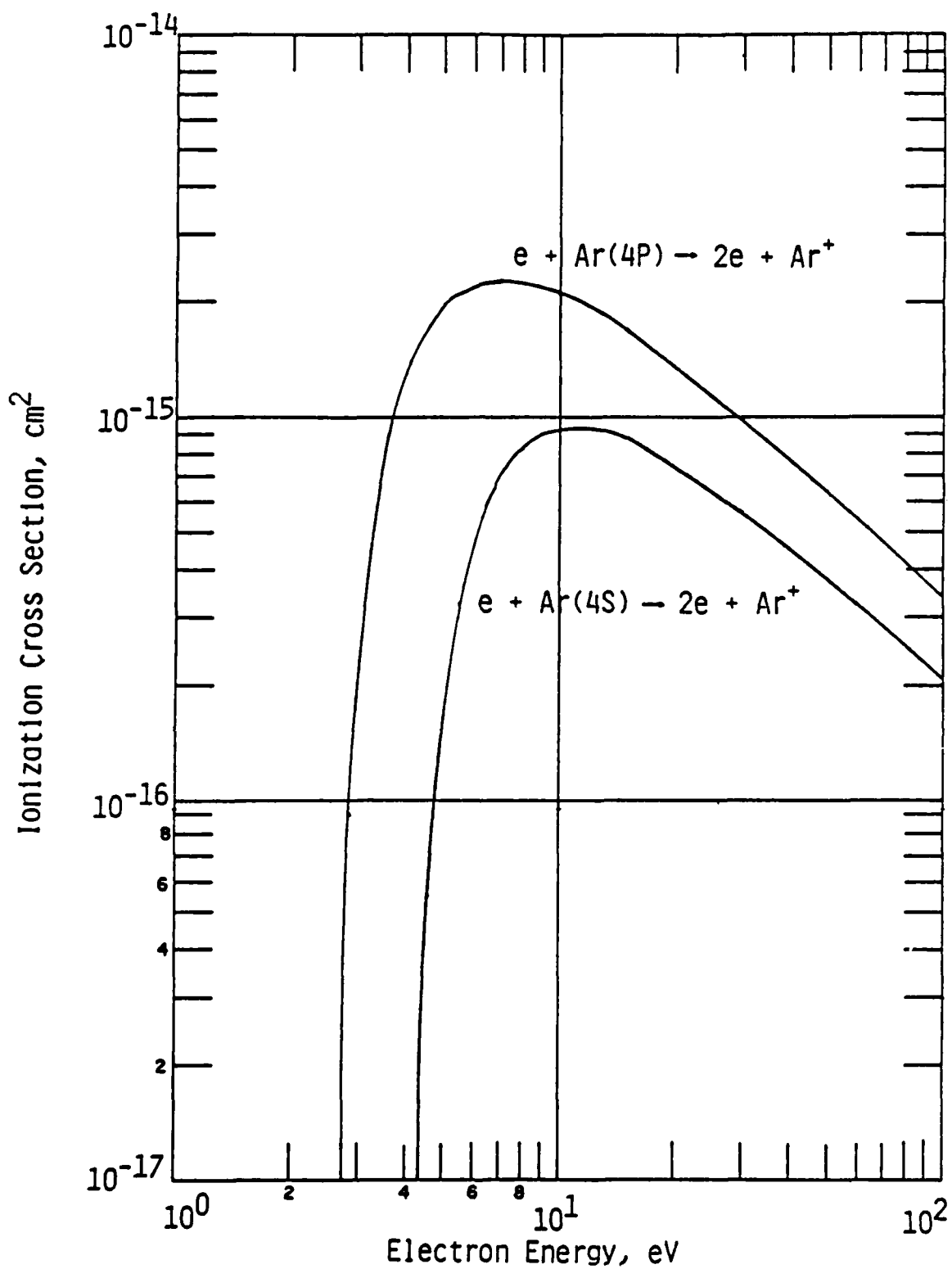
Figure 78. Electron impact ionization cross sections for Argon metastable states.
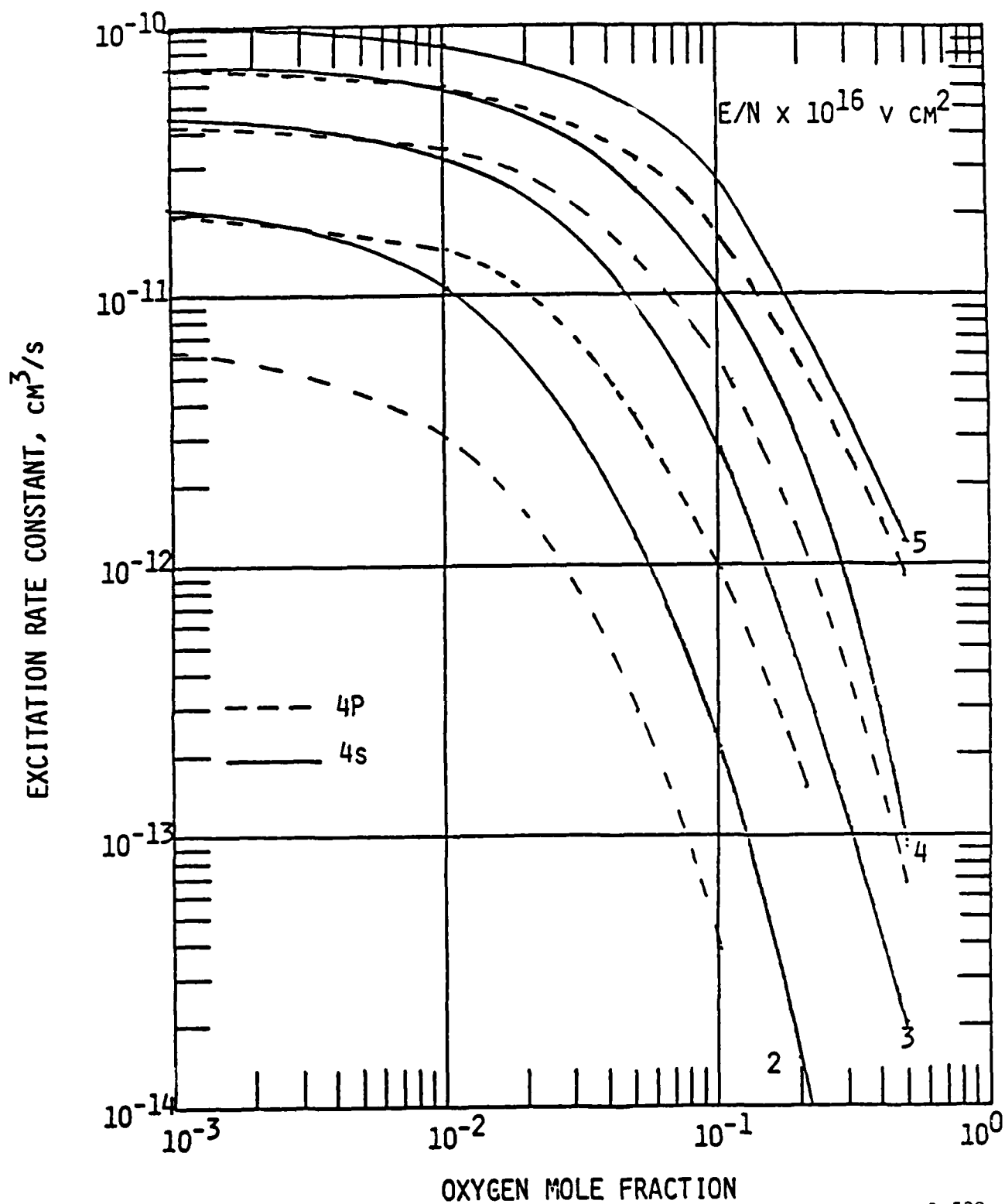
Figure 79. Argon electronic state excitation rate constants for
microwave excited O_2/Ar mixtures.

A-539
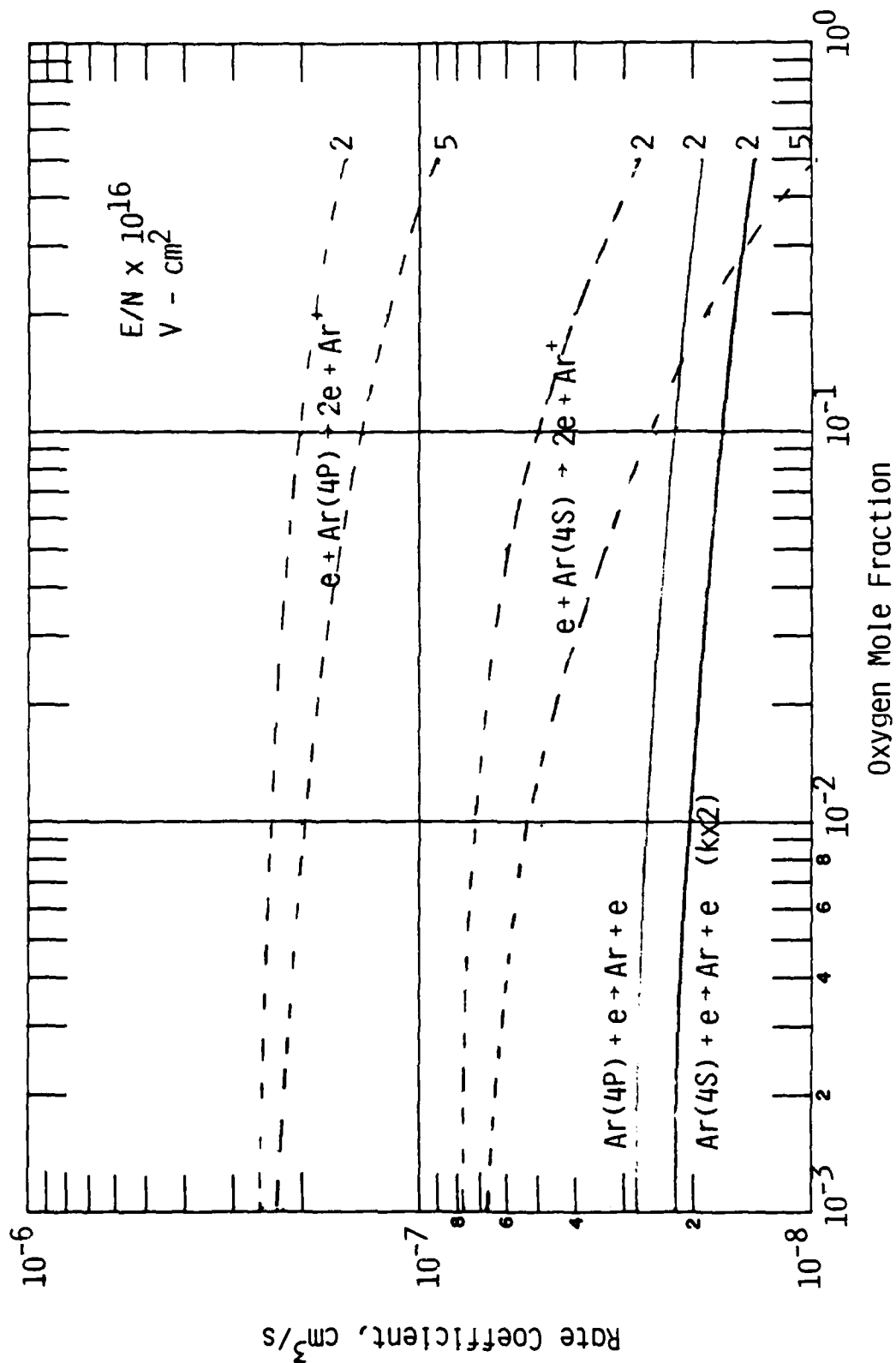
Figure 80. Argon metastable state ionization and de-excitation rate constants in microwave excited Ar/O_2 mixtures.

A-553
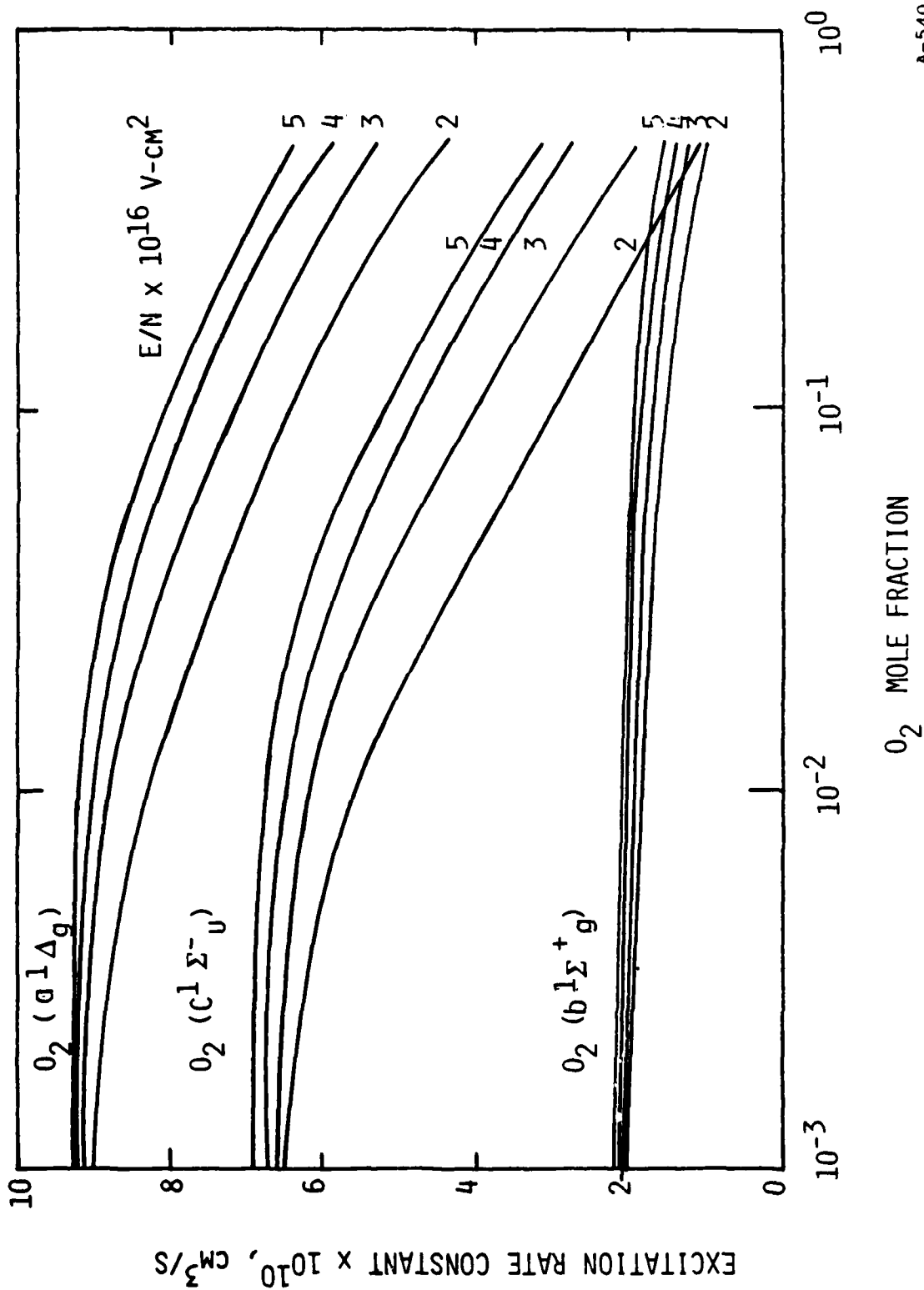
Figure 81. Rate constants for electron impact excitation of ground O_2 to several metastable states for microwave excited O_2/Ar mixtures.

A-540
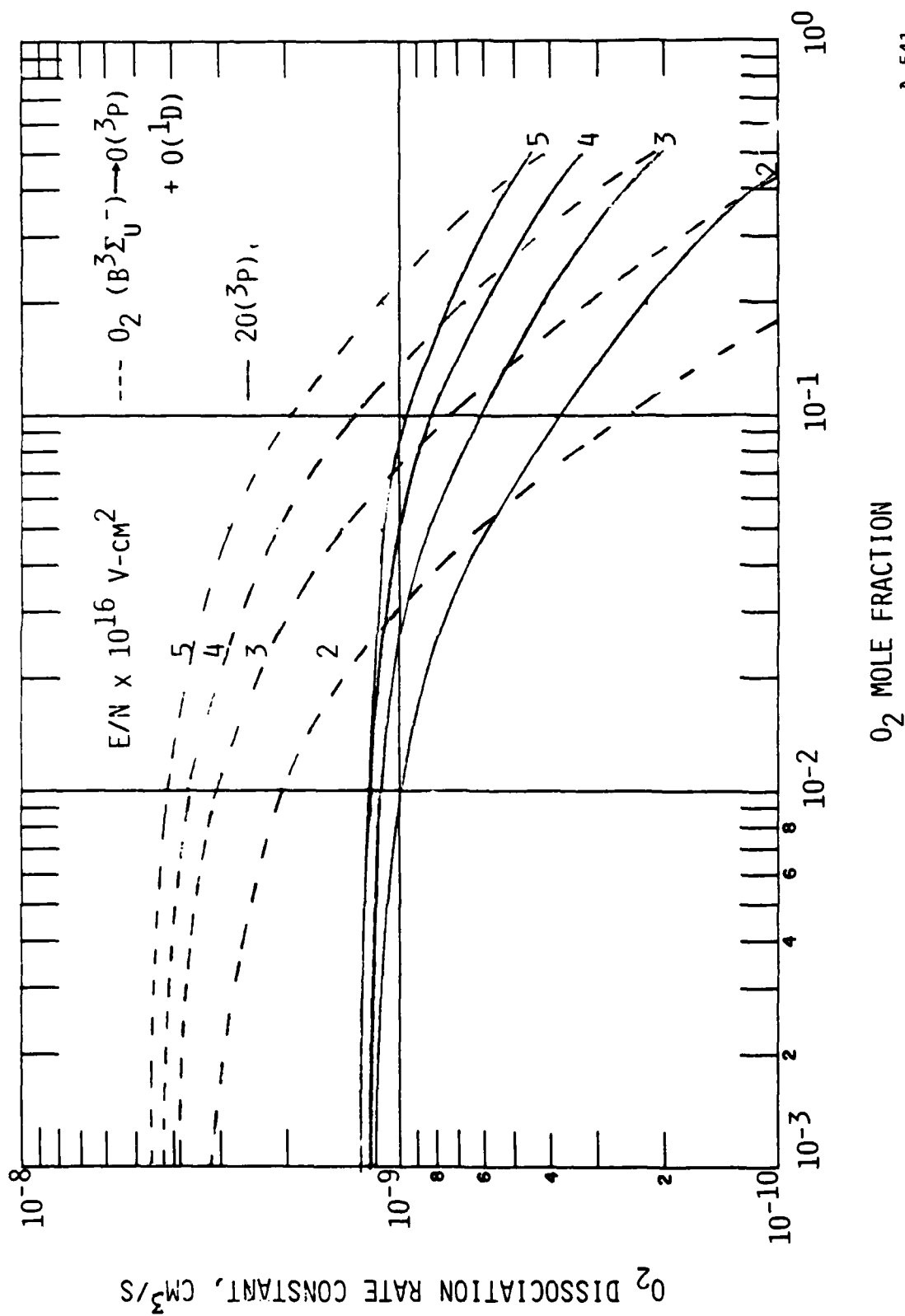
Figure 82. Predicted rate constants for O_2 dissociation in microwave excited O_2/Ar discharges.

A-541
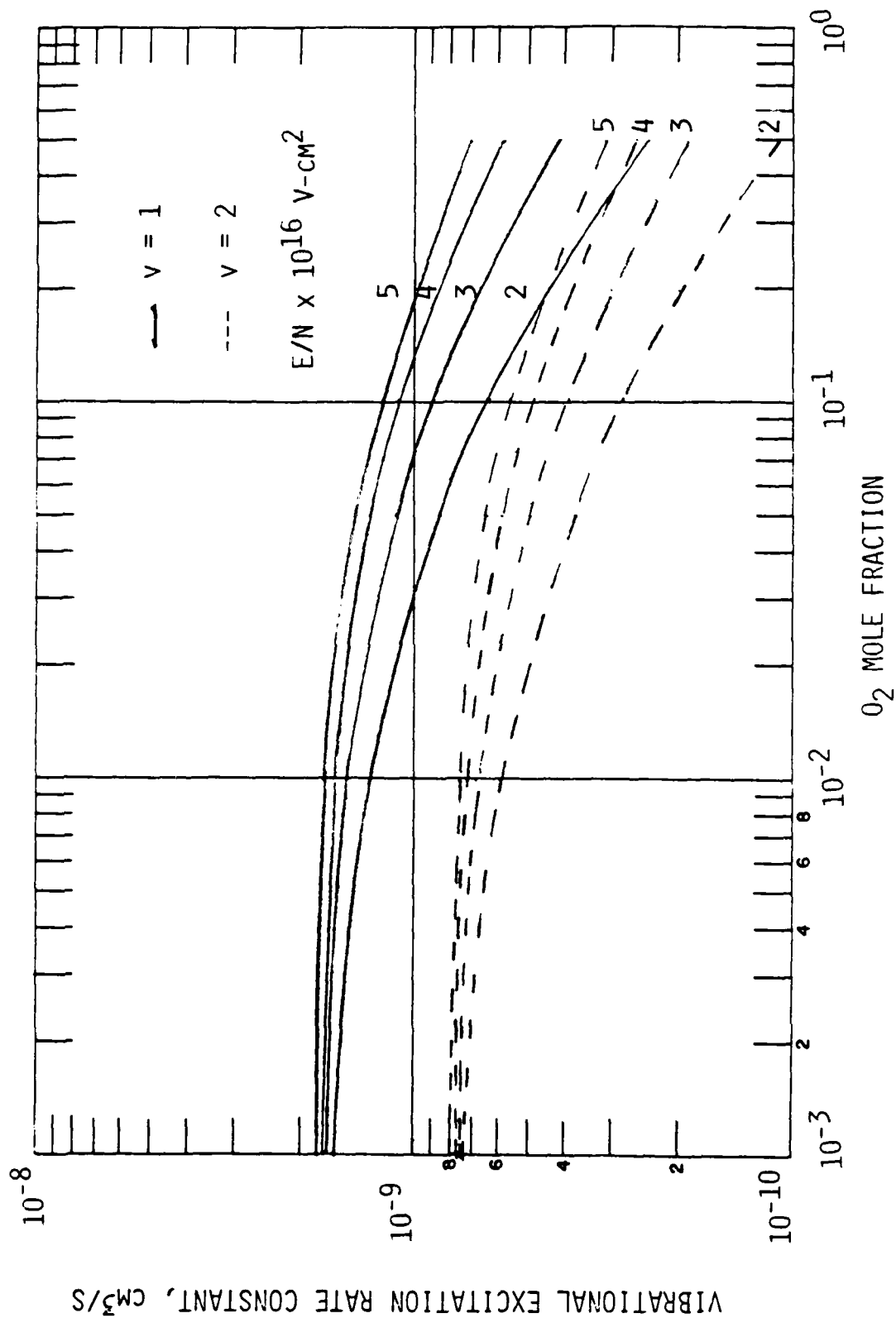
Figure 83. Predicted rate constants for direct excitation of vibrational levels v = 1 and 2 of O_2 in microwave excited mixtures of O_2/Ar.

A-542
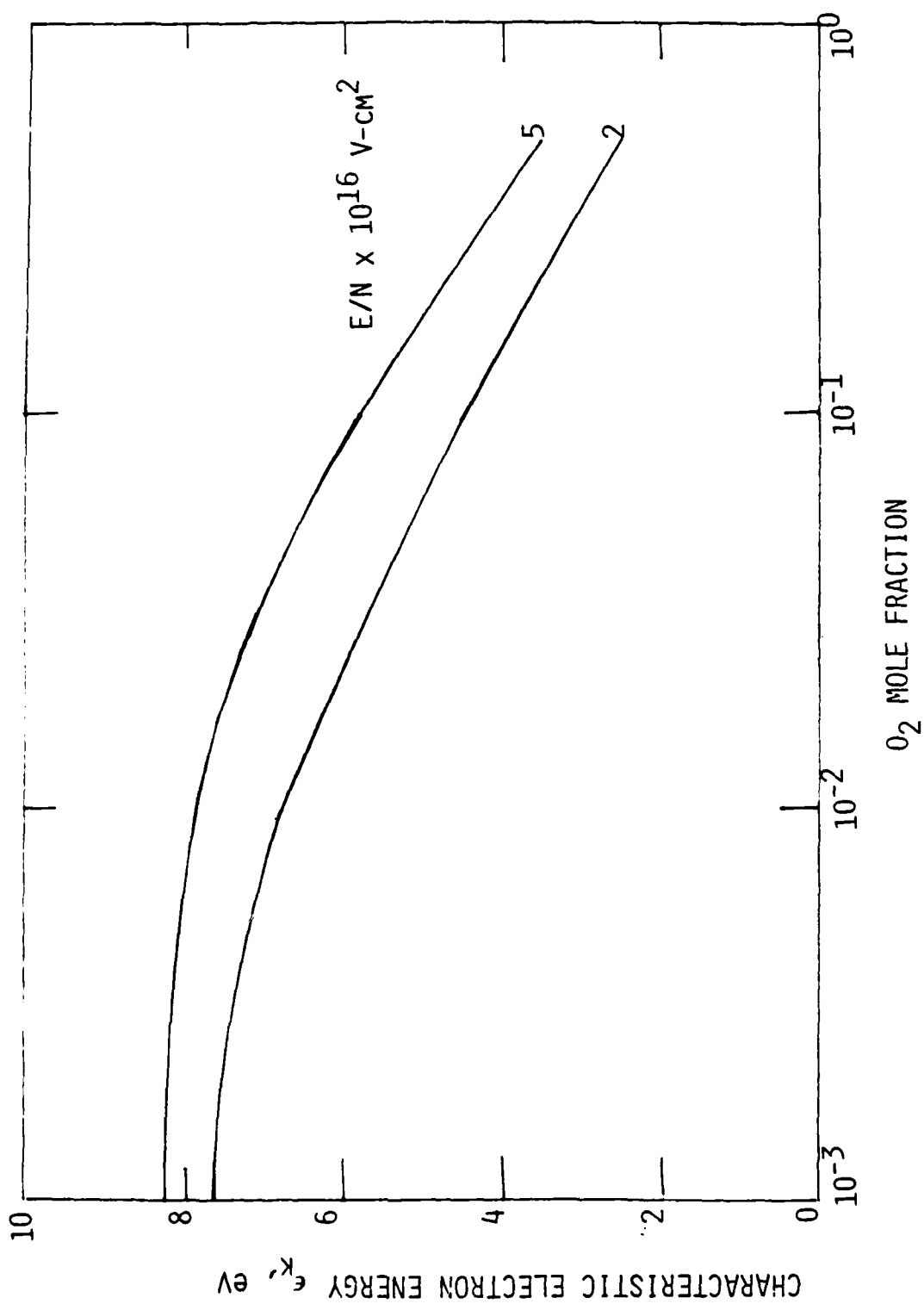
Figure 84. Predicted characteristic energies in microwave excited
mixtures of O_2/Ar.

A-545
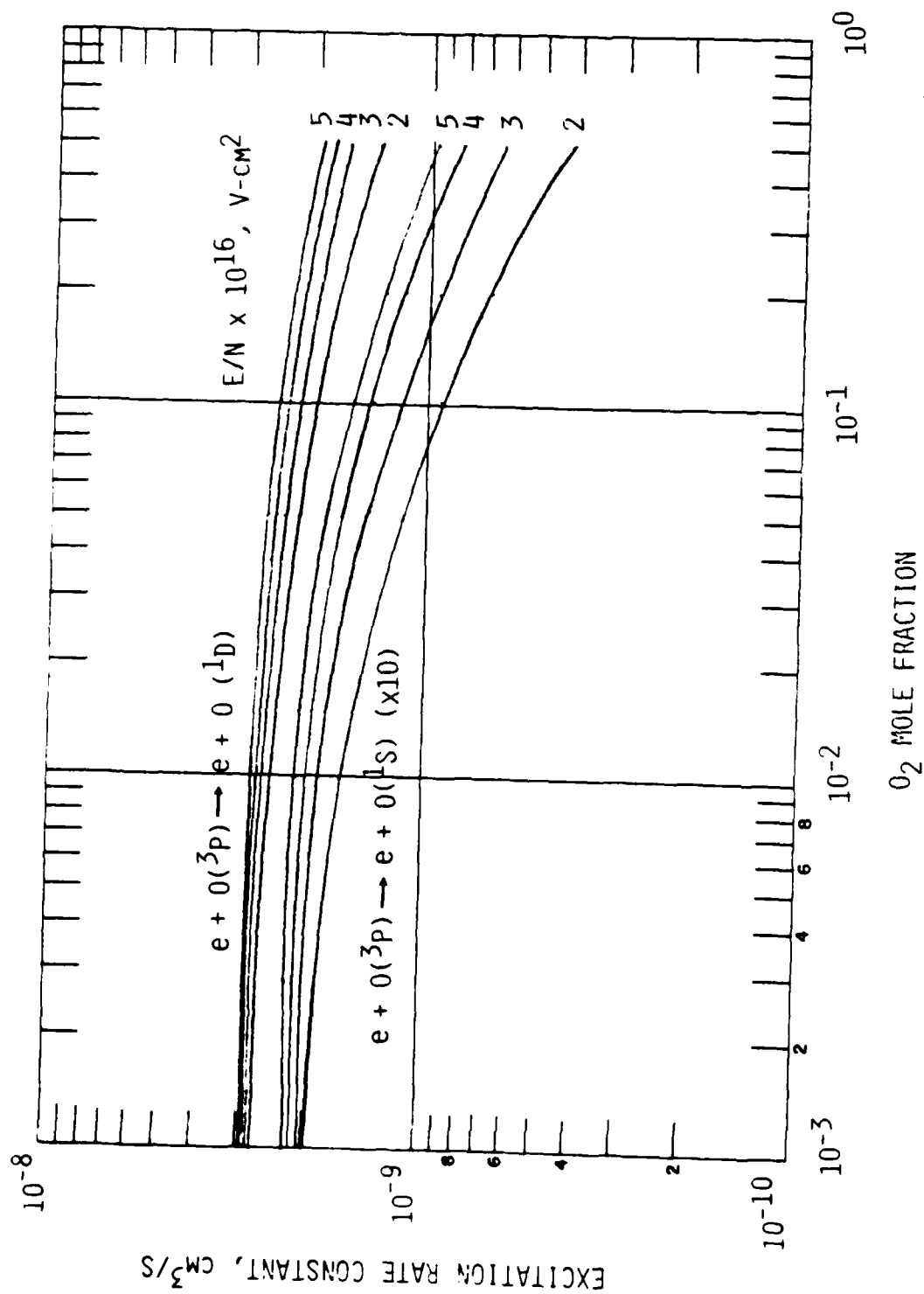
Figure 85. Predicted rate constants for electron impact excitation of $O(^3P)$ to $O(^1D)$, $O(^1S)$ in microwave excited O_2/Ar mixture.

A-543
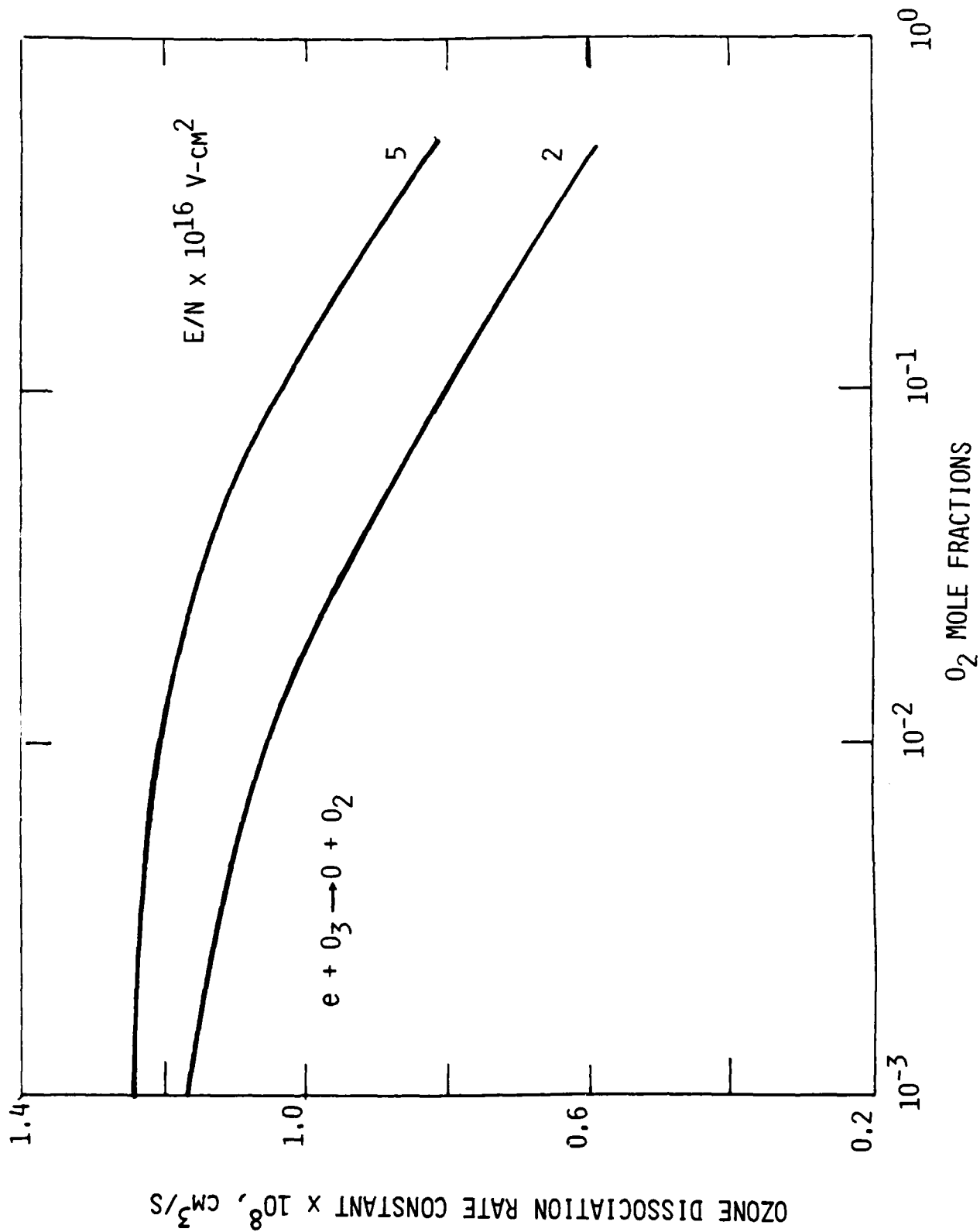
Figure 86. Predicted rate constant for electron impact dissociation of O_3 in microwave excited O_2/Ar mixtures.

A-544

found to have significant excitation rates over the full range of discharge parameters. The rate constants for electron impact dissociation of O_2 are shown in Fig. 82. Two processes are shown: (1) the excitation of continuum states leading to $2O(^3P)$ atoms; and (b) excitation of the $B^3\Sigma$ state which we have assumed leads to formation of $O(^1D) + O(^3P)$ with unit efficiency. Once again both processes exhibit high rate constants.

Rate constants for excitation of the $v = 1$ and $v = 2$ vibrational levels or O_2 are shown in Fig. 83. Only results for the direct excitation process (4.5 eV) are shown. The rate constants for the lower energy resonant states could not be calculated accurately because of the coarseness of the energy mesh used in the calculations (0.2 eV). Given the large characteristic energies of the electron distribution (See Fig. 84) it is anticipated that resonant excitation will be less important than direct excitation.

The predicted rate constants for electron impact excitation of $O(^3P)$ to $O(^1D)$ and $O(^1S)$ and for electron impact dissociation of O_3 are shown in Figs. 85 and 86, respectively. The rate constant for excitation of $O(^1D)$ is an order of magnitude larger than that for $O(^1S)$ as would be expected from the cross sections shown in Fig. 77. Dissociation of O_3 is very effective, reflecting its weak bond strength and the availability of low-lying dissociative states.

Superelastic de-excitation rate coefficients have also been calculated for the electronic states of O and O_2 considered. In general, these are large for states with low (~ 1 eV) excitation energies, i.e., vibration, $O_2(^1\Delta,^1\Sigma)$ and $O(^1D)$. In this instance, the excitation and de-excitation rate constants are of the same order of magnitude, reflecting the high characteristic electron energy in the discharge. For high lying electronic states, the de-excitation rates can be several orders of magnitude larger than the excitation rates.

It must be noted that these predictions should not be considered to be exact. Indeed, at these high characteristic energies the adequacy of the first order expansion of the transport equation is in question. Furthermore, superelastic collisions have not been accounted for and it has been assumed

that the O and O_3 concentrations are traces relative to those for O_2. If the latter assumption is valid, and given the accuracy of the cross sections, we expect the rate constants to be accurate to within a factor of two. Furthermore, at very high excitation levels additional processes should be considered, for example electron impact dissociation of the metastable states of O_2.

7.3   The Kinetic Scheme

It now remains to develop a full kinetic scheme for the prediction of product species formation within the discharge. A number of species are created directly through mediation of the discharge electrons and these in turn can interact with each other, the base species, or the discharge electrons. Reactive species deactivation/recombination can also occur via interaction with the discharge tube walls.

We have developed a reaction scheme which couples the species Ar, Ar*, Ar^+, Ar_2^+, O_2, $O_2(^1\Delta)$, $O_2(^1\Sigma)$, O_2^+, $O(^3P)$, $O(^1D)$, $O(^1S)$ and O_3. The species Ar* encompasses both the (4S) and (4P) manifold. Although the 4P states exhibit optically allowed transitions to the ground state, the strong self absorption by $Ar(^3P)$ effectively traps the radiation and thus the 4P states behave similarly to the 4S metastable states.

The literature has been reviewed to define both appropriate reaction mechanisms and rate constants. The resulting kinetic package, with the exception of the electron impact excitation reactions discussed in Section 7.2, is tabulated in Table 80. Kinetic information is available on most reactions of interest although some reaction branching ratio evaluations are lacking. We have purposely excluded high lying states of O_2 and vibrational kinetics from the reaction scheme. These could be incorporated at a later date as required. Furthermore, for the most part, excited-state plus excited-state reactions have been excluded. At high excitation levels additional reactions, such as

argon metastable interactions with oxygen metastables, might become important.

We are also concerned with diffusion losses in the narrow discharge tubes. If wall deactivation occurs on every collision the diffusive loss is given by the boundary layer relation

$$k_w = 0.62 \ D/(R/2.4)^2 \tag{13}$$

where R is the tube radius of 0.55 cm and D is the species diffusion coefficients. This may be rewritten as

$$k_w = 11 \ D, \ s \tag{14}$$

where D is in units of cm^2/s and evaluated at the conditions of interest. If the species has a low wall de-activation effeciency, the wall loss may be written as

$$k_w = \frac{\gamma \bar{c}}{2R} \tag{15}$$

where γ is the deactivation effiency and $\bar{c}$ is the mean molecular speed.

We have performed a quick review of available measurements of the diffusion coefficients of the species of interest and the results are given in Table 12. For example from Eq. (14) characteristic diffusive loss rates for 1 Torr and 100K would be $\sim 300 \ s^{-1}$. This value is close to Eq. (15) evaluated at $\gamma = 0.01$. Most of these species are not readily deactivated at the walls and we have chosen to model them using relationship (15) and a γ of 0.01. This will not have a large impact inasmuch as typical wall loss times will be > 10 ms, slightly larger than characteristic flow times.

The information assembled above is sufficient to provide kinetic predictions for COCHISE excitation as required.

7-26

TABLE 12. O_2/Ar DISCHARGE REACTION LIST.

	REACTION	RATE CONSTANT cm^3/s OR cm^6/s	COMMENTS	REFERENCE
1.	$Ar^+ + O_2 \rightarrow Ar + O_2^+$	5.2×10^{-11}		16
2.	$Ar^+ + 2Ar \rightarrow Ar_2^+ + Ar$	$2 \times 10^{-31}(300/T)^2$	T dep. not measured	17,18
3.	$Ar_2^+ + O_2 \rightarrow O_2^+ + 2Ar$	1.2×10^{-10}		19
4.	$Ar_2^+ + O_3 \rightarrow$	5×10^{-9}	Products Unknown	20
5.	$O_2^+ + e \quad \overset{0.11}{\rightarrow} \quad O(^3P) + O(^1S)$ $\overset{0.89}{\rightarrow} \quad O(^3P) + O(^1D)$	$1.95 \times 10^{-7}\left(\frac{300}{Te}\right)^{0.7}$	Branching ratio uncertain (See Ref. 22,23	21-23
6.	$Ar_2^+ + e \rightarrow Ar^* + Ar$	$9.1 \times 10^{-7}\left(\frac{Te}{300}\right)^{-1.9}$	Approximate as one excited product	24
7.	$O(^3P) + O(^3P) + M \rightarrow O_2 + M$	$5.2 \times 10^{-35}e^{900/T}$	$M = O_2, Ar, O$ $dO/dt = -2kO^2M$	25
8.	$O(^3P) + O_2 + Ar \rightarrow O_3 + Ar$	$3.9 \times 10^{-34}(T/300)^{-1.9}$	T > 220 K (See also 41)	26
9.	$O(^3P) + O_2 + O_2 \rightarrow O_3 + O_2$	$6.9 \times 10^{-34}(T/300)^{-1.25}$	T > 200 K (See also 32)	26
10.	$O_3 + O(^3P) \rightarrow 2 O_2$	$1.8 \times 10^{-11}e^{-2300/T}$		26
11.	$O_2(^1\Delta) + O_2 \rightarrow 2 O_2$	$1.9 \times 10^{-18}(T/300)^{0.78}$	Average Ref. 10,26	10,26
12.	$O_2(^1\Delta) + Ar \rightarrow O_2 + Ar$	1×10^{-20}	Average	10
13.	$O_2(^1\Delta) + O_3 \rightarrow O(^3P) + 2 O_2$	$5.2 \times 10^{-11}e^{-2840/T}$	T = 280 - 360	26

TABLE 12. O_2/Ar DISCHARGE REACTION LIST (CONTINUED).

	REACTION	RATE CONSTANT cm^3/s OR cm^6/s	COMMENTS	REFERENCE
14.	$O_2(^1\Delta) + O(^3P) \rightarrow O_2 + O(^3P)$		Upper Bound	27
15.	$O_2(^1\Delta) + O_2(^1\Delta) \rightarrow O_2(^1\Sigma) + O_2$	$7 \times 10^{-28} T^{3.8} e^{700/T}$		28
16.	$O_2(^1\Sigma) + O_2 \rightarrow O_2 + O_2$	4.0×10^{-17}	T = 300 K only	26
17.	$O_2 (^1\Sigma) + Ar \rightarrow O_2 + Ar$		probably small	--
18.	$O_2(^1\Sigma) + O_3 \xrightarrow{0.7} O(^3P) + 2\ O_2$ $\xrightarrow{0.3} O_2(^1\Delta) + O_3$ $\rightarrow O_2 + O_3$	2.2×10^{-11}	T = 300 K	26
19.	$O_2(^1\Sigma) + O(^3P) \rightarrow O_2 + O(^3P)$	8×10^{-14}	Cannot distinguish last two products	29
20.	$O(^1D) + O_2 \xrightarrow{0.8} O(^3P) + O_2\ (^1\Sigma)$ $\xrightarrow{0.2} O(^3P) + O_2$	$3.2 \times 10^{-11}\ e^{67/T}$		26
21.	$O(^1D) + Ar \rightarrow O(^3P + Ar$	5.0×10^{-13}	T = 110-330 K	30
22.	$O(^1D) + O_3 \xrightarrow{0.5} 2O(^3P) + O_2$ $\xrightarrow{0.5} 2\ O_2$	2.4×10^{-10}	T = 100-400 K	26
23.	$O(^1D) + O(^3P) \rightarrow 2O(^3P)$	7.5×10^{-11}	Estimate Only	22
24.	$O(^1S) + O_2 \xrightarrow{0.31} O(^1D) + O_2$ $\xrightarrow{0.69} O(^3P) + O_2$	$4.8 \times 10^{-12} e^{-850/T}$	Branching ratio Ref.33 T=200-450, Ref. 31	31-33

TABLE 12. O₂/Ar DISCHARGE REACTION LIST (CONTINUED).

REACTION	RATE CONSTANT cm^3/s OR cm^6/s	COMMENTS	REFERENCE
25. $O(^1S) + Ar \rightarrow O(^3P) + Ar$	4.8×10^{-18}	$O(^1D)$ Product?	32
26. $O(^1S) + O_3 \rightarrow 2\ O_2$ $\rightarrow O(^3P) + O(^3P, {}^1D) + O_2$ $\rightarrow O(^3P) + O_3$	5.8×10^{-10}	Product Unknown Reaction likely	34
27. $O(^1S) + O(^3P) \rightarrow O(^1D) + O(^1D)$ $\rightarrow O(^1D) + O(^3P)$ $\rightarrow 2\ O(^3P)$	2×10^{-14}	See 37 Earlier Refs wrong. Theory only activation energy expected. Upper branch preferred.	32, 35, 37
28. $O(^1S) + O_2(^1\Delta) \xrightarrow{0.17} O(^1D) + O_2\ (^1\Sigma)$ $\xrightarrow{0.19} 3\ O(^3P)$ $\xrightarrow{0.64} O(^3P) + O_2^*$	1.7×10^{-10}	O_2^* a triplet	36,37
29. $Ar^* + O_2 \xrightarrow{0.02} O(^3P) + O(^1S) + Ar$ $\xrightarrow{0.52} O(^3P) + O(^1D) + Ar$ $\xrightarrow{0.46} O(^3P) + O(^3P) + Ar$	2.1×10^{-10}		38,39
30. $Ar^* + O(^3P) \rightarrow Ar + O(^3P)$	8×10^{-11}		
31. $Ar^* + O_3 \rightarrow$		No information probably fast	40

TABLE 13. DIFFUSION COEFFICIENTS OF DISCHARGE SPECIES.

SPECIES	CARRIER	$D/N(T=300 \text{ K})^*$ $cm^{-1}s^{-1}$	REF.
O	Ar	7.5×10^{18}	42
O	O_2	8.1×10^{18}	42
$O(^1S)$	Ar	8.6×10^{18}	43
$O_2(^1\Delta)$	Ar	2.8×10^{18}	10
$O_2(^1\Delta)$	O_2	4.9×10^{18}	44
$O_2(^1\Sigma)$	O_2	5×10^{18}	9
Ar*	Ar	1.8×10^{18}	45

* Scales As $T^{1/2}$

7.4 References

1. Cobine, J.D., "Gaseous Conductors," Dover Publications, New York (1958) pp. 205-289.

2. Kaufman, F., "The Production of Atoms and Simple Radicals in Glow Discharges," in Advances in Chemistry Series #80, "(Chemical Reactions in Electric Discharges"), American Chemical Society (1969) pp. 29-47.

3. Brown, S.C., "Breakdown in Cases: Alternating and High Frequency Fields," in Encyclopedia of Physics, Vol. XXII Gas Discharges II, ed. S. Flugge, Springer-Verlag, Berlin (1956), pp. 531-575.

4. Frost, L.S. and Phelps, A.V., "Momentum-Transfer Cross Sections for Slow Electrons in He, Ar, Kr, and Xe from Transport Coefficients," Phys. Rev. 136A, 1538 (1969).

5. Ferreira, C.M. and Loureiro, J., "Characteristics of High-Frequency and Direct Current Argon Discharges at Low Pressures; a Comparative Analysis, J. Phys. D. 17, 1175 (1984).

6. Ellis, H.W., Thackston, M.G., McDaniel, E.W. and Mason, E.A., Atom - Data and Nucl. Data Tables 31, 113-151 (1984).

7. Dutton, J., "A Survey of Electron Swarm Data," J. Phys. Chem. Ref. Data 4, 577 (1975).

8. Kieffer, L.J., "A Compilation of Electron Collision Cross Section Data for Modeling Gas Discahrge Lasers," JILA Information Center Report 13, Sept. 30, 1973.

9. Lawton, S.A. and Phelps, A.V., "Excitation of the $b^1\Sigma_g^+$ State of O_2 by Low Energy Electrons," J. Chem. Phys. 29, 1055 (1978).

10. Tachibana, K. and Phelps, A.V., "Excitation of the O_2 ($a^1\Delta_g$) State by Low Energy Electrons," J. Chem. Phys. 75, 3315 (1981).

11. Phelps, A.V., private communication, 1982.

12. Jackman, C.H., Garvey, R.H. and Green, A.E.S., "Electron Impact on Atmospheric Gases I. Updated Cross Sections," J. Geophys. Res. 82, 5081 (1977).

13. Keto, J.W., "Electron Beam Excited Mixtures of O_2 in Argon, II, Electron Disbributions and Excitation Rates," J. Chem. Phys. 74, 4445 (1981).

14. Bretagne, J., Godart, J. and Puech, V., "Low-Energy Electron Distribution in an Electron-Beam-Generated Argon Plasma," J. Phys. D 15, 2205 (1982).

15. Bozin, J.V., Urosevic, V.V. and Petroniz, Z.Lj., "Experimental Investigation of Excitation of Argon Metastables by an Electron Swarm in Argon Nitrogen Gas Mixtures," J. Phys. A: Atoms & Nuclei 312, 349 (1983).

16. Adams, N.G. and Smith, D., "The Selected Ion Flow Tube (SIFT); A Technique for Studying Ion-Neutral Reactions," Int. J. Mass Spectrom. Ion Phys. 21, 349 (1976).

17. Good, A., "Third-Order Ion-Molecule Clustering Reactions," Chem. Rev. 75, 561 (1975).

18. Meot-ner (Mautner), M., "Temperature and Pressure Effects in the Kinetics of Ion-Molecule Reactions," Chapter 6 in Gas Phase Ion Chemistry, Vol. I Academic Press, New York (1979).

19. Bohme, D.K., Adams, N.G., Moseman, M., Dunkin, D.B. and Ferguson, E.E., "Flowing Afterglow studies of the Reactions of the Rare Gas Molecular ions He_2^+, Ne_2^+ and Ar_2^+ with Molecules and Rare-Gas Atoms," J. Chem. Phys. 52, 5094 (1970).

20. Keto, J.W., Hartz, C.F. and Kuo, C.Y., "Electron Beam Excited Mixtures of O_2 in Argon. III. Energy Transfer to O_2 and O_3," J. Chem. Phys. 74, 4450 (1981).

21. Alge, E., Adams, N.G. and Smith, D., "Measurements of the Dissociative Recombination Coefficients of O_2^+, NO^+, NH_4^+ in the Temperature Range 200-600 K," J. Phys. B.: At. Mol. Phys. 16, 1433 (1983).

22. Keto, J.W., Hart, C.F. and Kuo, C.Y., "Electron Beam Excited Mixtures of O_2 in Argon. I. Spectroscopy," J. Chem. Phys. 74, 4433 (1981).

23. Link, R., McConnell, J.C. and Sheperd, G.G., "A Self-Consistent Evaluation of the Rate Constants for the Production of the OI 6300 Å Airglow," Planet. Space Sci. 29, 589 (1981).

24. Shiu, Y.J. and Biondi, M.A., "Dissociative Recombination in Argon: Dependence of the Total Rate Coefficient and Excited State Production on Electron Temperature," Phys. Rev. A 17, 868 (1978).

25. Baulch, D.L., Drysdale, D.D., Duxbury, J. and Grant, S.J., "Evaluated Kinetic Data for High Temperature Reactions: Volume 3," Butterworths, London-Boston (1976).

26. Baulch, D.L., Cox, R.A., Crutzen, P.J., Hampson, Jr., R.F., Kerr, J.A., Troe, J. and Watson, R.T., "Evaluated Kinetic and Photochemical Data for Atmospheric Chemistry: Supplement I. CODATA Task Group on Chemical Kinetics," J. Phys. Chem. Ref. Data 11, 327 (1982).

27. Clark, I.D. and Wayne, R.P., "The Reaction of O_2 $(a^1\Delta g)$ with Atomic Nitrogen and with Atomic Oxygen," Chem. Phys. Lett. $\underline{3}$, 405.

28. Cohen, N. and Westberg, K.R., "Chemical Kinetic Data Sheets for High Temperature Chemical Reactions," J. Phys. Chem. Ref. Data $\underline{12}$, 531 (1983).

29. Slanger, T.G. and Black, G., "Interactions of $O_2(b^1\Sigma_g^+)$ with $O(^3P)$ and O_3," J. Chem. Phys. $\underline{70}$, 3434 (1979).

30. Davidson, J.A., Schiff, H.I., Brown, T.J., Streit, G.E. and Howard, C.J., "Rate Constants for the Deactivation of $O(^1D)$ by Xe, Kr and Ar over the Range 110-330 K," J. Chem. Phys. $\underline{69}$ 1213 (1978).

31. Atkinson, R. and Welge, K.H., "Temperature Dependence of $O(^1S)$ Deactivation by CO_2, O_2, N_2 and Ar," J. Chem. Phys. $\underline{57}$, 3689 (1972).

32. Schofield, K., "Rate Constants for the Gaseous Interactions of $O(2^1D_2)$ and $O(2^1S_0)$ - A Critical Evaluation," J. Photochem. $\underline{9}$, 55 (1978).

33. Slanger, T.G. and Black, G., "Products of the $O(^1S)$ $-O_2$ Interaction," J. Chem. Phys. $\underline{68}$, 998 (1978).

34. London, G., Gilpin, R., Schiff, H.I. and Welge, K.H., "Collisional Deactivation of $O(^1S)$ by O_3 at Room Temperature," J. Chem. Phys. $\underline{54}$, 4512.

35. Krauss, M. and Neumann, D., "On the Interacton of $O(^1S)$ with $O(^3P)$," Chem. Phys. Lett. $\underline{36}$, (1975).

36. Slanger, T.G. and Black, G., "The Product Channels in the Quenching of $O(^1S)$ by O_2 $(a^1\Delta g)$," J. Chem. Phys. $\underline{75}$, 2247 (1981).

37. Slanger, T.G. and Black, G.," Quenching of $O(^1S)$ by O_2, Geophys. Res. Lett. $\underline{8}$, 535 (1981).

38. Velazco, J.E., Kolts, J.H. and Setser, D.W., "Rate Constants and Quenching Mechanisms for the Metastable States of Argon, Kyrpton and Xenon," J. Chem. Phys. $\underline{69}$, 4357 (1978).

39. Balamuta, J. and Golde, M.F., "Formation of Electronically Excited Oxygen Atoms in the Reaction of $Ar(^3P_{0,2})$ and Xe $(^3P_2)$ Atoms with O_2," J. Phys. Chem. $\underline{86}$, 2765 (1982).

40. Piper, L.G., Clyne, M.A.A. and Monkhouse, P.B., "Electronic Energy Transfer Between Metastable Argon Atoms and Ground-State Oxygen Atoms," J. Chem. Soc. Faraday Trans. 2 $\underline{78}$, 1373 (1982).

41. Arnold, I. and Comes, F.J., "Temperature Dependence of the Reactions $O(^3P) + O_3 \rightarrow 2\ O_2$ and $O(^3P) + O_2 + M \rightarrow O_3 + M$," Chem. Phys. $\underline{4}$, 231 (1979).

42. Morgan, J.E. and Schiff, H.I., "Diffusion Coefficients of O and N Atoms in Inert Gases," Can. J. Chem. $\underline{42}$, 2300 (1964).

43. Corney, A. and Williams, O.M., "Measurement of the Radiative Lifetime of the $^1S_0$ Metastable Level of Atomic Oxygen," J. Phys. B: Atom. Molecule Phys. $\underline{5}$, 686 (1972).

44. Vidaud, P.H., Wayne, R.P. and Varon, M., "Diffusion Coefficient Measurement of O_2^* ($^1\Delta_g$) in Ground State O_2" Chem. Phys. Lett. $\underline{38}$, 306, (1976).

45. Lawson, S.A. and Phelps, A.V., "Excitation of the $b^1\Sigma_g^+$ State of O_2 by Low Energy Electrons," J. Chem. Phys. $\underline{69}$, 1055 (1978).

46. Kolts, J.H. and Setser, D.W., "Decay Rates of Ar ($4S$, $^3P_2$), Ar($4S$, $^3P_0$) Kr($5S$, $^3P_2$) and Xe ($6S$, $^3P_2$) Atoms in Argon," J. Chem. Phys. $\underline{68}$, 4848 (1978).

APPENDIX A

LINUS ANALYSIS

This appendix is TR-362, prepared as the Third Quarterly
R&D Status Report for Contract No. F19628-82-C-0050,
1 October through 31 December 1982.

A

PSI TR-362

LINUS ANALYSIS

Peter Nebolsine, Guy Weyl, and W. Terry Rawlins

Quarterly Status Report #3

1 October 1982 - 31 December 1982

Air Force Contract #F19628-82-C-0050

Contract Monitor

R. A. Armstrong
Air Force Geophysics Laboratory/OPR

TABLE OF CONTENTS

LIST OF FIGURES

1. INTRODUCTION

Physical Sciences Inc. is supporting the LINUS (Laser Initiated Nuclear Simulation) experiments being performed at AFGL. The LINUS experiments involve the measurement of the radiative properties of a plasma created by a Q-switched Nd^{3+}-YAG laser. Measurements such as broadband emission, spectral features, temporal history, etc. have been performed. The emphasis of the PSI effort has been in applying existing models to a laser-produced plasma to further understand the phenomena. The efforts have included spectroscopy studies, an experiment definition task to measure the radial temperature profile, and hydrodynamics to model the temperature-density field. Since PSI was involved in the initial scoping LINUS experiments, we have included an assessment of those results in an effort to more fully understand them.

Figure 1 shows the generic experimental arrangement. A Q-switched Quanta Ray Nd^{3+}-YAG laser is used in an unstable resonator configuration. The output beam is an annulus of 1.06 μm radiation with a pulse duration of approximately 10 ns and a full beam divergence of 0.5 mrad. After numerous beam directing optical elements, the laser beam is focused by a lens (focal length ~ 8 cm) into a test cell. The test cell is vacuum tight and can be filled with the desired gas to the desired pressure. Most experiments have been performed from 3 to 125 torr. The test cell has windows perpendicular to the laser beam to allow for observation and also a rear window which is used to monitor the transmitted laser energy. No detectable absorption of the laser energy is observed at the low pressures even though a breakdown exists.

A spectrometer has been the principal diagnostic. It has been used in zero order for broadband measurements and in first order for spectroscopic measurements. A Spex spectrometer (0.5 m focal length, f/8.6) was used with a CaF_2 collecting lens providing a nominal 1:1 magnification. The entrance slit is narrow compared to the spark length and the entrance slit height is comparable to the spark diameter.
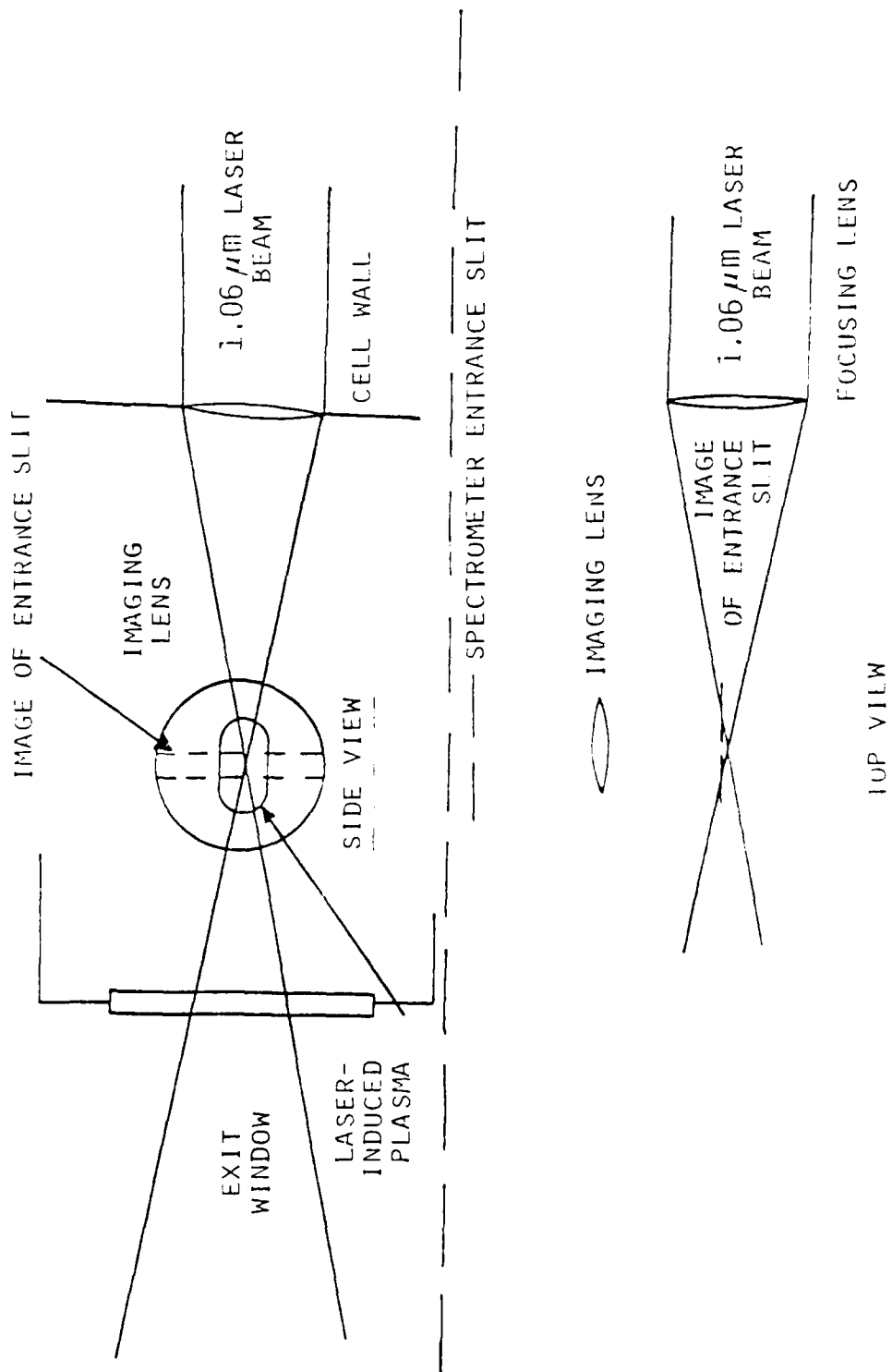
Fig. 1 Experimental schematic.

Section 2 of this report is devoted to an examination of the data collected by Roy Lucht in 1981.[1] Section 3 discusses experiments that can be performed to obtain more information to characterize the spark. Section 4 is devoted to blast wave analysis of a laser-produced spark and Section 5 is a short data analysis of data taken by John Swanton measuring broadband optical emission from the spark.[2]

2. REVIEW AND ANALYSIS OF SCOPING EXPERIMENTS

Roy Lucht obtained data using the apparatus outlined in the introduction. Breakdown thresholds as a function of pressure were measured for N_2, Ar, and O_2; Fig. 2 is the compilation of the data.[1] Both breakdown data and spectra were taken for these gases. The monochromator was operated with a 35 µm wide entrance slit which is small compared to the luminous length of the plasma. A boxcar integrator was used for the spectral measurements. The time gate was adjusted to be 200 ns and most of the emitted light within the field of view was collected. Line spectra were observed and radiating species were identified. At 125 torr pressure continuum radiation was observed in addition to the line radiation. Other data was taken by fixing the wavelength of the monochromator and shifting a 5 ns gate from the initiation of the laser pulse. Figure 3 is a typical trace for spectral lines of N^+, N^{++}, and N^{+++}. The peak emission appears to occur substantially after the laser pulse is off. Since the boxcar does not give an origin of time, the precise sequencing of the emission of one line to another and to the laser pulse is unknown. The temporal sequence of the peaks in the radiation of N^{+++}, N^{++} and N^+ is compatible with cooling of the plasma with time. Because the field of view of the monochromator is small compared to the spark dimension, the time profile may not be accurate for the entire N^{+++}, N^{++}, and N^+ radiation from the spark. The decay times from observed lines are on the order of 1 to 20 times the lifetime of a specific transition.

Using this apparatus, color temperature measurements were made using at least six lines from a radiating species. Color temperatures of 18,000 to 28,000 K were observed using a time gate of 200 ns. Because the temperature from blast wave theory is strongly varying within the spark, the color temperature can only be used as a gross indication of the plasma conditions.

An examination of the techniques and data will now be discussed. This discussion should be considered to be instructive in designing better experiments rather than criticizing the scoping experiments that were performed.

Much of the breakdown data in the literature is qualitative because it is difficult to quantitatively measure breakdown. In a colloquial sense, it
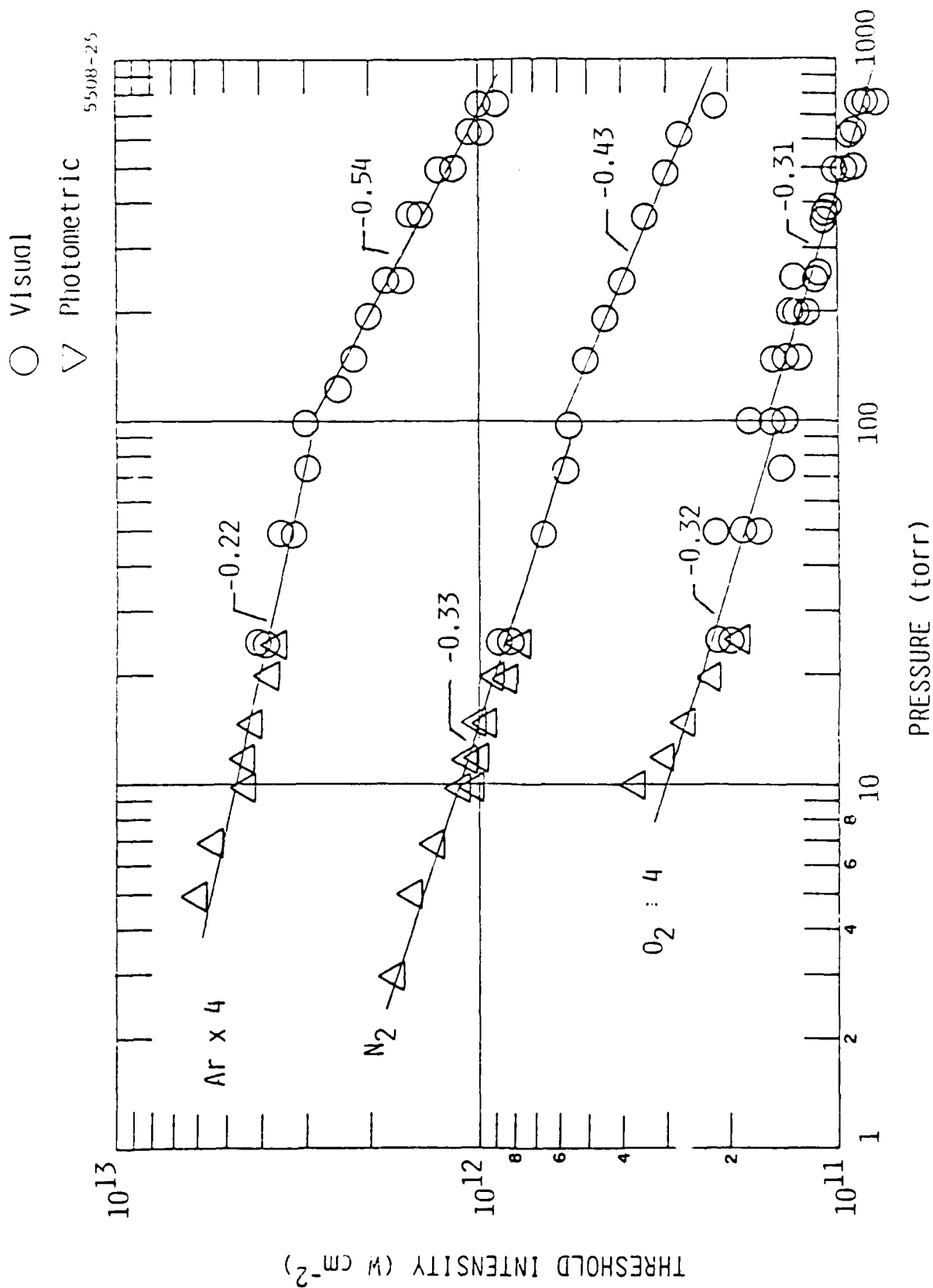
Fig. 2 Apparent breakdown thresholds for Ar, N_2 and O_2. Pressure exponents obtained from least squares fits (solid lines) for $p \gtrsim 100$ torr and $p \lesssim 100$ torr are indicated.
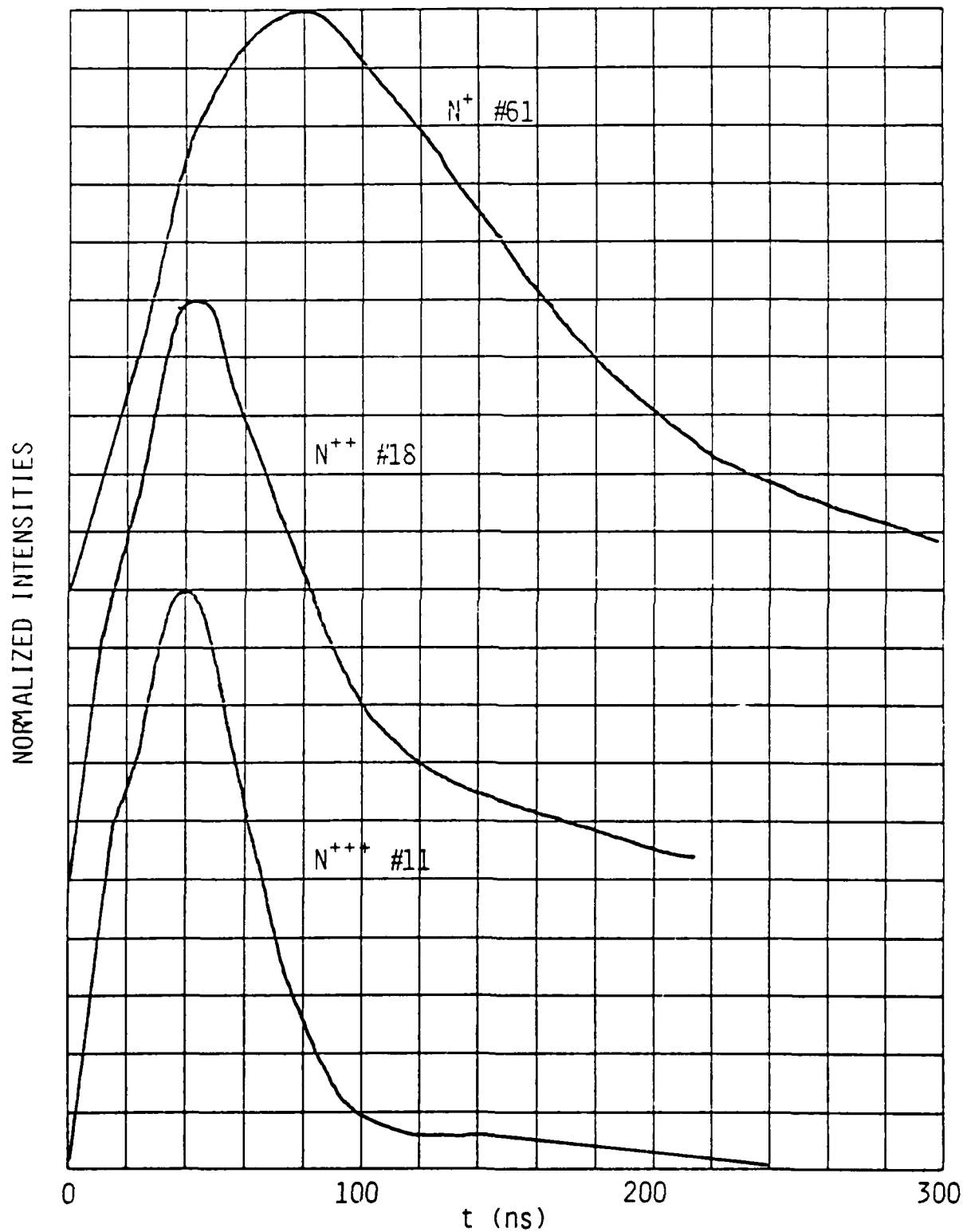
Fig. 3 Line profiles using 10 torr N_2 and 2.9 x 10^{12} W/cm^2.

A-6

is one of those "you know" events. At high pressure (e.g., 1 atm) there is no question whether or not there is breakdown because the transition is so abrupt from no visible plasma to a highly ionized absorbing plasma. Potential definitions of breakdown include:

1) visible flash

    a) detection by eye
    b) detection by a photo-detector

2) specific amount of radiation

    a) independent of pressure
    b) normalized by pressure

3) specific percentage of ionization.

Eye observation of a breakdown is the definition used by a number of investigators. A measurement of the degree of ionization is the preferred definition of breakdown. Unfortunately such a measurement is not trivial, hence radiation is typically used as a measure of breakdown. A broadband measurement of radiation normalized to the ambient density can provide a reasonable definition for experiments. This definition approximately specifies an equal amount of ionization to determine a breakdown threshold.

To take high quality breakdown data, the only parameters that should be varied are the laser beam irradiance and gas pressure. Also the repetition rate of the laser (in our case 10 Hz) should be low enough that residual ionization from previous pulses is not a factor in determining the breakdown threshold. (This should be carefully checked for each gas.) The purity of the gas is also an issue. Particulates and trace impurities can lower the breakdown threshold.

The scoping data taken by Roy Lucht were acquired by varying the flash-lamp pump energy to vary the laser output energy. This process of controlling the laser output energy also varied the laser's near field irradiance. This could have also varied the fluence distribution (peak fluence

and/or irradiance) at focus. Operating the laser at fixed output conditions and using a variable attenuator to vary the irradiance in the focal plane is the preferred technique. The irradiance distribution in the focal plane can be determined by using a long focal length lens to obtain a spatial extent of reasonable size. (If no lens is used, the laser beam would have to propagate 200 m to have the observation plane be in the far field.) Using a lens with a focal length of 30 m is probably a reasonable compromise between distance, fluence, and spatial extent.

The irradiance fluence distribution can be determined by scanning a detector in the focal plane. An unaberrated unstable resonator beam in the far field looks similar to the Airy pattern. However, the dark rings are not quite in the same location and less energy is within the first dark ring than for a uniformly illuminated aperture. Such measurements of the laser beam parameters will allow both a peak and average laser beam fluence to be calculated. The deduced fluence distribution can be scaled for the lens used in the experiment as long as aberrations are not important. Spherical aberration will limit the fluence level as the focal length of the focusing lens is reduced. The minimum focal length without significant spherical aberration and the use of multiple lenses or an aspheric lens will be discussed in the next section so that data at higher irradiances can be taken.

The data shown in Fig. 2 shows a weak dependence on pressure. Some of this dependence may be due to the changing beam divergence with output power. The use of an attenuator to change the laser beam irradiance in the cell, without changing the spot size, will provide a capability to take well characterized breakdown data.

3. SUGGESTED EXPERIMENTS

Experiments that can be done to characterize the laser breakdown process include:

3.1   Breakdown Data

Higher quality breakdown data can be taken by using a more accurately characterized laser beam and a quantitative definition for breakdown. The technique to scan fluence distribution in the focal plane of a long focal length lens was dicussed in Sec. 2. The temporal pulse shape of the laser pulse needs to be measured. The addition of the line narrowing feature in the laser will prevent spontaneous mode-locking. (Spontaneous mode-locking will generate high intensity fluctuations on the laser pulse which makes data interpretation more difficult.) Shorter focal length lenses than used to date will allow higher laser beam irradiances at the focus, permitting breakdown below 1 torr to be studied.

Figure 4 shows the breakdown data for N_2 that was obtained by Roy Lucht and also tne maximum irradiances that can be obtained using one, two and tnree lenses. The irradiance limit was calculated knowing the laser energy, spot size and choosing a focal length so that the aberrated spot size would be two-thirds the beam divergence spot size. Breakdowns for pressures below 1 torr can be studied with shorter than 6 cm focal length lenses. The practical alternative to multiple lenses to reduce spherical aberration is to use an aspheric lens. Aspheric lenses are commercially available with short focal lengths and low f/numbers.

The use of attenuators to vary only the peak irradiance but not the irradiance distribution is advocated. Care must be taken to utilize a non-aberrating attenuator. Fresnel reflections are an established technique to vary the energy in a laser beam without affecting the distribution of energy.[3]
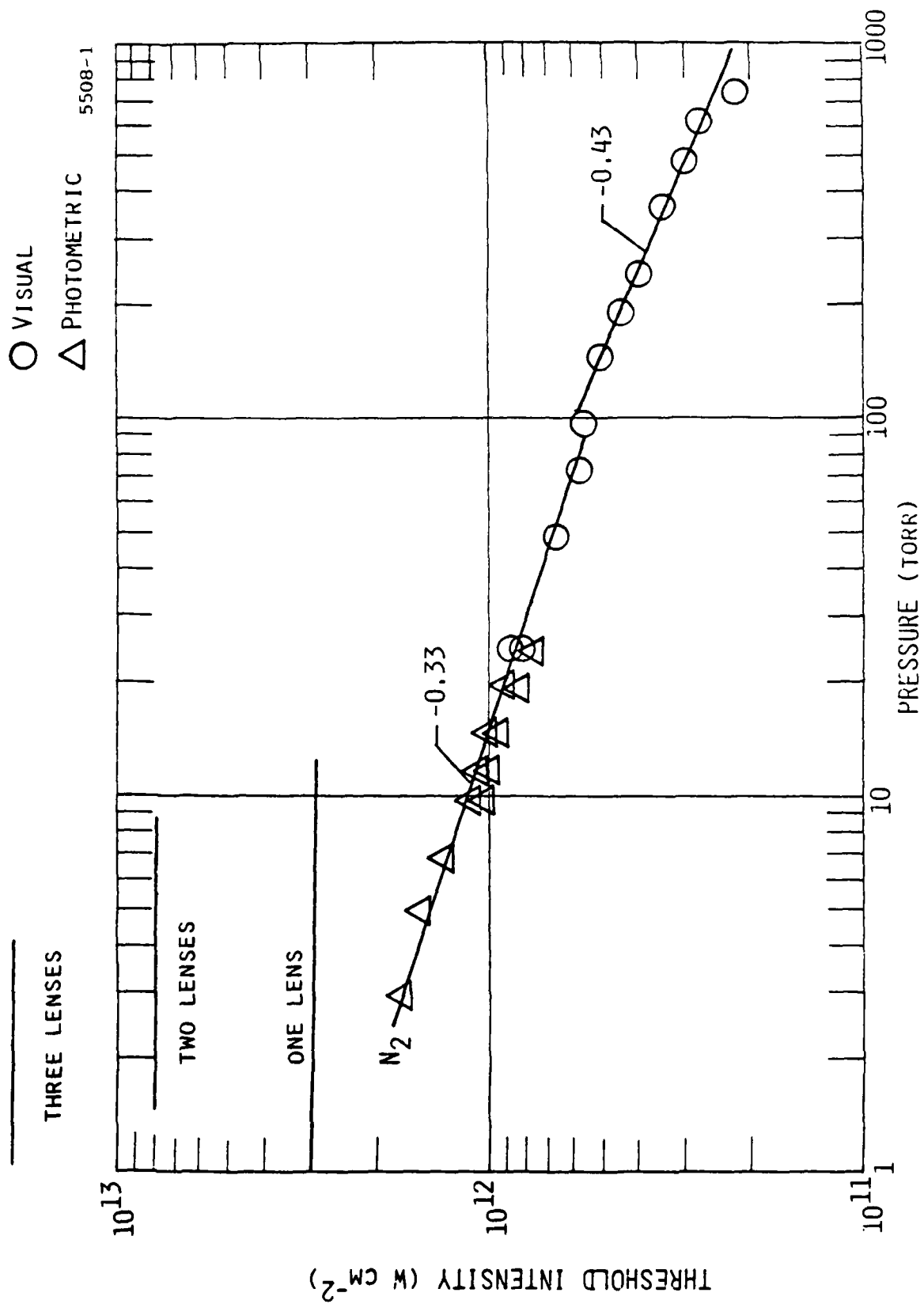
Fig. 4 Breakdown threshold for N_2 and maximum intensities for 1, 2 and 3 lenses.

3.2   Optical Characterization of the Spark

3.2.1.   No Spectral Resolution or Spatial Resolution

A pyroelectric detector can be used to measure the total optical radiation from the plasma. Pyroelectric detectors are rather insensitive ($\sim 10^{-6}$ A/W responsivity) but do have very broad wavelength coverage from the VUV to LWIR. This measurement would provide a lower bound on the energy deposited into the gas by the YAG laser beam. Care must be taken not to have this measurement corrupted by scattered 1.06 μm light from the laser or flash lamp. With baffling of the detector and a proper background it should be straight-forward to obtain good measurements. Given the detector's responsivity and the anticipated signal strengths, probably only a measurement of radiant energy in units of J/sr is possible.

The ratio of radiated energy to laser energy is a measure of the efficiency of depositing laser energy. A discussion of the relationship of radiated energy in a finite bandpass to laser energy as a function of gas pressure is presented in Sec. 5.

Finite bandwidth detectors such as photomultiplier tubes and other high quantum efficiency detectors can be used to measure the temporal emission of the spark.

3.2.   Spectral Resolution/No Spatial Resolution

The measurement would be of $P_\lambda(t)$ in units of W/sr-μm, i.e., radiant power per steradian per unit bandwidth. To perform this measurement, the total spark needs to be imaged into the entrance slit. Using 10 μm as a nominal entrance slit width, an image reduction of 200:1 is appropriate to collect all the visible light. With such an image reduction the f/number of the collecting optics will be very high (~ 2000) when matching the f/8.6 optics of the spectrometer.

Measurements can be made both time-resolved or time-integrated to provide spectral information. Doing measurements as a function of pressure will provide data for pressure-dependent effects. Roy Lucht's data gave an indication that first and second maximum existed for these laser sparks. Because the field of view was limited ($\sim$ 35 μm compared to the spark length of

~ 500 µm), only a rough compari....n to phenomena pertinent to the whole spark
can be made. Changing the field of view to include the whole spark will allow
the observation for first and second maximum.

The measurements will provide data for the time evolution of the radi-
ation from specific species. Figure 3 is an example of past work with a lim-
ited field of view. Similar measurements should be performed when observing
the whole spark. It is expected that the radiation from the most highly ion-
ized species would decay sooner than the singly ionized or neutral atoms be-
cause of the cooling of the spark.

Even though the temperature is not expected to be uniform within the
spark, a color temperature could be computed by measuring the ratio of inten-
sities from different radiating lines of a specific specie. The plasma is
optically thin (see Sec. 3.2.4c) so that radiation will be observed from all
the radiating species.

These measurements will provide additional information on the optical
radiation loss mechanism of the spark. For example, continuum radiation as
well as line radiation was observed at 125 torr. The measurements will allow
the computation of the amount of energy lost from the spark from specific
lines and also continuum emission.

3.2.3. Spatial Resolution/No Spectral Resolution

The laser energy is deposited in the spark in a volume determined by
the outline of the laser beam. The absorbed laser energy raises the pressure
of the ambient gas and the gas expands. Blast wave theory can be applied to
estimate the energy deposition, rate of expansion and shock temperatures and
cooling rates. Blast wave theory gives a power law dependence for the shock
front position versus time. The shock front can be measured by the presence
of the luminous front for strong shocks and Schlieren photography for weaker
shocks. Section 4 will be devoted to a discussion of blast wave physics and
its application to this problem.

3.2.4. Spectral and Spatial Resolution

Measurements would be made with spatial resolution fine compared to
any dimension of the spark. These measurements would provide radiometric
information in units of W/cm^2-sr-µm for temporal resolved measurements or

A-12

J/cm^2-sr-μm for time integrated measurements. If the spark is optically thin, then an Abel inversion can be used to obtain local values. For example, the local radiant emission in units of W/cm^3-sr-μm would be obtained. This data can be analyzed assuming local thermodynamic equilibrium to deduce a temperature of an emitting species. These results can provide information on the thermal profile within the spark. Blast wave theory for a spherical expansion (see Sec. 4) predicts a very strong radial dependence, e.g.,

$$T(r) \sim T_o \left(\frac{r_o}{r}\right)^{3/\gamma-1} \qquad r < r_o \qquad\qquad 3.1$$

where T_o is the temperature at shock location r_o and r is the radius within r_o. We note that the central core of the spark will be much hotter than the outside region. Once the gas is shock heated, it isentropically expands dropping its temperature and pressure. Two types of gas will exist: 1) gas directly heated by the laser pulse, and 2) gas shock-heated by the laser-heated gas. The spatial and temporally resolved measurements will be able to resolve the properties of these two differently heated gases. We will now discuss the measurement to deduce a local temperature.

We wish to calculate line emission from a hot (15,000 < T < 30,000 K) plasma and find the optimum spectral bandwidth for temperature measurements using line radiation from the plasma.

a) <u>Line Intensities</u>

Consider a small volume element containing N_u atoms in some excited (u) state, that are radiating to some lower (ℓ) state. The power emitted per unit time in 4π steradians is

$$P = N_u h\nu A_{u\ell} \qquad\qquad 3.2$$

where $A_{u\ell}$ is the Einstein A coefficient (s^{-1}) for the transition and is tabulated in Ref. 4. The power radiated per unit volume is given by

$$\mathcal{P} = \frac{ph\nu}{kT} \frac{c_\alpha g_u e^{-\varepsilon_u/kT}}{z_\alpha} A_{u\ell} \qquad\qquad 3.3$$

A-13

where p = pressure, C_α = concentration of species α, Z_α = partition function of species $\alpha(N, N^+, N^{++},$ etc.$)$, g_u = degeneracy of upper state. We show in Figs. 5 and 6 the molar concentrations of N_2, N, N^+, N^{++} as a function of temperature for pressures P = 10 and 1000 torr. These were obtained by solving (on a hand calculator) the simultaneous Saha equation for N_2, N^+, N^{++} and N. These concentrations were defined such that $2C_{N_2} + C_N + C_{N^+} + C_{N^{++}} = 1$. In order to take into account the dilution due to the electron concentration, we must divide the concentration of Figs. 5 and 6 by $(1 + C_{N^+} + 2C_{N^{++}})$.

The partition functions of interest are given in the table below.

Partition Functions $Z\alpha$

SPECIES	N	N^+	N^{++}
T = 300 K	4	9	6
T = 30,000 K	10	11.35	6.8

The only species whose partition function variation with temperature has to be considered is N. However, the concentration of nitrogen atoms above 15,000 K is negligible, and we will not be concerned with nitrogen lines.

We now calculate the radiation from a line plasma which enters the slit of the spectrometer, with the optical system shown in Fig. 7. The magnification at the slit is $f_2/f_1(= 10/25)$ and the solid angle subtended by the line plasma is $\Delta\Omega = (\pi d^2/4\ell_1^2) = \pi/(4f_1^2)$ where d = diameter of lens and ℓ_1 = distance from lens to the plasma. f_1 and f_2 are the f numbers associated with the collection lens shown in Fig. 7. The amount of radiation entering the slit during the measurement time Δt is given by

$$E = \left(\mathcal{J}\Delta t\right)\ (A'\ell\Delta\Omega)\qquad\qquad 3.4$$

where $\mathcal{J}$ is given by Eq. (3.3) and $A'\ell$ is the volume of the radiating element imaged onto the slit. We are interested in determining the energy incident on
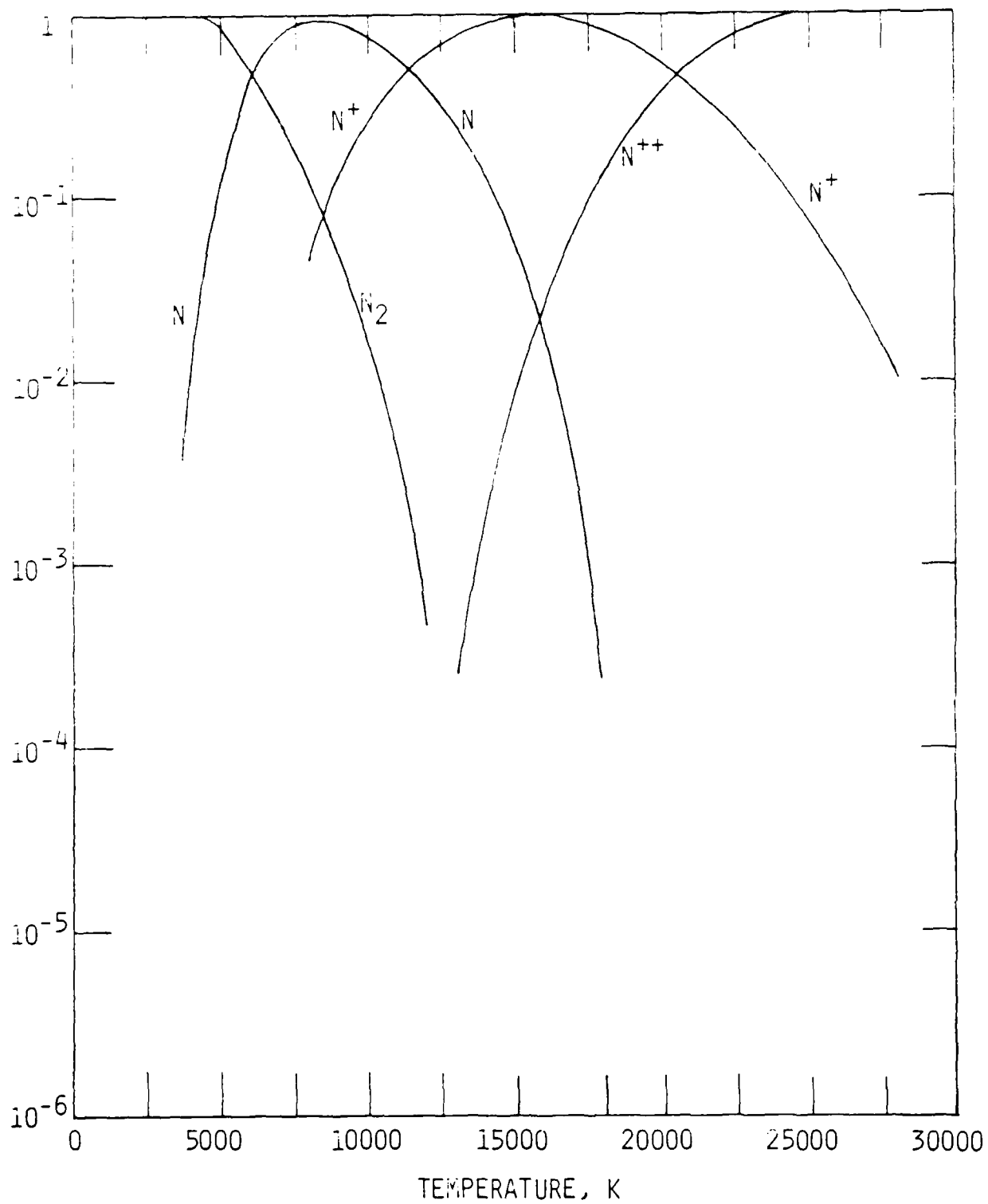
Fig. 5 Concentration of nitrogen species at 10 torr.
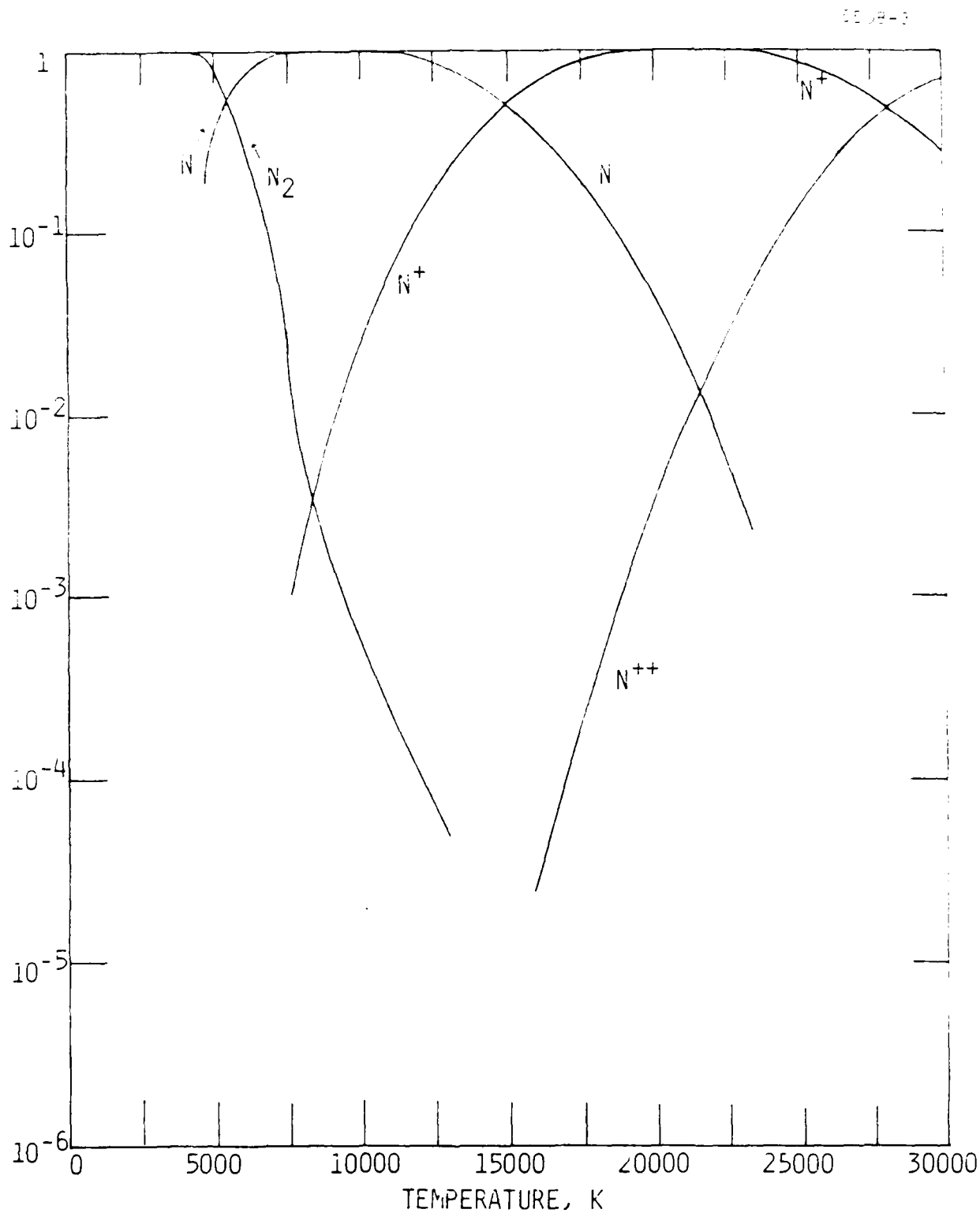
Fig. 6 Concentration of nitrogen species at 1,000 torr.
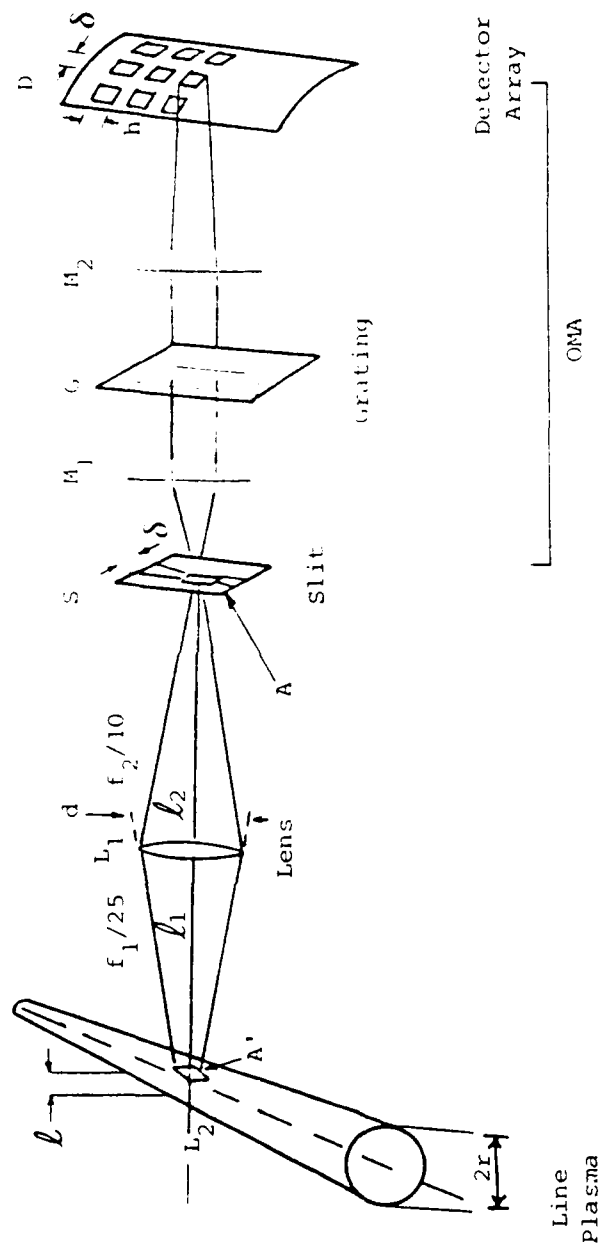
Fig. 7 Schematic of optical system and OMA.

individual detectors in the detector array of the optical multi-channel analyzer (OMA). This array is two dimensional, one dimension giving the spectral resolution, the other dimension, to the image of the slit in the plane of the detector array, gives spatial resolution at each wavelength. We also assume that the magnification of the spectrometer is unity. In this case the effective area of the slit imaged onto the detector is $(f_2/f_1)^2 A' = \delta h$ where $\delta =$ slit width and $h =$ detector dimension parallel to slit. If the radius of the plasma that is radiating is r, we have, for the central rays (those passing through the axis of the plasma)

$$A'\ell = (\delta h) \times (f_1/f_2)^2 \times 2r = 2rh\delta(f_1/f_2)^2 \qquad 3.5$$

The number of photon counts on the detector is given by

$$N = \frac{E}{h\nu} = \frac{\pi}{2} \frac{\delta h}{f_1^2} r \frac{p}{kT} \frac{C_\alpha e^{-\epsilon_u/kT} g_u}{Z_\alpha} \Delta t A_{u\ell} \qquad 3.6$$

We will now present results under the specific conditions $\delta = h = 25$ μm, $T = 25,000$ K, $f_1 = 25$

$$N = 3 \times 10^5 \frac{C_\alpha e^{-\epsilon_u/kT}}{Z_\alpha} A_{u\ell}\Delta t p(torr)$$

We will be concerned with measurement times Δt of the order of 50 ns and pressure $p \approx 10$ torr. Typical values of $A_{u\ell}$ for visible transition are $\sim 10^8 s^{-1}$ so that we will have $N \cong (3 \times 10^5) \times (10^8 \times 50 \times 10^{-9}) \times 10 \times X_{\alpha u} \cong 10^7 X_{\alpha u}$ where $X_{\alpha u}$ is the concentration of species α in the upper state u. We require $X_{\alpha u} > 10^{-7}$ in order that more than one photon be incident on the (central) detector in one measurement interval.

We show in the table below calculations for specific lines of N^+ and N^{++} which are the most intense in the band 3000-7000Å. We consider the two temperatures $T = 17,000$ K and $T = 30,000$ K.

TRANSITION Å	ε_u (cm^{-1})	g_u	A_{ul} (10^8s^{-1})	T = 17,000 K		T = 30,000 K	
				$X_{\alpha u}$	N	$X_{\alpha u}$	N
N$^+$ 4040.9	211332	27	2.64	2^{-8}	0.8	1.6^{-7}	6.3
4239.4	211053	21	2.04	1.5^{-8}	0.5	1.3^{-7}	4.1
4630.54	170667	5	0.84	1.7^{-7}	2.2	2^{-7}	2.6
5001.4	186572	7	1.08	2.5^{-8}	0.4	1^{-7}	1.6
5005.14	186653	9	1.22	3^{-8}	0.5	1.3^{-7}	2.4
5179.5	223787	11	1.02	5.5^{-10}	0.008	1.1^{-8}	0.17
5679.56	166579	7	0.56	2.2^{-7}	2	3.4^{-7}	2.9
N^{++} 4097.3	245102	4	0.96	x	x	1.6^{-6}	2.3
4514.9	304857	8	0.8	x	x	1.5^{-7}	2.12

From the above table we see that a temperature measurement using lines of N$^+$ can be done over the temperature range 17,000-30,000 K, but one has to span the spectral range 4239Å to 5001Å. There are three energy levels that can be used for N$^+$ = 211,000 cm^{-1}, 186,000 cm^{-1} and 166,000 cm^{-1}. Temperature measurements using the two lines of N^{++} at 4097Å and 4515Å can be used only for the highest temperatures.

b)   Line Widths

A line width is determined by the dominant of the three broadening mechanisms: 1) lifetime of upper state; 2) Doppler broadening; and 3) collision or Stark broadening. Due to the high temperature and electron densities of the present study mechanisms 2 and 3 dominate. Stark broadening parameters can be found in Table 4-5 of the book by Griem.[5] The line width $\Delta\lambda$ (in Å) is, following Griem, given by (n_e: electron concentration in cm^{-3}).

$$\Delta\lambda = W(T) \left(\frac{n_e}{10^{16}}\right) \qquad 3.7$$

As a typical example consider the line at 4630Å for which at 10,000 K where the nitrogen is dissociated and partially ionized, W = 6.4 x 10^{-3}. We calculate an electron density at T = 20,000 K, where the nitrogen is singly ionized, p = 10 torr of 2.8 x 10^{15} cm^{-3}, so that $\Delta\lambda(\lambda = 4630$Å$)$ = 2 x 10-3 Å.

A-19

Consider now Doppler broadening at the same temperature

$$\frac{\Delta\lambda}{\lambda} = \frac{\Delta\nu}{\nu} = \frac{U_{th}}{c} = \frac{4.5 \times 10^5}{3 \times 10^{10}} = 1.5 \times 10^{-5} \underline{\text{ or }} \frac{\Delta\nu}{\nu} = 3.6 \times 10^{-7} \quad \frac{T}{M}$$

where U_{th} is the thermal velocity. This gives a line width, for the same line, $\Delta\lambda = 7 \times 10^{-2}\text{Å}$. Since each detector is expected to span approximately a few tenths of an angstrom, we would expect no line overlaps to occur between detectors due to the finite line widths. The 0.5 m Spex monochromator with a 1,200 line/mm grating has a dispersion of 0.4 Å/picture element. An entrance slit of 10 μm will give 0.6 Å resolution and the line width will not be resolved.

c)   Optical Density of Plasma

The formulae that we have used neglected stimulated emission and are strictly valid only for a plasma that is quite optically thin. Knowing the line widths, we can easily calculate the optical density of the plasma by comparing $2r\mathcal{P}(\lambda)$ with the black body expression for the power. The black body intensity is given by

$$I = \frac{2h\nu^3}{c^2} \frac{1}{(e^{h\nu/kT}-1)} \qquad\qquad 3.8$$

The intensity at the center of a given line is given by:

$$\frac{2r\mathcal{P}}{\Delta\nu} = \frac{2rph\nu}{kT} \frac{C_\alpha g_u e^{-\epsilon_u/\ell T}}{z_\alpha \Delta\nu} A_{ue} \qquad\qquad 3.9$$

For the line at 4630.5Å and T = 17,000 K, we find that $(2rP/I\Delta\nu) = 3 \times 10^{-4}$, i.e., that the plasma is quite optically thin, even at the line center. The emission will be optically thin for all lines of the observed species.

4. BLAST WAVE THEORY

The Nd^{+++}-YAG/laser pulse deposits energy in the gas during the laser pulse duration of approximately 10 ns. The gas expands due to the pressure rise and entrains gas as it expands. When the laser induced shock wave is strong, then blast wave theory is applicable. In its usual form, blast wave theory does not have any loss mechanisms, assumes a constant ratio of specific heats (γ), thermal equilibrium and continuum fluid mechanics.

Blast wave theory was originally developed for the case of instantaneous release of energy and then was extended to a power-law time-dependence of energy release.[6] In all cases the energy is released into zero mass at a point, in a line, or in a plane. Hence, the temperature goes to infinity at the origin.

The general formulas for the shock radius as a function of time for both an instantaneous deposition of energy and power law deposition are:[6]

$$r_s = Kt^n \tag{4.1}$$

where

$$n = \frac{2 + \beta}{3 + \alpha} \quad \text{and} \quad K = \left(\frac{W_\alpha a_o^2}{p_o n^2 J_o}\right)^{1/\alpha+3} \tag{4.2}$$

and

$$E_\alpha = W_\alpha t^\beta \tag{4.3}$$

where $\beta = 0$ for instantaneous and $\beta = 1$ for constant input power and E_α = energy input/unit area ($\alpha = 0$), $= \frac{1}{2\pi}$ energy input/unit length ($\alpha = 1$), $= \frac{1}{4\pi}$ energy input ($\alpha = 2$). a_o = ambient sound speed and p_o is the ambient pressure.

Geometry	Dimensionality	α	$J_o(\beta=0)$
plane	1 Dimensional	0	1.67
line	2 Dimensional	1	0.88
point	3 Dimensional	2	0.60

Once the shock front position is determined, the pressure behind the shock is determined by:

$$P_s = \frac{2}{\gamma+1} \rho_o \left(\frac{dr}{dt}\right)^2$$

The similarity profiles of pressure, particle velocity, density and temperature are determined by computation. Figure 8 is an example of these profiles for $\gamma = 1.23$ and instantaneous release of energy at a point.[6] The pressure drops to about one-half the shock pressure for $0 < r < 0.8 \ r_s$, the density drops nearly to zero and the temperature asymptotes to a very high temperature (ideally infinity) with $r \rightarrow 0$.

The characteristic amount of energy deposited by the laser pulse will now be computed for an f/6 laser beam. The energy will be computed by first looking at the degree of ionization from Figs. 5 and 6 and the fact that a color temperature of ~ 28,000 K was determined by Roy Lucht.[1] We see that most of the nitrogen will be doubly ionized. To compute the energy per nitrogen molecule we add the energy to dissociate N_2(10 eV) + twice the ionization potential (2(14 eV)) + twice the ionization potential of N^+(2(25 eV)) + six times the heat capacity at 30,000 K (~6(2.5eV)) = $\frac{103 \text{ eV}}{N_2 \text{ molecule}}$. We multiply this energy/molecule by the number of molecules/cm^3 times the breakdown volume. At 10 torr the ambient number density is 3×10^{17}/cm^3 and the volume is computed from optics.

The volume in which there is breakdown will now be estimated. Figure 9 snows the energy contours for a diffraction limited beam from a uniformly illuminated aperture. The ordinate is scaled to the distance from the focal plane ($U = \frac{\pi}{2\lambda} (D/f)^2 Z$). The abscissa is scaled radially from the optical axis ($V = \frac{\pi}{2} \frac{D}{f} \cdot R$). The position of the node of the Airy Disk is annotated as well as the radius for a 0.25 mrad half angle beam divergence of the Quanta Ray laser. (This is the beam divergence specified by the manufacturer of the laser). The third line which is provided for reference is the geometrical shadow line. The minimum deposition volume is the volume bounded by the beam divergence ($V = 7.8$) and the intersection with the geometrical shadow ($U = 7.8$). However, because the beam divergence is not likely to be measured for the greatest extent of the laser beam but some nominal extent, we'll use the intersection of the $V = 7.8$ and the 50% energy contour ($U = 12.5$ which is $Z \sim \pm 290 \ \mu m$). The deposition volume is thus $2 \times (290 \ \mu m)(\pi)(14 \ \mu)^2 = 3.5 \times 10^{-7}$ cm^3. Combining the 103 eV/molecule, 3×10^{17} molecules/cm^3 and $V = 3.5 \times 10^{-7}$ cm^3, we obtain a deposition energy of 2×10^{-6} J. We will now provide a number of figures which plot blast wave results for this case of 2×10^{-6} J energy deposition.
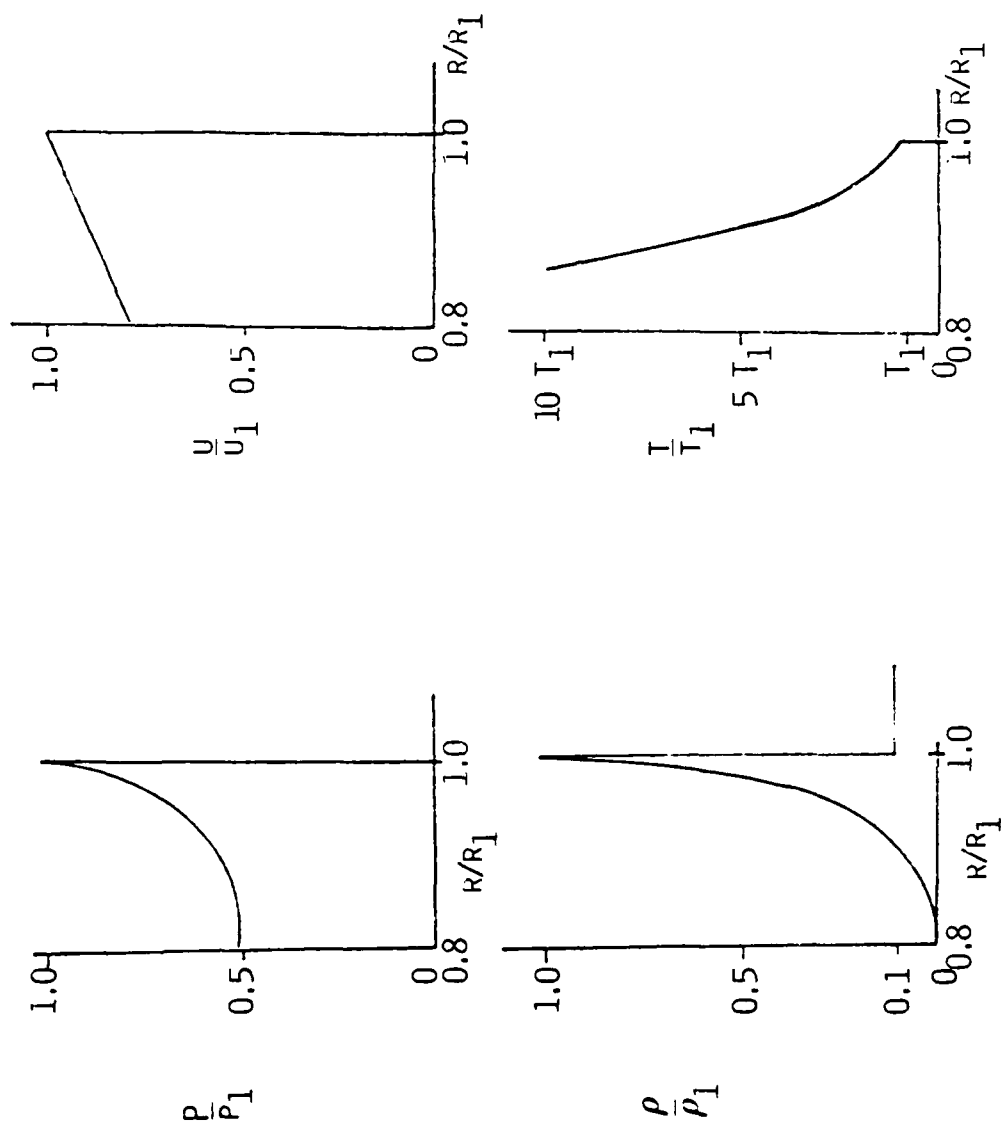
A-22
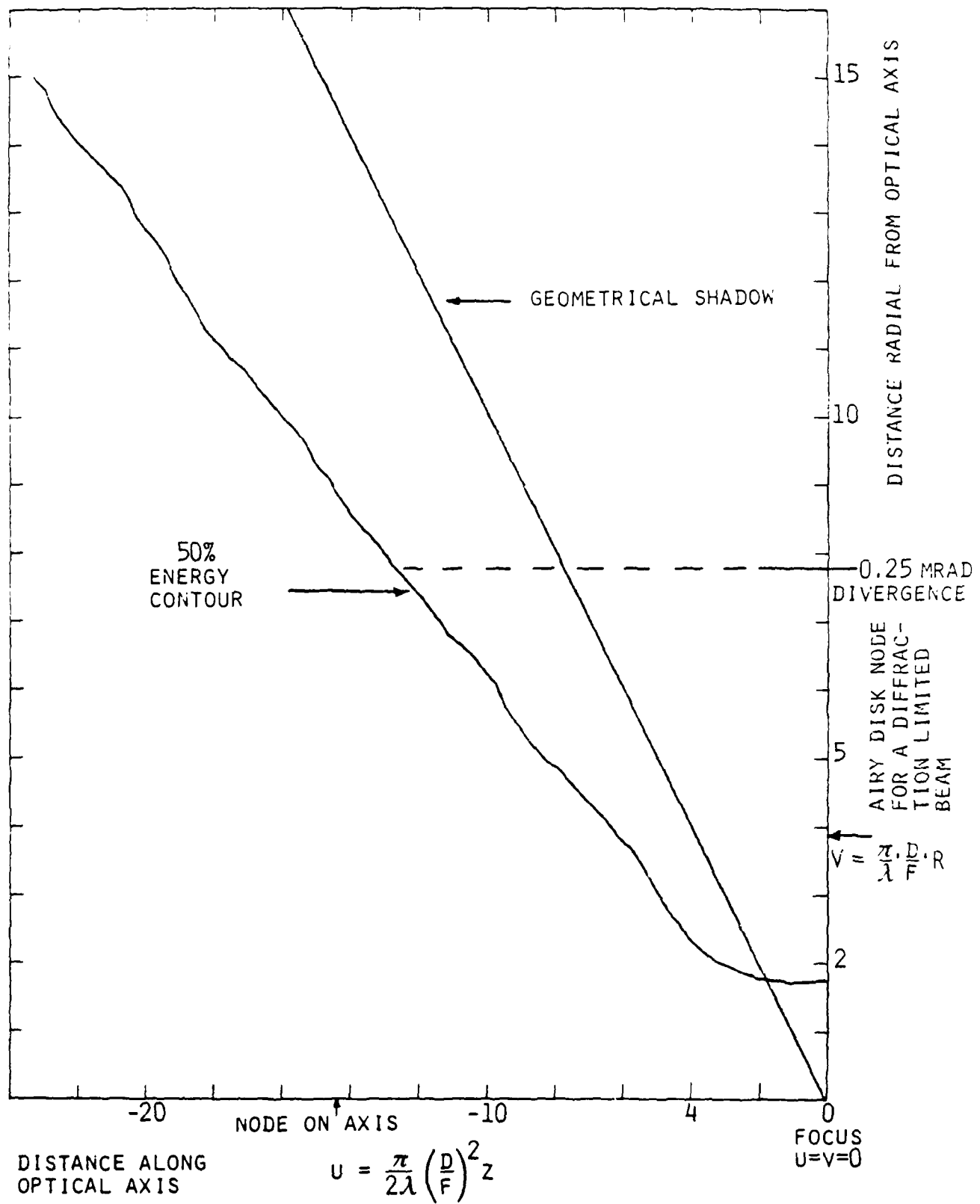
$\gamma = 1.23$

Fig. 8 Spherical blast wave profiles.

Fig. 9 Deposition contour around focus.

3-D Expansion - Instantaneous Energy Deposition

Figure 10 is a plot of the shock radius as a function of time. The radius increases as $t^{2/5}$. This computation yields a radius of 100 µm at 10 ns after energy deposition. This is a dimension considerably larger than the 14 µm beam radius computed from the laser beam divergence and focal length. Later on in this section we'll discuss the comparison to depositing the energy in 10 ns.

Figure 11 is a plot of the shock pressure versus time where $p \propto t^{-6/5}$. It will take over 1 µs for the shock pressure to relax to ambient pressure.

Figures 12 and 13 provide temperature information. Figure 12 is the temperature at the shock front versus time. The temperature jump is due to the shock heating. Figure 13 is the temperature of the shock where it occurs in radius. For example, when the shock has expanded to 200 µm, the temperature at the shock is 1,200 K.

The temperature profile within the shock is a very rapidly rising temperature as $r \to 0$. The functional form is:

$$T \sim T_o \left(\frac{r_s}{r}\right)^{3/\gamma - 1} \qquad \qquad 4.5$$

so for $\gamma = 1.4$

$$T \sim T_o \left(\frac{r_s}{r}\right)^{7.5}. \qquad \qquad 4.6$$

Profiles are shown in Fig. 14 for r_s = 100 µm and 210 µm which occur at 10 ns and 65 ns. A γ of 1.4 is chosen as a representative γ.

The last figure provides information about the cooling rate that the gas undergoes. The gas is shock heated and then isentropically expands and therefore cools. Figure 15 shows the cooling rate of gas which is originally at the shock front at the times specified on the ordinate. For example, gas that was shock heated at 10 ns, (r = 100 µm from Fig. 10) was shock heated to 9,000 K (Fig. 13) and then cooled at 1.5×10^{11} K/s. If the gas continually cooled at this rate, the gas would cool to ambient temperature in 60 ns. The cooling rate is fast because expansion velocity is high and the length scale is small.
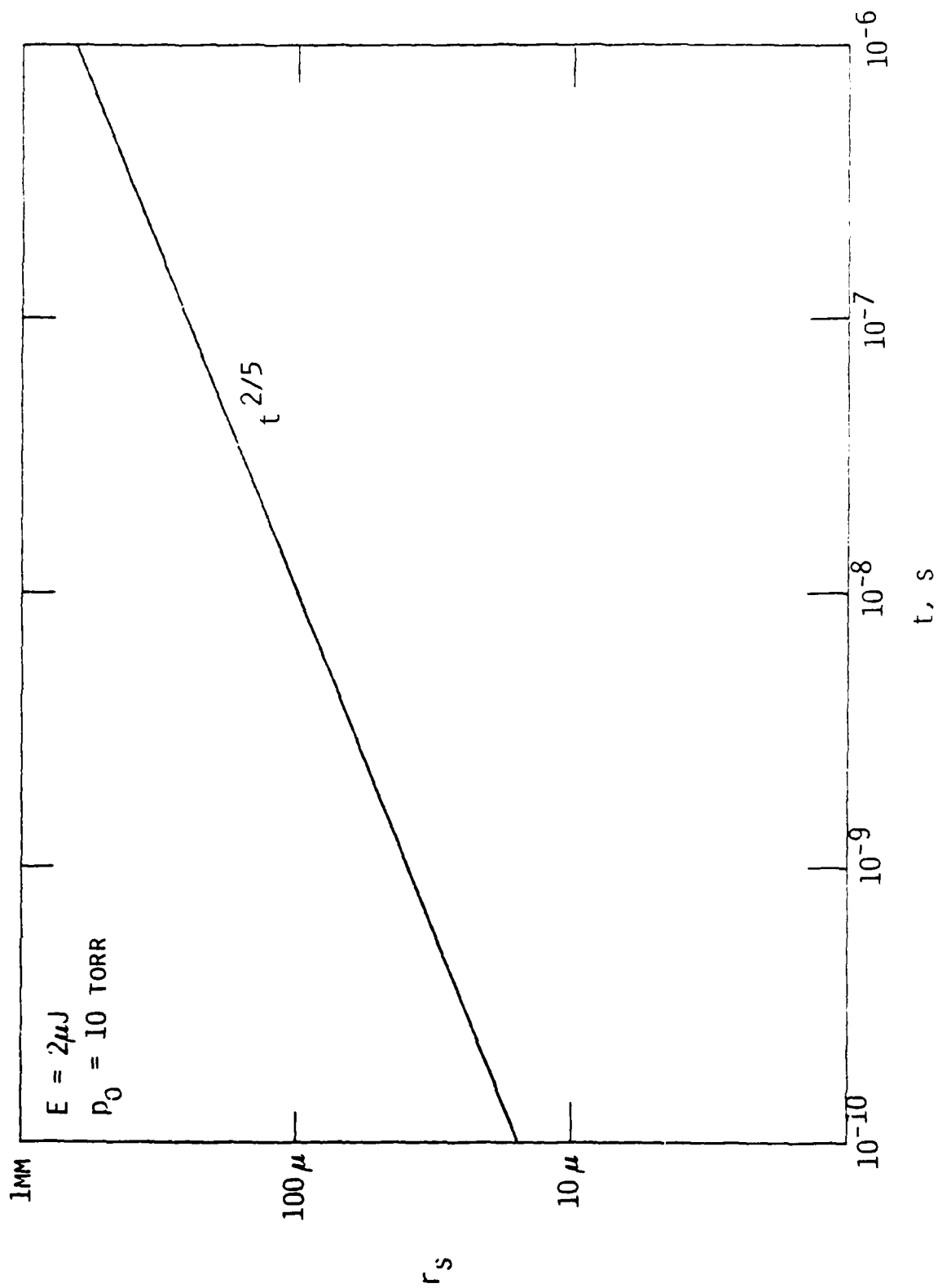
Fig. 10 Shock wave position vs. time.

$E = 2\mu J$

$p_0 = 10$ TORR

$t^{2/5}$

1MM

$100\,\mu$

$10\,\mu$

r_s

10^{-10} 10^{-9} 10^{-8} 10^{-7} 10^{-6}

t, s

Fig. 11 Pressure vs. time.

E = 2μJ
P₀ = 10 TORR

t⁻⁶/⁵

P₀

TIME, s

PRESSURE, DYNES/CM²
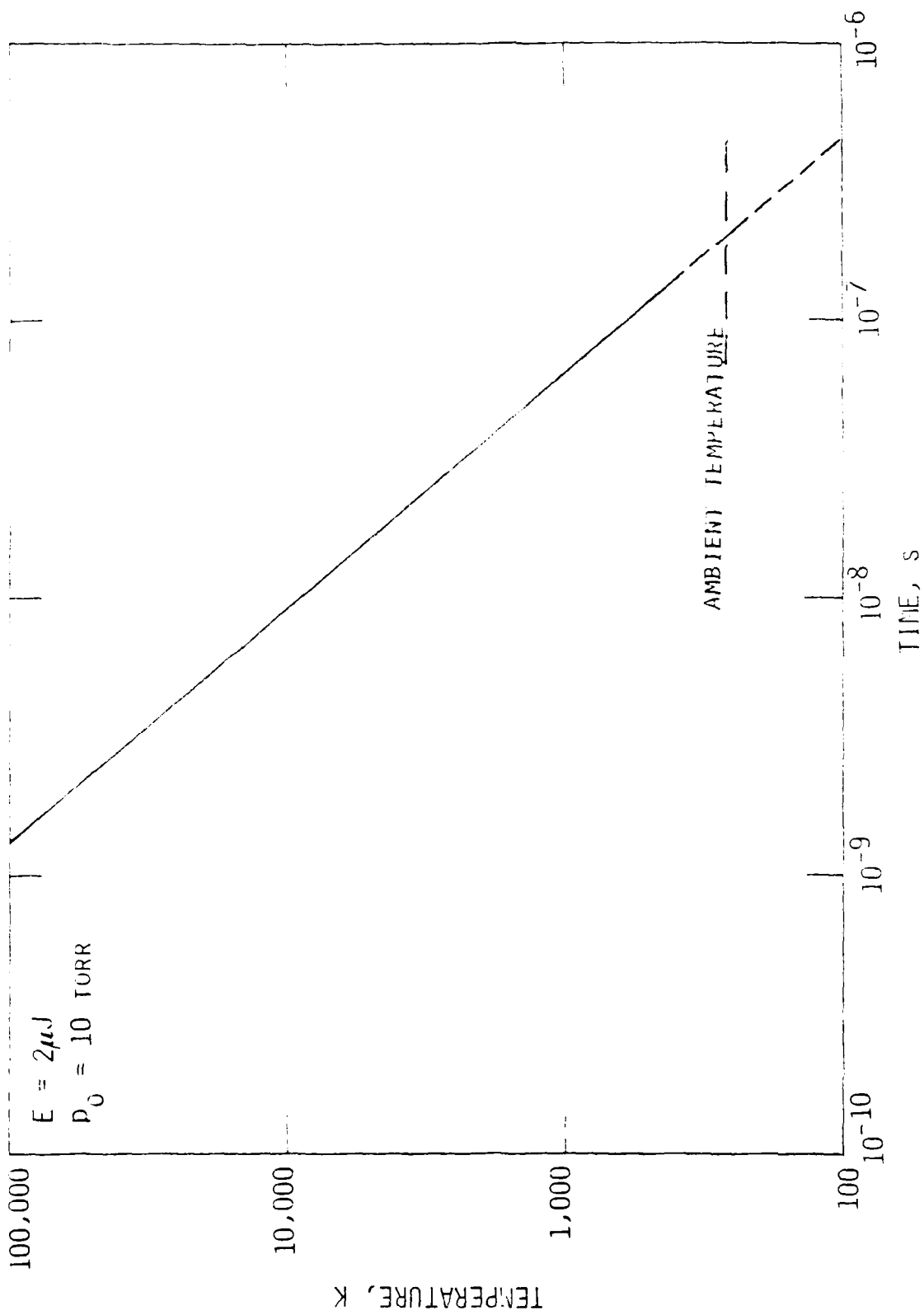
Fig. 12 Temperature behind shock vs. time.
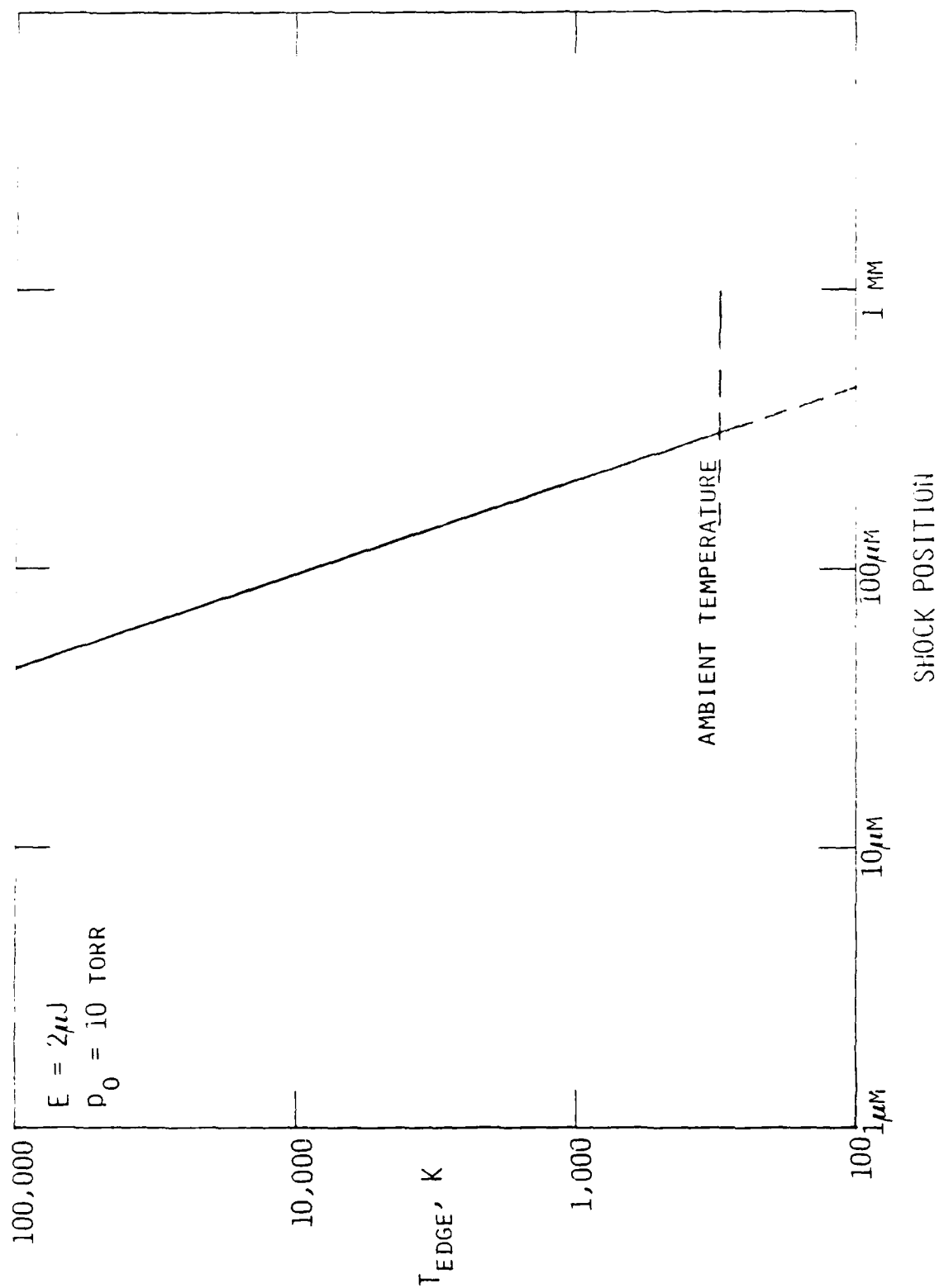
Fig. 13 Temperature at shock front vs. shock position.
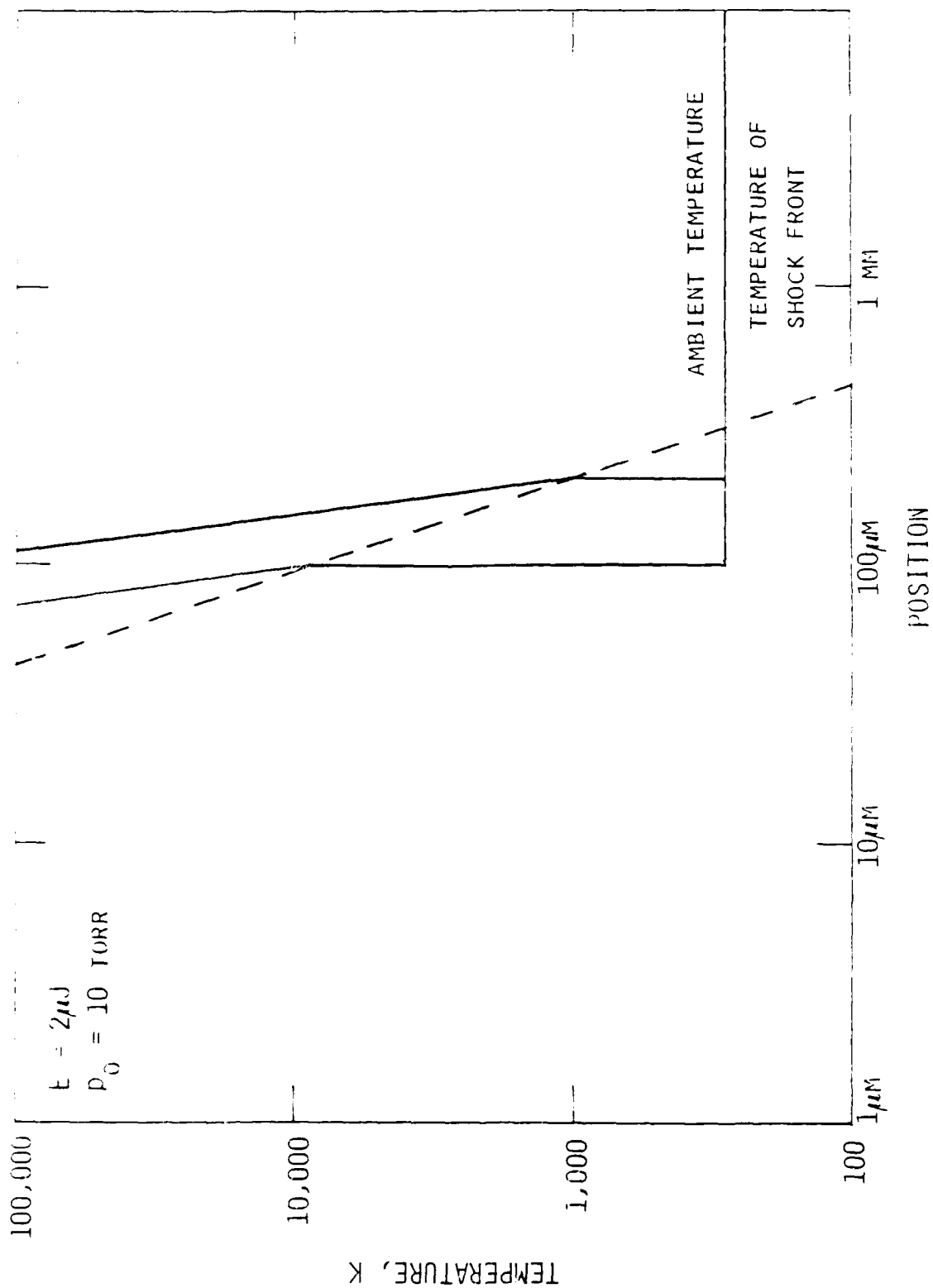
Fig. 14 Temperature profiles within shock when shock is at 100 μm and 200 μm.
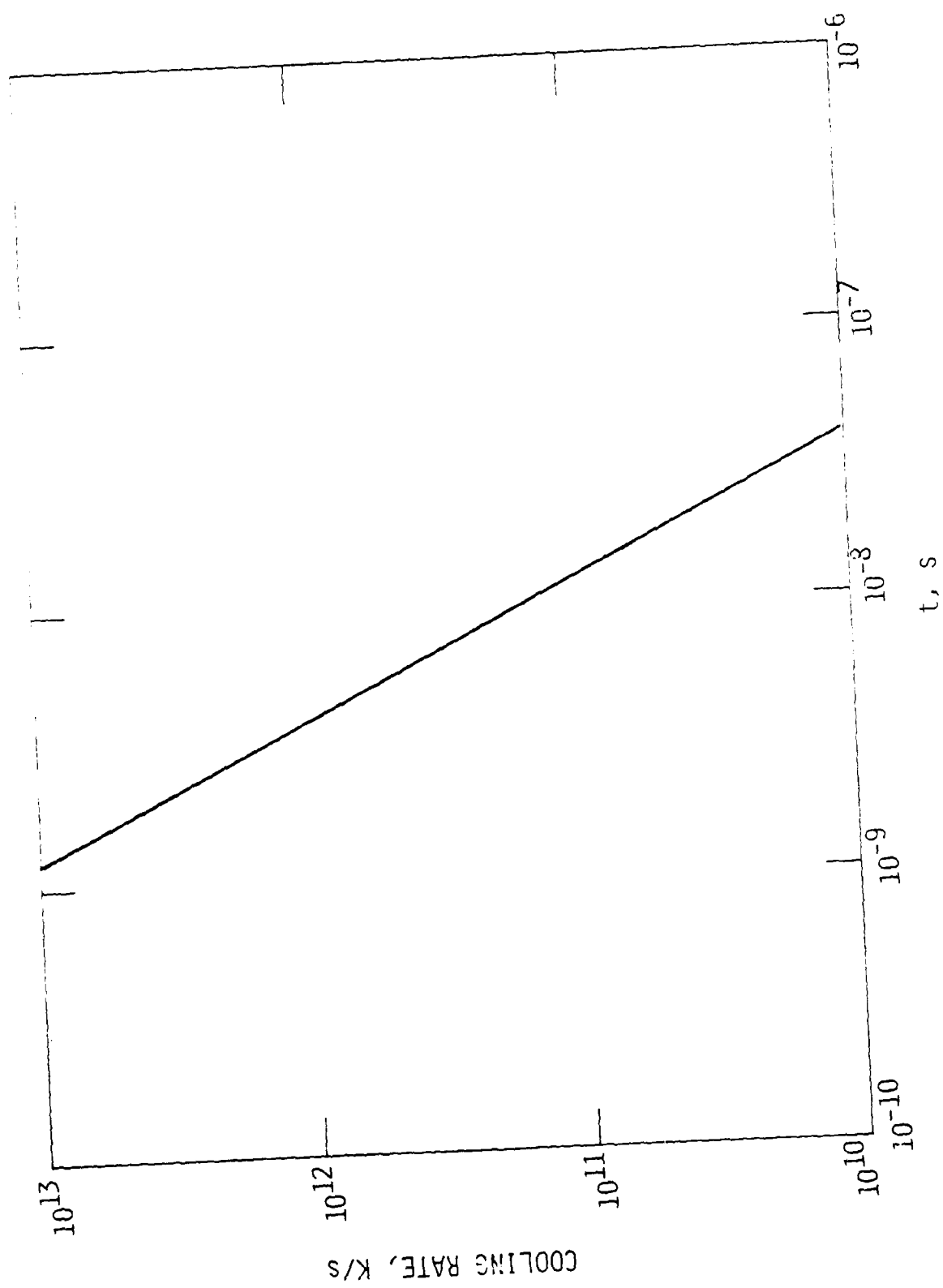
Fig. 15 Cooling rate versus time.

2-D Expansion

The approximately f/6 laser beam creates a breakdown region longer than it is wide. Hence, it is reasonable to model the breakdown as an expansion from a line. The computation is done by computing energy deposited per centimeter. In this case it is the 2×10^{-6} J discussed above over the depth of field (580 μm). The following figures are straight forward applications of the formulas given above.

$$r_s = Kt^{1/2} \qquad\qquad 4.1$$

where $K = 65 \frac{cm}{s^{1/2}}$ for $E = 2 \times 10^{-6}$ J along 580 μm.

This result is plotted in Fig. 16.

The shock front pressure is given by

$$p_s = \frac{2}{\gamma+1} \rho_o \left(\frac{dr_s}{dt}\right)^2 \qquad\qquad 4.4$$

so

$$p_s = 1.5 \times 10^{-2} \frac{1}{t}$$

for $\gamma = 1.4$ and this is plotted in Fig. 17.

The temperature is computed using the strong shock approximation and is plotted in Fig. 18 as a function of time and in Fig. 19 as a function of shock radius.

The cooling rate of the gas which is originally at the shock front at the specified time on the *abscissa* is given in Fig. 20. For example, at 20 ns, the gas at the shock front was 2,800 K (see Fig. 19) and this gas cools at a rate of 4×10^{10} K/s (see Fig. 20 at t = 20 ns). Within a factor of 2, this cooling rate applies to all the shocked gas at each specific time.
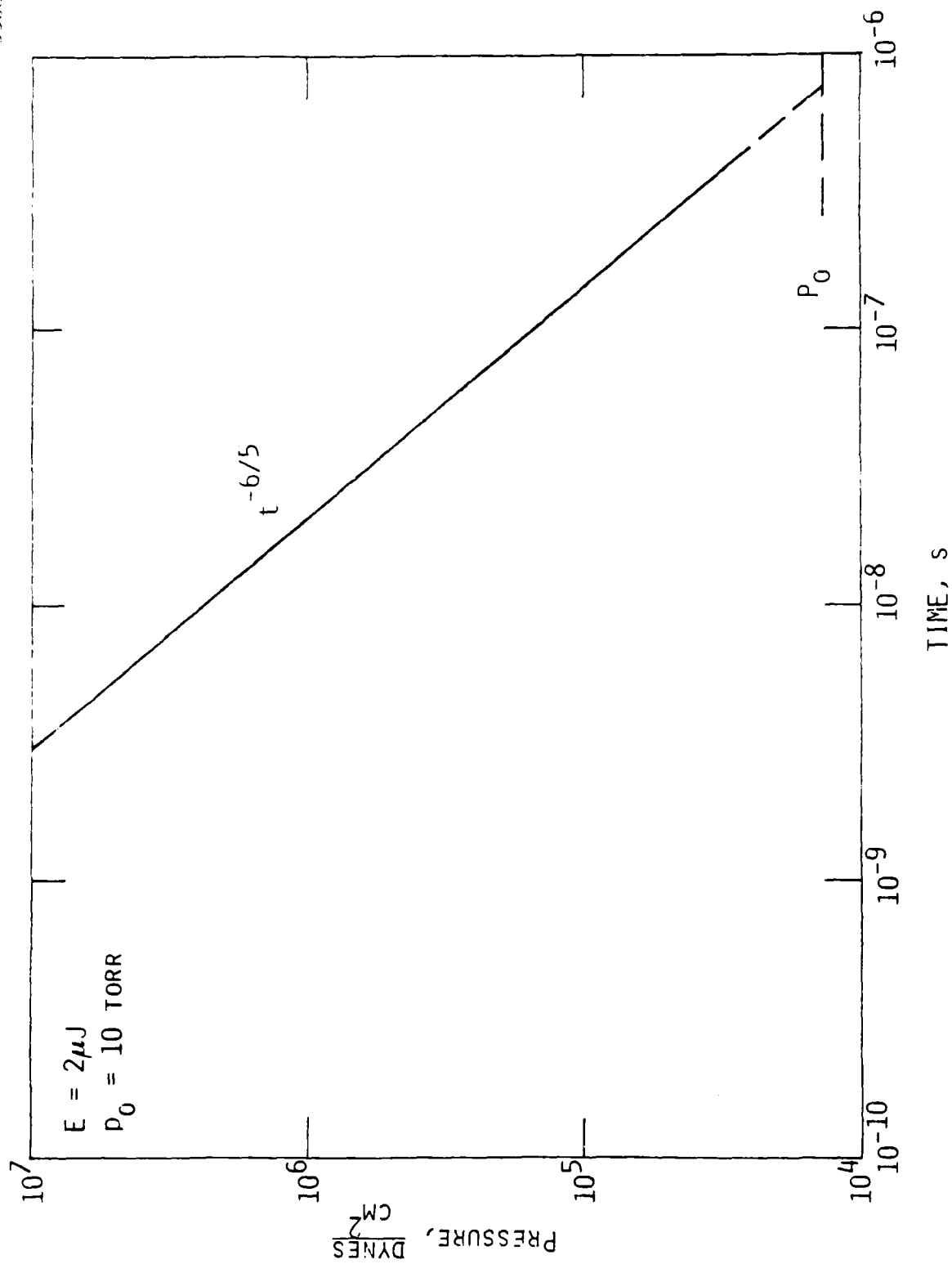
A-32
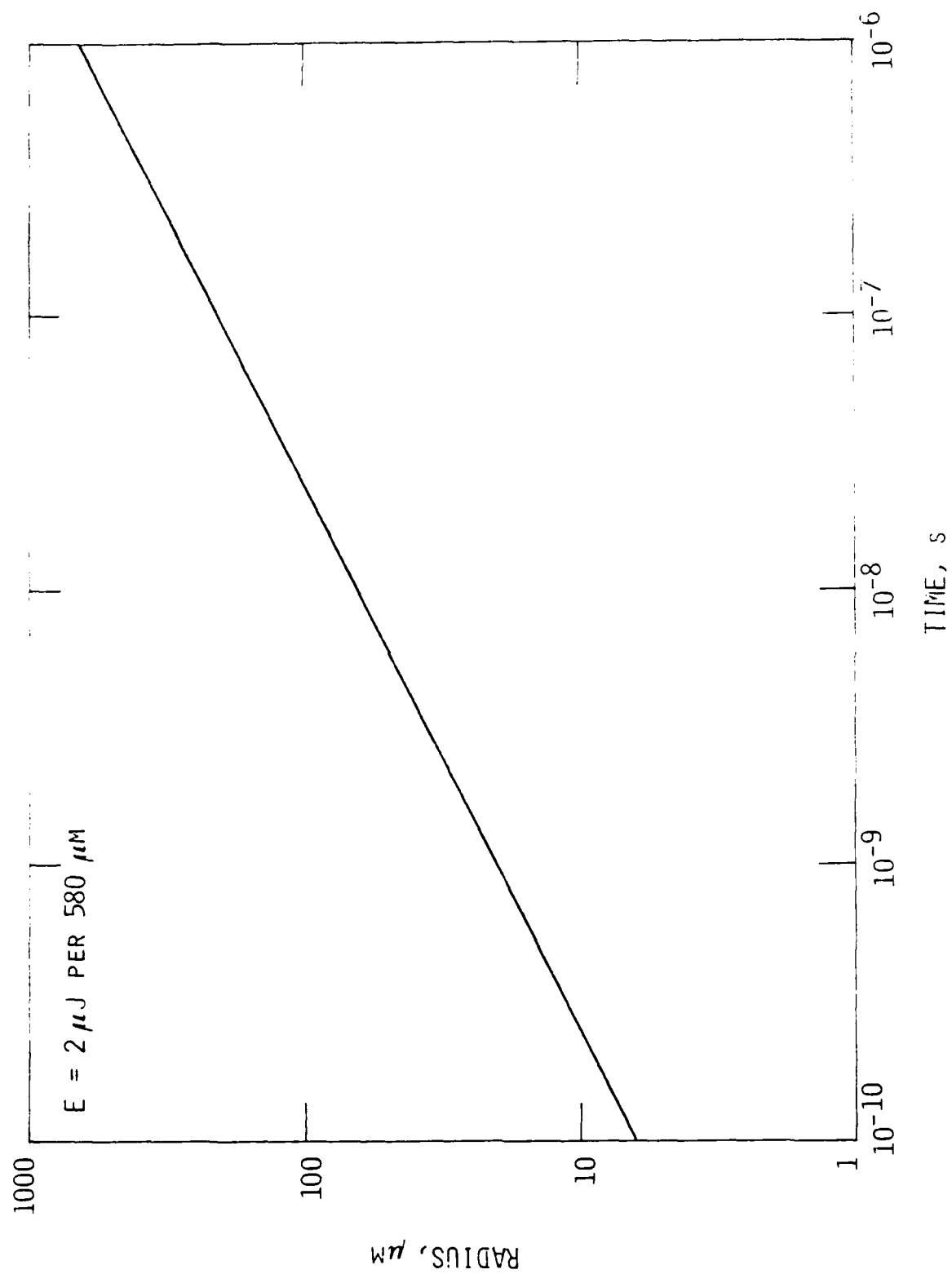
Fig. 16 Shock radius vs. time for 2-D expansion.
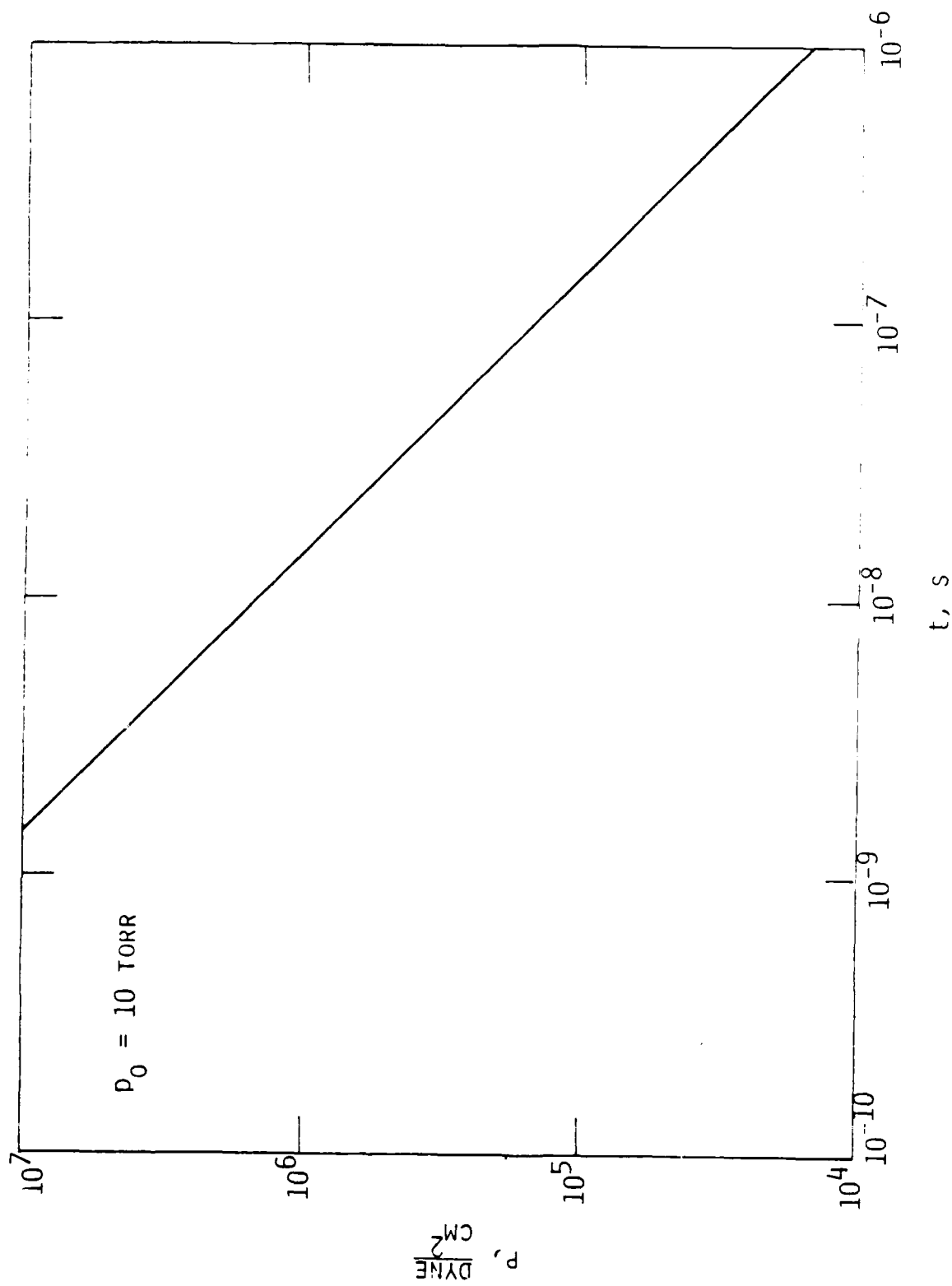
Fig. 17 Shock pressure vs. time.
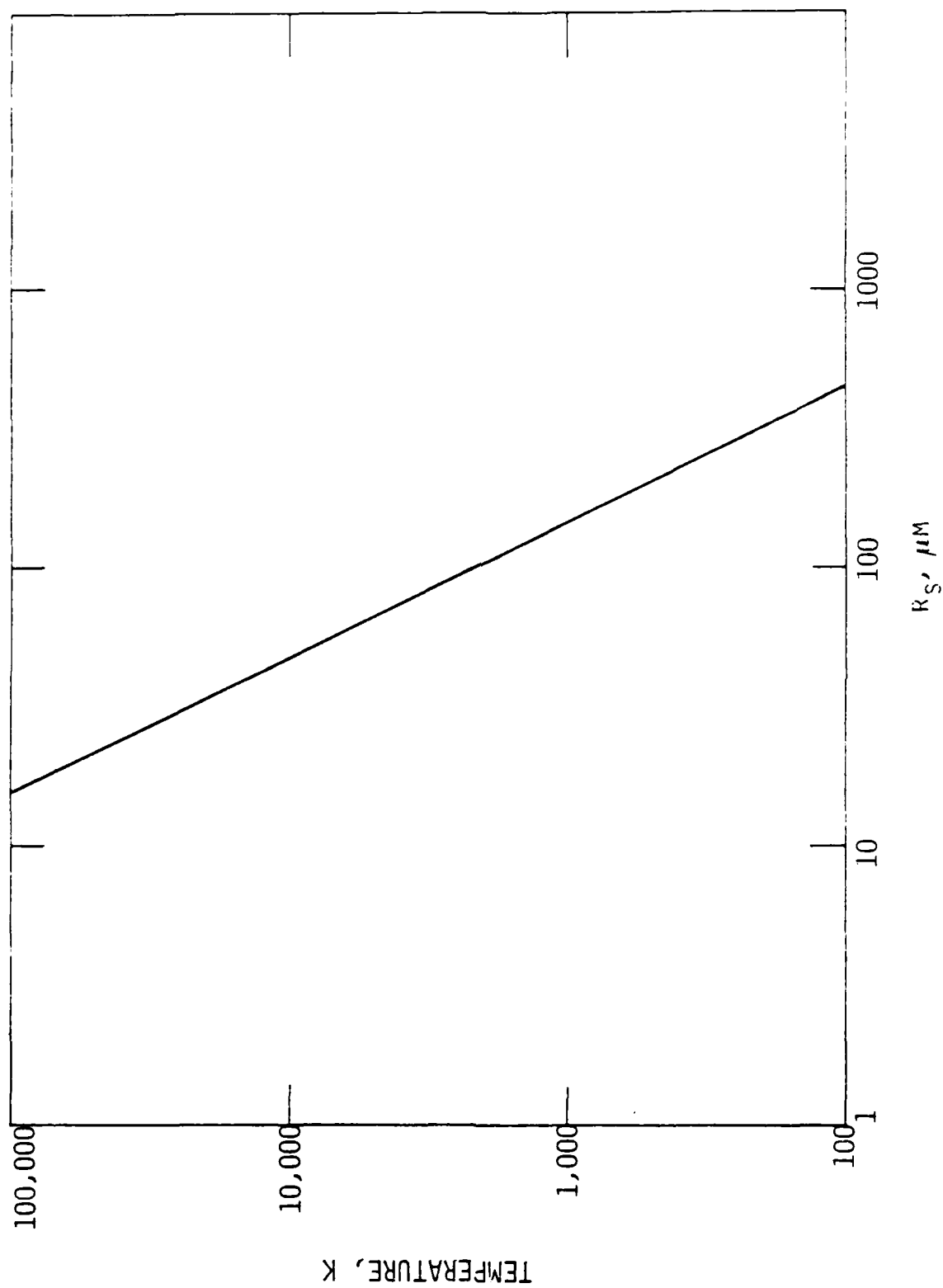
Fig. 18 Temperature at shock front.

TEMPERATURE, K

R_S, μM
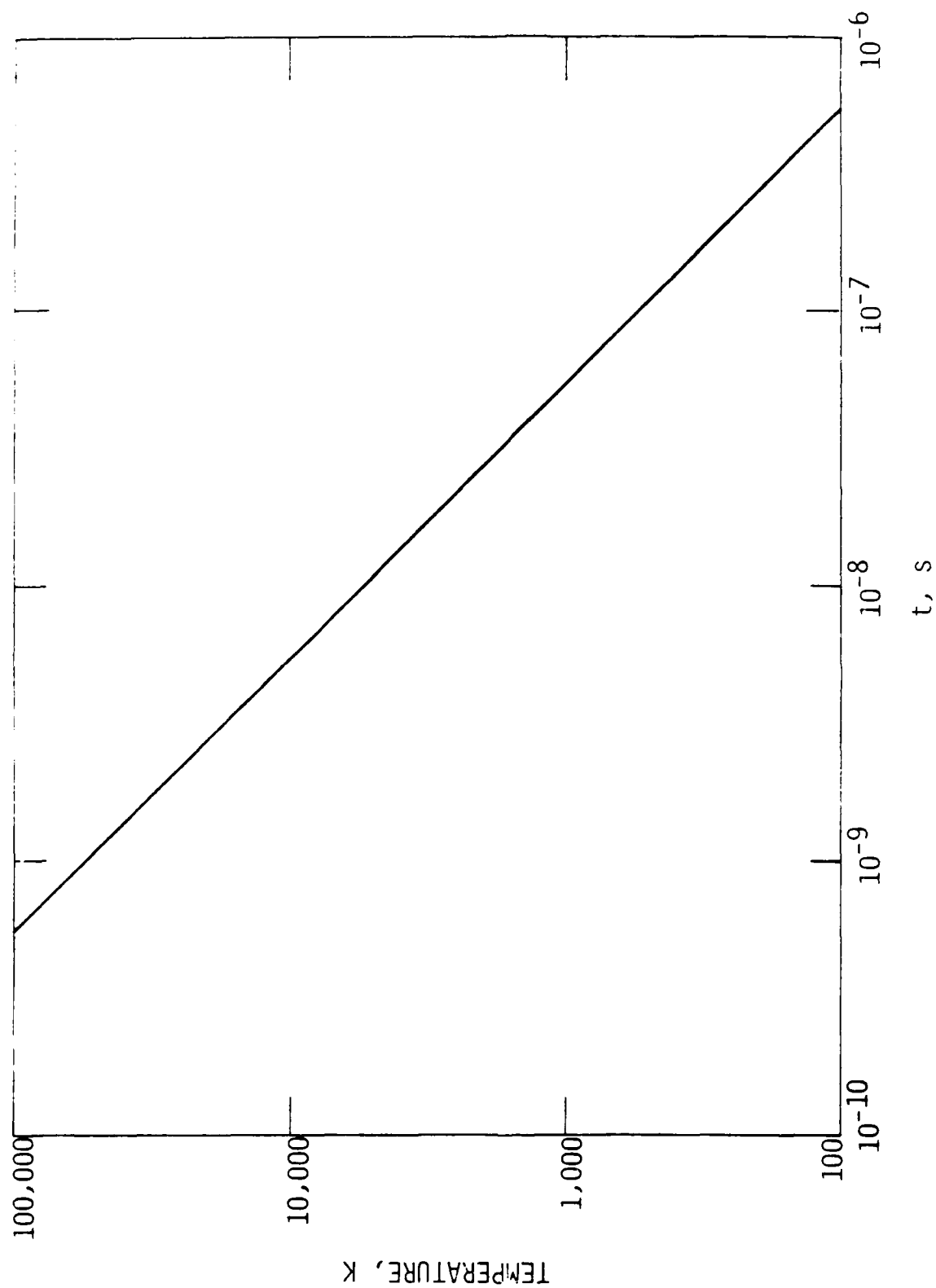
Fig. 19 Temperature at shock front vs. time.
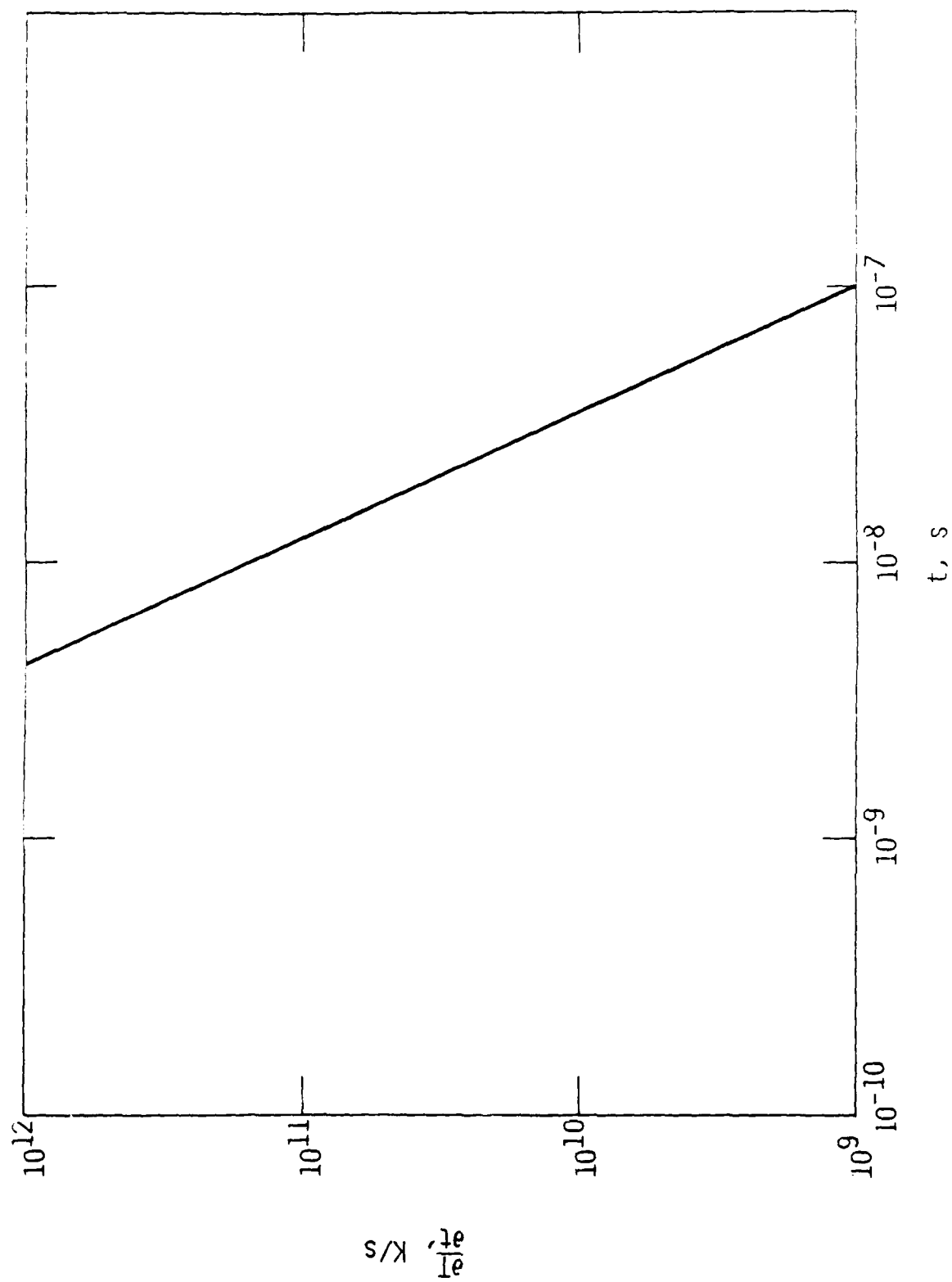
Fig. 20 $\dot{T}$ vs. t for gas initially at the shock front.

Variable Energy Blast Waves

Equation 4.1 provides a general formula for the position of the blast wave shock front.[7] We will compare the computed shock front position for an instantaneous release of energy and a finite release rate. To perform this comparison we'll compare the shock position at the time when the same amount of energy has been delivered to the gas over a finite time or instantaneously.

We'll evaluate r_S for the cases where

$$E_\alpha(\beta=0) = W_\alpha t^0$$

and   4.3

$$E_\alpha(\beta) = W_\alpha t^\beta .$$

Examining Eq. (4.1), we will calculate the ratio of shock radii for the case $E_\alpha(\beta=0) = W_\alpha(\beta)t^\beta$. Using Eq. (4.1) to compute the ratio, we have

$$\frac{r_s(\beta=0)}{r_s(\beta)} = \left[\frac{n^2(\beta)J_o(\beta)}{n^2(\beta=0)J_o(\beta=0)}\right]^{1/\alpha+3}$$ 4.7

We note the ratio is a constant independent of energy and is close to unity (1.08 for $\alpha=2$ and $\beta=1$). Hence, the shock wave will expand to nearly the same location independent of the rate of energy deposition.

5. DATA ANALYSIS

5.1   Introduction

The data taken by John Swanton to characterize the emission from the spark was analyzed for trends.[2] Data was taken with the Nd^{+++}-YAG laser operating at an output level so that breakdown was consistent at a specific pressure and also at twice that output energy. Measurements were made to characterize the laser induced sparks in N_2 gas at 3, 5, 10, and 20 torr.

The 0.5 m Spex spectrometer was operated in zero order viewing the spark through a sapphire window. The spark was imaged using a CaF_2 lens onto the entrance slit with 1:1 magnification. The photomultiplier tube (RCA C31034) has a rather uniform responsivity from 200 to 900 nm. The slit width was 10 µm and the height was 1.2 mm. Scans were made horizontally along the optical axis and vertically perpendicular to the optical axis.

5.2   Horizontal Scans

The scans along the optical axis appear Gaussian. Hence, the 1/e width was used to characterize the lateral extent of the spark. Figure 21 is a sample trace of the variation in signal with horizontal position. The PMT was operated using the input impedance of an oscilloscope as the load resistor and the voltage was read off the oscilloscope screen. Because the RC time constant was long compared to the spark duration, the electronic circuit acted as an integrator for the emitted light.

Figure 22 shows the reduced data of the full width at the 1/e points versus N_2 pressure with the laser operated at a flux level to cause consistent breakdowns and also at an output energy twice that level. The observed size of the luminous zone is somewhat dependent on the pressure and power level. We do note that the size of the luminous zone is always longer than the minimum laser energy deposition length. Because the luminosity peaks approximately 10's of nanoseconds after the laser pulse has terminated the plasma has had time to expand and excite molecules that were out of the laser beam.
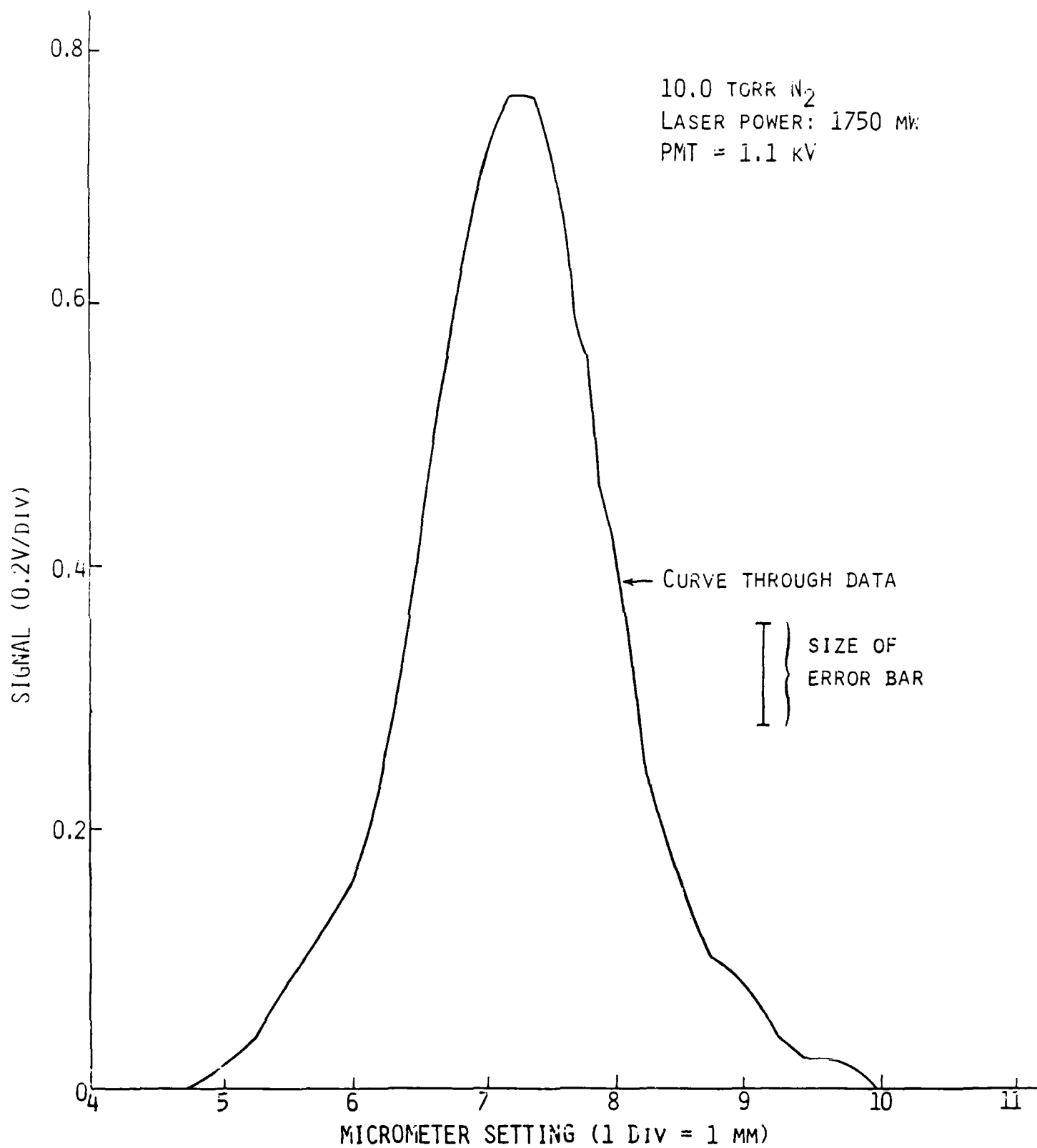
Fig. 21 Signal vs. micrometer setting.

A nominal line showing the depth of field for the f/6 laser beam has been included in Fig. 22. This line is deduced from Fig. 9 as the distance along the optical axis where 50% the energy contour from geometrical optics matches the minimum laser beam diameter given by the laser beam divergence. A nominal depth of field of 580 µm is calculated. It is expected that the luminous plasma length would be at least this long and above threshold, even greater than this. Thus data support our understanding of plasma lengths.

5.3 Vertical Scans

The spark diameter is more difficult to determine precisely because the slit height was comparable to the spark dimension. The lens and cell were vertically translated to obtain the measurements. Figure 23 is a typical trace at the same conditions as Fig. 21. We note that the characteristic dimension of the spark height is on the order of 1 mm. Because the translation (1 mm) is much less than the beam size (1 cm) or lens diameter, (~2.5 cm), the laser beam is not expected to be significantly affected by the translation of the lens.

The vertical height of the slit being 1.2 mm does not allow an accurate determination of the radius of the luminous spark. However, a comparison of the results compared to what would be observed if the spark had been a Gaussian irradiance distribution indicates that the 1/e width is approximately 0.4 mm + 0.2 mm. This dimension is much larger than the 14 µm radius of the laser beam divergence. This is undoubtedly because the laser heated gas has expanded and shock heated additional gas to a radius of hundreds of microns before cooling. As predicted by blast wave theory (Section 4), an estimate of the volume from which radiation was measured is 10^{-4} cm^3. This is to be compared to a deposition volume of 10^{-8} cm^3 for the laser beam.

5.4 Optical Radiation

The measured signals were analyzed to obtain the optical radiation versus pressure. The measured voltage is proportional to the optical energy radiated by the spark in the pass band determined by the optical system. The radiated energy was computed assuming the spark is optically thin and the radiation is isentropic. Nominal values of 15% for the PMT quantum efficiency, 10% transmission of the spectrometer (grating operated in zero order) and PMT gain of 2.6×10^4 were used. Figure 24 is a plot of the radiated energy versus nitrogen

A-41
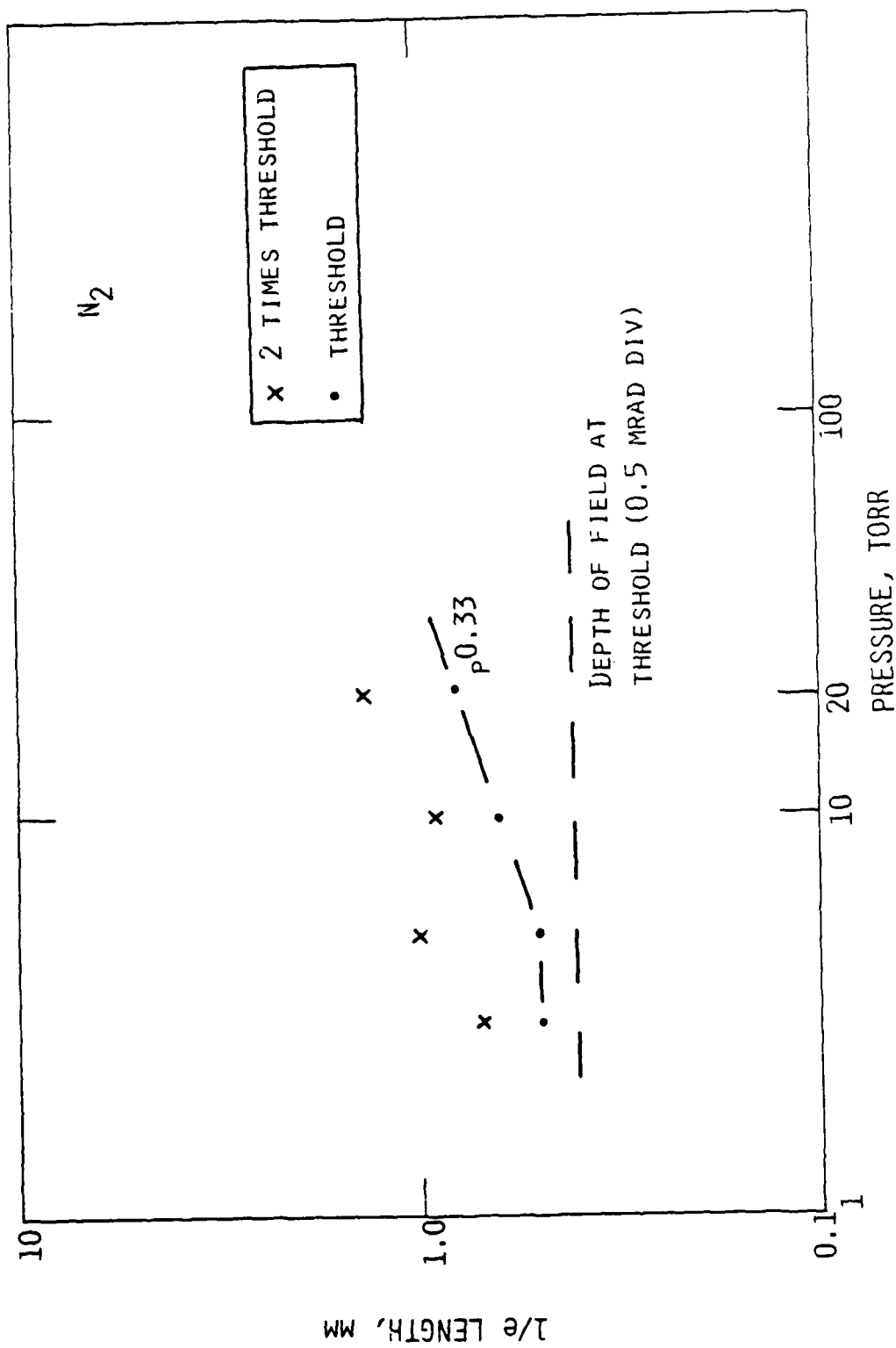
Fig. 22 Spark 1/e length vs. pressure.
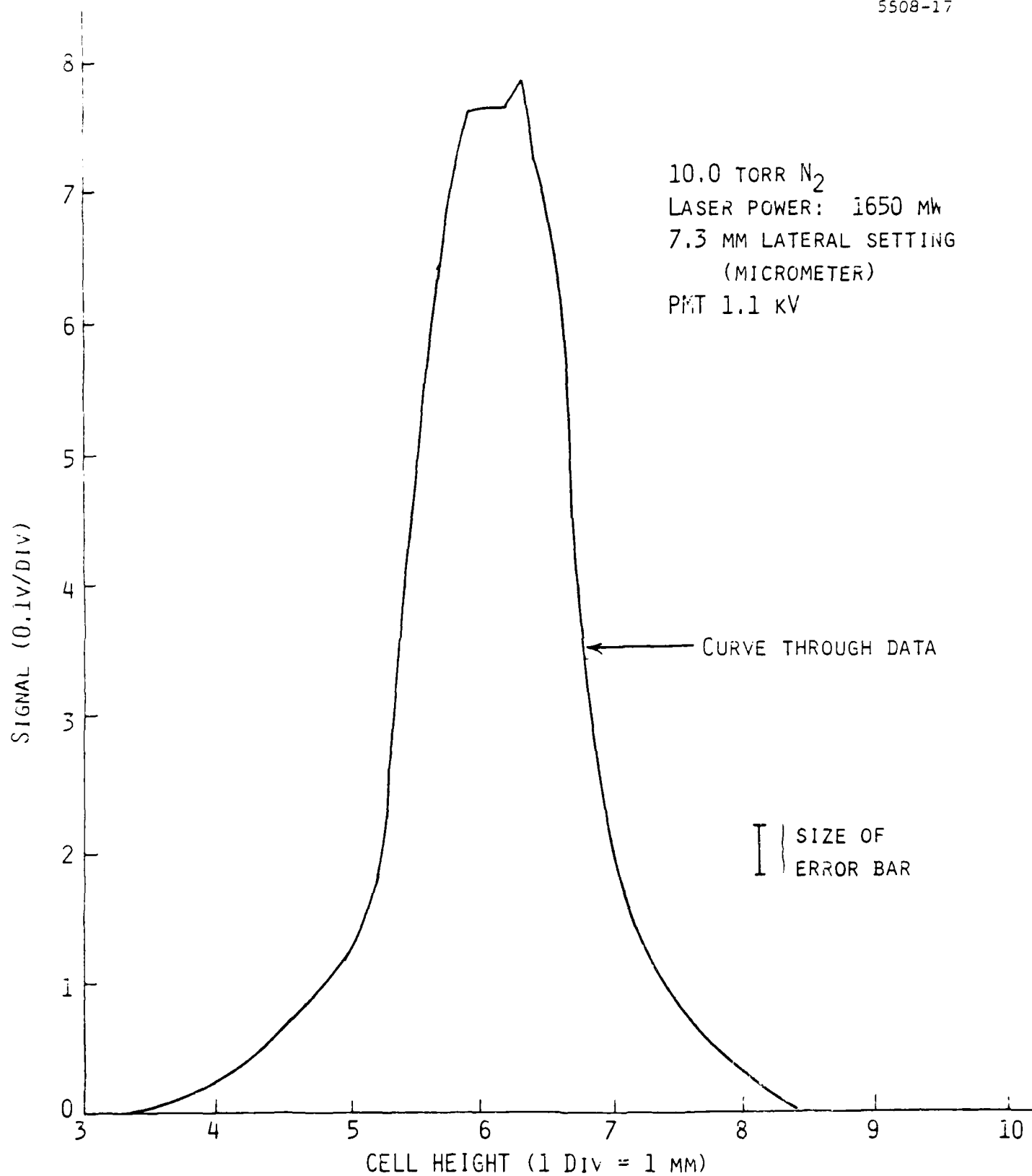
Fig. 23 Signal vs. cell height.
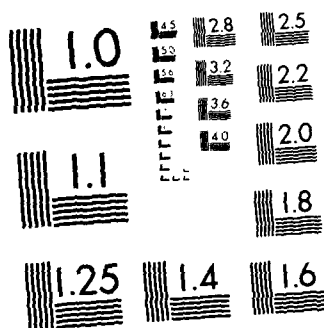
gas pressure in the test cell for the laser operated at an output energy just sufficient to obtain consistent sparks and at twice that output energy. The data shows a cubic pressure dependence. Because the laser energy is also changing with pressure, it is also instructive to plot the radiated energy normalized by the incident laser energy. This behavior is shown in Fig. 25. This ratio is a radiant efficiency of the spark. Because increased laser energy is needed as the pressure is reduced to obtain a spark, the pressure dependence in Fig. 25 is stronger than in Fig. 24. The data to show irradiance vs. pressure is shown in Fig. 26. Though the data was taken to characterize the optical radiation rather than measure breakdown thresholds, we have compared this data with that taken by Roy Lucht. This comparison is shown in Fig. 27. We note the close agreement between the two sets of data at 10 and 20 torr. John Swanton undoubtedly used a higher laser energy to obtain consistent breakdowns as compared to Roy Lucht's breakdown thresholds at 3 and 5 torr.
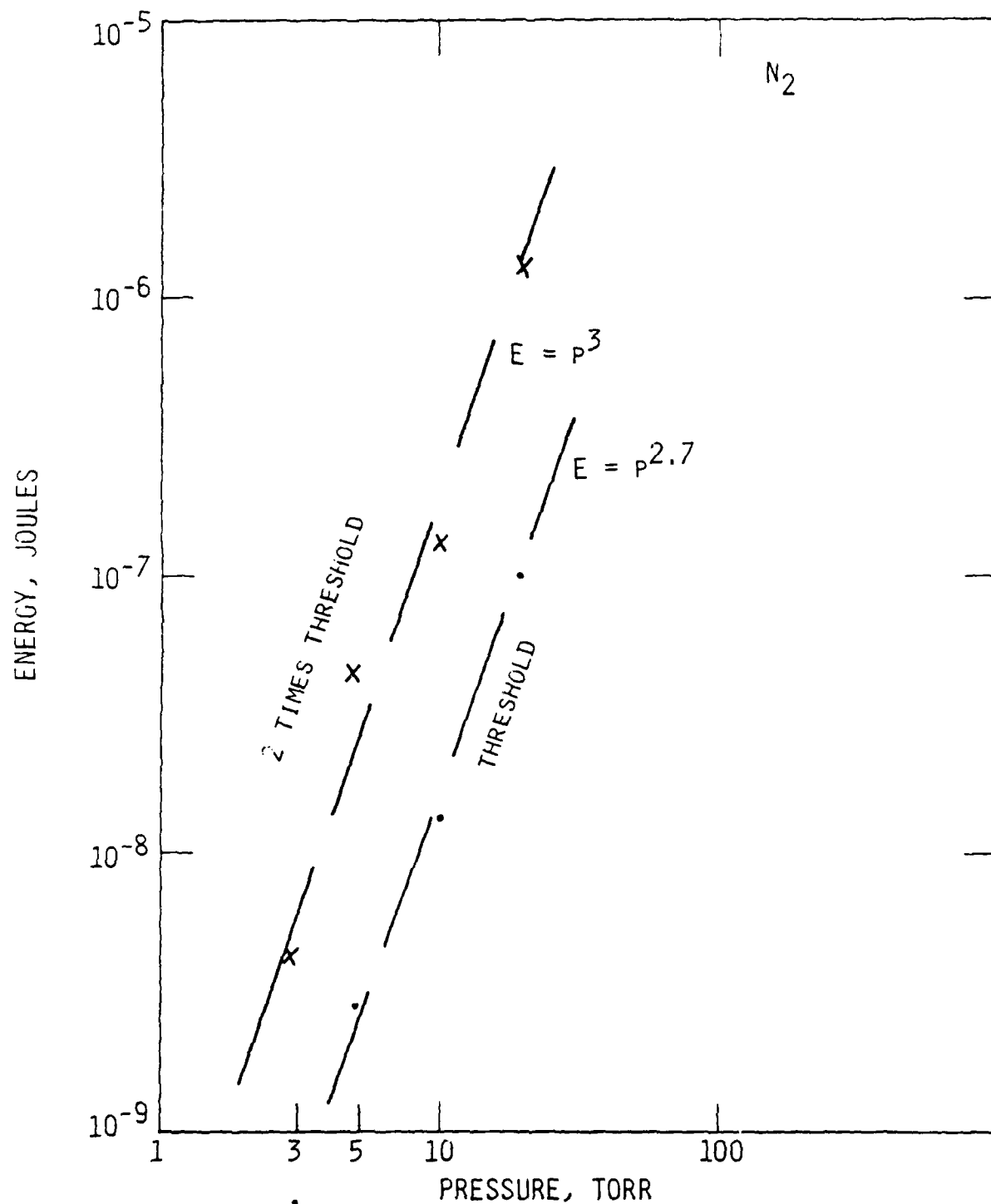
Fig. 24   Radiated energy vs. pressure.
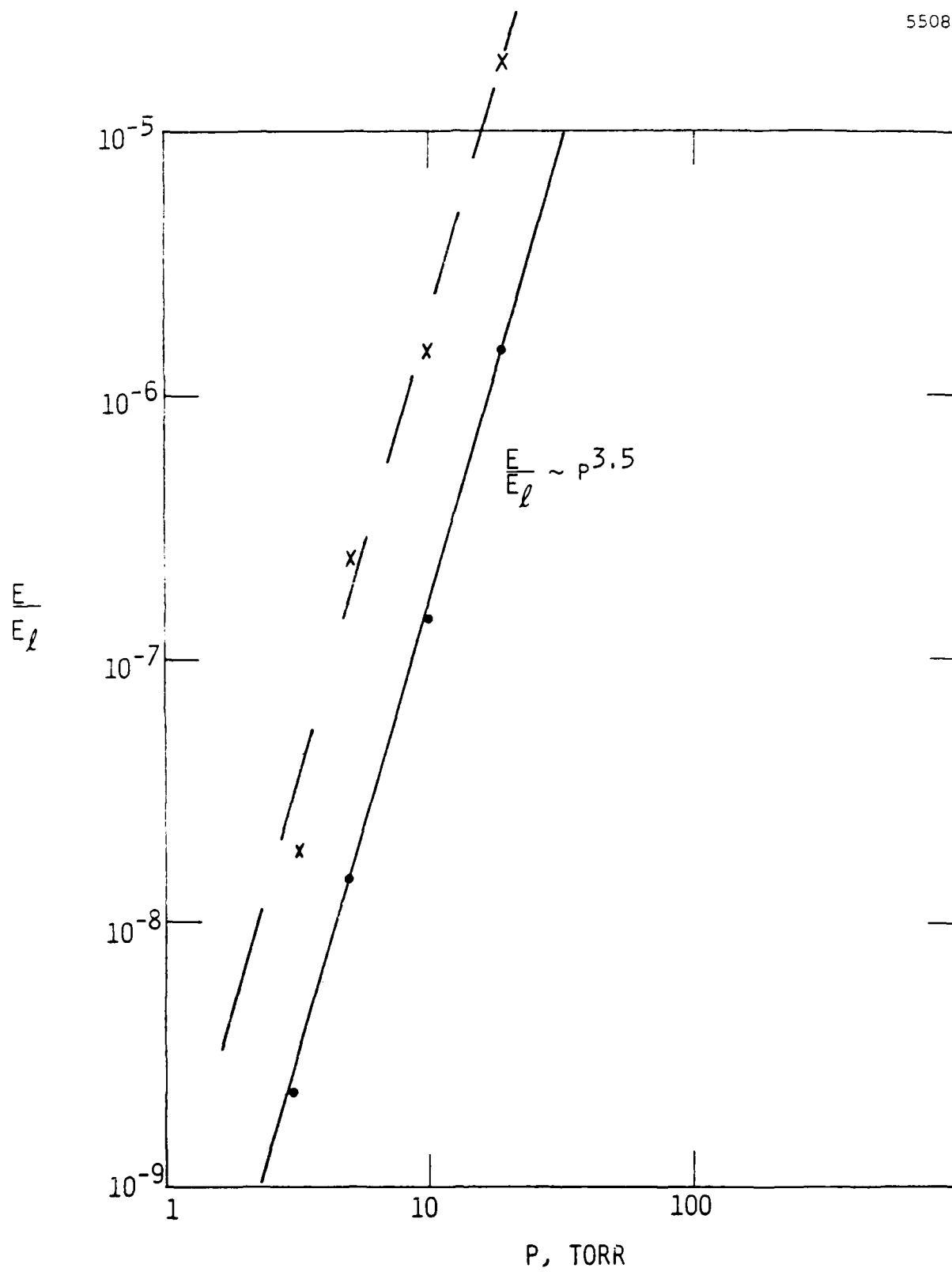
Fig. 25 $\frac{E}{E_\ell}$ vs. pressure.
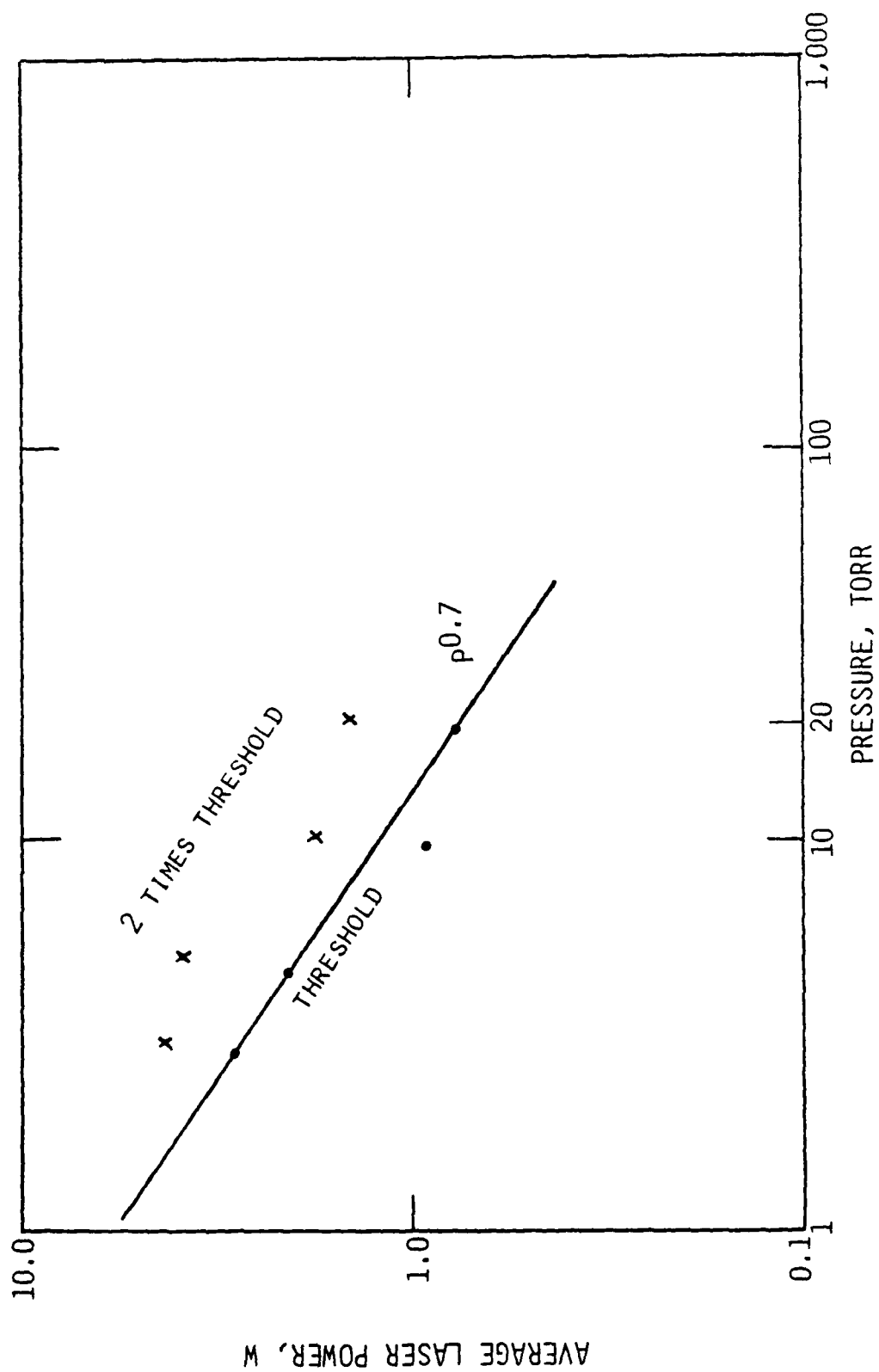
Fig. 26 Threshold laser power vs. N_2 pressure.

A-47
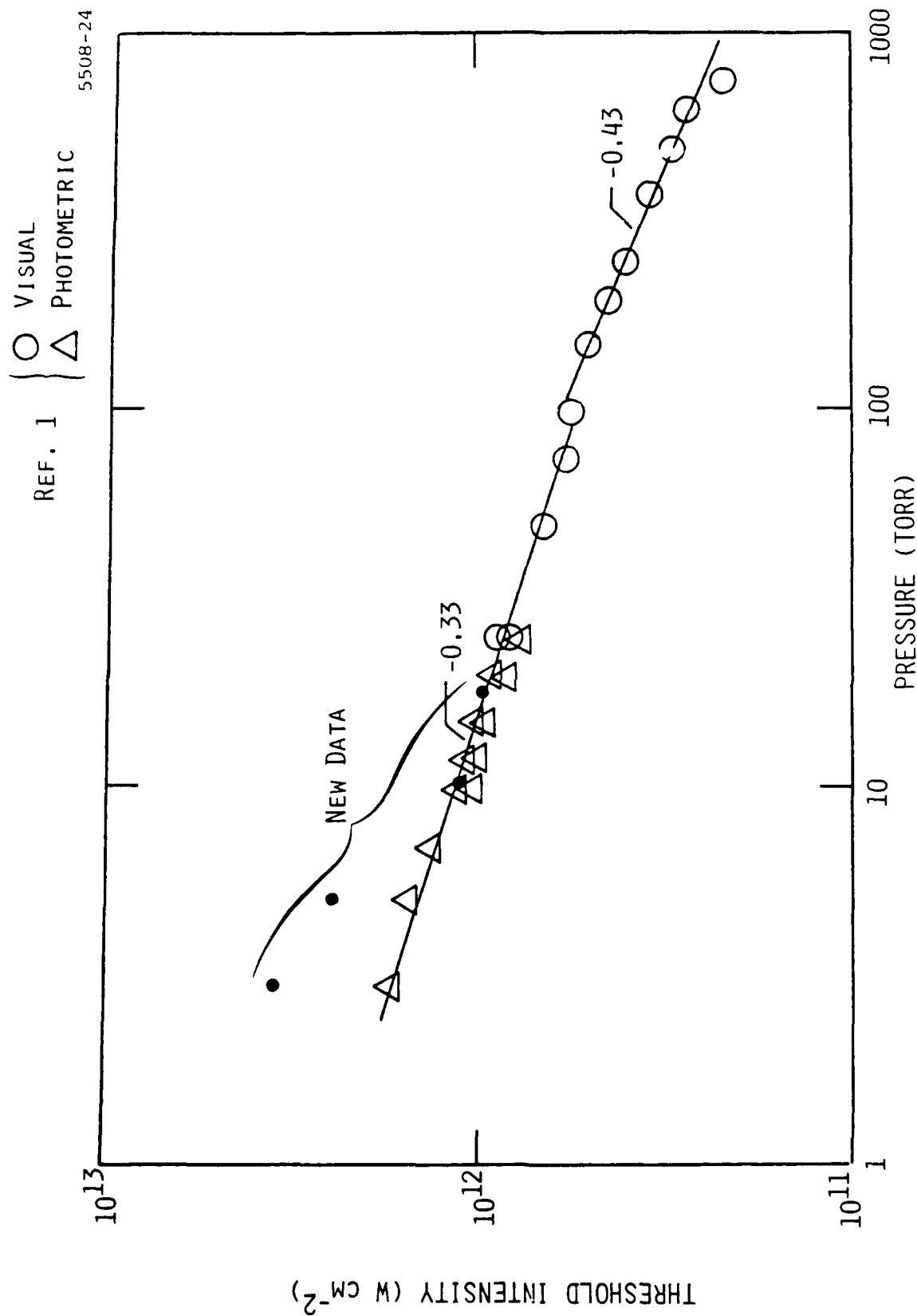
Fig. 27 N_2 breakdown thresholds.

6. SUMMARY

Scoping experiments were done by Roy Lucht to identify breakdown thresholds, radiating species, and time histories of radiating species for low pressure gases. An average color temperature was computed from integrated spectral measurements. The results of these studies indicated that more careful studies of the radiative properties and an analysis of the phenomenon was warranted. Section 3 of this report outlines a series of radiometric measurements that could be made to quantify the spark radiation in radiometric units. Spatially, spectrally, and temporally resolved measurements can be analyzed to obtain local color temperatures of radiating species.

Section 4 of this report discussed blast wave physics and its application to this problem. Blast wave solutions were calculated for 3-D and 2-D expansions. The shock radius for an instantaneous release of energy was compared to a constant energy input and found to be the same within 8% when the input energies are equal. Hence, the time scale over which energy is deposited does little to affect the position of the shock wave. Using the computed energy to obtain a 30,000 K plasma, the blast wave will expand to many laser beam diameters before the laser pulse is over. Blast wave theory provides estimates of the temperature-time history as the gas expands.

The data reduction of the integrated radiometric measurements of the spark radiation shows a strong pressure dependence. The radiometric efficiency (Joules of radiated energy/Joules of laser energy) scaled as the 3.5 power of ambient pressure.

During the next phase of the program, we will model the radiation emitted from the spark. Because the time scale for expansion is short, the plasma may not remain in equilibrium. Calculations will be made of the optical radiation as a loss mechanism as well as cooling due to expansion. The work in the next phase is aimed at providing a physical understanding of the radiation levels and decay time of the laser produced spark.

REFERENCES

1. Lucht, R., unpublished.

2. Swanton, J., unpublished.

3. Nichols, D. B. and Hall, R. B., "Laser-Beam Attenuation for Spatial Profiling of Small Focal Spot," Rev. Sci. Instrum. 51, 1131 (1980).

4. Wiese, W., Smith, M. and Glennon, B., "Atomic Transition Probabilities," Vol. 1, National Bureau of Standards, NSROS-NBS4, May 1966.

5. Griem, H., Plasma Spectroscopy, McGraw Hill, New York (1964).

6. Zel'dovich, Yn. B. and Raizer Yn. P., Physics of Shock Waves and High Temperature Hydrodynamic Phenomena, Academic Press, New York (1966).

7. Dabora, E. K., "Variable Energy Blast Waves," AIAA J 10, 1384 (1972).

APPENDIX B

THEORETICAL ANALYSIS OF NITROGEN PLASMA RADIATION
IN THE LINUS EXPERIMENT

This appendix is TR-386, prepared as the Fifth Quarterly R&D Status Report
for Contract No. F19628-82-C-0050,
1 April through 30 June 1983

COCHISE ATMOSPHERIC NITROGEN/OXYGEN EXCITATION STUDIES

Theoretical Analysis of Nitrogen Plasma Radiation in the LINUS Experiment

Fifth Quarterly Report
For the period 1 April 1983 - 30 June 1983
Under Contract No. F19628-82-C-0050

G. Weyl, P. E. Nebolsine and W. T. Rawlins

Prepared for

Air Force Geophysics Laboratory/OPR
R. Armstrong, Contract Monitor

Prepared by

Physical Sciences Inc.
Research Park, P.O. Box 3100
Andover, MA 01810

Sponsored by

Electronic Systems Division PKR
Air Force Systems Command
U.S. Air Force
Hanscom AFB, MA 01731

This report is intended only for the internal
management use of the contractor and the Air Force

TABLE OF CONTENTS

LIST OF ILLUSTRATIONS

LIST OF ILLUSTRATIONS (Continued)

LIST OF ILLUSTRATIONS (Continued)

LIST OF ILLUSTRATIONS (Continued)

1. INTRODUCTION

A series of experiments have been carried out and reported[1] under the LINUS (Laser Induced Nuclear Simulation) program in which visible radiation emitted by a nitrogen plasma in the pressure range 10 to 100 torr was measured. The plasma was created through laser-induced breakdown in the focus of a $\lambda = 1.06$ μm Nd:Yag laser beam. The plasma, after expansion to pressure equilibrium, was found to be of cigar shape with length $\cong 0.45$ mm and diameter ≈ 0.2 mm. The purpose of this investigation is to develop a physical model of the plasma that will explain the major features of the radiation data. In particular, time integrated spectra of plasma radiation indicate a continuum in the visible which has a peak at 4500 Å. Such a spectrum is shown in Fig. 1. Previous attempts at explaining the features of this continuum as due to electron bremsstrahlung radiation have been unsuccessful. Another series of data involved measurements of the temporal behavior of line radiation, as shown in Figs. 2 through 4. The following observations on line radiation were made that could only be understood for optically thick line radiation.

1) All lines originating from the same ionic species have similar profiles, independent of energy level from which they originate.

2) The decay times increase as one goes from N^{2+} to N^+ and then to N.

3) The higher the pressure the slower is the decay time.

4) The decay time increases as the laser intensity is increased above breakdown threshold.

Previous calculations, however, have shown that all lines are optically thin.[1,2]

The temporal behavior of line radiation and decay cannot be obtained under the assumption of LTE (local thermodynamic equilibrium). The decay times are one to two orders of magnitude longer than the radiative lifetimes of the excited states. A possible explanation, as we shall see further on in this study, is that the population of excited states and radiation from these states are determined by the rate of (three body) recombination. This rate varies as $T_e^{-9/2}$ (T_e = electron temperature) so that the rate of cooling of the plasma determines the rate at which excited states are populated and the level of radiation from those states.

B-1
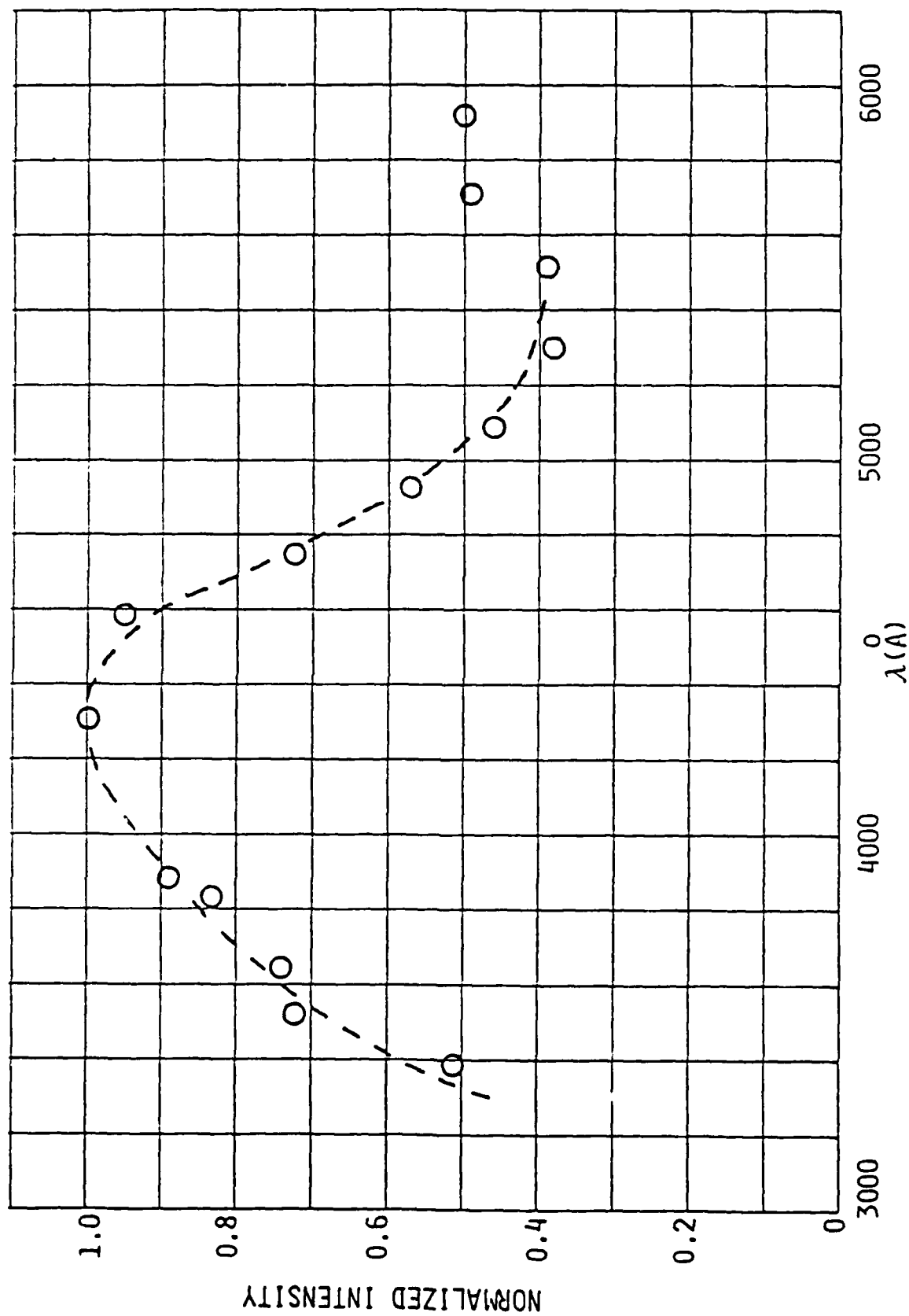
Fig. 1 Continuum spectrum using 125 torr N_2 and $I = 9.8 \times 10^{11}$ W/cm^2.

5195-11
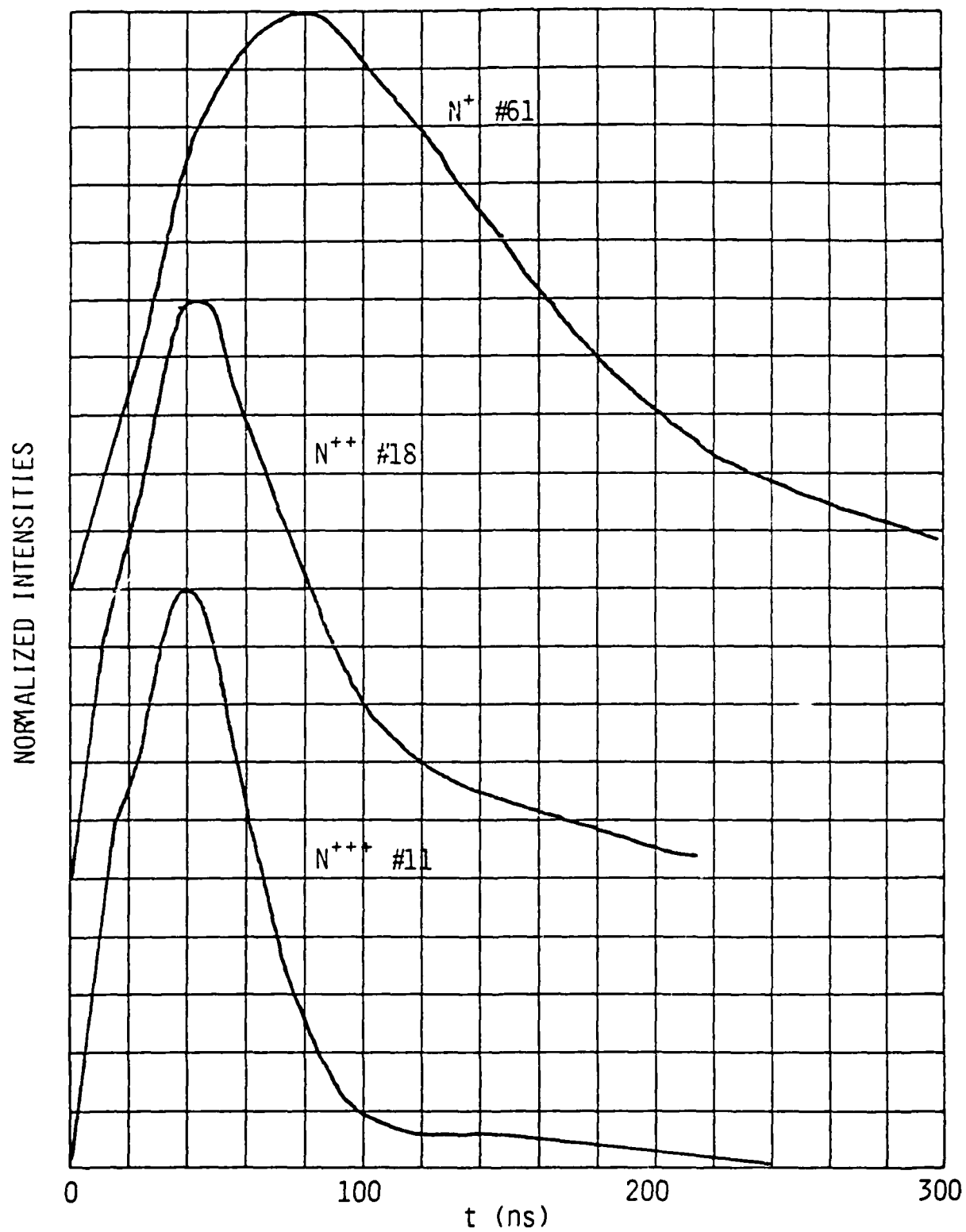
Fig. 2 Line profile using 10 torr N_2 and $I = 2.9 \times 10^{12}$ W/cm^2.
Note curves are normalized and displaced with respect
to each other.

B-3
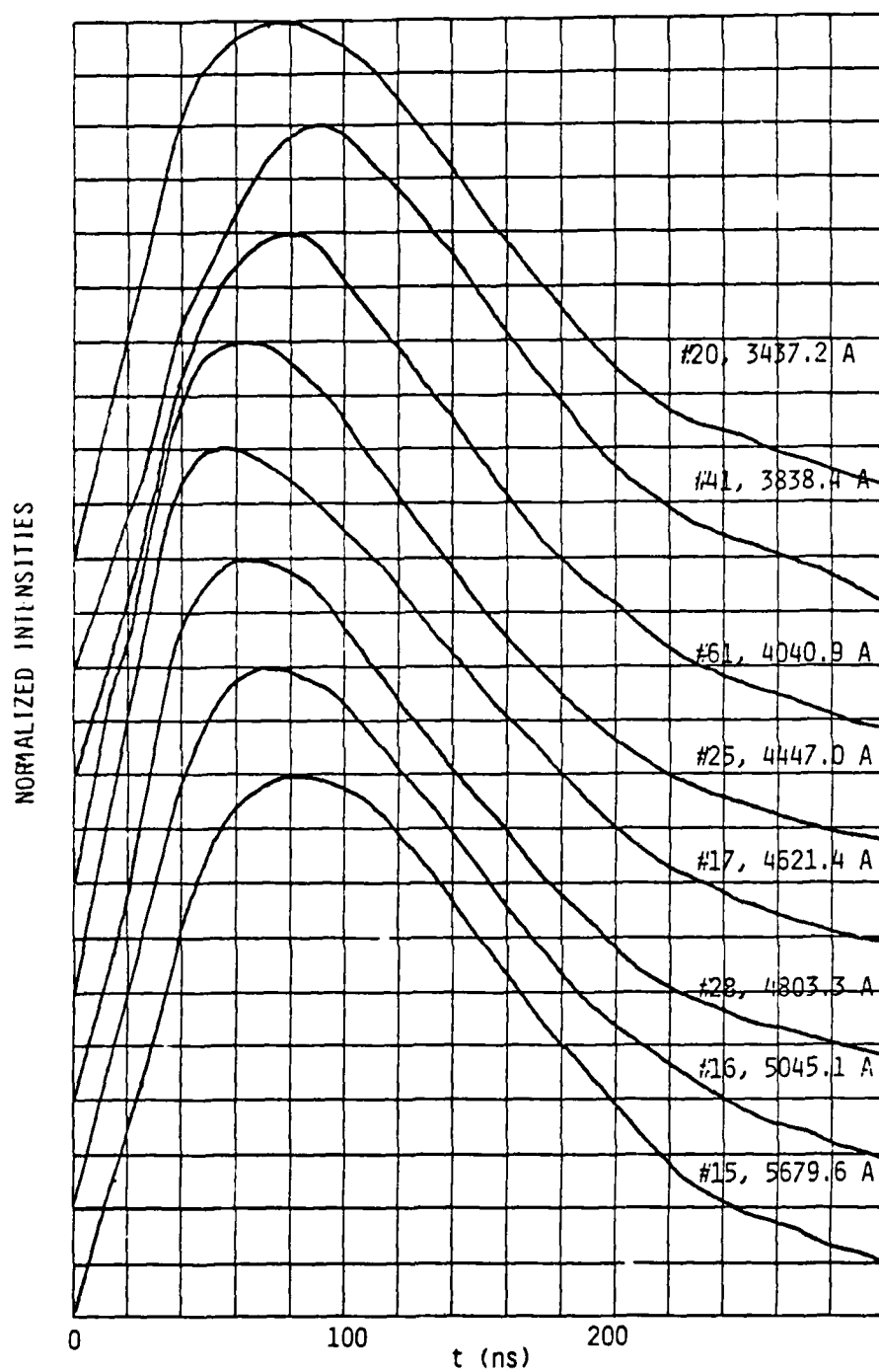
Fig. 3 N$^+$ line profiles using 125 torr N$_2$ and I =
2.9 x 10^{12} W/cm^2. Curves displaced as in
Fig. 2.
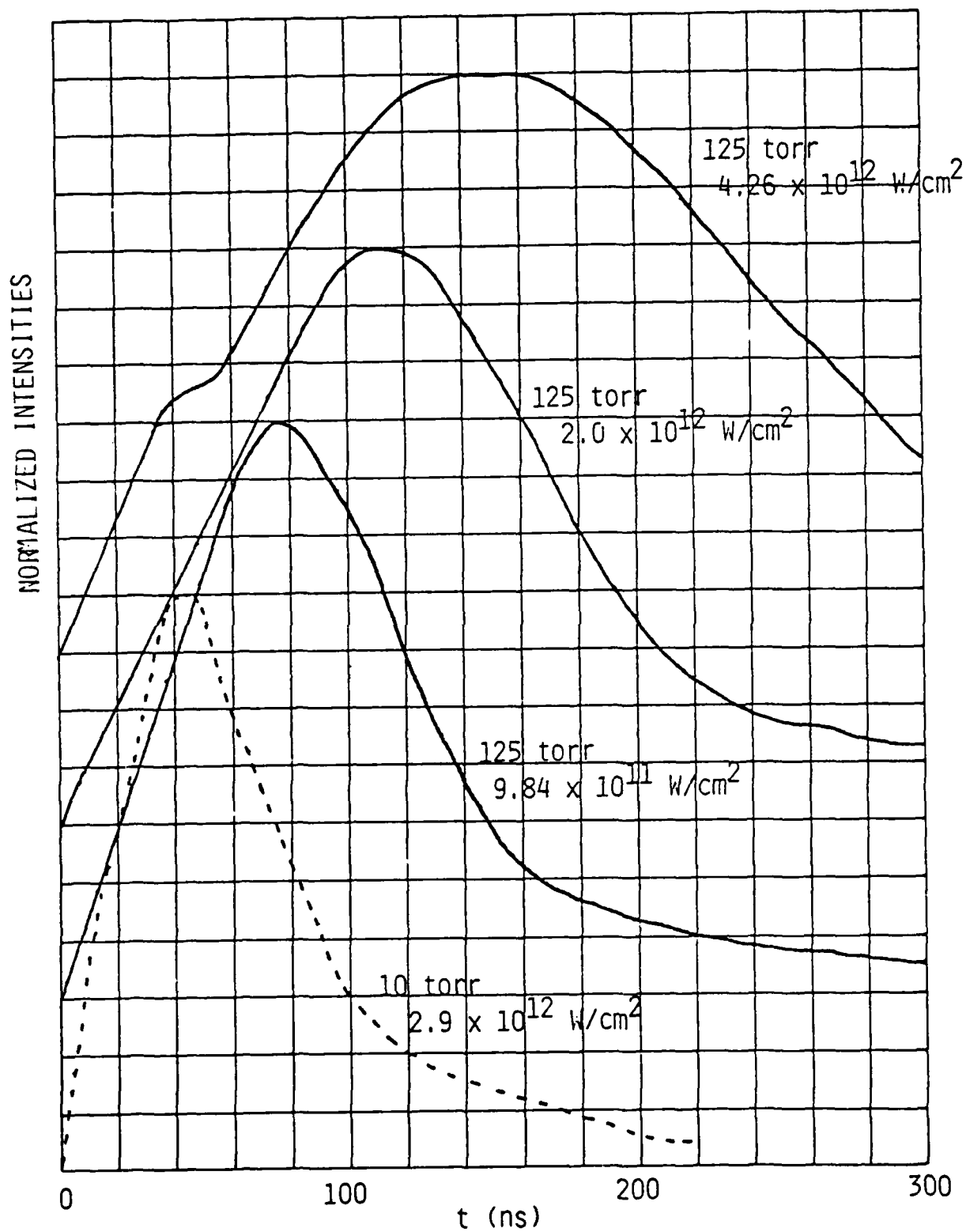
Fig. 4 N^{++} line profiles. Curves
displaced as in Fig. 2.
B-5

In order to provide a quantitative prediction for the plasma radiation one would have to evaluate the:

- Amount and spatial distribution of laser radiation deposited in the gas.

- Energy lost to the surrounding gas during the blast wave expansion.

- Cooling of the plasma by conduction and radiation.

- Chemistry occurring during the cooling.

- Absorption of radiation by the surrounding (cold) gas.

Such detailed analysis is beyond the scope of this study. The approach followed is to survey the many physical processes involved and to determine the most important of these. A more quantitative analysis would be reserved for more detailed further studies.

The various stages in the LINUS experiment are shown in Fig. 5. They are: (a) breakdown, (b) absorption, (c) expansion, and (d) cooling and radiation. They are analyzed in Sections 2 through 4 and in Appendix A. The breakdown threshold analysis, which is given in Appendix A, was performed for the most part under another contract and is included in this report only for completeness. Self absorption by the surrounding gas is studied in Appendix B. Our conclusions are given in Section 5.
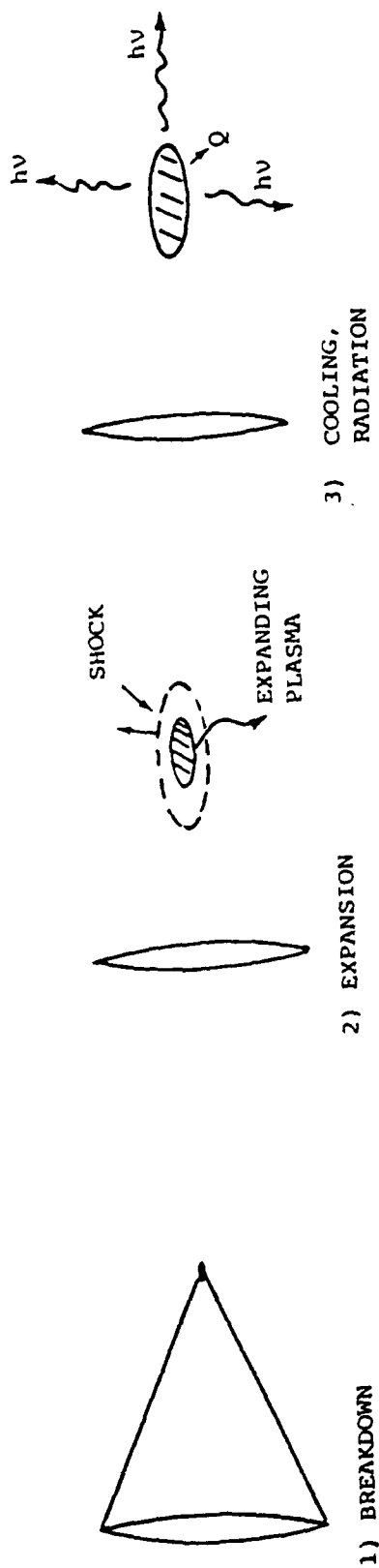
Fig. 5 Various stages of gas/plasma behavior in LINUS experiment.

1) BREAKDOWN

2) EXPANSION

SHOCK

EXPANDING
PLASMA

3) COOLING,
RADIATION

hν

Q

hν

hν

2. PHYSICAL PROCESSES OCCURRING DURING THE LASER PULSE

A detailed analyses of the breakdown process, the highlights of which are given in Appendix A, will be presented elsewhere. Suffice it to say here that multiphoton ionization and electron cascade ionization play equally important roles at λ = 1.06 μm for the pressures of interest 1 < p < 100 torr in the breakdown process. The initial electrons are created by multiphoton ionization of N_2 and impurities having low ionization potential. Build up of ionization then proceeds by cascade ionization of the neutrals through collisions with the laser-heated electrons.

2.1   Time Scales

We have looked at the time scales for various collisional processes and from these time scales we can conclude that

- Electron-electron collisions are sufficiently fast that one can define an electron temperature $T_e \gg T_{gas}$.

- Neutral-neutral, neutral-ion and ion-ion collisions occur on a time scale that is comparable or longer than the pulse time τ_p so that for all practical purposes heavy-heavy collisions are unimportant.

- The time for electrons to transfer their energy to heavy particles by momentum transfer collisions is so long (due to the factor M/m where M = heavy mass, m = electron mass) that the electrons cannot heat the gas by the time the pulse is over.

- The time scale for expansion of the gas is shorter than the pulse time so that the gas has already expanded before the major part of the energy has been deposited.

We have plotted the time scales for various physical processes in Fig. 6. These time scales are for a practically totally (singly) ionized plasma before expansion with electron temperature T_e. The pressure of the gas before breakdown for this figure was p = 10 torr and the scaling of all quantities with p is indicated. The formulae used for the derivation of Fig. 6 are given below, as well as numerical values for T_e = 20,000 K.

Electron neutral momentum transfer

$$\tau_{en} = \left(n \; \sigma_M V_e\right)^{-1} = 3 \times 10^{-11} \left(\frac{10}{p}\right) \; s \qquad\qquad (1)$$
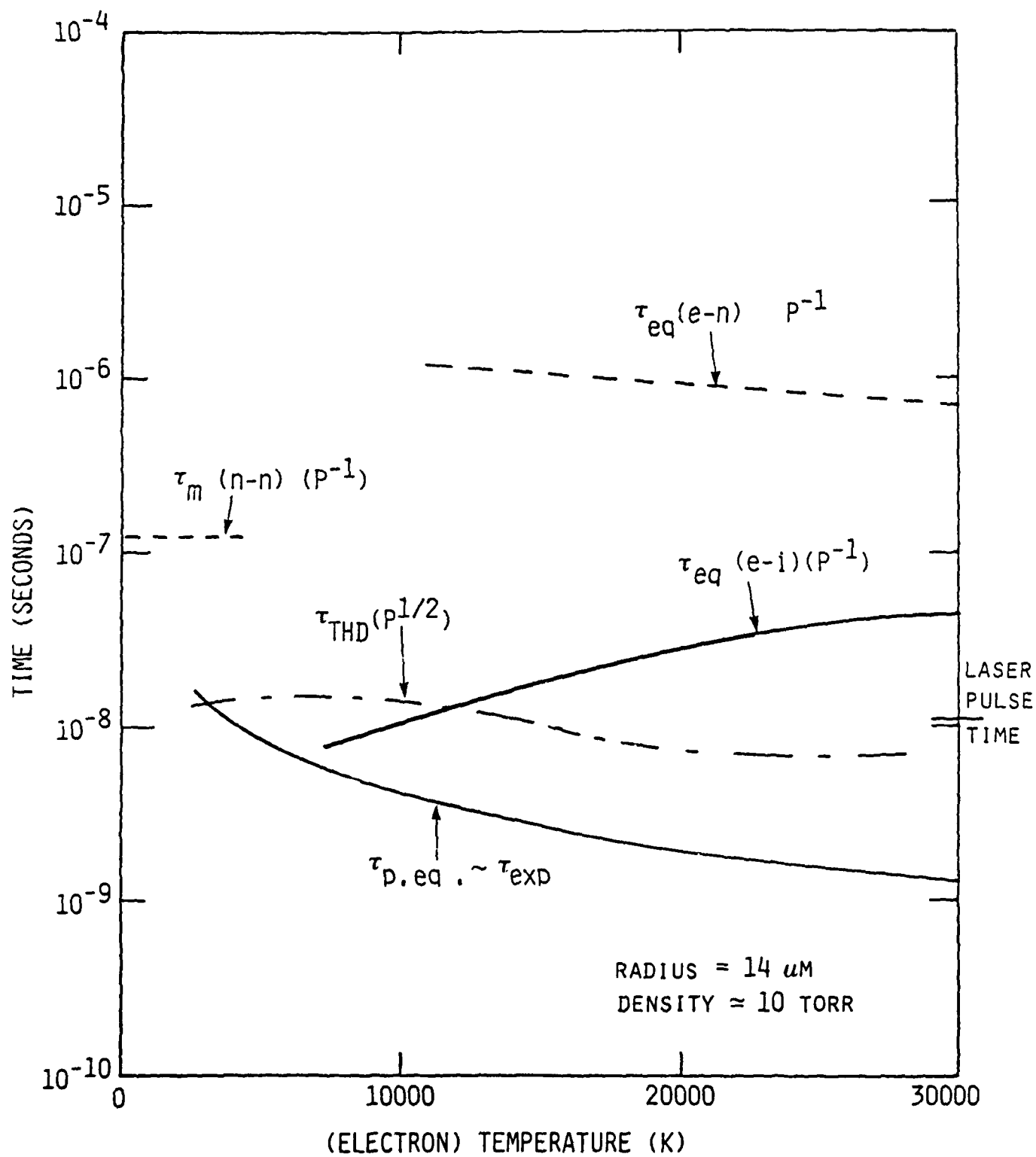
Fig. 6 Time scales of various physical processes before plasma expansion.

Electron-electron equilibration

$$\tau_{ee} = \frac{0.266 \, T_e^{3/2}}{n_e \ell n \Lambda} = 4 \times 10^{-12} \left(\frac{10}{p}\right) \quad \text{s} \tag{2}$$

Neutral-neutral collision time

$$\tau_{nn} = \left(n \sigma_M V\right)^{-1} = 10^{-7} \left(\frac{10}{p}\right) \quad \text{s} \tag{3}$$

Electron-ion equilibration time

$$\tau_{ei} = \frac{M}{2m} \tau_{ee} = 5 \times 10^{-8} \left(\frac{10}{p}\right) \quad \text{s} \tag{4}$$

Pressure equilibration time

$$\tau_{peq} = \frac{a}{\left(\gamma k T_e / M\right)^{1/2}} = 10^{-9} \quad \text{s} \tag{5}$$

Thermal diffusion time

$$\tau_{thdiff} = \frac{a^2}{K} \cong 10^{-8} \left(\frac{p}{10}\right)^{1/2} \quad \text{s} \tag{6}$$

where we defined $V = (2kT_g/M)^{1/2}$, $V_e = (2kT_e/m)^{1/2}$, $\ell n \Lambda$ = coulomb logarithm ($\cong 6$), a = beam radius (= 14 μm) and where σ_M is hard sphere cross-section of neutrals ($\approx 10^{-15}$ cm^2). The thermal conductivity used was taken as that of equilibrium high temperature nitrogen.[2]

Note that the plasma expansion time is estimated to be 10^{-9} s which is a factor of ten shorter than the pulse time. One would expect from such a short time that, if one operates the laser well above threshold, breakdown will occur early in the pulse and that because the plasma is expanding rapidly out of the beam, the latter portion of the laser pulse will be ineffective in depositing much more energy into the plasma.

Possible reactions that we have not included but may result in heating of the heavy particles are dissociation and dissociative recombination.

$$N_2 + e \rightarrow N_2^* + e \tag{7}$$

followed by

$$N_2^* \rightarrow N + N \qquad \text{(hot atom)}$$

and

$$N_2 + e \rightarrow N_2^+ + e + e \qquad \qquad (8)$$

followed by

$$N_2^+ + e \rightarrow N + N \qquad \text{(hot atom)}$$
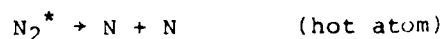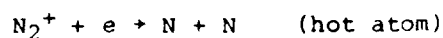
2.2   Length Scales

In order to gain better insight into the importance of various phys-ical processes during the breakdown, it is also worthwhile to estimate the various length scales entering into the problem. These are shown in Fig. 7. The length scales imposed by the optics are the focal radius $a \cong 14$ µm and the depth of focus ~ 300 µm. The importance of electron diffusion out of the beam during the breakdown is measured by the diffusion length $\ell_D \sim \sqrt{\mathcal{D}\tau_p}$ where $\mathcal{D}$ is the electron diffusivity and τ_p the pulse length. The free electron diffu-sion coefficient $\mathcal{D}$ as a function of 1.06 µm laser intensity at one amagat density is shown in Fig. 8. It was obtained by use of a Boltzmann code (see Appendix). ℓ_D' scales as $p^{-1/2}$. This length is so much larger than the beam radius that diffusion of electrons out of the beam will represent a signifi-cant loss process for cascade ionization. However, if multiphoton ionization processes can build up the electron concentration to $n_e > 10^{11}$ cm^{-3} where space charge effects limit diffusion to being ambipolar in nature, then the diffusivity is reduced by the factor $(m/M)^{1/2} = 4 \times 10^{-3}$. We show in Fig. 9 as a function of focal radius the electron density that has to be exceeded for space charge effects to be important.

The thermal diffusion length is given by

$$\ell_\theta = \sqrt{k\tau_p} \cong 14 \left(\frac{10}{p}\right)^{1/2} \text{µm.} \qquad (9)$$

For $p < 10$ torr we will have $\ell_\theta > a$ so that thermal losses during the pulse are important.
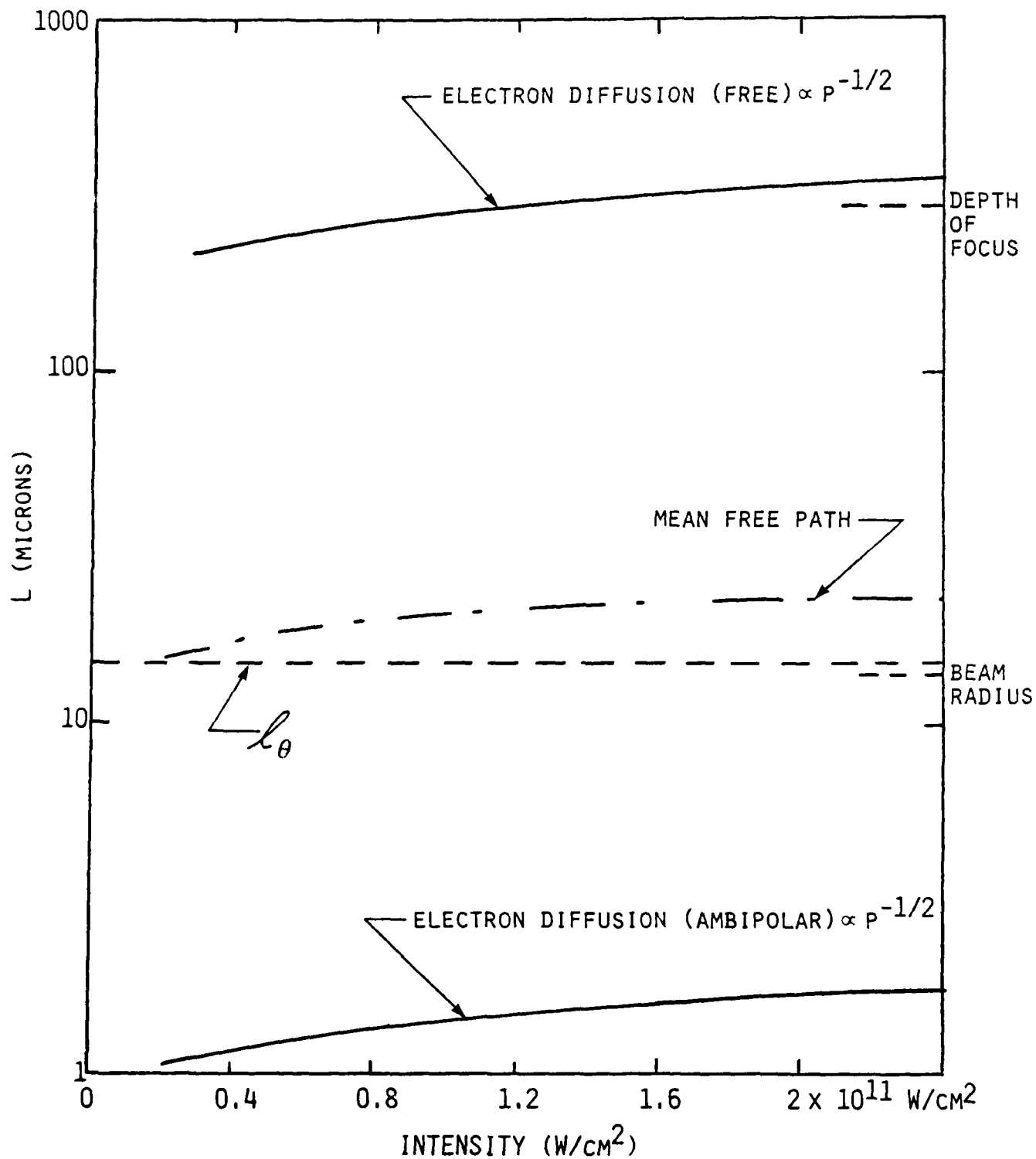
Fig. / Length scales of interest at p = 10 torr.
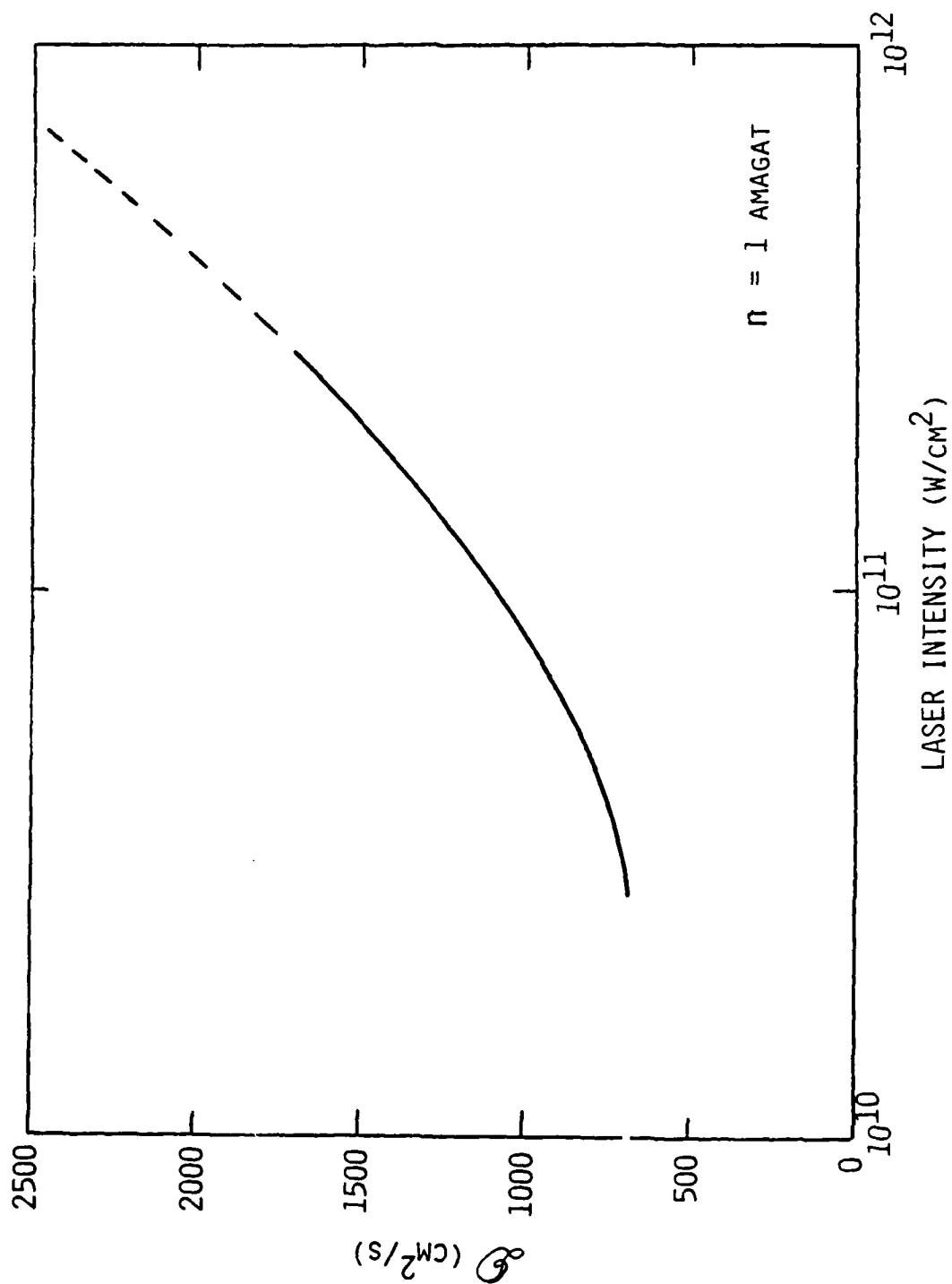
Fig. 8 Free electron diffusivity in N_2 at 1 amagat.
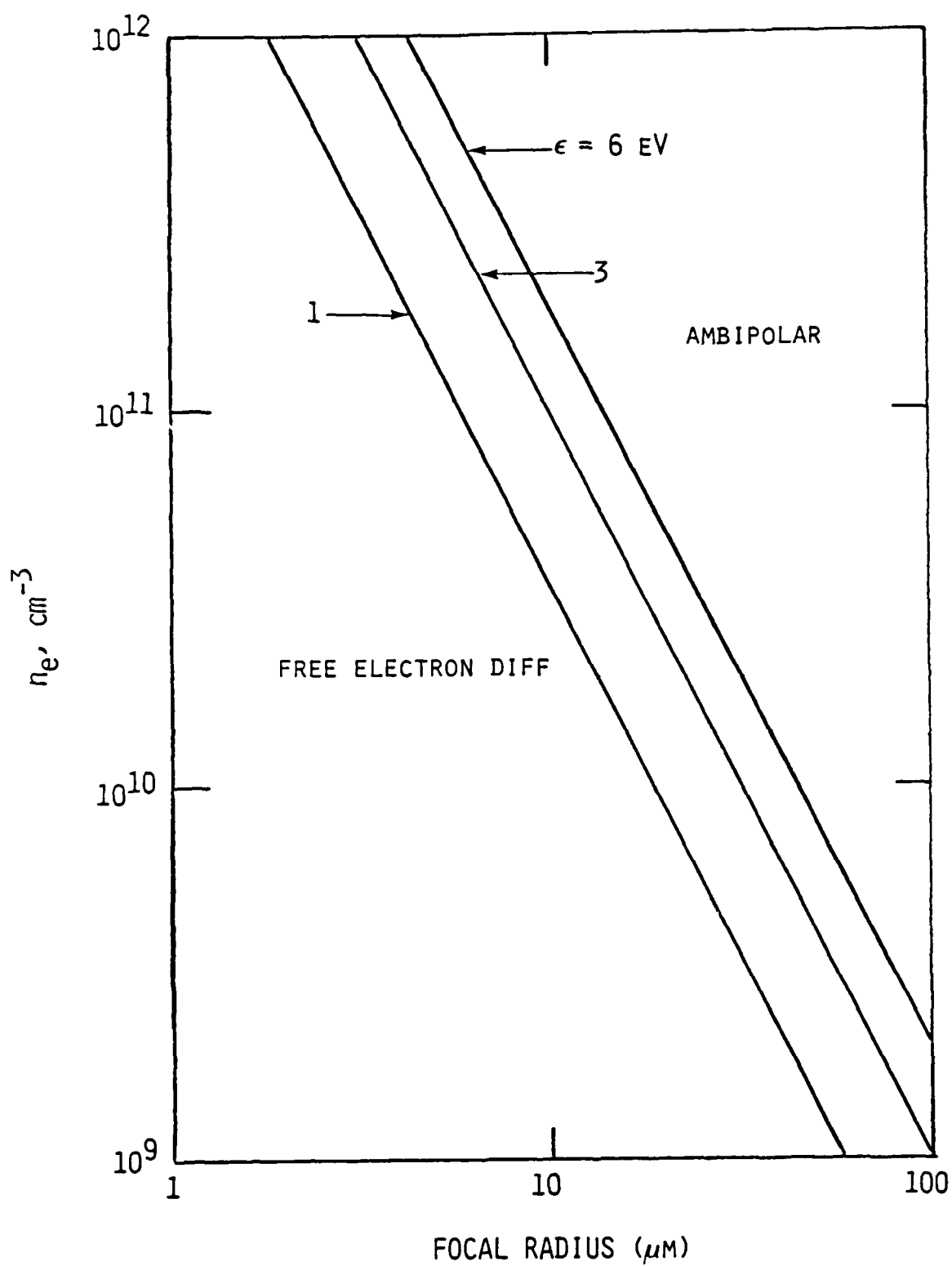
Fig. 9 Critical electron density for ambipolar diffusion.

Finally, the electron mean free path is $\ell_e = (N\sigma_M)^{-1} \cong 15 \, (10/p)$ µm. The mean free path, therefore, at $p < 10$ torr is of the order or larger than the beam radius. Continuum treatment of the gas will not be a valid approach at the low pressures.

3. EXPANSION OF THE GAS

The absorption of the laser radiation creates a high pressure in the focal volume. The gas expands in a finite time to return the pressure to ambient. Several treatments can be used to estimate the pressures and expansion times. Reference 2 by Nebolsine and Weyl describes two approaches - regular blast wave and variable energy blast wave theory and the application to this problem.

A zeroth order estimate of a characteristic expansion time is given by the spot radius divided by the speed of sound of the gas. Using 30,000 K as a temperature, the time scale for a 15 µm spot radius is several nanoseconds. Since the expansion time is shorter than the pulse duration, the gas will already be expanding before the laser pulse is over. With such a short characteristic time, the pressure will significantly drop on a time scale of the order of the laser pulse duration. We will now discuss the time scale for the pressure to return to ambient.

Using an estimate of 30,000 K for a plasma temperature, the peak pressure is expected to be on the order of 1,000 torr for an initial 10 torr gas pressure. The plasma will expand predominately radially because the laser beam diameter is approximately ten times shorter than the depth of field. Two dimensional blast wave theory yields a pressure that scales inversely with time. If at τ = 10 ns the pressure is 1000 torr, it will therefore decay to 10 torr (ambient) after 1 µs.

The average temperature of the expanded gas can be computed as a function of the ratio of specific heats, γ. Because γ is varying, examples will be given for a range of γ. Using the isentropic expansion relations for p and T, we find that T drops from 30,000 K to 4,700 K for a pressure drop of 100 and a γ of 1.67. On the other hand, if γ = 1.2, the average temperature will be 14,000 K for the same initial temperature and pressure drop. Thus, we find that the plasma can still be very hot and continue to radiate after gas dynamic effects are over.

4. RADIATION BY THE NITROGEN PLASMA

4.1 Radiation of Nitrogen Plasma in Thermodynamic Equilibrium

In order to get an idea of the radiation characteristics of the laser-produced nitrogen plasma, we have used a radiation code that was developed at PSI under a previous program to study plasma radiation coupling to metallic surfaces.[3] This code as written takes into account line radiation and continuum radiation (free bound and free free) from a plasma containing electrons, N and N^+. We have modified the code to include also radiation from excited states of N^{2+}. All lines included are those for which oscillator strengths are known and tabulated, excepting those lines connecting to lower states having two excited electrons. The code uses detailed balance to relate plasma emissivity to plasma absorptivity and is therefore valid only for a plasma in thermodynamic equilibrium at some temperature T. All lines of a same multiplet have been lumped into a single line whose strength is the sum of the line strengths of its constituent lines and having the stark broadening parameters as given by Griem.[4]

If the plasma is in thermodynamic equilibrium then the concentration of the various ions of nitrogen are related by the following Saha equations.

$$\frac{n_e [N^+]}{N} = \frac{A\ T^{3/2}\ g^+}{g}\ \exp-(\epsilon_1/kT) \tag{10}$$

$$\frac{n_e [N^{2+}]}{[N^+]} = \frac{AT^{3/2}\ g^{2+}}{g^+}\ \exp - (\epsilon_2/kT) \tag{11}$$

$$\frac{n_e [N^{3+}]}{[N^{2+}]} = AT^{3/2}\ \frac{g^{3+}}{g^{2+}}\ \exp - (\epsilon_3/kT) \tag{12}$$

where $A = 2\ (2\pi mk/h^2)^{3/2} = 4.83 \times 10^{15}\ cm^{-3}\ deg^{-3/2}$, the g's are partition functions of the heavies, $\epsilon_1 = 14.54$ eV, $\epsilon_2 = 29.6$ eV and $\epsilon_3 = 47.4$ eV. We must add to the above the equation of state

$$([N^+] + [N^{2+}] + [N^{3+}] + [N] + n_e)\ kT = p \tag{13}$$

and the equation of conservation of charge:

$$[N^+] + 2[N^{2+}] + 3[N^{3+}] = n_e \quad . \tag{14}$$

It is straightforward to solve Eqs. (10) through (14) for the concentration of species as a function of p and T by noting that at any p, T there will only be two major ionic species and the others may be treated as a perturbation. For example, below 20,000 K we need only consider Eqs. (10) and (11). If B_1 and B_2 are the right-hand sides of Eqs. (10) and (11) and if we write $[N] = n_o(1-x-y)$, $[N^+] = n_o x$ and $[N^{2+}] = n_o y$, Eqs. (10) and (11) become

$$\frac{x(x + 2y)}{1 - x - y} = \frac{B_1}{n_o} \tag{15}$$

$$\frac{y(x + 2y)}{x} = \frac{B_2}{n_o} \tag{16}$$

and Eq. (13) yields

$$n_o = \frac{P}{(1 + x + 2y)} \tag{17}$$

Equations (15) through (17) were solved on a programmable hand calculator by several iteration schemes. For $x > y$ (low temperature range). We solve for x as a function of y from Eq. (15), given n_o,

$$x = \frac{-(B_1/n_o + 2y) + \sqrt{(B_1/n_o + 2y)^2 - 4(1 - y)}}{2} \tag{18}$$

and then calculate y from Eq. (16)

$$y = \frac{(B_2/n_o)\, x}{x + 2y} \quad .$$

Inserting the value of y and the value of x in Eq. (17) yields an updated n_o. We then solve for x again using Eq. (18). This scheme does not converge for $x < y$, and we proceed as follows. We take the ratio of Eqs. (10) and (11) and solve for y as a function of x.

$$y = \frac{(1 - x) + \sqrt{(1 - x)^2 - (B_2/B_1)x^2}}{2} \quad .$$

We then solve for x from Eq. (11)

$$x = \frac{y(x + 2y)\, n_o}{B_2}$$

and recalculate n_o by use of Eq. (17).

A similar procedure is used above 20,000 K, where Eqs. (11) and (12) are used rather than Eqs. (10) and (11). The results of these calculations are shown in Fig. 10 for the three pressures $p = 1$, 10 and 100 torr. One sees from this figure that nitrogen becomes significantly ionized above 10,000 K and that N^{2+} becomes a dominant species above 18,000, 22,000 and 25,000 K for $p = 1$, 10 and 100 torr, respectively.

We show in Figs. 11 through 29 computer-generated plots of radiation emitted by a plasma slab of thickness 0.2 mm. These figures also show the black body emission and comparison of the two curves show that the plasma is quite optically thin to its own radiation. Figures 11 through 29 were gen-erated using a grid size of 20 cm^{-1} which is considerably larger than the stark broadened line widths. Therefore most lines whose centers fall well be-tween the grid points are not apparent. In order to make the lines more ap-parent, we have generated special plots, two of which are shown in Figs. 30 and 31, which give absorption coefficient at line center in the wavelength in-terval 0.2 - 0.9 μm. One verifies from Figs. 30 and 31 that, indeed, even at line center, a plasma of thickness ~ 0.2 mm is optically thin. A plot such as Fig. 30 was expanded so that the wavelength scale was identical to those of the visible spectra taken by R. Lucht.[1] We were able to verify that prac-tically all experimentally observed lines, excepting the band systems of N_2 and N_2^+, are included in the radiation code. The sudden rise in continuum ra-diation at wave numbers larger (wavelengths smaller) than some critical wave-numbers $\bar{\nu}_c$ (wavelengths λ_c) that are apparent in Figs. 11 through 29 are as-sociated with free-bound radiation following the reaction

$$N^{Z+} + e \rightarrow \left(N^{(Z-1)+} \right)^* + h\nu \, . \tag{19}$$

where the * represents an excited state of energy ϵ^* and $\nu = (\epsilon_I^{Z-1} + \epsilon - \epsilon^*)/h$, ϵ_I^{Z-1} being the ionization energy of the ion of charge $Z - 1$ and ϵ the free electron energy.
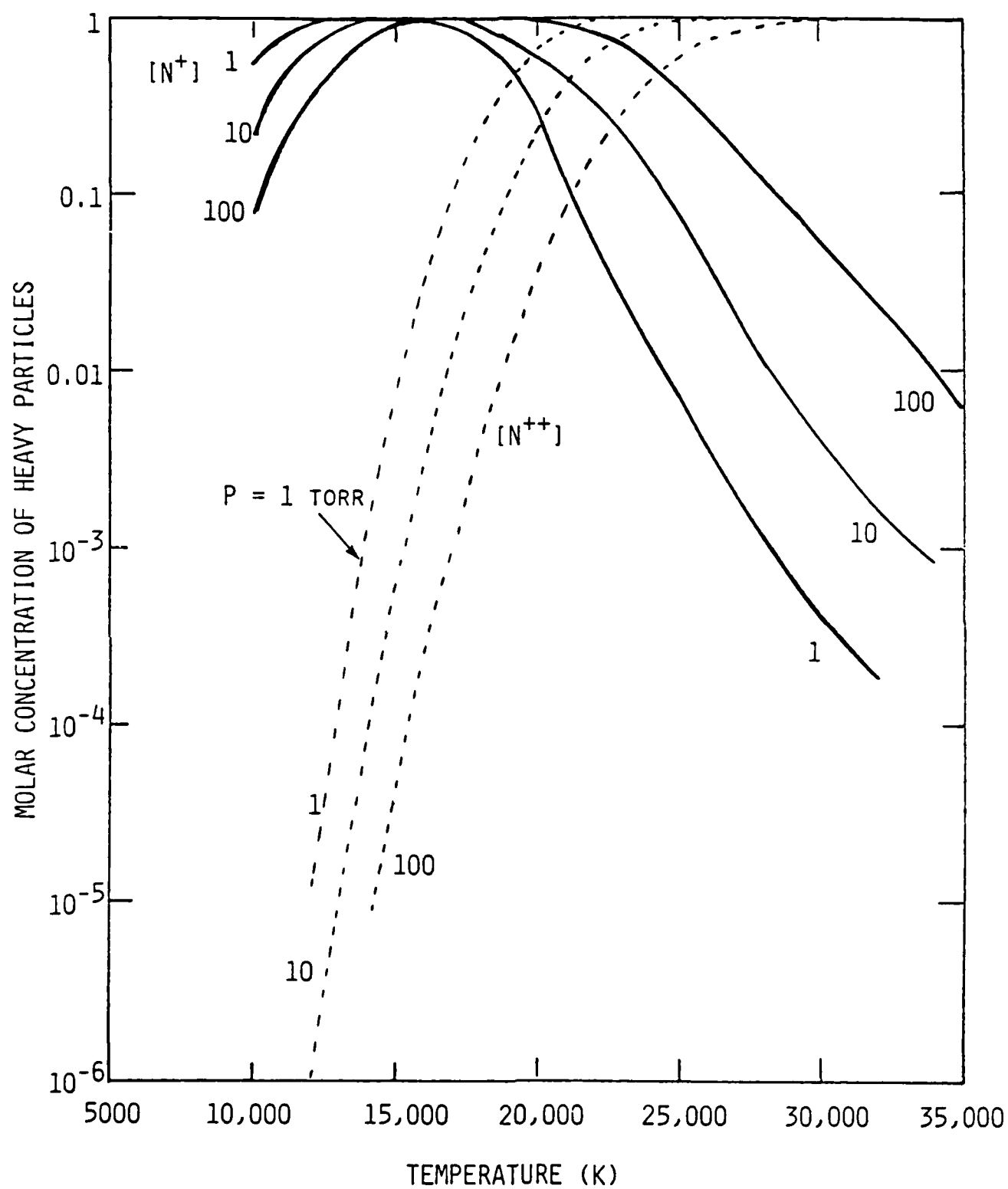
Fig. 10   Species concentrations in equilibrium plasma.
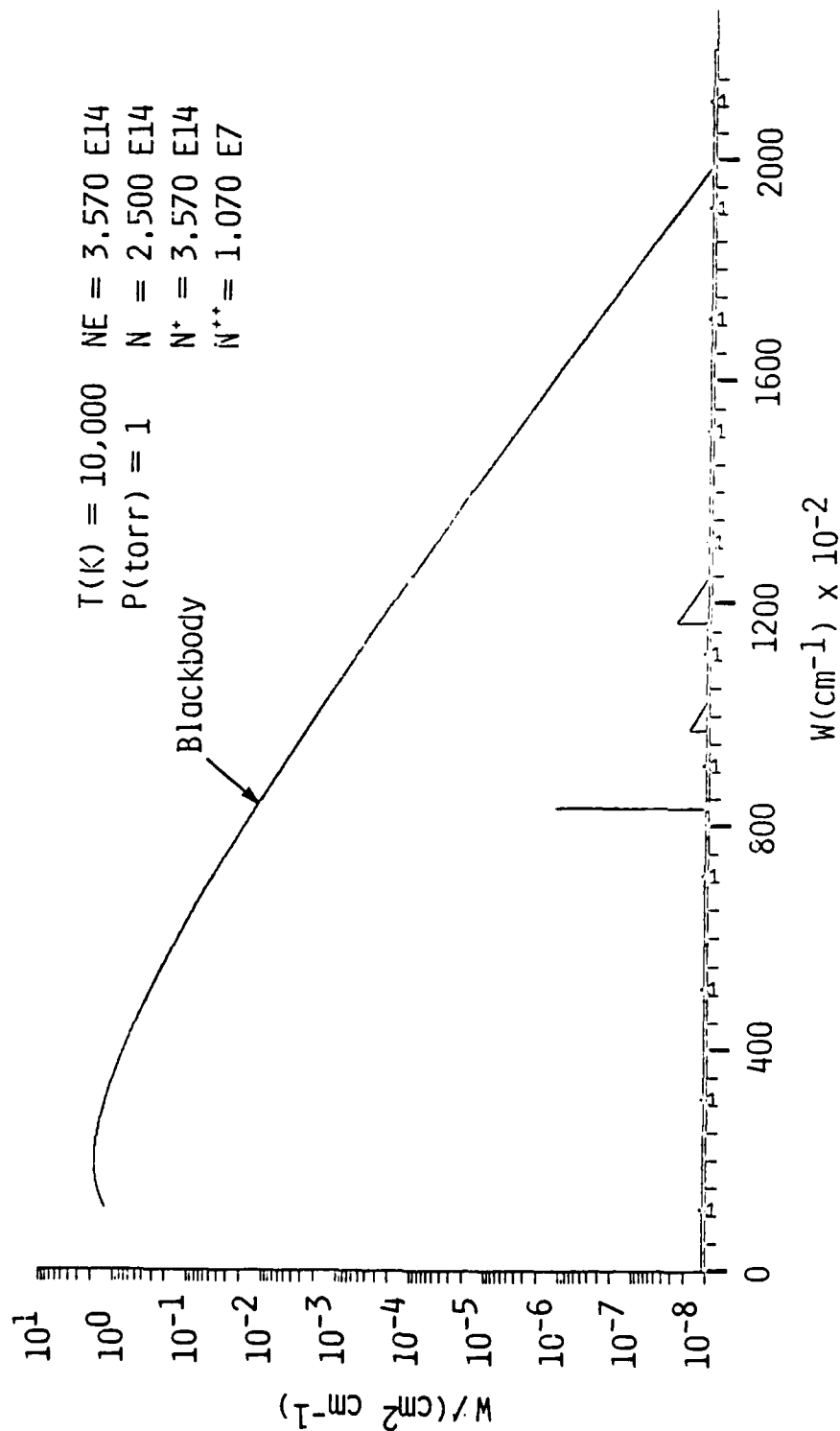
Fig. 11 Emission by an equilibrium nitrogen plasma slab of thickness 0.2 mm in the 0 to 250,000 cm^{-1} band, T = 10,000 K, p = 1 torr.
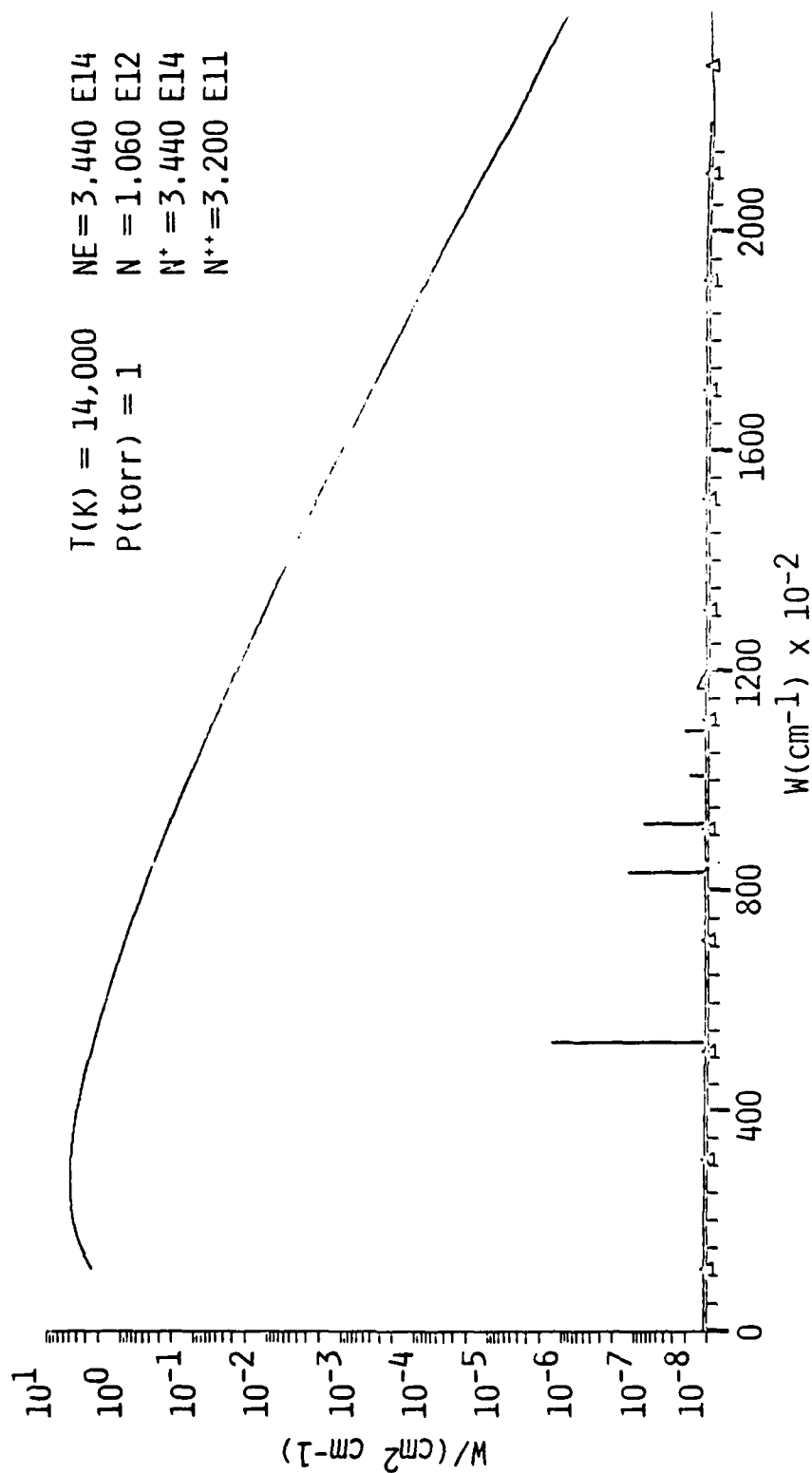
Fig. 12 Emission by an equilibrium nitrogen plasma slab of thickness 0.2 mm in the 0 to 250,000 cm^{-1} band, T = 14,000 K, p = 1 torr.
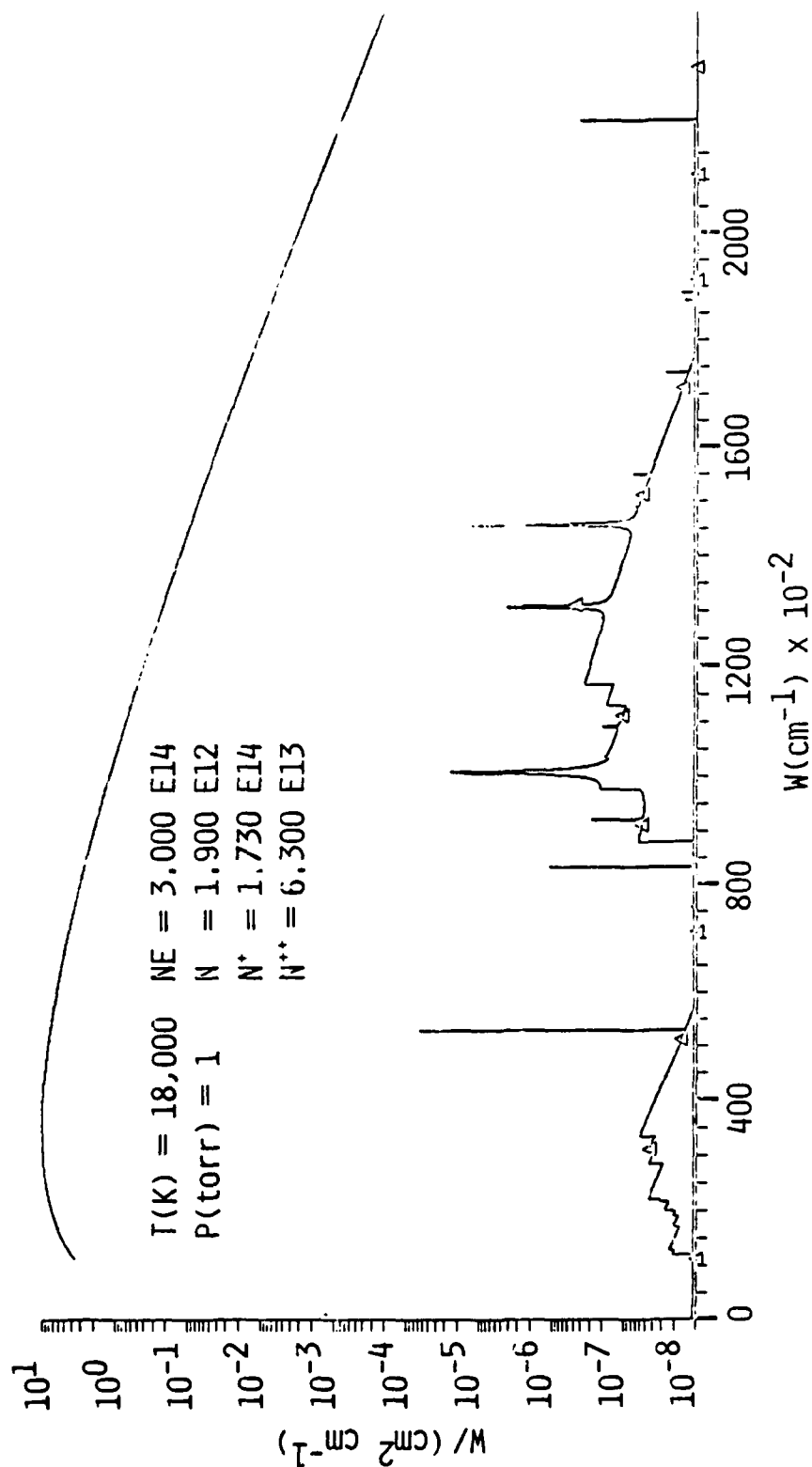
Fig. 13 Emission by an equilibrium nitrogen plasma slab of thickness 0.2 mm in the 0 to 250,000 cm^{-1} band, T = 18,000 K, p = 1 torr.

T(K) = 18,000 NE = 3.000 E14
P(torr) = 1   N = 1.900 E12
               N$^+$ = 1.730 E14
               N^{++} = 6.300 E13

W(cm^{-1}) × 10^{-2}

W/(cm^2 cm^{-1})
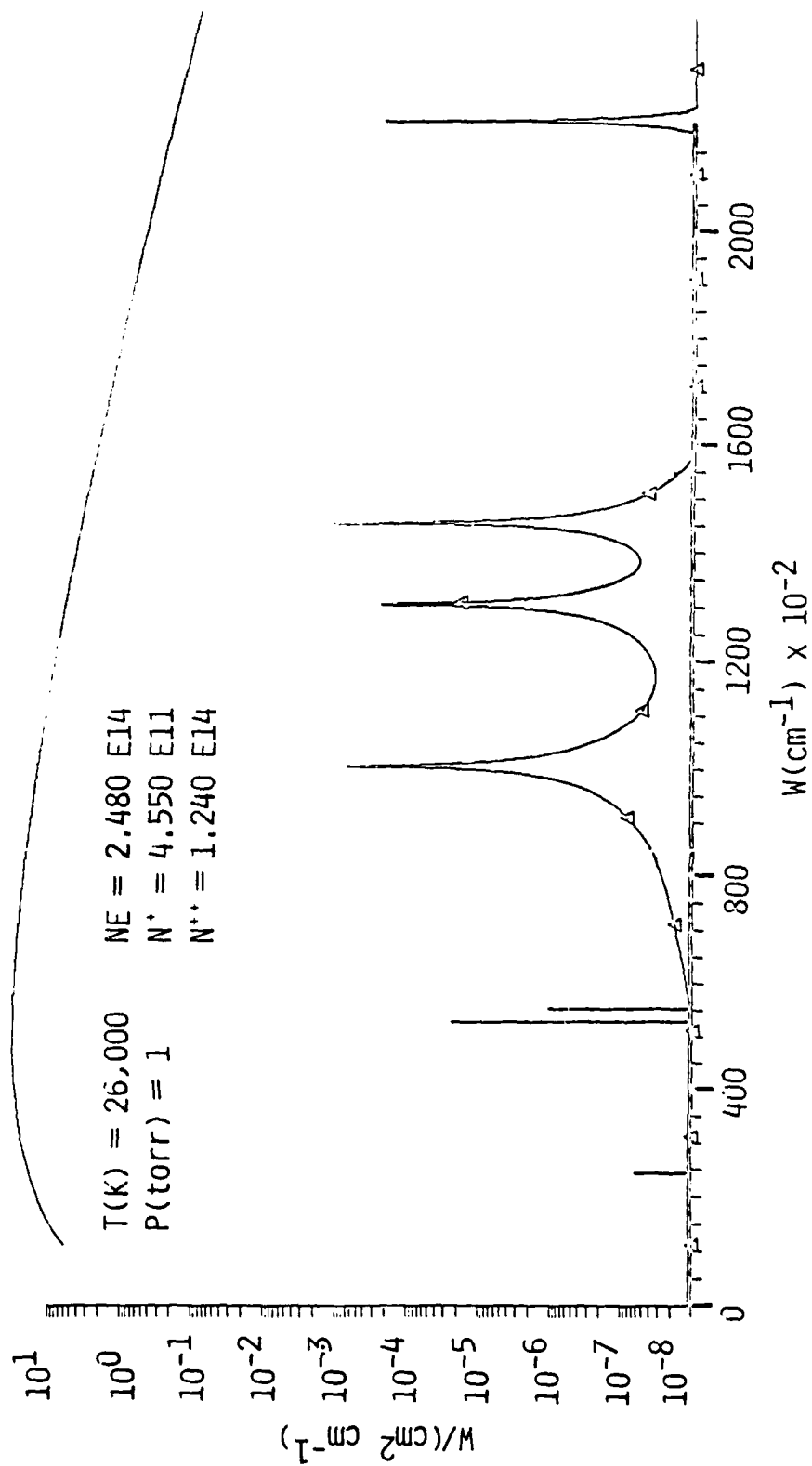
Fig. 14 Emission by an equilibrium nitrogen plasma slab of thickness 0.2 mm in the 0 to 250,000 cm^{-1} band, T = 26,000 K, p = 1 torr.

T(K) = 26,000   NE = 2.480 E14
P(torr) = 1   N$^+$ = 4.550 E11
                   N^{++} = 1.240 E14

W(cm^{-1}) x 10^{-2}

W/(cm^2 cm^{-1})
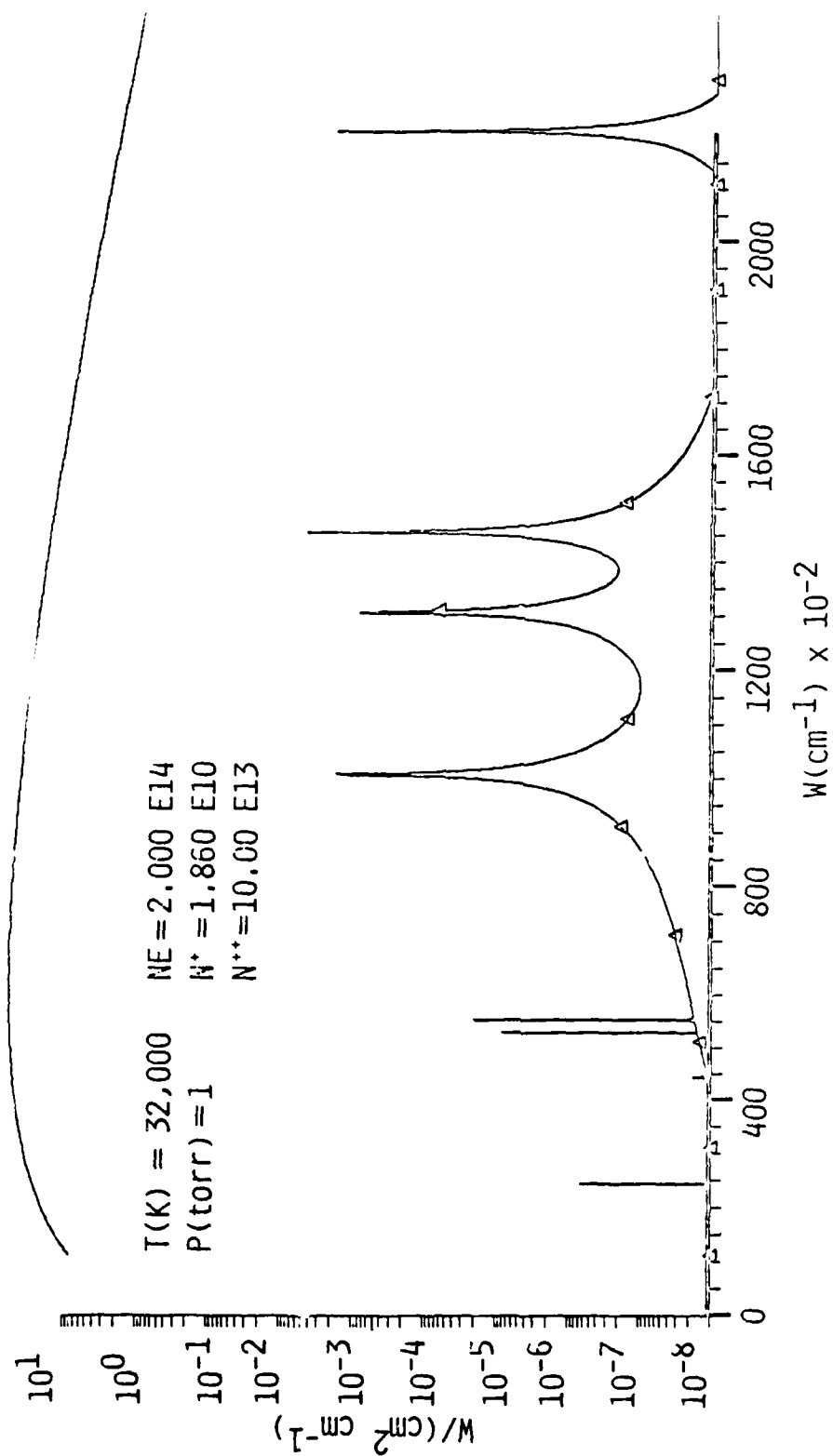
Fig. 15 Emission by an equilibrium nitrogen plasma slab of thickness 0.2 mm in the 0 to 250,000 cm^{-1} band, $T = 32,000$ K, $p = 1$ torr.
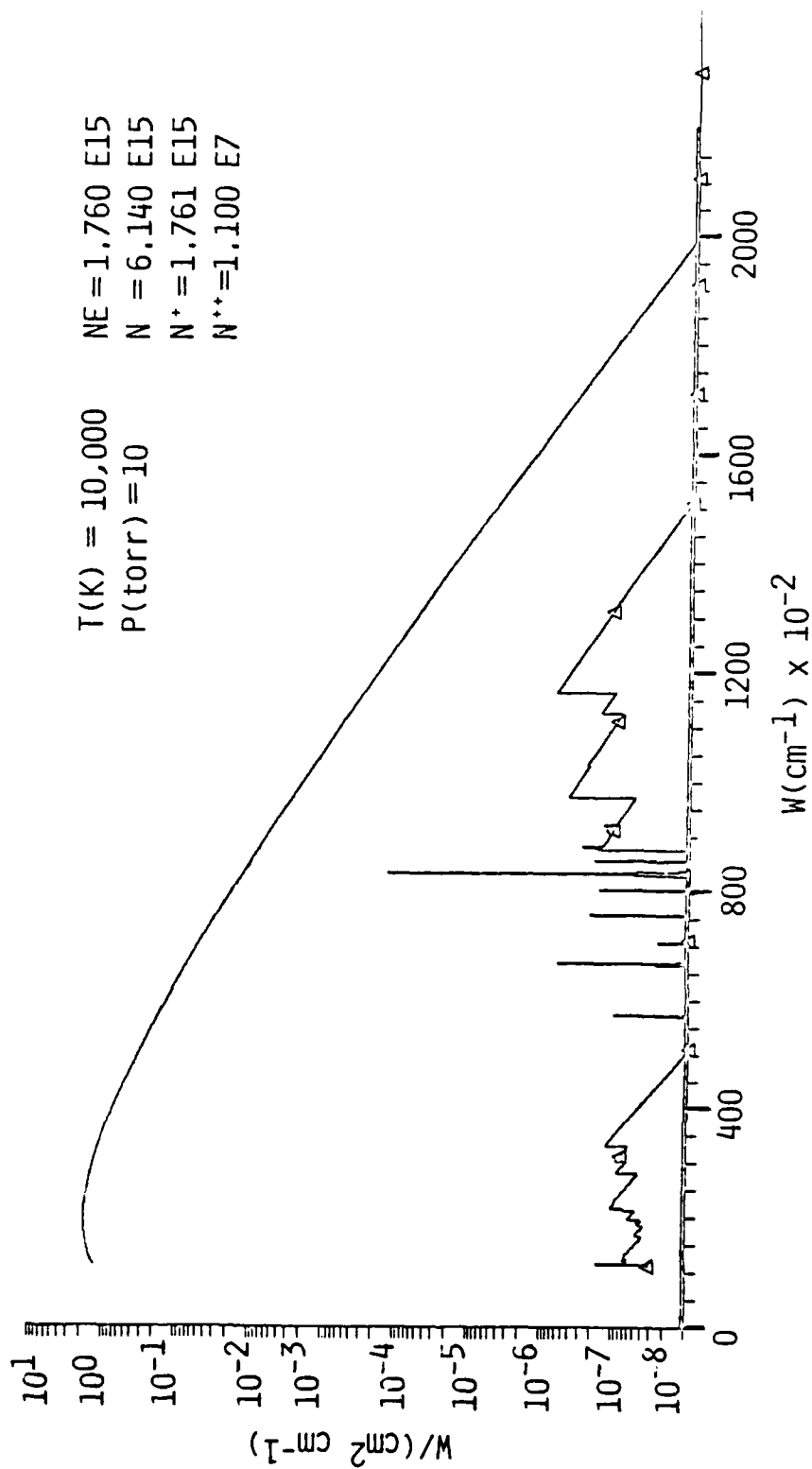
Fig. 16 Emission by an equilibrium nitrogen plasma slab of thickness 0.2 mm in the 0 to 250,000 cm^{-1} band, T = 10,000 K, p = 10 torr.
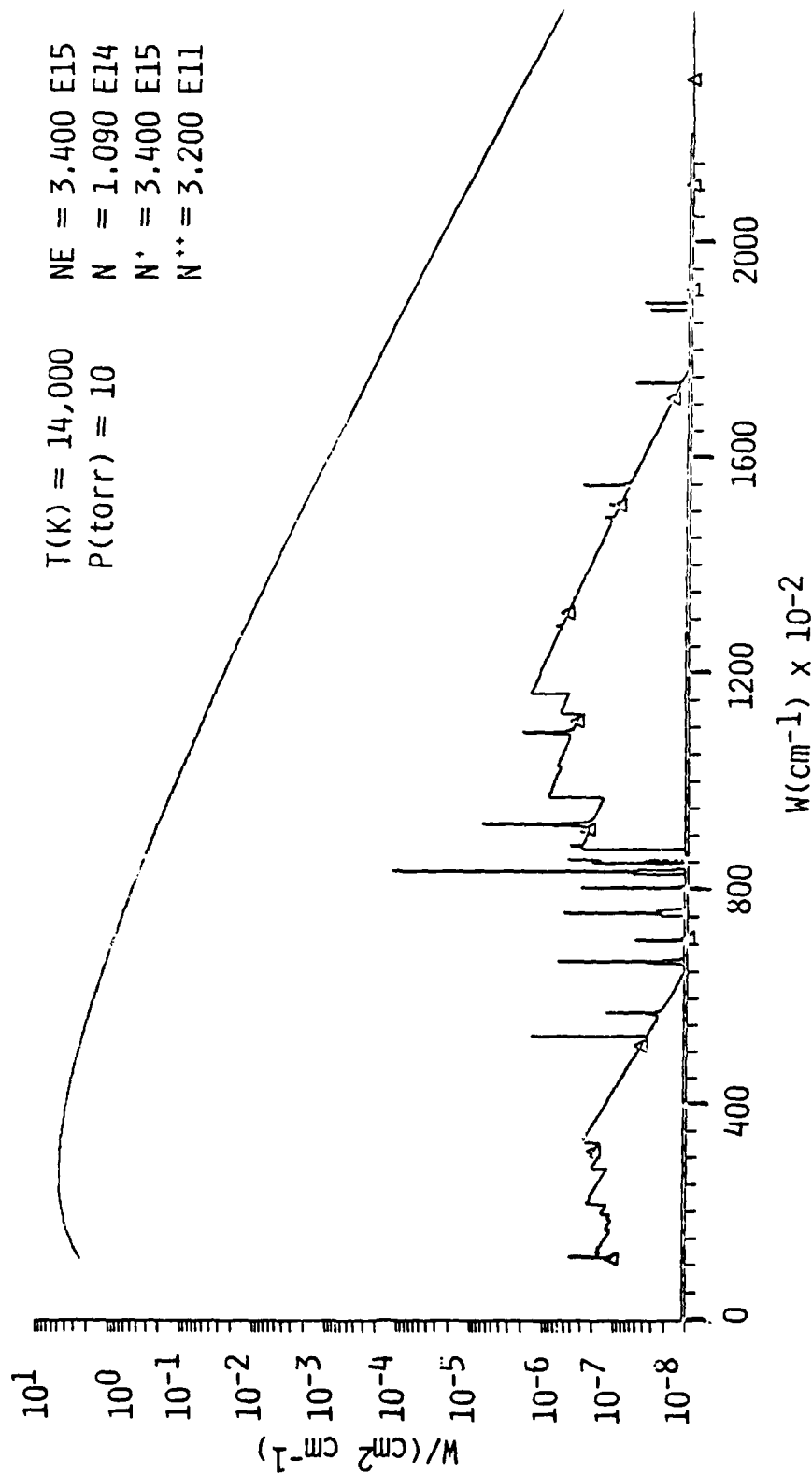
Fig. 17 Emission by an equilibrium nitrogen plasma slab of thickness 0.2 mm in the 0 to 250,000 cm^{-1} band, T = 14,000 K, p = 10 torr.

T(K) = 14,000   NE = 3,400 E15

P(torr) = 10   N = 1.090 E14

N$^{\cdot}$ = 3.400 E15

N$^{\cdot\cdot}$ = 3.200 E11

5750-
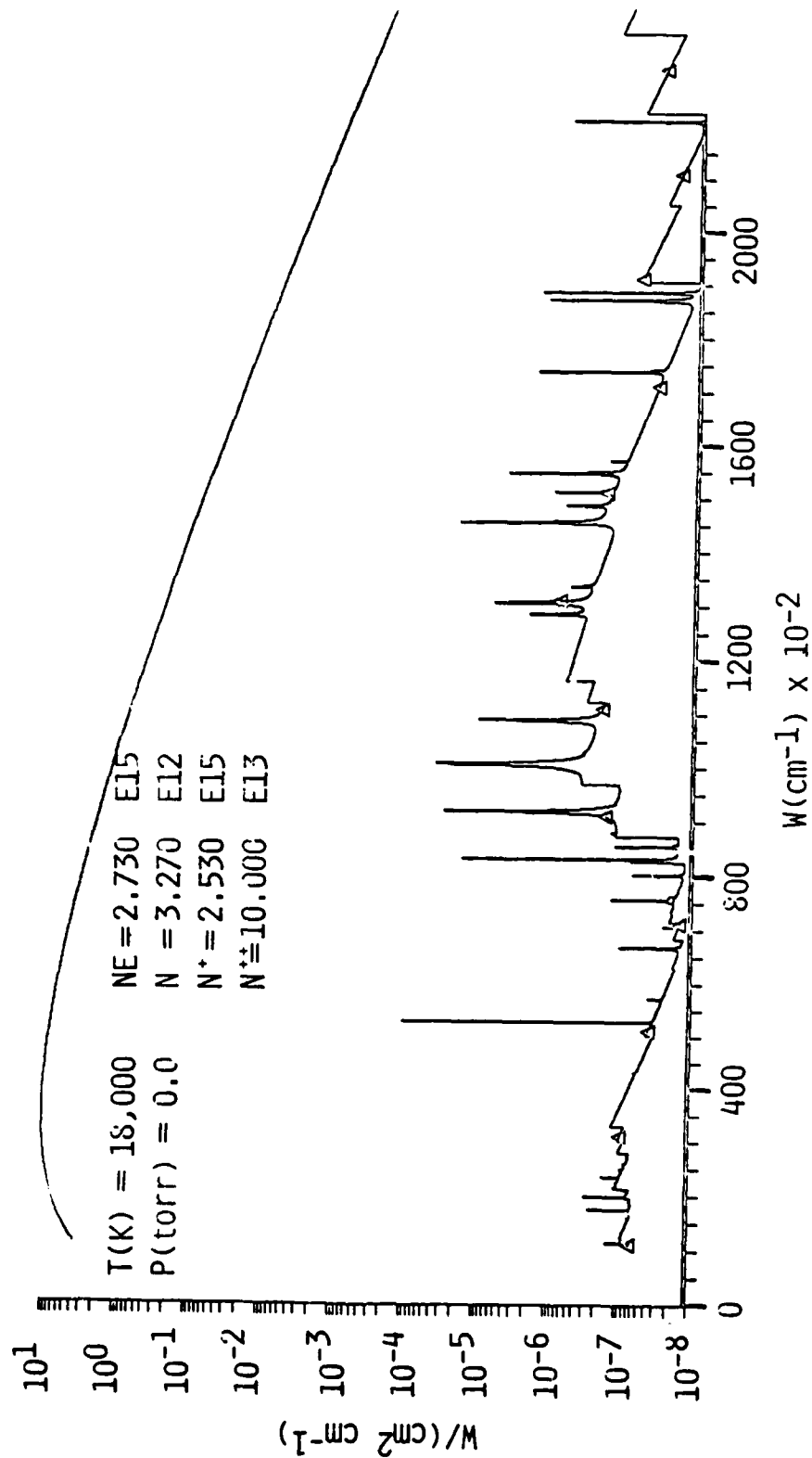
Fig. 18 Emission by an equilibrium nitrogen plasma slab of thickness 0.2 mm in the 0 to 250,000 cm^{-1} band, T = 18,000 K, p = 10 torr.

5750-8

B-30
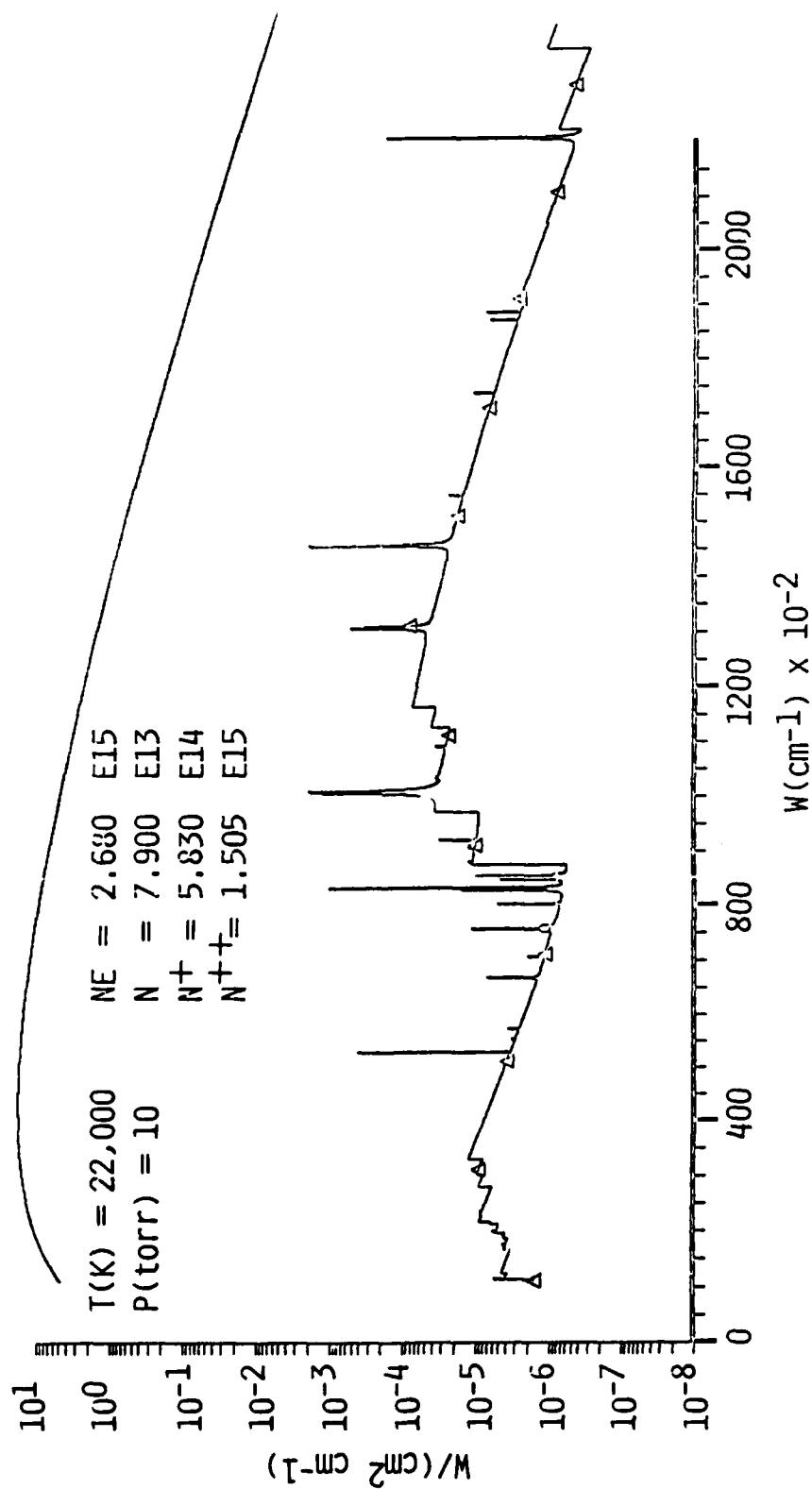
Fig. 19 Emission by an equilibrium nitrogen plasma slab of thickness 0.2 mm in the 0 to 250,000 cm^{-1} band, T = 22,000 K, p = 10 torr.
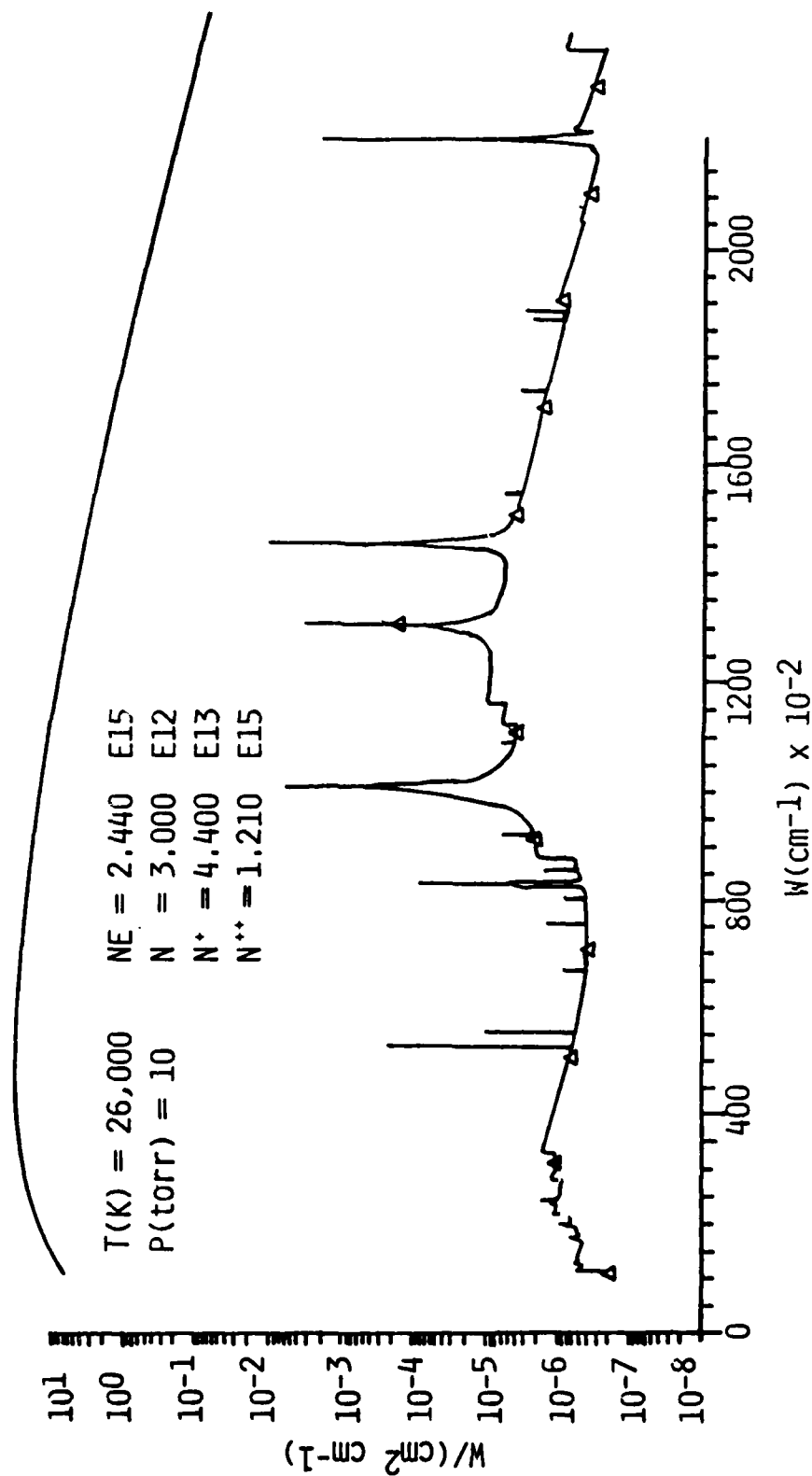
Fig. 20 Emission by an equilibrium nitrogen plasma slab of thickness 0.2 mm in the 0 to 250,000 cm^{-1} band, T = 26,000 K, p = 10 torr.
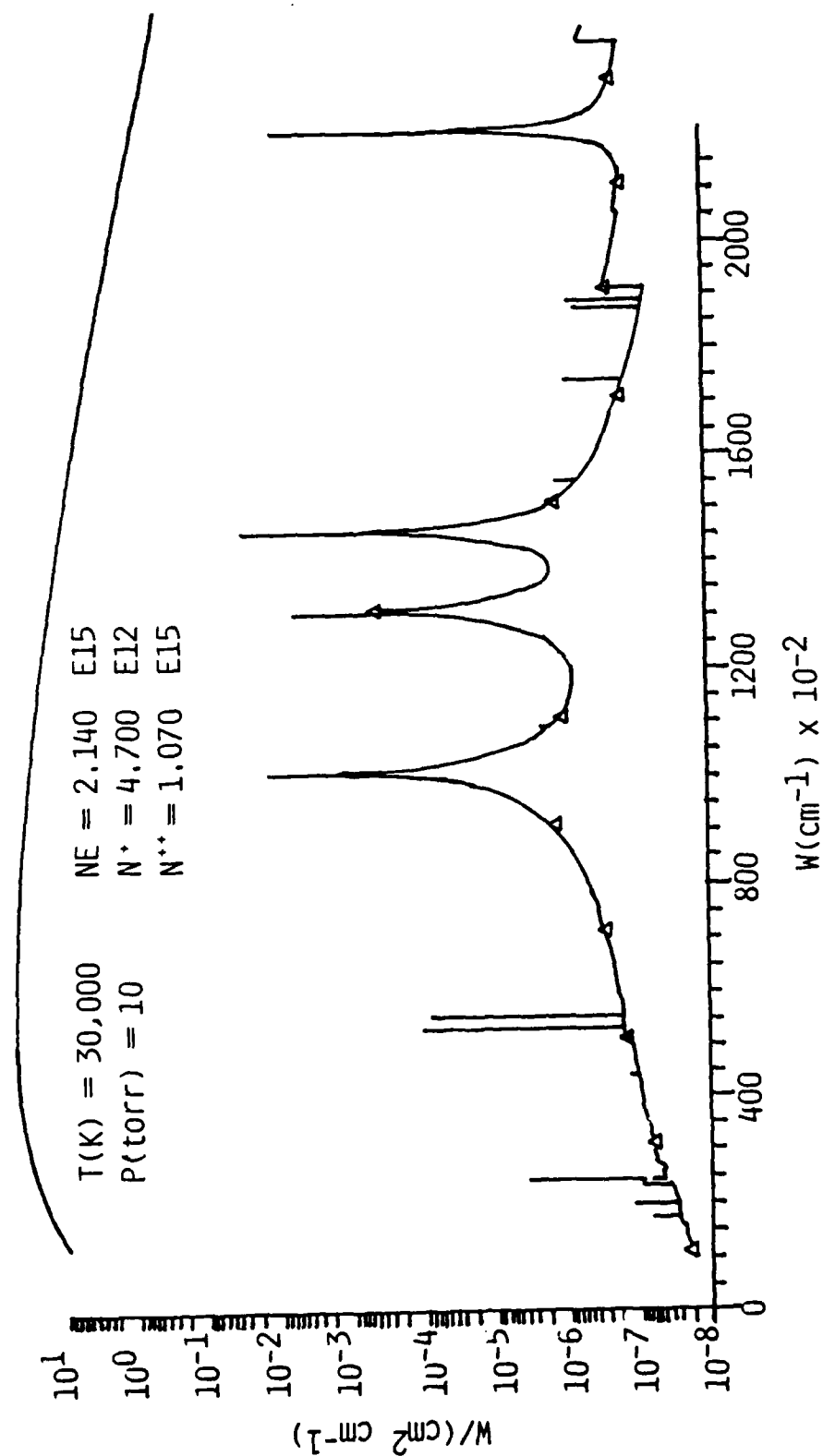
Fig. 21 Emission by an equilibrium nitrogen plasma slab of thickness 0.2 mm in the 0 to 250,000 cm⁻¹ band, T = 30,000 K, p = 10 torr.
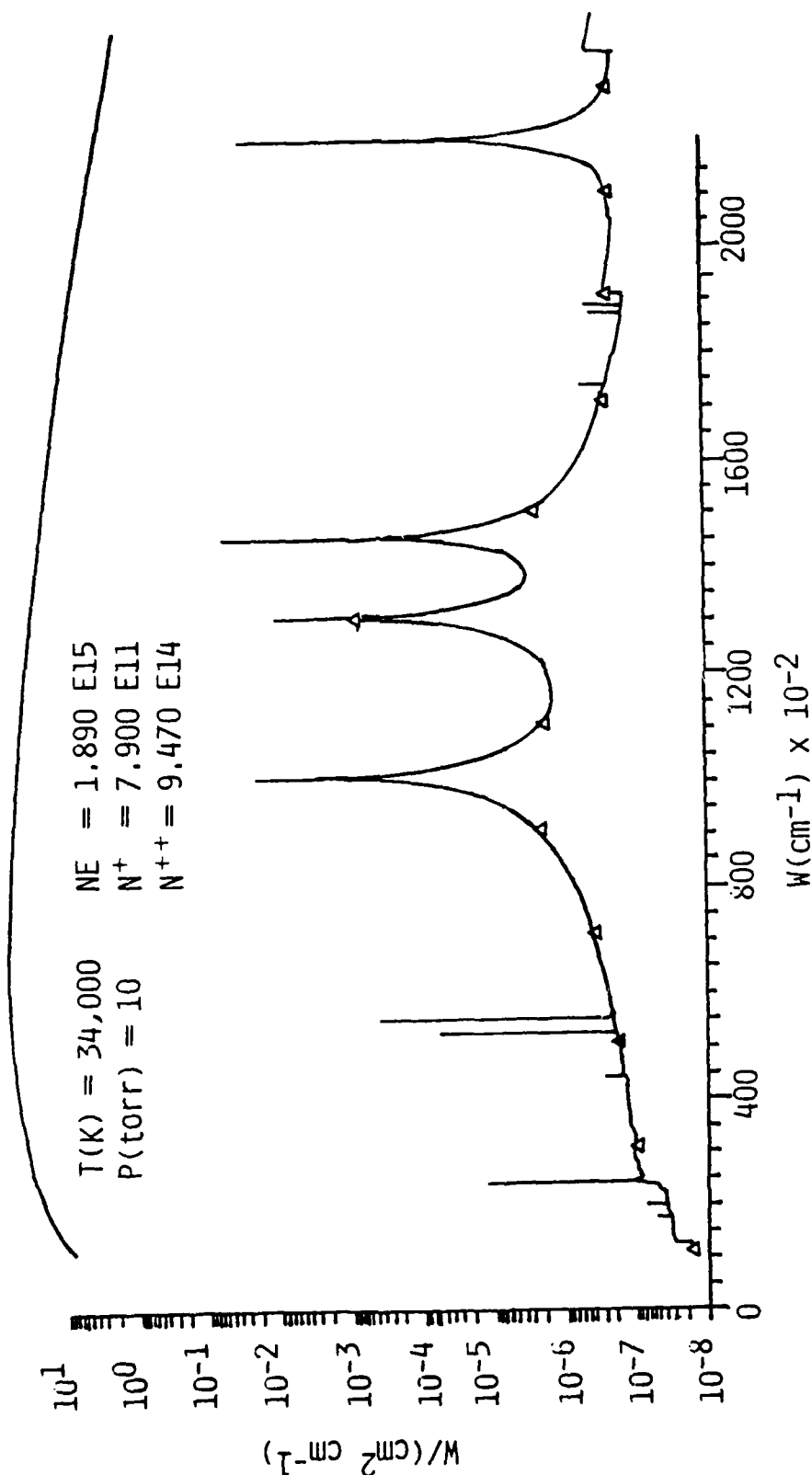
Fig. 22 Emission by an equilibrium nitrogen plasma slab of thickness 0.2 mm in the 0 to 250,000 cm^{-1} band, $T = 34,000$ K, $p = 10$ torr.

$T(K) = 34,000$ $NE = 1.890$ E15

$P(torr) = 10$ $N^+ = 7.900$ E11

$N^{++} = 9.470$ E14

$T(K) = 10,000$ $NE = 6.550$ $E15$
$P(torr) = 100$ $N = 6.300$ $E16$
$N^+ = 6.550$ $E15$

$W(cm^{-1}) \times 10^{-2}$

$W/(cm^2 \ cm-1)$
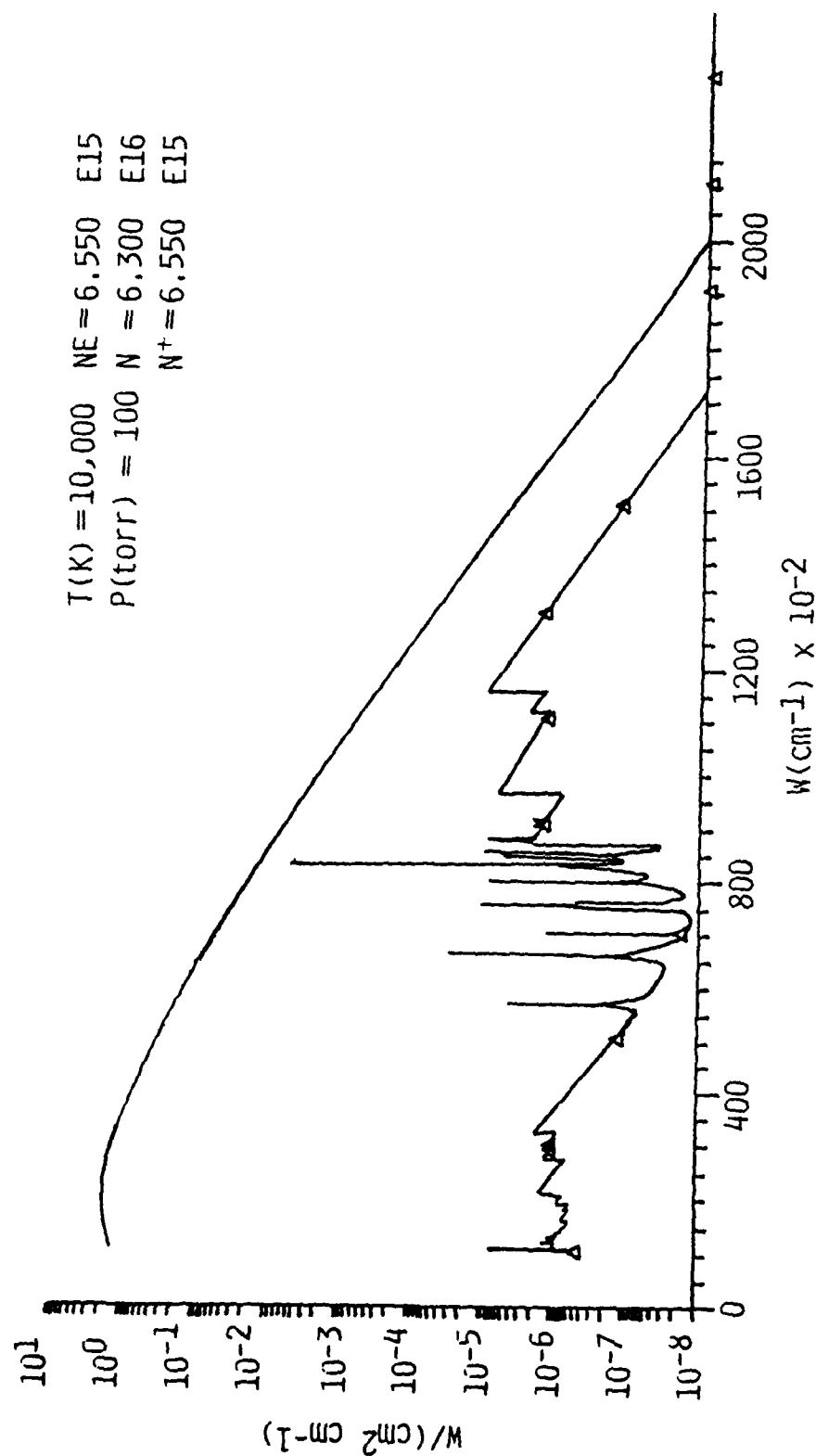
Fig. 23 Emission by an equilibrium nitrogen plasma slab of thickness 0.2 mm in the 0 to 250,000 cm^{-1} band, $T = 10,000$ K, $p = 100$ torr.
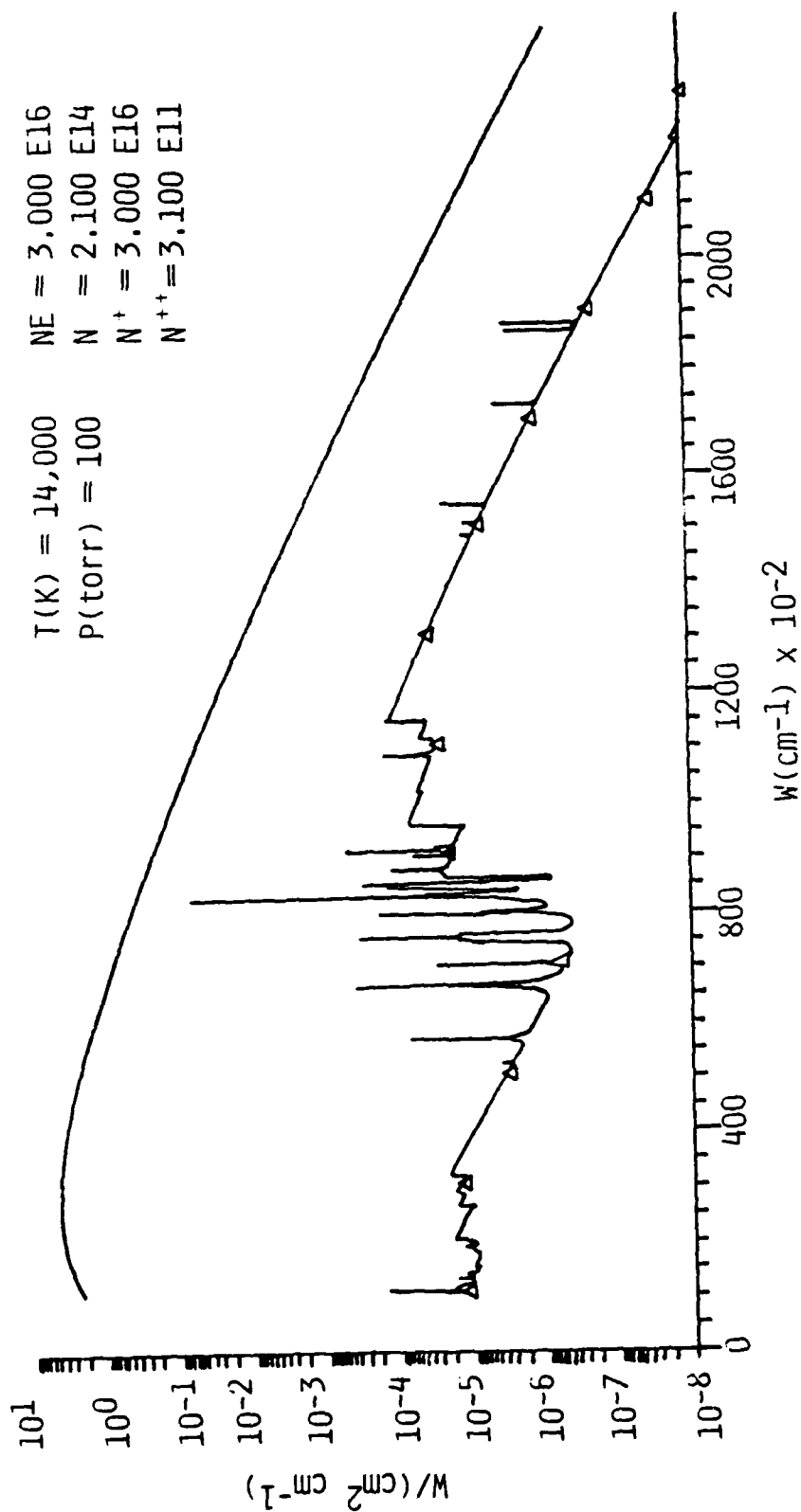
Fig. 24 Emission by an equilibrium nitrogen plasma slab of thickness 0.2 mm in the 0 to 250,000 cm^{-1} band, T = 14,000 K, p = 100 torr.
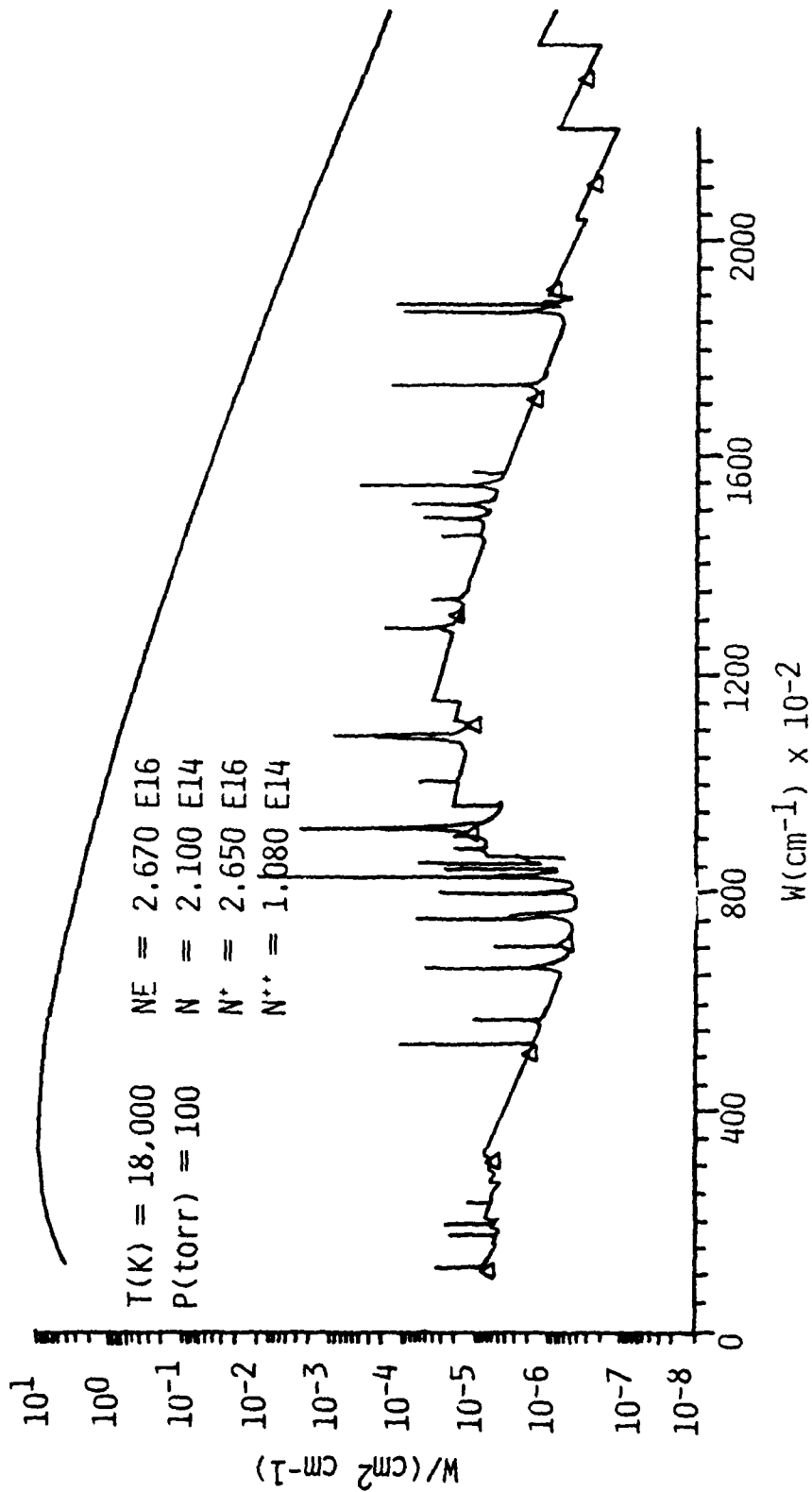
Fig. 25 Emission by an equilibrium nitrogen plasma slab of thickness 0.2 mm in the 0 to 250,000 cm^{-1} band, T = 18,000 K, p = 100 torr.

T(K) = 18,000   NE = 2.670 E16
P(torr) = 100   N = 2.100 E14
                 N$^+$ = 2.650 E16
                 N^{++} = 1.080 E14

W(cm^{-1}) × 10^{-2}

W/(cm^2 cm-1)
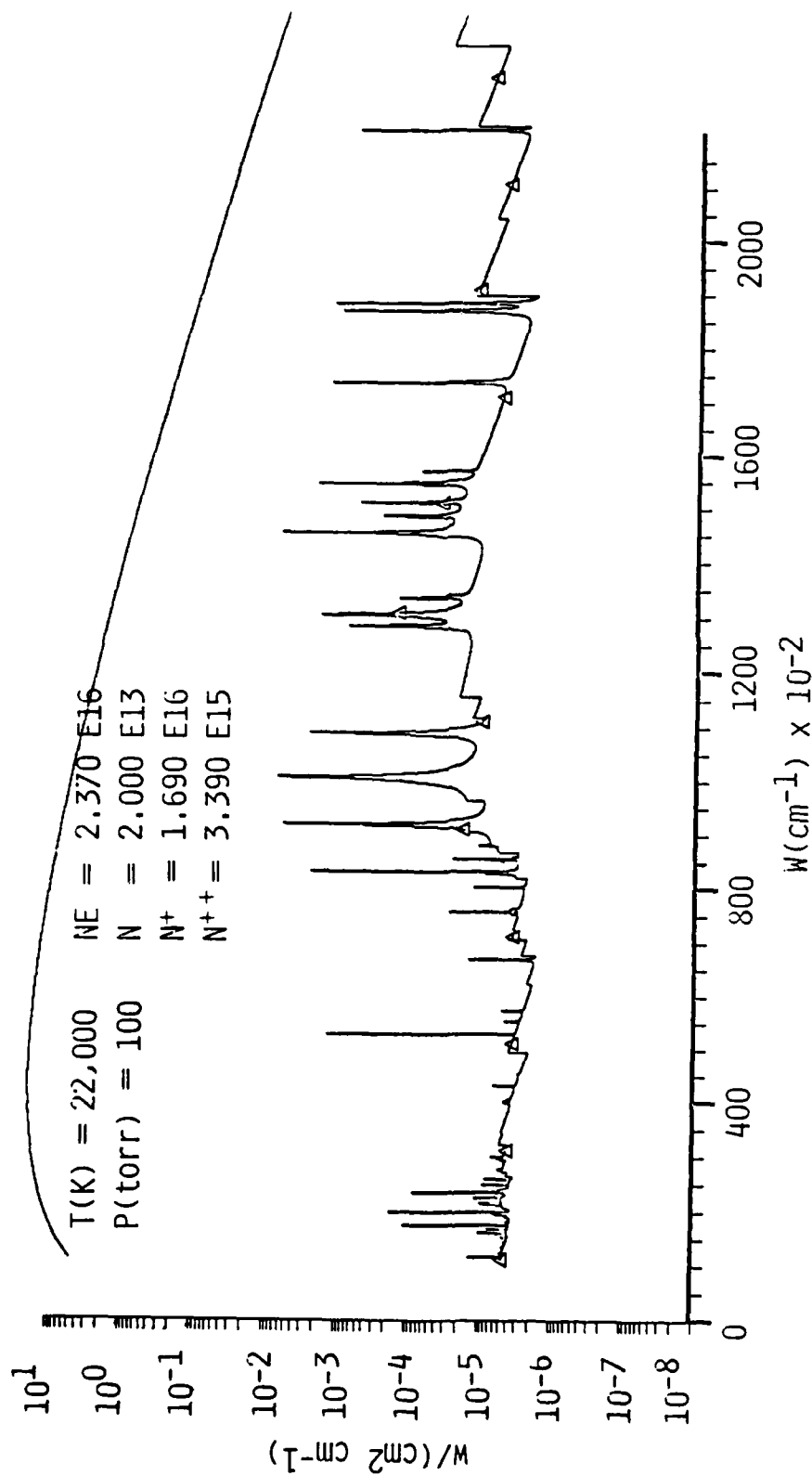
Fig. 26 Emission by an equilibrium nitrogen plasma slab of thickness 0.2 mm in the 0 to 250,000 cm^{-1} band, $T = 22,000$ K, $p = 100$ torr.
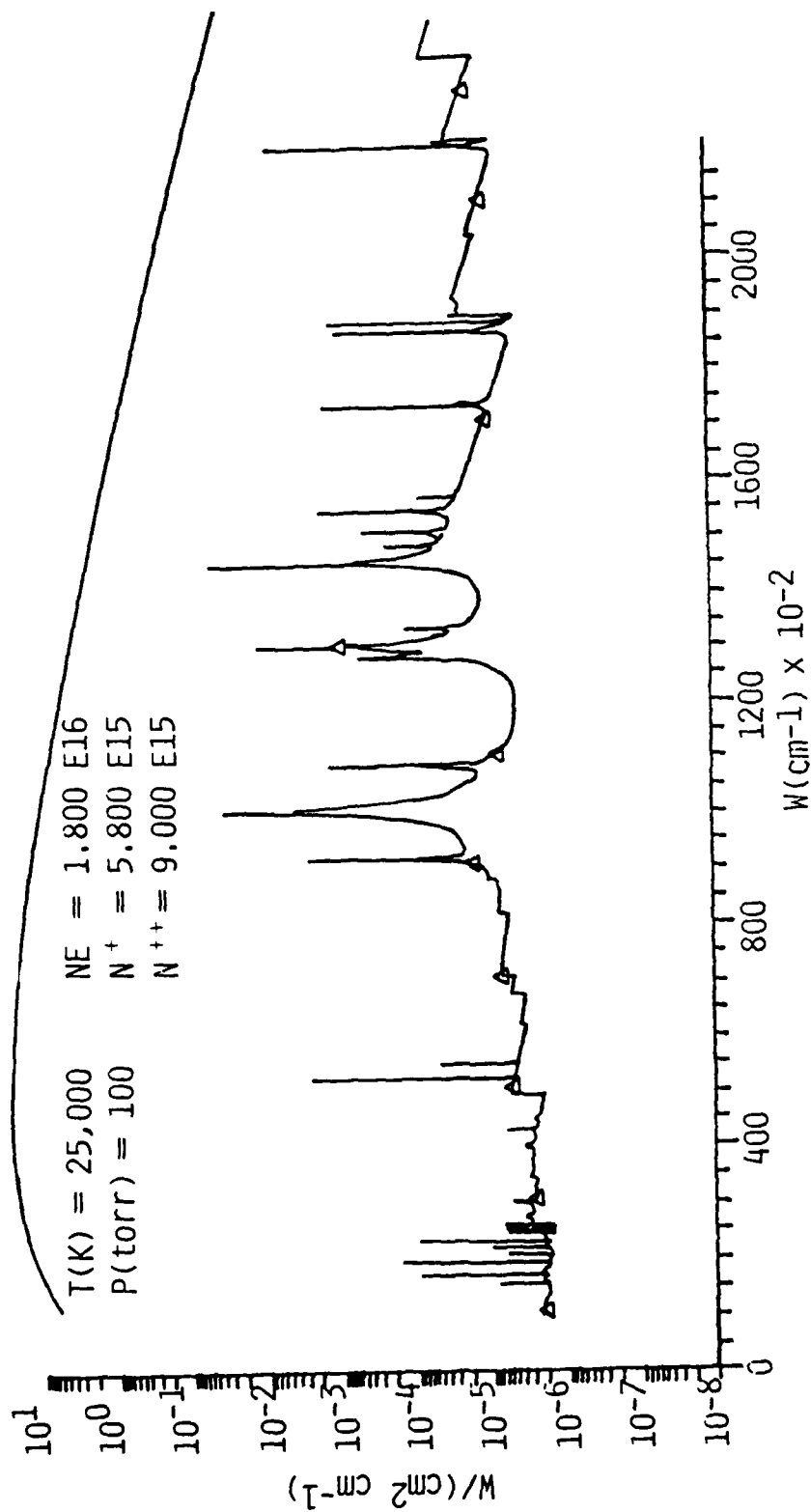
Fig. 27 Emission by an equilibrium nitrogen plasma slab of thickness 0.2 mm in the 0 to 250,000 cm^{-1} band, T = 25,000 K, p = 100 torr.
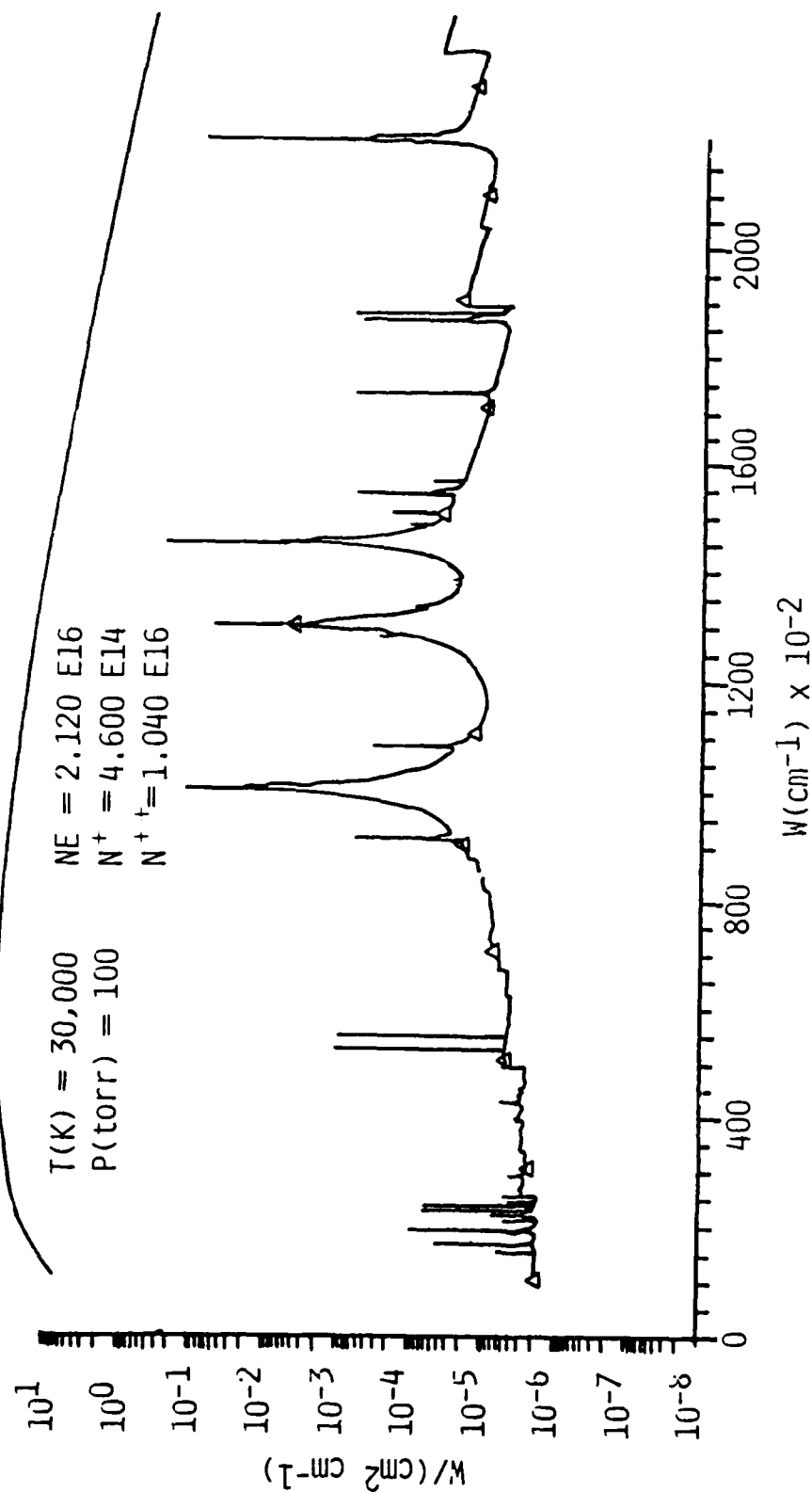
Fig. 28 Emission by an equilibrium nitrogen plasma slab of thickness 0.2 mm in the 0 to 250,000 cm⁻¹ band, T = 30,000 K, p = 100 torr.
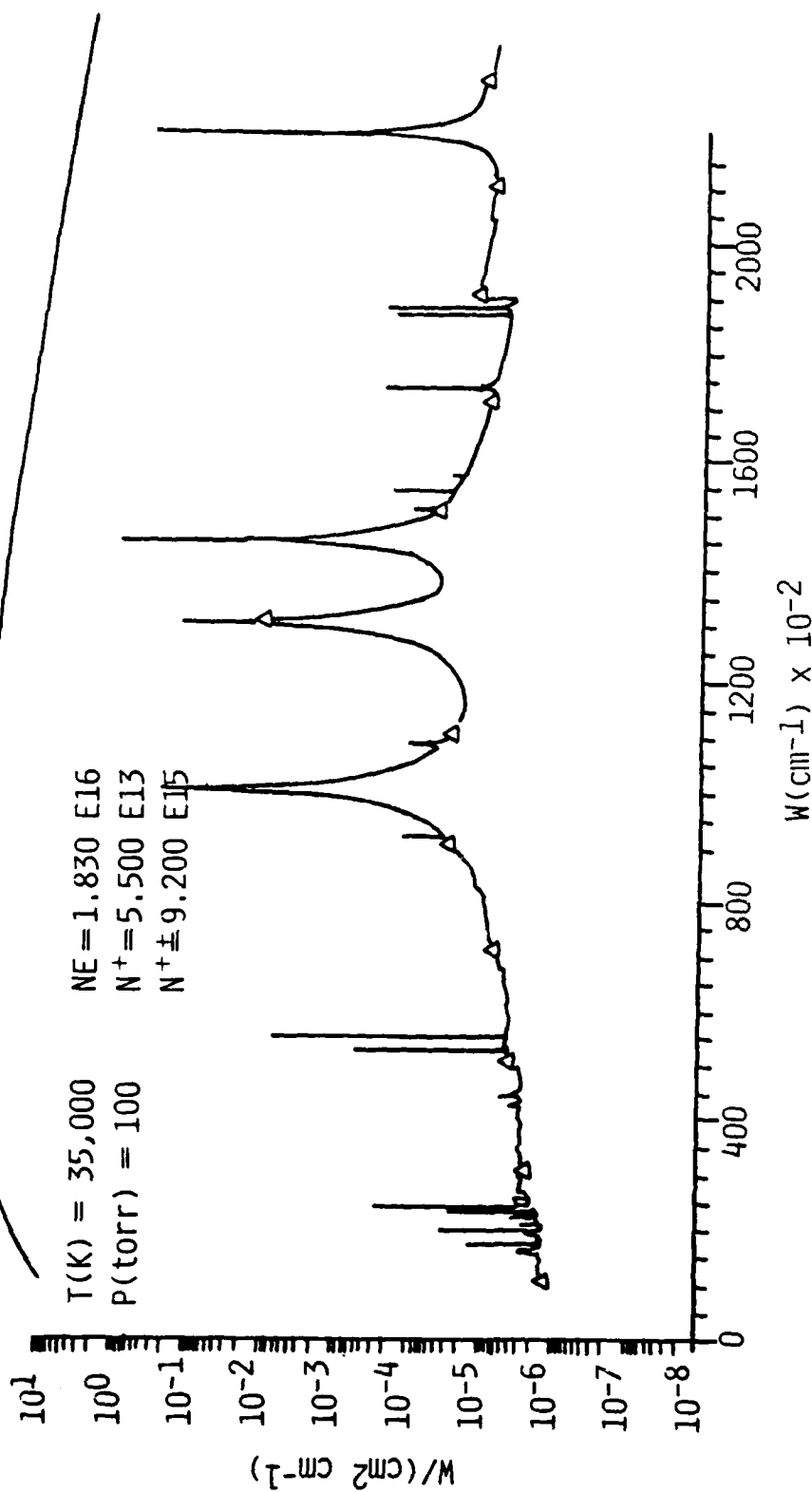
Fig. 29 Emission by an equilibrium nitrogen plasma slab of thickness 0.2 mm in the 0 to 250,000 cm^{-1} band, T = 35,000 K, p = 100 torr.
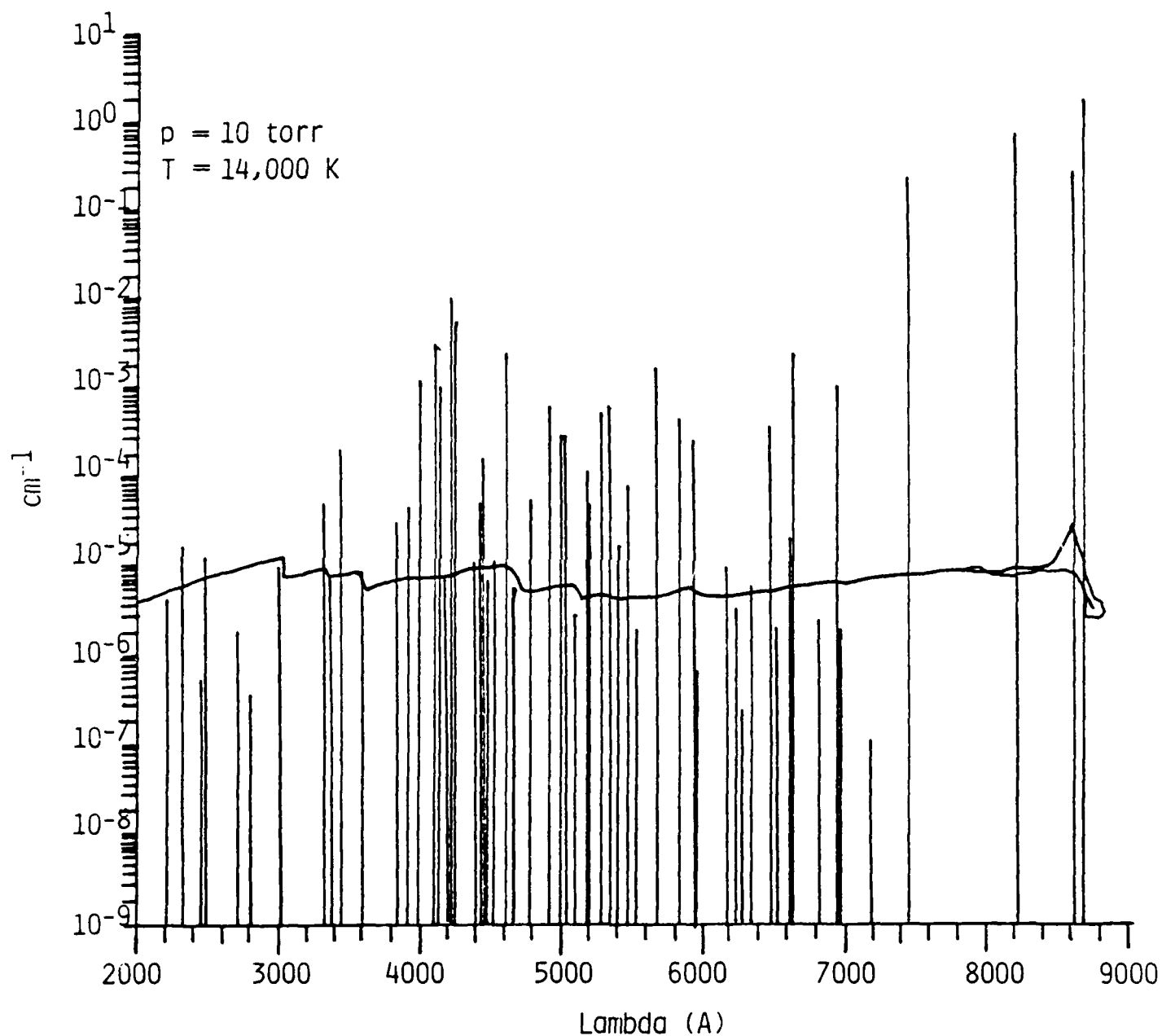
Fig. 30 Absorption coefficient at line center in the 0.2 - 0.9 μm band, nitrogen,
T = 14,000 K, p = 10 torr.
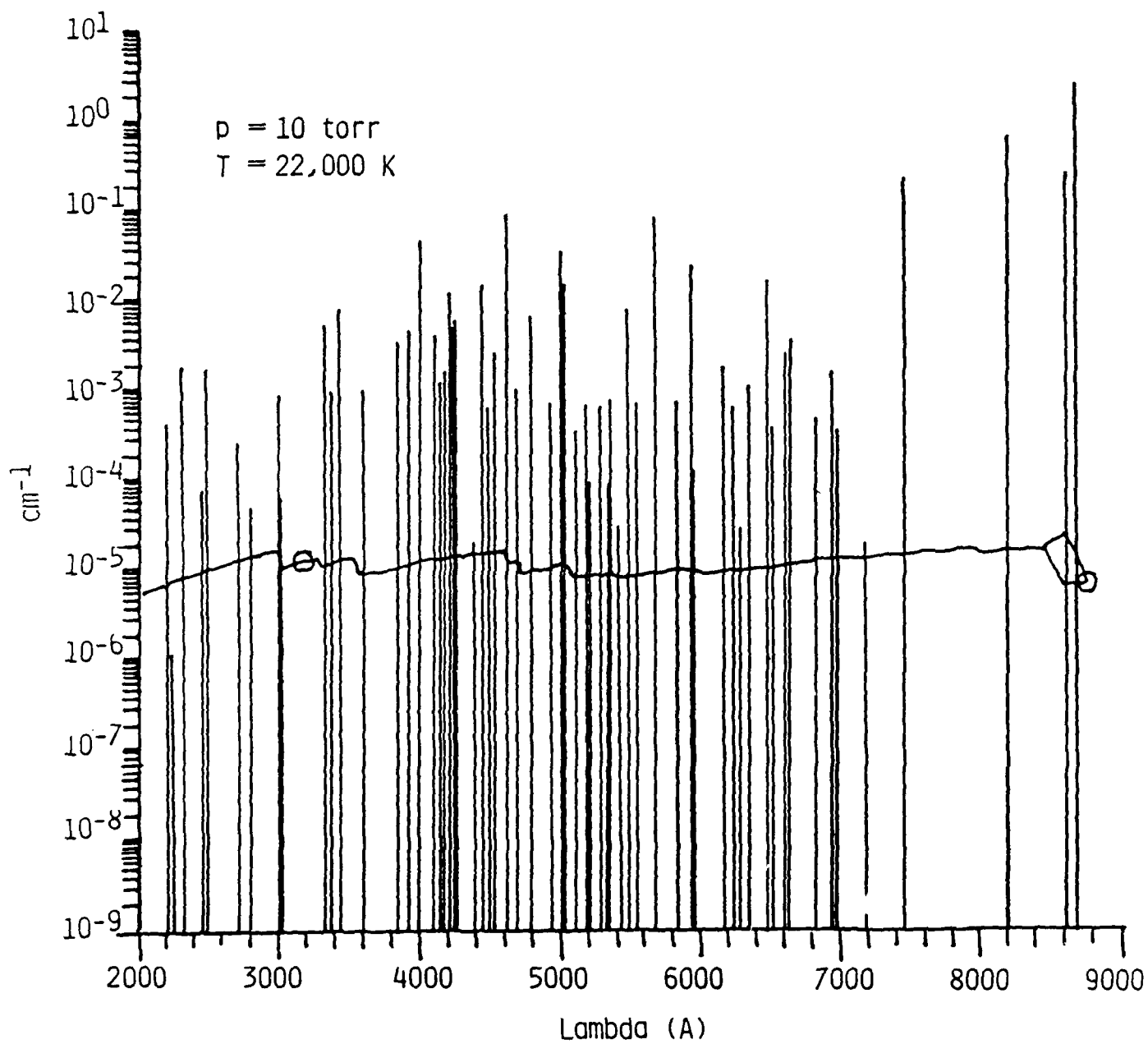
Fig. 31 Absorption coefficient at line center in the 0.2 - 0.9 µm band, nitrogen,
T = 14,000 K, p = 10 torr.

We show in Fig. 32 radiation emitted in the wave number band $0 < \bar{\nu} < 250,000$ cm^{-1} (500 Å $< \lambda < \infty$) and in Fig. 33 the integrated emission in the spectral band of the radiometer $0.2 < \lambda < 0.9$ μm. A comparison of Figs. 32 and 33 indicate that the radiometer would be measuring less than 1% of the radiation emitted by the plasma if it were in thermal equilibrium. Analysis of the validity of local thermodynamic equilibrium (LTE) for line radiation is presented in Section 4.3

4.2   Free Bound Continuum in the Visible

We show in Fig. 34 calculated radiation in the visible (mainly due to bound-bound and *free-bound* transitions) for $p = 100$ *torr* and $T = 10,000$ K. Also shown in this figure is time integrated spectrometer data in which line radiation has been eliminated. This curve was reproduced from the normalized spectrum shown in Fig. 1. The abscissa at the maximum was chosen in such a way as to superimpose the data and computed radiation. There is a strong indication from a comparison of the two curves that the continuum radiation in the visible is due to free-bound transitions. We examine free-bound radiation in the visible in more detail below, especially with regard to the relaxation of the assumption of LTE. Free-bound radiation can be calculated by detailed balance by looking at the reverse process of reaction 19, which is photoionization of excited states,

$$N^* + h\nu \rightarrow N^+ + e .$$ (20)

The threshold for reaction (6) is

$$h\nu_c = \epsilon_I - \epsilon^* ,$$

and the cross section, following Zel'dovich and Raizer,[5] is given by

$$\sigma_{phi} = 7.9 \times 10^{-18} \frac{n}{Z^2} \left(\frac{\nu_c}{\nu}\right)^3 \quad cm^2$$ (21)

where n is the principal quantum number, Z the charge of the remaining core ($Z = 1$ for N^+) and $\nu > \nu_c$. By detailed balance we must have
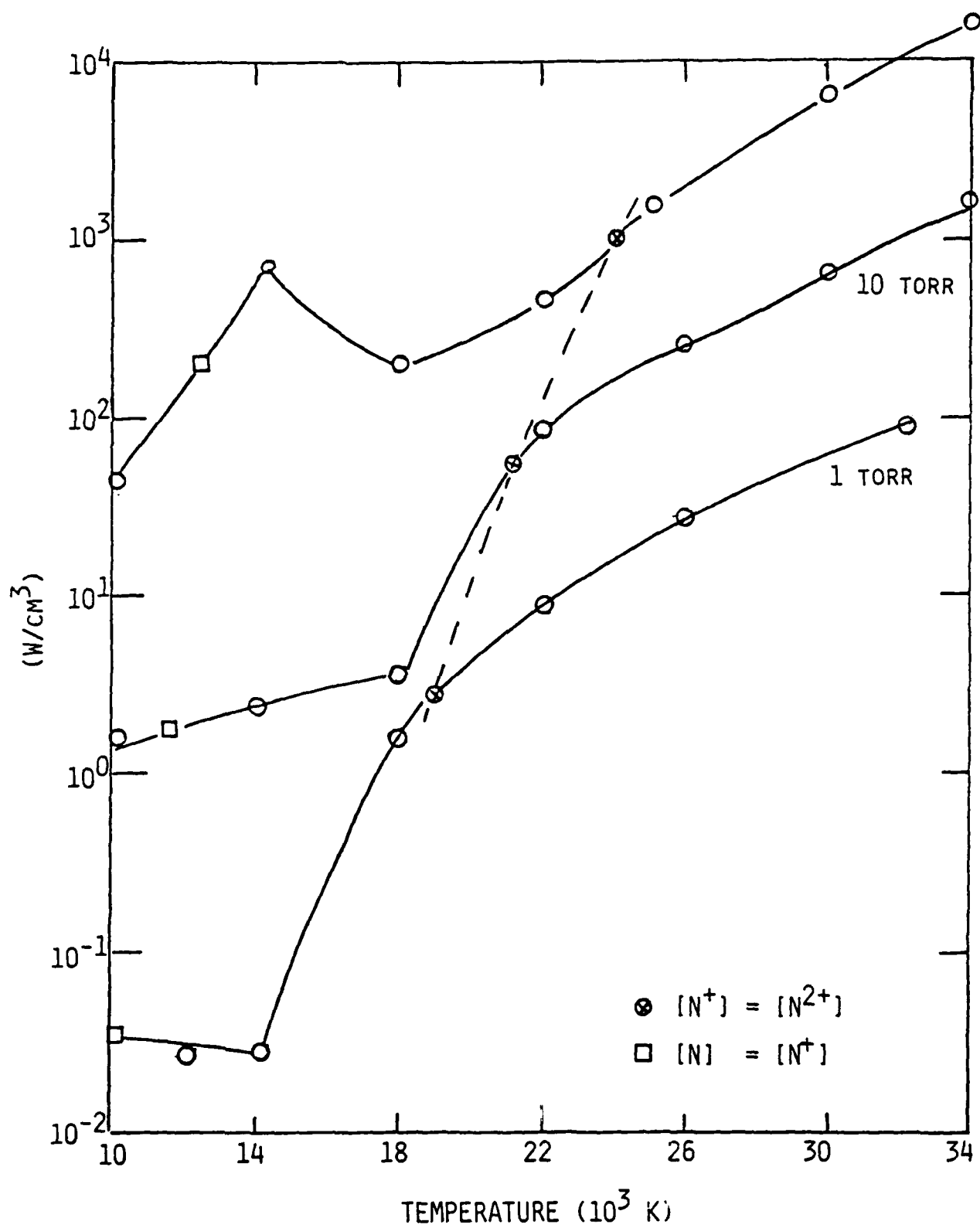
Fig. 32   Integrated emission in the wavenumber band $0 < \bar{\nu} < 250,000$ cm^{-1}.
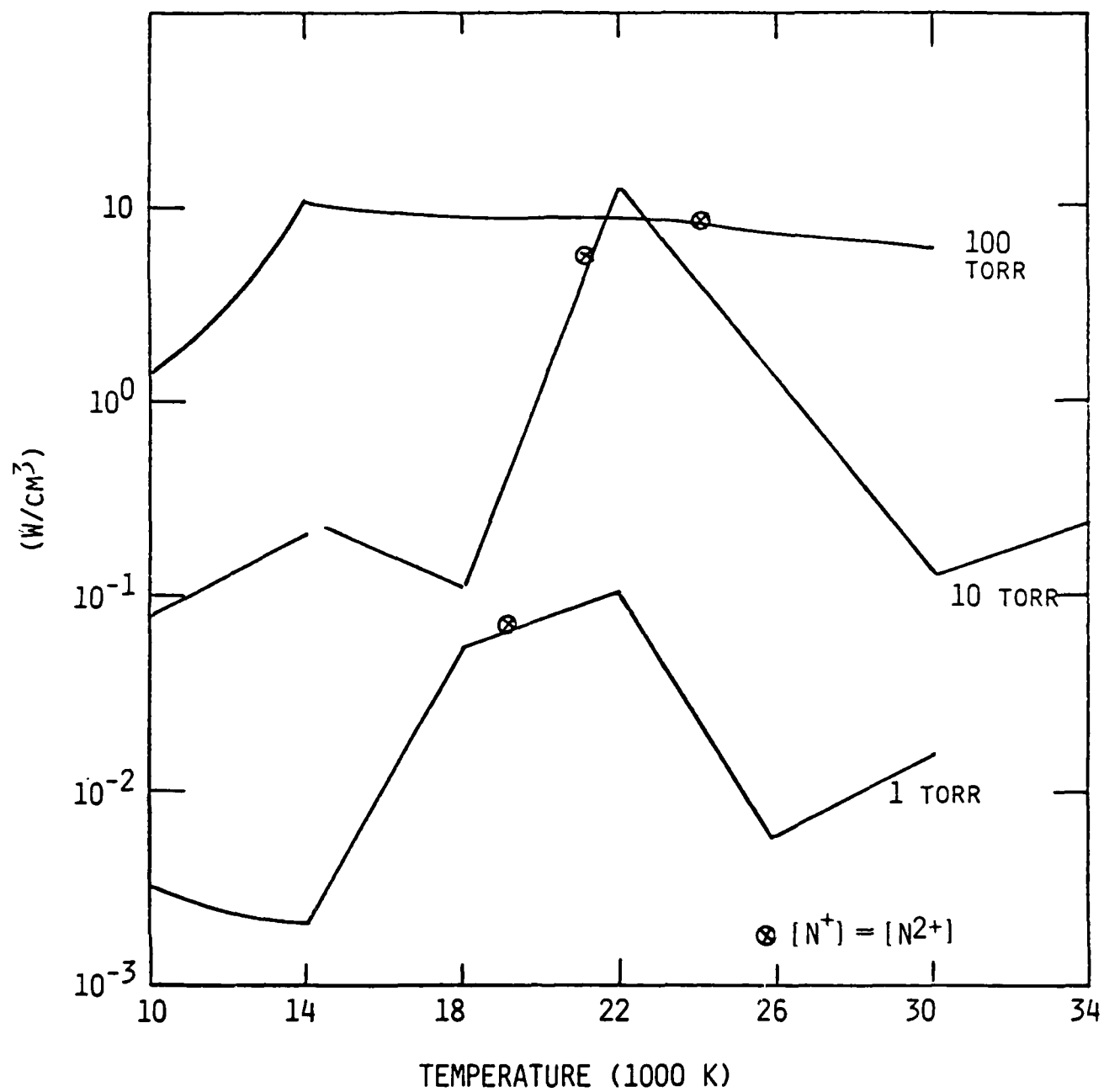
Fig. 33   Integrated emission in the radiometer band $0.2 < \lambda < 0.9$ μm.
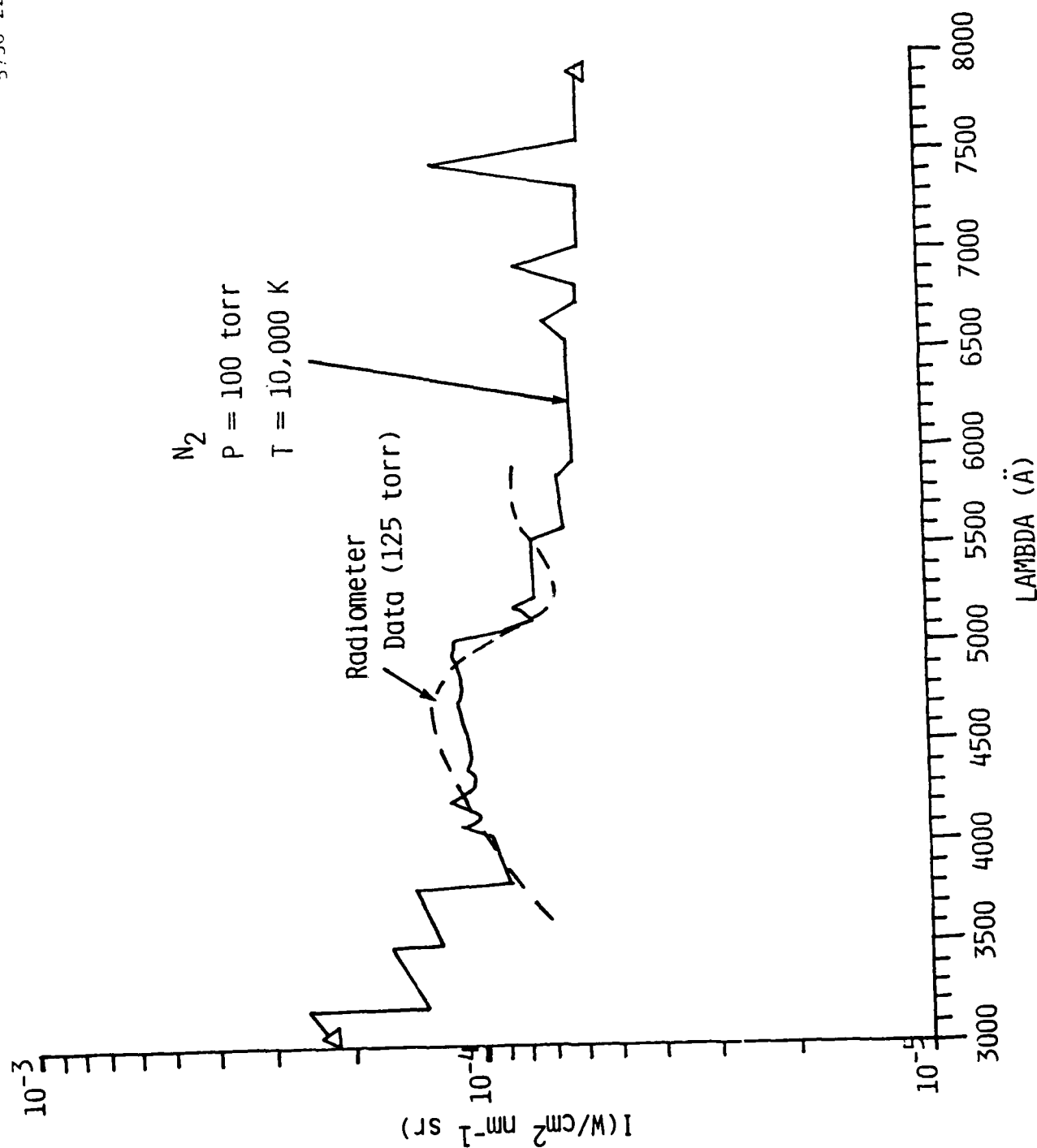
Fig. 34 Radiation in the visible (0.2 mm slab).

$$\left(1 - e^{-h\nu/kT}\right) \frac{\rho_{BB}(\nu,T)c}{h\nu} \, d\nu \, \sigma_{phi} \, [N^*] = n_e [N^+] \, f_B(\epsilon,T) \, \sigma_{FB}(\epsilon) \, \sqrt{\frac{2\epsilon}{m}} \, d\epsilon \quad (22)$$

where $d\epsilon = hd\nu$, f_B is a Maxwell Boltzmann distribution function for electrons at T and ρ_{BB} is the energy density of black body radiation per unit frequency interval. The concentrations of electrons, $[N^*]$ and $[N^+]$ are related by the equations of LTE,

$$\frac{[N^+][n_e]}{[N^*]} = \frac{[N^+][n_e]}{[N]} \frac{[N]}{[N^*]} = \frac{AT^{3/2}g^+}{g^*} e^{-\left(\frac{\epsilon_I - \epsilon^*}{kT}\right)} \quad (23)$$

The radiation code that we have used uses the left-hand side of Eq. (22) to calculate the plasma radiation while in reality it is the right-hand side which represents emission. After the rapid expansion the plasma is far from LTE, as we shall see in Section 4.3, since recombination is slow. The radiation per unit volume is given by

$$\int W(\nu)d\nu = \int h\nu n_e [N^+] \sqrt{\frac{2\epsilon}{m}} \, f(\epsilon) \sigma_{FB} \frac{d\epsilon}{d\nu} \, d\nu$$

$$= \int h^2 \nu n_e [N^+] \sqrt{\frac{2\epsilon}{m}} \, f(\epsilon) \, \sigma_{FB}(\epsilon) \, d\nu$$

where $f(\epsilon)$ is the distribution function of electrons in energy space. The free-bound cross section is found to be, from Eqs. (21) through (23),

$$\sigma_{FB}(\epsilon) = \frac{\sigma_{phi}(\nu)}{2} \frac{(h\nu)^2}{mc^2\epsilon} \frac{g^*}{g^+}$$

$$\cong \frac{h\nu n^2}{mc^2\epsilon} \sigma_{phi} \quad (\nu = \nu_C + \epsilon/h) \quad (24)$$

where in the last step we used the fact that $g^* \cong 2n^2$ (n = principal quantum number). If we assume that $f(\epsilon)$ is a Boltzmann distribution at temperature T,

$$f_B(\varepsilon) = \frac{2}{\sqrt{\pi}} \frac{\sqrt{\varepsilon}}{(kT)^{3/2}} e^{-\varepsilon/kT} \tag{25}$$

we obtain the radiation emitted per unit volume in the bandwidth $\Delta\nu$

$$W(\nu)\Delta\nu = h\nu n_e [N^+] \, f_B(\varepsilon,T)\sigma_{FB} \sqrt{\frac{2\varepsilon}{m}} \frac{d\varepsilon}{d\nu} \Delta\nu$$

$$= \sqrt{\frac{8}{\pi m}} \frac{1}{(kT)^{3/2}} n_e [N^+] \, e^{-\varepsilon/kT} \frac{(h\nu)^2}{mc^2} n^2 \sigma_{phi} (\nu = \nu_c + \varepsilon/h) \, \Delta\nu$$

$$= B \, e^{-\varepsilon/kT} \left(\frac{\nu_c}{\nu}\right) \Delta\nu \, , \tag{26}$$

where in the last step we lumped into the factor B all quantities that do not depend on ν, and note that, by conservation of energy, $\varepsilon = h(\nu - \nu_c)$.

We show in Table 1 the wavelengths $\lambda_j (= c/\nu_j)$ and corresponding energy levels which represent the threshold below which a free-bound radiative transition can occur. The actual radiation at $\lambda(\nu)$ will correspond to the sum of those transitions for which $\lambda_j > \lambda$ (or $\nu_j < \nu$).

$$W(\nu) = \sum_{\nu_j < \nu} B_j \, e^{-h(\nu - \nu_j)/kT} \left(\frac{\nu_j}{\nu}\right) \tag{27}$$

We have used Eq. (27) to model free-bound radiation in the visible. Since the spectrometer measured $W(\lambda)$ rather than $W(\nu)$ it is more convenient to rewrite (27) as

$$W(\lambda) = \sum_{\lambda_j > \lambda} B_j \left(\frac{\lambda}{\lambda_j}\right)^3 e^{-\left[\frac{hc}{kT}\left(\frac{1}{\lambda} - \frac{1}{\lambda_j}\right)\right]} \tag{28}$$

TABLE 1

Energy levels for free-bound radiation in the visible

SPECIES	λ_j (Å)	STATE			ε_j^* (cm^{-1})
N	8180	$2p^2$	$3d$	^2D	105030
	7850	$2p^2$	$3d$	^1P	104600
	7270	$2p^2$	$4s$	^4P	103600
	5650	$2p^2$	3_s	^2D	99660
	5108	$2p^2$	$3p$	$^2P^o$	97770
	4867	$2p^2$	$3p$	$^2D^o$	96800
	4855	$2p^2$	$3p$	$^4S^o$	96750
	4570	$2p^2$	$3p$	$^4P^o$	95476
	4442	$2p^2$	$3p$	$^4D^o$	94770
	4208	$2p^2$	$3p$	$^2S^o$	93582
	3213	$2p^2$	3_s		86223
N$^+$	5680	$2p$	$5f$	$^3G, ^1G$	221200
	4067	$2p$	5_s	^3P_o	214250
	3655	$2p$	$4f$	$^3D, ^1G$	211490
	3630	$2p$	$4f$	^3G	211300
	3590	$2p$	$4f$	$^1F, ^3F$	211000
	3550	$2p$	$4d$	$^3P^o$	210705

We have plotted Eq. (28) in Fig. 35 assuming B_j was the same for all transitions and with T chosen so that

$$\frac{W(\lambda = 4200\text{Å})}{W(\lambda = 3500\text{Å})} = 2$$

as was experimentally observed. This yields an electron temperature of 1.4 eV (16,000 K). The resulting free-bound continuum thus obtained has a strikingly similar shape than the experimentally observed continuum. Note, however, that, because the radiation was measured with a relatively long (200 ns) box car integrator, it is likely that the electron temperature varied significantly during the measurement.

We also have plotted, as a dashed line, in Fig. 35 free-bound radiation due to the reaction

$$N^{2+} + e \rightarrow (N^+)^* + h\nu.$$
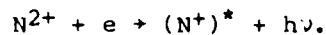
It is clear from the figure that recombinations of N^{2+} cannot explain the radiation peak observed at 4500Å.

4.3   Temporal Behavior of Line Radiation

We have shown in Figs. 2 through 4 some of the data taken that show the temporal behavior of line radius in the LINUS. This behavior can be summarized as follows.

a)   The radiation first increases with time, reaches a maximum and then decreases.

b)   Peaks in radiation occur first for lines from N^{2+}, then N^+ and finally N.

c)   The decay times increase with increasing pressure, decrease with increasing ionization and are in the range 20-200 ns.

d)   All lines originating from the same ionic species have roughly the same decay times irrespective of the upper energy level from which they originate.

Since the lifetime for transitions measured in the visible is $\sim 10^{-8}$ s i.e., much shorter than the observed decay times of the line radiation, one
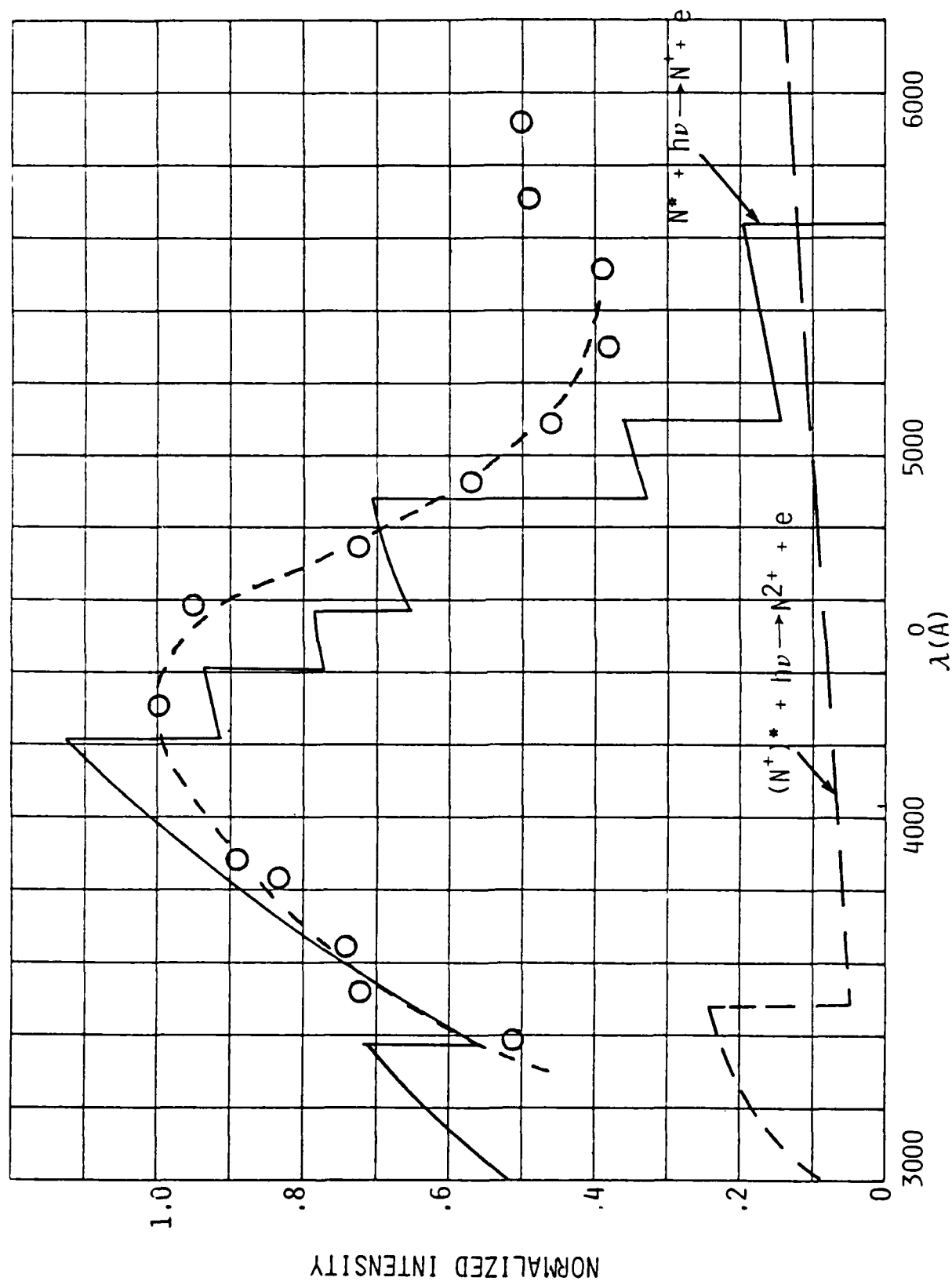
Fig. 35 Free bound continuum due to the reactions $N^+ + e \rightarrow N^* + h\nu$ and $N^{++} + e \rightarrow N^+ + h\nu$.

must recognize that the excited states are being replenished. Therefore, observation c together with observations a and b are consistent with the hypothesis that local thermodynamic equilibrium (LTE) is maintained during and after the expansion. The rise and decay of line radiation would be associated, then, with the shift in dominant ionic species from N^{3+} to N^{2+}, N^+ and, finally, N as the plasma cools by expansion and later by thermal conduction. We must verify, however, that observation d obtained from the decay rate of line radiation (see Fig. 3) is satisfied. We now analyze decay of N^+ line radiation. If LTE were maintained, the concentration of N^+ ions would be given by the Saha equation, Eq. (10),

$$\frac{n_e [N^+]}{[N]} = AT^{3/2} \frac{g^+}{g} \exp\left(- \epsilon_1/kT\right) \tag{10}$$

Also, the population of the excited state is proportional to its Boltzmann factor.

$$\frac{[N^+]^*}{[N^+]} = \frac{g^*}{g_+} \exp\left(- \epsilon^*/kT\right) \tag{29}$$

where ϵ^* is the energy with respect to the ground state of the ion. When $[N^+] \gg [N]$, we can neglect the variation of n_e and N^+ with temperature and, taking the logarithmic deviative of Eq. (29), we obtain the decay of line intensity S_{ij},

$$\frac{d\ell n S_{ij}}{dt} = \frac{d\ell n\ (N^+)}{dt} - \frac{\epsilon^*}{kT} \frac{d\ell n T}{dt} \tag{30}$$

At lower temperatures, however, when N^+ is rapidly disappearing by recombination, we have $[N^+] \propto T^{3/4} \exp\left(-\epsilon_1/2kT\right)$, so that taking the logarithmic derivative of Eq. (29), we obtain

$$\frac{d\ell n S_{ij}}{dt} = - \frac{2\epsilon^* + \epsilon_1}{2kT} \frac{d\ell n T}{dt} \tag{31}$$

We apply the above to Fig. 3. Information on the lines is given in Table 2. We compare line #15 having the lowest energy $\epsilon^* = 20.63$ eV with line #61 having the highest energy $\epsilon^* = 26.2$ eV. From Fig. 10 we expect the N^+ concentration to become important and that N^+ line radiation peaks when the

TABLE 2

Energy levels of observed transition

Line Number	Wavelength (Å)	Upper Energy Level (cm-1)
20	3437.2	178274
41	3838.4	196712
61	4040.9	211332
25	4447.0	187092
17	4621.4	170573
28	4803.3	187493
16	5045.1	168893
15	5679.6	166679

temperature of the plasma has decreased to ~ 1.6 eV at p = 10 torr. The con-
centration of the 4 f state of N^+ (upper level of line #61) has decreased by a
factor of ten when the temperature has changed by an amount - θ such that

$$0.1 = \exp - 26.2 \left(\frac{1}{1.6 + \theta} - \frac{1}{1.6} \right)$$

which yield θ = 0.2 eV = 2300 K. The concentration of the 3 p state of N^+
(line #15) using the same change in temperature has decreased by a factor of
only 6.1. The data in Fig. 1 at t = 285 ns indicate that when line #61 is at
1/10th of its peak, line #15 is at 1/8th of its peak value rather than at
1/6th. There is, therefore, some indication from the relative decay of line
radiation that LTE is not maintained. The deviation is not sufficiently large
to infer in a conclusive way that LTE is not maintained.

The line profiles, however, imply a drop of 2300 K in 180 ns x (T/θ) =
1.6 µs. We can readily show that the thermal decay time is much shorter
than this. The plasma is cooled by three processes: a) by expansion during
the blast wave, b) by radiation, and 3) by conduction to the surrounding
cooler gas. From Sec. 3 the rate of cooling of the plasma at time t due to
the expansion is

$$\frac{d\ell nT}{dt} = - \left(\frac{\gamma - 1}{\gamma} \right) t^{-1} \tag{32}$$

so that for γ = 1.2, corresponding to LTE being maintained and t ~ 10^{-7} s, we
find dℓnT/dt ~ 16 x 10^6 s^{-1} which is a factor of three larger than the decay
rate inferred from line radiation.

The plasma cooling rate due to conduction and radiative losses can be
estimated from the enthalpy equation for the plasma

$$\rho \frac{dh}{dt} = \frac{1}{r} \frac{\partial}{\partial r} \left(rK \frac{\partial T}{\partial r} \right) + \phi_R \tag{33}$$

where K = heat conductivity, h = enthalpy and ρ = density. The second term on
the right-hand side of Eq. (33) represents radiation losses. The decay rates
due to thermal conduction and radiative losses are, respectively

$$\tau_C^{-1} = \frac{1}{h}\frac{d_C h}{dt} \approx \frac{KT}{\rho h L^2} \tag{34a}$$

$$\tau_R^{-1} = \frac{1}{h}\frac{d_R h}{dt} \approx \frac{\phi_R}{\rho h} \tag{34b}$$

We use the equilibrium high temperature air properties of Yos[11] to obtain ρ, h and K as a function of T for various pressures. These are shown in Figs. 36 through 38. Open shutter photographs of the plasma indicate a plasma diameter after expansion of 0.2 mm, so that we may take L = 0.1 mm as an upper bound on plasma radius during the expansion. Using the above values, we obtain the times τ_L and τ_R shown in Figs. 39 and 40. We see that thermal conduction losses will dominate the cooling process. At T = 20,000 K and p = 10 torr the cooling rate is 5×10^8 s^{-1}, which would lead to a line decay rate (ϵ^*/kT) $\times$ $5 \times 10^8 = 5 \times 10^9$ to 3×10^{10} s^{-1}, a rate faster than the decay rate of the highly excited states (10^8 s^{-1}). We, therefore, can conclude that the plasma cooling rate by conduction is inconsistent with the observation of decay of line radiation and with the assumption of LTE. Some mechanism must play a role in limiting the population of the excited states from following LTE. We believe that the bottleneck is three-body recombination, as discussed in the next subsection.

We close the subsection by noting that the pressure dependence of the decay of line radiation is more consistent with the conclusion that thermal conduction rather than blast wave expansion determines the cooling rate of the plasma at t ⩾ 100 ns. The blast wave formulas do not have a pressure dependence in the decay rate of temperature. We note from Fig. 40 that the thermal decay time τ_C scales roughly as p. Fig. 2 shows the decay time of line radiation increases as some positive power of p.

4.4   Recombination of Plasma During and After Expansion

There are two mechanisms through which the fully ionized nitrogen plasma may recombine:
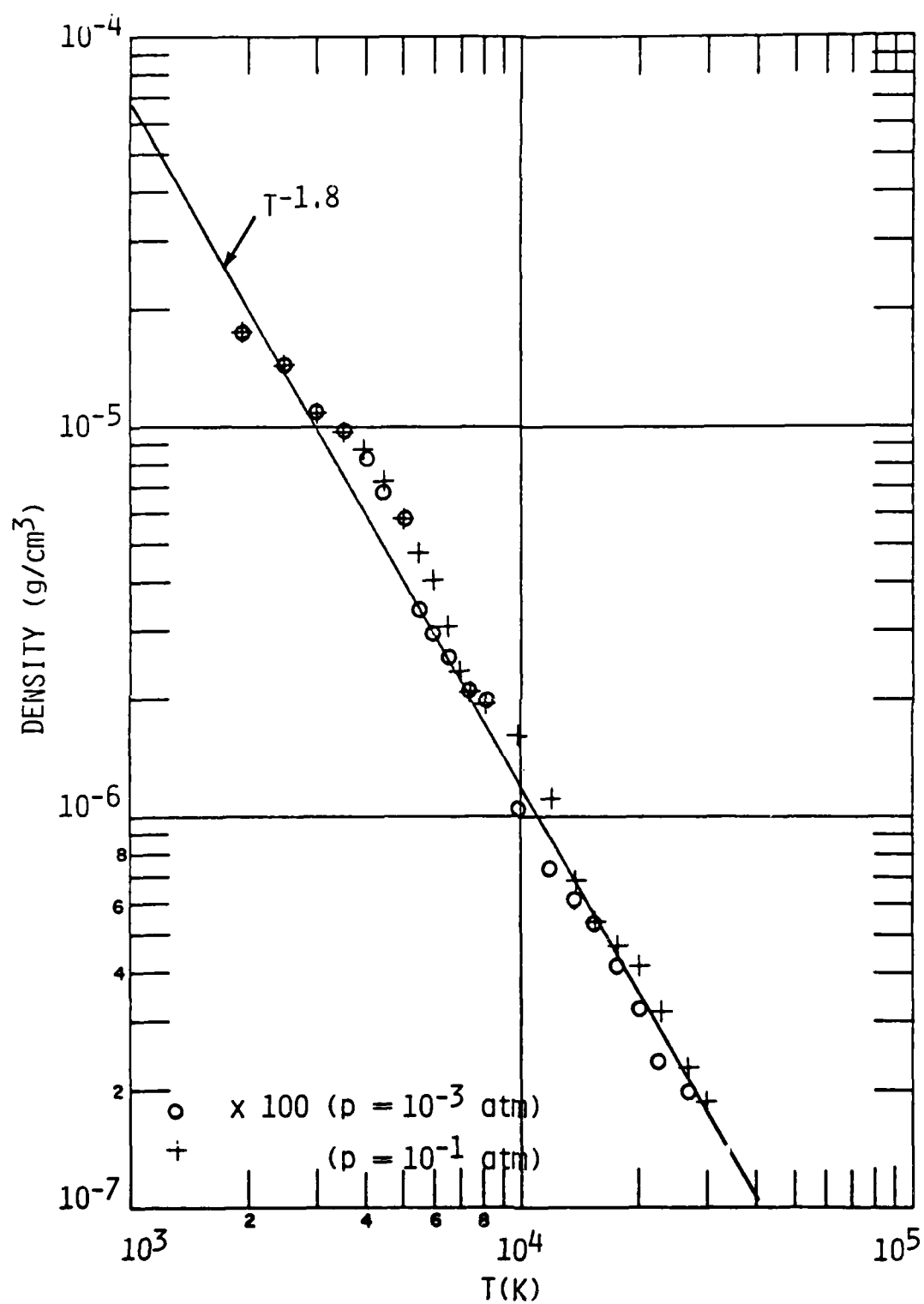
Fig. 36 Density of nitrogen.
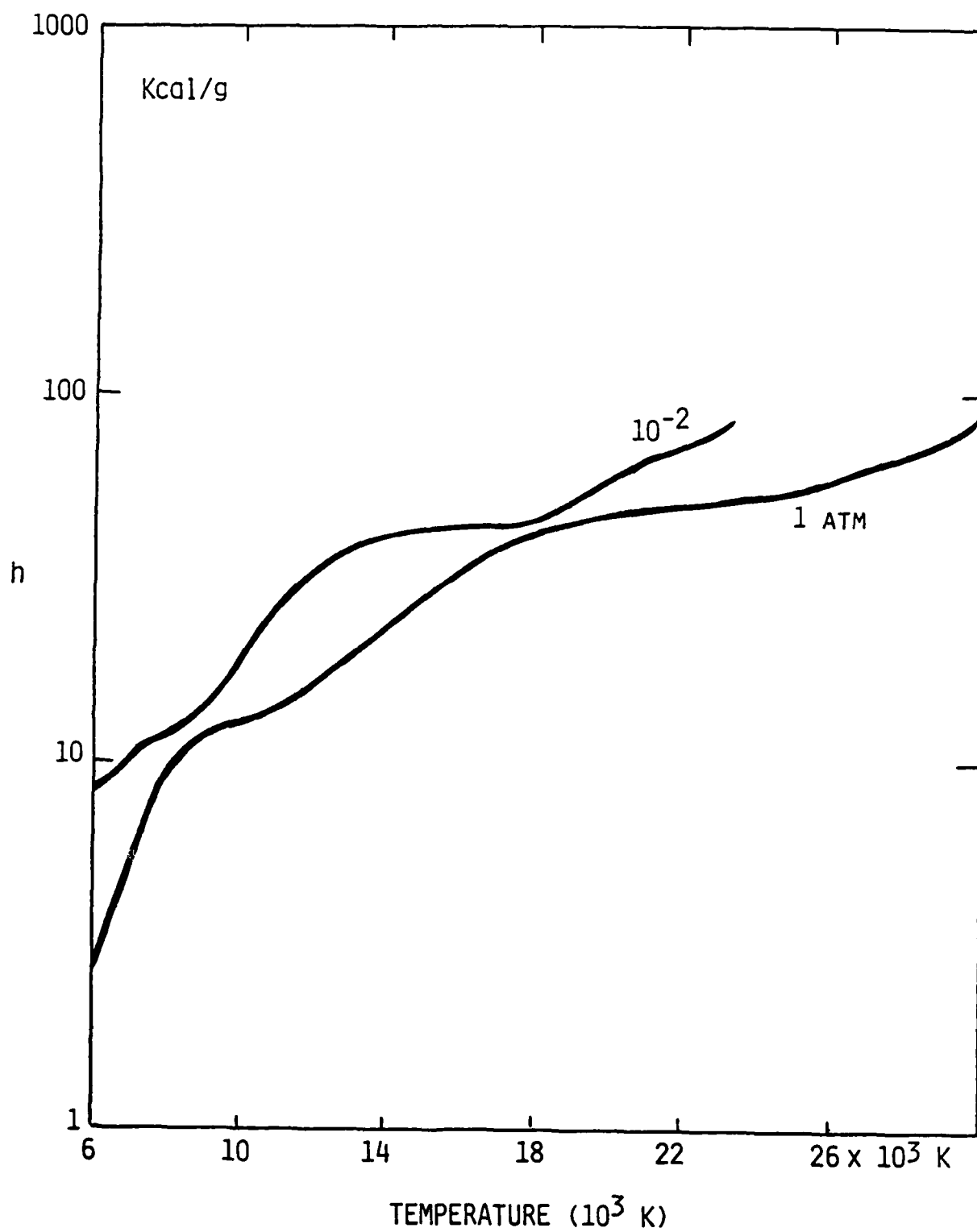
Fig. 37 Enthalpy of nitrogen.
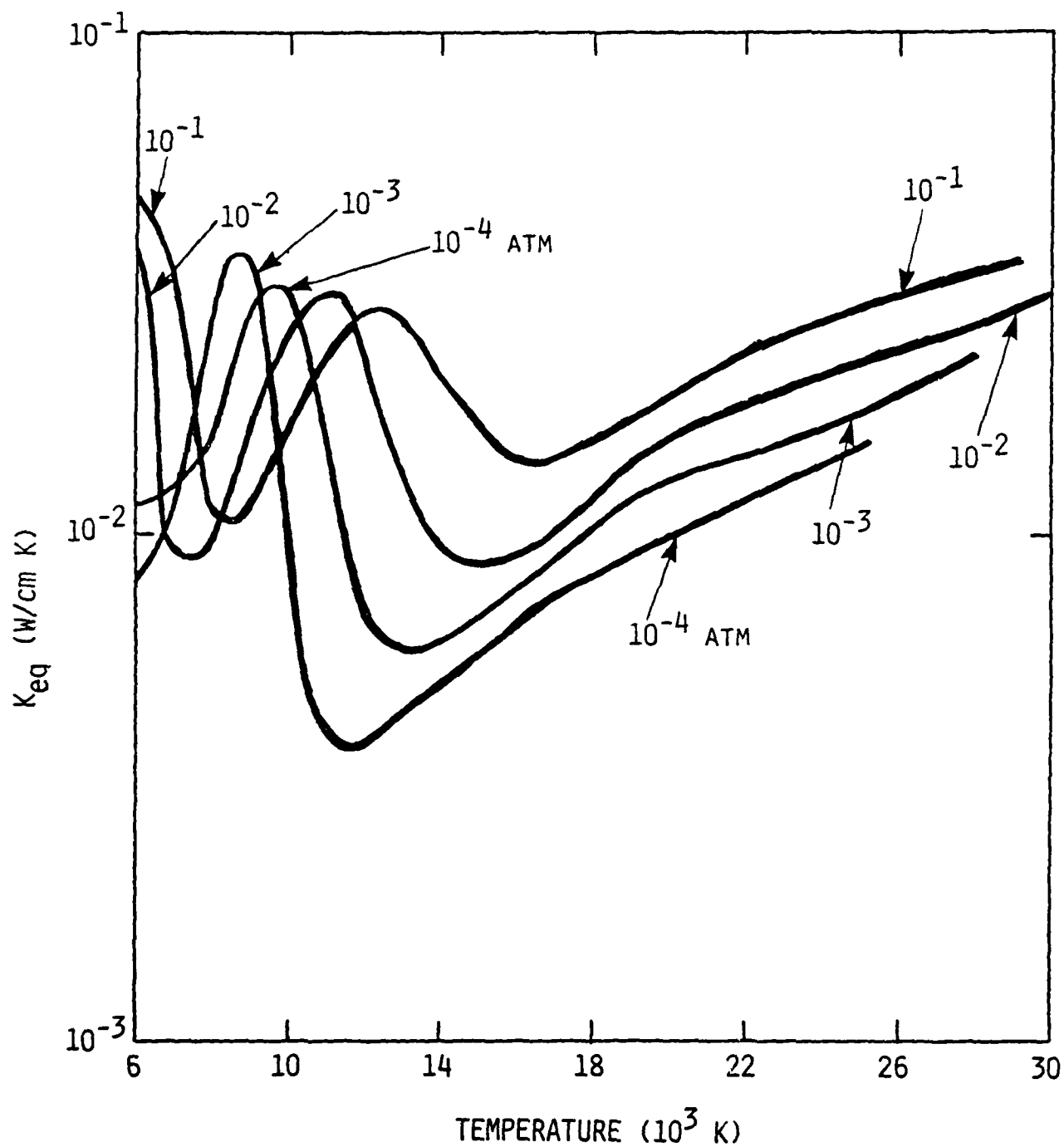
Fig. 38 Thermal conductivity of nitrogen.
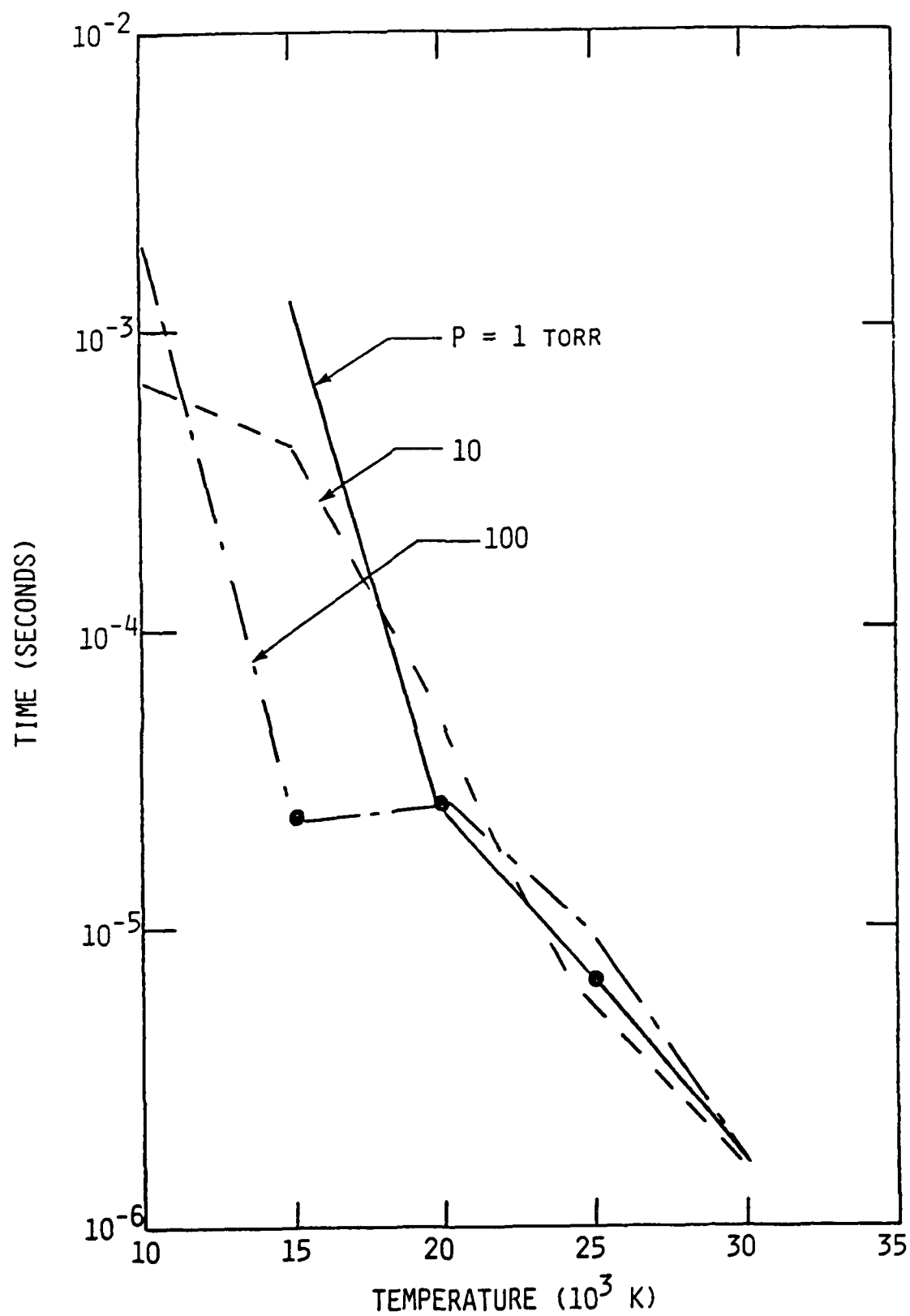
Fig. 39 Thermal decay time due to radiation - τ_R.
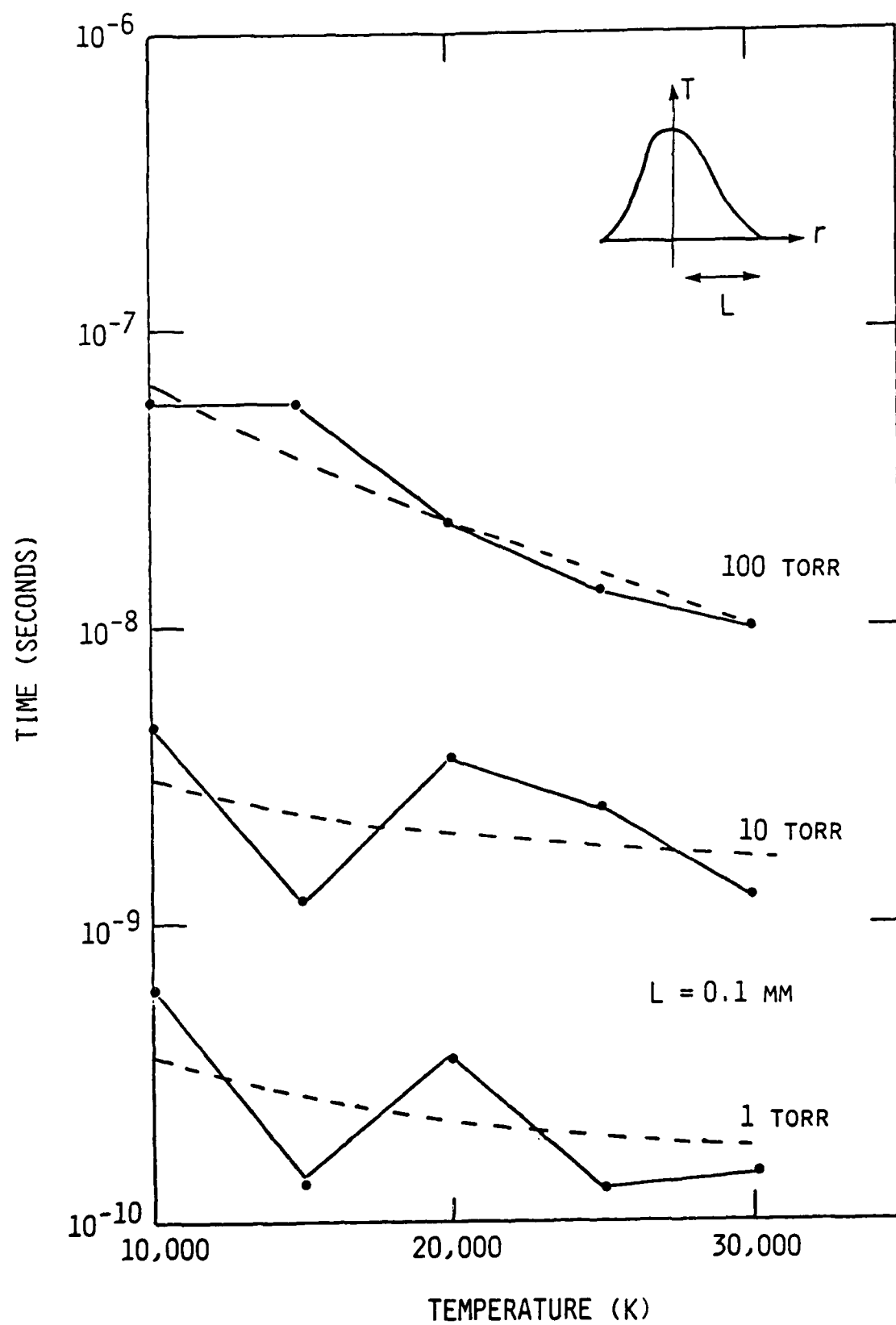
Fig. 40   Thermal decay time due to thermal conduction.   Plasma radius = 0.1 mm.

a)   Radiative recombination

$$N^{Z+} + e^- \xrightarrow{b_\nu} N^{(Z-1)+} + h\nu \tag{35}$$

b)   Three-body recombination

$$N^{Z+} + e^- + M \xrightarrow{k_R} N^{(Z-1)+} + M \tag{36}$$

Following Zel'dovich and Raizer[6] the radiative recombination rate is given by

$$b_\nu \cong \frac{2 \times 10^{-11} Z^2}{T^{1/2}} \qquad cm^3/s \tag{37}$$

while the three-body recombination rate is given by

$$k_R = \frac{1.65 \times 10^{-8} Z^2 n_e}{T^{9/2}} \qquad cm^3/s \tag{38}$$

where we chose the third body in reaction b to be an electron. Three-body recombination is found to dominate two-body recombination when

$$n_e > 1.3 \times 10^{-3} T^4$$

The above inequality is expected to be satisfied under the conditions of the LINUS experiment so that we need only consider three-body recombination.

Following the analysis of Pitaevskii[7] and others,[8] electron three-body recombination is a process whereby a third body (an electron for the problem at hand) carries away the energy that is lost when a free electron gets captured into a highly excited state. The radiative lifetime of the excited state then formed is sufficiently long that many more collisions occur with free electrons exciting and deexciting the excited states till finally a sufficiently strongly bound state is formed which can radiate (in the UV and deep UV) to the ground state of the ion (atom). Pitaevskii treats the problem of recombination as a diffusion of electrons in energy space subject to the boundary condition $f(\epsilon) = 0$ for $\epsilon < \epsilon^*$ where $f(\epsilon)$ is the electron distribution function and ϵ^* is the lowest lying excited state above which radiation by a transition to the ground (or low lying) state can be neglected.

In order to ascertain the importance of two and three body recombination reactions in the LINUS, we have developed a map, Fig. 41, which shows rates as a function of n_e and T. We show in Fig. 41 n_e versus T for a plasma in LTE at 1, 10 and 100 torr. The dashed line corresponds to equality of the two recombination rates. The region of the map to the left of this dashed line is the region where three-body recombination dominates. The dash-dotted line in Fig. 41 represents the lines of constant recombination rate for the reactions

$$N^+ + 2e \rightarrow N + e \tag{39}$$

and

$$N^{++} + 2e \rightarrow N^+ + e . \tag{40}$$
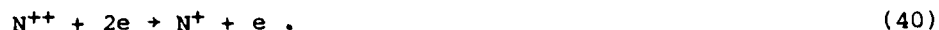
Since the rate scales as Z^2, the lines to right of the graph representing reaction (40) are displaced downward by a factor of $\sqrt{Z^2} = 2$ as compared to those representing reaction (39). Recombination is seen to be fast at p = 100 torr but slow when p < 10 torr. The recombination rate, however, following Eq. (4) depends strongly on the electron temperature. During the recombination process there will be a tendency for T_e to increase. Cooling of the electrons will occur due to collisions with the heavies. We showed in Fig. 6 the electron-ion equilibration time (τ_{ei}) before expansion. After expansion, when the pressure has decreased by a factor of 100 to 1000 and the density by a somewhat smaller amount, the electron-ion equilibration time is expected to be ~ 100 times longer than that shown on Fig. 6. We believe that the electron cooling time will be sufficiently lengthened as recombination occurs as to significantly slow down this recombination process.

4.5   Validity of Assumption of LTE for Line Radiation

The line radiation that has been monitored in the LINUS experiment originates from highly excited states of N, N^+ and N^{++} that are being populated by the three-body recombination process. Depending on how high these states are the relative population of the states with respect to each other will be related through a Boltzmann relation with some effective temperature
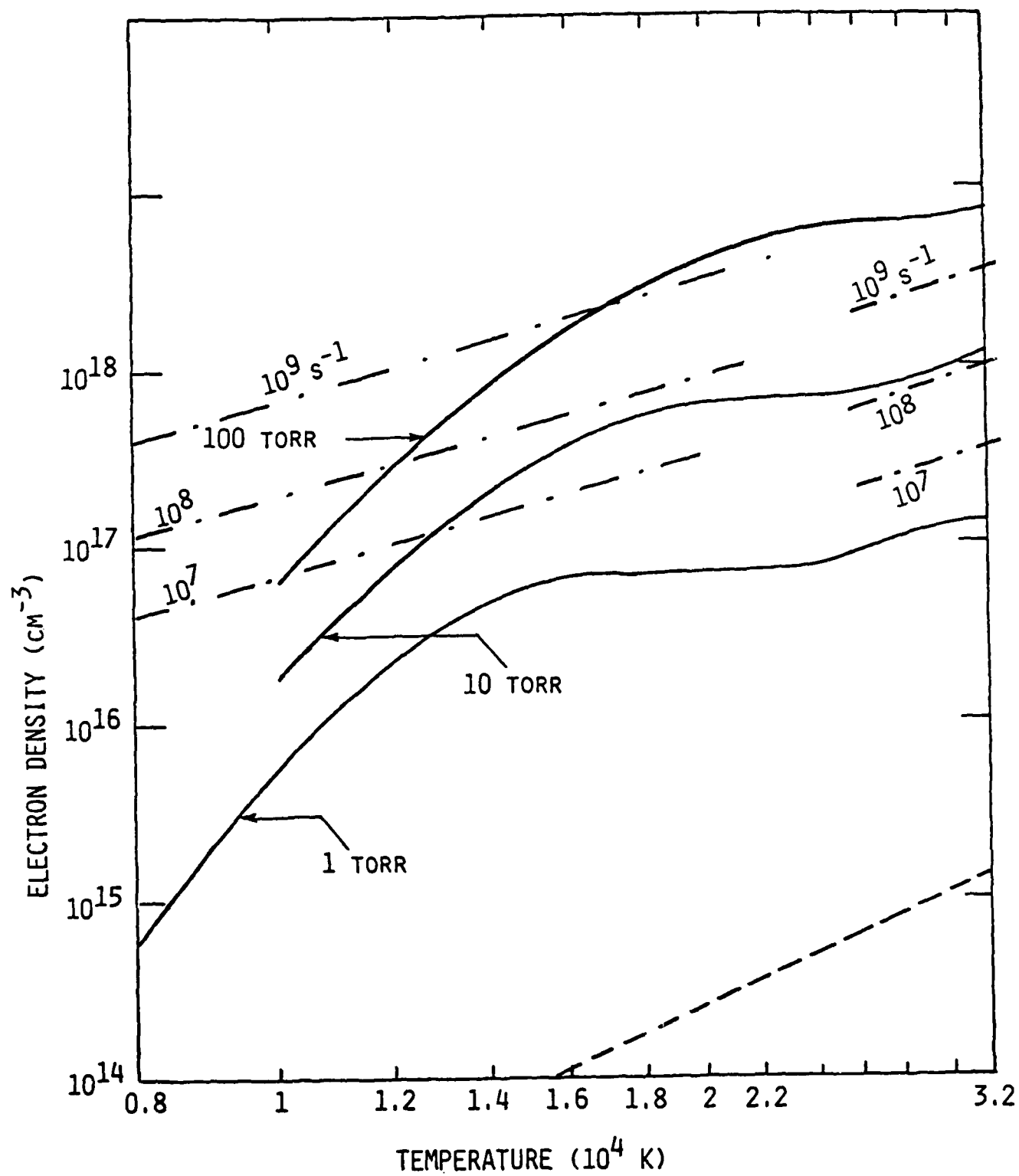
Fig. 41   Equilibrium electron density in a nitrogen plasma.

T_e or will only be related by the branching ratios for radiative decay from excited states above the state of interest. Following Griem[9] the validity of LTE for a given state depends on the electron density exceeding the critical value.

$$N_e = 7 \times 10^{18} \frac{Z^7}{n^{17/2}} \left(\frac{kT}{\varepsilon_H Z^2} \right)^{1/2} \quad cm^{-3}$$

where Z = ionic charge as seen by the outer electron, n = principal quantum number of the state considered and ε_H = 13.6 eV. The validity of LTE has to be determined on a line by line basis. As an example consider the 4040 Å line of N^+ for which $n = 4$, $Z = 2$. If we choose $T = 20,000$ K we obtain $n_e > 1.2 \times 10^{15}$ cm^{-3} for LTE to be maintained for the line. If, on the other hand, we had considered the 4059 Å line of N^{++} ($n_{eff} = 2.5$, $Z = 3$, $T = 25,000$ K) we would have the much more stringent condition $n_e > 7 \times 10^{17}$ cm^{-3}. These densities are to be compared with the calculated n_e for LINUS: $n_e = 2.4 \times 10^{16}$, 2.7×10^{15}, and 3×10^{14} at pressures of 100, 10 and 1 torr, respectively. One will, therefore not expect to obtain an LTE population of the upper state corresponding to the 4059 Å transition of N^{++}; LTE for the 4040 Å transition of N^+ may, however, hold at the highest pressure considered.

5. CONCLUSIONS

From the discussion of the previous sections we can draw the following conclusions with respect to visible radiation in the LINUS experiment:

1) Continuum radiation observed in the 3500-7000 Å band is very probably due to the two-body radiative recombination reaction

$$N^+ + e \rightarrow N^* + h\nu .$$
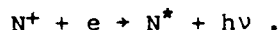
The spectral characteristics of the continuum indicate an electron temperature $T_e \cong 14000$ K. Since spectral measurements were obtained with an open shutter camera over a period of time which is long as compared to the plasma expansion time and cooling time, the measured electron temperature can only be considered as a time averaged one.

2) The line radiation observed cannot be analyzed on the basis of LTE since a) the electron density is too low to maintain a temperature equilibrium between free and most bound electronic states, and b) the decay of line radiation is much longer than the calculated cooling times (multiplied by kT/ε_I) based on thermal conduction losses.

3) The temporal behavior of line radiation is dominated by three-body recombination which populates highly excited states of the ions and atoms. These excited states then radiate by bound-bound transitions, a fraction of which spans the visible spectrum. The rise and decay of N^{2+}, N^+ and N^* radiation is associated with the population growth and decay of these ions and atoms by successive recombination. The recombination rate scales as $n_e^2/T_e^{9/2}$. As the plasma cools down (by conduction losses) it contracts so that n_e increases. The increase in n_e and decrease in T_e makes the recombination rate, and thus radiation, increase with time. The ultimate decay of line radiation will be then associated with disappearance of the particular species considered.

4) The pressure dependence of the time scales for line radiation is due to heat conduction losses which scale as $1/p$. The radial diffusion of charged species which increases as the pressure is decreased, should, however, slow down the recombination and may counterbalance somewhat the effect of more rapid heat losses at the lower pressures.

Finally, one must consider radiation and cooling during the blast wave expansion. The time for pressure equilibrium is of the order of 100 ns, i.e., of the same order as the duration of line radiation. Though blast wave expansion times should be independent of pressure for a constant energy per unit mass deposited, the breakdown mechanisms should be somewhat dependent on pressure, i.e., the efficiency of laser coupling to the nitrogen would depend on p. If we assume that recombination is slow during the expansion, then n_e is

proportional to density ρ and we obtain a radiation per unit volume which scales as $n_e^2/T_e^{9/2} = \rho^2/T^{9/2}$. Since the spectrometer is looking at a slice of the plasma, the radiation will be proportional to $R^2\rho$, but, by conservation of mass for the laser heated gas, $R^2\rho = $ constant. Radiation will therefore scale as $R^2\rho^2/T^{9/2} \propto \rho/T^{9/2} \propto (t/t_o)^{9\gamma-11/2\gamma}$, where in the last step we used cylindrical blast wave results for a gas of constant γ. For frozen gas chemistry (i.e., slow recombination), $\gamma = 5/3$ and the radiation will scale as $t^{6/5}$, i.e., practically linearly with time. However, as the recombination rate increases and recombination becomes important, the value of γ should decrease. Indeed when $\gamma < 11/9$ (which should occur under equilibrium conditions) blast wave scaling will yield a <u>decrease</u> in line radiation with time. Thus, blast wave effects could also explain the rise and fall of line radiation.

REFERENCES

1. R. Armstrong, R. Lucht and W. T. Rawlins, J. Appl. Optics, $\underline{22}$, 1573 (1973).

2. P. Nebolsine and G. Weyl, "LINUS Final Report for the period Oct. 1, 1981 - Sept. 30, 1982," PSI TR-348, Oct. 1982.

3. A. Pirri, R. Root and P. Wu, "Analytical Laser/Material Interaction Investigation -- Part I, Theory," Final Report, PSI TR-104.

4. H. Griem, Plasma Technology, McGraw Hill, New York (1964), see table 4-5

5. Ya Zel'dovich and Yu Raizer, Physics of Shock Waves and High Temperature Hydrodynamic Phenomena, Academic Press, New York (1966), p. 265.

6. Same as reference (5), p. 405.

7. L. Pitaevskii, Sov. Phys. JETP $\underline{15}$, 919 (1962).

8. D. Bates, R. Kingston and R. McWhirter, Proc. Roy. Soc. (London) $\underline{A270}$, 144 (1962).

9. Same as reference (4), p. 148.

10. R. Huffman, Y. Tanaka and J. Lanobee, J. Chem. Phys. $\underline{39}$, 910 (1963).

11. J. Yos, "Revised Transport Properties for High Temperature Air and its Components," Avco Systems Division Memorandum, 28 Nov. 1967.

12. R. E. Huffman, Y. Tanaka and J. C. Larabee, J. Chem. Phys. $\underline{39}$, 910 (1963).

APPENDIX B-1

Laser Induced Breakdown of Nitrogen

Under a powerful laser beam, electrons are generated and grow by two mechanisms: cascade ionization and multiphoton ionization. We have, for the first process, the reaction

$$N_2 + e \rightarrow N_2^+ + e^- + e^- \tag{A1}$$

The electrons must have an energy that exceeds the ionization potential ($\varepsilon_I = 15.5$ eV) of nitrogen for reaction (A1) to occur. The heating mechanism that furnishes energy to the electrons is called inverse bremmstrahlung absorption and is a process whereby electrons, upon colliding with heavy particles (neutrals) absorb one or more photons. Multiphoton ionization on the other hand is a process whereby a molecule will absorb m simultaneous photons, gaining sufficient energy for it to become ionized.

$$N_2 + m \; h\nu \rightarrow N_2^+ + e \tag{A2}$$

Reaction (A2) would require m $\geq$ 13, if one considers $\lambda = 1.06$ μm radiation ($h\nu \approx 1.17$ eV) and an ionization potential $\varepsilon_I = 15.5$ eV.

The growth of electron density in the focal volume of the laser beam is described by the differential equation:

$$\frac{d \; n_e}{dt} = \nu_i \; n_e + [N_2] \; \sigma_m \; I^m + D \; \nabla^2 \; n_e. \tag{A3}$$

where ν_i is the ionization rate due to reaction (A1)

$$\nu_i = \langle\sigma_i \; v_e\rangle[N_2] \tag{A4}$$

σ_i being the electron impact ionization cross section, σ_m the multiphoton ionization cross section, I the laser intensity and D the diffusion coefficient of electrons. The last term in Eq. (A4) represents diffusion of electrons out of the focal volume.

PRECEDING PAGE BLANK-NOT FILMED

The ionization rate ν_i was determined by scaling to 1.06 µm the results of a Boltzmann code calculation that had been run to study breakdown at CO_2 wavelengths.[†] The results are shown in Fig. A1, for p = 10 torr. The results can be extended to different pressures since ν_i scales proportionately with p. One sees from this figure that if one requires 10 cascades to break down the gas by the end of the pulse (corresponding to an electra growth from 10^{12} to 10^{17} cm^{-3}), one would expect breakdown at I ≥ 3 × 10^{12} W/cm^2 for τ_p = 10 ns and p = 10 torr.

The cross section for multiphoton ionization of N_2 has recently been determined by Baravian et al.[††] They found that m = 9 and σ_9 = 2.9 × 10^{-111} W^{-9} cm^{18} s^{-1}. The explanation given by these authors for an exponent m = 9 rather than 13 is that ionization occurs through a two step process

$$N_2(X \ ^1\Sigma_g^+) + 9 \ h\nu \rightarrow N_2^* \ (W \ ^1\Delta_u, \ v' = 9) \tag{A5}$$

followed by

$$N_2^*(W \ ^1\Delta_u, \ v' = 9) + 5h\nu \rightarrow N_2^+ + e. \tag{A6}$$
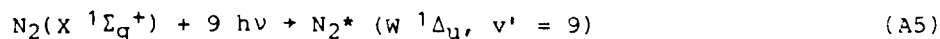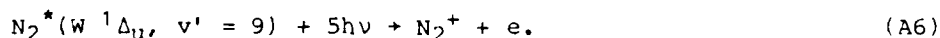
Reaction (A5) is the rate limiting step at low intensities. At laser intensities above 2 × 10^{12} W/cm^2, Baravian et al.[††] found an exponent m = 12 associated with the formation of N^+ ions rather than N_2^+ ions, They explain their result as predissociation of N_2 by absorption of 8 and then 4 photons followed by ionization of nitrogen atoms which requires simultaneous absorption of 12 photons. The 12 photon ionization of N occurs with a cross section σ_{12} = 9 × 10^{-151} W^{-12} cm^{24} s^{-1}. We show in Fig. A2 the ionization rate (per molecule) following the results of Baravian et al.[††] When the intensity exceeds 3 × 10^{12} W/cm^2 the ionization rate exceeds 10^2 s^{-1} so that in 10^{-9} s, the gas would have a degree of ionization ~ 10^{-7}. For p = 10 torr this corresponds to an electron density n_e = 3 × 10^{10}. At such an electron density diffusion out of the focal volume will be ambipolar for focal radii in excess of ~ 10 µm. Since the ambipolar diffusion coefficient is smaller than the free electron diffusion coefficient by a factor of 200, diffusion losses can be neglected under the conditions of the LINUS experiment.

[†]G. Weyl, J. Phys. D12, 33 (1979).
[††]G. Baravian, J. Godart and G. Sultan, Phys. Rev. A 25, 1483 (1982).
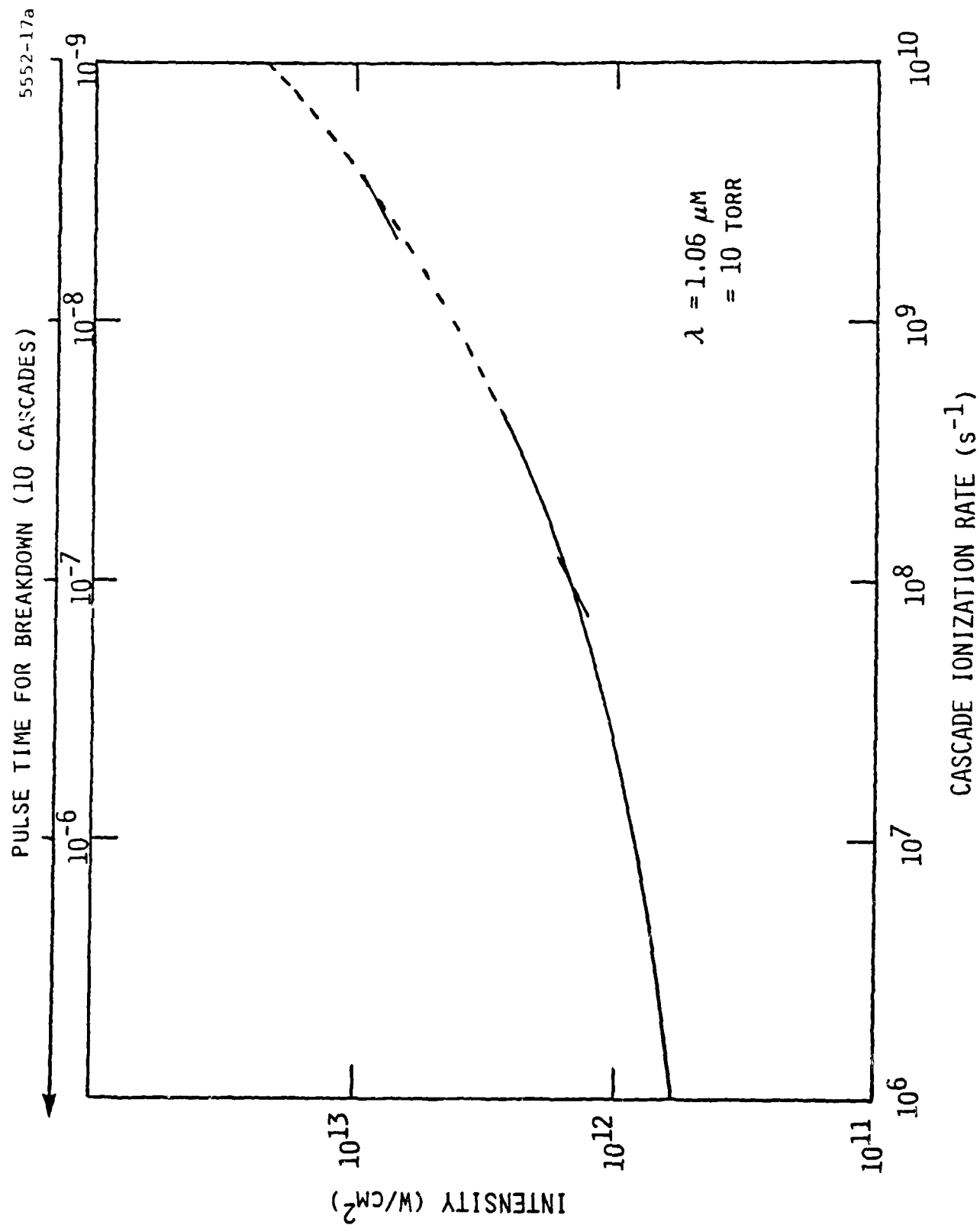
Fig. Al Cascade ionization rate in nitrogen at $\lambda = 1.06$ μm and 10 torr.
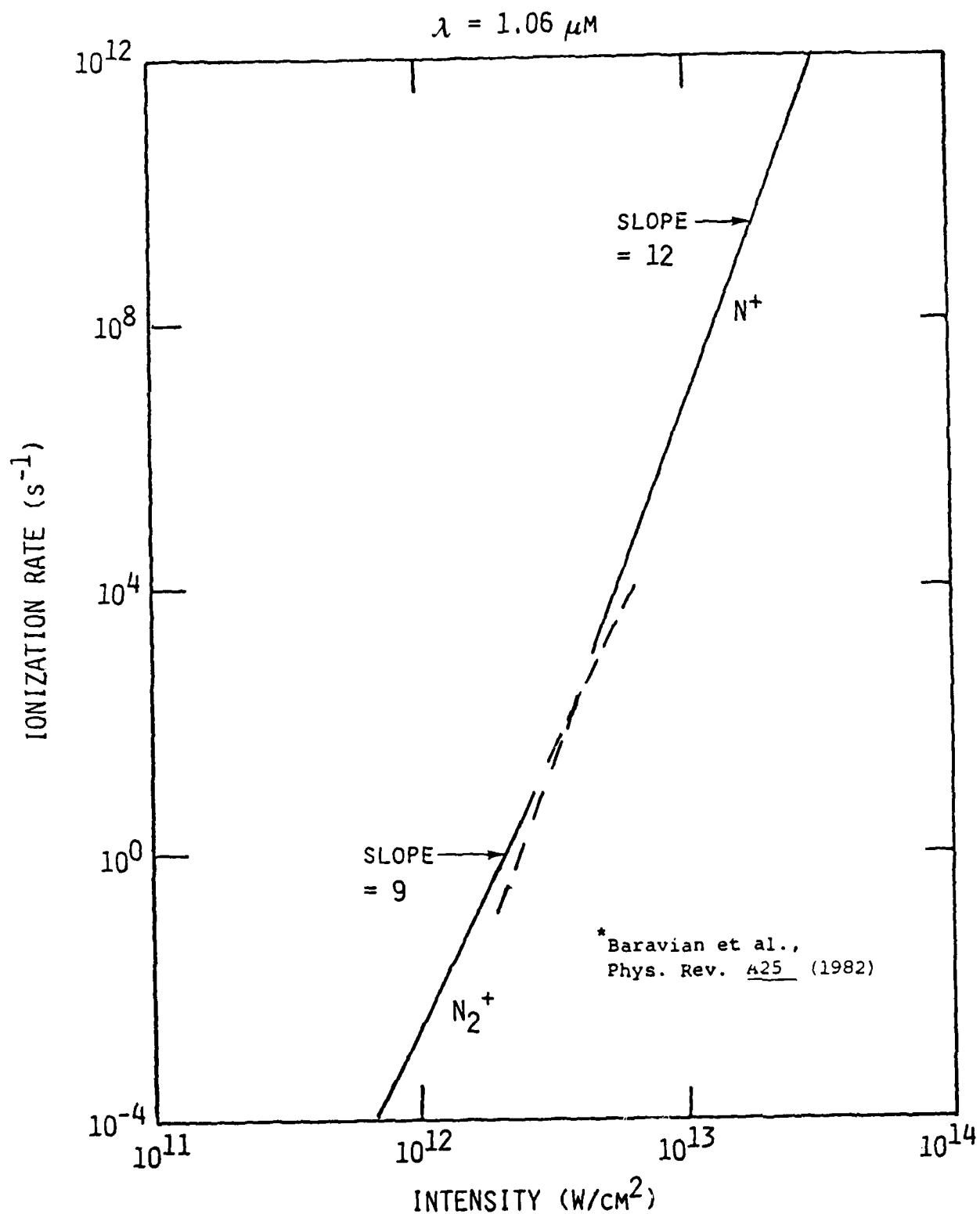
Fig. A2 Multiphoton ionization rate in nitrogen*.

We rewrite Eq. (A3) using the appropriate coefficients as described above.

$$\frac{dn_e}{dt} = [5 \times 10^6 \, i^2 + 3.3 \times 10^{16} \, (3 \times 10^{-3} \, f_1 + 9 \times 10^{-7} \, f_2 \, i^2) \, i^9 \, n_e]p \quad (A7)$$

where $i = I(W/cm^2)/10^{12}$ and p is the pressure in torr. The factors f_1 and f_2 are correction factors for photon statistics. If the beam is perfectly coherent then $f_1 = f_2 = 1$. If, however, the beam is composed of many modes with random phases then $f = m!$, the enhancement being due to the spikiness of the intensity when looked at on a microscopic time scale. Equation (A7) was numerically integrated assuming a coherent beam with Gaussian FWHM = 10 ns. The results are shown in Fig. A3 and are compared with the experimental data. Given the fact that the theory lines represents intensity on the axis and that the experimental data represent intensity averaged over the angular spread of the beam, the beam profile not being known, one can conclude that reasonable agreement is obtained if one assumes the beam to be incoherent. The growth of electron density on axis, neglecting diffusion losses is shown in Fig. A4 for three threshold conditions.
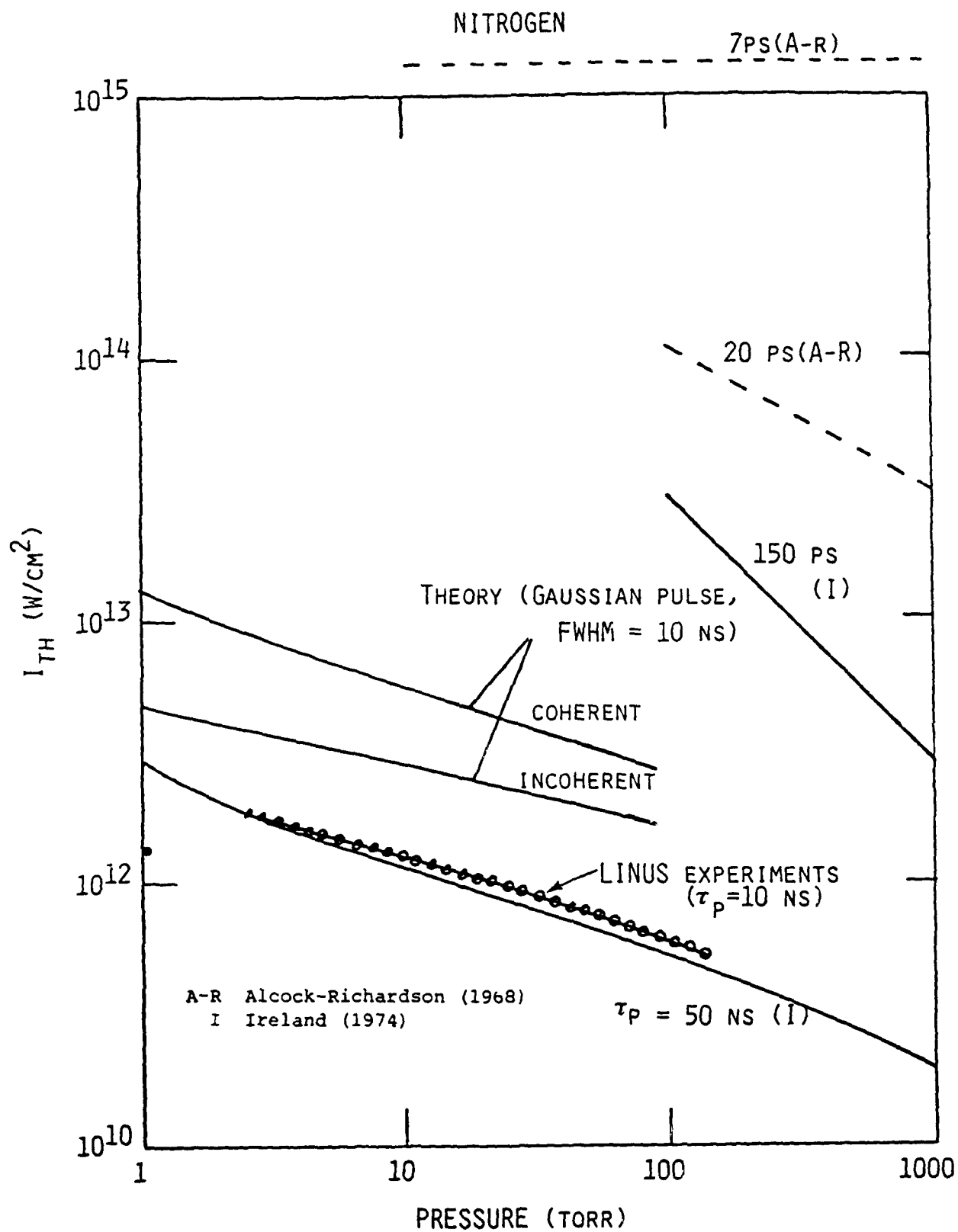
Fig. A3 Experiments on breakdown at 1.06 μm.
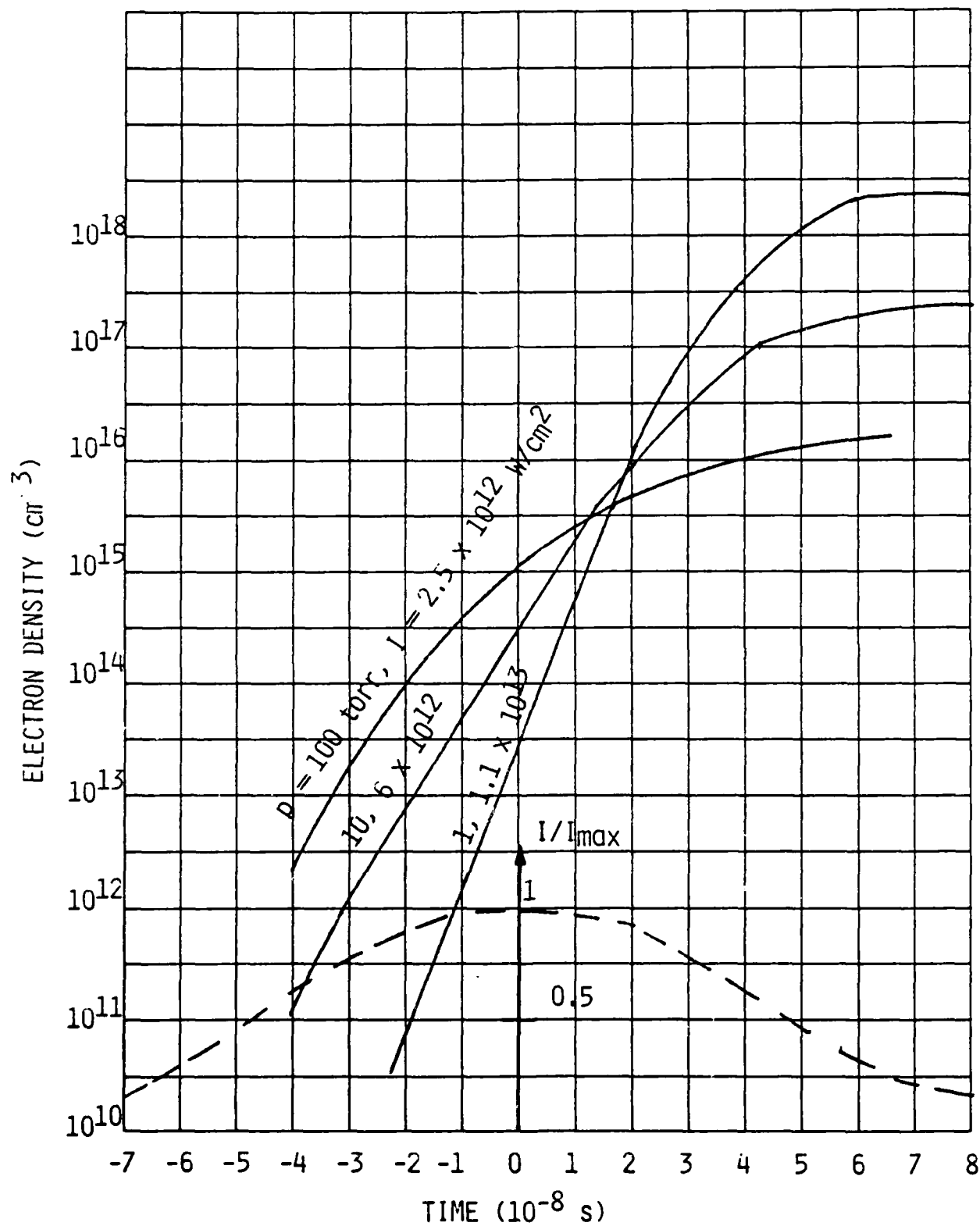
Fig. A4 Breakdown in Gaussian pulse (FWHM = 10 ns).

APPENDIX B-2

Absorption of Vacuum UV Radiation by the Surrounding Nitrogen Gas

We examine in this section continuum deep UV radiation by nitrogen. The main concern here is to find out how much of the UV radiation emitted by the hot nitrogen plasma will escape through the cold nitrogen surrounding the plasma and reach the detector or the walls. In order to be definite, we choose a typical cell dimension of 2 cm and background pressures of 1, 10 and 100 torr. The absorption coefficient k at (STP) below which 50% of the radiation reaches the walls is given in the table below.

	p = 1 torr	10 torr	100 torr
k (cm^{-1}) at STP	520	52	5

We show in Fig. 42 the measured absorption coefficient in nitrogen referred to standard conditions. The measurements in the wavelength interval 600 to 1,000 Å were taken by R. E. Huffman, Y. Tanaka and J. C. Larabee.[12] Absorption at wavelengths longer than 1,000 Å is extremely weak and can be neglected for all practical purposes.

The following conclusions can be drawn from Fig. B.

a) Wavelength band 1,000-900 Å. Less than 10% of the UV radiation will be transmitted in the windows between the absorption bands of N_2 at p = 100 torr, this number increases to 70% at 10 torr and 80% at 1 torr.

b) Wavelength band 900-800 Å. Less than 2% reaches the walls at 100 torr, between 20 and 30% at 10 torr and 75% at 1 torr.

c) Between 800 and 700 Å. Practically no radiation reaches the walls at 100 torr and 10 torr. Only 20-25% reaches the wall at 1 torr, the transmissivity averaging 12% at wavelengths shorter than 770 Å and being close to one in the windows between bands at $\lambda > 770$ Å.

d) Between 700 and 660 Å. Average transmissivity of 12% for p = 1 torr.

e) Below 660 Å, average transmissivity of 7% for p = 1 torr and negligible transmission at the higher pressures.

PRECEDING PAGE BLANK-NOT FILMED
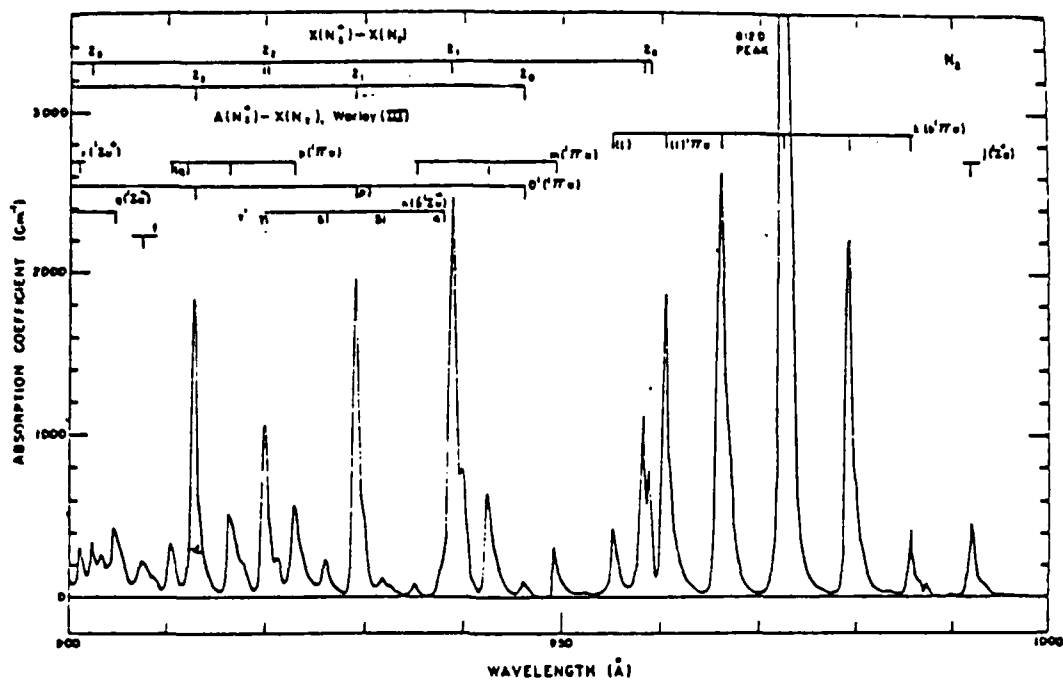
Fig. Ba Nitrogen absorption coefficients in the 1000-900 Å wavelength
region.
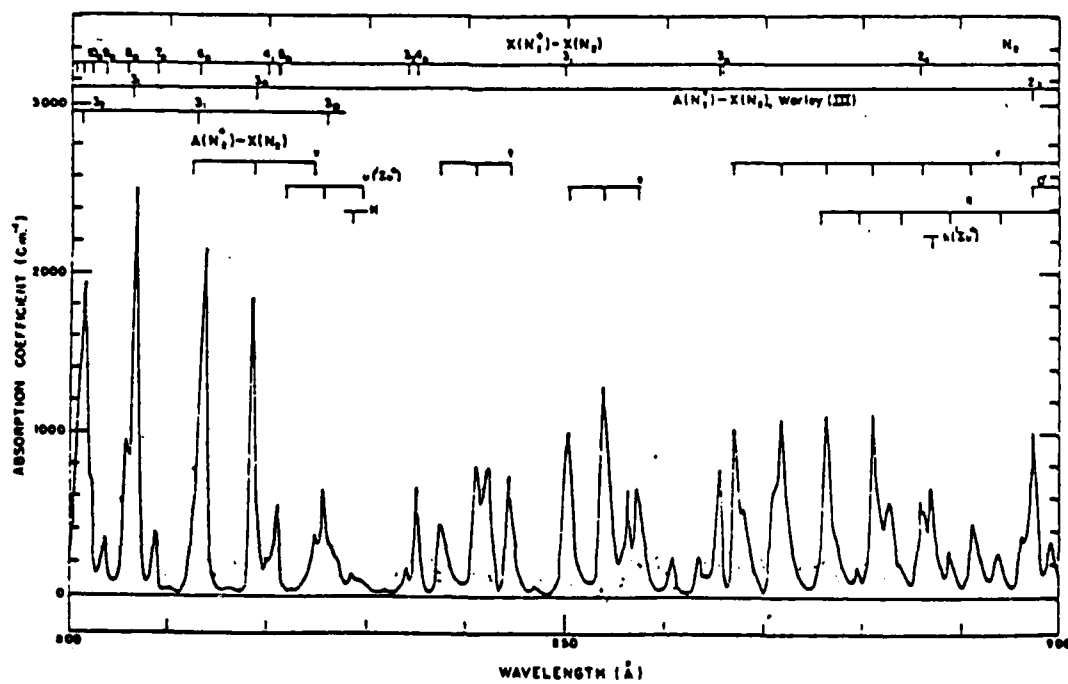
Fig. Bb Nitrogen absorption coefficients in the 900-800 Å wavelength
region.
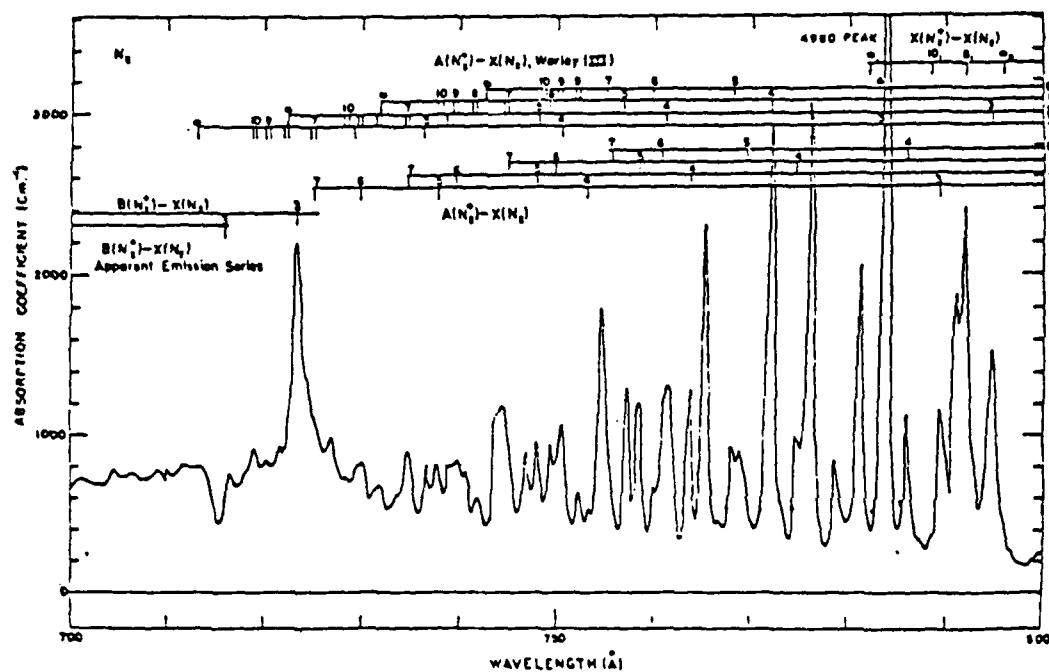
Fig. Bc Nitrogen absorption coefficients in the 800-700 Å wavelength region.
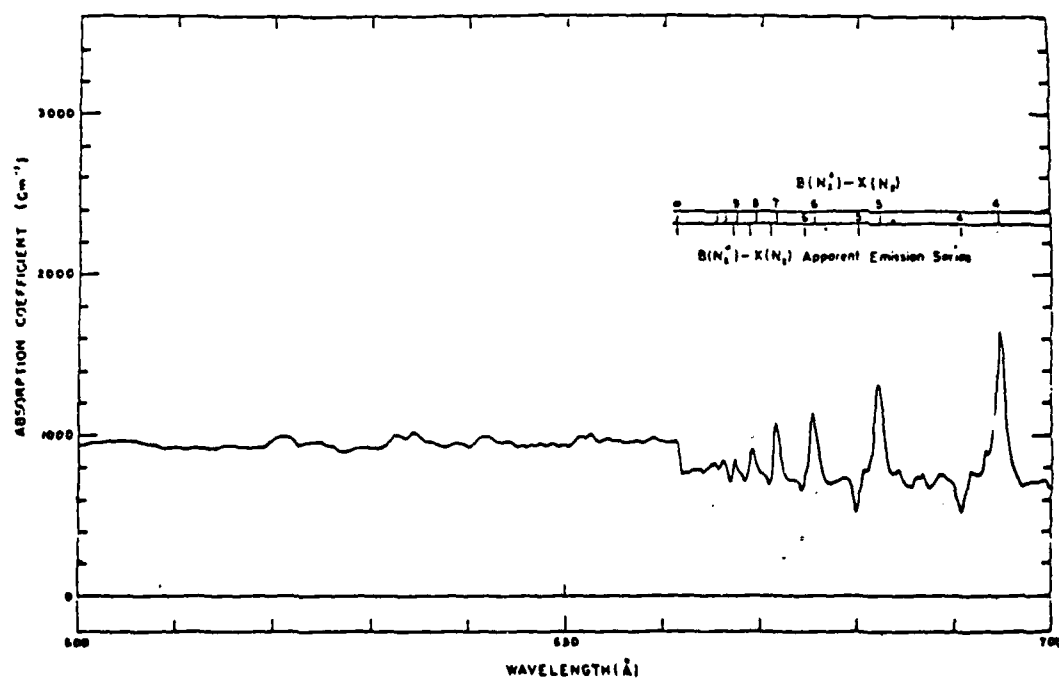
Fig. Bd Nitrogen absorption coefficients in the 700-600 Å wavelength region.

APPENDIX C

O-ATOM YIELDS FROM MICROWAVE DISCHARGES IN
N_2O/Ar MIXTURES

This appendix is SR-152A.

O-ATOM YIELDS FROM MICROWAVE DISCHARGES IN N_2O/Ar MIXTURES

Lawrence G. Piper and Wilson T. Rawlins

Physical Sciences Inc.
Research Park, P. O. Box 3100
Andover, MA 01810

ABSTRACT

We have studied the products of Ar/N_2O microwave discharges to determine their fitness as sources of atomic oxygen in discharge-flow reactors. For N_2O feed rates below 10 and 20 $\mu mol\ s^{-1}$, the discharge converts about 75% of the N_2O to atomic oxygen, and in addition produces small quantities of atomic nitrogen, generally less than 10% of the O-atom product. At higher N_2O feed rates the O-atom production efficiency decreases, and some nitric oxide accompanies the O-atoms out of the discharge. At intermediate N_2O feed rates, only atomic oxygen is observed, and neither N nor NO leaves the discharge. The exact point at which this occurs is a function of the discharge power and the Ar/N_2O mixing ratio. Adding molecular nitrogen to the discharge eliminates any NO product, but at the penalty of a slightly reduced O-atom production efficiency. Atomic oxygen flows in excess of 20 $\mu mol\ s^{-1}$ are produced at pressures near 1 torr and discharge powers of only 30 watts.

In kinetic modeling of the discharge chemistry, we can account for the experimental observations only if the electron-impact dissociation of the N_2O in the discharge proceeds through a spin-forbidden channel to produce $O(^3P)$. In addition, the model indicates that about 10 to 20% of the N_2O dissociations result from collisions between metastable argon atoms in the discharge and N_2O.

I. INTRODUCTION

Atomic oxygen sources for flow reactors take a variety of forms, and each has its own particular strengths and weaknesses. The simplest technique for making atomic oxygen is to dissociate molecular oxygen, usually in some form of discharge, the 2.45 GHz microwave discharge being most common.[1] These sources are somewhat limited in overall yield and generally produce large quantities of accompanying electronically excited metastable singlet molecular oxygen -- $O_2(a^1\Delta_g, b^1\Sigma_g^+)$.[2-5] In pure molecular oxygen the dissociation efficiency is generally only a few percent.[5] If the oxygen is highly diluted in a rare gas buffer such as argon or helium, dissociation efficiencies can exceed 50%,[2,6] but due to the large dilution, the overall atomic oxygen yield is still low.

The other major technique is to convert N-atoms to O-atoms by titration with NO:[7]

$$N + NO \rightarrow N_2 + O \quad . \tag{1}$$

This technique has the advantage that the absolute flow rates will be equal to the flow rate of the nitric oxide added, provided atomic nitrogen is in excess. Even in this instance, if significant O-atom recombination occurs, a large fraction of the molecular oxygen formed will be $O_2(a^1\Delta_g)$.[8] The yields of atomic nitrogen from conventional discharge sources are generally even lower than those from oxygen discharges, so the maximum O-atom flow rates again are limited.

The thermal decomposition of O_2, O_3, or N_2O in contact with a Nernst glower is also useful for certain applications.[9,10] The claims for the lack of reactive-impurity production by this technique conflict and yields are small, being limited to atomic-oxygen flow rates less than a micromole s^{-1}.[9]

Photolysis of molecular oxygen or some other oxygen-donating species with vacuum ultraviolet laser pulses provides a potentially very clean source of atomic oxygen.[11] Producing radially and axially uniform number densities

of O-atoms in the flow tube, however, requires extreme care. In addition, current laser development limits this technique to atomic-oxygen flow rates on the order of 0.1 μmol s^{-1} or less.

Several years ago, Ung reported that microwave discharges through mixtures of Ar/N$_2$O/N$_2$ would produce significant quantities of atomic oxygen, free from molecular oxygen.[12] He deduced atomic-oxygen production rates in N$_2$O discharges to be an order of magnitude greater than he could obtain using a molecular-oxygen discharge operating under the same conditions. His measured yields were not large, a maximum O-atom flow rate of 0.5 μmol s^{-1}, but the atomic oxygen his discharge produced clearly suffered severe depletion by recombination in the flow region between the discharge and the detector.

Intrigued by Ung's results, and desiring a technique to produce relatively large flows of atomic oxygen without large accompanying flows of molecular oxygen, we decided to investigate further the characteristics of Ar/N$_2$O discharges. We determined number densities of atomic-oxygen and either atomic-nitrogen or nitric oxide products in a discharge-flow reactor from measurements of the air afterglow intensity[13,14] as a function of the number density of nitric oxide injected downstream of the discharge. Our results will not support Ung's claim that oxygen-atom production is an order of magnitude more efficient using N$_2$O as the discharge gas as opposed to molecular oxygen. However, we do find that Ar/N$_2$O discharges produce large flow rates of atomic oxygen and that, furthermore, under certain conditions negligible flow rates of atomic nitrogen or nitric oxide accompany the atomic-oxygen flow.

In trying to rationalize our experimental observations with a kinetic model, we were surprised to discover that the spin-forbidden pathway for electron-impact dissociation of N$_2$O to produce O(^{3}P) must dominate the more endoergic but spin-allowed channel which produces O(^{1}D). Furthermore dissociation of N$_2$O by metastable argon atoms in the discharge also appears to be an important dissociation pathway. We describe the experimental methods, results and the kinetic analysis in the following sections.

II. EXPERIMENTAL
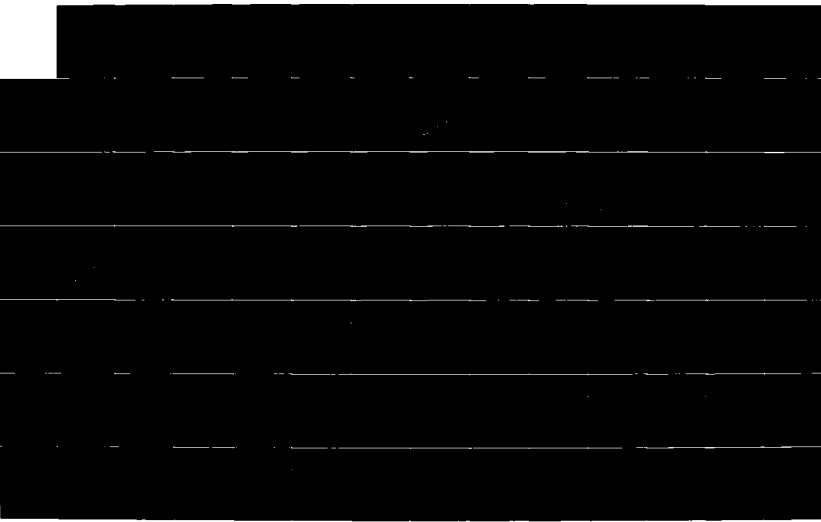
A. <u>Apparatus</u>

The apparatus is a modification of one we have used previously in a number of other studies.[15-19] It consists of a 2-in. flow tube pumped by a Leybold-Heraeus Roots blower/forepump combination capable of producing linear velocities up to 3×10^3 cm s^{-1} at pressures of one torr. The flow-tube design is modular (see Fig. 1), with separate source, reaction, and detection sections which clamp together with O-ring joints. The detection region is a rectangular stainless-steel block bored out internally to a 2-in. circular cross section and coated with Teflon® (DuPont Poly TFE #852-201) to retard surface recombination of atoms.[20] The surface was primed with black primer prior to the Teflon® coating to reduce scattered light inside the block. Two viewing positions consisting of four circular ports each on the four faces of the block are separated by a distance of 7.5 cm. The circular ports, all of which contain MgF$_2$ windows, can accommodate vacuum ultraviolet resonance lamps, monochromator interfaces, laser delivery side-arms, or in the case of these studies, a spatially filtered photomultiplier/interference filter combination.

The optical train of the filtered photomultiplier consists of two circular apertures and a one-inch diameter f/1 lens which was 2 inches away from both the center of the flow tube and the photocathode of the photomultiplier. The apertures reduced scattered light from the discharge by a factor of twenty. The interference filter in front of the photomultiplier is centered at 580 nm and has a full-width-at-half-maximum band pass of 10 nm. This wave-length is near the peak of the emission from the $\Delta v=4$ sequence of the nitrogen first-positive bands when they are excited by atomic nitrogen recombination,[21] and also is near the peak of the air-afterglow intensity distribution.[22,23] In addition, this band pass is insensitive to chemiluminescence from the nitric oxide/ozone system which has a short wavelength cutoff of 500 nm,[24] and eliminates the strong argon lines scattered from the discharge, most of which are to the red of 700 nm.

A picoammeter (Keithley 417S)/strip-chart recorder (Heath SR 205) combination amplifies and displays the photomultiplier (HTV R955) output. In several experiments a 0.5 m monochromator/thermoelectrically cooled photomultiplier
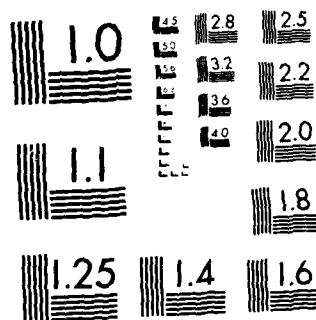
(EMI 9659QA)/photon-counting rate meter (PARC 1105) combination obtained the chemiluminescence spectra in the flow tube between 185 and 800 nm under a variety of conditions to verify the interpretation of the measurements using the filtered photomultiplier.

Flows of argon, nitrous oxide, and, in some cases, nitrogen, pass through a 12 mm o.d. Pyrex® tube surrounded by a McCarroll microwave-discharge cavity[25] before entering the main flow tube. Nitric oxide in a substantial flow of helium ($\approx$ 7% of the total flow) joins the discharged gases in the main section of the flow tube through an injector fabricated from a one-inch diameter loop of 2 mm o.d. polyethylene containing a large number of small holes around both its inner and outer perimeters. The helium flow out of the injector gives injected gases a significant velocity as they enter the main flow, thus aiding their mixing.

Mass-flow meters monitor the flow rates of argon and nitrogen, rotameters measure those of nitrous oxide and helium, and measurement of the rate of increase in pressure with time in a calibrated volume determines the flow rate of nitric oxide. All flow meters were calibrated by measuring rates of increase of pressure with time into 6.5 or 12 ℓ flasks, using appropriate differential pressure transducers (Validyne DP-15) which had themselves been calibrated with silicon oil or mercury manometers. Typically the flow rates for argon, nitrous oxide, and helium were 1400, 0-100, 120 μmol s^{-1}, respectively, the total pressure was 1.25 torr, and the flow velocity was 1150 cm s^{-1}.

The argon and nitrogen flow through molecular-sieve traps to remove water and carbon dioxide prior to entry into the flow reactor, while the helium flows through the injector straight from the cylinder. Most experiments used nitrous oxide (>99.0%) straight from the cylinder without further purification. The major impurity in nitrous oxide is air.[26] We tried removing any air from one lecture bottle of nitrous oxide by freezing the contents of the bottle with liquid nitrogen and then pumping on it until the pressure was below 1 mtorr. No volatile residue remained after a few cycles of thawing, refreezing, and pumping. Experiments with nitrous oxide purified in this manner gave identical results to those in which the nitrous oxide was used straight from the cylinder.

Nitric oxide was purified by flowing it slowly at atmospheric pressure and room temperature through an Ascarite® trap, then through a trap immersed in a liquid nitrogen/methanol slush bath (175 K). It was stored in a 5 ℓ bulb. Final nitric oxide purification involved several freeze, pump, thaw cycles of the gas in the storage bulb. The Ascarite® trap previously had been baked overnight under vacuum.

B.   Determination of O and N or NO Number Densities by Air-Afterglow Measurements

Mixtures of atomic oxygen and nitric oxide emit a continuum radiation called the air afterglow, which extends from 375 nm to beyond 3000 nm.[13,14,22,23,27-31] The intensity of this emission is directly proportional to the product of the number densities of atomic oxygen and nitric oxide,[13] and independent of pressure of bath gas, at least at pressures above about 0.2 torr.[14] Thus, the emission intensity of the air afterglow is

$$I_{O/NO} = \kappa(\lambda)[O][NO] \tag{2}$$

where $\kappa(\lambda)$ is a calibration constant specific to the particular viewing geometry and incorporates such things as detection system efficiency, the size of the observation volume and the absolute air-afterglow rate coefficient. κ is a function of wavelength both through the detection system's spectral response as well as through the wavelength variation of the air-afterglow rate coefficient. We have described elsewhere in great detail how to determine κ.[11,16,32]

The experimental measurements involved monitoring the air-afterglow intensity at three to five different number densities of added nitric oxide. (An experimental data set is illustrated in supplementary Fig. S1.) The atomic-oxygen number density is given by the ratio of the slope of the $I_{O/NO}$ vs. [NO]$_{added}$ plot to the calibration constant, κ. An intercept of the $I_{O/NO}$ vs. [NO] line on the ordinate indicates that nitric oxide is an N_2O-discharge product along with the atomic oxygen, and the number density of this product NO is the ratio of the intercept and slope of the $I_{O/NO}$ vs. [NO] line. An intercept on the abscissa indicates that nitrogen atoms, produced in the N_2O discharge along with the atomic oxygen, consumed some of the added NO (reaction (1)). The initial N-atom number density is equal to the added NO

number density at the point of intersection of the $I_{O/NO}$ vs. [NO] line and the abscissa. O-atom number densities determined from the slope of such plots must be corrected for the additional atomic oxygen made in the titration of the initial N atoms with the NO. The large rate coefficient for reaction (1)[33-35] and the long flow time from the discharge to the observation point ($\approx$ 45 ms) precludes the possibility that both atomic nitrogen and nitric oxide will coexist as far as the detection region.

A series of calibrations taken over a period of time established κ to $\pm$ 8%. The slopes of the $I_{O/NO}$ vs. [NO] plots for the determination of [O] had standard deviations less than 5%. Thus, the determination of [O] is in principle accurate to $\pm$ 10%.

After determining the O-atom and N-atom or NO number densities, we converted them to flow rates so that we could make reasonable comparisons from one set of conditions to another. This approach affords greater recognition of the similarities and differences between experimental runs. For example, runs with 1400 μmol s^{-1} of argon through the discharge generated approximately the same O- and NO-product flow rates from a given input of N_2O whether the pressure was 0.52 torr or 1.25 torr. The number densities of the products from the two experiments, however, differed by a factor of 2.5. Under our baseline set of conditions, $F_{Ar} \approx 1400$ μmol s^{-1}, $F_{He} \approx 115$ μmol s^{-1}, $p \approx 1.2$ torr, and 30 watts forward power from the discharge, an atomic-oxygen flow rate of 20 μmol s^{-1} corresponds to an O-atom number density of about 5×10^{14} atoms cm^{-3}. In one experiment we produced more than thirty millitorr of atomic oxygen 150 ms downstream from the discharge at a power of only 30 watts.

One complication in using the air-afterglow technique to measure O-atom number densities is the slow removal of atomic oxygen in a three-body recombination reaction with NO:

$$O + NO + M \rightarrow NO_2 + M \quad (k_6 = 7 \times 10^{-32} \text{ cm}^6 \text{ molecule}^{-2} \text{ s}^{-1}$$

$$\text{for } M = Ar)^{36} \tag{3}$$

$$O + NO_2 \rightarrow NO + O_2 \quad (k_7 = 9.5 \times 10^{-12} \text{ cm}^3 \text{ molecule}^{-1} \text{ s}^{-1})^{36}. \tag{4}$$
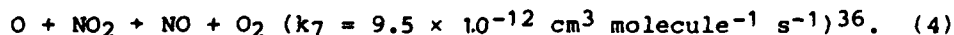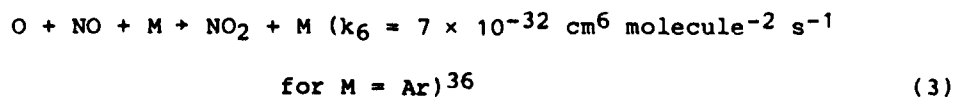
The second reaction is fast, and maintains a constant NO number density, while

doubling the effective rate at which O is removed in reaction (3). The effect of these reactions is strongest at higher pressures ($\gtrsim$ 1.5 torr), longer mixing times ($\gtrsim$ 30 ms) and large NO number densities ($\gtrsim 10^{14}$ molecules cm^{-3}). Corrections for this effect were generally less than 5% in the calibration experiments to determine κ. However, in a few of the experimental runs at higher pressures, slower flow velocities, and large product nitric oxide number densities, the corrections were large. The iterative procedure for these corrections is detailed elsewhere.[32]

III. RESULTS

A. General Observations

Figure 2 shows how the emission intensity at 580 nm varies with the flow rate of N_2O through the discharge for several different discharge powers. As the N_2O flow rate increases from zero, the emission intensity rises to a peak, then drops to zero (see inset), increases again very sharply, and finally levels off at the highest N_2O flow rates. The color of the chemiluminescence is yellow-orange at low flow rates, changes to a very faint blue near where the 580 nm signal drops to zero, and finally turns grey-green at high N_2O flow rates. While the observed color variations and the subsequent results of the O, N, and NO number density measurements suggested a fairly obvious interpretation of these observations, we took spectra[32] of the emissions in the reactor under several different sets of conditions so that our interpretation would be unequivocal.

The ultraviolet spectrum (available in the supplementary material as Fig. S2) was strongest at N_2O flow rates between those giving the initial small 580 nm intensity peak and the dark point. Prominent spectral features were the NO β-, γ-, and δ-bands which result from three-body recombination of O and N atoms.[37,38] For N_2O additions past those giving the 580 nm dark point, this spectrum is completely extinguished.

The major spectral features between 500 and 800 nm (supplementary material Fig. S3), when the N_2O flow rates are adjusted to give the initial 580 nm intensity peak in the I_{580} vs. F_{N_2O} plot, were the nitrogen first-positive $(B^3\Pi_g \text{ -- } A^3\Sigma_u^+)$ bands with a vibrational distribution peaked at vibrational levels 10, 11, and 12, characteristic of three-body N-atom recombination.[21] Minor features were the 558 nm line from OI (^1S -- ^1D) and the $O_2(b^1\Sigma_g^+$ -- $X^3\Sigma_g^-$) atmospheric-oxygen band at 762 nm, both of which are excited in three-body O-atom recombination,[37,39] and also, in the case of $O(^1S)$, in the transfer from $N_2(A^3\Sigma_u^+)$ to $O(^3P)$.[17] Atomic-nitrogen recombination produces the $N_2(A)$.[21]

Adjusting the N_2O flow rate beyond the dark point in the I_{580} vs. F_{N_2O} plot resulted only in the air-afterglow continuum emission which results from recombination of atomic oxygen and nitric oxide and the previously observed atmospheric-oxygen band at 762 nm.

The preceding observations identify atomic nitrogen and atomic oxygen as discharge products at low N_2O flow rates. At high N_2O flow rates nitric oxide accompanies the atomic oxygen, and at some intermediate N_2O flow rate, the discharge produces neither nitric oxide nor atomic nitrogen, only atomic oxygen. Figure 2 shows that this intermediate point where neither N nor NO is made is a function of discharge power, occurring at higher N_2O flow rates when the discharge power is higher. The initial peak in intensity at 580 nm which is due to atomic-nitrogen recombination is much more intense at higher discharge powers, indicating greater N-atom production rates at higher powers. The dramatic increase in the air-afterglow signal at higher discharge powers that is observed at high N_2O flow rates shows that the higher-power discharges produce much more O and NO. At low discharge powers the O and NO production reaches a plateau when 25-30% of the available discharge power is consumed dissociating N_2O.

B.   Quantitative Observations

Figure 3 shows how the flow rates of O and N or NO out of the discharge vary with the flow rate of N_2O into the discharge. At low N_2O flow rates, the discharge converts approximately 75% of the N_2O into atomic oxygen. Under similar conditions in our system, Ar/O_2 discharges convert only about 30% of the molecular oxygen to atoms, while Ar/N_2 discharges dissociate only about 5% of the molecular nitrogen.

Atomic-nitrogen yields from the Ar/N_2O discharges at low flow rates are generally 10% or less of those of atomic oxygen. Nitric oxide production at the higher N_2O flow rates, on the other hand, approaches that of atomic oxygen under certain conditions. An additional interesting feature is that the product-NO flow rates appear to increase linearly as the N_2O flow rate through the discharge is increased.

Experiments with different argon flow rates at constant total pressure or constant discharge residence time showed that higher Ar/N_2O mixing ratios suppress nitric oxide production: the onset of NO formation is delayed to higher N_2O flow rates, and the efficiency of NO production as a function of N_2O flow rate is smaller for larger flows of argon through the discharge. At constant argon flow rate, however, nitric oxide formation depends upon neither discharge residence time nor pressure.

A He/N_2O discharge produces nitric oxide at all N_2O flow rates, and in addition, is 25-30% less efficient as a source of atomic oxygen than is the Ar/N_2O discharge (Fig. 4). This lower efficiency is consistent with our observations that the fractional O_2 dissociations in He/O_2 discharges are only about 20-25% in our system compared to the ~ 30% fractional dissociation in an Ar/O_2 discharge. We discuss the differences between the Ar/N_2O and He/N_2O discharges further in the next section.

Adding molecular nitrogen to the discharge suppresses nitric oxide formation, but at the expense of a reduced atomic-oxygen production efficiency (Fig. S2). For low initial nitrous oxide flows ($\leq$ 20 μmol s^{-1}), fairly small flows of N_2 remove all the NO whereas, for high initial nitrous oxide flows ($\geq$ 60 μmol s^{-1}), N_2 additions must exceed 30% of the total flow through the discharge to remove the NO.

Increased discharge power enhances significantly atomic-oxygen yields at the higher N_2O flow rates. At the low N_2O flow rates, the 30 watt and 50 watt discharges produce O atoms from N_2O with equal efficiency. However, at the highest N_2O flow rate studied, the 50 watt discharge produces 30% more atomic oxygen than does the 30 watt discharge. The higher power discharge also delays nitric oxide formation to larger N_2O flows. The above observations are illustrated further in the supplementary material, Figs. S4 through S10.

IV. KINETIC INTERPRETATIONS

A.   General Considerations

To provide a better understanding of the discharge kinetics, we have assembled and exercised a simple kinetic model, assuming typical (and somewhat idealized) discharge properties and surface recombination efficiencies. The model includes the major production and loss terms for each reagent, metastable intermediate, and product which is likely to contribute significantly to the observed results. The resulting rate equations are sufficiently coupled so as to require numerical solution by computer. Kinetic modeling in this context substantiates mechanistic interpretations of the experimental data. It does not determine quantitative rate coefficients or species concentrations, nor is it intended to. However, the results of the modeling do give useful estimates of the magnitudes of concentrations of species not observed directly in the experiments.

Following Ung,[12] we expected N_2O decomposition in a microwave dis-charge would occur primarily via the spin-allowed electron-impact dissociation pathway,

$$e^- + N_2O \rightarrow N_2 + O(^1D) + e^- \, , \tag{6}$$
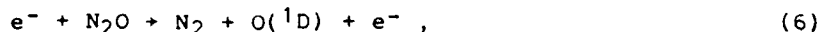
with the $O(^1D)$ rapidly quenched to $O(^3P)$ by Ar and wall collisions or converted to NO by reaction with N_2O:

$$O(^1D) + N_2O \rightarrow NO + NO \, . \tag{7}$$

Given the rate coefficients for $O(^1D)$ removal by N_2O,[40] N_2[41] and Ar[41] and our typical experimental conditions one would expect at least one-third of the $O(^1D)$ produced in Reaction (6) to form NO via Reaction (7). This would give about one NO molecule for every two N_2O molecules destroyed, or roughly equal NO and $O(^3P)$ yields. This conflicts with our observation of [O] >> [NO]. The cou-pled nature of the equations, however, precludes reliable estimates of the species production rates in the absence of time-dependent calculations. A further complication of this line of reasoning is its failure to account for

N-atom production in the discharge. N formation from electron-impact dissocia-
tion of N_2O, N_2, or NO should be much too slow to compete with NO formed from
Reaction (7). The kinetic model confirms that the decomposition of N_2O by re-
actions (6) and (7) fails to explain our observed O and NO yields, and indi-
cates that the spin-forbidden process,

$$e^- + N_2O \rightarrow N_2 + O(^3P) + e^- , \qquad (8)$$
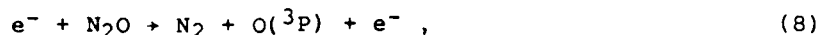
must be the major N_2O decomposition channel. The dissociation of N_2O by $Ar(^3P)$
metastables,

$$Ar^* + N_2O \rightarrow N_2(B^3\Pi_g) + O(^3P) + Ar , \qquad (9)$$
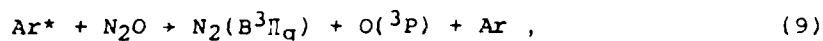
appears to be another important pathway for O-atom production. Electron-
impact dissociation of metastable N_2, primarily $N_2(A^3\Sigma_u^+)$ formed by rapid
cascade from $N_2(B^3\Pi_g)$ produced in reaction (9), is an important source of N at
low initial N_2O levels:

$$e^- + N_2^* \rightarrow N + N + e^-. \qquad (10)$$

NO is formed primarily in reaction (7), the $O(^1D)$ coming from electron-impact
excitation of $O(^3P)$. The supplementary material details the choice of
important reactions in the model and their rate parameters.

B.   Results of Calculations

The calculations used a modified predictor-corrector computer code
designed to solve numerically "stiff" systems of coupled differential
equations. Time-dependent solutions extend 500 μs; typical residence times in
our discharges are $\approx$ 300 μs. Our calculations indicate that the kinetics are
nearly in steady state after $\approx$ 200 μs (supplementary material, Fig. S11).
Figure 4 shows the species concentrations as functions of initial N_2O level at
300 μs. This represents the neutral gas composition at the exit of the active
discharge.

Since the actual measurements of O, N, and NO are made some distance downstream from the discharge, we must correct the predicted concentrations to reflect the completeness of the N plus NO reaction (1) between the discharge exit and the measurement station. Figure 5 compares the final, predicted concentrations of O, N, and NO at the measurement port as functions of $[N_2O]_0$ with experimental results obtained under comparable conditions. Figure 5 also indicates predictions for the case where N_2O dissociation by electrons proceeds entirely via the $O(^1D)$ product channel (reaction (6)). The $O(^3P)$ case clearly compares very nicely with the observations, while the $O(^1D)$ case gives too much NO and not enough O. More significantly, the predicted [O]/[NO] ratio is inconsistent with experimental results.

NO formation is overpredicted in the case where reactions (6) and (7) are assumed because at early times, before significant N_2 has built up, N_2O is the major quenching partner for $O(^1D)$. In that case every three N_2O molecules form two NO molecules but no $O(^3P)$. As N_2 and NO accumulate, this branching ratio moderates somewhat, but most of the NO has already been formed at this point. Increasing the rate of reaction (6) increases [O] but does not change [NO]. Consuming N_2O by electrons faster than the $O(^1D)$ can react with it requires an unreasonably large rate for reaction (6).

Thus direct production of $O(^3P)$ from N_2O appears necessary. Reacting N_2O with Ar* provides one such source. To obtain [O]>[NO], however, requires an extraordinarily high [Ar*]. Therefore, we must conclude that, in a microwave discharge, the electron-impact dissociation of N_2O proceeds primarily, if not entirely, by formation of $O(^3P)$ in a spin-forbidden process.

Comparison with data obtained for other gas mixtures at similar pressures, flow rates, and discharge powers (i.e., comparable discharge conditions) strengthen our interpretations. Calculations on He/N_2O mixtures use the same mechanism except, of course, for the reactions involving Ar*. He* reactions with N_2O are unlikely sources of atomic oxygen[32] so we have omitted He* kinetics from our calculations. In accord with the measurements, the calculations predict a 20-30% reduction in O production for He/N_2O discharges and production of NO at all N_2O levels (supplementary material, Fig. S12). We conclude that the observed reduced O yields result from the absence of the

Ar* + N_2O reaction, and that the continuous production of NO results from the absence of Ar* which virtually eliminates N_2*, and thereby N atoms, the major sink for NO.

Calculations on $Ar/N_2O/N_2$ mixtures also predict the general behavior observed in the experiments (supplementary material, Fig. S13). In this case, we overpredicted the N production, undoubtedly because the assumed rate coefficient for dissociation of N_2 by electrons is too large. While this process is insignificant for Ar/N_2O mixtures, it is the major source of N when N_2 is present initially. Furthermore, the addition of such large amounts of N_2 to the discharge will alter significantly the characteristic electron energy distribution and number density and might render kinetic processes involving atomic-nitrogen metastables consequential, although still minor. We considered neither of these factors. The important point, however, is that the kinetic calculations and experimental measurements both show that fairly large amounts of N_2 are required to produce enough N to remove the NO that is formed in reaction (7).

V. SUMMARY AND CONCLUSIONS

The experimental results show that Ar/N_2O discharges are indeed pro-
lific sources of atomic oxygen. We were able to generate O-atom flows over 20
μmol s^{-1} at modest discharge powers. The source is also very efficient, con-
verting about 75% of the nitrous oxide to atomic oxygen at nitrous oxide feed
rates less than 10-20 μmol s^{-1}. Judicious manipulation of discharge power, and
the addition of molecular nitrogen to the discharge prevents atomic-nitrogen or
nitric oxide from accompanying the atomic oxygen product. The point at which
atomic nitrogen and nitric oxide both are absent is indicated readily by the
absence of emission at 580 nm, N-atom and O/NO recombination both being strong
sources of 580 nm emission.

Kinetic calculations reproduce the experimental results reasonably well
under the assumptions that the electron-impact dissociation of N_2O proceeds
through the spin-forbidden channel to produce $O(^3P)$, and that about 20% of the
dissociations result from collisions between metastable argon atoms and N_2O.
The modeling calculations also indicate that perhaps as much as 20% of the
nitrous oxide fed to the discharge is undissociated, and that the molecular
oxygen flow rates out of the discharge are generally an order of magnitude less
than those of atomic oxygen. Thus, the argon/nitrous oxide discharge can be a
relatively clean source of atomic oxygen with only minor amounts of atomic
nitrogen, nitric oxide, or molecular oxygen accompanying the O-atoms out of the
discharge region, with the two former products being controllable to some
extent.

ACKNOWLEDGMENTS

SUPPLEMENTARY MATERIAL AVAILABLE

Fourteen additional figures are available to quantify the trends in the data discussed in the text, and to illustrate further the comparison between experimental observations and kinetic-model predictions. In addition we provide a table of reactions and rate coefficients used in the model and discuss our reasons for making the choices.

REFERENCES

1. C. J. Howard, J. Phys. Chem. <u>83</u>, 3 (1979).

2. L. Elias, E. A. Ogryzlo, and H. I. Schiff, Can. J. Chem. 37, 1680 (1959).

3. A. Mathias and H. I. Schiff, Discuss. Faraday Soc. 37, 38 (1964).

4. R. E. March, S. G. Furnival, and H. I. Schiff, Photochem. Photobiol. <u>4</u>, 971 (1965).

5. T. J. Cook and T. A. Miller, Chem. Phys. Lett. <u>25</u>, 396 (1974).

6. L. G. Piper, unpublished results (1978).

7. F. Kaufman and J. R. Kelso, 7th Int. Symp. Combustion, 53 (1958).

8. G. Black and T. G. Slanger, J. Chem. Phys. <u>74</u>, 6517 (1981).

9. O. R. Lundell, R. D. Ketcheson, and H. I. Schiff, 12th Int. Comb. Symp., 307 (1969).

10. J. L. McCrumb and F. Kaufman, J. Chem. Phys. <u>57</u>, 1270 (1972).

11. W. T. Rawlins, L. G. Piper, G. E. Caledonia, and B. D. Green, "COCHISE Research," PSI TR-298 (1981). Available from the authors upon request.

12. A. Y. M. Ung, Chem. Phys. Lett. <u>32</u>, 351 (1975).

13. F. Kaufman, Proc. Roy. Soc. (London) A <u>247</u>, 123 (1958).

14. F. Kaufman, Chemiluminescence and Bioluminescence, M. J. Cormier, D. M. Hercules, and J. Lee, eds. pp. 83-100 (1973).

15. L. G. Piper, G. E. Caledonia, and J. P. Kennealy, J. Chem. Phys. <u>74</u>, 2888 (1981).

16. L. G. Piper, G. E. Caledonia, and J. P. Kennealy, J. Chem. Phys. <u>75</u>, 2847 (1981).

17. L. G. Piper, J. Chem. Phys. <u>77</u>, 2373 (1982).

18. W. T. Rawlins and L. G. Piper, Proc. Soc. Photo.-Opt. Instrum. Eng. <u>279</u>, 58 (1981).

19. L. G. Piper, A. A. Clyne, and P. B. Monkhouse, J. Chem. Soc., Faraday Trans. 2 <u>78</u>, 1373 (1982).

20. H. C. Berg and D. Kleppner, Rev. Sci. Instrum. <u>33</u>, 248 (1962).

21. M. F. Golde and B. A. Thrush, Rep. Prog. Phys. <u>36</u>, 1285 (1973).

22. A. Fontijn, C. B. Meyer, and H. I. Schiff, J. Chem. Phys. $\underline{40}$, 64 (1964).

23. M. Sutoh, Y. Morioka, and M. Nakamura, J. Chem. Phys. $\underline{72}$, 20 (1980).

24. P. N. Clough and B. A. Thrush, Trans. Faraday Soc. $\underline{63}$, 915 (1967).

25. B. McCarroll, Rev. Sci. Instr. $\underline{41}$, 279 (1970).

26. D. Manson, Matheson Gas Co., Gloucester, MA. Private communication to L. G. Piper (1982).

27. M. Vanpee, K. D. Hill, and W. R. Kineyko, AIAA Journal $\underline{9}$, 135 (1971).

28. M. F. Golde, A. E. Roche, and F. Kaufman, J. Chem. Phys. $\underline{59}$, 3953 (1973).

29. D. Golomb and J. H. Brown, J. Chem. Phys. $\underline{63}$, 5246 (1975).

30. G. A. Woolsey, P. H. Lee, and W. D. Slafer, J. Chem. Phys. $\underline{67}$, 1220 (1977).

31. A. M. Pravilov and L. G. Smirnova, Kinet. and Catal. $\underline{19}$, 202 (1978).

32. L. G. Piper and W. T. Rawlins, and R. A. Armstrong, "O-Atom Yields from Microwave Discharges in N_2O/Ar Mixtures," AFGL-TR-83-0031, Air Force Geophysics Laboratory, Hanscom AFB, MA 1983. Available from the authors on request.

33. D. Husain and N. K. H. Slater, JCS. Faraday II $\underline{76}$, 606 (1980).

34. J. H. Lee, J. V. Michael, W. A. Payne, and L. J. Stief, J. Chem. Phys. $\underline{69}$, 3069 (1978).

35. M. A. A. Clyne and I. S. McDermid, JCS Faraday I $\underline{71}$, 2189 (1975).

36. D. L. Baulch, D. D. Drysdale, D. G. Horne, and A. C. Lloyd, _Evaluated Kinetic Data for High Temperature Reaction. II. Homogeneous Gas Phase Reactions of the H_2 - N_2 - O_2 System._ (Butterworths, London, 1973).

37. R. A. Young and R. L. Sharpless, J. Chem. Phys. $\underline{39}$, 1071 (1963).

38. W. Groth, D. Kley, and U. Schurath, J. Quant. Spectrosc. Radiat. Transfer. $\underline{11}$, 1475 (1971).

39. G. Slanger and G. Black, J. Chem. Phys. $\underline{64}$, 3767 (1976).

40. K. Schofield, J. Photochem. $\underline{9}$, 55 (1978).

41. L. Lam, D. R. Hastie, B. A. Ridley, and H. I. Schiff., J. Photochem. $\underline{15}$, 119 (1981).

FIGURE CAPTIONS

PICOAMMETER

HIGH
VOLTAGE

PMT

IRIS

FILTER
(580 ± 5 NM)

LENS

PRESSURE
PORT

TO BLOWER

NO
INLET

μ WAVE
DISCHARGE

Ar/N₂O

A-949

Piper/Rawlins
PSI SR-152A
Figure 1

C-20

Piper/Rawlins
PSI SR-152A
Figure 2

A-951

Piper/Rawlins
PSI SR-152A
Figure 3
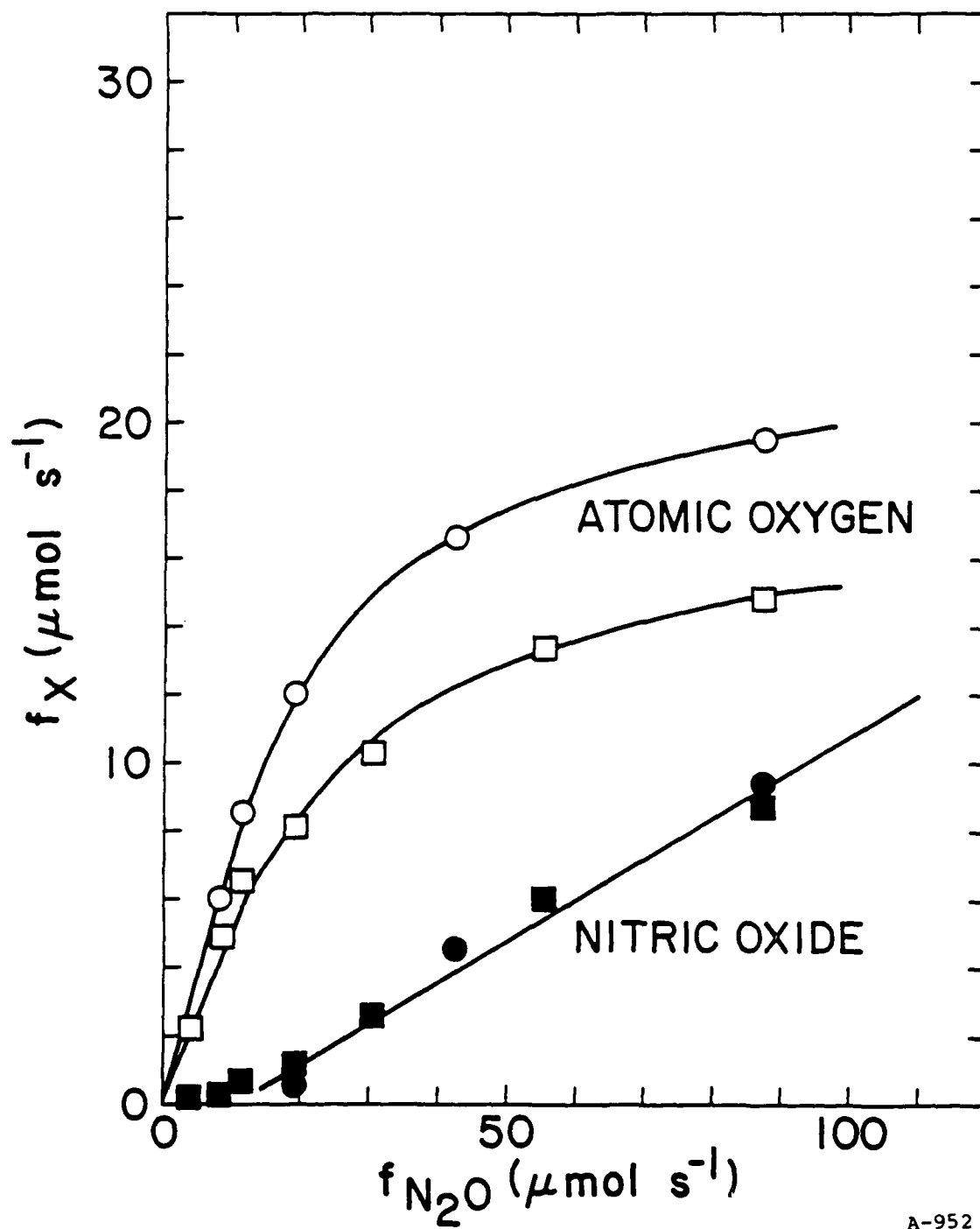
A-952
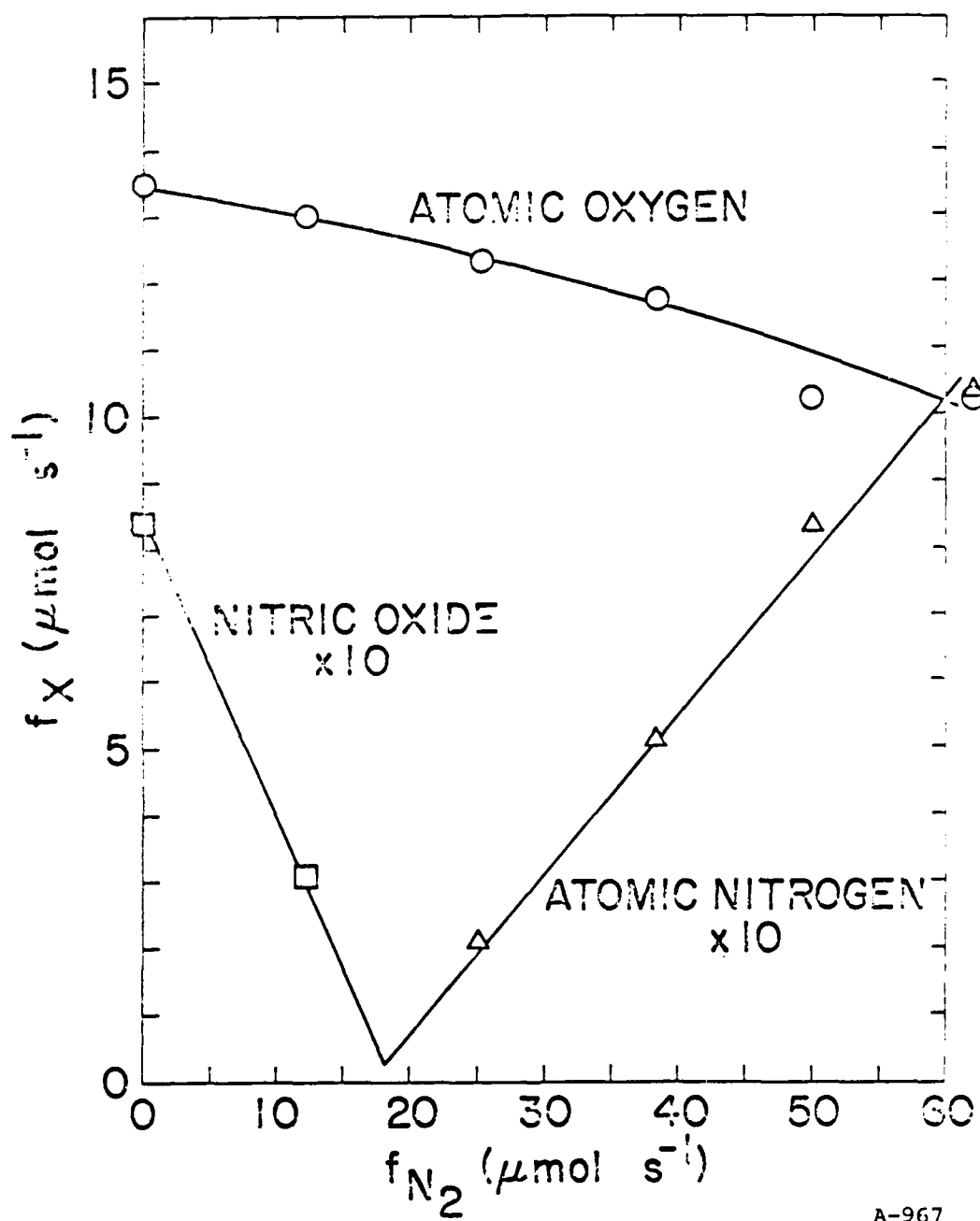
A-967

$\tau = 300 \mu s$

A-953

Piper/Rawlins
PSI SR-152A
Figure 6

Figure 7

SPECIES CONCENTRATION (cm^{-3}) vs $[N_2O]_0$ (10^{15} cm^{-3})

EXPERIMENTAL RESULTS

PREDICTED, $N_2O \rightarrow O(^3P)$

PREDICTED, $N_2O \rightarrow O(^1D)$
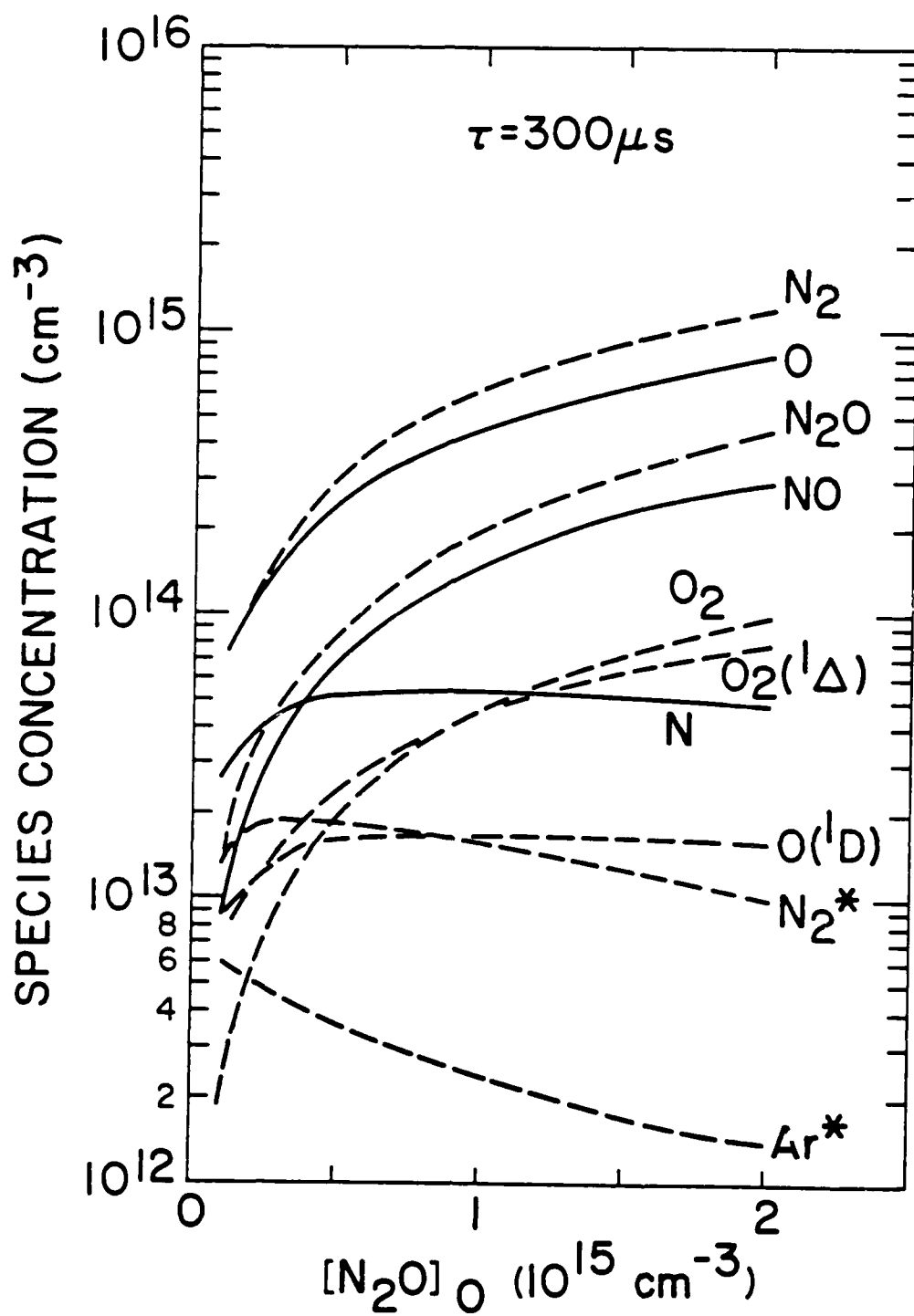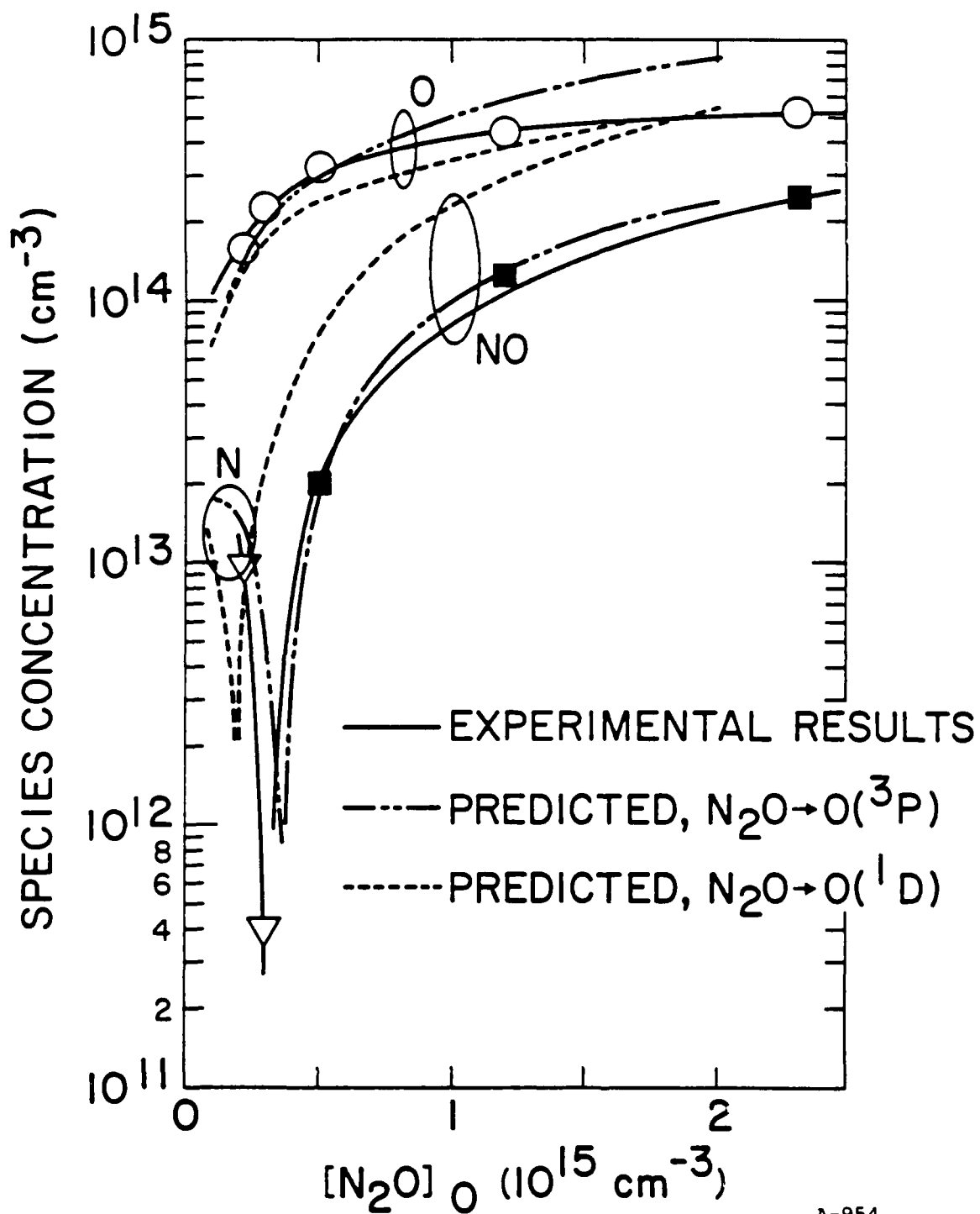
A-954

Piper/Rawlins
PSI SR-152A
Figure 7

O-ATOM YIELDS FROM MICROWAVE DISCHARGES IN N_2O/Ar MIXTURES

Lawrence G. Piper and Wilson T. Rawlins

Physical Sciences Inc.
Research Park, P. O. Box 3100
Andover, MA 01810

S U P P L E M E N T A R Y   M A T E R I A L

CHOICE OF REACTIONS AND RATE COEFFICIENTS

We present here a brief synopsis of our representation of the chemistry of the active discharge. Table S1 lists the important reactions and their rate coefficients. In the table, Ar^* denotes collectively the $^3P_0$ and $^3P_2$ metastable states of argon, and N_2^* denotes metastable $N_2(A^3\Sigma_u^+)$ as formed by rapid cascade from the higher electronic states which are the actual initial products of the reactions. Some of the N_2^* removal rate coefficients incorporate the possibility of vibrational excitation. Rate coefficients for the neutral bimolecular reactions come from information available in the literature with no further adjustments.

Electron-impact and surface removal processes govern the production and loss terms for critical species such as $O(^1D)$, Ar^*, and N_2^*. The rate parameters for these processes are difficult to estimate to better than an order of magnitude because they are strong functions of conditions in the discharge. The absence of dissociation cross-section data for N_2O and N_2^* further compounds this problem. While we can estimate coefficients for the surface-removal processes fairly reliably from diffusion arguments and previous observations, we must rely on intuition to estimate the electron-impact coefficients based on knowing energy thresholds, cross sections for the desired species or similar molecules, and electron-energy distributions normally obtained in such discharges. Kaufman[S1] has discussed these considerations in some detail and we follow the same principles here. We assume typical discharge conditions $P \sim 1$ torr, $T \sim 500$ K, $E/N \sim 10^{-16}$ V cm^2, average electron energy $\sim 3-8$ eV, and primary electron density $\sim 3 \times 10^{11}$ cm^{-3}, with uniform properties along the entire length of the active discharge. These conditions are representative of those encountered in our experiments.

The dissociation of N_2O by electrons can proceed by three possible pathways, forming $O(^3P)$, $O(^1D)$, or NO. The N-NO branch has the largest energy

threshold (4.93 eV as opposed to 1.68 eV for N_2-$O(^3P)$ and 3.66 eV for N_2-$O(^1D)$)[S2] and should be unimportant. $O(^1D)$ is a critical precursor to NO through its reaction with N_2O. Thus the predicted NO yields are extremely sensitive to the extent of $O(^1D)$ production (see below). $O(^1D)$ also is formed from electron-impact excitation of $O(^3P)$ and is quenched to $O(^3P)$ in collisions with a number of species in the discharge. For these reasons, the N_2O dissociation branching ratio is the most critical parameter in determining the O/NO ratio obtained in the discharge.

One branch of the $O(^1D)$ + N_2O reaction forms significant amounts of N_2 and O_2, but the bulk of the N_2 formed arises from N_2O dissociation. In gas mixtures containing Ar, the reaction between Ar metastables and N_2O provides a direct source of $O(^3P)$ and leads to the formation of significant levels of metastable N_2.[S3] The dissociation of N_2^* by primary electrons probably proceeds with a large rate coefficient,[S4] so that this process should compete with the N-NO dissociation channel of N_2O as a source of atomic nitrogen. In gas mixtures containing He, the interaction between He metastables and N_2O leads primarily to Penning ionization,[S5] followed by surface recombination of N_2O^+ and/or dissociative recombination with secondary electrons to give atomic oxygen; in this case, N_2^* is not important and N may not be formed at significant levels.

We estimated first-order surface removal rates for $O(^1D)$ and N_2^* by assuming unit deactivation probability and using the diffusion equation $k = (2.4/r)^2\ D/P\ (T/300)^{3/2}$, where r is the radius of the discharge tube, D is the diffusion coefficient in $cm^2\ s^{-1}$ at 1 torr and 300 K, P is the pressure in torr, and T is the temperature. Diffusion coefficients for $O(^1D)$/Ar[S6] and N_2^*/Ar[S7] are in the literature. Our previous observations of atomic concentrations in partially self-reversed discharge resonance lamps allowed us to estimate recombination coefficients for $O(^3P)$ and N.[S8,S9] These two species do not appear to exhibit unit recombination efficiency, even in active discharges.

The kinetics of Ar discharges are somewhat complicated, and representation of the Ar* formation and removal processes presents a special problem. We have chosen to express Ar* production and loss in a shorthand form using direct electron-impact excitation and an effective first-order removal which is consistent with other observations in the active discharge. In previous observations of atomic-nitrogen resonance radiation excited by direct energy transfer from Ar* in a nearly-pure Ar discharge, we noted that the addition to the active discharge of significant amounts of Xe, a strong quencher of Ar*, reduced the steady-state number density of Ar* only moderately, implying that the net loss rate for Ar* must be near 10^5 s^{-1} in pure Ar.[S10] This effect is probably due largely to ionization of Ar*. Using this value to describe Ar* removal, we then adjusted the Ar* production coefficient to give a large enough Ar* number density to match the observed N and O yields as described below. The resulting rate coefficient is consistent with a pure Ar discharge but is about a factor of 10 greater than we might expect for Ar with impurity levels of a few percent. However, we have not considered other Ar* sources (e.g., cascade from higher states formed in dissociative recombination of Ar_2^+ with electrons), and our assumed electron density may be too small. In any case, the relevant factor is the steady state Ar* number density which is in the 10^{12} atoms cm^{-3} range, consistent with Ar and He metastable number densities required to explain flux levels of O and N resonance radiation observed in microwave-discharge line sources.[S8-S10] Furthermore, the predicted Ar* number density is only weakly dependent on the initial N_2O concentration, as we previously observed for Xe as a collision partner.[S10] This latter effect is important for our analysis, because e^- + N_2O is not sufficient by itself to explain our observed [O]/[NO] ratios, and we require that 20-50% of the early-time O production take place via Ar* + N_2O over a 20-fold variation in $[N_2O]_0$.

REFERENCES FOR SUPPLEMENTARY MATERIAL

S1. F. Kaufman, Advances in Chemistry Series 80, 29 (1969).

S2. D. R. Stull and H. Prophet, JANAF Thermochemical Tables, Nat'l. Stand. Ref. Ser. - NBS 37, (1971).

S3. L. A. Gundel, D. W. Setser, M. A. Clyne, J. A. Coxon, and W. S. Nip, J. Chem. Phys. 64, 4390 (1976).

S4. E. C. Zipf, Bull. Am. Phys. Soc. 27, 100 (1982).

S5. J. P. Riola, J. S. Howard, R. D. Rundel, and R. F. Stebbings, J. Phys. B: Atom. Molec. Phys. 7, 376 (1974).

S6. A. Corney, And O. M. Williams, J. Phys. B: Atom. Molec. Phys. 5 686 (1972).

S7. D. Levron, and A. V. Phelps, J. Chem. Phys. 69, 2260 (1978).

S8. W. T. Rawlins and F. Kaufman, J. Quant. Spectrosc. Radiat. Transfer 18, 561 (1977).

S9. W. T. Rawlins, Applications of OI and NI Resonance Apsorption in the Vacuum Ultraviolet to Studies of Electronic Energy Transfer in Active Nitrogen, Line Broadening in Low Pressure He Discharge Lamps, and Thermo-spheric $O(^3P)$ and $N(^4S)$ Densities, Thesis, University of Pittsburgh (1977).

S10. W. T. Rawlins and L. G. Piper, Proc. Soc. Photo.-Opt. Instrum. Eng. 279, 58 (1981).

TABLE S1

Reactions Contributing to N_2O Dissociation
in $N_2O/N_2/Ar$ Microwave Discharges

Reaction	Approximate Rate Coefficient†	Source
N_2O Dissociation		
$e^- + N_2O \rightarrow O(^1D) + N_2 + e^-$	0	See text
$\rightarrow O(^3P) + N_2 + e^-$	1×10^{-8}	Discharge estimate
$\rightarrow N + NO + e^-$	1×10^{-9}	Discharge estimate
$O(^1D)$ Quenching		
$O(^1D) + N_2O \rightarrow NO + NO$	7.2×10^{-11}	a,b
$\rightarrow N_2 + O_2$	4.8×10^{-11}	a,b
$O(^1D) + Ar \rightarrow O(^3P) + Ar$	3×10^{-13}	a
$O(^1D) + N_2 \rightarrow O(^3P) + N_2$	3×10^{-11}	a
$O(^1D) + NO \rightarrow O(^3P) + NO$	1.5×10^{-10}	c
$O(^1D) + wall \rightarrow O(^3P)$	8×10^3	Diffusion estimate
Ar Metastable Reactions		
$Ar + e^- \rightarrow Ar^* + e^-$	1×10^{-10}	Optimized-see text
$Ar^* + N_2O \rightarrow N_2^* + O(^3P) + Ar$	4.4×10^{-10}	d
$Ar^* + N_2 \rightarrow Ar + N_2^*$	3×10^{-11}	d
$Ar^* + NO \rightarrow Ar + N + O(^3P)$	1.5×10^{-10}	d
$Ar^* + O_2 \rightarrow Ar + O(^3P) + O(^3P)$	2×10^{-10}	d
$Ar^* + O \rightarrow Ar + O^*$	8×10^{-11}	e
$Ar^* + N \rightarrow Ar + N^*$	1.5×10^{-10}	f
$Ar^* \rightarrow Ar$	1×10^5	Optimized-see text
N_2 Metastable Reactions		
$N_2^* + e^- \rightarrow N + N + e^-$	1×10^{-8}	Discharge estimate
$N_2^* + Ar \rightarrow N_2 + Ar$	7×10^{-15}	g
$N_2^* + N_2O \rightarrow N_2 + N_2 + O(^3P)$	6×10^{-12}	h
$N_2^* + O \rightarrow N_2 + O^*$	3×10^{-11}	i
$N_2^* + N \rightarrow N_2 + N^*$	5×10^{-11}	j
$N_2^* + wall \rightarrow N_2$	6×10^3	Diffusion estimate
N, O Reactions		
$O(^3P) + e^- \rightarrow O(^1D) + e^-$	1×10^{-8}	Discharge estimate
$O(^3P) + wall \rightarrow 1/2\ O_2^*$	5×10^2	Diffusion estimate
$e^- + N_2 \rightarrow N + N + e^-$	1×10^{-10}	Discharge estimate
$N + wall \rightarrow 1/2\ N_2$	5×10^2	Diffusion estimate
$N + NO \rightarrow N_2 + O(^3P)$	3×10^{-11}	k

†Rate coefficients are in units of cm^3 molecule^{-1} s^{-1} for bimolecular reactions and s^{-1} for first-order surface deactivation/recombination processes.

REFERENCES FOR TABLE S1

a. K. Schofield, J. Photochem. $\underline{9}$, 55 (1978).

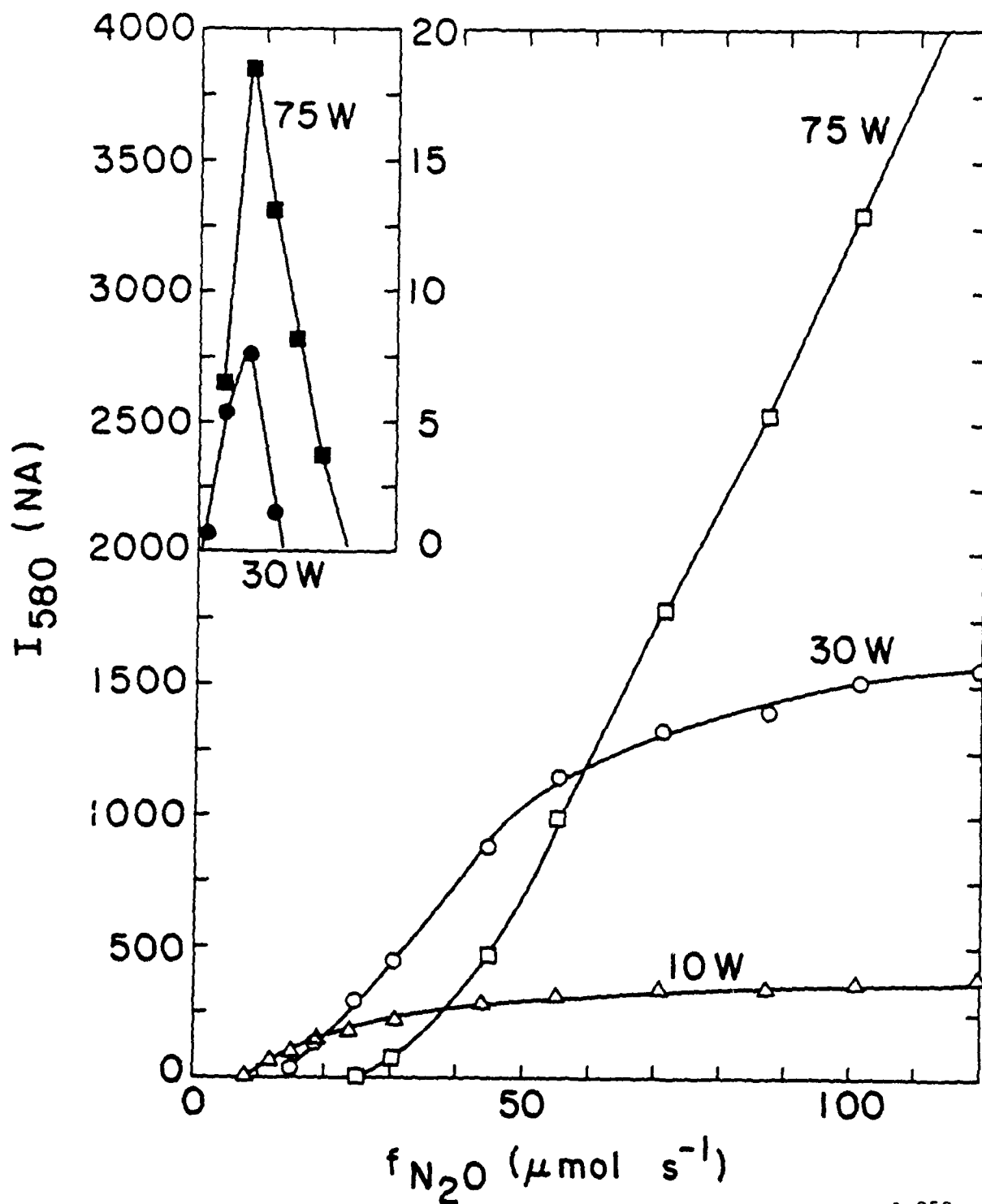b. L. Lam, D. R. Hastie, B. A. Ridley, and H. I. Schiff., J. Photochem. 15 119 (1981).

c. M. J. McEwan, and L. F. Phillips, Chemistry of the Atmosphere, John Wiley & Sons, New York, p. 138 (1975).

d. L. G. Piper, J. E. Velazco, D. W. Setser, J. Chem. Phys. $\underline{59}$, 3323 (1973).

e. L. G. Piper, M. A. A. Clyne, and P. B. Monkhouse, J. Chem. Soc., Faraday Trans. $\underline{2\ 78}$, 1373 (1982).

f. L. G. Piper, M. A. A. Clyne, and P. B. Monkhouse, Chem. Phys. $\underline{51}$, 107 (1980).

g. J. W. Dreyer and D. Perner, J. Chem. Phys. $\underline{58}$, 1195 (1980).

h. W. G. Clark, and D. W. Setser, J. Phys. Chem. $\underline{84}$, 2225 (1980).

i. L. G. Piper, G. E. Caledonia, and J. P. Kennealy, J. Chem. Phys. $\underline{75}$, 2847 (1981).

j. O. J. Dunn, and R. A. Young, Int. J. Chem. Kinet. $\underline{8}$, 161 (1976).

k. C. T. Cheah, and M. A. A. Clyne, J. C. S. Faraday $2\ \underline{76}$, 1543 (1980).

S1. Intensity at 580 nm as a function of added NO number density for discharged N_2O/Ar. The N_2O flow rates in μmol s^{-1} are as follows: O - 7.8, $\triangle$- 11, ■ - 18.5, ● - 42, ▲ 87. The ordinates for the 42 and 87 μmol s^{-1} runs have been reduced by 600 and 1580 n A, respectively.

S2. Ultraviolet spectrum produced in N + O + Ar recombination. $\Delta\lambda$ = 0.2 nm. f_{Ar} = 1470 μmol s^{-1}, f_{N_2O} = 21 μmol s^{-1}, p = 1.18 torr, power = 50 watts.

S3. Nitrogen-atom recombination spectrum from discharged N_2O/Ar. Argon lines scattered form the discharge appear at $\lambda > 700$ nm. f_{Ar} = 4882 μmol s^{-1}, f_{N_2O} = 18.5 μmol s^{-1}, p = 3.50 torr, Power = 50 watts.

S4. The production of O and NO from Ar/N_2O discharges as a function of N_2O flow rate for two different Ar flow rates but constant pressure. P=1.25 *torr*, power = 30 watts; circles: f_{Ar} = 1415 μmol s^{-1}, discharge residence time = 0.32 ms; squares: f_{Ar} = 4510 μmol s^{-1}, discharge residence time = 0.11 ms.

S5. The production of O and NO from Ar/N_2O discharges as a function of N_2O flow rate for two different Ar flow rates but constant pressure. P=0.52 torr, power = 30 watts; circles: f_{Ar} = 1325 μmol s^{-1}; squares: f_{Ar} = 400 u mol s^{-1}.

S6. The production of O and NO from Ar/N_2O discharges as a function of N_2O flow rate at three different argon flow rates and pressures, but similar discharge residence times ($\approx$ 0.37 ms). Triangles: f_{Ar} = 400 μmol s^{-1}, p = 0.53 torr; circles: f_{Ar} = 1461 μmol s^{-1}; p = 1.24 torr; squares: f_{Ar} = 4352 μmol s^{-1}, p = 3.1 torr.

S7. The production of O and NO from Ar/N_2O discharges as a function of N_2O flow rate at constant Ar flow rate but varying pressures and discharge residence times. Triangles: p = 0.52 torr, discharge residence time = 0.15 ms; circles: p = 1.24 torr, discharge residence time = 0.32 ms; squares: p = 3.6 torr, discharge residence time = 0.98 ms.

S8. The production of O, NO, and N from Ar/N_2O/N_2 discharges as a function of N_2 flow rate. f_{Ar} = 1385 μmol s^{-1}, f_{N_2O} = 42.5 μmol s^{-1}, p $\approx$ 1.35 torr, power = 30 watts.

S9. Variation in the flow rates of atomic oxygen and nitric oxide products from $Ar/N_2/N_2O$ discharges as a function of N_2 flow rate. $f_{Ar} = 1405$ μmol s^{-1}, $f_{N_2O} = 87$ μmol s^{-1}, $p \approx 1.4$ torr, power $= 30$ watts.

S10. The production of O and NO from Ar/N_2O discharges as a function of N_2O flow rate at two different discharge powers. $f_{Ar} \approx 1430$ μmol s^{-1}; $p = 1.2$ torr; circles: 30 watts; squares: 50 watts.

S11. Predicted species evolution in an Ar/N_2O microwave discharge plasma, using the reaction set of Table 1. $[Ar] = 2.4 \times 10^{16}$ cm^{-3}, $[N_2O]_o = 1 \times 10^{15}$ cm^{-3}.

S12. Predicted concentrations of O, N, and NO at the measurement station for Ar/N_2O and He/N_2O microwave discharges.

S13. Experimental and predicted concentrations of O, N, and NO at the measurement station for an $Ar/N_2/N_2O$ microwave discharge, $[N_2O]_o = 8 \times 10^{14}$ cm^{-3}. The experimental data are from Fig. S8.

The y-axis is labeled I(NA) with values 100, 200, 300. The x-axis is labeled [NO] ADDED (10^{13} MOLECULES cm^{-3}) with values 0, 1.0, 2.0, 3.0, 4.0, 5.0, 6.0.

A-955

Piper/Rawlins
PSI SR-152A
Figure S1

NO($B^2\Pi-X^2\Pi$)

$v'=0$

NO($A^2\Sigma^+-X^2\Pi$)

NO($C^2\Pi-X^2\Pi$)$v'=0$

WAVELENGTH (nm)

A-965
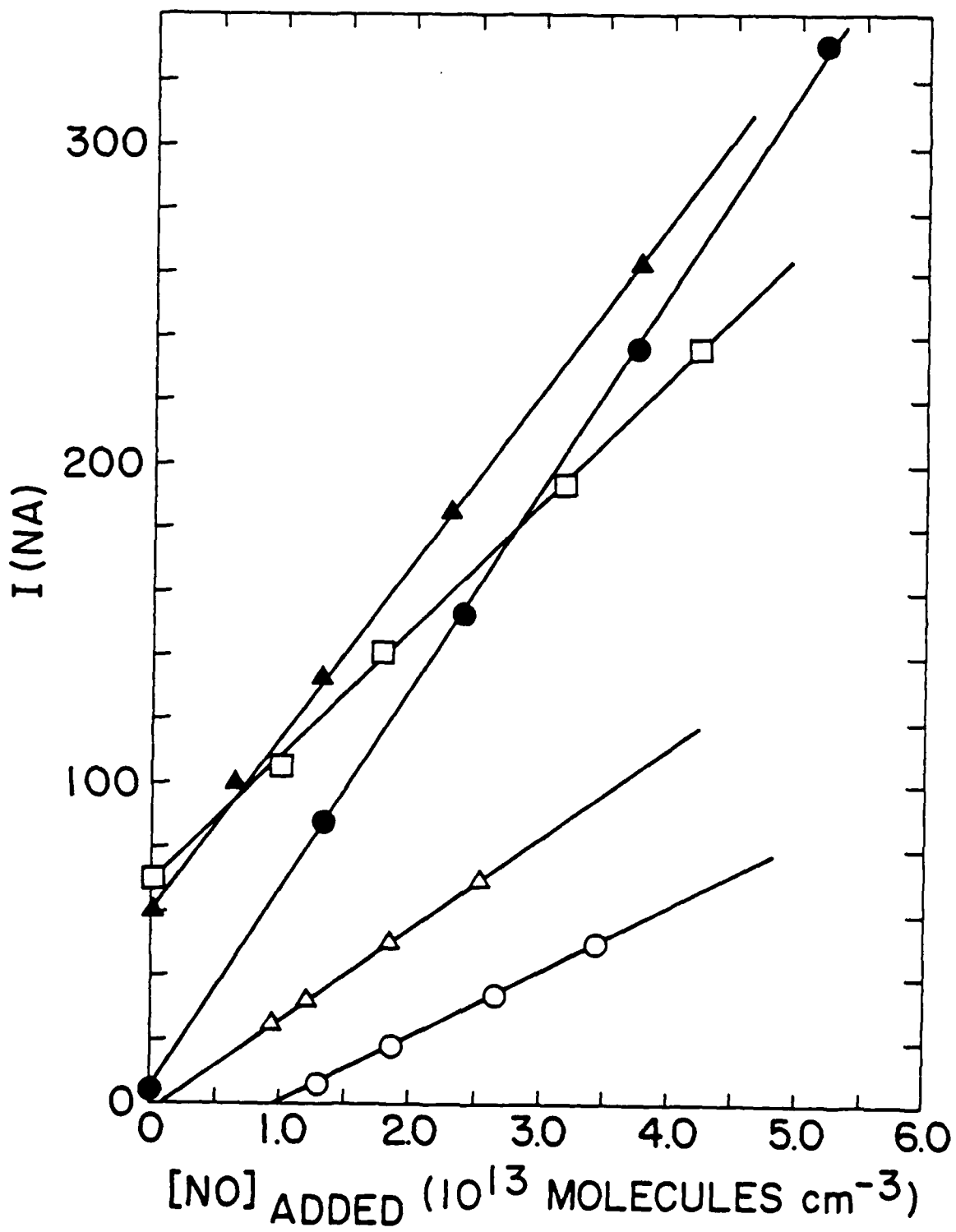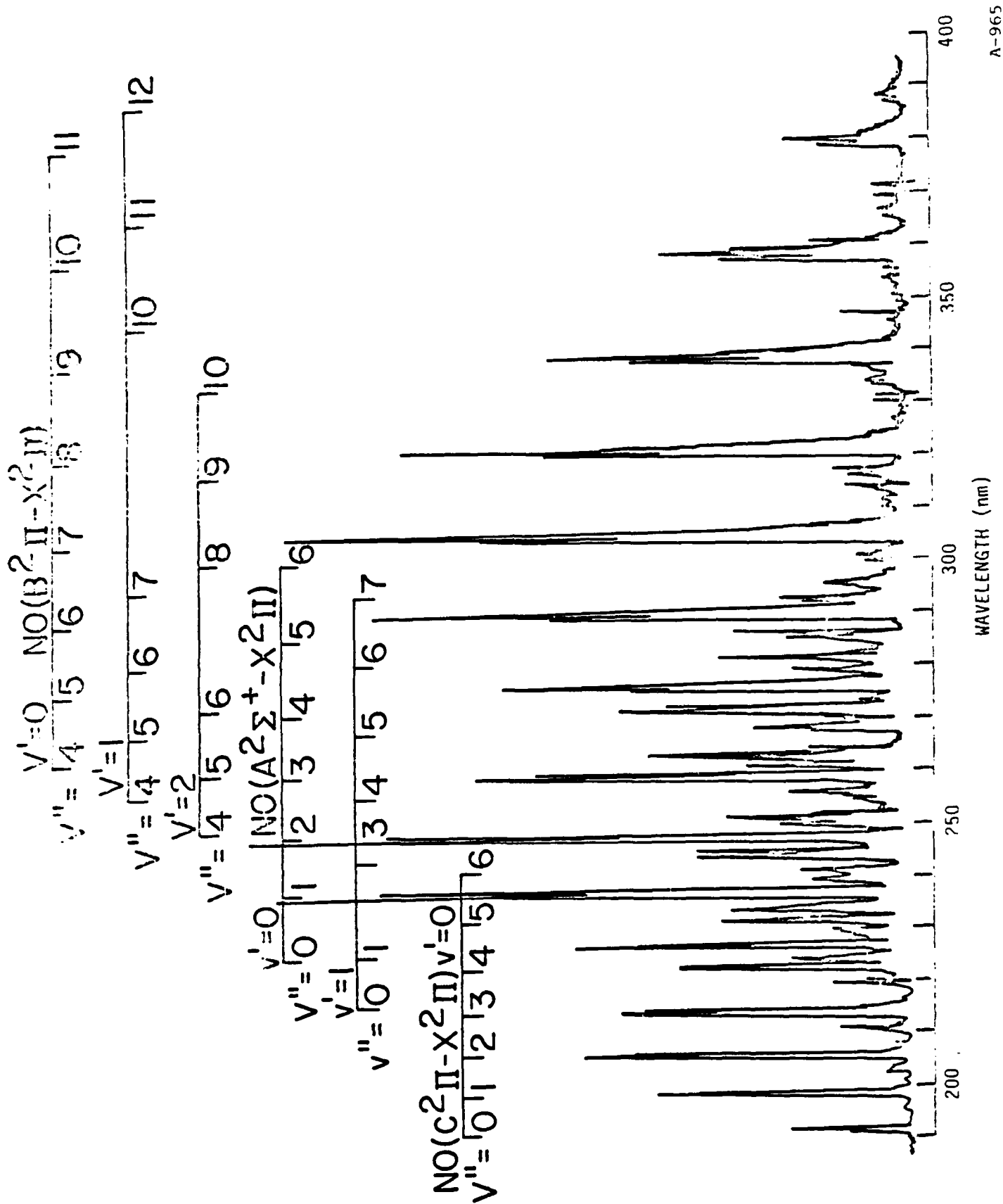
S-10

Piper/Rawlins
PSI SR-152A
Figure S2

RELATIVE SPECTRAL RESPONSE

$\Delta\lambda = 1.3$ nm
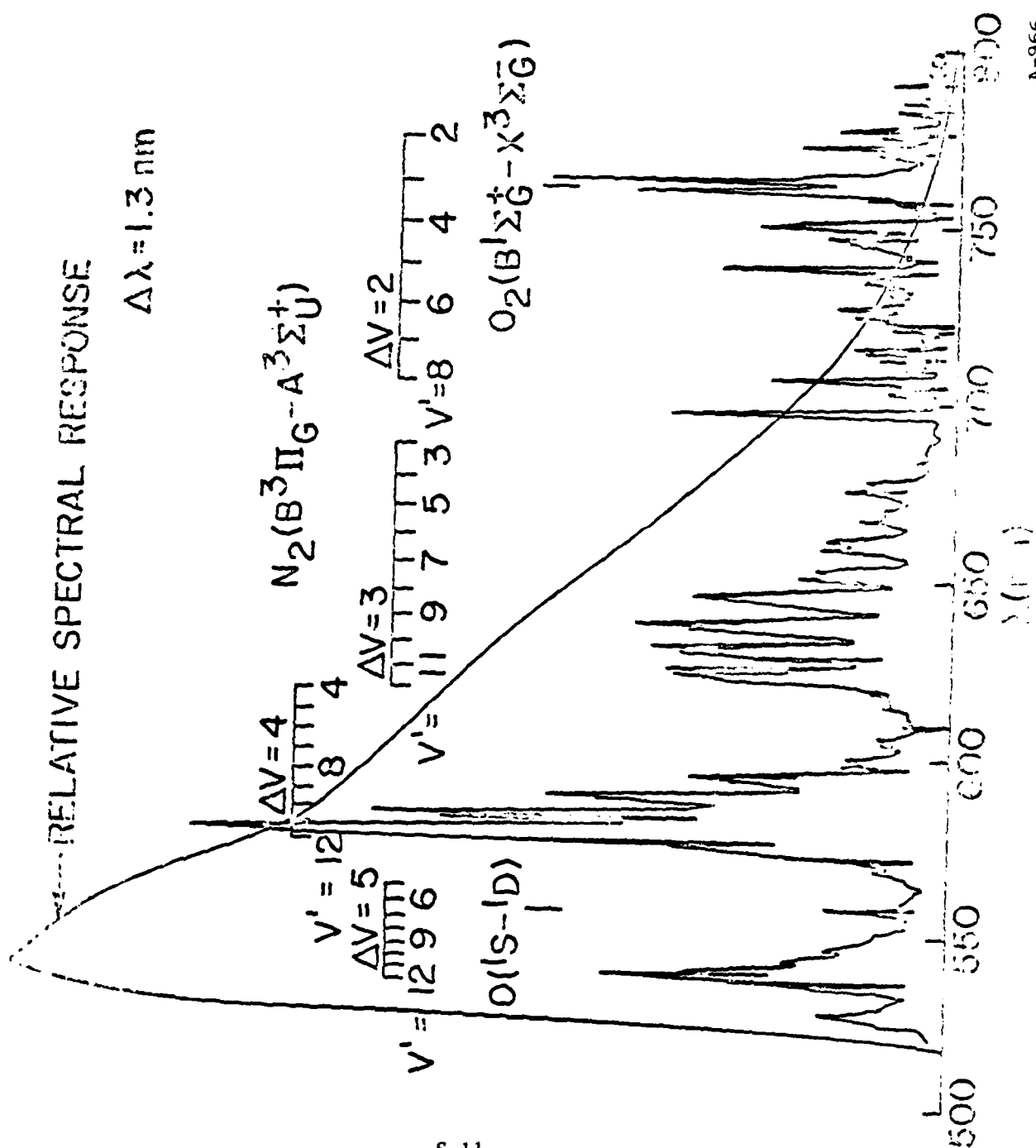
$N_2(B^3\Pi_G - A^3\Sigma_U^+)$

$O_2(B^1\Sigma_G^+ - X^3\Sigma_G^-)$

$O(^1S - ^1D)$

A-966

S-11

ATOMIC OXYGEN

NITRIC OXIDE

A-956

S-12

f_X (μmol s^{-1}) vs f_{N_2O} (μmol s^{-1})

ATOMIC OXYGEN

NITRIC OXIDE
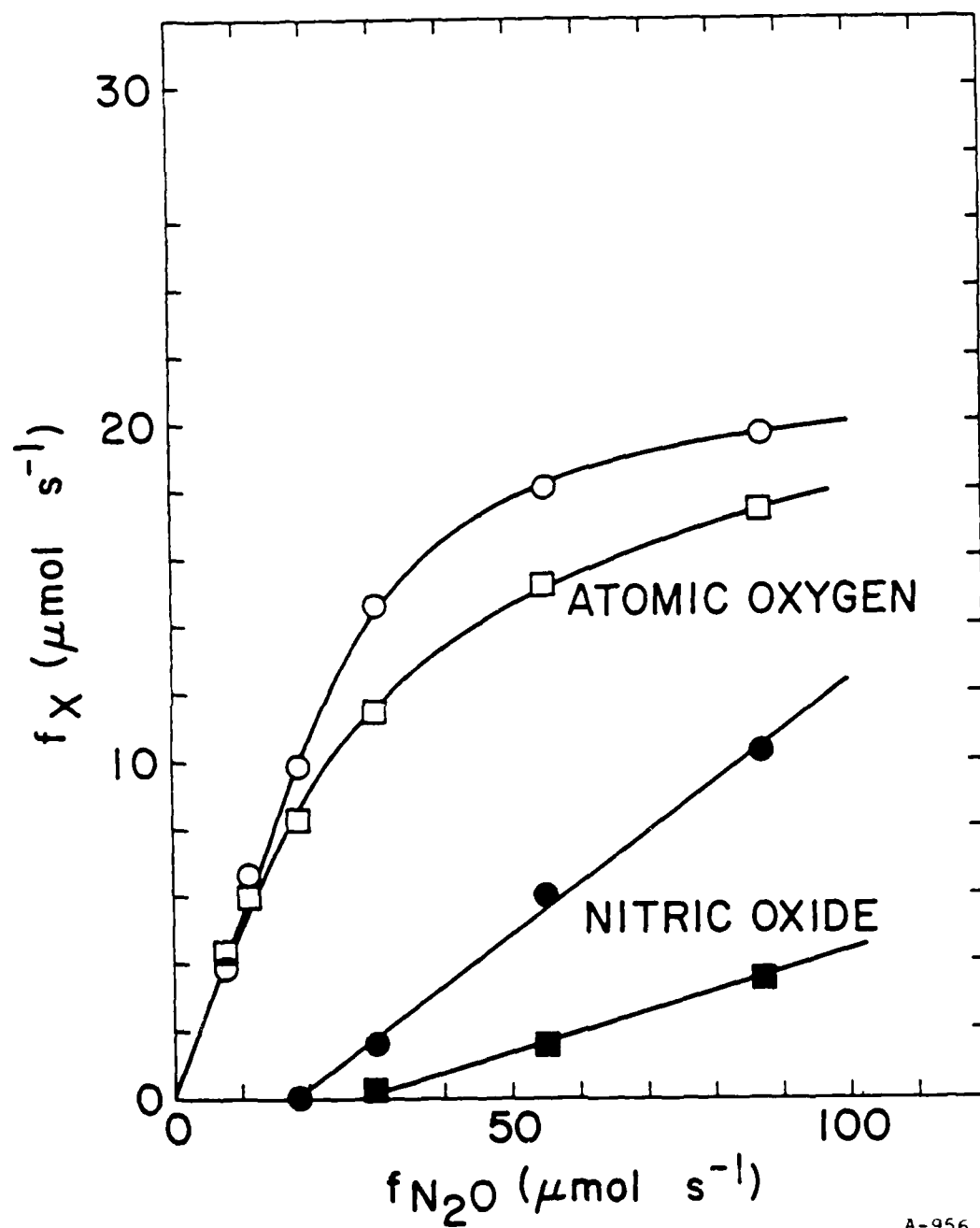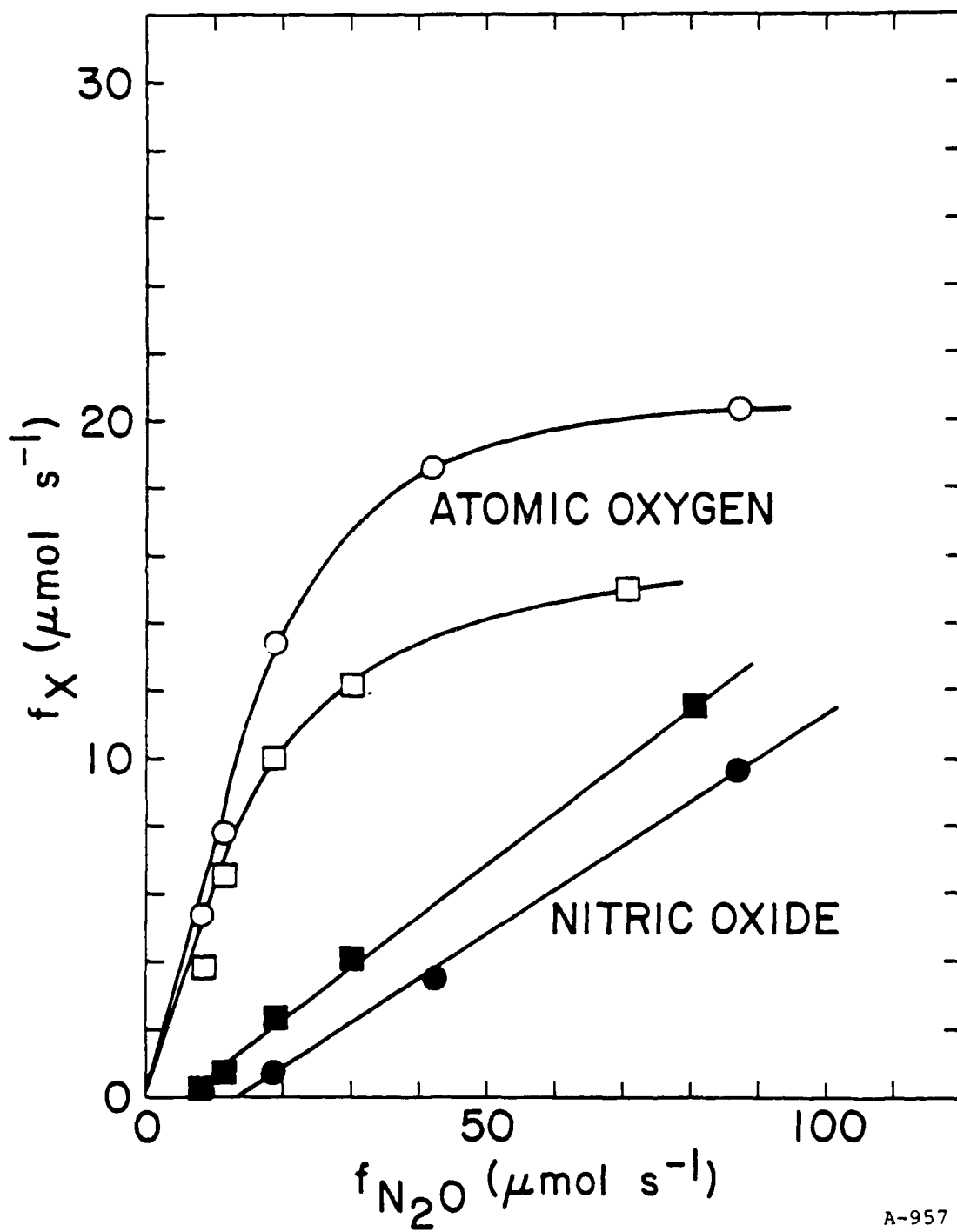
A-957

Piper/Rawlins
PSI SR-152A
Figure S5

S-13
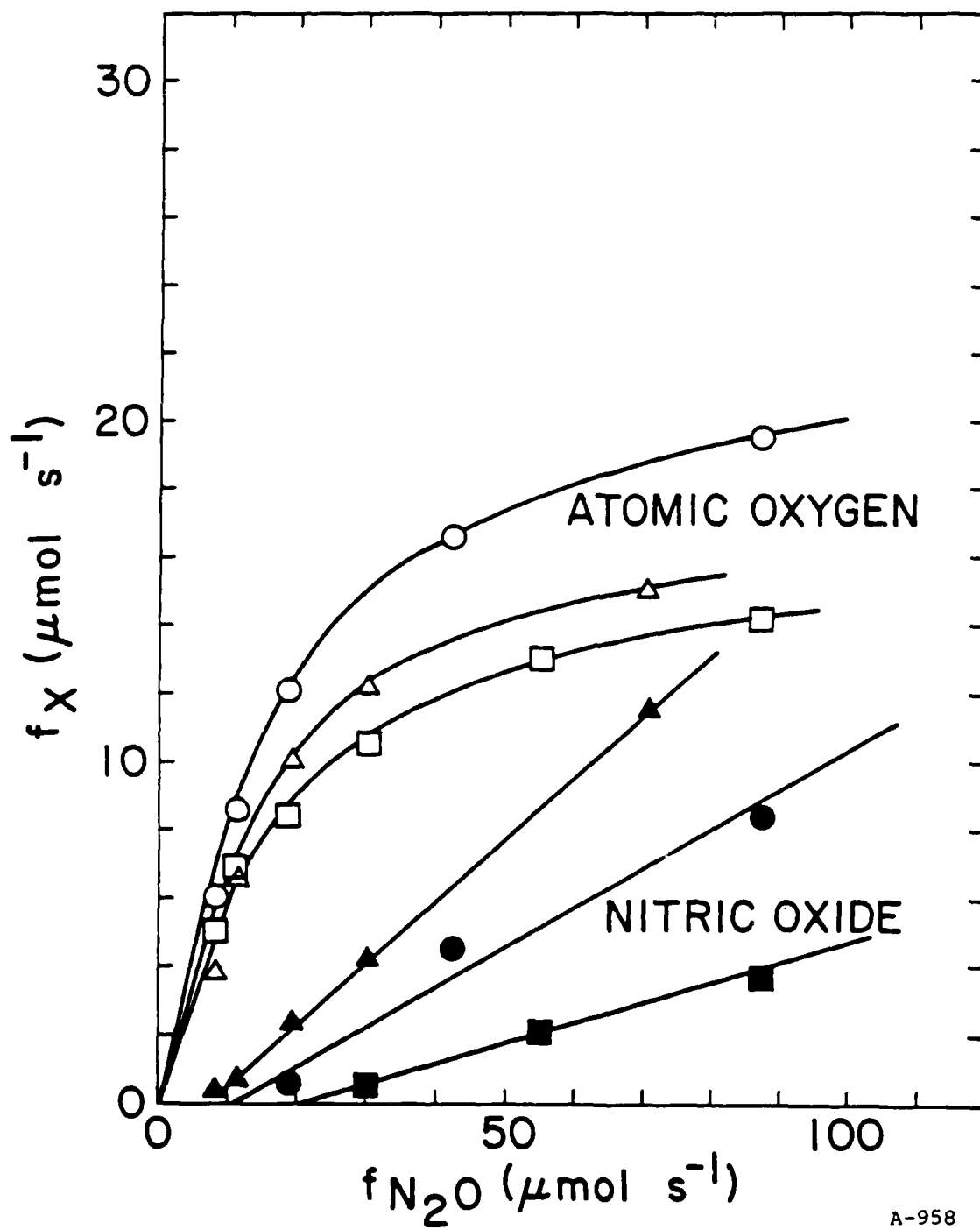
A-958

Piper/Rawlins
PSI SR-152A
Figure S6
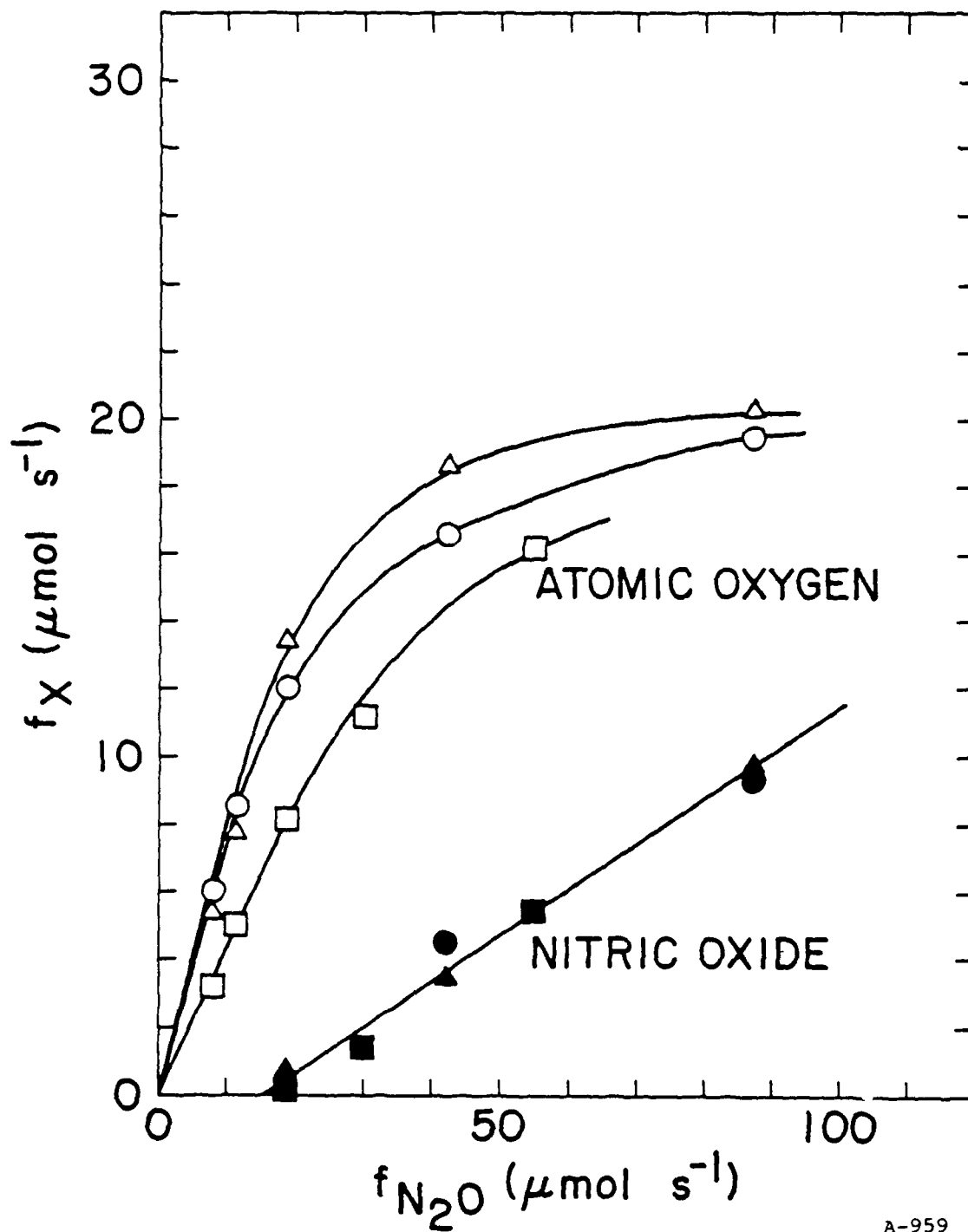
A-959

Piper/Rawlins
PSI SR-152A
Figure S7
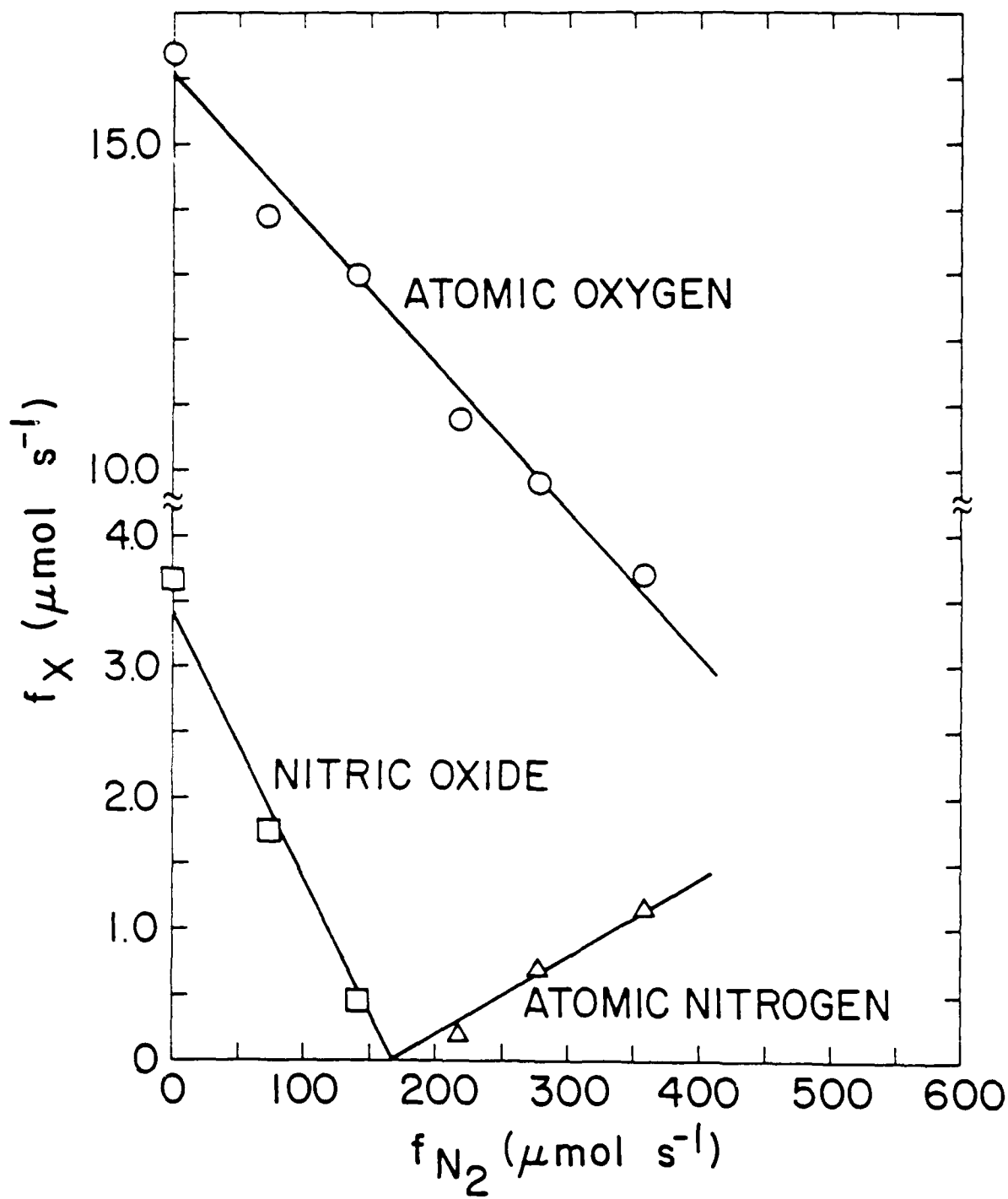
A-960

Piper/Rawlins
PSI SR-152A
Figure S8
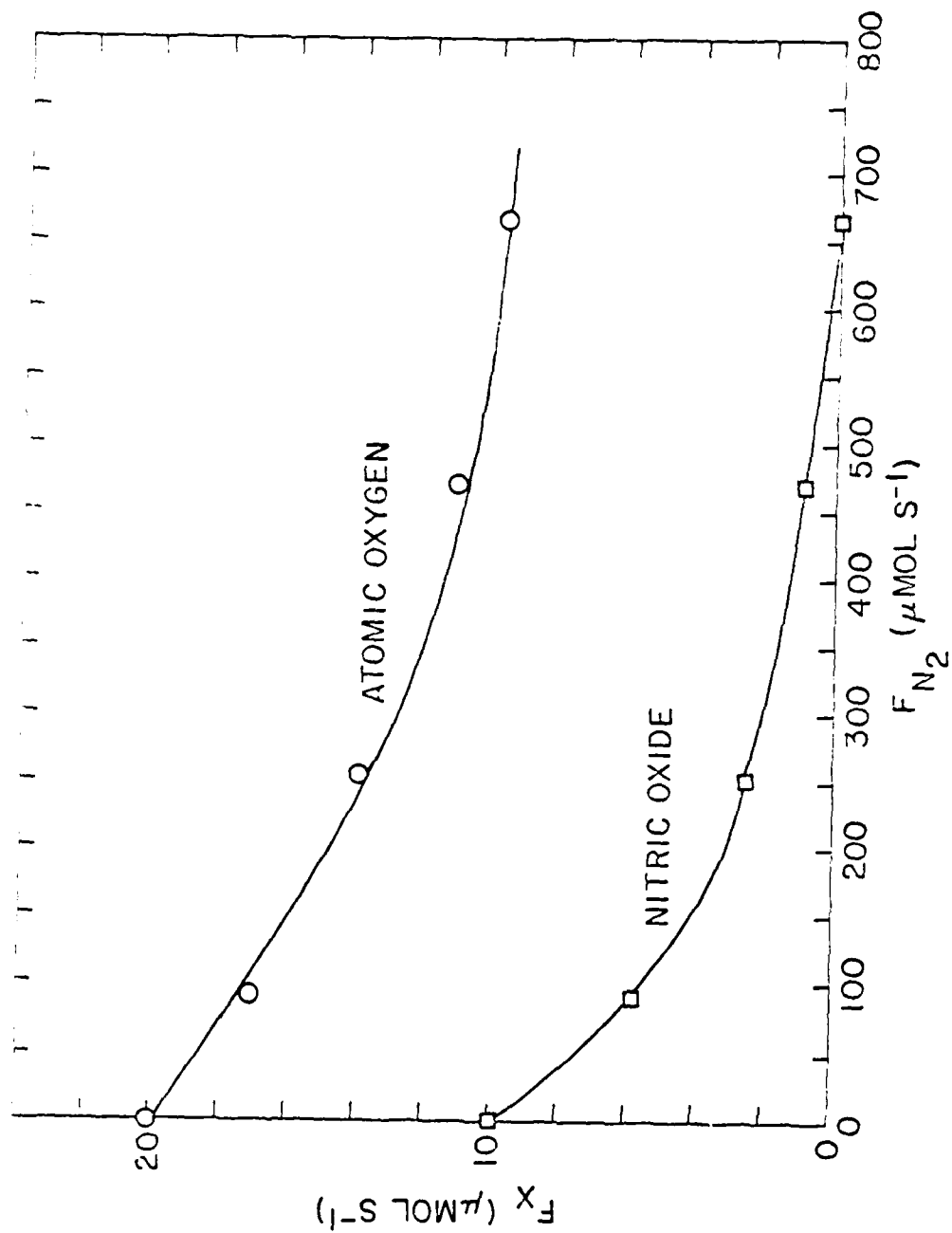
Piper/Rawlins
PSI SR-152A
Figure S9

A-968
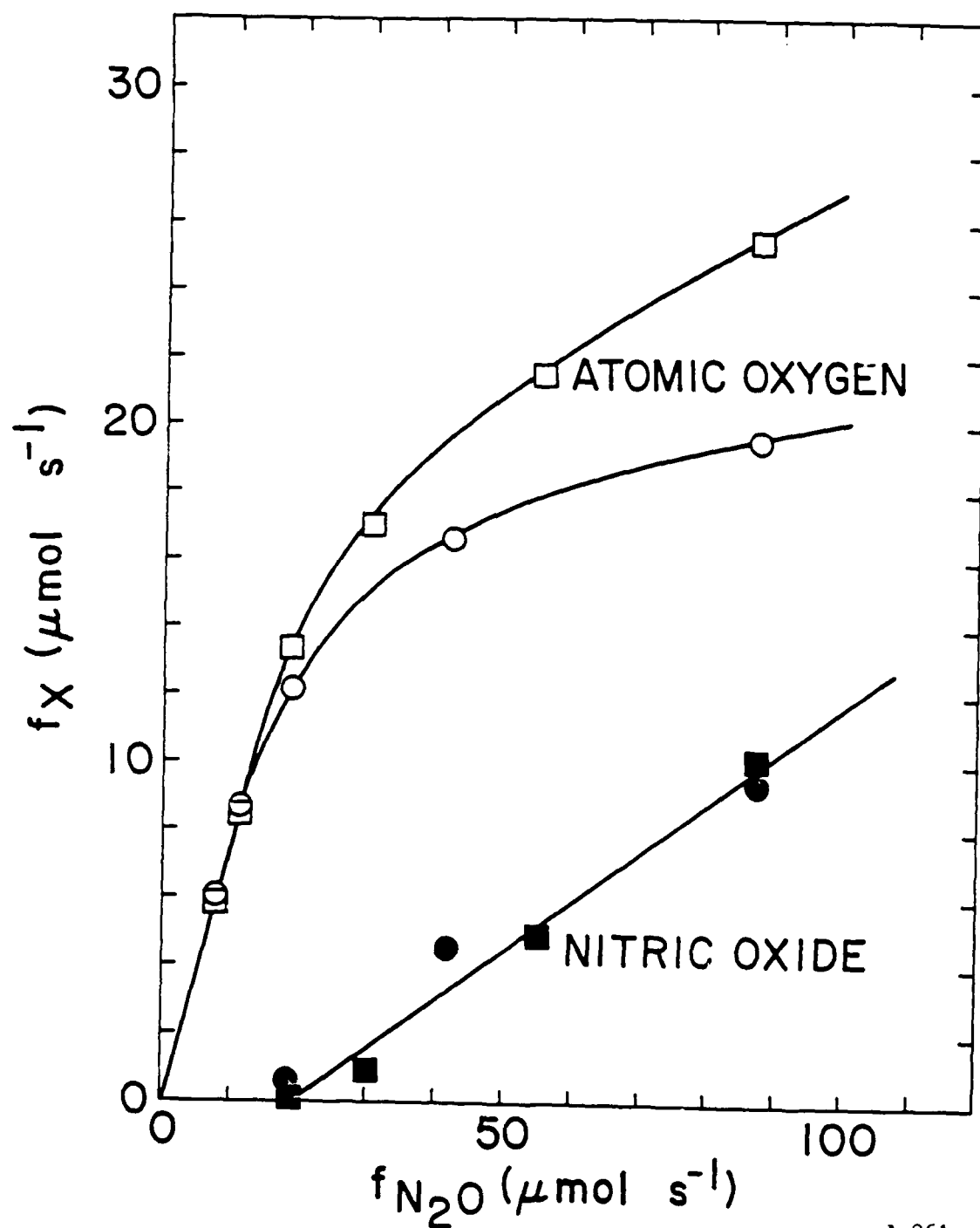
A-961

Piper/Rawlins
PSI SR-152A
Figure S10
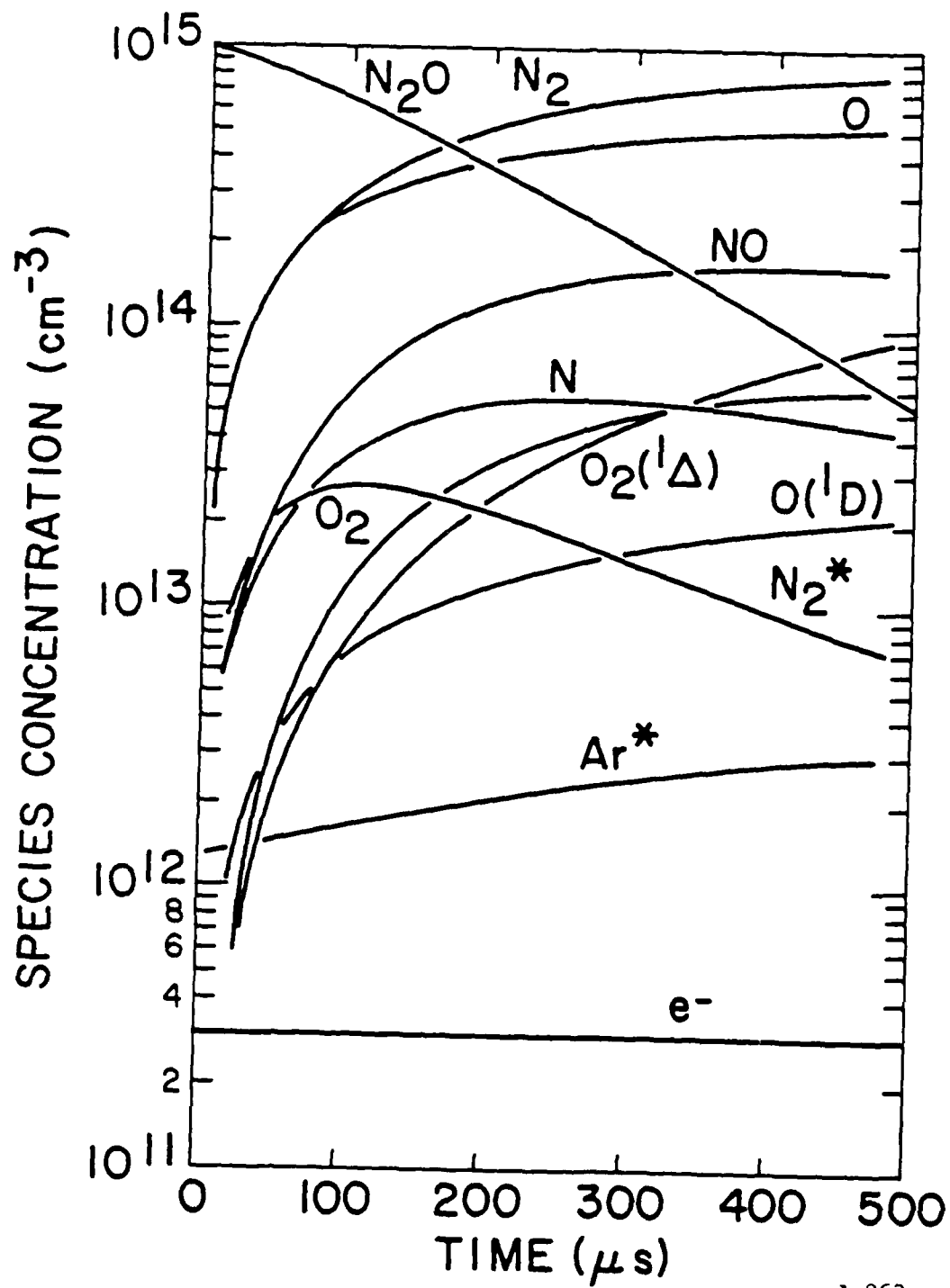
A-962

Piper/Rawlins
PSI SR-152A
Figure S11
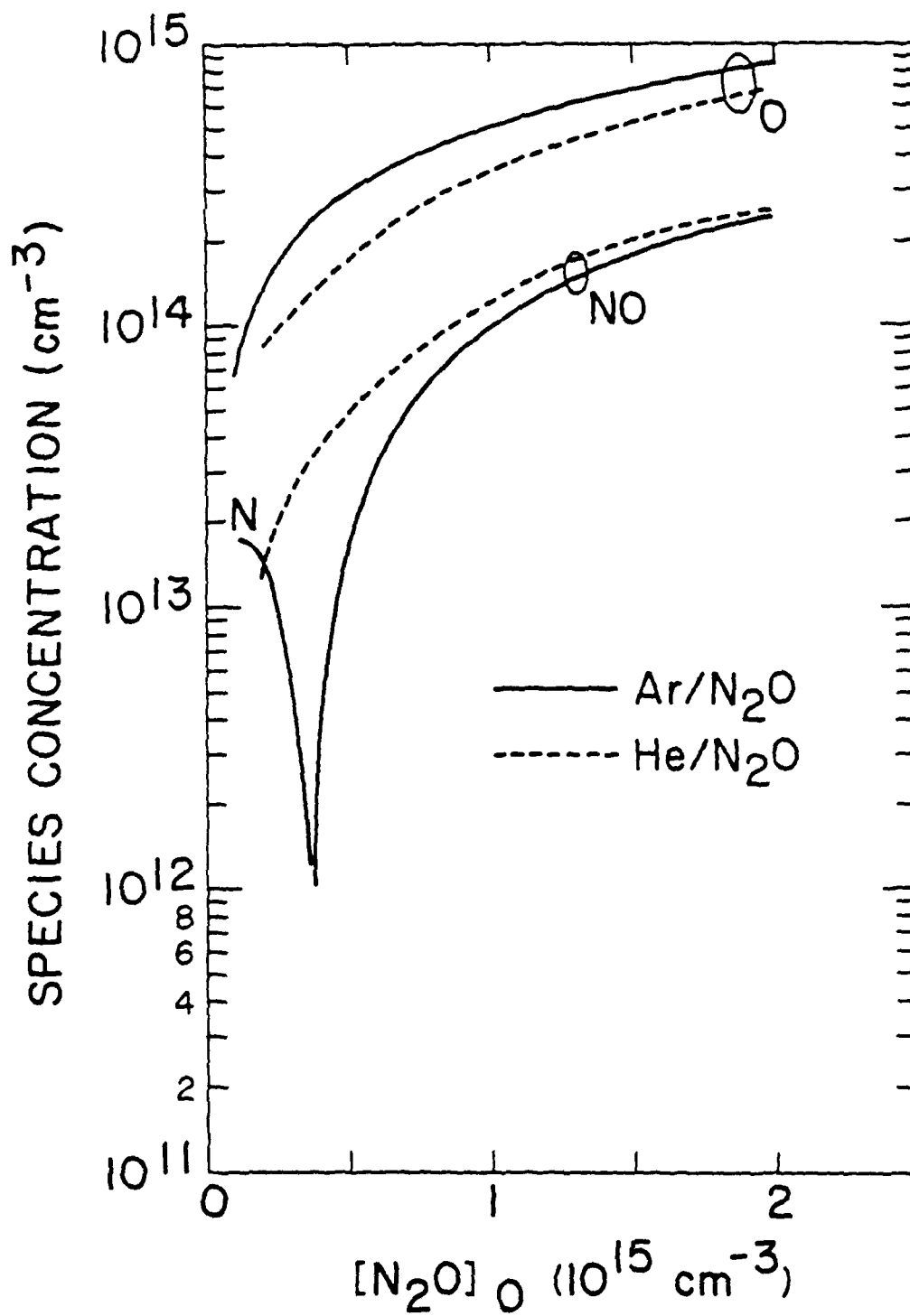
A-963

Piper/Rawlins
PSI SR-152A
Figure S12
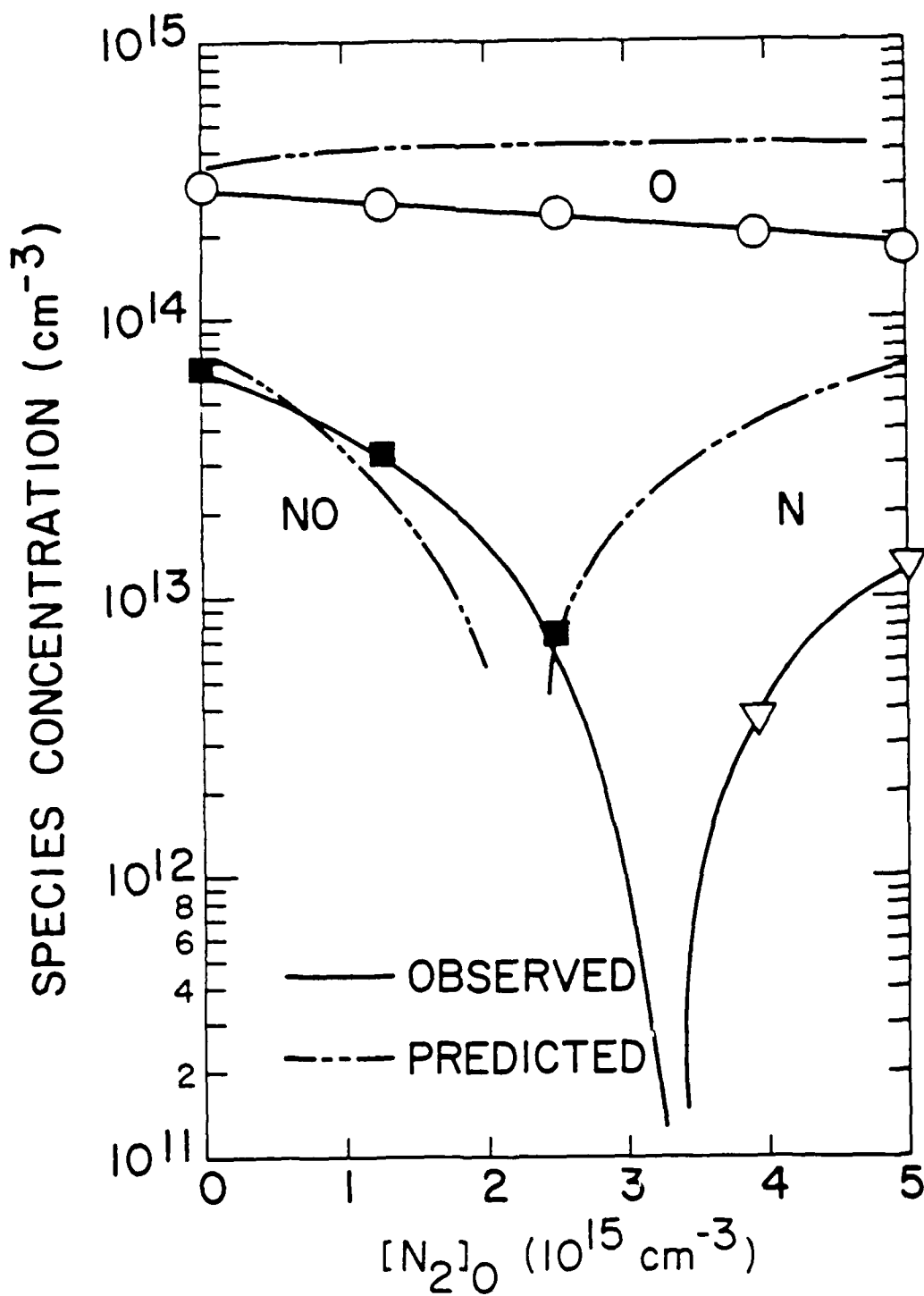
A-964

Piper/Rawlins
PSI SR-152A
Figure S13

APPENDIX D

INFRARED SPECTRA (2-16 μm) OF ArI RYDBERG EMISSION
FROM A MICROWAVE DISCHARGE PLASMA

This appendix is SR-160.

D

Infrared Spectra (2-16 μm) OF ArI Rydberg Emission
from a Microwave Discharge Plasma

W. T. Rawlins and A. Gelb

Physical Sciences Inc.
Research Park, P. O. Box 3100
Andover, MA   01810

R. A. Armstrong

Infrared Technology Division
Air Force Geophysics Laboratory
Hanscom AFB, MA   01731

ABSTRACT

Infrared (2 to 16 μm) emission from Ar Rydberg atoms, excited in a conventional low-pressure microwave discharge plasma, has been observed in the cryogenic COCHISE reactor/spectrometer facility. The observed spectrum is very complex but is identifiable using the detailed energy level structure and optical selection rules for ArI. Detailed transition probabilities for dipole-allowed transitions between 2 and 16 μm were computed using the Coulomb approximation. Comparisons of observed and predicted spectra show that substantial long wavelength infrared (LWIR) emission (~ 12 μm) arises from Rydberg states near the ionization limit; these states must have kinetically enhanced populations in order to account for the observed emission intensities. The results are interpreted in terms of a radiative/collisional cascade sequence initiated by dissociative recombination of Ar_2^+ with energetic electrons in the active discharge.

I. INTRODUCTION

Studies of the radiative and collisional properties of atomic Rydberg states have generated a rich literature for over 100 years.[1] A great many of the more recent experimental investigations have employed optical excitation methods to form highly excited states, and the bulk of the work in this area deals with alkali metals. Relatively little attention has been given to Rydberg state spectroscopy for more complex atoms such as O, N, and Ar, which are significant constitutents of the upper atmosphere. Furthermore, in high-altitude electron bombardments, as in low-pressure laboratory electric discharges, Rydberg species can be formed by kinetic processes which may give rise to non-Boltzmann population distributions among the upper energy levels. Thus it is informative to study the excitation of atmospheric species under laboratory conditions representative of the high altitude environment. We report here the first direct observations of long-wavelength infrared (LWIR) fluorescence from Rydberg states of argon excited in a low-pressure microwave discharge, as studied in the COCHISE cryogenic infrared fluorescence facility.

The principal objectives of this investigation are to characterize the Ar spectrum from 2 to 16 μm at the highest possible spectral resolution, and to identify as fully as possible the sources of the emission and the kinetic mechanism of the excitation. Our greatest interest lies in the spectral region beyond 8 μm, where the data are unique and exhibit an unusual spectral distribution peaking near 12 μm. To accomplish these goals, we (1) obtained considerable spectral data over a range of spectral resolution and discharge operating conditions; (2) compared the observed emissions to transitions predicted from optical selection rules; and (3) compared the data to simulated

•

dipole-allowed spectra computed using transition probabilities estimated from the Coulomb approximation.

For Rydberg atoms in which a single electron is excited to an orbital of large principal quantum number, i.e., near the point of ionization, the excited electron moves in a near-Coulombic field of essentially unit charge. Thus, the transition frequencies in Rydberg spectra are often represented in terms of a simple hydrogenic approximation. In COCHISE, we observe infrared transitions from states with principal quantum numbers $4 < n < 12$ (20,000 to 1,000 cm^{-1} below the ionization limit); for these transitions, we find that the hydrogenic approximation does not apply, even if quantum defects are considered. Furthermore, for the lower energy levels, whose transitions predominate at shorter wavelengths ($\lambda < 5$ μm), we observe that certain optical selection rules break down, and that the Coulomb approximation is clearly inappropriate for predicting spectral intensities. Finally, the spectral distribution at long wavelengths suggests excitation of the emitting species via a cascade mechanism initiated by ionic recombination.

II. EXPERIMENTAL OBSERVATIONS

The design and operation of the COCHISE facility have been described in detail elsewhere.[2-4] In brief, the entire radiative environment of the experiment is maintained at a base temperature of ~ 20 K, which effectively eliminates background radiation within the 2-20 μm operating range of the apparatus. The detection system consists of a scanning grating monochromator and a liquid-helium-cooled Si:As detector. Reagent gases are introduced through temperature-controlled feed lines to the reaction cell shown in Fig. 1. Flowing Ar at ~ 1 torr passes through four parallel conventional microwave discharges (2450 MHz, 50 W, 1.1 cm i.d.) prior to expanding into a low-pressure (~ 3 mt), cryogenically pumped interaction volume. A counterflow gas enters the volume from the opposite side to combine with the discharged gas in a stagnation region near the axis of the cylindrical field of view of the detector. In some cases (e.g., Ref. 2), this interaction consists of a chemical reaction under nearly single-collision conditions. In other experiments, all the emission observed arises in the field-of-view from long-lived species formed in the discharge sidearms.[5,6] The Ar spectral studies reported here were carried out for pure Ar (Matheson, UHP) at discharge pressures of 0.1-2 torr and temperatures of 80-150 K. The approximate discharge residence times ranged from 5 ms at 0.1 torr to 0.8 ms at 2 torr. Measurements were made with spectral resolutions in the range 0.013 -0.080 μm. For all conditions, a large number of sharp spectral features, apparently atomic lines and multiplets, were observed between 2 and 16 μm. The observed intensities of these features are comparable to those observed for molecular chemiluminescence from the field-of-view when other reagents are present.

The Ar-related intensities and spectral distributions are completely insensitive to the flow rate or identity of the counterflow gas. This estab-

lishes that the emission arises not from the field of view but from the dis-
charge tubes themselves, and reaches the field of view by multiple reflections
within the reaction chamber. This is consistent with our expectation that the
emitting species can be excited only in the active discharge and that their in-
frared radiative lifetimes ($\sim$ 1-10 μs for atoms) would be much shorter than the
$\sim$ 0.5 ms transit time from the end of the discharge tubes to the detector's
field of view. By comparison with other experiments containing molecular
fluorescence signals, we expect the reduction in the initial line intensities
due to the multiple reflections is at least three orders of magnitude (i.e., of
order 10 reflections). This means that we can observe only the most intense
features of the many that must arise from such discharges, i.e., primarily
those of neutral Ar. The data are corrected for the relative responsivity of
the optical train and detection system, but not for that of the scattering sur-
face. We present the observed intensities in arbitrary units proportional to
W/cm^{-2} sr^{-1} μm^{-1} (as determined by blackbody calibrations) to give a measure of
the __apparent__ relative intensity on a consistent scale.

Spectra of the observed Ar-related emission are shown in Figs. 2-4. In
general, there are many intense features from 2 to 5 μm, a striking "window"
between 5 and 10 μm, and several moderately strong features from 10 to 15 μm.
Although the general appearance of this spectrum is insensitive to pressure and
temperature, the total spectral intensity increases by a factor of $\sim$ 4 as the
pressure is reduced from 2 to 0.1 torr. This effect is difficult to interpret
in terms of quenching because changing Ar pressure in the discharge sidearms
simultaneously alters the flow velocity (i.e., the residence time) and the E/N
in the discharge plasma, as well as other characteristics of the discharge. In
general, as N_2 or O_2 are added to the discharge, the intensities of Ar-related

emissions decrease. The decrease in signal upon reagent addition may be due to quenching of the emission or to slight reduction in the high-energy electron-impact rates due to the presence of diatomic molecules. Most of the detailed spectral studies were carried out at 0.1 torr, where the S/N ratios were the most favorable. All the features exhibit spectral characteristics typical of atomic lines or multiplets; in addition, many of the line groupings cannot be separated even at the highest resolution ($\Delta\lambda$ = 0.013 μm) possible for these measurements.

The possible sources of this emission are Rydberg states of Ar or Ar^+ excited in the discharge. However, the levels of excitation in such discharges are rather low ([e^-] ~ 10^{11} cm^{-3}, average electron energy ~ 8 eV),[9] so the total Ar^+ number density is several orders of magnitude smaller than that of the neutral atom. Thus, the observed transitions appear to arise from high Rydberg-like energy levels of neutral argon. However, since the spectroscopic literature does not extend beyond ~ 4 μm, considerable analysis is required to make the spectral assignments. The observed spectra are clearly complex and bear no resemblance to what one might predict from a simple quantum defect approach. Indeed, Ar exhibits strong spin-orbit coupling as well as coupling of orbital angular momentum between the outer electron and the core, so hydrogenic approximations are expected to be inadequate. Thus, in order to interpret the spectral data, it was necessary to predict all possible transitions according to the energy levels and optical selection rules for Ar. In addition, transition probabilities had to be estimated in order to compare the experimental spectra to simulated spectra convolved with the instrumental resolution function.

III. INFRARED SPECTROSCOPY OF ARI

A. Argon Rydberg States

The excited states of Ar, $1s^2 2s^2 2p^6 3s^2 3p^5 \, n\ell$, are described using the intermediate or j-ℓ coupling scheme. Specific states are denoted as $n\ell[K]_J$ or $n\ell'[K]_J$ where $K = \ell + j_c$ and $J = K + S$. K is the resultant angular momentum formed by coupling the core electron angular momentum j_c to the outer electron orbital angular momentum ℓ. Primed states denote $j_c = 1/2$ and unprimed states denote $j_c = 3/2$. J is the total atomic momentum formed by coupling the outer electron spin angular momentum, S, to K. A superscript zero is used to denote states of even orbital angular momentum ($\ell = s, d, g$). The primed and unprimed manifolds rapidly divide with increasing n into two distinct groups of levels. The $j_c = 1/2$ manifold approaches in its ionization limit the $^2P_{1/2}$ state of the argon ion; $j_c = 3/2$ approaches the $^2P_{3/2}$ ion. The respective ionization limits of the $j_c = 3/2$ and $j_c = 1/2$ manifolds are 127109.9 cm^{-1} and 128541.3 cm^{-1}. Energy level tables have been compiled by Moore[8] and more recently by Bashkin and Stoner.[9]

B. Calculation of Radiative Transition Probabilities

We shall summarize the calculation of radiative transition probabilities within the framework of a one-electron dipole approximation. The selection rules that result for the transition between states $n_1 \ell_1 [K_1]_{J_1}$ and $n_2 \ell_2 [K_2]_{J_2}$ are:

$$
\begin{aligned}
\ell_1 - \ell_2 &= \pm 1 \\
K_1 - K_2 &= 0 \ (K_1 \neq 0), \ \pm 1 \\
J_1 - J_2 &= 0 \ (J_1 \neq 0), \ \pm 1 \\
j_{c_1} - j_{c_2} &= 0 \ .
\end{aligned}
\tag{1}
$$

The computed line strength is given by

$$\mathcal{S} = \frac{1}{3}(2J_1 + 1)(2J_2 + 1)(2K_1 + 1)(2K_2 + 1)$$

$$\cdot \begin{Bmatrix} J_1 & J_2 & 1 \\ K_2 & K_1 & 1/2 \end{Bmatrix}^2 \begin{Bmatrix} \ell_2 & K_2 & j_c \\ K_1 & \ell_1 & 1 \end{Bmatrix}^2 |\langle \ell_1 \| T \| \ell_2 \rangle|^2 , \qquad (2)$$

where the bracketed quantities are 6-j symbols and $\langle \ell_1 \| T \| \ell_2 \rangle$ is the reduced matrix element of the dipole operator. The matrix element is expressed as the following:

$$|\langle \ell_1 \| T \| \ell_2 \rangle|^2 = \frac{3}{4\pi}(2\ell_1 + 1)(2\ell_2 + 1)C(\ell_1,1,\ell_2;000)^2$$

$$\times \left| \int_0^\infty f_{\ell_1}(r) f_{\ell_2}(r) r \, dr \right|^2 , \qquad (3)$$

where $C(\ell_1,1,\ell_2;000)$ is the Clebsch-Gordan coefficient and $f_{\ell_1}(r)$ and $f_{\ell_2}(r)$ are radial wave functions for the outer electron. We will use the Coulomb approximation for the evaluation of the radial integral.

In the Coulomb approximation the radial wave functions are approximated by hydrogenic wave functions, i.e.,

$$I \equiv \int_0^\infty f_{\ell_1}(r) f_{\ell_2}(r) r \, dr \approx \int_0^\infty \phi_{\ell_1}^{coul}(r) \, \phi_{\ell_2}^{coul}(r) r \, dr \qquad (4)$$

where ϕ_ℓ^{coul} is a hydrogenic wave function. Several methods of evaluation of I are available. Bates and Damgaard[10-12] presented an analytic expression for I:

$$I = \frac{2^{n_1+n_2}}{(n_1)^{n_1+1}(n_2)^{n_2+1}} \left[\Gamma(n_1+\ell_1+1)\Gamma(n_1-\ell_1)\Gamma(n_2+\ell_2+1)\Gamma(n_2-\ell_2) \right]^{-1/2}$$

$$\times \sum_{k_1=0} \sum_{k_2=0} a_{k_1} a_{k_2} \left[\frac{n_1 n_2}{(n_1+n_2)} \right]^{n_1+n_2+2-k_1-k_2} \Gamma(n_1+n_2+2-k_1-k_2). \qquad (5)$$

The principal quantum numbers n_1 and n_2 are non-integers and are evaluated for each state from the relation

$$n = \left(\frac{109737}{E_\infty - E}\right)^{1/2} \qquad (6)$$

where E_∞ is the ionization limit (cm^{-1}) of the state manifold and E is the term value (cm^{-1}) of the state. The coefficients a_{k_1} and a_{k_2} are evaluated from the recurrence relation

$$a_k = \frac{n a_{k-1}}{2k}\left[\ell(\ell+1) - (n-k)(n-k+1)\right] , \qquad (7)$$

with $a_0 = 1$ for each set of coefficients. The summation is truncated by the condition $k_1 + k_2 < n_1 + n_2 - 1$. This procedure is computationally very rapid and works well for $n_1 + n_2 < 18$ using double precision arithmetic.

For higher effective principal quantum numbers, cancellation between large numbers in the summation causes computational difficulties. In this instance we use the method of Friedrich et al.,[13] which employs a semi-numerical procedure in which I is approximated as:

$$I = \int \phi_{\ell_1}^{coul}(r)\phi_{\ell_2}^{coul}(r) r \, dr \approx \Delta r \sum_{\nu=0}^{\nu_{max}} \phi_{\ell_1}^{coul}(r_\nu)\phi_{\ell_2}^{coul}(r_\nu) . \qquad (8)$$

The hydrogenic wave functions are approximated as

$$\phi_\ell^{coul}(r) = \frac{1}{[n^2 \Gamma(n+\ell+1)\Gamma(n-\ell)]^{1/2}} \left(\frac{2r}{n}\right)^n e^{-r/\nu} \sum_{t=0}^{t_{max}} a_t r^{-t} \qquad (9)$$

with t_{max} determined by the inequality

$$t_{max} < n + 1 < t_{max} + 1$$

and with the a_t defined as in the Bates-Damgaard method. The step size Δr is generally taken to be 0.125. Larger values, $\Delta r = 0.30$, give identical results

for the cases studied. The starting point r_o is taken to be 0.25. The value of ν_{max} is determined by the relation

$$\frac{|\phi_\ell^{coul}(r_{\nu_{max}})|}{max|\phi_\ell^{coul}(r)|} < e^{-13} \tag{10}$$

for the wavefunction with the smaller principal quantum number.

We have found that these two methods give virtually identical results in cases when comparison is possible. The Bates-Damgaard method is more computationally efficient and therefore is used when applicable.

The Einstein coefficient, A, of the emitting species is inversely proportional to its radiative lifetime. These coefficients are related to the wavelength-independent atomic linestrengths, $\mathcal{S}$, by the relationship:

$$gA = \frac{2.026 \times 10^{-6}}{\lambda^3} \times \mathcal{S}, \tag{11}$$

where λ is the transition wavelength given in centimeters and g is the degeneracy of the radiating state. We have computed gA factors for radiating states from n=4 to n=22 for transitions between 2 and 16 μm. Additionally, simulations of radiation from hot argon gas have been computed. The results of these calculations are presented in the next section.

IV. RESULTS OF SPECTRAL ANALYSIS

In Table I we list tentatively identified Rydberg transitions. For most observed spectral features more than one transition is given. This is a consequence of the large density of spectral lines for excited argon and limited spectral resolution to discriminate between the various transitions. The possible transitions are determined using a weaker set of selection rules than those discussed above for spectral computations. For the weaker selection rules the restriction of core angular momentum invariance is dropped and hence transitions between the $^2P_{1/2}$ and $^2P_{3/2}$ manifolds are allowed. Experimentally these transitions are found to be important at shorter wavelengths. Indeed, Humphreys[14] notes many core-changing transitions, several quite intense, in his compilation of observed argon lines between 1.2 and 4.0 µm. Table I includes the observed peak wavelength, identified possible transitions and the predicted wavelength based on the state energies listed in C. Moore's[8] and Bashkin and Stoner's[9] tables. An "H" after the listing indicates that the transition is listed in Humphreys' compilation.[14] Table I includes the entire range of the present spectral measurements, from approximately 2.0 to 16.0 µm.

Some general conclusions about the types of identified transitions may be made. First, there is a general tendency to see radiation from higher energy states, i.e., higher principal quantum numbers, at longer wavelengths. This is as expected since the energy gaps are too large for states with low quantum numbers to radiate in the LWIR. However, with the exception of the peaks observed around 12.2-12.4 µm (and to some extent around 2.4 µm) it is rarely necessary to invoke states of quantum numbers greater than eight. Two possible explanations are that excited state argon formation does not produce such

TABLE I

TENTATIVELY IDENTIFIED SPECTRAL TRANSITIONS
FOR ARGON BETWEEN 1.95 AND 16.0 μm

Observed Peak Wavelength (μm)	Upper Level Energy (cm^{-1})	Transition	Lower Level Energy (cm-1)	Predicted Wavelength (μm)	gA (s^{-1})	
1.960	123505.536	$5d'[5/2]_2^0 \rightarrow 5p'[3/2]_1$	118407.494	1.9616	2.04×10^5	
	122282.134	$5d[5/2]_2^0 \rightarrow 5p[3/2]_2$	117183.654	1.9614	1.95×10^1	
1.995	117151.387	$5p[3/2]_1 \rightarrow 3d[3/2]_2^0$	112138.980	1.9950	1.44×10^5	H
2.050	125066.501	$6d'[3/2]_2^0 \rightarrow 4f[3/2]_2$	120188.660	2.0501		
	125066.501	$6d'[3/2]_2^0 \rightarrow 4f[3/2]_1$	120188.340	2.0500		
	125482.700	$6f'[7/2]_3 \rightarrow 4d'[3/2]_2^0$	120600.944	2.0484	4.52×10^6	
	125483.160	$6f'[5/2]_3 \rightarrow 4d'[3/2]_2^0$	120600.944	2.0483	4.38×10^6	
	125483.340	$6f'[5/2]_2 \rightarrow 4d'[3/2]_2^0$	120600.944	2.0482	3.13×10^5	
2.100	111818.090	$3d[1/2]_1^0 \rightarrow 4d[1/2]_0$	107054.319	2.0992	1.59×10^6	H
	118407.494	$5p'[3/2]_1 \rightarrow 5s[3/2]_1^0$	113643.260	2.0989		H
2.212	111818.090	$3d[1/2]_1^0 \rightarrow 4p'[3/2]_2$	107131.755	2.2083		H
	116660.054	$5p[1/2]_1 \rightarrow 3d[3/2]_2^0$	112138.980	2.2119	1.12×10^6	H
2.280	124609.917	$7d[7/2]_4^0 \rightarrow 4f[5/2]_3$	120229.810	2.2830	1.62×10^3	
2.290	121932.908	$5d[1/2]_1^0 \rightarrow 5p[1/2]_0$	117563.020	2.2883	3.86×10^5	
	124051.440	$6f[5/2]_2 \rightarrow 4s[3/2]_2^0$	119683.113	2.2892		H
	124051.650	$6f[5/2]_3 \rightarrow 6s[3/2]_2^0$	119683.113	2.2891		H
	124554.939	$7d[1/2]_1^0 \rightarrow 4f[3/2]_1$	120198.660	2.2902	8.37×10^4	
	124554.939	$7d[1/2]_1^0 \rightarrow 4f[3/2]_2$	120188.340	2.2901	1.67×10^4	
	125637.930	$9d[3/2]_1^0 \rightarrow 6p[3/2]_2$	121270.683	2.2898	5.84×10^4	
2.406	117183.654	$5p[3/2]_2 \rightarrow 3d[7/2]_3^0$	113020.390	2.4021		
	121161.356	$6s'[1/2]_1^0 \rightarrow 5p'[5/2]_2$	116999.389	2.4027		
	125353.310	$8s'[1/2]_1^0 \rightarrow 6p[5/2]_2$	121191.920	2.4030		

TABLE I (Cont.)

TENTATIVELY IDENTIFIED SPECTRAL TRANSITIONS
FOR ARGON BETWEEN 1.95 AND 16.0 μm

Observed Peak Wavelength (μm)	Upper Level Energy (cm^{-1})	Transition	Lower Level Energy (cm-1)	Predicted Wavelength (μm)	gA (s^{-1})	
2.445	122601.290	$6p'[1/2]_1 \rightarrow 4d[1/2]_0^0$	118512.170	2.4455		
	125286.280	$6d'[3/2]_1^0 \rightarrow 6p[5/2]_2$	121191.920	2.4424		
2.462	125072.600	$9p[3/2]_1 \rightarrow 4d'[3/2]_1^0$	121011.979	2.4627		
	125074.900	$9p[3/2]_2 \rightarrow 4d'[3/2]_1^0$	121011.979	2.4613		
	125331.930	$10s[3/2]_1^0 \rightarrow 6p[3/2]_2$	121270.682	2.4623	6.69×10^3	
	125329.990	$10s[3/2]_2^0 \rightarrow 6p[3/2]_2$	121270.682	2.4635	5.90×10^4	
2.544	126257.400	$13p[3/2]_2 \rightarrow 5d[5/2]_3^0$	122329.720	2.5460	2.61×10^4	
	117563.020	$5p[1/2]_0 \rightarrow 5s[3/2]_1^0$	113643.260	2.5505	1.25×10^6	H
2.582	122282.134	$5d[5/2]_2^0 \rightarrow 5p'[3/2]_1$	118407.494	2.5809		
	125066.501	$6d'[3/2]_2^0 \rightarrow 6p[5/2]_2$	121191.920	2.5809		
	125150.000	$6d'[5/2]_3^0 \rightarrow 6p[3/2]_2$	121270.682	2.5778		
	125135.898	$8d[1/2]_1^0 \rightarrow 6p[3/2]_1$	121257.227	2.5782	8.75×10^3	
	125353.310	$8s'[1/2]_1^0 \rightarrow 6p[1/2]_0$	121470.304	2.5753		
	127131.000	$9d'[3/2]_2^0 \rightarrow 7p[3/2]_1$	123254.990	2.5800		
	127131.000	$9d'[3/2]_1^0 \rightarrow 7p[3/2]_1$	123254.990	2.5800		
	118870.981	$5p'[1/2]_0 \rightarrow 5s'[1/2]_1^0$	114975.070	2.5667	1.23×10^6	
2.634	125066.501	$6d'[3/2]_2^0 \rightarrow 6p[3/2]_2$	121270.682	2.6345		
	120753.520	$4d'[5/2]_3^0 \rightarrow 4p[5/2]_3$	116942.815	2.6235		H
2.672	118407.494	$5p'[3/2]_1 \rightarrow 3d'[5/2]_2^0$	114461.040	2.6550	2.23×10^6	H
	117183.654	$5p[3/2]_2 \rightarrow 3d[5/2]_2^0$	113426.050	2.6613	1.75×10^5	H
2.690	117183.654	$5p[3/2]_2 \rightarrow 5s[3/2]_2^0$	113468.550	2.6917	4.99×10^6	H

TABLE I (Cont.)

TENTATIVELY IDENTIFIED SPECTRAL TRANSITIONS
FOR ARGON BETWEEN 1.95 AND 16.0 μm

Observed Peak Wavelength (μm)	Upper Level Energy (cm^{-1})	Transition	Lower Level Energy (cm-1)	Predicted Wavelength (μm)	gA (s^{-1})	
2.715	117151.387	$5p[3/2]_1 \rightarrow 5s[3/2]_2^0$	113468.550	2.7152	5.44×10^5	H
	122707.940	$5f[5/2]_3 \rightarrow 4d[7/2]_4^0$	119023.669	2.7142	4.66×10^4	
2.721	120619.076	$4d'[5/2]_2^0 \rightarrow 5p[5/2]_3$	116942.815	2.7202		
	122695.700	$5f[9/2]_{4,5} \rightarrow 4d[7/2]_4^0$	119023.669	2.7233	8.40×10^6	
2.740	118469.117	$5p'[3/2]_2 \rightarrow 3d'[5/2]_3^0$	114821.990	2.7419	3.38×10^6	
	118459.662	$5p'[1/2]_0 \rightarrow 3d'[3/2]_2^0$	114805.180	2.7364	2.02×10^6	H
2.750	123826.850	$6d[5/2]_2^0 \rightarrow 4f[3/2]_2$	120188.660	2.7486	2.38×10^2	
	123826.850	$6d[5/2]_2^0 \rightarrow 4f[3/2]_1$	120188.340	2.7483	2.14×10^3	
	124651.050	$7p'[1/2]_1 \rightarrow 4d'[3/2]_1^0$	121011.979	2.7480	6.05×10^4	
	123205.830	$7p[5/2]_3 \rightarrow 4d[5/2]_3^0$	119566.110	2.7475	1.42×10^5	
2.769	122479.459	$7s[3/2]_1^0 \rightarrow 5p'[1/2]_0$	118870.981	2.7712		
2.870	122695.700	$5f[9/2]_4 \rightarrow 4d[7/2]_3^0$	119212.930	2.8713	8.15×10^6	H
	118459.662	$5p'[1/2]_1 \rightarrow 5s'[1/2]_1^0$	114975.070	2.8698	1.92×10^6	H
	124643.540	$7p'[3/2]_1 \rightarrow 6s'[1/2]_1^0$	121161.356	2.8718	2.49×10^4	
	124649.549	$7d[7/2]_3^0 \rightarrow 6p[5/2]_3$	121165.431	2.8702	2.53×10^3	
	124554.939	$7d[1/2]_1^0 \rightarrow 6p[1/2]_1$	121068.804	2.8685	7.71×10^4	
3.022	123557.459	$5d'[5/2]_3^0 \rightarrow 4f[7/2]_4$	120250.150	3.0236		
	123557.459	$5d'[7/2]_3^0 \rightarrow 4f[7/2]_3$	120250.150	3.0236		
	125748.900	$9f[7/2]_{3,2} \rightarrow 7s[3/2]_2^0$	122440.109	3.0223		
3.194	122695.700	$5f[9/2]_4 \rightarrow 4d[5/2]_3^0$	199566.110	3.1953		H
3.200	124137.450	$5f'[7/2]_2 \rightarrow 4d'[3/2]_1^0$	121011.979	3.1995	5.01×10^6	H

TABLE 1 (Cont.)

TENTATIVELY IDENTIFIED SPECTRAL TRANSITIONS
FOR ARGON BETWEEN 1.95 AND 16.0 μm

Observed Peak Wavelength (μm)	Upper Level Energy (cm⁻¹)	Transition		Lower Level Energy (cm-1)	Predicted Wavelength (μm)	gA (s⁻¹)	
3.205	122686.400	$5f[3/2]_2$	$\rightarrow 4d[5/2]^0_3$	119566.110	3.2048	1.16×10^5	H
3.217	125391.040	$8f[5/2]_3$	$\rightarrow 5d[5/2]^0_2$	122282.134	3.2166	1.07×10^4	
3.505	116999.389	$5p[5/2]_2$	$\rightarrow 3d[3/2]^0_1$	114147.750	3.5068	5.37×10^4	H
3.531	124865.040	$7f[5/2]_3$	$\rightarrow 5d[7/2]^0_4$	122036.134	3.5349	5.89×10^3	
	124868.770	$7f[7/2]_{3,4}$	$\rightarrow 5d[7/2]^0_4$	122036.134	3.5302	1.08×10^5	
	123903.795	$8s[3/2]^0_2$	$\rightarrow 6p[1/2]_1$	121068.804	3.5280	1.28×10^5	
3.593	119444.880	$4d[5/2]^0_2$	$\rightarrow 5p[1/2]_1$	116660.054	3.5909		
3.697	124865.040	$7f[5/2]_3$	$\rightarrow 5d[7/2]^0_3$	122160.220	3.6971	3.18×10^2	
	124865.190	$7f[5/2]_2$	$\rightarrow 5d[7/2]^0_3$	122160.220	3.6969	6.35×10^3	
	124868.770	$7f[7/2]_{3,4}$	$\rightarrow 5d[7/2]^0_3$	122160.220	3.6920	1.29×10^5	
3.913	121011.979	$4d'[3/2]^0_1$	$\rightarrow 5p'[1/2]_1$	118459.662	3.9180	1.06×10^6	H
3.925	117183.654	$5p[3/2]_2$	$\rightarrow 3d'[5/2]^0_2$	114641.040	3.9330		
	123815.530	$5d'[3/2]^0_1$	$\rightarrow 6p[3/2]_2$	121270.682	3.9296		
	121191.920	$6p[5/2]_2$	$\rightarrow 4d[1/2]^0_1$	118651.447	3.9363		
	125059.800	$9p[1/2]_2$	$\rightarrow 5d[3/2]_1$	122514.290	3.928	1.87×10^3	
3.961	124857.420	$7f[3/2]_2$	$\rightarrow 5d[5/2]_3$	122329.720	3.956	1.86×10^4	
	125219.880	$8d[7/2]_4$	$\rightarrow 5f[9/2]_{4,5}$	122695.700	3.962	2.14×10^5	
	125135.898	$8d[7/2]_1$	$\rightarrow 6p'[3/2]_1$	122609.760	3.959		
	125039.600	$9p[1/2]_1$	$\rightarrow 5d[3/2]_1$	122514.290	3.960	3.93×10^3	
4.005	125286.280	$6d'[3/2]^0_1$	$\rightarrow 6p'[1/2]_0$	122790.612	4.0069	7.67×10^3	
	119683.113	$6s[3/2]^0_2$	$\rightarrow 5p[3/2]_2$	117183.654	4.0009	1.50×10^6	H
	124658.520	$7p'[3/2]_2$	$\rightarrow 5d[7/2]^0_3$	122160.220	4.0027		

TABLE 1 (Cont.)

TENTATIVELY IDENTIFIED SPECTRAL TRANSITIONS
FOR ARGON BETWEEN 1.95 AND 16.0 μm

Observed Peak Wavelength (μm)	Upper Level Energy (cm^{-1})	Transition	Lower Level Energy (cm-1)	Predicted Wavelength (μm)	gA (s^{-1})
4.116	125066.501	6d$'$[3/2]$_2^0$ → 6p[3/2]$_2$	122635.128	4.1129	
4.278	123808.600	6d[3/2]$_1^0$ → 6p[1/2]$_0$	121470.304	4.2766	3.89×10^3
4.297	122514.290	5d[3/2]$_1^0$ → 4f[3/2]$_2$	120188.660	4.2999	6.96×10^3
	122514.290	5d[3/2]$_1^0$ → 4f[3/2]$_1$	120188.340	4.2993	3.48×10^4
4.370	123385.130	7p[1/2]$_0$ → 6s$'$[1/2]$_0^0$	121096.670	4.3698	
	123557.459	5d$'$[5/2]$_3^0$ → 6p[3/2]$_1$	121270.682	4.3730	
	121161.356	6s$'$[1/2]$_1$ → 5p$'$[1/2]$_0$	118870.981	4.3661	2.95×10^5
	124376.380	8p[1/2]$_1$ → 5d[3/2]$_2^0$	122086.974	4.3680	1.37×10^4
	125791.940	8p$'$[3/2]$_2$ → 5d$'$[5/2]$_2^0$	123505.536	4.374	2.58×10^4
4.378	120753.520	4d$'$[5/2]$_3^0$ → 5p[3/2]$_2$	118469.117	4.3775	
	119847.810	4d[3/2]$_1^0$ → 5p[1/2]$_0$	117563.020	4.3768	8.57×10^5
	122514.290	5d[3/2]$_1^0$ → 4f[5/2]$_2$	120230.070	4.3779	1.80×10^6
	121191.920	6p[5/2]$_2$ → 4d[5/2]$_2^0$	118906.665	4.3759	4.50×10^3
4.440	118906.665	4d[3/2]$_2^0$ → 5p[1/2]$_1$	116660.054	4.4511	1.78×10^6
	123508.960	6d[1/2]$_0^0$ → 6p[3/2]$_1$	121257.227	4.4410	2.14×10^4
4.536	124137.450	5f$'$[5/2]$_1$ → 5d[1/2]$_1^0$	121932.908	4.5361	
4.720	116942.815	5p[5/2]$_3$ → 3d$'$[5/2]$_3^0$	114821.990	4.7151	
	122717.900	5f[7/2]$_3$ → 4d$'$[3/2]$_2^0$	120600.944	4.7238	
	124051.650	6f[5/2]$_2$ → 5d[1/2]$_1^0$	121932.908	4.7198	
	123773.920	6d[7/2]$_3^0$ → 4f$'$[5/2]$_2$	121654.580	4.7185	
	123773.920	6d[7/2]$_3^0$ → 4f$'$[5/2]$_3$	121654.320	4.7179	
	123773.920	6d[7/2]$_3^0$ → 4f$'$[7/2]$_{3,4}$	121653.400	4.7158	
	125291.450	8d[5/2]$_2^0$ → 7p[1/2]$_1$	123172.090	4.7184	

TABLE I (Cont.)

TENTATIVELY IDENTIFIED SPECTRAL TRANSITIONS
FOR ARGON BETWEEN 1.95 AND 16.0 μm

Observed Peak Wavelength (μm)	Upper Level Energy (cm^{-1})	Transition		Lower Level Energy (cm-1)	Predicted Wavelength (μm)	gA (s^{-1})
6.617	121270.682	6p[3/2]$_2$	→ 6s[3/2]$_1^0$	119760.220	6.6205	1.18×10^5
	122609.760	6p'[3/2]$_1$	→ 6s[1/2]$_0^0$	121096.670	6.6090	
	126161.900	7d'[3/2]$_1^0$	→ 7p[1/2]$_1$	124651.050	6.6188	
10.050	120207.770	4f[9/2]$_4$	→ 4d[7/2]$_3^0$	119212.930	10.052	
	122160.220	5d[7/2]$_3^0$	→ 6p[5/2]$_3$	121165.431	10.052	7.46×10^4
10.330	122160.220	5d[7/2]$_3^0$	→ 6p[5/2]$_2$	121191.920	10.327	1.40×10^6
10.840	123557.459	5d'[5/2]$_3^0$	→ 6p'[3/2]$_2$	122635.128	10.842	1.39×10^6
11.115	121653.400	4f'[7/2]$_{3,4}$	→ 4d'[5/2]$_3^0$	120753.520	11.113	
	121654.320	4f'[5/2]$_3$	→ 4d'[5/2]$_3^0$	120753.520	11.0889	
11.480	123505.536	5d'[5/2]$_2^0$	→ 6p'[3/2]$_2$	122635.128	11.489	7.81×10^4
	122036.134	5d[7/2]$_4^0$	→ 6p[5/2]$_3$	121165.431	11.484	1.40×10^6
12.010	123468.034	6d[1/2]$_1^0$	→ 6p'[3/2]$_2$	122635.128	12.006	
12.130	125135.898	8d[1/2]$_1^0$	→ 8p[1/2]$_1$	124311.720	12.133	2.30×10^4
12.182	126458.800	13f[3/2.$_{,2}$	→ 9d[3/2]$_2^0$	125637.930	12.182	1.24×10^3
	126674.400	18s[3/2]$_{1,2}^0$	→ 11p[3/2]$_2$	125853.800	12.186	1.47×10^2
	126211.570	9s'[1/2]$_1^0$	→ 8f[5/2]$_2$	125391.170	12.189	
12.229	126204.100	11d[3/2]$_1^0$	→ 8f[3/2]$_{1,2}$	125386.410	12.230	1.07×10^3
12.255	122086.974	5d[3/2]$_2^0$	→ 6p[3/2]$_2$	121270.682	12.251	3.18×10^5
12.318	125680.520	9d[5/2]$_3^0$	→ 7f[7/2]$_{3,4}$	124868.770	12.319	9.38×10^4
12.352	126292.710	12d[1/2]$_1^0$	→ 6f'[5/2]$_3$	125483.340	12.355	
	126079.400	12p[5/2]$_{2,3}$	→ 8d[7/2]$_3^0$	125269.520	12.348	3.21×10^4

TABLE I (Cont.)

TENTATIVELY IDENTIFIED SPECTRAL TRANSITIONS
FOR ARGON BETWEEN 1.95 AND 16.0 μm

Observed Peak Wavelength (μm)	Upper Level Energy (cm⁻¹)	Transition	Lower Level Energy (cm-1)	Predicted Wavelength (μm)	gA (s⁻¹)
12.378	125523.200	$10p[5/2]_2 \rightarrow 7d[5/2]_3^0$	124715.160	12.376	1.07×10^3
12.385	126313.100	$12d[5/2]_2^0 \rightarrow 10p[1/2]_1$	125505.500	12.382	
	126458.800	$13f[5/2]_{2,3} \rightarrow 9d[7/2]_3^0$	125652.040	12.388	7.35×10^1
	126651.500	$16d[1/2]_{1,0}^0 \rightarrow 11p[1/2]_1$	125844.300	12.389	1.76×10^3
12.427	125519.900	$10p[5/2]_3 \rightarrow 7d[5/2]_3^0$	124715.160	12.426	2.07×10^4
13.060	124137.290	$5f'[5/2]_3 \rightarrow 5d'[3/2]_2^0$	123372.987	13.084	1.21×10^6
	124137.450	$5f'[5/2]_2 \rightarrow 5d'[3/2]_2^0$	123372.987	13.081	8.64×10^4
	123205.830	$7p[5/2]_3 \rightarrow 7s[3/2]_2^0$	122440.109	13.060	5.16×10^5
13.271	122686.200	$5f[3/2]_1 \rightarrow 5d[1/2]_1^0$	121932.908	13.275	1.24×10^5
	122686.400	$5f[3/2]_2 \rightarrow 5d[1/2]_1^0$	121932.908	13.272	6.18×10^5
13.500	121932.908	$5d[1/2]_1^0 \rightarrow 6p[5/2]_2$	121191.920	13.495	
	123254.990	$7p[3/2]_1 \rightarrow 5d[3/2]_1^0$	122514.290	13.500	1.00×10^6
13.665	123172.090	$7p[1/2]_1 \rightarrow 7s[3/2]_2^0$	122440.109	13.662	1.66×10^6
14.625	120250.150	$4f[7/2]_{3,4} \rightarrow 4d[5/2]_3^0$	119566.110	14.619	
	125334.750	$8s'[1/2]_0^0 \rightarrow 7p'[1/2]_1$	124651.050	14.626	4.42×10^4
15.570	125791.940	$8p'[3/2]_2 \rightarrow 6d'[5/2]_3^0$	125150.000	15.578	3.77×10^5
	123903.795	$8s[3/2]_2^0 \rightarrow 7p[3/2]_2^0$	123861.593	15.584	1.82×10^5

states or that such states, which have larger radiative lifetimes, are quenched by gas phase or wall collisions. Second, as mentioned above, core-changing transitions are quite important at shorter wavelengths. Several peaks seem to be directly attributable to such transitions: 2.100, 2.212, 2.445, 2.634 and 4.116 μm. The prominence of such transitions makes the use of the Coulomb approximation rather dubious since they are beyond the scope of that treatment. It seems that for longer wavelengths (8-16 μm) core changing transitions play a less significant role. It is therefore expected that the Coulomb approximation will be more reliable for longer wavelength radiation. (The 12.2-12.4 μm feature may be an exception - see below). This conclusion is also physically appealing since for higher quantum numbers the outer electrons should become more "hydrogen-like."

The gA factors for all selection-rule allowed transitions in the λ = 2 to 16 μm wavelength range have been computed for initial states of n = 4, 5, 6, 7, 8, 10, 12, 14, 16, 18, 20 and 22. The results of these calculations are presented in Table I for each identified transition. An example of the behavior of gA with λ is shown in Fig. 5 for n = 7 transitions. Plots similar to Fig. 5 are given for all values of n in a report available from the authors.[15]

Upon inspection of the contents of Table I, several general trends in the values of gA can be seen. Values of gA tend to decrease with increasing transition wavelength and/or increasing values of principal quantum number, n. The values of gA vary over more than four orders of magnitude. For values of n less than or equal to 6 there are many lines with submicrosecond values of $(gA)^{-1}$. However, for n > 10 the strongest lines are in the several microsecond lifetime regime and occur at the shorter wavelengths, 2-4 μm. In the

8-16 μm range, lifetimes are usually much longer. In that range, there are

very few submicrosecond values of $(gA)^{-1}$, which occur only for n < 7. For

n > 10 there are no allowed transitions with lifetimes less than 10 μs and for

n > 14 (essentially) none with lifetimes less than 100 μs. Consequently, in

the relatively high density environment of the discharge tubes, excited states

with high quantum values of n, if formed, may not be observed (between 8 and

16 μm) due to rapid gas phase or wall quenching processes.

These calculations were made within the framework of the Coulomb ap-

proximation, usually taken to be order-of-magnitude in accuracy[16] and, of

course, applicable only to dipole-allowed transitions. There is some evidence

that we may have more confidence in the general accuracy of these calculations

for the dipole-allowed transitions of argon. Recently, Borge and Campos[17]

have measured lifetimes for several $ns[3/2]_2^0$ (n = 6, 7, 8, 9) states and com-

pared their results to computed Coulomb approximation lifetimes and the re-

sults of more accurate calculations. Their comparisons indicate agreement

between the Coulomb approximation predictions and measured values to well

within a factor of two. However, it should be noted that their work covers a

limited set of states, so it is difficult to assess the confidence over the

range of states used here.

Calculations were performed to simulate argon spectra for 8-16 μm as

observed in COCHISE. To compute theoretical spectra, a distribution of popu-

lations of states must be chosen. We have chosen a Boltzmann distribution

with a temperature of 10,000 K. Calculations were also performed at tempera-

tures of 20,000 and 50,000 K, but showed no significant variation, since the

states of interest are at high energy and exhibit only slight relative popula-

tion changes with temperature. We present only results computed at 10,000 K.

D-19

We emphasize that the use of a Boltzmann distribution in defining state populations is convenient but not realistic, since it is unlikely that equilibrium is achieved in the disturbed environment of a microwave discharge. The theoretical spectra were computed using triangular slit functions to simulate the resolutions of the experimental spectra. The energy radiated at a given wavelength is given by the formula:

$$I(\lambda) = \sum g_i A_{i \rightarrow j} e^{-\epsilon_i / kT} \sigma(\lambda - \lambda_{ij}) \epsilon_{ij}$$

where $g_i A_{i \rightarrow j}$ is the product of the upper state degeneracy and the Einstein coefficient for the transition between states i and j, $e^{-\epsilon_i / kT}$ is the Boltzmann factor for the upper state, ϵ_{ij} is the energy of the transition and $\sigma(\lambda - \lambda_{ij})$ is the triangular slit function. The su is over all possible transitions allowed in the dipole approximation which are within the instrumental bandpass at a given wavelength setting.

Predicted and observed spectra for 8-16 μm are compared in Fig. 6, normalized to the intensities of the features near 11.5, 15.0, and 15.5 μm. The comparison between theory and experiment is mixed. In the interval 8.5-10 μm very little radiation is measured where the calculations predict substantial emission. The calculations also do not predict the shape and relative magnitude of the large spectral feature around 12.4 μm. However, with these exceptions the theoretical predictions correlate fairly well with the observed peak positions and, within factors of 2-3, with relative peak heights over the rest of the spectrum, i.e., the theoretical predictions seem to agree best with experiment in the 10-12 μm and 12.6-16.0 μm ranges.

The poor comparison between 8 and 10 μm may occur because the Coulomb approximation happens to fail for the transitions occurring in that region. It

is curious, however, that several of the observed transitions in the 10-12 μm and 12.6-16.0 μm regions originate from upper states in the same $n\ell$ manifolds as the unobserved transitions in the 8.5-10 μm region. This may indicate that there are non-equilibrium populations within manifolds due to selective excitation or cascade processes in the radiating gas. The strongest predicted transitions in the 8.5 to 10.0 μm region are listed in Table II. We have examined this group to see if transitions arising from the same upper state appear in other portions of the spectrum. Most do not appear as singly identified transitions but several appear identified with other transitions that may well cause the observed features. Only transitions from the $4f'[7/2]_3$, $4f'[5/2]_3$ and $5d[3/2]_2$ states seem to be definitely identified at 11.115, 11.115 and 12.255 μm, respectively. Thus for the strong transitions predicted between 8.5 and 10 μm we speculate that, for states not radiating elsewhere in the observed spectrum, non-equilibrium effects from selective excitation or cascade may cause them not to be populated. In addition, the seemingly missing predicted radiation from 4f' states between 9.497 and 9.671 μm might well be due to the breakdown of the Coulomb approximation for 4f states. The Coulomb approximation limits are generally accepted to be $n - \ell > 1$ so that this case is borderline at best. The possibility of selective population within the $n\ell$ manifolds is quite intriguing although we readily admit to the quantitative limitations of the Coulomb approximation.

A high-resolution spectrum of the surprisingly intense 12.4 μm feature from Fig. 6 is shown in Fig. 7. As listed in Table I, most of the observed features can be confidently assigned to individual transitions, as labeled in the figure. Note that most of the intensity between 12.1 and 12.5 μm arises

TABLE II

UNOBSERVED SPECTRAL TRANSITIONS: 8.50 TO 10.00 μm

Transition	Predicted Wavelength μm
$4f'[7/2]_3 \rightarrow 4d'[5/2]_2^0$	9.668
$4f'[5/2]_3 \rightarrow 4d'[3/2]_2^0$	9.493
$5d[3/2]_2^0 \rightarrow 6p[3/2]_1$	9.822
$5d[5/2]_2^0 \rightarrow 6p[1/2]_1$	9.757
$5d'[3/2]_1^0 \rightarrow 6p'[1/2]_0$	9.757
$5d[3/2]_1^0 \rightarrow 6p[1/2]_0$	9.579
$5d[5/2]_3^0 \rightarrow 6p[3/2]_2$	9.443
$5d[5/2]_2^0 \rightarrow 6p[5/2]_2$	9.172
$5d[5/2]_3^0 \rightarrow 6p[5/2]_3$	8.589
$6d'[5/2]_3^0 \rightarrow 5f[7/2]_4$	9.859
$6d[7/2]_3^0 \rightarrow 5f[9/2]_4$	9.275
$6d[5/2]_2^0 \rightarrow 5f[7/2]_3$	9.018
$7f'[5/2]_2 \rightarrow 6d'[3/2]_1^0$	9.913
$7f[7/2]_4 \rightarrow 6d[5/2]_3^0$	9.650
$4p[5/2]_2 \rightarrow 5d[7/2]_3^0$	9.429
$7p'[5/2]_1 \rightarrow 5d'[5/2]_2^0$	8.787
$7s[3/2]_2^0 \rightarrow 6p[3/2]_2$	8.551
$7p[5/2]_3 \rightarrow 5d[7/2]_4^0$	8.548

from transitions out of very high states, $8 < n < 12$. Furthermore, the spectral distribution cannot be described by a Boltzmann distribution. By comparing relative intensities and transition probabilities, we deduce relative emitting state populations of $5d[3/2]_2^{\circ}:8d[1/2]_1^{\circ}:9d[5/2]_3^{\circ}:10p[5/2]_2:10p[5/2]_3:11d[3/2]_1^{\circ}:12p[5/2]_{2,3} = 0.2:2.2:1.0:130:4.5:44:3.7$. In contrast, for a 10^4 K Boltzmann distribution, these states would have nearly identical relative populations, to within 30%. The discrepancies could be due at least in part to inadequacy of the Coulomb approximation; however, some of the variations seem too large to be explained in this way. The apparent $5d[3/2]_2^{\circ}$ population is very low relative to those of the higher levels, which is consistent with our failure to observe its emission at shorter wavelengths as discussed above. Other states exhibit marked population enhancements, particularly $10p[5/2]_2$ and $11d[3/2]_1^{\circ}$. Furthermore, the 9d, 10p and 12p transitions account for more than 70% of the observed intensity between 12.1 and 12.5 μm. We conclude by inspection of the spectral comparison in Fig. 6 that the intense feature near 12 μm probably results from an enhancement of the populations of these states by roughly an order of magnitude relative to those of the $n = 4,5$ states responsible for neighboring emission between 10 and 16 μm.

V. DISCUSSION

Careful inspection of the transitions listed in Table I leads to several interesting observations. For convenience, the observed manifold-to-manifold transitions are depicted on energy-level diagrams in Figs. 8-10.

First, emission is observed from states up to within a few hundred cm^{-1} of the ionization limit for the j_c = 3/2 (unprimed) core configuration. This is far higher in the energy manifold than has been probed in other electron bombardment experiments,[18] in which only emission in the visible was monitored.

Second, emitting states above 124,000 cm^{-1} are not uniformly represented by observable transitions. This is contrary to what we might expect for excitation solely by direct electron impact. Electron impact excitation will occur in the tail of the electron energy distribution with cross sections similar to that for ionization. This should give rise to a uniform population distribution, with the relative state populations decreasing with increasing energy. Collisional relaxation may modify this distribution somewhat; however, this modification probably does not strongly affect the distributions under our conditions. Quenching studies[19-21] for the 4p and 4p' manifolds yield collisional deactivation rate coefficients in the 10^{-11} cm^3 s^{-1} range, probably occurring via curve crossings on the Ar_2 potential surface.[21] For our conditions, 0.1 torr, 100 K, and [Ar] = 10^{16} cm^{-3}, the collisional lifetime of Ar* would be ~ 10 μs, i.e., on the order of the infrared radiative lifetimes for the higher levels (n ~ 10). Additional rapid quenching by electronic-to-translational energy transfer may be expected for states above n ~ 12, where the energy defects are on the order of kT or less. Thus, we expect quenching to deplete levels above 125,000 cm^{-1}, but in a non-selective

way. The implication is, then, that the few observed emitting states above 125,000 cm^{-1}, which radiate predominantly at long wavelengths, are directly populated by some rapid kinetic process. This is consistent with the results of the spectral analysis, which show that the upper-level electronic population distribution cannot be described by a Boltzmann expression, but rather exhibits a population <u>enhancement</u> for LWIR - radiating states. The LWIR emissions from these states, as well as their collisional deactivation, appear to be the initial steps in a (largely radiative) cascade sequence which populates the lower levels. As the cascade moves down the energy "ladder," the radiative lifetimes become shorter, quenching becomes less important, and the radiative transitions occur at shorter wavelengths. Below ~ 122,000 cm^{-1}, virtually every electronic state manifold can be accounted for in the infrared spectrum. Note that the relative populations within manifolds can still be non-Boltzmann owing to the selectivity of the radiative transitions in and out. This effect has been observed even at high pressures.[19,20] Such selective excitation within manifolds can explain the observed absence of certain predicted transitions, as discussed in the previous section.

Third, the observed transitions occur primarily in the $j_c = 3/2$ manifold. Of the few $j_c = 1/2$ transitions we observe, most of them occur at shorter wavelengths, and the highest states observed lie at substantially lower energies than those observed for $j_c = 3/2$. The implication here is that there is little or no direct formation of Ar* with the $j_c = 1/2$ core, and that the higher states we observe are populated initially by collisional energy transfer from Ar* ($j_c = 3/2$).

Fourth, there are some manifolds at intermediate points in the cascade for which there are several radiative inputs and few radiative outputs. This

is especially true for the 6p manifold, and also to some extent for 5d, 4f, 4d, and 5p. The "bottleneck effect" in evidence for these manifolds may be expected to give unusual state distributions within each manifold and intense radiative transitions at selected wavelengths.

It remains to identify the excitation process responsible for initiating the cascade. The most obvious candidate is dissociative recombination of Ar_2^+:

$$e^- + Ar_2^+ \rightarrow Ar + Ar^* \tag{12}$$

where Ar* is in one of many possible Rydberg states. Direct recombination of Ar^+ with electrons is a three-body, dielectronic process and will be extremely slow in a low-pressure, weak plasma such as occurs in our discharges. Similarly, two-body radiative recombination of Ar^+ will not be significant under our conditions. Reaction (12) has been carefully studied by Shiu and Biondi[18] for electron temperatures of 300-7500 K. By monitoring radiation in the visible, they observed formation of Ar(4p, 4p') in the recombination of Ar_2^+ with 300 K electrons, and formation of states as high as 5d when 7200 K electrons were used. The authors deduced that the observed states were populated directly from Ar_2^+, whose zero-point energy lies near 117,000 cm^{-1} (binding energies of 1.4, 1.23 ± 0.02, and 1.33 ± 0.02 eV are reported in Refs. 22-24, respectively). However, since infrared emission was not monitored in their experiments, it is not clear whether the observed states were populated directly or by radiative cascade from above. In any case, Shiu and Biondi's experiments show that energetic electrons can recombine with Ar_2^+ to form Ar* with most of the excess energy going into electronic excitation of the Ar*. For the microwave discharge case, with an electron temperature of 10^{4-5} K, one can

expect population of states near the ionization limit, as we observe spectro-scopically. (There may also be substantial formation of $Ar^+(^2P_{3/2})$ by this route.) Of course, we cannot eliminate the possibility that intermediate states of Ar* are directly populated as well; this will exacerbate the non-Boltzmann character of the cascade process.

Reaction (12) can only explain our observations if there is sufficient formation of Ar_2^+ in a microwave discharge. Ar_2^+ can be formed by three-body recombination of Ar^+:

$$Ar^+ + Ar + Ar \rightarrow Ar_2^+ + Ar \qquad (13)$$

However, reaction (13) has a rate coefficient of the order of 10^{-31} cm^6 s^{-1} at room temperature,[25] giving it an effective bimolecular rate coefficient of $\sim 10^{-15}$ cm^3 s^{-1} at 0.1 torr. By comparison, direct electron impact excitation of Ar* should occur with an effective rate coefficient similar to that for ionization; Caledonia[26] has calculated the latter quantity to be in the range $10^{-12\pm1}$ cm^3 s^{-1} for typical microwave discharges. Thus we anticipate that the Ar_2^+ mechanism, with Reaction (13) as a rate-limiting step, would not be able to compete with electron impact excitation as a source for Ar* unless the pressure is considerably larger. However, as pointed out by Shiu and Biondi,[18] the reverse of Reaction (12), associative ionization of Ar*, is probably very facile, with a rate coefficient of at least 10^{-9} cm^3 s^{-1}. Thus, it is pos-sible to form Ar_2^+ from less energetic Ar* produced in electron impact, and then recombine the Ar_2^+ with "hot" electrons to form highly energetic Ar**:

$$e^- + Ar \rightarrow Ar^* + e^- \qquad (a)$$

$$Ar^* + Ar \rightarrow Ar_2^+ + e_{cold}^- \qquad (b)$$

$$e_{hot}^- + Ar_2^+ \rightarrow Ar^{**} + Ar \qquad (c)$$
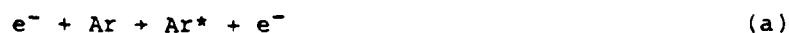
Here e_{hot} denotes the relatively energetic "average" electron in the plasma. Although the recombination coefficient decreases with increasing electron energy, the electron energy distribution is such that most recombinations will occur with relatively energetic electrons. Ar** is then a highly excited Rydberg species with a $^2P_{3/2}$ core configuration, and is subject to collisional and radiative deactivation as outlined above, as well as to rapid electron-impact ionization. The specificity of the process for the $^2P_{3/2}$ core can be understood in terms of the adiabatic dissociation of the Ar_2^+ -- e^- associated pair along the Ar -- $Ar^+(^2P_{3/2})e^-$ coordinate: the complex behaves like Ar_2^+ and dissociates to form the lowest-energy configuration of the atomic "ion."

Reactions (b) and (c) in effect set up a quasi-equilibrium between Ar_2^+ and the atomic Rydberg manifold, such that the net removal of Rydberg atoms is controlled primarily by radiative and collisional cascade. Recombination of --Ar_2^+ and e_{cold}^- (the reverse of (b)) can also occur; however, this reaction only feeds back Ar* and should not constitute a major loss term for Ar_2^+. Since this reaction is dominated by ambient-temperature electrons, we anticipate that, in the active discharge, the principal fate of Ar_2^+ is recombination with e_{hot} in Reaction (c). In steady state, the Ar_2 and Ar** number densities are given by:

$$[Ar_2^+] = \frac{k_a[e^-]}{k_c[e_{hot}^-]} [Ar] \tag{14}$$

$$[Ar^{**}] = \frac{k_a[e^-][Ar]}{L} \tag{15}$$

where L is the effective first-order loss rate of Ar** by collisional and radiative deactivation and is of order 10^6 s^{-1}. We can see from Eq. (15) that

[Ar**] depends upon the effective rate for electron-impact excitation of Ar*. This rate is extremely sensitive to pressure through the field/density ratio E/N for the discharge; indeed, the ionization rate coefficient increases two orders of magnitude for a two-fold increase of E/N.[26] Thus, the pressure effect we observe is undoubtedly influenced strongly by changes in discharge conditions such as E/N and [e⁻].

Clearly, direct observation of the discharge plasma in COCHISE would provide a great deal more information. However, such experiments require extensive reconfigurations which are presently incompatible with our on-going chemiluminescence investigations. We are considering future experiments incorporating such modifications.

VI. SUMMARY AND CONCLUSIONS

We have used the COCHISE apparatus to obtain a unique set of spectro-
scopic observations of the infrared emission from Ar Rydberg atoms using scat-
tered light emanating from a low-pressure microwave discharge plasma. These
measurements are the first laboratory observations of LWIR Rydberg emission,
and exhibit a rich spectrum from 2 to 16 μm. Commonly used hydrogenic approx-
imations often applied to other Rydberg atoms cannot account for the complex
nature of this spectrum, but all the observed transitions can be identified as
ArI lines or groupings using tabulated energy levels together with the strong
(dipole-allowed) selection rules and, in several cases, also allowing the core
configuration to change in the transition. A Coulomb approximation to the di-
pole moment function is fairly successful in accounting for the observed in-
tensities of the dipole-allowed transitions, but fails to predict detailed
spectral structure at shorter wavelengths (λ < 5 μm) where core-changing tran-
sitions are important. The spectral distribution in the LWIR portion of the
spectrum exhibits a remarkable peak near 12 μm that seems to indicate a non-
Boltzmann population distribution with a strong enhancement of very high
states within a few hundred cm^{-1} of the ionization limit. (However, strong-
coupling enhancements[27] of the line strengths of the particular transitions
cannot be ruled out a priori.) The most likely source of a non-Boltzmann dis-
tribution is the dissociative recombination of Ar_2^+ with energetic electrons
in the active discharge, followed by rapid collisional and radiative cascade.
These infrared measurements are the first observations of such high excitation
in dissociative recombination; previous workers have studied only visible
emissions, which are the end results of the cascade process.

Based on the results given here, Ar is not likely to be a significant
infrared radiator in normal atmospheric perturbations owing to the kinetic

D-30

limitations of forming Ar_2^+ at high altitudes.[15] However, the COCHISE results

for ArI may hold implications for atmospheric OI and NI emission in the in-

frared. Unlike Ar_2^+, O_2^+ and N_2^+ are readily formed by direct ionization of air.

The recombination of these ions with energetic electrons may lead to the for-

mation of Rydberg states of O and N in much the same way as in the case

of Ar_2^+, although the attainable energy is moderated considerably by the large

dissociation energies of O_2^+ and N_2^+. If the initially populated Rydberg states

are high enough, substantial infrared line radiation could occur in a strong

aurora. However, the spectral signature is difficult to predict theoretically

because of the non-Boltzmann character of the initial formation and cascade.

We plan to pursue this point with laboratory experiments on low-pressure (< 1

torr) Ar/N_2 and Ar/O_2 discharges and with spectral simulations using the

methodologies we have applied to the ArI data.

ACKNOWLEDGEMENTS

REFERENCES

1. S. Feneuille and P. Jacquinot, Adv. Atomic Molec. Physics 17, 99 (1981).

2. J. P. Kennealy; F. P. DelGreco; G. E. Caledonia, and B. D. Green

    J. Chem. Phys. 69, 1574 (1978).

3. J. P. Kennealy; F. P. DelGreco; G. E. Caledonia, and W. T. Rawlins, Proc.

    Soc. Photo-Opt. Instrum. Eng. (G. A. Vanesse, ed.) 191, 151 (1979).

4. W. T. Rawlins, H. C. Murphy, G. E. Caledonia, J. P. Kennealy, F. X.

    Robert, A. Corman, and R. A. Armstrong, Appl. Opt. to be submitted,

    1984.

5. W. T. Rawlins, G. E. Caledonia and J. P. Kennealy, J. Geophys. Res., 86,

    5247 (1981).

6. W. T. Rawlins and R. A. Armstrong, AFGL-TR-82-0273, NTIS No. ADA-123653,

    Air Force Geophysics Laboratory, 1982.

7. F. Kaufman, Advances in Chemistry Series 80, 29 (1969).

8. C. E. Moore, Atomic Energy Levels, Vol. 1, NSRDS-NBS35 (1971).

9. S. Bashkin and J. O. Stoner, Jr., Atomic Energy - Level and Grotrian

    Diagrams 2, North-Holland Publishing Co., New York (1978).

10. D. R. Bates and A. Damgaard, Phil. Trans. Roy. Soc. A242, 101 (1949).

11. H. Statz, C. L. Tang, and G. F. Koster, J. Appl. Phys. 34, 2625 (1963).

12. G. F. Koster and H. Statz, J. Appl. Phys. 32, 2654 (1964).

13. H. Friedrich, K. Katterbach, and E. Trefftz, J. Quant. Spectrosc. Radiat.

    Transfer 10, 11 (1970).

14. C. J. Humphreys, J. Phys. Chem. Ref. Data, 2, 519 (1974).

REFERENCES (CONT.)

15. W. T. Rawlins, A. Gelb, and R. A. Armstrong, AFGL-TR-83-0201, NTIS No. 137916, Air Force Geophysics Laboratory, Hanscom AFB, MA, 1983.

16. W. L. Wiese, in Progress in Atomic Spectroscopy, Part B, Edited by W. Haule and H. Deinpoppen, Plenum Publishing Corp., New York (1979).

17. M. J. G. Borge and J. Campos, Phys. Rev. A27, 1910 (1983).

18. Y. J. Shiu and M. A. Biondi, Phys. Rev. A 17, 868 (1978).

19. J. W. Keto, and C. Y. Kuo, J. Chem. Phys. 74, 6188 (1981).

20. C. Y. Kuo and J. W. Keto, J. Chem. Phys. 78, 1851 (1983).

21. R. S. F. Chang and D. W. Setser, J. Chem. Phys. 69, 3885 (1978).

22. R. S. Mullikan, J. Chem. Phys. 52, 5170 (1970).

23. C. Y. Ng, D. J. Trevor, B. H. Mahan, and Y. T. Lee, J. Chem. Phys. 66, 446 (1977).

24. J. T. Moseley; R. P. Saxon; B. A. Huber; P. C. Cosby; R. Abouaf, and M. Tadjeddine, J. Chem. Phys. 67, 1659 (1977).

25. A. Good, Chemical Reviews 75, 561 (1975).

26. G. E. Caledonia, unpublished work. See Appendix C of W. T. Rawlins, L. G. Piper, A. Gelb, R. A. Lucht, and G. E. Caledonia, "COCHISE Research," PSI TR-349, Physical Sciences Inc., Research Park, Andover, MA 01810, January 1983, available from the authors upon request.

27. C. M. Lee and K. T. Lu, Phys. Rev. 48, 1241 (1971).

FIGURE CAPTIONS

Fig. 1   COCHISE reaction chamber. The cross-hatched region delineates the field-of-view of the detector (not shown).

Fig. 2   High resolution spectrum of Ar emission from 2 to 4 μm, 0.007 μm resolution, 0.1 torr. The spectrum was taken using a 2 μm long-pass interference filter and a grating blazed at 3 μm, operating in first order.

Fig. 3   Medium resolution spectrum of Ar emission, 4-5 μm, 0.013 μm resolution, 0.1 torr. The spectrum was taken using a 4 μm long-pass interference filter and a grating blazed at 3 μm, operating in first order.

Fig. 4   Medium resolution spectrum of Ar emission, 10-12 μm, 0.027 μm resolution, 0.1 torr, using an 8 μm long-pass interference filter and a 10 μm grating in first order.

Fig. 5   Computed values of gA as a function of transition wavelength (2-16 μ m) for argon excited states, $[1s^2 2s^2 2p^6 3s^2 3p^5]$ nℓ, n=7. Plotted values are normalized to the maximum value of gA, $(gA)_{max}$, noted on figure.

Fig. 6   Predicted and observed ArI spectra for 0.1 torr, 0.08 μm resolution. The normalization is such that coincidence between theory and experiment occurs at 11.5, 15.2, and 15.6 μm.

Fig. 7   High resolution spectrum of Ar emission near 12.3 μm, 0.013 μm resolution, 0.1 torr. Emitting states for the individual transitions are indicated; see Table I for more complete identification.

Fig. 8   Observed ArI transitions, 2 - 3.5 μm.

Fig. 9   Observed Ar: transitions, 4 - 7 μm.

Fig. 10   Observed ArI transitions, 10 - 16 μm.

Microwave
Discharges

5690-7

APPARENT RELATIVE SPECTRAL RADIANCE

WAVELENGTH, μm

W.T. Rawlins
PSI SR-160
Fig. 2

D-37

APPARENT RELATIVE SPECTRAL RADIANCE

WAVELENGTH, μm
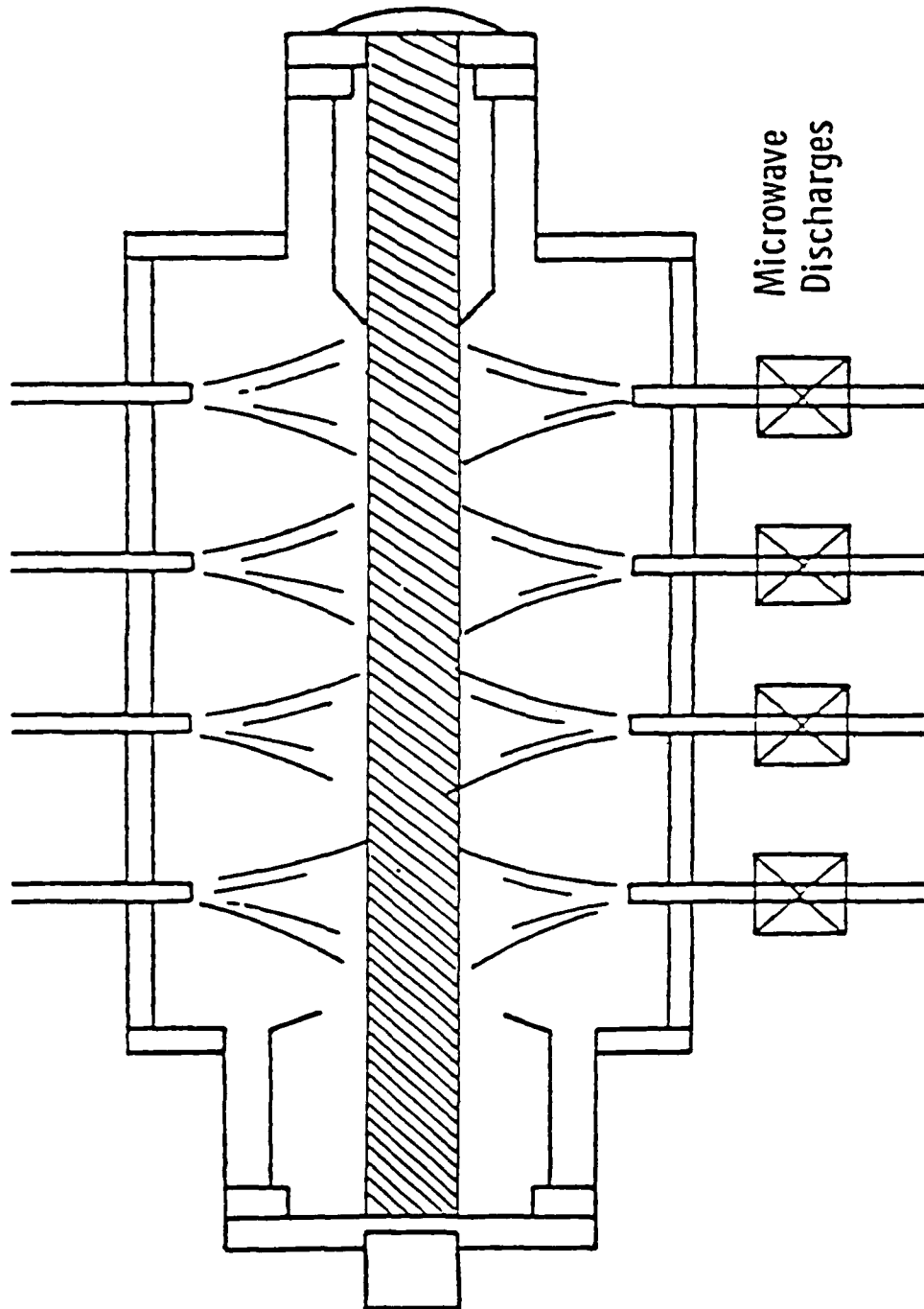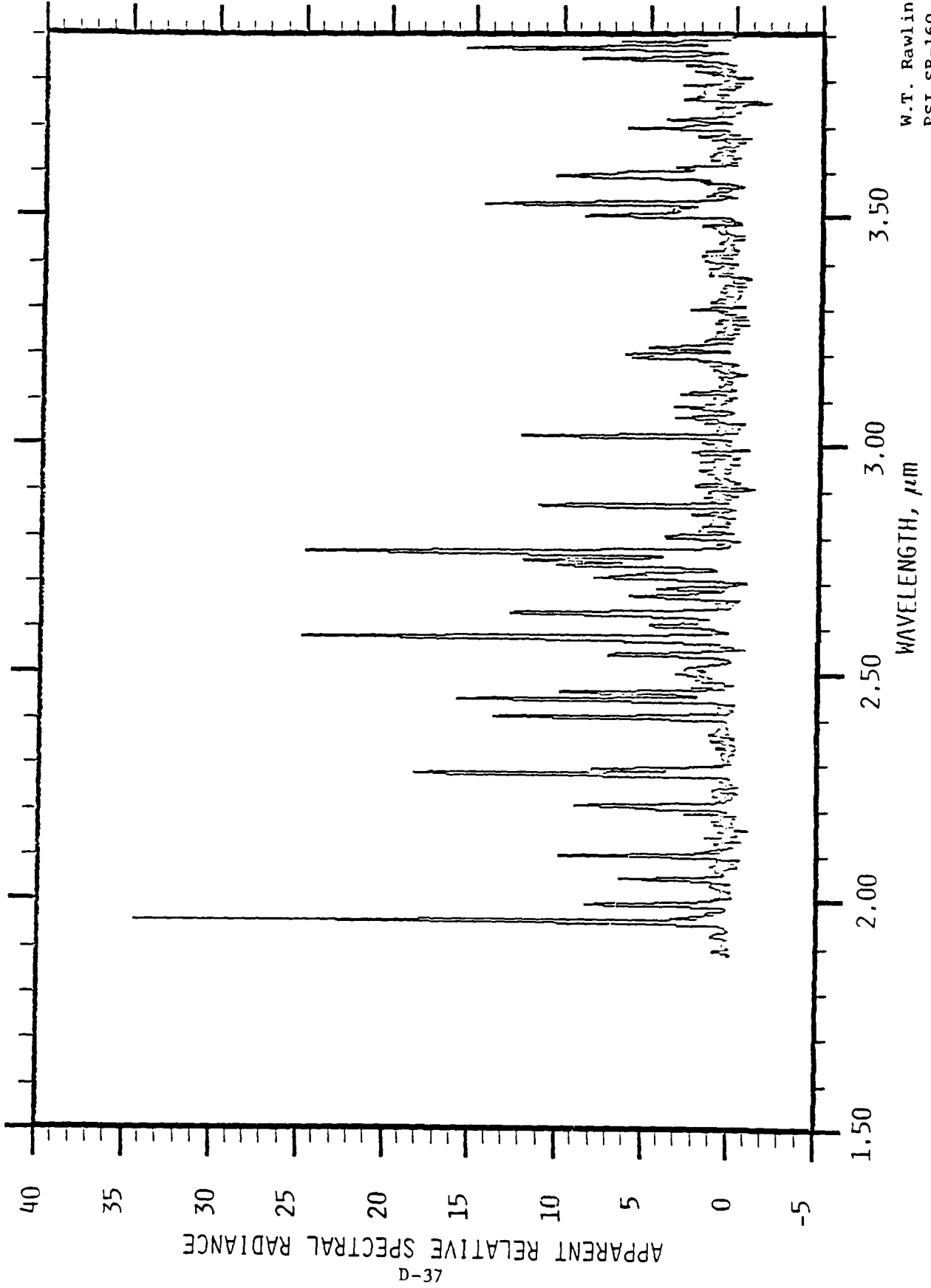
5690-8

W.T. Rawlins
PSI SR-160
Fig. 3
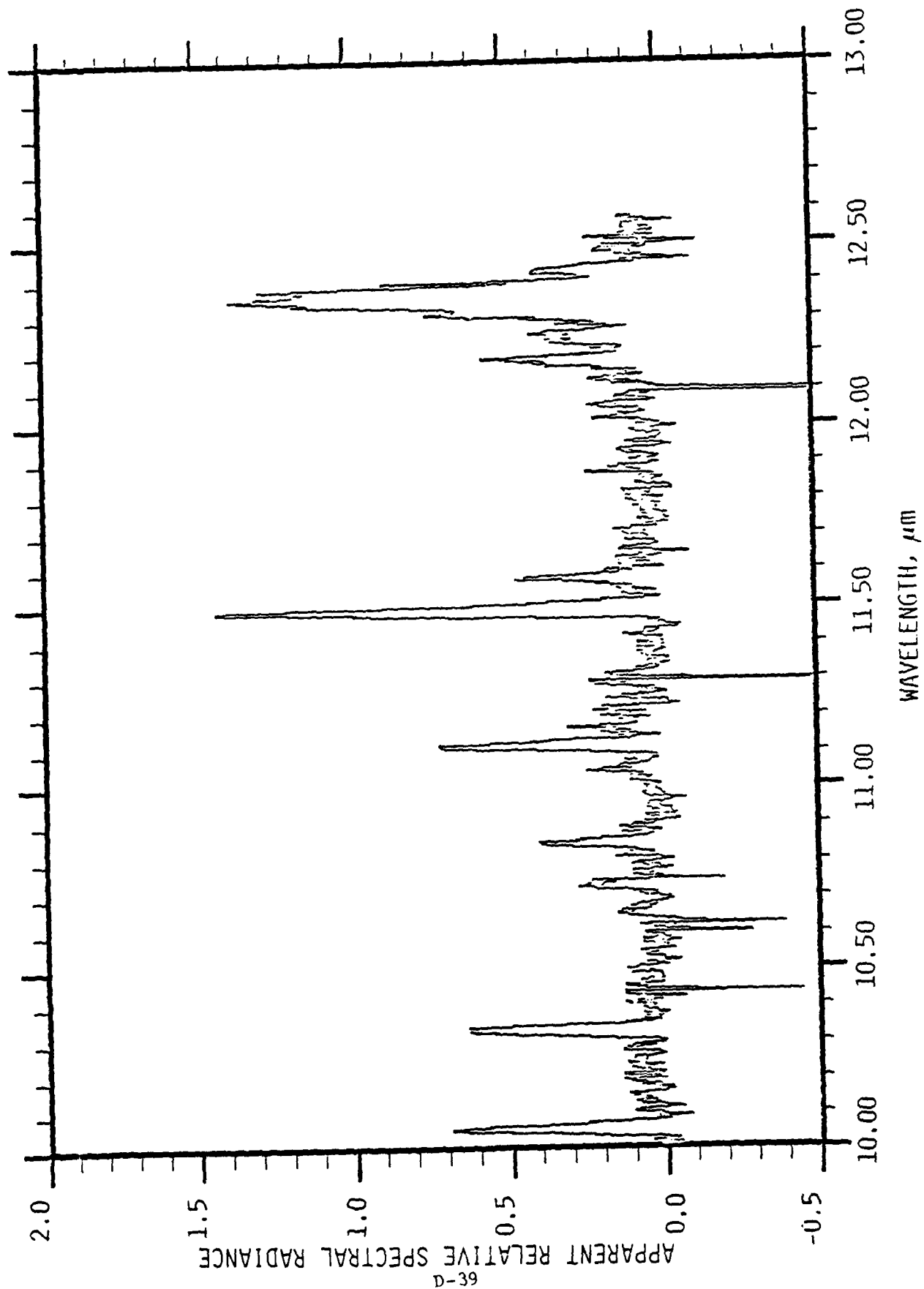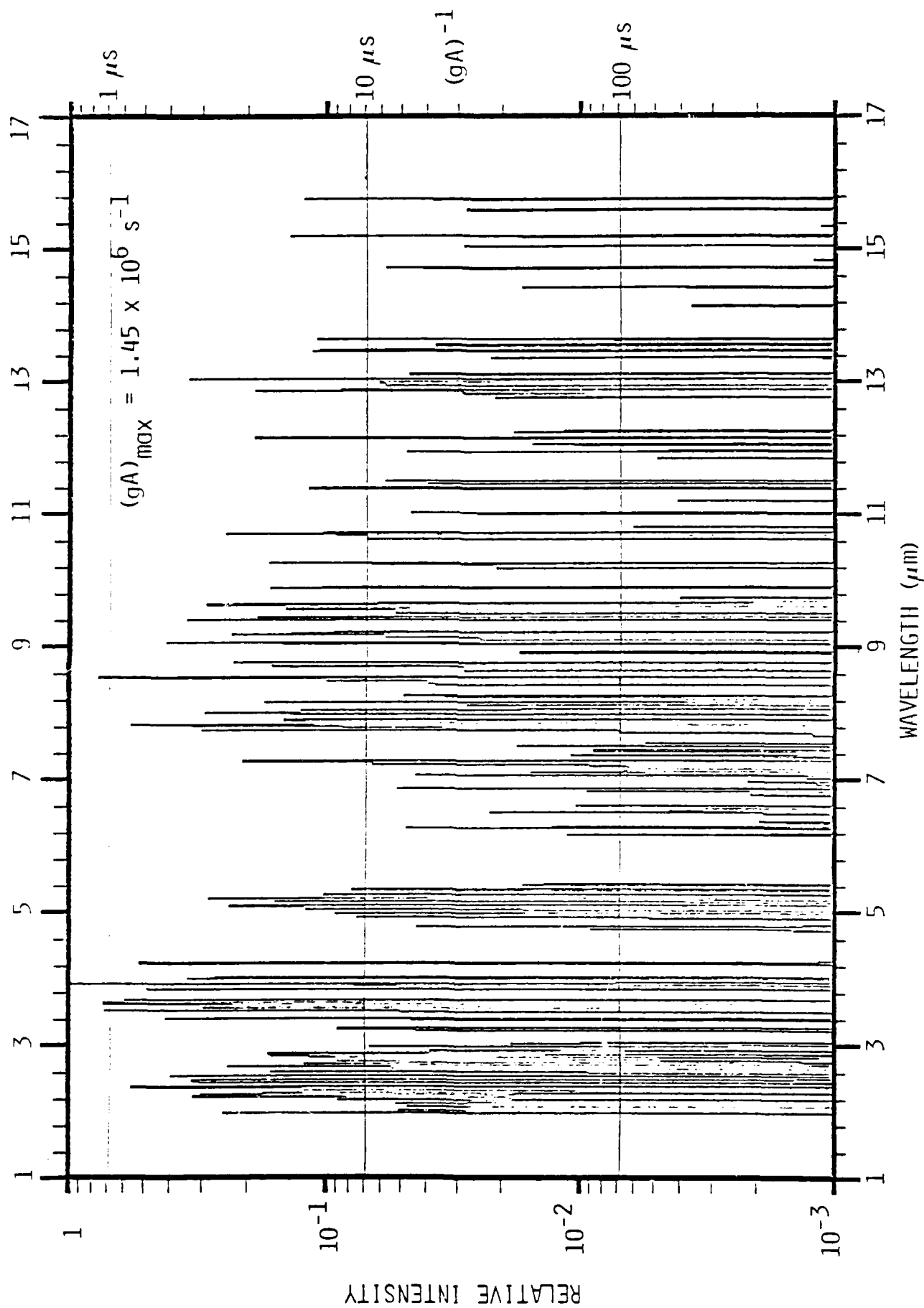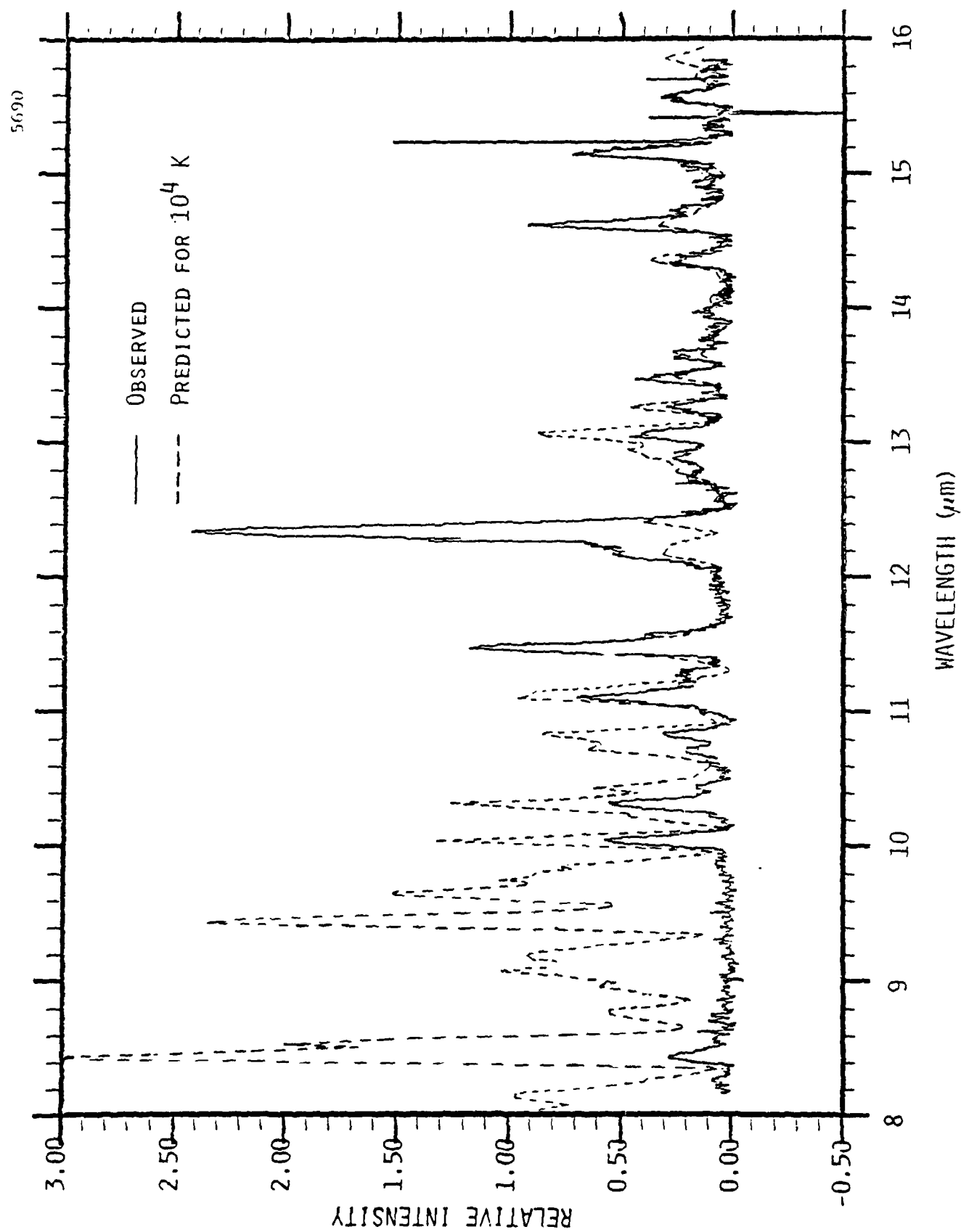
D-38

APPARENT RELATIVE SPECTRAL RADIANCE

WAVELENGTH, μm

W.T. Rawlins
PSI SR-160
Fig. 4

5690-10

D-39

RELATIVE INTENSITY

WAVELENGTH (μm)

$(gA)_{max} = 1.45 \times 10^6 \text{ s}^{-1}$

$1 \mu s$

$10 \mu s$

$(gA)^{-1}$

$100 \mu s$

W.T. Rawlins
PSI SR-160
Fig. 5

D-40

W.T. Rawlins
PSI SR-160
Fig. 6

WAVELENGTH, μm

APPARENT RELATIVE SPECTRAL RADIANCE

5690-12

W.T. Rawlins
PSI SR-160
Fig. 7

D-42

Fig. 8

5690-26

ENERGY, cm⁻¹

W.T. Rawlins
PSI SR-160
Fig. 10

APPENDIX E

CLASSICAL TRAJECTORY STUDY OF
ENERGY TRANSFER BETWEEN ARGON ATOMS AND
VIBRATIONALLY-ROTATIONALLY EXCITED
OZONE MOLECULES

E
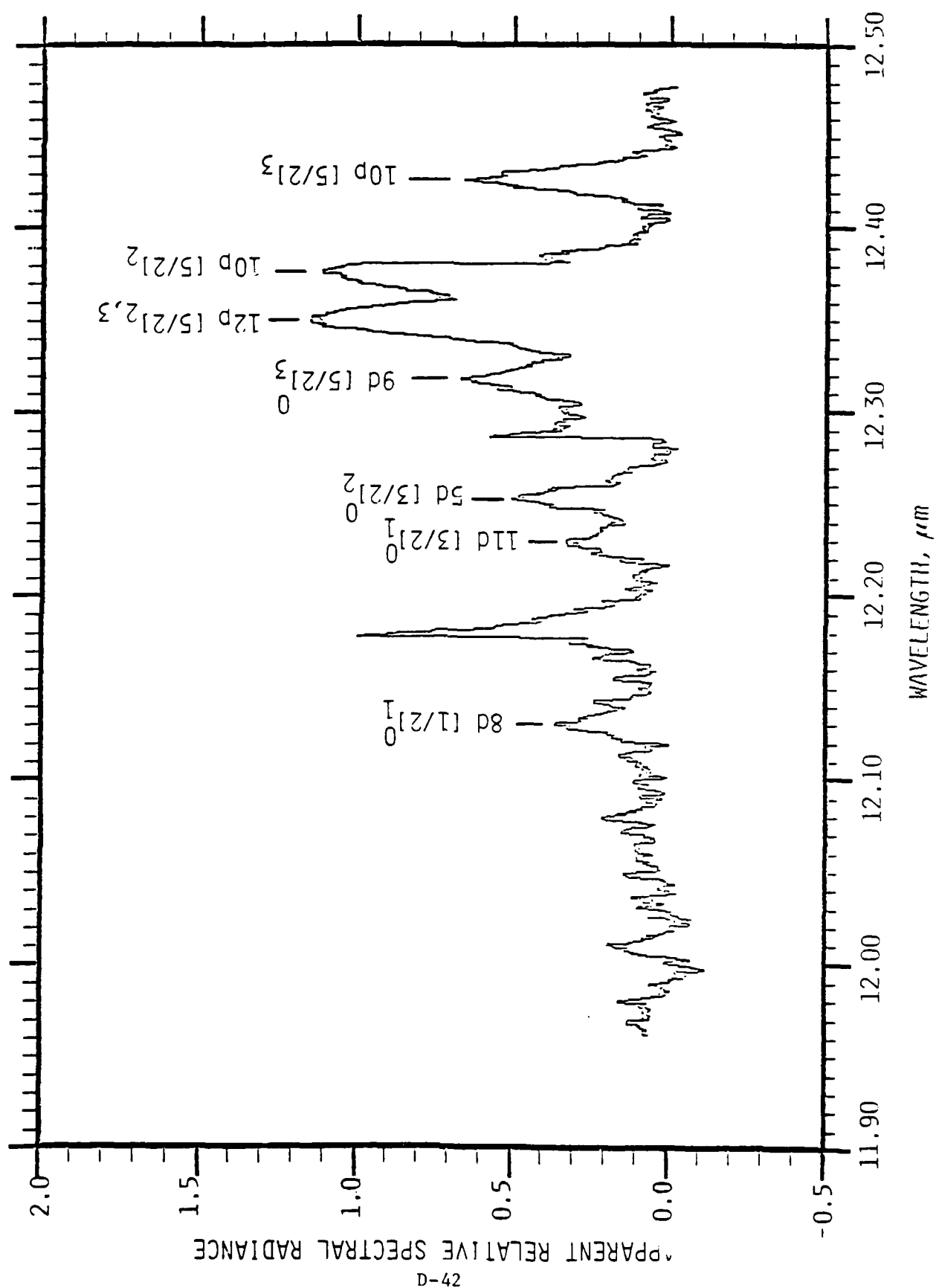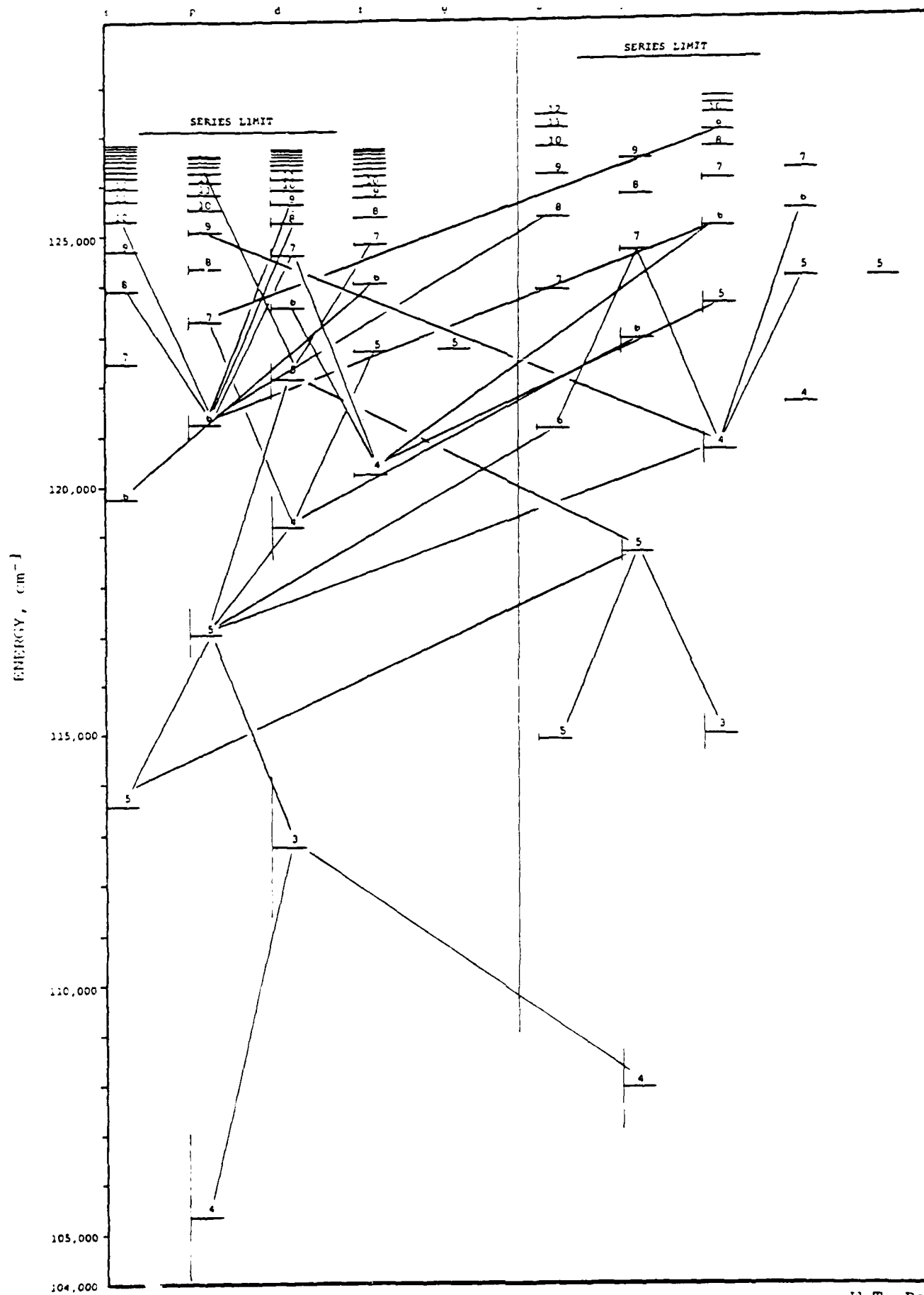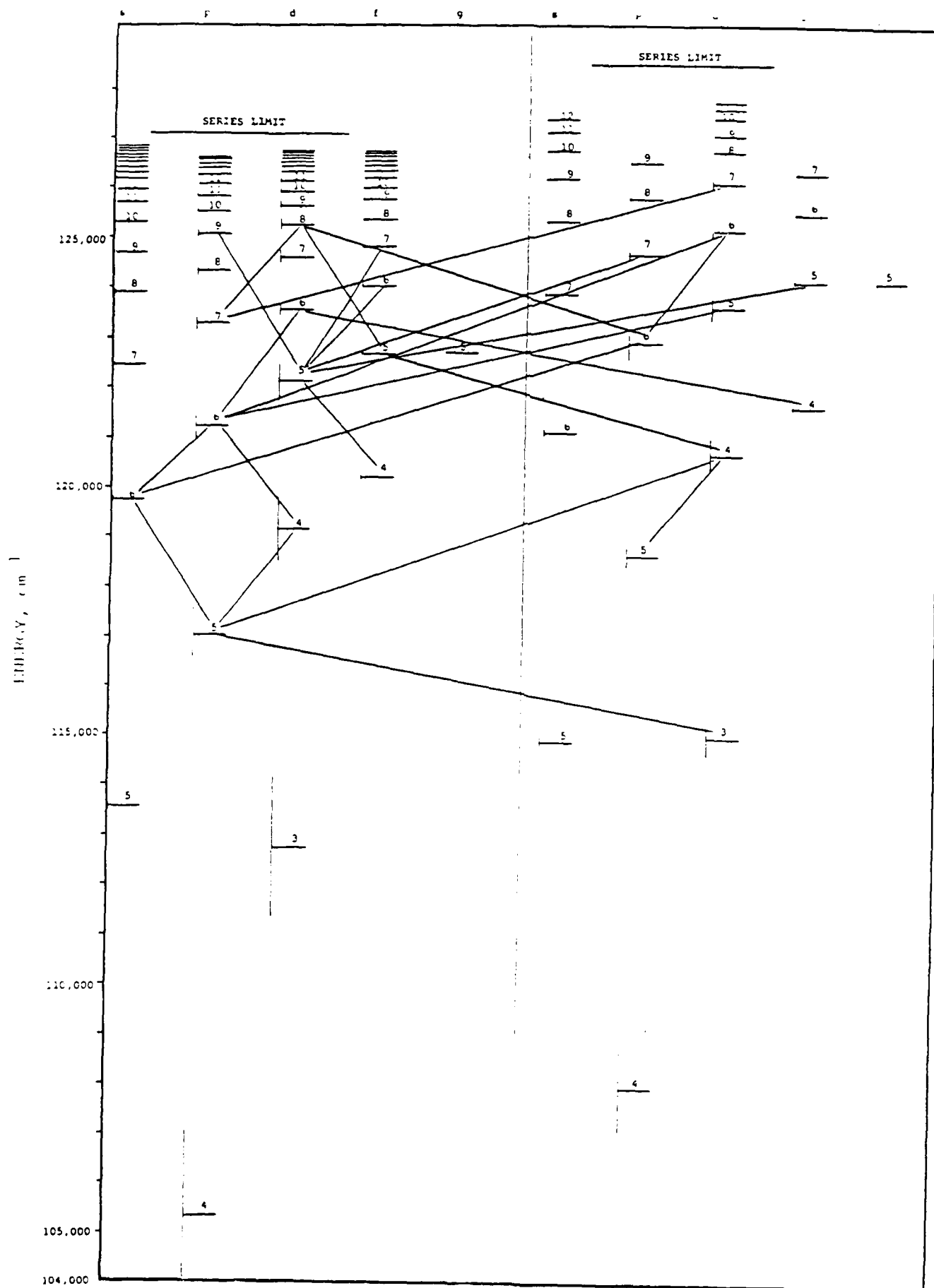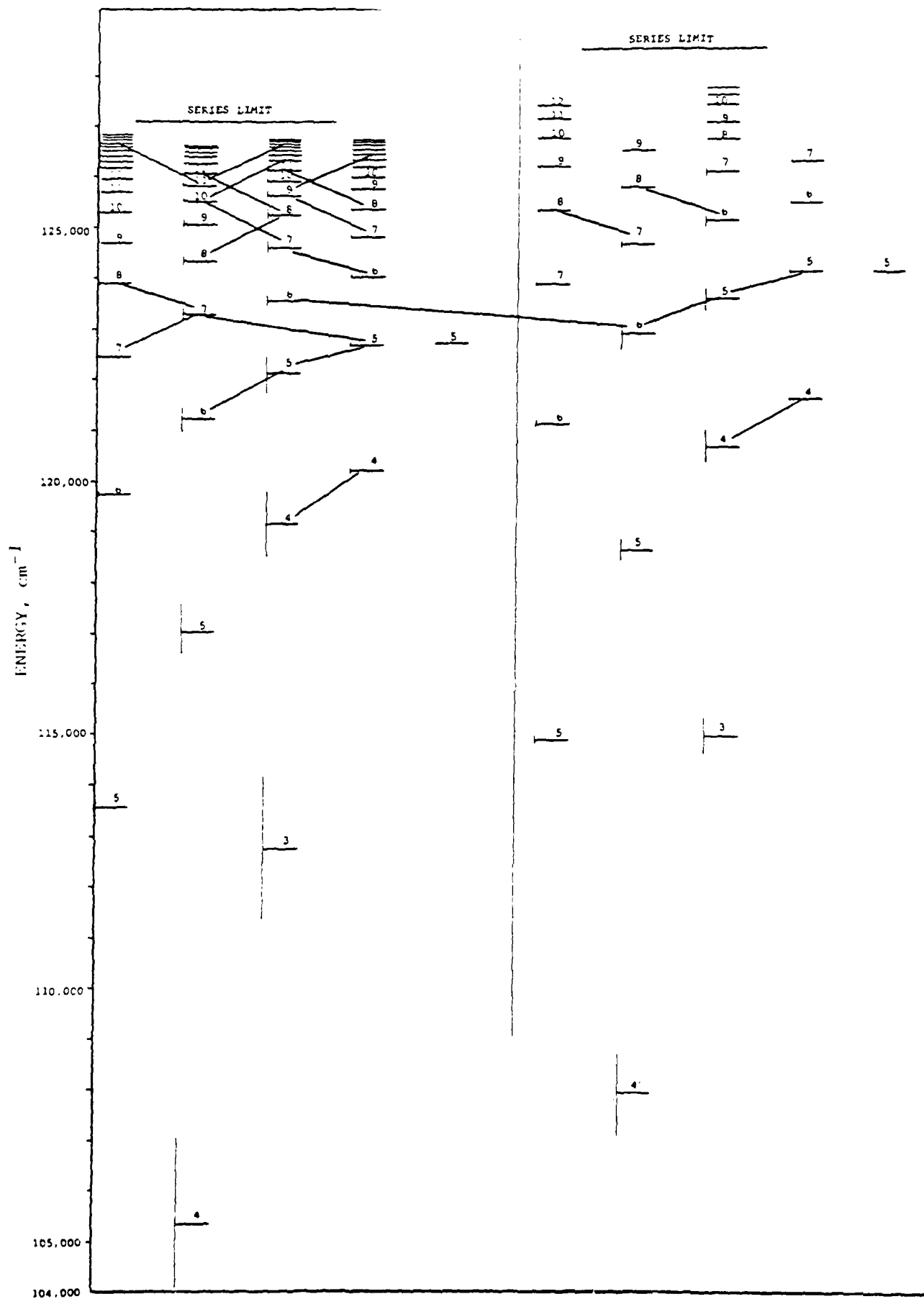
APPENDIX E

CLASSICAL TRAJECTORY STUDY OF ENERGY TRANSFER
BETWEEN ARGON ATOMS AND VIBRATIONALLY-ROTATIONALLY
EXCITED OZONE MOLECULES

ABSTRACT

The results of a classical trajectory study of collisions between argon atoms and vibrationally-rotationally excited ozone molecules are presented. The calculations indicate that energy transfer is controlled by the ozone angular momentum. Even highly vibrationally excited molecules with low angular momentum gain energy upon collision with Ar atoms for all translational energies considered.

I. INTRODUCTION

Ozone three-body recombination and relaxation is of interest for several applications including modeling of ozone chemistry in the upper atmosphere. At high altitudes ozone can be formed by three-body recombination, i.e.,

$$O + O_2 + M \rightarrow O_3^* + M$$
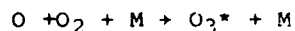
where O_3^* is thought to be a vibrationally-rotationally excited molecule. The newly recombined ozone molecules are important radiators in the infrared in the upper mesosphere.[1] Reaction rate calculations coupled with atmospheric fluorescence observations can provide insight into key chemical processes and molecular concentrations. It is thus important to develop an understanding of the dynamics of the recombination reaction as well as the relaxation processes of highly excited ozone.

Experimental studies of the ozone recombination reactions are ongoing at several centers. Several investigations of high altitude ozone chemistry have been performed on the COCHISE facility at the Air Force Geophysics Laboratory.[2] These experiments have included measurements of infrared emission from ozone recombination with argon as a third-body and have inferred early time distributions of ozone internal state distributions. Interpretation of experimental data is complicated due to experimental limitations in controlling very early time relaxation of the nascent distribution. The goal of this effort is to provide a theoretical description of the three-body ozone recombination dynamics and short time relaxation of the nascent ozone distribution.

In this paper we present a classical trajectory study of energy transfer from vibrationally-rotationally excited ozone by collisions with argon atoms. Our immediate goal is to develop an understanding of energy relaxation processes that occur in highly excited ozone formed by three-body recombination. To this end we have systematically examined energy transfer as a function of relative translational energy and the ozone molecular angular momentum.

Relatively little work has been done on the collisional relaxation of highly excited triatomic molecules. Gallucci and Schatz[3] studied collisions of He with highly excited HO_2. They used the quasiclassical trajectory method to compute cross-sections for energy transfer, stabilization and dissociation of HO_2 excited above the dissociation threshold. Their work is quite relevant to our effort in describing three-body recombination of ozone. Brown and Miller[4] computed classical trajectories to describe energy transfer between He and HO_2 for HO_2 excited to energies near the dissociation threshold. They investigated the dependence of the energy transfer on bath temperature, total energy and the molecular angular momentum. Their calculations indicate that energy transfer increases with molecular angular momentum. A similar result will be presented here for $Ar-O_3$ energy exchange.

Stace and Murrell[5] studied energy transfer between rare gas atoms and several triatomics, in particular ozone. Their work concentrated on energy transfer of thermalized molecules in a bath of rare gas atoms. However some calculations were performed on highly excited ozone with all the internal

E-2
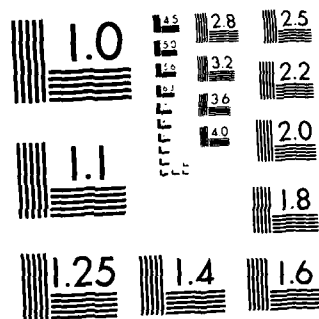
CROCOPY RESOLUTION TEST CHART

NATIONAL BUREAU OF STANDARDS-1963-A

energy either as rotation or as vibration. Their limited calculations indicate that the energy exchange process is qualitatively different for molecules in which all the molecular energy is exclusively in rotational or in vibrational excitation. The calculations of Stace and Murrell used an earlier version of the ozone potential surface developed by Murrell, et al.[6] The calculations presented here use the more recent version of the ozone potential surface developed by Varandas et al.[7,8]

Mulloney and Schatz[9] computed classical trajectories for rare gas atom-ozone collisions using the Stace and Murrell potential surface.[6] They compared the results of energy transfer calculations using the centrifugal and rotational sudden approximations with exa t classical trajectory results. They also conclude that most of the energy transfer is rotational. A recent review of the quasiclassical trajectory studies of collsional energy transfer in polyatomic molecules is given in Ref. 10.

In addition to single collision energy transfer studies we present some results for multi-collisional relaxation of excited ozone. The multi-collisional method was developed to examine non-equilibrium effects in diatom three-body recombination[10] and is appropriate for computing the energy relaxation of an ensemble of excited molecules in a thermal heat bath.

II.   CLASSICAL TRAJECTORY METHODOLOGY

The calculation of classical trajectories consists of three tasks: (1) selection of initial conditions, (2) integration of Hamilton's equations of motion and (3) final state analysis. Several reviews have described each of these tasks in considerable detail. The reader is referred especially to the reviews by Bunker[12] and Porter and Raff.[13] Only points specific to the present calculations will be discussed here.

We use a four-body coordinate system with fixed center of mass at the origin. A convenient coordinate system for integration of Hamilton's equations of motion is defined by the following relations:

$$\bar{q}_i = \bar{r}_i - \bar{r}_4$$

$$i = 1,2,3$$

$$\bar{p}_i = m_i \dot{\bar{r}}_i$$

where $\bar{r}_i$ are the coordinates of the four particles relative to the center of mass and are defined by the relations

$$\sum_{i=1}^{4} m_i \bar{r}_i = 0$$

$$\sum_{i=1}^{4} m_i \dot{\bar{r}}_i = 0.$$

In the $\bar{q}_i$ coordinate system the Hamiltonian, H, becomes

$$H = 1/m_4 \sum_{i=1}^{3} (m_i + m_4) \bar{p}_i^2 / 2m_i + 1/m_4 \sum_{i>j} \bar{p}_i \cdot \bar{p}_j + U$$

where U is the potential energy function. Hamilton's equations are written as:

$$\dot{\bar{q}}_i = \frac{\partial H}{\partial \bar{p}_i} = \frac{m_i + m_4}{m_i m_4} \bar{p}_i + \frac{1}{m_4} (\bar{p}_{j \neq i} + \bar{p}_{k \neq j \neq i})$$

and

$$\dot{\bar{p}}_i = -\frac{\partial H}{\partial \bar{q}_i} = -\frac{\partial U}{\partial \bar{q}_i}$$

E-4

The numerical integrations were performed using a fourth order fixed step-size Runge-Kutta integrator for the first five integration points. Subsequent points were computed using a fixed stepsize, fourth order Adams-Moulton integrator.

Computed trajectories were checked for numerical accuracy by back integration of selected trajectories and observation of conservation of energy and angular momentum. In most cases total energy was constant to a few parts in 10^6. Angular momentum components were conserved to better than two parts in 10^6. The integrations were performed using 60 bit CDC single precision arithmetic. Most calculations were performed on the Cyber 750 computer at the Air Force Geophysics Laboratory.

Potential Surface

For collisions of Ar with O_3 we use the Varandas-Murrell potential surface.[7] The ozone portion of this potential was derived by Murrell et al.[7,8] using available spectroscopic data.

The potential function is written as

$$U = V_{Ar-O_3} + V_{O_3}$$

where V_{Ar-O_3} is the Ar-O_3 interaction and V_{O_3} is the potential function for ozone. V_{Ar-O_3} is given by a sum of pairwise Ar-O Lennard-Jones 6-12 potentials between the Ar atom and each oxygen atom, i.e.

$$V_{ArO_3} = \sum_{i=1}^{3} 4\epsilon_{ArO} \left[\left(\frac{\sigma}{|\bar{q}_i|} \right)^{12} - \left(\frac{\sigma}{|\bar{q}_i|} \right)^6 \right].$$

The ozone interaction, V_{O_3}, is written as a function of the oxygen interatomic distances, r_1, r_2, and r_3, defined by

$$\bar{r}_1 = \bar{q}_1 - \bar{q}_2$$

$$\bar{r}_2 = \bar{q}_2 - \bar{q}_3$$

$$\bar{r}_3 = \bar{q}_1 - \bar{q}_3$$

and is given by:

$$V_{O_3} = \left[P(r_1 r_2 r_3) + G(r_1 r_2 r_3) \right] \left[1 - \tanh 2.2 Q_1 \right]$$

$$+ V_{O_2}(r_1) + V_{O_2}(r_2) + V_{O_2}(r_3)$$

where

$$V_{O_2}(r) = C_1 \left[1 + C_2(r - C_1) \right] e^{-C_4(r - C_3)},$$

$$Q_1 = C_{12} \left[(r_1 - C_{13}) + (r_2 - C_{13}) + (r_3 - C_{13}) \right],$$

$$Q_2 = C_{14} \left[(r_2 - C_{13}) - (r_3 - C_{13}) \right],$$

$$Q_3 = C_{15}(r_1 - C_{13}) + C_{16}(r_2 - C_{13}) + C_{17}(r_3 - C_{13}),$$

$$P = C_5 + C_6 Q_1 + C_7 Q_1^2 + C_8(Q_2^2 + Q_3^2) + C_9 Q_1(Q_2^2 + Q_3^2)$$

$$+ C_{10}(Q_3^3 - 3Q_2^2 Q_3) + C_{11}(Q_2^2 Q_3^2)^2,$$

$$G = g_1(1 + g_3 Q_1) g_p^5 e^{-g_4(Q_2^2 + Q_3^2)}$$

and

$$g_p = \left[g_3 + \sum_{i=1}^{3} (r_i^2 - r_j^2 - r_h^2)/2 r_j r_h \right].$$

The values of the constants are given in Ref. (5) and (7). The ozone por-
tion of this potential surface has been used previously by Varandas and
Murrell[7] to study the dynamics of the $O + O_2$ exchange reaction. Their results
give reasonably good agreement with experiment thus lending some credence to
the use of this potential surface.

The use of additive atom-atom potentials for the intermolecular
potential, V_{Ar-O_3}, arises because of the lack of a more accurate one. This
form has been used for most rare gas atom triatom energy transfer studies.
Redmon, et al.,[14] have shown that this choice of intermolecular potential pro-
vides a reasonable zeroth-order description adequate for qualitative purposes.
This is consistant with the goal of this work which is to gain insight into the
basic features of the collisional energy exchange process.

III. COMPUTATIONS

Calculations were performed at various fixed $Ar-O_3$ relative translational
energies. Translational energies of 0.5, 1.0, 2.0 and 4.0 kcal/mol were con-
sidered (corresponding to average kinetic energies for temperatures of 250,
500, 1000 and 2000 K). Ozone molecular energies of 25, 20, 15 and 10 kcal/mol
were used for each translational energy. (The ozone dissociation energy on
this potential surface is approximately 26 kcal/mol from the well minimum).
For each ozone internal energy, the molecular angular momentum was varied
between 0 and a value for which almost all the molecular energy was in rota-
tion. For calculations at fixed ozone angular momentum, impact parameters were
chosen randomly with maximum value 4Å. Calculations were done in batches of
500-1000 (usually 750) for each set of translational energy, molecular energy
and molecular angular momentum. Approximately 80,000 trajectories were com-
puted for this effort.

Calculations were also performed at fixed total molecular energy with
different partitionings of molecular energy (set equal to 25 kcal/mol) between
rotation and vibration. Initial vibrational energy was equal to 0, 12.5 and
25 kcal/mol. Each calculation was done for a relative translational energy of

2 kcal/mol and fixed impact parameter. Impact parameters were varied between
0 and 4Å in steps of 0.5Å. Batches of usually 1000 trajectories were done for
each set of initial conditions. About 27,000 trajectories were computed for
these initial conditions.

Multiple collision simulations of vibrationally-rotationally excited ozone
have also been performed. These calculations provide an approximate descrip-
tion of the temporal behavior, i.e. relaxation, of ozone in a bath of argon.
The relaxation of ensembles of 60 ozone molecules by 250 sequential collisions
with argon has been computed. Two cases were treated, both with initial total
molecular energy equal to 15 kcal/mol. The two batches differed by the amount
of angular momentum in the initial molecules. The relative translational ener-
gy for each collision in the sequence was fixed at a value of 2.388 kcal/mol
corresponding to an approximate bath temperature of 597°K. Some calculations
have also been performed for relaxation and dissociation of highly excited
ozone with 25 kcal/mol initial vibrational energy.

IV. RESULTS AND DISCUSSION

In our examination of energy transfer from highly excited ozone by colli-
sion with argon, our primary focus is the energy transfer from highly excited
ozone as a function of molecular angular momentum, i.e. the effect on energy
transfer of partitioning of the total molecular internal energy between rota-
tion and vibration. The primary quantity of interest then, is the mean energy
transferred in a collisional event, $\langle \Delta E \rangle$. This quantity is computed by suit-
ably averaging over an ensemble of trajectories with randomly chosen initial
conditions. Computed values of $\langle \Delta E \rangle$ versus initial ozone angular momentum are
shown in Fig. 1-4, for total ozone internal energies of 25, 20, 15 and
10 kcal/mol respectively. For each initial ozone internal energy, relative
translational energies of 0.5, 1.0, 2.0 and 4.0 kcal/mol were considered.
Molecular angular momentum was varied from zero (non-rotating molecule) to a
value such that almost all the internal energy was present as rotational
energy. Molecular angular momentum is plotted in units of 16 $\hbar$ for
convenience. The significance of these initial calculations to the relaxation
of nascent recombined ozone molecules will be discussed briefly later.

We discuss first the results for collisions with ozone with 25 kcal/mol internal excitation. The adiabatic dissociation energy of ozone via the reaction

$$O_3 \rightarrow O_2 + O$$

requires slightly more than 26 kcal/mol (from the well bottom). Thus in this case we are considering energy transfer from molecules excited to within 1 kcal/mol of their dissociation limit. The computed values of $\langle \Delta E \rangle$ are displayed in Fig. 1. Two points are immediately obvious and noteworthy. First, despite the high internal energy, molecules with low angular momentum gain energy per collision. This occurs for all relative translational energies. This gain in energy is correlated with a transfer of relative orbital angular momentum into molecular angular momentum. Second, as the molecular angular momentum is increased the energy transfer is reversed and the ozone molecules lose energy per collision. The results indicate that transfer of energy to ozone by collision occurs most readily by transfer into rotational energy.

The dominance of R→T energy transfer has also been observed by Suzukawa, Wolfsberg and Thompson[15] in their study of energy transfer between rare gas atoms and CO_2. They noted that at relative translational energies below several electron volts almost all the energy transferred in a collision was T→R energy transfer. Similar behavior was noted by Schatz and Redmon[16] in collisions of $O(^3P)$ with CO_2. Due to the difficulty of separating rotational and vibrational modes for highly excited molecules we have not attempted to compute a partitioning of energy transfer. However we note that for the calculations presented here the magnitude and size of the energy transfer directly correlates with changes in angular momentum of the ozone molecule and may be identified as primarily rotational energy transfer.

We note also the dependence of energy transfer on relative translational energy. At zero initial ozone angular momentum the average energy transferred per collision, $\langle \Delta E \rangle$, decreases with increasing translational energy, i.e. the amount of energy into the molecule increases with increasing translational

energy. Thus for the range of translational energy considered here, which corresponds to an approximate translational temperature range of 250-2000 K, the net effect of collisions with non-rotating ozone is to pump energy into the molecule and the magnitude of the energy transferred increases with the available translational energy. As the initial ozone angular momentum is increased the sign of the energy transfer changes and energy is transferred from the molecule. Energy transfer from the molecule as a function of molecular angular momentum occurs first for the lowest translational energy, 0.5 kcal/mol. Thus at intermediate values of the initial molecular angular momentum the average energy transfer increases with decreasing relative translational energy. As the molecular angular momentum is increased further the dependence of the energy transferred on translational energy changes again. At high values of initial molecular angular momentum $\langle \Delta E \rangle$ again increases with increasing translational energy. This transition occurs for the translational energies considered when a large fraction of the initial molecular energy of 25 kcal/mol is present as rotational energy. (Note however that at internal energies of 25 kcal/mol a strict separation of rotational and vibrational energy is not meaningful.)

A qualitative understanding of the dependence of energy transfer on molecular angular momentum may be obtained by consideration of the relative time scales of the translational, rotational and vibrational motion. Characteristic time scales for rotational and translational motion are similar. Thus exchange between these modes is quite facile. However the characteristic time scales (or frequencies) for vibration are much faster than translation. Hence the argon atom impinging on the vibrating ozone sees a rapidly fluctuating forcefield that averages the energy transfer over the course of a trajectory to zero.

At low initial angular momentum the impinging Ar atom sees a cold rotational mode and transfers energy into it. As mentioned, the vibrational motion is highly energetic but does not couple readily to the atom translation. Thus the net effect is energy transfer into the molecule. At intermediate values of molecular angular momentum the rotational mode and translational

energy are balanced so that they do not exchange energy. Energy exchange
between vibration and translation does not occur readily and the net effect is
that the average energy passes through zero for each translational energy. As
expected, this occurs at higher values of molecular angular momentum for
higher translational energies. At high values of molecular angular momentum
the impinging atom sees a hot rotational mode which readily loses energy to
translation and thus the net effect of collisions is that the molecule loses
energy. If molecular angular momentum could be increased indefinitely its
characteristic time scale would become too short to effectively couple with
translation and a decrease in energy transfer is expected.

The computed values of $\langle\Delta E\rangle$ for ozone internal energies of 20,15 and
10 kcal/mol are shown in Figs. 2, 3 and 4 respectively. These results are
extraordinarily similar to those for internally excited ozone of 25 kcal/mol
and are in accordance with the fact that energy transfer occurs primarily
between translational and rotational modes. At the lower vibrational energies
this should be even more true due to the shorter timescale of vibrational
motion as one goes down into the potential well. For this model of Ar-O_3 only
rotational energy transfer seems significant for internal energies spanning
almost the entire well depth (at the translational energies considered).

Selected calculations have been performed for $\langle\Delta E\rangle$ as a function of
impact parameter. Three cases for ozone with initially 25 kcal/mol internal
energy have been computed: (1) all internal energy in vibration, (2) the
internal energy divided equally between vibration and rotation and (3) all
internal energy as rotation. The calculations are for relative translational
energy of 2 kcal/mol. The results are displayed in Fig. 5.

For the non-rotating case (E_{ROT} = 0) the energy transfer is negative
at all impact parameters, i.e. energy is pumped into the molecule. This shows
that the net negative values discussed earlier which were averaged over impact
parameters had no positive energy transfer range. The magnitude of the energy
transfer increases initially due to the increasing orbital angular momentum of

the relative translational motion. At large impact parameters the energy
transfer decreases rapidly due to the fairly rapid drop-off of the potential
with intermolecular distance. For the case when all the initial triatom
energy is in rotation, very large average energy transfers are computed. In
this case the average energy transfer decreases monotonically with increasing
impact parameters. The case of equally divided initial rotational and vibra-
tional energy resembles the $E_{VIB} = 0$ case. Here the magnitude of energy
transferred per collision is somewhat reduced due to the lesser amount of
rotational energy.

It is also of interest to examine the distribution of energy transfers
per collision. Distributions of magnitudes of energy transfers are shown in
Fig. 6 for initial molecular excitation of 25 kcal/mol, and translational
energy of 2 kcal/mol for two values of initial angular momentum: 31 $\hbar$ and
125 $\hbar$. As before, positive values of energy transfer signify that energy is
lost from the molecule while for negative values the molecule gains energy in
a collision. As seen in both Figs. 6 and 7 most collisional encounters lead
to small energy transfers due to the fairly large maximum impact parameter of
4Å used in the calculations. For the lower value of molecular angular momen-
tum there are very few encounters in which more than 1-2 kcal/mole is trans-
ferred out of the molecule. Hence as previously mentioned the net collisional
transfer is into the ozone molecule despite its initial high vibrational-
rotational excitation. The higher molecular angular momentum case is quite
different. The average energy transfer is from the molecule to relative
translational motion. Additionally there is a substantial number of large
energy transfer collisions. The total cross section for energy transfers
greater than 10 kcal/mol is computed to be 2.4 Å^2. It is clear that the pre-
sence of large molecular angular momentum qualitatively changes the energy
transfer. A similar result was obtained by Stace and Murrell.[5]

Multiple collision calculations were performed to simulate the relaxation of excited ozone in a bath of argon. Two cases were treated in this preliminary effort; (a) molecules initially excited 15 kcal/mol with angular momentum equal to 16 $\hbar$ and (b) molecules excited 15 kcal/mol with angular momentum equal to 63 $\hbar$. The average molecular energy versus collision number is plotted in Fig. 8 for both cases. Average molecular angular momentum versus collision number is shown in Figure 9. A fixed value of the relative translational energy equal to 2.3 kcal/mol was chosen.

The effect of initial molecular angular momentum on energy relaxation is readily seen. Initially the low or angular momentum ensemble gain energy as angular momentum is built up by collisions. On the other hand the higher angular momentum ensemble undergo a rapid energy loss initially associated with a loss in average molecular angular momentum. The peak in the average molecular energy of the low initial angular momentum ensemble correlates well with the increase in molecular angular momentum shown in Fig. 9. Additionally, the rapid energy relaxation of the higher initial angular momentum is readily associated with the initial decrease in the ensemble angular momentum. These observations reinforce the observation that energy transfer is primarily between translational and rotational modes.

An implication of this behavior is that energy relaxation of highly excited ozone occurs via a V→R→T mechanism in this classical model. Thus it may not be possible to fully decouple rotational and vibration relaxation. The highly excited vibrational modes act as rotational energy sources causing full rotational relaxation (to equilibrium) to occur on a time scale much longer than without large vibrational excitation. This behavior has been observed in the relaxation of highly excited diatomic molecules.[10] This point requires further study. The difference in behavior between the two ensembles is highly transitory. After approximately fifty collisions the characteristic relaxation behaviors of both ensembles become identical. This behavior, however, has serious implications for the early relaxation of recombined molecules formed very close to the dissociation limit. For molecules with low

angular momentum, energy will be pumped into the molecule as angular momentum is increased by collisions. This will lead to dissociation for some molecules. However, molecules formed with high angular momentum will lose energy more readily and should have a substantially lower probability of dissociation.

Preliminary calculations of the relaxation of 25 kcal/mol vibrationally excited ozone (with zero angular momentum) show that on the order of one-third of the molecules are dissociated after 25 collisions. Dissociation, curiously, is a very low probability single collision event. Approximately 10,000 trajectories were computed in which the total energy exceeded the ozone dissociation energy. However only one trajectory was observed to lead to dissociation. The multicollisional calculations imply that dissociation is quite important for very highly excited molecules and makes a very significant contribution to the computed rates of recombination and relaxation. These early calculations would seem to establish the need for describing non-equilibrium effects in any realistic description of ozone recombination.

This work is part of an ongoing study of ozone recombination. Future work will treat the dynamics of quasibound O_3 formation by $O+O_2$ collisions, collisional stabiization of quasibound O_3 complexes and collisional relaxation of recombined ozone molecules.

V. ACKNOWLEDGMENT

REFERENCES

1. a) Stair, Jr., A. T., Ulwick, J. C., Baker, D. J., Wyatt, C. L. and Baker, K. C., Geophys. Rec. Lett. 1974, 1, 117.

    b) Stair, Jr., A. T., Ulwick, J. C. Baker, K. C. and Baker, D. J., in Atmospheres of the Earth and the Planets, edited by B. M. McCormack, D. Reidel, Dorerecht, Holland, 1975, 335-346.

2. a) Rawlins, W. T., Caledonia, G. E. and Kennealy, J. P., J. Geophys. Res., 1981, 86, 5247.

    b) Rawlins, W. T. and Armstrong, R. A., "COCHISE Observations of O_3 Formed by Three-Body Recombination of O and O_2," AFGL-TR-82-0273, Air Force Geophysics Laboratory, Hanscom AFB, MA, 1982.

3. Gallucci, C. R. and Schatz, G. C., J. Phys. Chem., 1982, 86, 2352.

4. Brown, N. J. and Miller, J. A., J. Chem. Phys. 1984, 80, 5568.

5. Stace, A. J. and Murrell, J. N., J. Chem. Phys., 1978, 68, 3078.

6. Murrell, J. N., Sorbie, K. S. and Varandas, A. J. C., Mol. Phys., 1976, 32, 1359.

7. Varandas, A. J. C. and Murrell, J. N., Chem. Phys. Lett., 1982, 88, 1.

8. Carter, S., Mills, I. M., Murrell, J. N. and Varandas, A. J. C., Mol. Phys. 1982, 45, 1053.

9. Mulloney, T. and Schatz, G. C., Chem. Phys. 1980, 45, 213.

10. Schatz, G. C., in Molecular Collision Dynamics, edited by J. M. Bowman, Springer-Verlag, Berlin, 1983, 25.

11. Gelb, A., Kapral, R. and Burns, G., J. Chem. Phys. 1972, 56, 4531.

12. Bunker, D. C., Meth. Comp. Phys. 1972, 10, 287.

13. Porter, R. N. and Raff, L. M., in Dynamics of Molecular Collisions Part B, edited by W. H. MIller, Plenum New York, 1976.

14. Redmon, M. J., Bartlett, R. J., Garrett, B. C., Purvis, G. D., Saatzer, P. M., Schatz, G. C. and Sharitt, I., in Potential Energy Surfaces and Dynamics Calculations, edited by D. G. Truhlar, Plenum, New York, 1981, 771.

15. Suzukawa, Jr., H. H. and Wolfsberg, M. J. Chem. Phys., 1978, 68, 455.

16. Schatz, G. C. and Redmon, M. J., Chem. Phys., 1981, 58, 195.
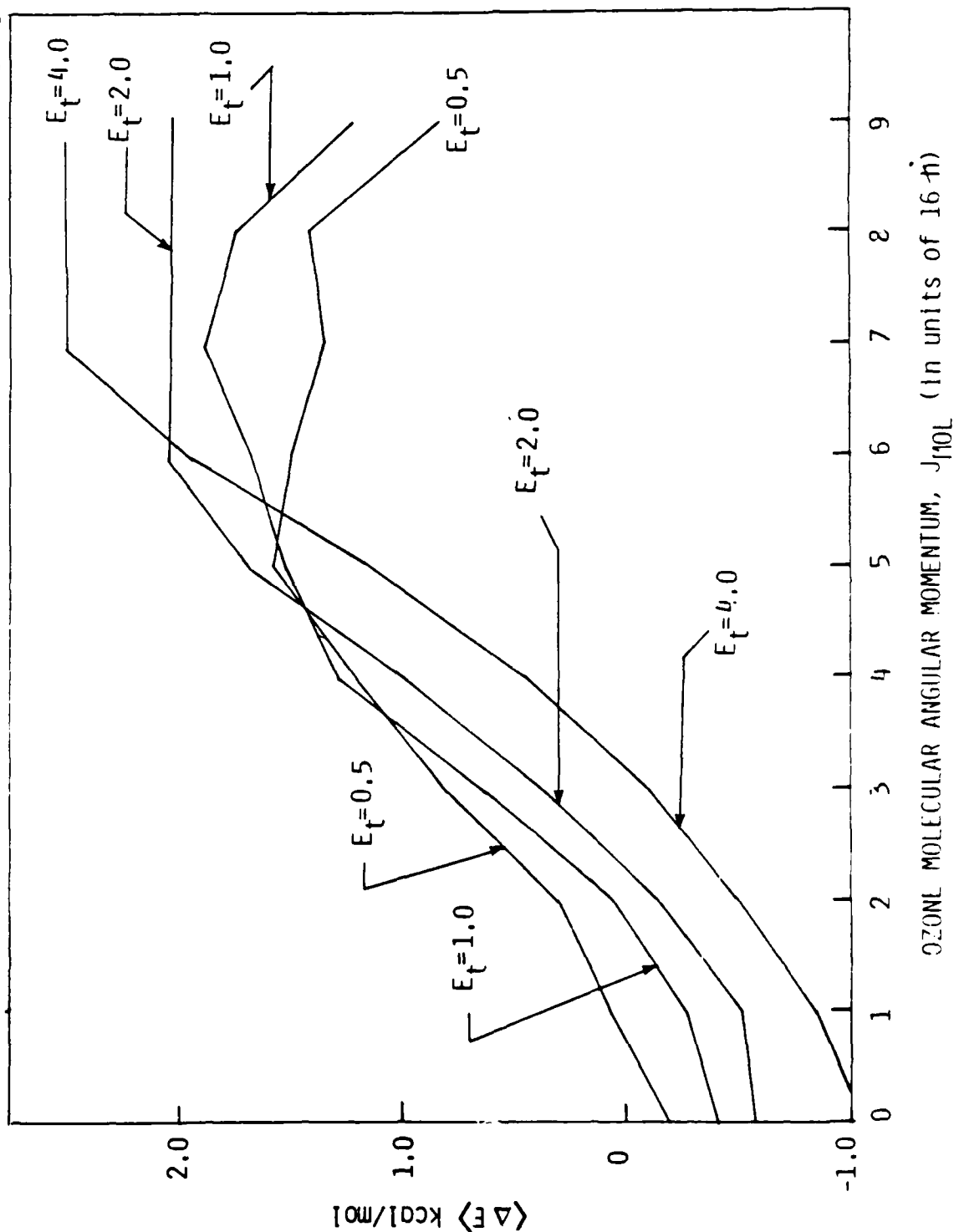
Fig. 1. Average energy transferred per collision, ⟨ΔE⟩, between ozone and argon as a function of initial ozone molecular angular momentum, J_{mol}, for relative translational energies of .5, 1.0, 2.0 and 4.0 kcal/mol. Initial ozone molecular energy equal to 25 kcal/mol.

INITIAL OZONE ENERGY = 20 KCAL/MOL

Fig. 2. Average energy transferred per collision, $\langle\Delta E\rangle$, between ozone and argon as a function of initial ozone molecular angular momentum, J_{mol}, for relative translational energies of .5, 1.0, 2.0 and 4.0 kcal/mol. Initial ozone molecular energy equal to 20 kcal/mol.

INITIAL OZONE ENERGY = 15 KCAL/MOL

6004-2

Fig. 3. Average energy transferred per collision, $\langle \Delta E \rangle$, between ozone and argon as a function of initial ozone molecular angular momentum, J_{mol}, for relative translational energies of .5, 1.0, 2.0 and 4.0 kcal/mol. Initial ozone molecular energy equal to 15 kcal/mol.

INITIAL OZONE ENERGY = 10 KCAL/MOL

6004-3
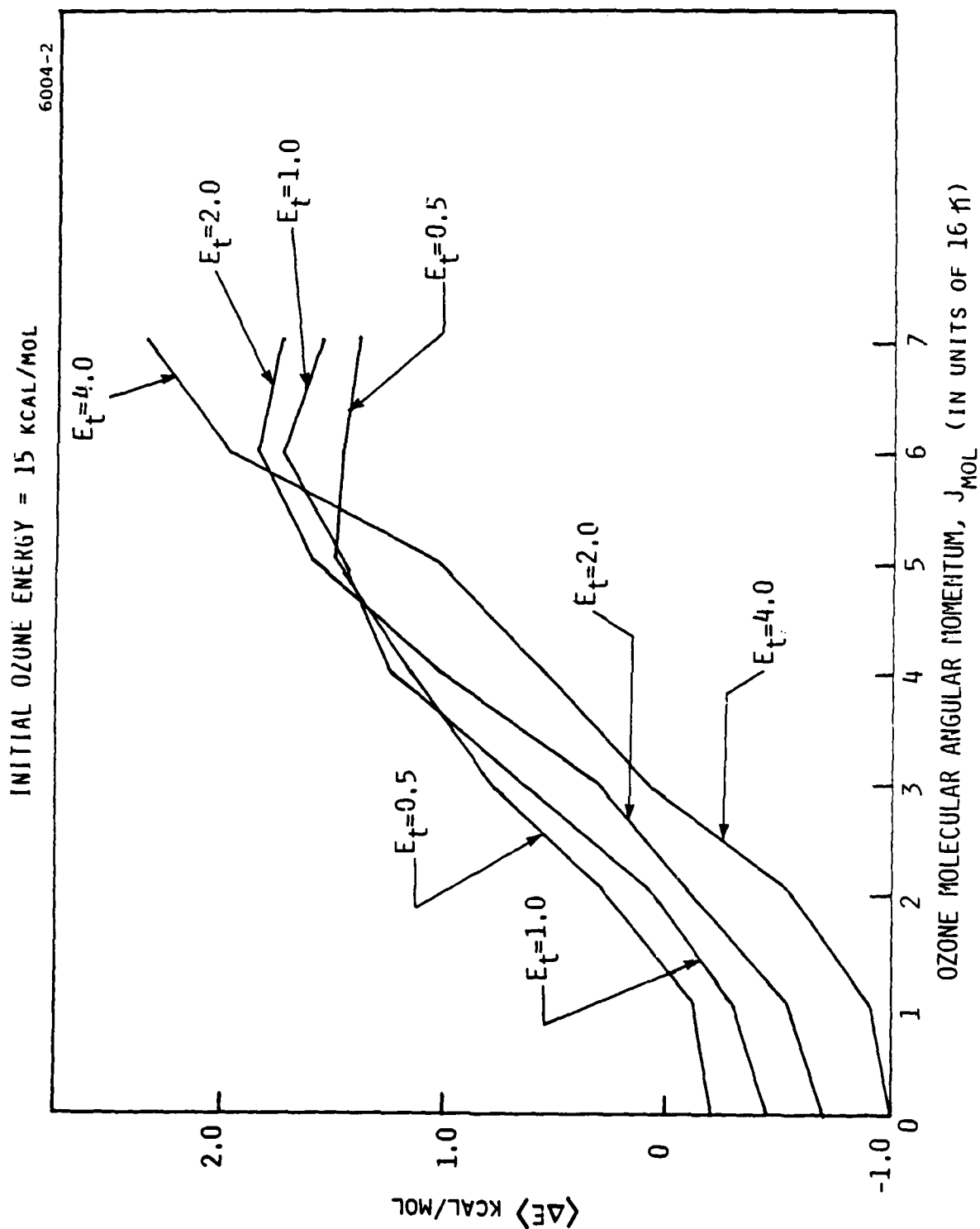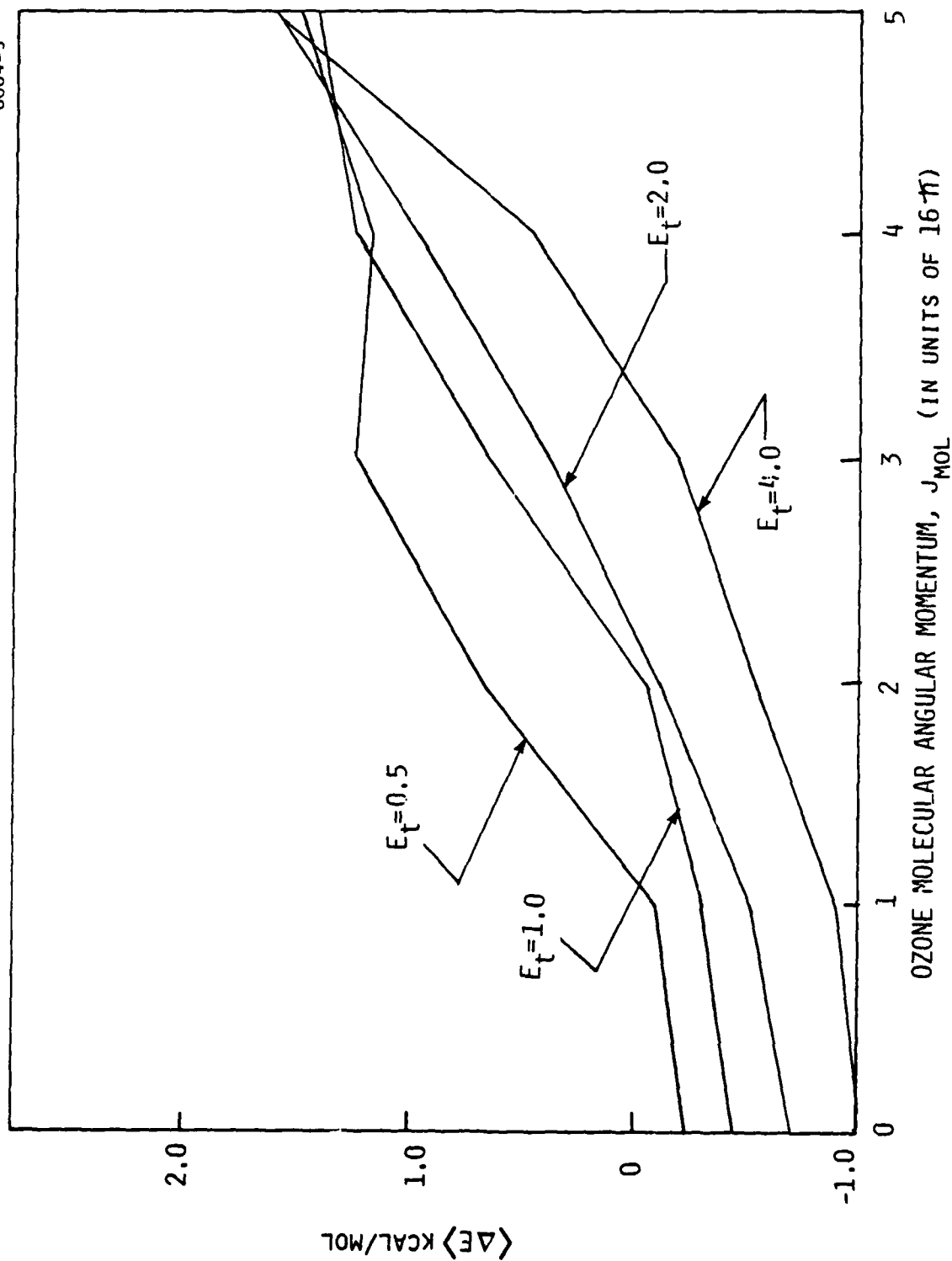
Fig. 4. Average energy transferred per collision, $\langle \Delta E \rangle$, between ozone and argon as a function of initial ozone molecular angular momentum, J_{mol}, for relative translational energies of .5, 1.0, 2.0 and 4.0 kcal/mol. Initial ozone molecular energy equal to 10 kcal/mol.

Fig. 5. Average energy transferred per collision, ΔE(b), between ozone and argon as a function of impact parameter for initial ozone rotational energy equal to 0, 12.5 and 25 kcal/mol. Total initial ozone molecular energy is equal to 25 kcal/mol.

E-20

ENERGY TRANSFERRED, ΔE (kcal/mol)

RELATIVE FREQUENCY

6004-8

Fig. 6. Relative frequency of energy transfers, ΔE, in argon-ozone collisions at initial relative translational energy of 2 kcal/mol, ozone molecular energy of 25 kcal/mol and initial molecular angular momentum equal to 31 ℏ.
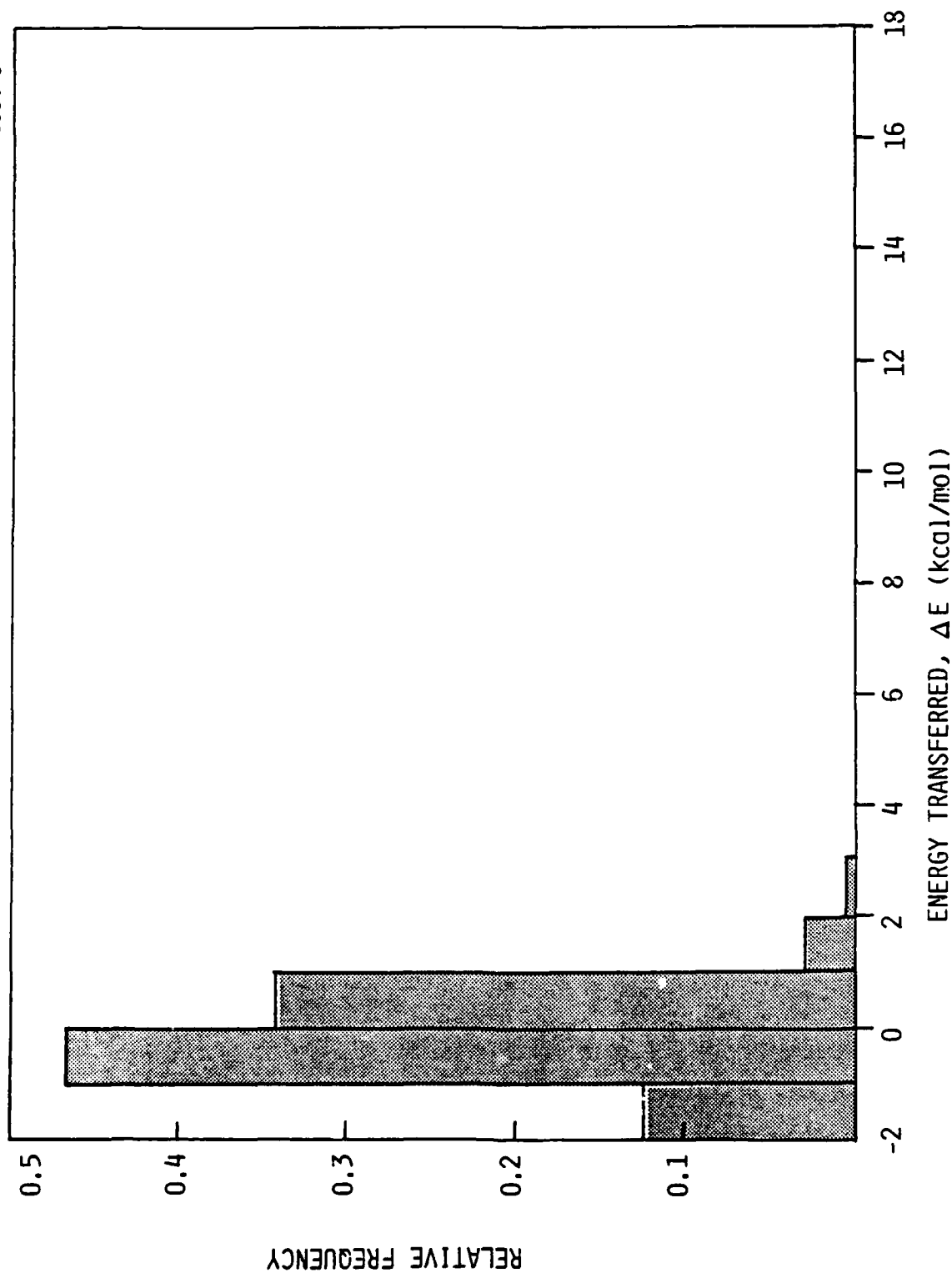
ENERGY TRANSFERRED, ΔE (kcal/mol)

RELATIVE FREQUENCY
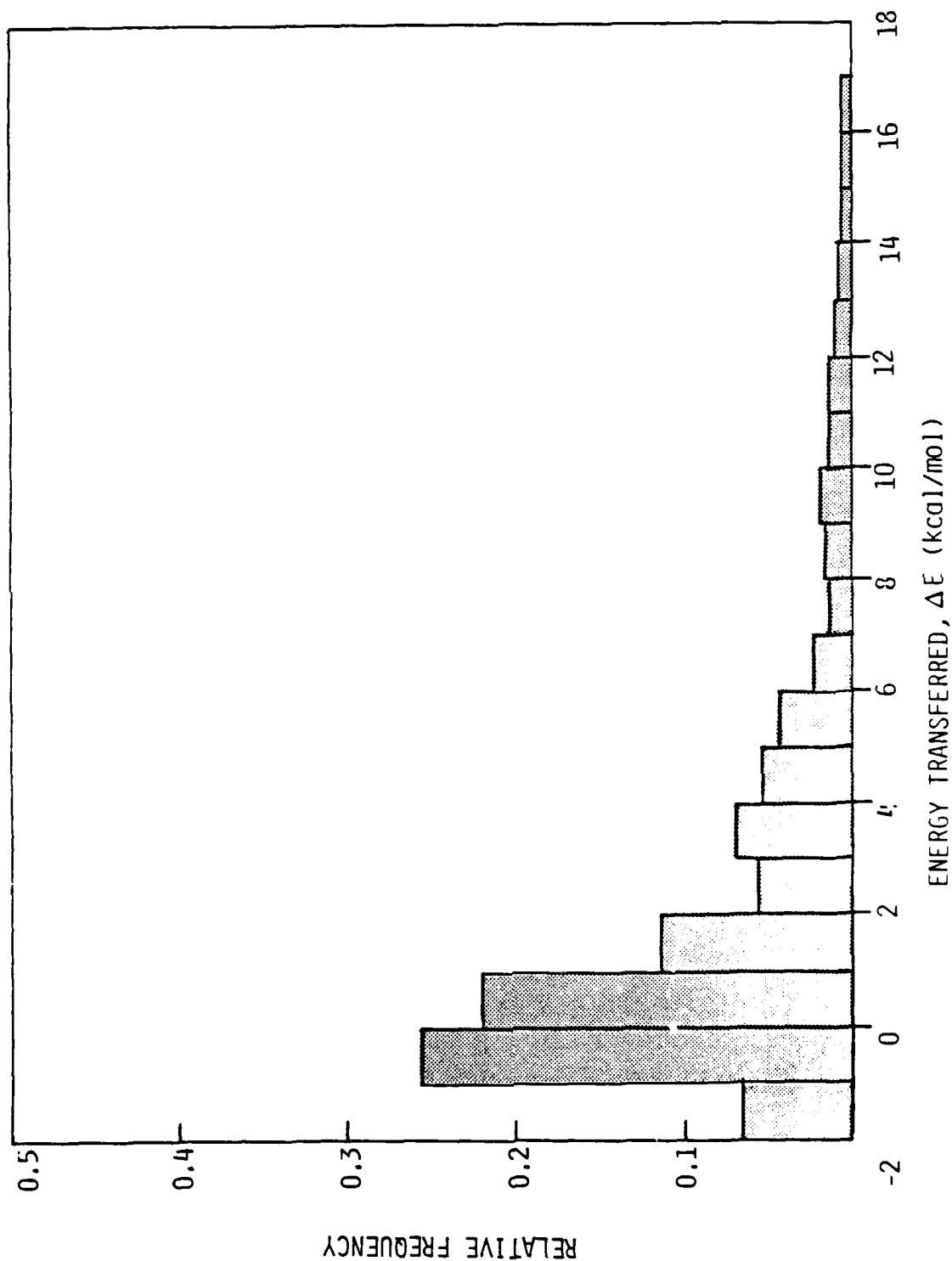
Fig. 7. Relative frequency of energy transfers, ΔE, in argon-ozone collisions at initial relative translational energy of 2 kcal/mol, ozone molecular energy of 25 kcal/mol and initial molecular angular momentum equal to 125 ℏ.

Fig. 8. Average molecular internal energy of an ensemble of ozone molecules as a function of number of collisions with argon atoms. The results for two ozone ensemble initial conditions are shown: (1) total ozone energy equal to 15 kcal/mol and initial ozone angular momentum, J_{int}, equal to 16 $\hbar$ and (2) total ozone energy equal to 15 kcal/mol and $J_{int} = 63\hbar$. Relative translational energy is equal to 2.3 kcal/mol in both cases.

APPENDIX F

QUANTUM CHEMICAL CALCULATIONS IN O_3

F

APPENDIX F
QUANTUM CHEMICAL CALCULATIONS ON O_3

D. Noid and M. Koszykowski

The ultimate goal of this project is a theoretical description of $O-O_3$ recombination dynamics. A prerequisite for such calculations is a reasonably accurate representation of the O_3-O potential energy surface. To this end ab initio quantum mechanical calculations are to be done at Sandia National Laboratories. As a first step in this effort we computed energies at selected configurations on the ozone potential surface. The results of these calculations will be used for evaluating the currently-used Murrell et al. ozone potential surface and for reparameterizing that surface if necessary. The results of the ozone potential surface calculation techniques and results are presented below.

Studies have shown that the calculation of spectroscopic properties and collision cross sections are frequently very sensitive to changes in the shape of the potential energy surface used for the calculations. No complete quantum chemically calculated surfaces exist for this system, primarily since calculations on three or four heavy atom systems are prohibitively computer intensive. A carefully constructed surface of O_3 does not exist but was fit with a heavy reliance on existing experimental data. In order to test this surface and possibly improve the parameters we have performed a series of quantum chemistry calculations on O_3 which sample various regions of the surface, especially at extended internuclear separations.

There are numerous approximations one can employ in these quantum chemical calculations. We will briefly discuss three types of calculations: (1) Hartree-Fock, (HF) (2) Configuration-Interaction, (CI) and (3) Many Body Perturbation Theory, (MBPT) and list the considerations which led us to use MBPT.

Hartree-Fock calculations are the simplest method we will discuss and also form the starting basis for the other two methods. We write the wavefunction ψ_0 as a determinant of one electron spin orbitals χ_i

$$\psi_0 = (n!)^{-1/2} \det(\chi_1 \cdot \cdot \cdot \chi_n)$$

where n is the number of electron and the χ are electron functions which are a product of space and spin. In the linear combination of atomic orbitals approximation, the χ_i are expanded in terms of N functions ϕ_j

$$\chi_i = \sum_{1=i}^{N} C_{ij}\phi_j$$

and in our case the ϕ_j are Gaussian approximations to Slater orbitals centered on the atoms. We now solve for the C_{ij} by minimizing the expectation value of the total energy variationally

$$E = \int \ldots \int \psi_0^* H \psi_0 d\tau$$

where H is the non-relativistic, non-magnetic Born-Oppenheimer Hamiltonian. This gives us the Hartree-Fock energy and wavefunction. In effect we have solved the equation for each electron in the average field of the (n-1) remaining electrons. Electrons, however, respond to each other via Coulomb's law instantaneously, i.e., the electrons do not move in an averaged field but are correlated. This correlation energy between the pairs of electrons is neglected in the Hartree-Fock treatment and is defined as

$$E_\rho = E_{exact} - E_{HF}$$

The self-consistent field (SCF) or Hartree-Fock energy is generally good for evaluating the overall surface topology and is excellent for calculations of

equilibrium geometries. However as the bond displacements increase the correlation energy increases and a correlation correction must be made to adequately describe the long-range interactions.

The most common method of calculating the correlation energy is commonly referred to as the Configuration Interaction (CI) method. The SCF wavefunction contains n orbitals $(\chi_1 . . . \chi_n)$ which are occupied and (N-n) orbitals $(\chi_{n+1} . . . \chi_n)$ which are virtual or unoccupied. An obvious way to go beyond the HF calculation is to variationally determine the total energy by including wave functions with different configurations, i.e., each new configuration replaces an occupied orbital from the SCF wavefunction with a virtual orbital. A common method of classifying configurations is by examining the total number of orbitals in the wave function which differ from the SCF reference wavefunction. We write the CI wavefunction as

$$\psi_{CI} = C_0 \psi_0 + \sum_i C_i \phi_i^S + \sum_j C_j \phi_j^D + . . .$$

where a single excitation function, ϕ_i^S, differs from the SCF reference χ_0 by one orbital and the double excitation function ϕ_j^D by two, and so on. The CI coefficients, C_i, are then determined variationally to yield the lowest possible total energy. In the limit of a complete basis set $(N \to \infty)$ and where all possible substitutions are included in ψ_{CI}, the variational energy approaches the correct non-relativistic Born-Oppenheimer results. Errors arise from a truncation of the functions used to determine the SCF reference wavefunction and from the truncation of the excitation functions series in ψ_{CI}. The reference wavefunction ψ_0 will typically be the same for a CI or Many Body Perturbation Theory (MBPT) calculation, however, for a molecule even as small as water, ψ_{CI} becomes a function of a very large number of basis functions. Because of this one must truncate the expansion and eliminate unimportant configurations. In general one can show that

$$\langle \psi_0 | H | \phi^T \rangle = \langle \psi_0 | H | \psi^0 \rangle = 0)$$

In words, the matrix elements between the reference wavefunctions and triple and quadruple excitations is zero. Thus to first order, only single and double excitations contribute. Because of this, many CI calculations attempt to include all single and double excitations in the expressions for ψ_{CI}. To go beyond this, generally more than one reference wavefunction is used.

In many body perturbation theory (MBPT) we will again begin with the SCF wavefunction (ψ_0) as our reference and attempt to account for E_c, the correlation energy. The concept of substitution or excitation functions described in the above section on CI calculations will carry over to the MBPT calculations. In MBPT one can write the wavefunction, ψ_p, as

$$\psi_p = e^T |\phi\rangle$$

where T is an excitation operator defined as

$$T = T_S + T_D + T_T + T_Q \ldots$$

where S, D, T, Q refer to Single, Double, Triple and Quadruple substitutions respectively. One can write T_n, in general, where n refers to the number of excitations as

$$T_n = \frac{1}{n!} \sum_{\ell,a} t_\ell^a \chi_a^+ \cdot \cdot \cdot \chi_\ell$$

where the sum over (a) represents excited orbitals and ℓ occupied orbitals. The total energy is now given by

$$E_{MBPT} = \langle \phi_0 | He^T | \phi_0 \rangle$$

What must be determined to evaluate E_{MBPT} are the t_ℓ^a from above. An equivalent expression which makes the perturbation expansion more clear is

F-4

$$E_{MBPT} = \sum_{K=0}^{\infty} \langle \phi_0 | H[(E_0 - H_0)^{-1} H]^k | \phi_0 \rangle$$

where the sur is over only so called linked diagrams, H_0 has eigenfunctions ϕ_0 and the expansior potential $V - H - H_0$, the perturbation. The $k = 0$ term gives the reference energy and for $k > 0$ correlation corrections are included. In practice the MBPT total energy is calculated by truncating te T operator expansion and projecting $He^{Tn}|\phi_0\rangle$ onto the appropriate n-space. This leads to a set of nonlinear coupled equations for the t_ℓ^a coefficients which correspond to the CI expansion coefficients. The equations are solved iteratively and E_{MBPT} evaluated. In practice T_4 is an upper limit which corresponds to quadruple substitutions. The series is an oscillatory convergent sum, which in practice has proven to be at least as accurate as E_{CI} with single and double excitations included.

The best possible method to use would be a full CI (all possible configurations) with a complete basis set. However since the number of configurations is proportional to $\langle n|^\ell$, where n is the number of basis functions and ℓ is the level of excitation, it would be prohibitive to even include all single and double excitations. This truncation causes the loss of size-consistency. Size consistency implies that the energy calculated for A and B far apart is the sum of the energy calculated for A and B separately. In a size extensive calculation the energy is proportional to the size of the system. These properties are very important if one wishes to compute correct relative energies on a potential energy surface. MBPT, on the other hand, is guaranteed to have the correct size-dependence because the expansions contain only the so-called linked diagrams. In addition because of the computational efficiency of MBPT, calculations can be performed up to fourth order in the perturbation expansion and include single, double, triple and quadruple excitations in the calculation of the correlation energy. For these reasons we have chosen to use MBPT in our investigation of the potential energy surface of O_3.

All calculations reported here were performed with a split valence plus polarization basis set, the so-called 6-31G** basis. This adequately spans the s, p space of occupied O_3 orbitals and includes one set of polarization

orbitals or d-functions. Test calculations without any polarization functions proved to be totally inadequate. Adding additional polarization functions or f-orbitals does not significantly alter the relative energies but does tremendously increase the computation time making it impractical to do a survey of the surface with this basis set. In Table 1 we compare six different calculations at various geometries where one bond distance and the O_3 bond angle were varied. The energies listed refer to Hartree-Fock (HF), second order perturbation theory (MP2), third order (MP3) and fourth order (MP4) with various types of substitutions accounted for. The dipole moment has also been listed for possible spectroscopic use in future dynamics calculations. From this comparison we see that MP4 (SDTQ) is significantly better than the lower levels and all further calculations will be done at this level. In addition we note that while the total energy is changing from level to level the overall shape of the surface the atoms move on is converging rapidly. In Table 2 we list MP4(SDTQ) energies and the dipole for a number of additional geometries. Next the relative shape of the MP4(SDTQ) points should be compared to the existing surface to determine if additional regions are important or if the existing surface can be improved.

TABLE F-1. Computed Ozone Total Borne-Oppenheimer Energies and Molecular Dipole Moment.

R1(Å)	θ(degs.)	HF	MP2	MP3	MP4(DQ)	MP4(SDQ)	MP4(SDTQ)	DIPOLE (a.u.)
				(ENERGY IN HARTREES)				
1.204	119.015	-224.2614	-224.8491	-224.8200	-224.8230	-224.8349	-224.8677	0.826
1.004	119.015	-224.1670	-224.6961	-224.6850	-224.6878	-224.6978	-224.7198	1.804
1.104	119.015	-224.2440	-224.8040	-224.7842	-224.7871	-224.7976	-224.8246	1.173
1.304	119.015	-224.2521	-224.8548	-224.8110	-224.8236	-224.8402	-224.8781	1.095
1.404	119.015	-224.2352	-224.8275	-224.7979	-224.8032	-224.8257	-224.8631	1.653
1.504	119.015	-224.2212	-224.7862	-224.7685	-224.7764	-224.7975	-224.8283	1.994
1.604	119.015	-224.2121	-224.7534	-224.7440	-224.7534	-224.7706	-224.7960	1.998
1.704	119.015	-224.2063	-224.7211	-224.7264	-224.7364	-224.7510	-224.7735	1.808
1.804	119.015	-224.2024	-224.7154	-224.7139	-224.7242	-224.7369	-224.7575	1.549
1.904	119.015	-224.1995	-224.7039	-224.7048	-224.7152	-224.7265	-224.7457	1.286
1.204	115.015	-224.2599	-224.8475	-224.8191	-224.8219	-224.8334	-224.8660	0.916
1.204	117.015	-224.2611	-224.8487	-224.8199	-224.8228	-224.8346	-224.8672	0.871
1.204	113.015	-224.2579	-224.8455	-224.8174	-224.8201	-224.8314	-224.8638	0.959
1.204	111.015	-224.2551	-224.8425	-224.8148	-224.8173	-224.8285	-224.8608	1.002
1.204	109.015	-224.2512	-224.8985	-224.8113	-224.8136	-224.8246	-224.8567	1.044
1.204	121.015	-224.2611	-224.8487	-224.8193	-224.8225	-224.8345	-224.8675	0.780
1.204	123.015	-224.2601	-224.8475	-224.8180	-224.8213	-224.8335	-224.8665	0.734
1.204	125.015	-224.2584	-224.8457	-224.8160	-224.8194	-224.8317	-224.8649	0.687
1.204	127.015	-224.2562	-224.8433	-224.8134	-224.8169	-224.8294	-224.8626	0.640
1.204	129.015	-224.2534	-224.8402	-224.8102	-224.8138	-224.8275	-224.8597	0.592
1.204	132.015	-224.2482	-224.8345	-224.8045	-224.8082	-224.8211	-224.8544	0.522
1.204	135.015	-224.2421	-224.8277	-244.7977	-224.8015	-224.8146	-224.8479	0.451
1.204	140.015	-224.2298	-224.8138	-224.7843	-224.7881	-224.8014	-224.8347	0.337

TABLE F-2. Ozone Borne-Oppenheimer Energies and Dipole Moment
for Several Extended Moleular Configurations
(MP4 (SDTQ) Level of Calculation)

r1(Å)	r2(Å)	θ(degrees)	E(hartrees)	Dipole (a.u.)
1.204	1.204	140.015	-224.8347	0.3372
1.1043	1.1043	119.0154	-224.7780	0.9289
1.0043	1.1043	119.0154	-224.6679	1.2584
1.3043	1.1043	119.0154	-224.8362	1.6999
1.4043	1.1043	119.0154	-224.8222	2.1678
1.5043	1.1043	119.0154	-224.7942	2.3591
1.1043	1.7043	119.0154	-224.7483	2.0423
1.0043	1.0043	119.0154	-224.5503	0.9932
1.0043	1.3043	119.0154	-224.7351	2.3437
1.0043	1.4043	119.0154	-224.7268	2.7145
1.0043	1.5043	119.0154	-224.7068	2.8204
1.0043	1.6043	119.0154	-224.6863	2.7042
1.0043	1.7043	119.0154	-224.6682	2.4645
1.3043	1.4043	119.0154	-224.8778	1.0913
1.3043	1.5043	119.0154	-224.8400	1.6440
1.3043	1.3043	119.0154	-224.8890	0.6968
1.3043	1.6043	119.0154	-224.8004	1.7915
1.3043	1.7043	119.0154	-224.7739	1.6685
1.4043	1.4043	119.0154	-224.8753	0.5650
1.0543	1.2043	119.0154	-224.7827	1.4712
1.1543	1.2043	119.0154	-224.8515	0.9385
1.2543	1.2043	119.0154	-224.8761	0.8866
1.3543	1.2043	119.0154	-224.8740	1.3748
1.0543	1.1043	119.0154	-224.7367	1.1297
1.1543	1.1043	119.0154	-224.8069	0.9874
1.2543	1.1043	119.0154	-224.8339	1.4255
1.3543	1.1043	119.0154	-224.8320	1.9587
1.3543	1.1543	119.0154	-224.8579	1.6675
1.2543	1.1543	119.0154	-224.8603	1.1290
1.1543	1.1543	119.0154	-224.8347	0.8816
1.0543	1.1543	119.0154	-224.7639	1.2175

APPENDIX G

EXCITATION OF NO($A^2\Sigma^+$) BY ENERGY TRANSFER
FROM $N_2(A^3\Sigma_u^+)$

APPENDIX G

EXCITATION OF NO(A$^2\Sigma^+$) BY ENERGY TRANSFER
FROM N$_2$(A$^3\Sigma_u^+$)

The energy transfer reaction between N$_2$(A$^3\Sigma_u^+$) and NO can be an important loss process for N$_2$(A) in an aurora or otherwise highly disturbed atmosphere. The primary product from this interaction is the NO(A$^2\Sigma^+$) state which radiates on the NO γ bands in the uv. Because the potential minima of the A and X states of NO are offset, most of the γ-band radiation will produce vibrationally excited NO. In a highly dosed atmosphere, this reaction could conceivably become a significant source of NO(v). The vibrational distribution of the ground state NO will depend to some extent upon the vibrational distribution of the NO(A) produced, which is in turn dependent upon the vibrational distribution of the N$_2$(A) involved in the energy transfer reaction. In this appendix, we detail the state-to-state kinetics of the energy transfer reaction between N$_2$(A) and NO.

During the course of these measurements, we found it necessary to re-examine the problem of the variation of the NO(A--X) transition moment with r-centroid. Our results show that contrary to what the majority of scientists believe, the transition moment of the NO(A--X) varies significantly with r-centroid. These findings impact a host of previous studies including measurements of mesospheric NO column densities, interpretations of NO(v) product yields in reactions such as that between N(^{4}S) and O$_2$, and even the reliability of uv spectrometer calibration which in turn affects all subsequent measurements made with these faulty calibrations. This appendix substantiates these findings.

2. EXPERIMENTAL

The apparatus is a two-inch flow tube pumped by a Leybold-Heraeous Roots blower/forepump combination capable of producing linear velocities up to 5×10^3 cm s^{-1} at pressures of one torr. The flow tube design is modular (see Figure G-1), with separate source, reaction, and detection sections which clamp together with O-ring joints. We have described it in its various configurations a number of times.[1-6] The detection region is a rectangular stainless-steel block bored out internally to a two-inch circular cross section and coated with Teflon® (Dupont Poly TFE #852-201) to retard surface recombination of atoms.[7-11] Use of a black primer prior to the Teflon® coating reduces scattered light inside the block dramatically. The block has two sets of viewing positions consisting of four circular ports each on the four faces of the block. These circular ports accommodate vacuum-ultraviolet resonance lamps, VUV and visible monochromator interaces, laser delivery side-arms and a spatially filtered photomultiplier/interference filter combination.
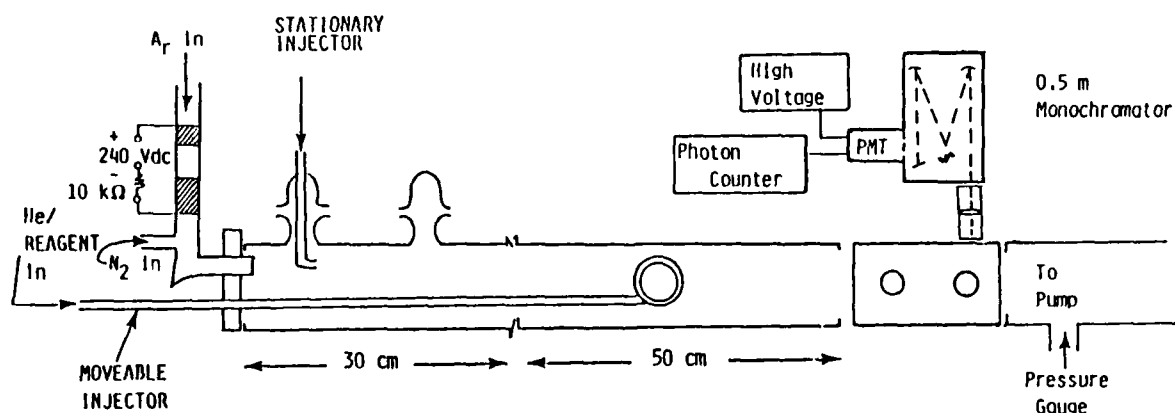
Figure G-1. Flow tube apparatus configured for $N_2(A)$ decay kinetics measurements.

G-2

In these experiments a suprasil lens collected light from the center of the flow tube and focussed it on the entrance slit of a 0.5 m Minuteman mono-chromator which is outfitted with a 1200 groove mm^{-1} grating blazed at 250 nm. A thermoelectrically-cooled photomultiplier (HTV/R943-02) detected photons with the aid of an SSR 1105 photon-counting rate meter. A laboratory computer system digitized the analog output from the rate meter and stored the informa-tion on floppy disks for further processing. The computer system comprises an IBM PC with 512 K of RAM, two 360 K diskette drives, a monochrome monitor, and a 160 cps dot-matrix printer with graphics capability. Data Translation manu-factures the I/O system (DT2801A), which features 16 channels of A/D inputs, two channels of D/A output, two 8-bit digital I/O ports, software programmable gain, single-ended or differential input, and data acquisition rates as fast as 14 kHz. Laboratory Technologies Inc. software package "Real-time Labora-tory Notebook," interfaces the computer to the D/A board and organizes data in a form compatible for analysis using the "Lotus 123" business spreadsheet software or for sending to the PRIME 400 computer in PSI's computer center for analysis on that machine. Much of the analysis revolves around least-squares fitting of spectra. Our code[12] generates basis functions consisting of a syn-thetic electronic spectrum for a unit population in each vibrational level of each electronic state appearing in the spectral region of interest. A least squares routine then finds the populations of each vibronic band which when multiplied by the appropriate basis function gives a composite spectrum most nearly matching the experimental spectrum.

Standard quartz-halogen and D_2 lamps were used to calibrate the spectral system for relative response as a function of wavelength. Excellent agreement between observed and calculated intensities of a number of bands of the $N_2(A\ ^3\Sigma_u^+ - X\ ^1\Sigma_g^+)$ system between 220 and 400 nm confirmed the reliability of the UV calibration.

The reaction between metastable $Ar(^3P_{0,2})$ and molecular nitrogen produces the metastable nitrogen molecules, $N_2(A^3\Sigma_u^+)$[13,14]. This transfer excites $N_2(C^3\Pi_u)$[15] which quickly cascades radiatively to the metastable $A^3\Sigma_u^+$ state via the $B(^3\Pi_g)$ state. A hollow-cathode discharge source operating at 240 V.d.c. and 3 mA produces the argon metastables. The argon and nitrogen are purified by flowing them through traps filled with 5A molecular sieve. Since

$N_2(C\,^3\Pi_u - B\,^3\Pi_g)$

$\Delta V = 3 \quad 2 \quad 1 \quad 0 \quad -1 \quad -2 \quad -3$

$N_2(A\,^3\Sigma_u^+ - X\,^1\Sigma_g^+)$

$V' = 0$
$V'' = 3 \quad 4 \quad 5 \quad 6 \quad 7 \quad 8 \quad 9 \quad 10 \quad 11$

$V' = 1$
$V'' = 3 \quad 4 \quad 5 \quad 7 \quad 8 \quad 9 \quad 10 \quad 11 \quad 12$

$V' = 2$
$V'' = 6 \quad 7 \quad 8 \quad 10 \quad 11 \quad 12$

$NO(A\,^2\Sigma^+ - X\,^2\Pi)$ $V' = 0$
$V'' = 0 \quad 1 \quad 2 \quad 4 \quad 5$

$\Delta\lambda = 1.7\ nm$

250   300   350   400

$\lambda\ (nm)$

A-1140
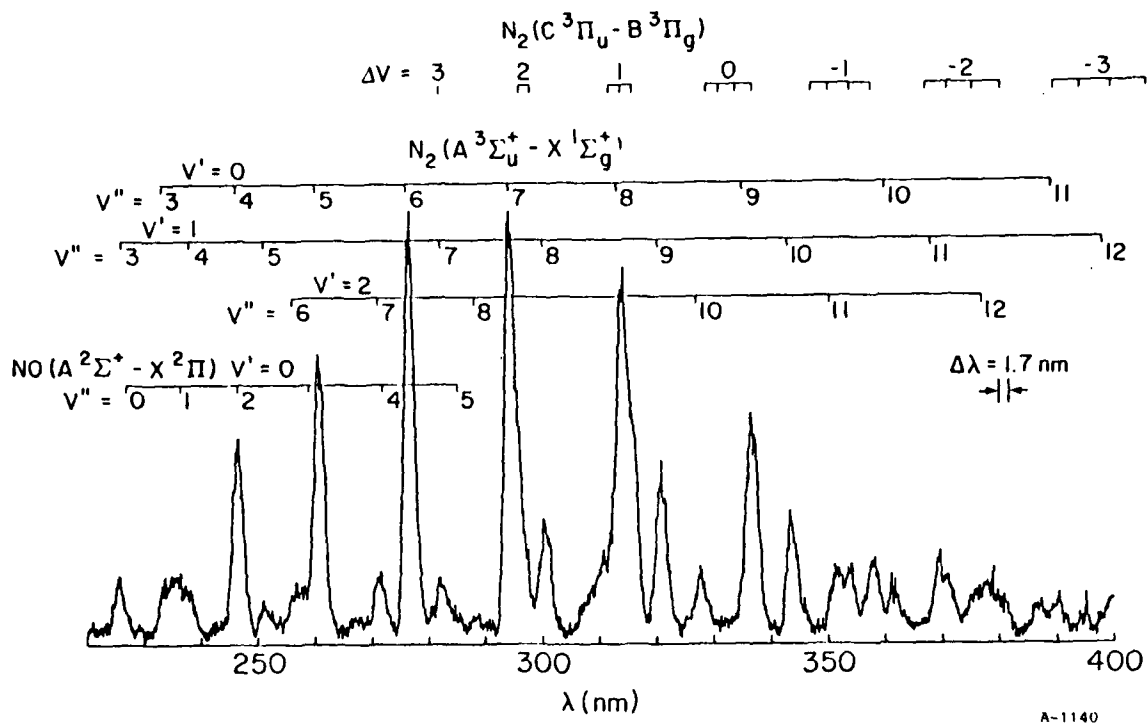
Figure G-2. Vegard-Kaplan emission in flow reactor 9 ms downstream from the discharge.

the experiments involve metastable nitrogen, it is not necessary to remove the nitrogen impurity from the argon carrier.

Observations of strong Vegard-Kaplan, $N_2(A\,^3\Sigma_u^+ - X\,^1\Sigma_g^+)$, emission downstream of the Ar/N_2 mixing zone confirms the production of the nitrogen metastables (Figure G-2). Co-discharging the nitrogen with the argon increases the $N_2(A)$ yield by a factor of about six[16] but we have found that this procedure also produces some atomic nitrogen, vibrationally excited N_2 and metastable $N_2(a'\,^1\Sigma_u^-)$.[17] Unequivocal measurements on $N_2(A\,^3\Sigma_u^+)$ reactions therefore, demand that the nitrogen be added downstream of the discharge.

Nitric oxide enters the flow tube through a 1 inch diameter loop injector seated on the end of a 1/4 inch diameter tube which slides along the bottom of the flow tube and parallel to its axis. This allows a variety of reaction distances for accurate kinetic studies. Adding CH_4, CF_3H, or CF_4 to the gas stream through a fixed, hook-shape injector, just downstream from where the

G-4

N_2A entered the flow reactor relaxed N_2A vibrational excitation without significant electronic quenching.[18,19]

Mass-flow meters or rotameters monitor gas flow rates. All flow meters were calibrated by measuring rates of increase of pressure with time into 6.5 or 12 ℓ flasks, using appropriate differential pressure transducers (Validyne DP-15) which themselves have been calibrated with silicon oil or mercury manometers. Typical flow rates for argon, nitrogen, and helium through the injector are 2000-5000, 100-500 and 50 μmol s^{-1}, while the NO flow rate ranges between 0 or 1 and 0 and 0.01 μmol s^{-1} for decay or excitation rate measurements, respectively. Total pressures, as measured by a Baratron® capacitance manometer, range from 0.3 to 10 torr, and flow velocities vary from 500 to 5000 cm s^{-1}.

The number density of reactant i is given by

$$N_i = \frac{f_i P_{tot}}{\sum\limits_i f_i} \times \frac{N_o}{RT}$$

where the f_i represent reagent flow rates, P_{tot} is the total flow tube pressure in torr, N_o Avogadro's number, R the gas constant (6.236×10^{-2} torr cm^3 μmol^{-1} K^{-1}), and T the absolute temperature.

Nitric oxide is purfied by slowly flowing it at atmospheric pressure through an Ascarite® trap and then through a cold finger surrounded by a methanol/ℓN$_2$ slush bath (- 100°C). The NO is then diluted in argon and the mixtures stored in 5-ℓ Pyrex® flasks. Mixtures of 5-8% NO sufficed for decay rate measurements while the excitation-rate determinations required NO mole fractions $\lesssim 10^{-3}$.

3. THE ELECTRONIC TRANSITION MOMENT FOR THE NO(A $^2\Sigma^+$ - X $^2\Pi$) TRANSITION

The issue of whether or not there is a significant variation in the elec-
tronic transition moment with r-centroid for the NO(A $^2\Sigma^+$ - X $^2\Pi$) transition
has been the subject of a number of papers over the last several decades.[20-31]
While a number of papers have shown evidence of a significant transition-
moment variation,[20-25] several groups have disputed this contention.[26-31]
References 25 and 29 review most of the relevant literature. The general
consensus in the scientific community seems to be that no significant transi-
tion moment variation occurs for the NO γ-bands. Recently, while studying the
electronic energy transfer between N_2(A $^3\Sigma_u^+$) and NO, we found inconsistencies
in NO(A $^2\Sigma^+$) excitation rates measured using different bands originating from
v'=0 if we invoked a constant transition moment. The excitation of the NO γ-
bands by N_2 (A $^3\Sigma_u^+$) energy transfer to NO (X $^2\Pi$) provides a source of γ-band
emission which is free from other significant overlapping band systems in the
spectral region. We find that our observed branching ratios for transitions
from a common vibrational level in the upper state cannot be explained by
variations in the Franck-Condon factors. Our observations show variation in
the electronic transition moment of more than 40% over the r-centroid range
1.13-0.97Å. We support this contention in the following paragraphs.

Correct transition probabilities for the NO A-X system bear directly upon
atmospheric science through such processes as the measurement of NO column
densities in the mesophere[32] or the interpretation of emissions in a strong
aurora. In addition proper NO A-X transition probabilities are needed to
calculate the gain for various transitions in the optically pumped NO A-X
laser. Proper NO(A-X) transition probabilities affect a wider range of
studies, however. Because they are easy to excite the NO γ-bands are often
used to establish the relative spectral response of monochromators in the
ultraviolet.[26,28] Using incorrect branching ratios for the A-X transition
will of course result in an incorrect response function, and will thereby
invalidate all other measurements which depend upon the spectral response
determined from the γ-band branching ratio measurements. The technique of
laser-induced flurorescence on NO A-X transitions has become an increasingly
important tool for probing the vibrational distributions of ground electronic

state NO produced in chemical or photolytic reactions.[33,34] Incorrect values
for the NO A-X transition probabilities invalidates the results of these mea-
surements, and thereby casts doubt on the validity of dynamical interpretations
of the results.

The intensity of emission from a given band is the product of the number
density in the upper state and the Einstein coefficient for spontaneous radia-
tion. The Einstein coefficient can be separated into a product of the Franck-
Condon Factor, the cube of the transition frequency, and the square of the
electronic transition moment. Thus

$$I_{v'v''} = N_{v'} A_{v'v''} = \text{const.} \times N_{v'} \; q_{v'v''} \nu^3_{v'v''} |R_e(\bar{r}_{v'v''})|^2 \qquad (1)$$

The transition-momentless population in the upper state is then determined from
the ratio of the integrated band intensity to the product of the Franck-Condon
factor and the cube of the transition frequency:

$$N^*_{v'v''} = \frac{I_{v'v''}}{q_{v'v''} \; \nu^3_{v'v''}} = N_{v'} |R_e(\bar{r}_{v'v''})|^2 \qquad (2)$$

The ratios of these transition-momentless populations to each other should be
constant unless the transition moment varies with r-centroid. The relative
variation in the transition moment with r-centroid results from the ratio of
the various momentless populations to one reference population. Scaling the
relative transition moments to experimentally determined lifetime or
oscillator-strength data is then a relatively simple process. The spectral
response function of the monochromator/detector system was accurately cali-
brated and verified by fitting the N_2 (A-X) Vegard-Kaplan transition features
which occurs in the same spectral region.

We determined the transition-momentless populations of the bands emanating
from v'=0 and 1 using a spectral fitting routine for each Δv sequence from $\Delta v=1$
to $\Delta v= -8$. The fitting routine corrected for spectral overlap between the
transitions for v'=0 and 1. The fit included different effective rotational

temperatures for the two vibrational levels. We ratioed each of these popula-
tions to the ones determined for the $\Delta v = -3$ sequence. This sequence is in the
middle of the wavelength range for the band system and thus should minimize any
systematic errors in the relative monochromator response function. The Franck-
Condon factors of both Nicholl's[35] and Albritton et al.,[36] gave similar
results. Our final results incorporate the latter set.

Figure G-3 shows the electronic transition moment relative to its value
for the $\Delta v = -3$ sequence plotted against r-centroid. The variation is small, but
consistent, up through the $\Delta v = -3$ sequence, but rises much more sharply for the
$\Delta v < -3$ sequences. The diamonds in Figure 3 show our re-analysis of the
branching-ratio measurements of McGee et al.[30] They excited NO (A, v'=0)
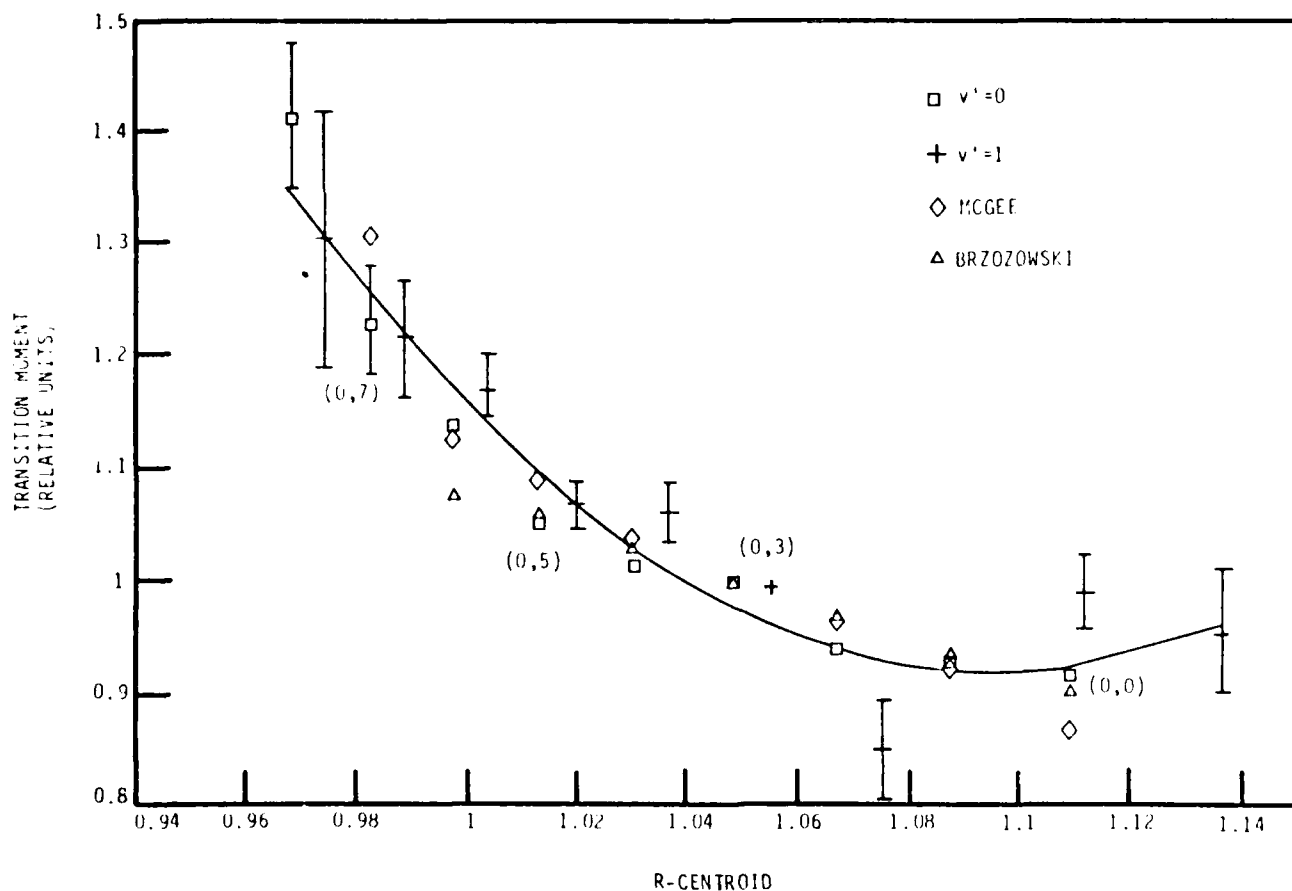
A-1145

Figure G-3. Variation in electronic transition moment with R-centroid for the
NO (A $^2\Sigma^+$ - X $^2\Pi$) transition.

G-8

with a laser and reported relative band emission intensities. Their results agree excellently with ours. Finally, we have also plotted the transition moment variation given by Brzozowski et al.[24] who observed γ-band emission in electron-beam excited NO during studies on NO predissociation.

We fit the results of the three experiments to a quadratic function of r-centroid:

$$\left| R_e(\bar{r}_{v'v''}) \right|_{rel} = 33.08 - 58.77\ \bar{r}_{v'v''} + 26.85\ \bar{r}_{v'v''}{}^2 \tag{3}$$

Using this functional form for the relative transition moment, we determined a smoothed set of branching ratios for emission from a given upper state as being

$$BR_{v'v''} = \frac{q_{v'v''}\ \nu^3{}_{v'v''}\ \left| R_e(\bar{r}_{v'v''}) \right|^2{}_{rel}}{\displaystyle\sum_{v''}\ q_{v'v''}\ \nu^3{}_{v'v''}\ \left| R_e(\bar{r}_{v'v''}) \right|^2{}_{rel}} \tag{4}$$

The Einstein coefficient for spontaneous radiation from each band is the product of the branching ratio for the given band to the total radiative decay rate of the upper state vibrational level. The average of nine apparently reliable determinations of the fluorescence lifetime of NO (A, v'=0) gives a value of (202 ± 14) ns.[27,29,37-43] Eight different determinations for the v'=1 level give a value of (192 ± 14) ns.[29,37,38,41,42,44-46] In both cases the error bars represent one standard deviation. Table G-1 lists the Einstein coefficients for each band.

Equation 5 relates the Einstein coefficient for a given v'v" transition to the absorption oscillator strength:

$$f^{abs}_{v'v''} = \frac{m_e\ c\ \lambda_o{}^2}{8\pi^2\ e^2}\ \frac{d_u}{d_1}\ A_{v'v''} \tag{5}$$

where m_e is the electron mass, e its charge in esu, c the speed of light, λ_o the transition wavelength, and d_u and d_1 are the electronic degeneracies of the upper and lower states, respectively. These last quantities are 1 and 2

G-9

TABLE G-1. EINSTEIN COEFFICIENTS FOR NO (A $^2\Sigma^+$ - X $^2\Pi$)

$v'=0$	v''	Wavelength (nm)	$Q_{v'v''}$	$\bar{r}_{(v'v'')}$ (Å)	$R_e(r)$	Branching Ratio	$A_{v'v''}$ (s^{-1})
	0	226.548	0.16697	1.1091	0.921429	0.202462	1.002E+06
	1	236.604	0.26345	1.0873	0.917005	0.277740	1.375E+06
	2	247.421	0.23646	1.067	0.935830	0.227041	1.124E+06
	3	259.087	0.15962	1.0481	0.973248	0.144364	7.147E+05
	4	271.700	0.090505	1.0303	1.026027	0.078883	3.905E+05
	5	385.377	0.045696	1.0135	1.091448	0.038894	1.925E+05
	6	300.252	0.021285	0.9977	1.166803	0.017777	8.801E+04
	7	316.482	0.009363	0.9827	1.250746	0.007673	3.799E+04
	8	334.256	0.003954	0.9684	1.342021	0.003166	1.568E+04
	9	353.794	0.001622	0.9548	1.439015	0.001259	6.235E+03
	10	375.362	0.000652	0.9419	1.540195	0.000485	2.405E+03
	11	399.283	0.000259	0.9295	1.645876	0.000183	9.061E+02
	12	425.947	0.000102	0.9177	1.754110	0.000067	3.339E+02

$v'=1$	v''	Wavelength (nm)	$Q_{v'v''}$	$\bar{r}_{(v'v'')}$ (Å)	$R_e(r)$	Branching Ratio	$A_{v'v''}$ (s^{-1})
	0	215.134	0.33353	1.1364	0.962957	0.451795	2.353E+06
	1	224.182	0.10295	1.1108	0.922847	0.113188	5.895E+05
	2	233.870	0.00097	1.0920	0.915801	0.000925	4.818E+03
	3	244.266	0.07231	1.0754	0.925357	0.061794	3.218E+05
	4	255.446	0.13381	1.0551	0.957153	0.106972	5.572E+05
	5	267.499	0.13257	1.0368	1.004782	0.101704	5.297E+05
	6	280.526	0.097792	1.0198	1.065139	0.073099	3.807E+05
	7	294.644	0.060554	1.0039	1.135635	0.044406	2.313E+05
	8	309.990	0.033426	0.9888	1.215151	0.024100	1.255E+05
	9	326.723	0.017042	0.9745	1.301742	0.012043	6.273E+04
	10	345.032	0.008212	0.9609	1.394282	0.005653	2.944E+04
	11	365.139	0.0038	0.9480	1.491236	0.002524	1.315E+04
	12	387.312	0.00171	0.9357	1.592003	0.001084	5.651E+03
	13	411.871	0.000753	0.9238	1.697225	0.000451	2.353E+03
	14	439.206	0.000327	0.9126	1.803203	0.000182	9.507E+02
	15	469.796	0.000141	0.9017	1.912810	0.000072	3.769E+02

$v'=2$	v''	Wavelength (nm)	$Q_{v'v''}$	$\bar{r}_{(v'v'')}$ (Å)	$R_e(r)$	Branching Ratio	$A_{v'v''}$ (s^{-1})
	0	204.952	0.29246	1.1654	1.050907	0.468229	2.573E+06
	1	213.147	0.017314	1.1516	1.003423	0.022467	1.234E+05
	2	221.886	0.15606	1.1194	0.932396	0.154996	8.516E+05
	3	231.223	0.07289	1.0947	0.915646	0.061695	3.390E+05
	4	241.217	0.00038	1.0770	0.923791	0.000288	1.584E+03
	5	251.936	0.034722	1.0644	0.939840	0.023936	1.315E+05
	6	263.459	0.08771	1.0440	0.983897	0.057946	3.184E+05
	7	275.873	0.10421	1.0265	1.039499	0.066934	3.678E+05
	8	289.281	0.088733	1.0103	1.105627	0.055919	3.072E+05
	9	303.801	0.062245	0.9951	1.180487	0.038608	2.121E+05
	10	319.569	0.038476	0.9807	1.262851	0.023464	1.289E+05
	11	336.744	0.021789	0.9671	1.350863	0.012995	7.140E+04
	12	355.514	0.011589	0.9542	1.443523	0.006707	3.685E+04
	13	376.099	0.005891	0.9419	1.540195	0.0003278	1.801E+04
	14	398.761	0.02897	0.9301	1.640572	0.001534	8.432E+03
	15	423.818	0.001392	0.9189	1.742761	0.000693	3.808E+03
	16	451.643	0.000688	0.9081	1.847680	0.000304	1.672E+03

for A $^2\Sigma^+$ and X $^2\Pi$, respectively. Applying our Einstein coefficients to
Eq. (5) gives absorption oscillator strengths for the 0,0 and 1,0 bands of
$(3.9 \pm 0.3) \times 10^{-4}$ and $(8.2 \pm 0.6) \times 10^{-4}$, respectively. These values agree
quite well with literature measurements of $(4.03 \pm 0.22) \times 10^{-4}$ for the 0,0
transition (five different experiments)[47-51] and $(8.26 \pm 0.48) \times 10^{-4}$ for the
1,0 transition (three different measurements).[48,50,51] Thus our transition
moment function satisfies the important criterion that the lifetime and
absorption measurements be consistent.

We have also calculated Einstein coefficients for v'=2 assuming the tran-
sition moment variation of Eq. (3) and a radiative-decay lifetime for v'=2
of (182 ± 10) ns.[29,37,38,41,42] Because transition moment variation was
extrapolated to regions outside the fit, the transition probabilities from
v'=2 are less reliable. This may be reflected in the modest disagreement
between the absorption oscillator strength of the 2,0 band calculated from the
transition probabilities given in Table 1 of $(8.1 \pm 0.4) \times 10^{-4}$ and the exper-
imental value of $(6.8 \pm 0.2) \times 10^{-4}$.[28,30,31]

Figures G-4 and G-5 show a comparison between the observed and the syn-
thetic best fit spectra for the case of no assumed transition moment varia-
tion, and the transition moment variation determined in this work. Clearly
including the transition moment variation makes a significant difference in
the quality of the fit. A poor fit could also be the result of our having an
incorrect relative monochromator response function. In that case our analysis
for the transition moment function would also be invalid. This does not
appear to be a significant problem in our work, however, because we very accu-
rately fit the Vegard-Kaplan bands of nitrogen over the same wavelength
region. In addition, the good agreement between our own results and those of
the two other groups alluded to previously[24,30] confirms that our wavelength
response function is accurate.
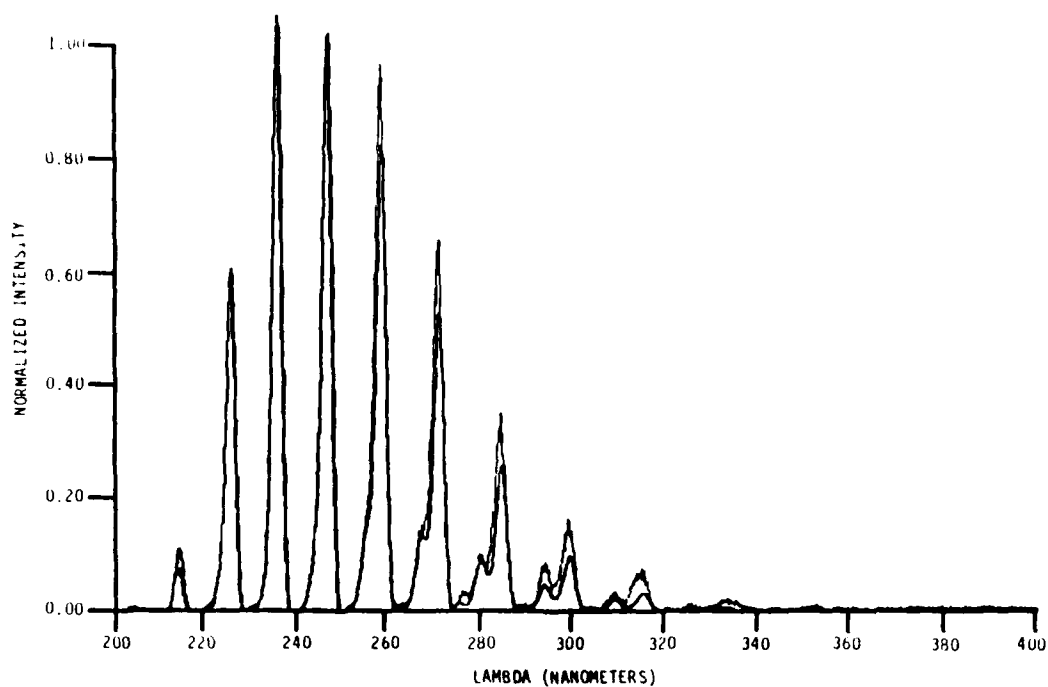
Figure G-4. Experimental (light line) and synthetic (heavy line) spectrum for the NO γ-bands assuming a constant electronic transition moment.
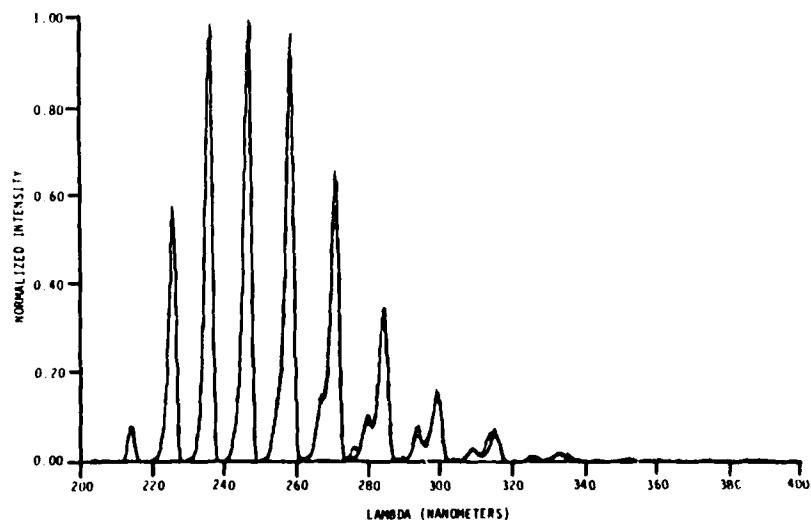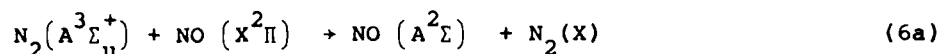

Figure G-5. Experimental (light line) and synthetic (neavy line) spectrum of the NO γ-bands using the electronic transition-moment function determined in this work. The major remaining areas of discrepancy between the two spectra at 260, 276, 294, and 313 nm result primarily from small additions to the experimental spectrum from the 0,5 through 0,8 bands of the N_2 Vegard-Kaplan system which were not included in the synthetic fit.

G-12

4. THE KINETICS OF THE $N_2(A)$ PLUS NO REACTION

Complete characterization of the energy-transfer reaction between $N_2(A)$ and NO,

$$N_2\left(A^3\Sigma_u^+\right) + NO\left(X^2\Pi\right) \rightarrow NO\left(A^2\Sigma\right) + N_2(X) \tag{6a}$$

$$\rightarrow \text{other channels} \tag{6b}$$

$$NO\left(A^2\Sigma^+\right) \rightarrow NO\left(X^2\Pi\right) + h\nu \tag{7}$$

involves measuring both the rate coefficient for removal of $N_2(A)$ by NO and the rate coefficient for the excitation of the NO γ-bands in the energy transfer reaction. The rapid vibrational relaxation of $N_2(A)$ by molecules such as CF_4, CF_3H, and CH_4, with no accompanying electronic quenching[18,19] allows us to alter the vibrational distribution of the $N_2(A)$. This makes state-to-state measurements possible.

4.1 The Quenching of N_2 (A $^3\Sigma_u^+$, v'=0) by NO

Measurements of the rate of removal of $N_2(A)$ by NO are not so easy as corresponding measurements of $N_2(A)$ quenching by other molecules. Ordinarily, one follows $N_2(A)$ number density decays by monitoring the Vegard-Kaplan emission.[2,3,19] The extremely bright NO γ-band emission in the same region of the spectrum however, masks the Vegard-Kaplan bands. Fortunately γ-band emission is a sensitive tracer of the $N_2(A)$ number density.

The differential equation describing the rate of change in the $NO(A^2\Sigma^+)$ number density with time is

$$\frac{d[NO(A)]}{dt} = k_6[N_2(A)][NO(X)] - k_7[NO(A)] . \tag{8}$$

The NO(A) is in steady state in the observation volume because the lifetime of NO(A) is short compared to the time a molecule resides within the field of view of the detector. Thus the intensity of the γ-band emission is

$$I_{NO*} = k_7 [NO*] = k_6 [N_2(A)][NO] \ . \tag{9}$$

Upon rearranging this equation, we relate the number density of $N_2(A)$ in the observation volume to the ratio of the γ-band emission intensity and the NO number density:

$$[N_2(A)] = \frac{I_{NO*}}{k_6 [NO]} \ . \tag{10}$$

The differential equation describing the decay of $N_2(A)$ in the reactor is

$$\frac{d[N_2(A)]}{dt} = -(k_6 [NO] + k_{wall}) \ [N_2(A)] \tag{11}$$

where k_{wall} is the first-order (pressure dependent) rate coefficient for $N_2(A)$ quenching in wall collisions. Because the NO number density is typically several orders of magnitude greater than the $N_2(A)$ number density, we can assume that the NO number density is a constant (the pseudo first-order approximation). This approximation leads to an analytical solution to Equation (11), viz,

$$\ln \frac{[N_2(A)]}{[N_2(A)]^o} = -(k_6 [NO] + k_{wall}) \ z/\bar{v} \tag{12}$$

where we have replaced the reaction time by the ratio of the distance from flow tube injector to observation volume, z, to the bulk flow velocity, in the reactor, $\bar{v}$. Inserting Equation (10) into Equation (12) gives

$$\ln \frac{I_{NO*}/[NO]}{I_{NO*}^o/[NO]^o} = - \ k_6 [NO] + k_{wall} \ z/\bar{v} \ . \tag{13}$$

The above equation shows that measurements of the logarithm of the ratio of γ-band intensity to NO number density as a function of NO number density but with fixed reaction time will give a linear relationship with a slope of $- k_6 \ z/\bar{v}$. Such measurements at several different reaction distances, under

otherwise constant conditions of pressure, temperature, total flow rate, etc., will correct for non-instantaneous mixing at the injector. The results must further be corrected by a factor of $(0.62)^{-1}$ to correct for the coupling of a radial density gradient in $N_2(A)$ number density with a parabolic velocity profile.[52-59]

Because we have shown previously[2] that rate coefficients measured using a tracer can be seriously in error if the tracer is sensitive to several different $N_2(A)$ vibrational levels each of which quenches at significantly different rates, we have relaxed the N_2A vibrational distribution to only $v'=0$. CF_3H, CF_4, and CH_4 all were used to relax $N_2(A)$ to $v'=0$. As expected, the results were invariant with relaxation partner.

Figure G-6 shows a plot of the ratio of the natural log of the γ-band intensity to the NO number density as a function of the NO number density for several different distances between the injector and observation volume. The linearity of these plots is quite good, extending over more than two orders of magnitude. Figure G-7 shows a plot of the slopes of the lines in Figure G-6 and two other sets of data not shown plotted as a function of the reaction time. The slope of this plot, when divided by the radial-profile correction factor, 0.62, gives the rate coefficient for quenching $N_2(A)$ by NO. Note the non-zero intercept, indicative of the finite time required for complete reagent mixing.

A number of experiments spanning a range in total gas pressures from 0.7 to 3.7 Torr and reaction times from 11 to 124 ms, and using several different NO/Ar gas mixtures all gave consistent results for the rate coefficient for $N_2(A, v'=0)$ quenching by NO of $(6.6 \pm 0.8) \times 10^{-11}$ cm^3 molecule^{-1} s^{-1}. The quoted error estimate is one standard deviation in the averaging process. The total experimental uncertainty, including estimates in the uncertainties in the calibrations of the flow meters, pressure gauges, etc. is about 15%. A few decay measurements in which the $N_2(A)$ was not vibrationally relaxed gave decays only slightly larger ($\lesssim$ 5%) than those measured for the relaxed $N_2(A)$. Thus we infer that NO quenches vibrationally excited $N_2(A)$ at a rate similar to that for quenching $v'=0$.
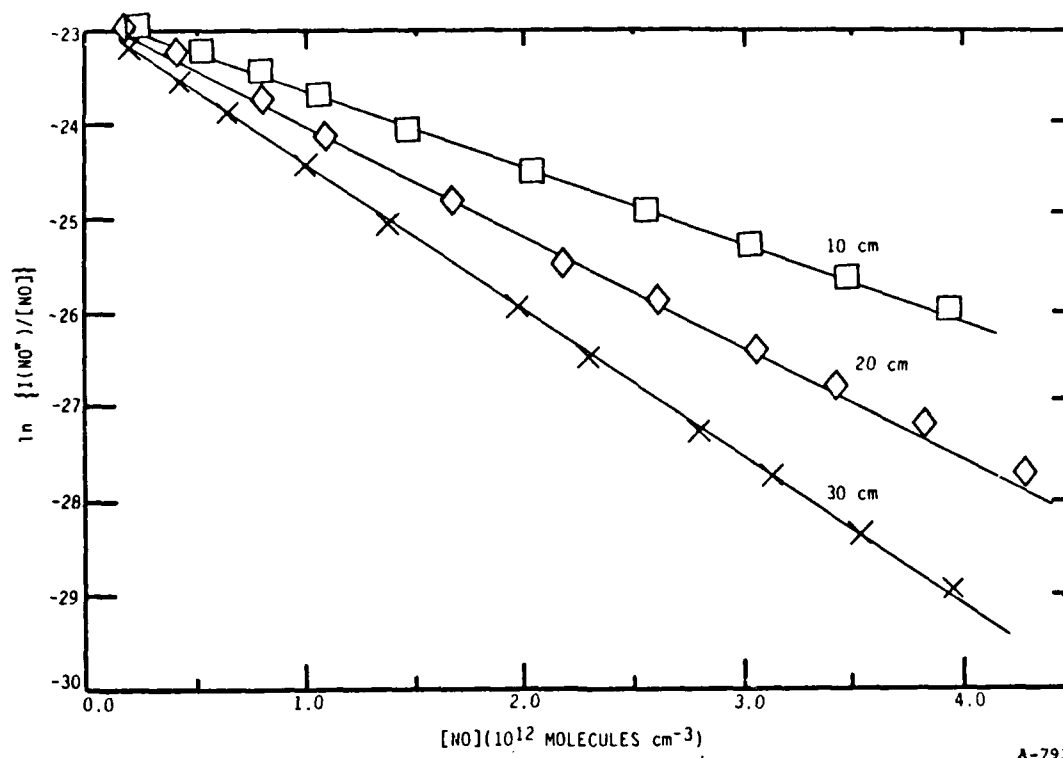
Figure G-6. Decay in the natural log of the $N_2(A, v'=0)$ number density as a function of NO number density at three different reagent mixing distances.
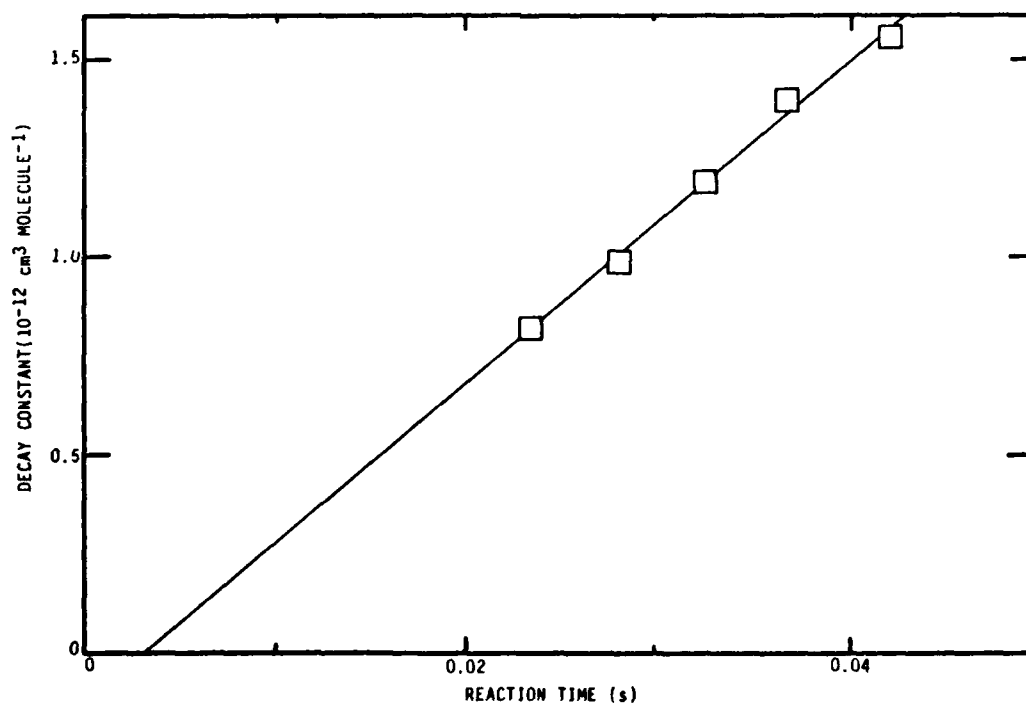
Figure G-7. $N_2(A, v'=0)$ decay constants in NO as a function of reaction time.

G-16

Our result disagrees markedly with Dreyer and Perner's reported value of 2.8×10^{-11} cm^3 molecule^{-1} s^{-1} also for v'=0.[60] We agree excellently with the recent result of Shibuya et al.[61], $(6.9 \pm 0.7) \times 10^{-11}$ cm^3 molecule^{-1} s^{-1}, and also quite well with early measurements by Callear and Wood[62], 8.0×10^{-11}, Young and St. John[63], 7.0×10^{-11}, Hill et al.[64], 7.5×10^{-11} and Piper[65] at 196 K, $(9 \pm 2) \times 10^{-11}$. Mandel and Ewing's[66], rate coefficient, 4.3×10^{-11} appears to be discordant with the rest of the literature. All the above rate coefficients are in units of cm^3 molecule^{-1} s^{-1}. All measurements excepting Dreyer and Perner's used tracer techniques, and were not state specific. As we have pointed out, however, our measurements indicate that the quenching of $N_2(A)$ by NO does not appear to show a strong dependance on the $N_2(A)$ vibrational level. Callear and Wood[62] also reached this conclusion when they attempted to relax $N_2(A)$ vibration with large additions of helium to their flash photolysis system.

4.2 The Excitation of NO(A $^2\Sigma^+$, v'=0) by $N_2(A\ ^3\Sigma_u^+$, v'=0)

We have determined the rate coefficient for excitation of NO(A $^2\Sigma^+$, v'=0) by measuring the increase in the intensity of several bands originating from NO(A, v'=0) as a function of added NO number density but for constant $N_2(A)$ number density. If we note that the $N_2(A)$ number density is the intensity of the Vegard-Kaplan bands divided by the Einstein coefficient[76] for spontaneous radiation, we can rearrange Equation (9) to give the working equation for our analysis.

$$I_{NO^*} = k_6 \frac{I_{VK}}{A_{VK}} [NO] \tag{14}$$

One convenient feature of this analysis is that the absolute calibrations for photon-emission rate measurements of the two intensities cancel and only the relative spectral response is important. Thus the intensity measurements do not introduce significant potential sources of systematic error. In practice, we determined total Vegard-Kaplan intensity from a spectral fit to the whole band system. We then measured the change in the peak intensity of one of the bands of NO(A) as a function of added NO number density, being careful to keep added NO number densities below the range giving significant N2(A) quenching. Multiplying the peak intensity by a correction factor gave

the total integrated intensity under that specific band. Dividing the integrated intensity by the appropriate branching ratio (see Section 3) determined the total emission from NO(A). We made observations on the 0,1, 0,4 and 0,5 γ-bands. Under our experimental resolution, the 1,5 and 1,6 bands overlap the 0,4 and 0,5 γ-bands and thus contribute to the observed emission intensity. We subtracted out this small contribution from our data. All three of the observed γ-bands gave excitation rate coefficients which were identical within experimental error.

Figure 8 shows that the intensity of the 0,1 band increases linearly with added NO number density in accord with Eq. (14). A number of such experiments yielded a rate coefficient for exciting NO(A, $v'=0$) by N_2(A, $v'=0$) of $(9.0 \pm 2.7) \times 10^{-11}$ cm^3 molecule^{-1} s^{-1}, where the error bars represent the total estimated statistical and systematic error. The major contribution to the uncertainty is in the 20% uncertainty quoted for the N_2(A) Einstein coefficient.[67] Variations of greater than a factor of five in pressure, and of more than an order of magnitude in N_2(A) number density gave consistent results. We also varied the distance between the NO injector and the observation region to insure that the NO was fully mixed. In addition using Xe* + N_2 as the N_2(A) source, and using several different NO/Ar gas mixtures did not change the results.

Relatively high resolution scans over the 0,6 and 1,7 bands as a function of pressure between 0.4 and 10 Torr showed that the ratio of NO(A, $v'=1$) to NO(A, $v'=0$) excitation by N_2(A, $v'=0$) was 0.54 ± 0.06, Figure G-9. Spectral scans between 200 and 400 nm indicated that excitation of NO(A, $v'=2$) and NO(B, $v'=0$) were both > 0.003 as compared to NO(A, $v'=0$). Thus the total rate coefficient for NO excitation by N_2(A, $v'=0$) is $(10 \pm 3) \times 10^{-11}$ cm^3 molecule^{-1} s^{-1}.

4.3 State-to-State Excitation of NO(A, $v'=0,1,2$) by N_2(A, $v'=0,1,2$)

We scanned a number of spectra of the NO γ-bands and N_2 Vegard-Kaplan bands with fixed NO number density but with varying CF_4 number density, and thus varying N_2(A) vibrational distribution (Figures G-10 and G-11). The total
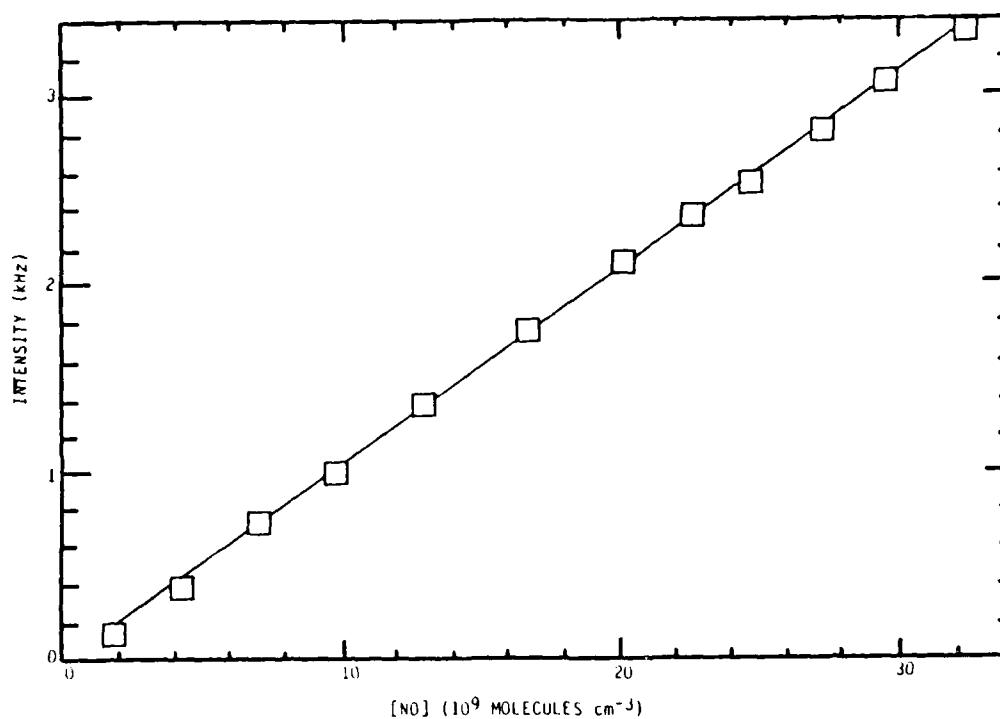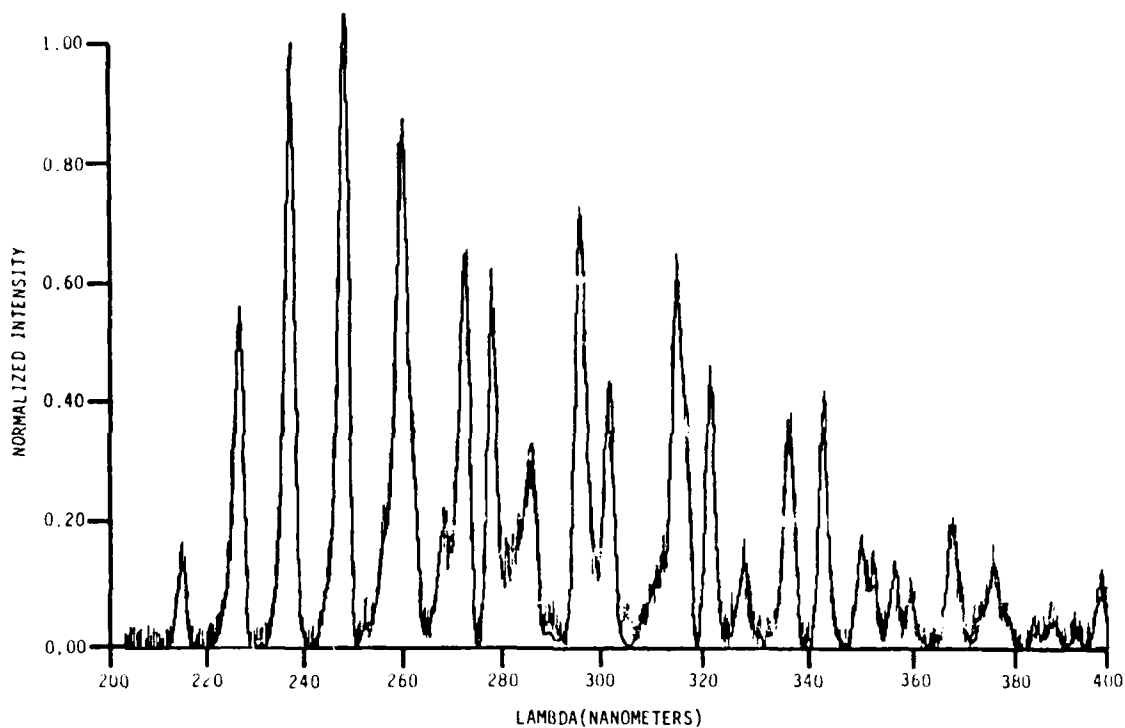
Figure G-8. Variation in the peak intensity of the NO(A-X, 0,1) band as a function of added NO number density.
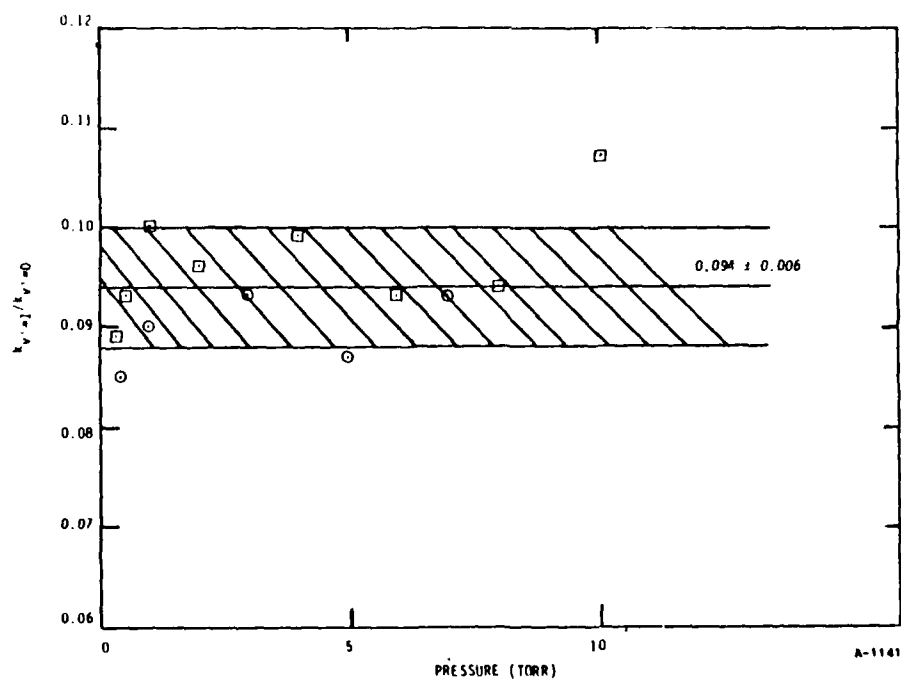
Figure G-9. Ratio in the rate coefficients for exciting NO (A, v'=1) to NO (A, v'=0) by N_2 (A, v'=0) as a function of argon pressure.

G-19

A-1147

Figure G-10. Spectrum of NO(A-X) and N_2(A-X) in the absence of CF_4. The light line shows the experimental data, while the heavy line shows the synthetic best fit to the data.
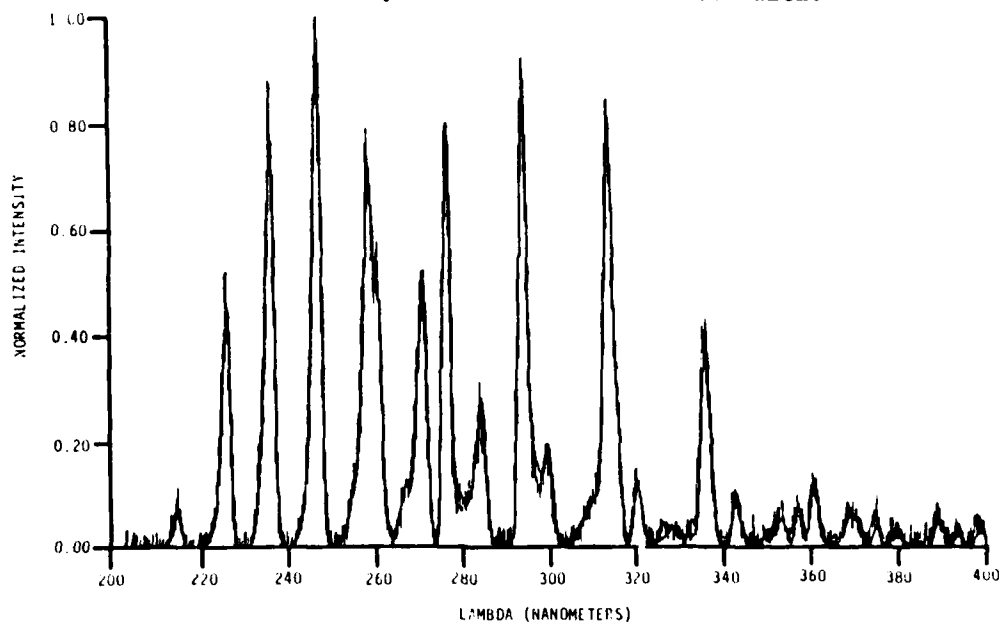
A-1146

Figure G-11. Spectrum of NO(A-X) and N_2(A-X) in presence of CF_4 which relaxes most of the N_2(A) vibrational energy. The light line is the experimental data while the heavy line shows the synthetic best fit.

G-20

$N_2(A)$ number density changed little over the series of experiments, but the vibrational distribution changed from one in which more than half of the $N_2(A)$ was vibrationally excited to one in whch well over 80% of the $N_2(A)$ was in $v'=0$. These measurements therefore tracked how the NO(A) vibrational distribution changed with changes in $N_2(A)$ vibrational distribution. We can express the observed intensity of a given NO(A) vibrational level by Eq. (15)

$$I_{NO^*{}_v} = k_{0v} \, [N_2A]_0 + k_{1v} \, [N_2A]_1 + k_{2v} \, [N_2A]_2 \quad [NO], \quad (15)$$

where the subscripts on the k's represent the vibrational level of the $N_2(A)$ and NO(A) respectively. CF_4 vibrationally relaxes $N_2(A)$ in $\Delta v=1$ transitions, and relaxes $v' \geq 2$ much more efficiently than it does $v'=1$.[17] Thus for small CF_4 additions, the $v'=1$ number density stays relatively constant, and primarily $v' \geq 2$ is quenched. For moderate to high amounts of vibrational relaxation, therefore, only $N_2(A)$ $v'=0$ and 1 remain in the reactor and further relaxation beyond that point changes only the ratio of $v'=1/v'=0$; thus Eq. (15) can be simplified and rearranged to give,

$$\frac{I_{NO^*{}_v}}{[N_2A]_0} = k_{0v} + k_{1v} \frac{[N_2A]_1}{[N_2A]_0} \quad [NO] \; . \quad (16)$$

The ratio of the slope to intercept of the linear plot implied by Eq. (16) will give the ratio of the rate coefficients k_{1v}/k_{0v}. Figures G-12 and G-13 show that this linear relationship does indeed obtain. Using the results for $v'=1$ excitation derived from the moderate-to-high relaxation data, we can subtract out the contribution to observed excitation from $v'=1$ for the data showing little relaxation and thereby probe contributions from $v' \geq 2$. The working equation then becomes

$$\frac{I_{NO^*{}_v}}{[N_2A]_0} - k_{1v} \frac{[N_2A]_1}{[N_2A]_0} \quad [NO] = k_{0v} + k_{2v} \frac{[N_2A]_2}{[N_2A]_0} \quad [NO] \; . \quad (17)$$
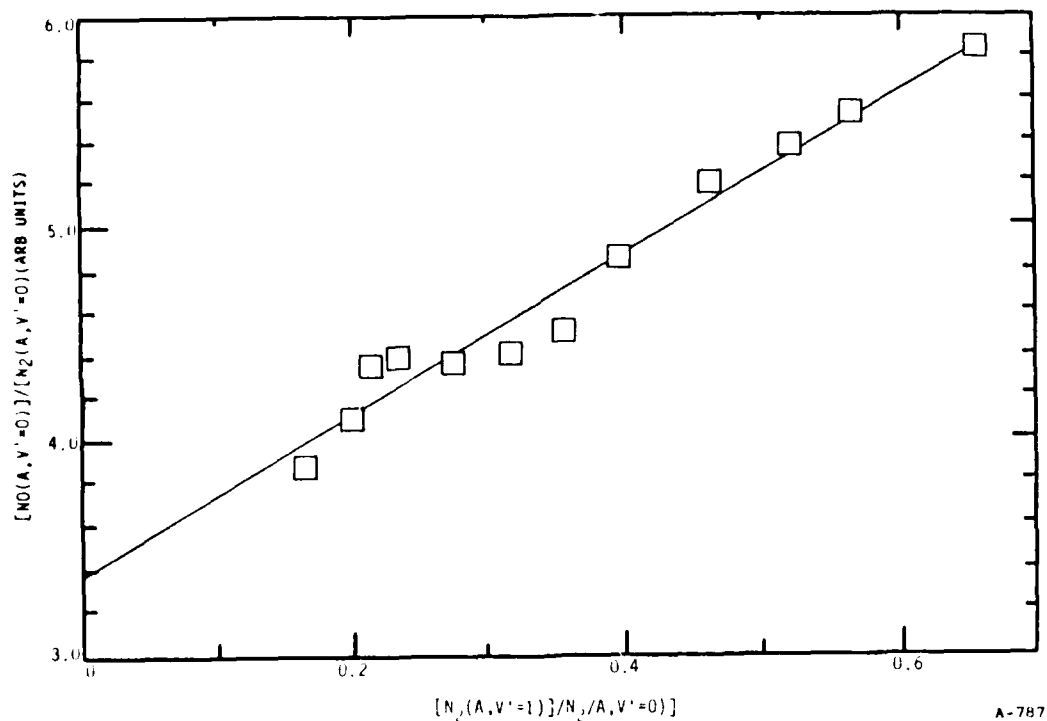
G-21

Figure G-12. Excitation of NO(A, v'=0) as a function of the ratio of
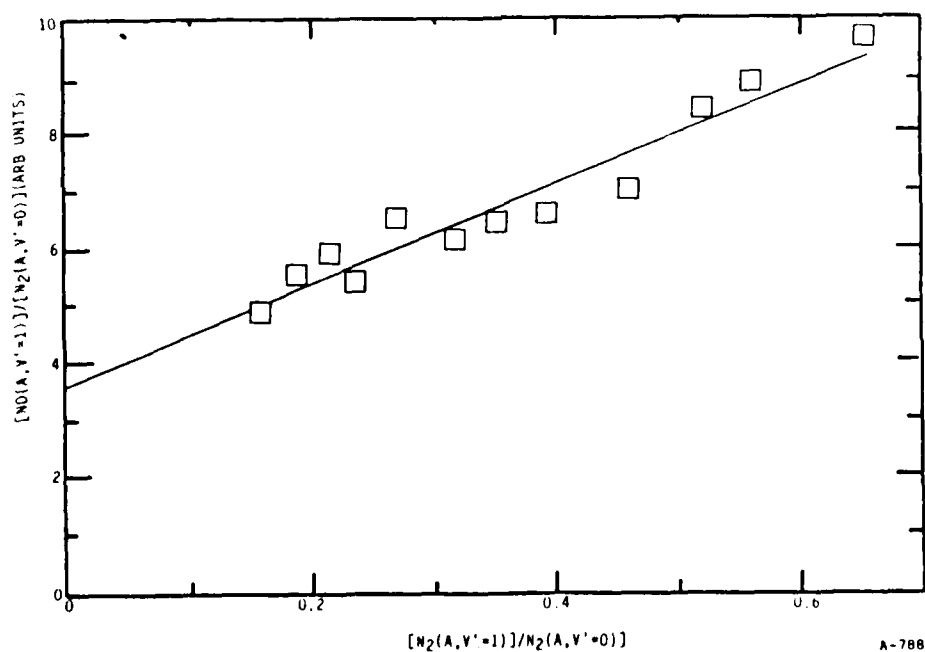N$_2$(A, v'=1) to N$_2$(A, v'=0).

Figure G-13. Excitation of NO(A, v'=1) as a function of the ratio of
N$_2$(A, v'=1) to N$_2$(A, v'=0).

Figures G-14 and G-15 show the linear relationship implied by this equation, and the ratio of the slope to intercept from these plots gives the ratio k_{2v}/k_{0v}. Because excitation of NO(A, v'=2) and NO(B, v'=0) were such minor channels, we only estimated their contributions to the total excitation by measuring the integrated intensity under the 2,0 gamma band and the 0,7 beta band in several spectra in which the $N_2(A)$ was vibrationally excited and several more in which it was relaxed. Thus we report only an excitation rate coefficient for excited and unexcited $N_2(A)$ for these two states. Table G-2 lists the relative excitation rate coefficients for the state-to-state excitation of NO(A, v'=0,1,2) and NO(B, v'=0) by $N_2(A, v'=0,1,2)$.

TABLE G-2. STATE-TO-STATE RELATIVE EXCITATION-RATE COEFFICIENTS.

| $N_2(A)$ v'	NO(A) v'=	0	1	2	NO(B,v'=0)
0		1*	0.094±0.006	0.003	0.0032±0.0007
1		1.11±0.07	0.22±0.03		
2		0.29±0.07	0.32±0.03	0.024	0.033±0.007
*1 = 9.0 x 10^{-11} cm^3 molecule^{-1} s^{-1}					

4.4 Discussion

If the energy transfer between $N_2(A)$ and NO proceeds only through exit channels of radiating NO states, then the rate coefficients for $N_2(A, v'=0)$ quenching by NO (6.6 x 10^{-11} cm^3 molecule^{-1} s^{-1}) and for NO(A,B) excitation by $N_2(A,v'=0)$ (10 ± 3) x 10^{-11} cm^3 molecule^{-1} s^{-1}) ought to be the same. We are therefore somewhat disturbed by the lack of congruency between the two measurements, even though they do overlap slightly at the extreme limits of their respective error bars. We have tried to cross check our data very care-fully, and to vary the experimental conditions over a fairly wide range, thereby hoping to find systematic trends which might explain the discrepancy. We have been unable to find any. Our conclusion, therefore, is that the Einstein coefficient for the $N_2(A-X)$ transition is in error by about 30% (it should be smaller).
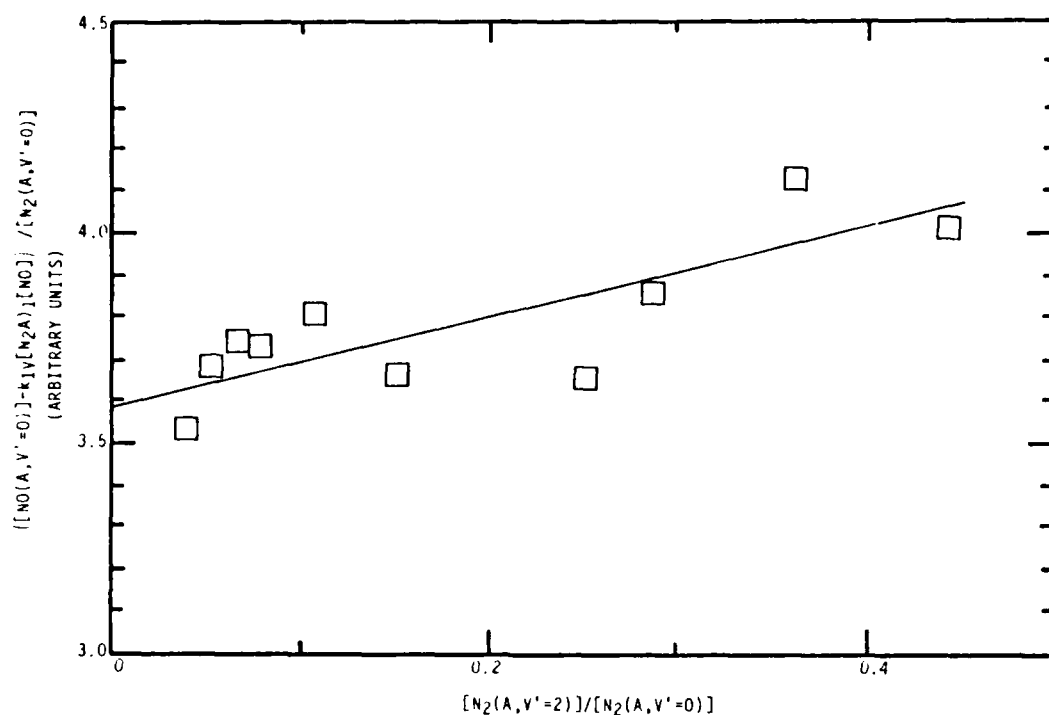
A-790

Figure G-14. Excitation of NO(A, v'=0) as a function of the ratio of N_2(A, v'=2) to N_2(A, v'=0).
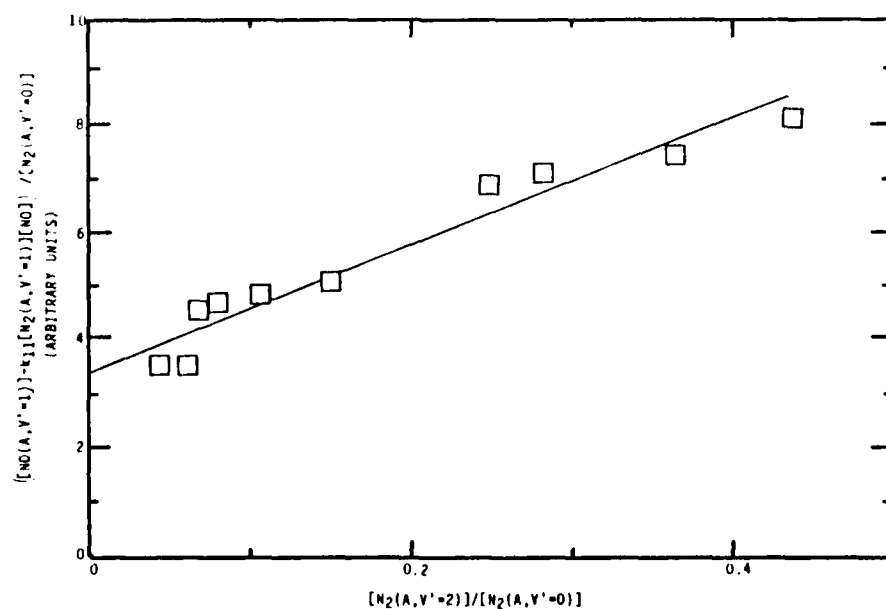
A-789

Figure G-15. Variation in the excitation of NO(A, v'=1) as a function of the Ratio of N_2(A,v'=2) to N_2(A, v'=0).

G-24

The experimental determination of lifetimes on the order of 2 seconds is extremely difficult and fraught with manifold uncertainties. The accepted value of the Einstein coefficient for the N_2(A-X) transition rests upon absorption measurements by Shemansky in the vacuum ultraviolet[67] and his reanalysis[68] of Carleton and Oldenberg's[25] absorption measurements of N_2(A) in a discharge.[69] His analysis requires a long extrapolation of the transition-moment function with r-centroid from the region encompassed by his absorption measurements into the region of r-centroid sampled by the strong transitions from the v'=0 level. He tied this extrapolation to the lifetime for the v'=0 level derived from the Carleton and Oldenberg reanalysis. Carleton and Oldenberg[69] attempted to measure simultaneously the absolute photon-emission rate of the 0,6 Vegard-Kaplan band and the absolute number density v'=0 level of the A state via resonance absorption on the 1,0 transition of the first-positive system (N_2 B-A). Assuming that the experimental observations of Carleton and Oldenberg are accurate, and that Shemansky's re-analysis of their observations is correct, then their derived lifetime for N_2(A, v'=0) depends directly upon the accuracy of the lifetime of the v'=1 level of N_2(B). While the recent lifetime measurements of Eyler and Pipkin[70] on the radiative lifetimes of N_2(B, v'=5-12) indicate that the transition probabilities of the first-positive system given by Shemansky[71] are essentially correct for $v' \gtrsim 3$, we do not feel confident that Shemansky's transition probabilities for the three lowest levels are necessarily accurate. The transition probabilities for these three levels depend predominantly upon an extrapolation of the electronic transition-moment function which Shemansky derived from relative intensity measurements of bands with r-centroid values between 1.35 and 1.6Å out to r-centroid values as small as 1.0. This is generally a risky procedure. The recent ab initio calculations of the transition-moment function by Werner et al.[72] show a much slower increase in the transition moment to smaller r-centroid than is given by Shemansky's extrapolation. The lifetimes Werner et al., calculate from their transition-moment function are consistently 16% larger than the lifetimes measured by Eyler and Pipkin,[70] but the relative variation of their calculated lifetimes with vibrational level matches that of Eyler and Pipkin quite well. They also match the relative variation in the lifetimes measured by Jeunehomme,[74] and by Carlson et al.[73]

and those calculated from Shemansky's transition probabilities for v'>4. They deviate markedly from the experimental results, however, for the lowest vibrational levels, with the calculated lifetimes of Werner et al., being somewhat longer. If we reduce the calculated lifetimes of Werner et al., by 16% to make them coincide with Eyler and Pipkin's measurements for the high vibrational levels, we obtain a lifetime for v'=1 of $N_2(B)$ of 9.5 μs in contrast to the value of 7.8 μs which results from Shemansky's transition probabilities. This large a change in the lifetime of the B state will reduce the transition probability for $N_2(A, v'=0)$ from Carleton and Oldenberg's experiment by 20%. This reduction would then bring our quenching- and excitation-rate measurements into reasonable agreement. Taking the ab initio transition probabilities at face value would result in a Vegard-Kaplan transition probability about 40% smaller than the currently accepted values, and would bring our two measurements into almost perfect congruence. A reduction in the transition probability of the $N_2(A)$ state on the order of 20-30% would still give a variation in the absolute transition moment of the A--X transition fully consistent with the absolute measurements of Shemansky that sampled smaller values of the r-centroid, and the relative transition-moment measurements of Broadfoot and Maran[75] which sampled larger r-centroid values, those sensitive to the Vegard-Kaplan transitions from v'=0. We feel that good experimental measurements of the relative transition-moment variation of the first-positive system which sample smaller values of r-centroid are imperative to clear up this conflict. This will require relative intensity measurements extending out into the infrared to 1.5 μm.

Our measurements on the vibrational-level dependence of NO excitation by $N_2(A)$ show that $N_2(A, v'=1)$ excites NO(A,B) about 25% more efficiently than does $N_2(A,v'=0)$. $N_2(A,v'=2)$ however, is somewhat less efficient at exciting NO transitions. Presumably in a laser system the pressures will be modest, $\gtrsim 10$ torr, and the $N_2(A)$ will essentially be relaxed into vibrational levels 0 and 1. Our results show that this relaxation does not compromise the projected efficiency of such a laser system.

The reduction in observed intensity from NO(A,B) from excitation by $N_2(A,v'=2)$ could result from one of three possibilities. The quenching efficiency could be smaller from some reason. The more highly excited $N_2(A)$ can access higher lying levels of NO(A,B) which might be collisionally coupled into other states of NO which our system cannot see, such as the b $^4\Sigma^-$ or a $^4\Pi$ states. A third possibility is that some of the encounters between $N_2(A,v'=2)$ and NO end up dissociating the NO. Only vibrational levels of $N_2(A)$ greater than or equal to two have sufficient energy to dissociate the NO. We have not yet attempted to look for atom production from this interaction, but such measurements would confirm this possibility.

The efficient transfer of vibronic energy from $N_2(A)$ to NO may occur by a Franck-Condon type of mechanism. Deperasinska et al.[76] have calculated Franck-Condon factors for the transitions relevant to the transfer of energy from $N_2(A,v'=0)$ to NO. The Franck-Condon factors for producing NO(A) are three orders of magnitude greater than those for producing NO(B), which they claim is reflected in the much smaller efficiency for producing NO(B) relative to NO(A). Their calculated Franck-Condon factors, however, would predict roughly equal probabilities for producing vibrational levels $v'=0$ and 1 of NO(A). In contrast, our observations show that NO(A,v'=0) is produced ten times more efficiently than NO(A,v'=1). They have not performed the relevant Franck-Condon calculations for $N_2(A,v'=1, 2)$.

The kinetics of the N_2A + NO energy transfer have been studied by several other investigators. Callear and Wood[62] estimated rate coefficient ratios from their work of k_{01}/k_{00} = 0.105 in reasonable agreement with our value of 0.094 ± 0.006 and k_{11}/k_{10} = 0.53 in disagreement with our value of 0.20 ± 0.03. Clark and Setser[65] determined a population ratio for NO(A, $v'=0,1,2$) of 1.0:0.15:0.014 respectively from excitation by $N_2(A)$ with the ratio $v'=1/v'=0$ of 0.61. With the same $N_2(A)$ vibrational distribution, we calculate an NO(A) vibrational distribution from our excitation rate coefficients of 1.0:0.14:0.011 respectively, in excellent agreement with Clark and Setser's observations. More recently Balamuta et al.[77] have measured vibrational distributions of NO(A) from $N_2(A)$ excitation of 1.00:0.90:0.007

for excitation by $N_2(A,v'=0)$ and 1.00:0.17:0.02 for excitation by $N_2(A)$ with a vibrational distribution of 1.00:0.48:0.19:0.14 for $v'=0-3$ respectively. Our rate coefficients would predict an NO(A) vibrational distribution of 1.00:0.19:0.013 given the same initial $N_2(A)$ vibrational distribution. Balamuta et al's. data show an 18% decrease in total NO(A) intensity for the vibrationally excited case whereas our results would indicate that the intensities of the NO(A) produced from vibrationally excited and unexcited $N_2(A)$ would be within 2% of each other.

ACKNOWLEDGEMENT

REFERENCES

1. Rawlins, W.T., Piper, L.G., Caledonia, G. E. and Green, B.D., "COCHISE Research," Physical Sciences Inc. Technical Report TR-298 (1981).

2. Piper, L.G., Caledonia, G.E. and Kennealy, J.P., "Rate Constants for Deactivation of $N_2(A\ ^3\Sigma_u^+\ v'=0,1)$ by O_2," J. Chem. Phys. $\underline{74}$, 2888 (1981).

3. Piper, L. G., Caledonia, G.E. and Kennaly, J.P., "Rate Constants for Deactivation of $N_2(A\ ^3\Sigma_u^+\ v'=0,1)$ by O," J. Chem. Phys. $\underline{75}$, 2847 (1981).

4. Piper, L.G., "The Excitation of $O(^1S)$ in the Electronic Energy Transfer Between $N_2(A\ ^3\Sigma_u^+)$ and O," J. Chem. Phys. $\underline{77}$, 2373 (1982).

5. Piper, L.G., Murphy, H.C. and Rawlins, W.T., "Development of COCHISE UV Absorption System: Final Report," TR-292 (November 1981), AFGL-TR-81-0318, Air Force Geophysics Laboratory Report (1981).

6. Rawlins, W.T. and Piper, L.G., "Effect of Excitation Mechanism on Linewidth Parameters of Conventional VUV Discharge Line Sources," Proc. Soc. Photo. Opt. Instr. Eng. $\underline{279}$, 58 (1981). Also presented at the Technical symposium East '81 of the Society of Photo-Optical Instrumentation Engineers, Washington, D.C. (April, 1981).

7. Krech, R.H., Diebold, G.J. and McFadden, D.L., "Kinetics of the $O + F_2$ Reaction: A Case of Low Reactivity of Elemental Fluorine," J. Am. Chem. Soc. $\underline{99}$, 4605 (1977).

8. Krech, R.H., "ESR Discharge - Flow Kinetics: The $O + F_2$ Reaction, Masters dissertation, Dept. of Chem., Boston College, 1976.

9. Pak, S.J., Krech, R.H., McFadden, D.L. and MacLean, D.I., "EPR Discharge - Flow Kinetics: The $H + ClF_3$ Reaction," J. Chem. Phys. $\underline{62}$, 3419 (1975).

10. Kaufman, M. and Kolb, C.E., "Molecular Beam Analysis of the Reaction Between Atomic Fluorine and Carbon Tetrachloride," NR 092-531, 8 (1971).

11. Berg, H.C. and Kleppner, D., "Storage Technique for Atomic Hydrogen," Rev. Sci. Instrum. $\underline{33}$, 248 (1962).

12. Lewis, P.F. and Green, B.D., "Computation of Electronic Spectra of Diatomic Molecules," PSI TR-413 (1984).

13. Setser, D.W., Stedman, D.H. and Coxon, J.A., "Chemical Applications of Metastable Argon Atoms. IV. Excitation and Relaxation of Triplet States of N_2," J. Chem. Phys. $\underline{53}$, 1004 (1970).

REFERENCES (Continued)

14. Stedman, D.H. and Setser, D.W., "Chemical Applications of Metastable Argon Atoms II. A Clean System for the Formation of $N_2(A\ ^3\Sigma_u^+)$," Chem. Phys. Lett. 2, 542 (1968).

15. Sadeghi, N. and Setser, D.W., "Primary $N_2(B)$ Vibrational Distributions from Excitation-Transfer Reactions Between $Kr(^3P_2)$ or $Xe(^3P_2)$ Atoms and N_2," Chem. Phys. Lett. 82, 44 (1981).

16. Thomas, J.M. and Kaufman, F., "Production and Kinetics of $N_2(A\ ^3\Sigma_u^+, v<3)$," Photochemistry Symposium, Harvard University, August (1984).

17. Golde, M.F., "Vacuum UV Emission by Electronically Excited N_2: The Collisional-Induced $N_2(a\ ^1\Pi_g\ v\approx 0)\ \sim\ N_2(a'\ ^1\Sigma_u^-,\ v'\approx 0)$ Transition," Chem. Phys. Lett. 31, 348 (1975).

18. Thomas, J.M., Jeffries, J.B. and Kaufman, F., "Vibrational Relaxation of $N_2(A\ ^3\Sigma_u^+, v'=1,2,3)$ by CH_4 and CF_4," Chem. Phys. Lett. 102, 50 (1983).

19. Piper, L.G., Marinelli, W.J., Green, B.D., Rawlins, W.T., Murphy, H.C., Donahue, M.E. and Lewis, P.F., "Kinetics of Iodine Monofluoride Excitation by Energitic Nitrogen," PSI-TR-051/460 prepared under Air Force Weapons Laboratories Contract # F29601-82-C-0051 (1984).

20. Robinson, D. and Nicholls, R.W., "Intensity Measurements on the O_2^+ Second Negative, CO Ångström and Third Positive an NO γ and β Molecular Band Systems," Proceedings of the Physical Society LXXI, 957 (1958).

21. Keck, J.C., Allen, R.A. and Taylor, R.L., "Electronic Transition Moments for Air Molecules," J. Quant. Spectrosc. Radiat. Transfer 3, 335 (1963).

22. Callear, A.B., Pilling M.J. and Smith, I.W.M., Trans, Faraday Soc. 62, 2997 (1966).

23. Bubert, H., "Population and Predissociation of Vibronic States of Nitric Oxide," J. Chem. Phys. 56, 1113 (1972).

24. Brzozowski, J., Erman, P. and Lyyra, M., "Predissociation Rates and Perturbations of the A, B, B', C, D and F States in NO Studied Using Time Resolved Spectroscopy," Physica Scripta 14, 290 (1976).

25. Kuz'menko, N.E., Kuznetsova, L.A., Monyakin, A.P. and Kuzyakov, Yu. Ya., "Probabilities for Electronic Transitions of Molecular Systems of High-Temperature Air Components--II. The γ and β Systems of NO and the (4+) System of CO," J. Quant. Spectrosc. Radiat. Transfer 24, 219 (1980).

END

DATE
FILMED

11-86

DTIC